Berliner Elektronenspeicherring-Gesellschaft
für Synchrotronstrahlung mbH

B E S S Y

A n n u a l   R e p o r t   2 0 0 1

Introduction

2001 was a year of many changes and new developments at BESSY. The annual report, now called "BESSY Highlights 2001", your are holding in your hands has a new look. This new format intends to reflect the full spectrum of science at BESSY including new developments of accelerator and experimental stations. The "good old" annual report is now published on compact disc.

In May 2001, Prof. Wolfgang Gudat handed over the position as director of science to Prof. Wolfgang Eberhardt, who will keep on developing BESSY's scientific profile and future. The accelerator of BESSY II shows an excellent performance, improving the life time of the electron beam at 200 mA to 10 h. In the past year, nearly 3900 h total user operation time has been achieved in three shift seven days a week operation mode and more than 160 projects were carried out.

At present, 36 beamlines are in operation. Among the beamlines put into operation in 2001 is a newly designed plane grating monochromator beamline of the Russian-German Laboratory, a joint venture of the University of St. Petersburg, the Freie Universität Berlin and BESSY. The inauguration was accompanied by the "Third Russian-German Workshop" on Synchrotron Radiation Research. By the end of the year, the new Infrared beamline run by the IR-Initiative Synchrotron radiation (IRIS) was operational, opening a whole new wavelength range for BESSY users.

The Application Center for Microtechniques started operation in November 2001. This is a cooperation with the Technical University Berlin, dedicated for applied research in lithography, enabeling developments for industry and small and medium sized companies.

Also, the conventional facilities of BESSY are expanding. The new wing of the building on Albert-Einstein-Straße has been inaugurated with a ceremony on October 4th 2001. It includes a lecture hall for 150 people and a library, improving the scientific communication on site as well as 1000 m^2 of additional office and laboratory area increased the space capacity for the growing BESSY crew. Another 1000 m^2 are dedicated to the Hahn-Meitner-Institute (HMI) including laboratory installations and office spaces, intensifying the BESSY-HMI collaboration.

"Visions of Science: The BESSY-FEL in Berlin-Adlershof" describes the technological challenges and the enthusiasm about the scientific opportunities of the planned free electron laser (FEL) (see CD). In context with this documentation of the "Scientific Case", a short description of the project "Development and Construction of a Free Electron Laser (SASE-FEL) in Berlin-Adlershof" was submitted and successfully presented to the Wissenschaftsrat on October 25th and 26th 2001. A statement by the

Wissenschaftsrat is expected by mid 2002. The importance of the FEL project is also recognised by the Berlin Senate, supporting the technical design study by the Zukunftsfonds for three years.

The BESSY Users' Meeting, traditionally held beginning of December, with more than 300 participants, also had a focus on the perspectives of the planned BESSY-FEL. The annual "Ernst-Eckhardt-Koch" Prize for the outstanding doctoral thesis was awarded to Dr. Karin Heister (University Heidelberg). For the first time the BESSY innovation prize, also funded by the VDFFB, was donated to Dr. Rolf Follath and Dr. Friedmar Senf (both BESSY).

A look behind the scenes of BESSY attracted more than 3800 visitors during the first "Lange Nacht der Wissenschaften" in Berlin. Additionally, more than 70 national and international groups visited BESSY in 2001. The importance of BESSY for the WISTA and greater area of Berlin concerning science and technological development was also expressed by the visits of high ranking persons like the Klaus Wowereit, (Governing Mayor of Berlin), Adrienne Goehler (Berlin Senator of science, research and culture), Werner Müller (Federal Minister of Economy), and Hans-Olaf Henkel, the new president of Wissenschaftsgemeinschaft Gottfried-Wilhelm-Leibniz.

The facility BESSY II is one of the most modern and efficient synchrotron radiation sources world wide, which is only possible due to the great dedication of all people involved. We want to thank the entire BESSY staff and all BESSY users for their commitment and the members of our various committees and the funding agencies for their support.

The BESSY Board of Directors   Berlin, February 2002

High-accuracy detector calibration for EUV metrology

F. Scholze, G. Brandt, P. Müller, B. Meyer, F. Scholz, J. Tümmler, K. Vogel, and G. Ulm.

Physikalisch-Technische Bundesanstalt, Abbestraße 2-12, 10587 Berlin, Germany

With the development of EUV-lithography, high-accuracy at-wavelength metrology has increasingly gained in importance. Characterization of detectors and sources using synchrotron radiation has been performed by the Physikalisch-Technische Bundesanstalt (PTB) for almost 20 years[1,2]. At their laboratory at BESSY II [3], PTB now has set up instrumentation which is suitable for high-accuracy EUV detector calibration. The detector calibration at PTB uses a cryogenic electrical substitution radiometer (ESR) as the primary detector standard [4]. The operating principle of an ESR is that an absorber transforms the incident radiant power into a heat flow directed through a heat link to a heat sink kept at constant temperature. In our case, the ESR is operated in the dynamic substitution mode, i.e. the absorber temperature is also kept constant, and the radiant power equals the change in the electrical heater power required for keeping the absorber temperature at a constant value when the radiation shutter is opened, see figure 1. First results of the application of this technique to the EUV spectral range were achieved at BESSY I about six years ago [5,6,7]. As compared to the previous operation, the electrical power fluctuations could now be reduced from 2.5 nW [4] to about 500 pW. This allowed us to perform high-accuracy detector calibrations down to 50 eV at the soft X-ray radiometry beamline at BESSY II.

The response of a detector to be calibrated and that of the ESR to monochromatized radiation are compared. This method requires that the higher order and stray light contribution be as small as possible since the spectral response of the ESR and the detector to be calibrated normally are different. Moreover, to avoid the use of monitor detectors, which would give rise to additional uncertainties, it is desirable for the photon flux at the beamline output to depend linearly on the electron beam current. Then the photon flux can be normalized to the stored beam current. The high stability of the normalized radiant power and the low contributions of higher diffraction orders and diffusely scattered light at the soft X-ray radiometry beamline have already been shown as a prerequisite for high-accuracy reflectometry [8]. The relative standard uncertainty for the measurement of a radiant power of 0.2 µW with the ESR is 0.11% and the spectral responsivity of a photodiode in the EUV spectral range is measured with a relative uncertainty of 0.28%, for details see reference [9].
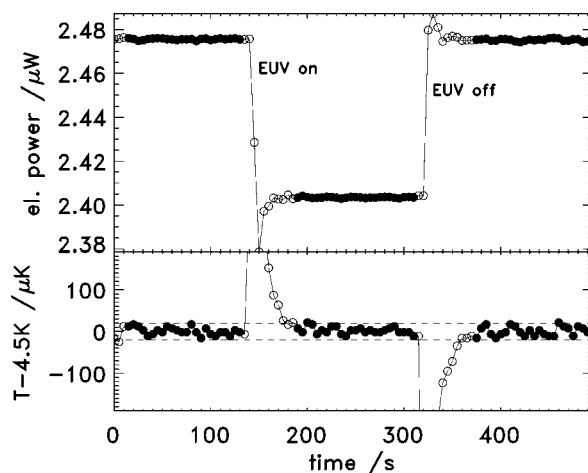
Figure 1 Radiant power measurement using the ESR. In the upper part the electrical heating power of the absorber is shown while the lower part shows the actual absorber temperature. After switching the EUV radiation on/off the control circuit takes about 50 s to settle; after this time the temperature returns to the set value of 4.5 K.

The temperature noise is 10 µK (1 σ). The corresponding standard deviation of the electrical power is about 500 pW. The difference in the heating power, which corresponds in the case shown here to a radiant power of only 80 nW, can be determined with a statistical uncertainty of 100 pW by averaging over all points (shown as solid circles) in which the temperature is at the value set.

(a)

(a)

(b)

(b)
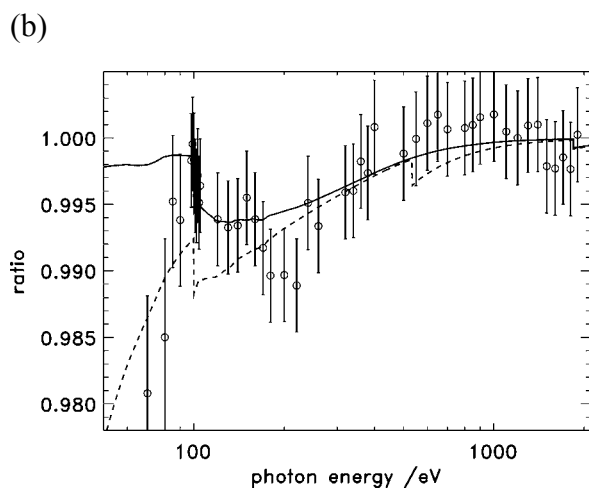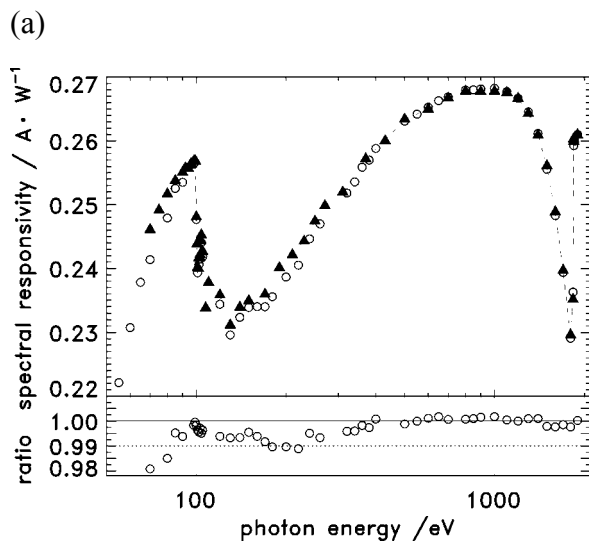
Figure 2 Spectral responsivity of an AXUV100G photodiode. Part (a) shows two measurements using a cryogenic ESR. The time between measurements was five months and the diode was stored in dry air and was not used for measurements. In the lower part of the figure, the ratio of the second measurement (open circles) to the first one (solid triangles) is shown. In the photon energy range above 400 eV, the measurements coincide well within the uncertainty of 0.25%.
Part (b) shows the ratio from part (a) and two models. The solid line is calculated assuming a decrease from 88.2% to 87.5% in collection efficiency directly beneath the front oxide interface. The dashed line additionally covers the absorption of by an oxygen layer of 91 ng/cm².
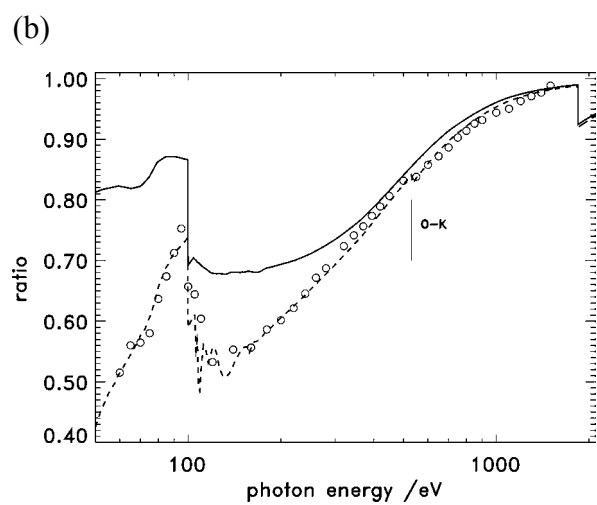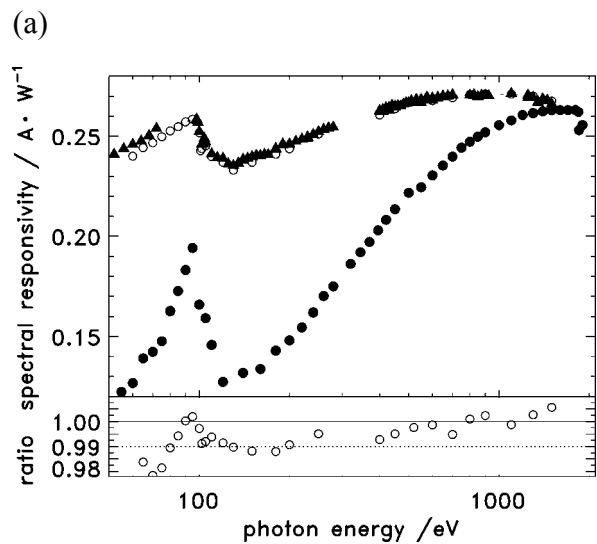
Figure 3 Spectral responsivity of an AXUV100G photodiode. Part (a) shows measurements of 1995 (triangles), 1997 (open circles), and 2001 (solid circles). Between the first two measurements, the diode was stored in dry air and used only occasionally in ultra high vacuum at moderate irradiance levels below 1 μW/cm². In the lower part of the figure, the ratio of the first two measurements is shown.
Part (b): ratio of first and last measurement (open circles). The solid line is calculated assuming a decrease from 91.5% to 60% in collection efficiency directly beneath the front oxide interface and a simultaneous increase from 150 nm to 370 nm in thickness of the incomplete charge collection layer. The dashed line additionally covers the absorption by a silicon oxide layer of 20 nm in thickness.

The soft X-ray radiometry beamline was used for the calibration of photodiodes with reference to the ESR in the spectral range from 50 eV to 1900 eV. Starting with the measurements at BESSY I, the responsivity of individual photodiodes has been observed over a period of up to six years. Our results on the long-term stability of AXUV photodiodes which are widely assumed to be stable in the EUV spectral range [10,11] are of sufficient accuracy to show that even diodes which are rarely used and carefully stored, degrade. After a period of

three years, the degradation becomes ever stronger. The typical behaviour is summarized in figures 2 and 3.

First, results from two calibrations performed at BESSY II within only five months are shown in figure 2. The measurements agree within 1% for nearly all but the lowest photon energies. A close view at the ratio reveals, however, that the differences are of a systematic nature. The responsivity decreased by about 1% relative in the range between 100 eV and 300 eV and also significantly below 90 eV. Assuming only a decrease in collection efficiency directly beneath the front oxide interface would not explain the drop in responsivity below 100 eV. In addition, oxidation must have occurred, see model calculations in figure 2 (b).

There is one diode which could be used all the time from 1995 to 2001. Calibration data for that diode from 1995, 1997 and 2001 are summarized in figure 3. During the first interval, the diode was stored in dry air and used only occasionally in ultra high vacuum at moderate irradiance levels (below 1 µW/mm²). The two calibration curves for the spectral sensitivity are nearly identical. A close view at the ratio reveals, however, the same systematic differences as discussed above. Here too, oxidation must have occurred. Later on that diode was used during the installation of the new laboratory at BESSY II for radiant power measurements at the newly installed soft X-ray beamlines, and during these measurements it was exposed to higher irradiance levels of several µW/mm². It was observed during these measurements that the diode became unstable and inhomogeneous. The result of a final calibration in 2001 is also shown in figure 3. Now the responsivity dropped by about 50% in some regions of the spectrum and a rather significant oxidation can be concluded from the spectral slope.

References

1   B. Wende, "Radiometry with synchrotron radiation," Metrologia **32**, 419-424 (1996)

2   G. Ulm, and B. Wende, "Radiometry laboratory of Physikalisch-Technische Bundesanstalt at BESSY," Rev. Sci. Instrum. **66**, 2244-2247 (1995)

3   G. Ulm, B. Beckhoff, R. Klein, M. Krumrey, H. Rabus, and R. Thornagel, "The PTB radiometry laboratory at the BESSY II electron storage ring," Proc. SPIE **3444**, 610-621 (1998)

4   H. Rabus, V. Persch, and G. Ulm, "Synchrotron-Radiation Operated Cryogenic Electrical-Substitution Radiometer as High-Accuracy Primary Detector Standard in the Ultraviolet, Vacuum Ultraviolet and Soft X-Ray Spectral Ranges," Appl. Optics **36**, 5421-5440 (1997)

5   H. Rabus, F. Scholze, R. Thornagel, and G. Ulm, "Detector calibration at the PTB radiometry laboratory at BESSY," Nucl. Instr. and Meth. **A377**, 209-216 (1996)

6   F. Scholze, H. Rabus, G. Ulm, "Spectral responsivity of silicon photodiodes: High-accuracy measurements and improved self calibration in the soft X-ray spectral range," Proc. SPIE **2808**, 534-543 (1996)

7   F. Scholze, H. Rabus, and G. Ulm, "Mean energy required to produce an electron-hole pair in silicon for photons of energies between 50 and 1500 eV," J. Appl. Phys. **84,** 2926-2939 (1998)

8   F. Scholze, B. Beckhoff, G. Brandt, R. Fliegauf, A. Gottwald, R. Klein, B. Meyer, U. Schwarz, R. Thornagel, J. Tümmler, K. Vogel, J. Weser, and G. Ulm, "High-Accuracy EUV Metrology of PTB Using Synchrotron Radiation," Proc. SPIE **4344**, 402–413 (2001)

9   F. Scholze, G. Brandt, P. Müller, B. Meyer, F. Scholz, J. Tümmler, K. Vogel, and G. Ulm, "High-accuracy detector calibration for EUV metrology," to appear in Proc. SPIE **4688** (2002)

10   E.M. Gullikson, R. Korde, L.R. Canfield, and R.E. Vest, "Stable silicon photodiodes for absolute intensity measurements in the VUV and soft X-ray regions," J. Electron Spectrosc. Rel. Phenom. **80**, 313-316 (1996)

11   R. Korde, J.S. Cable, and L.R. Canfield, "One gigarad passivating nitrided oxides for 100% internal quantum efficiency silicon photodiodes," IEEE Trans. Nucl. Sci. **40**, 1655-1659 (1993)

Detector calibration at the BAM*line*

M. Krumrey, U. Linke, G. Ulm

Physikalisch-Technische Bundesanstalt, Abbestraße 2-12, 10587 Berlin, Germany

The Bundesanstalt für Materialforschung und -prüfung (BAM) and the Physikalisch-Technische Bundesanstalt (PTB) are jointly operating the BAM*line* [1]. The PTB is using this beamline mainly for radiometric applications in the photon energy range above 8 keV. In the year 2001, several X-ray detectors have been characterized and calibrated.

Energy-dispersive detectors can be calibrated by direct irradiation with the calculable spectral photon flux from the wavelength shifter (WLS). To access the hard X-ray range, low energy photons, otherwise dominating the spectrum, have to be suppressed by filters. The filter transmittance is measured separately at the same beamline with monochromatic radiation. Fig. 1 shows measured and calculated spectra for HPGe detector. As the detector operates in the photon counting mode, the stored electron current of BESSY II has to be reduced from typically 200 mA to 25 pA.
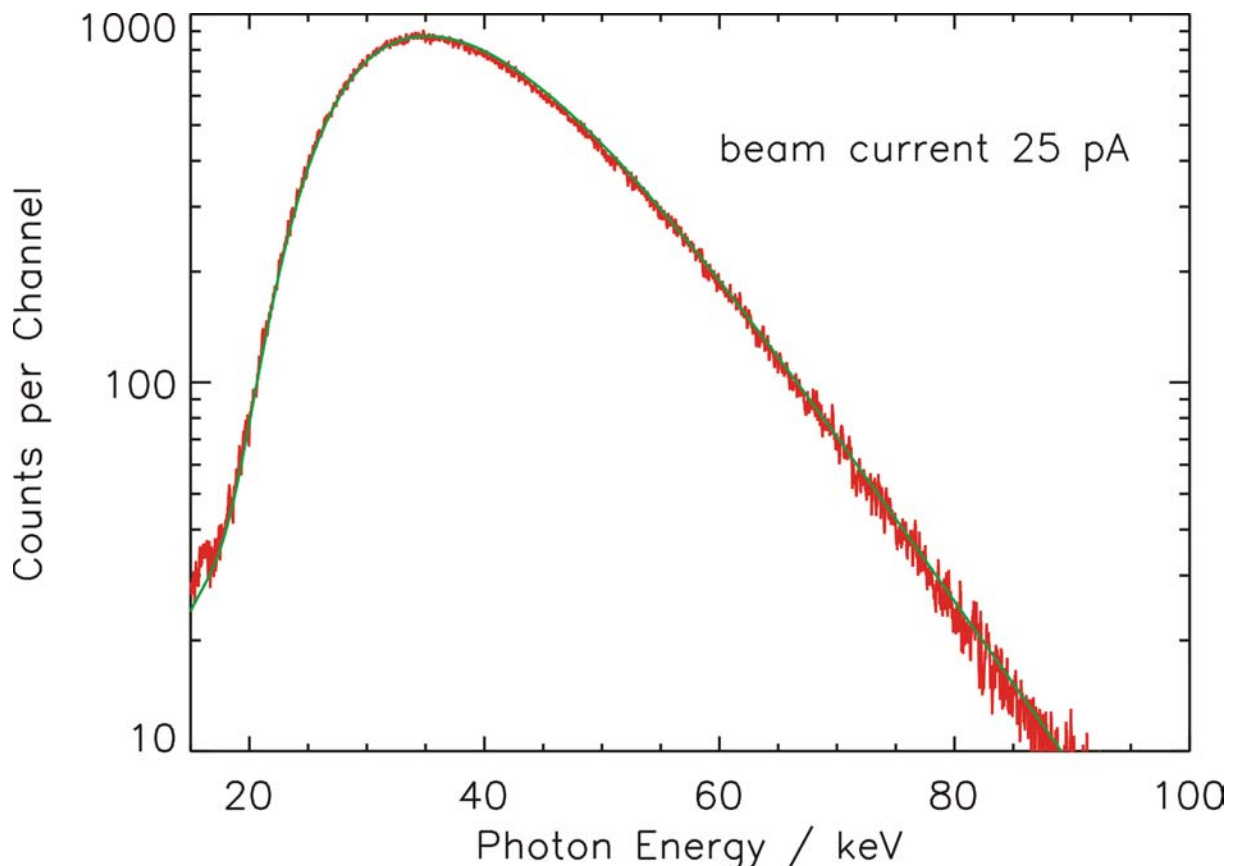
Figure 1: Calculated and measured spectrum of a HPGe detector in undispersed WLS radiation behind a 1 mm Al filter and a 0.145 mm Cu filter

For the calibration of non energy-dispersive detectors like semiconductor photodiodes, monochromatic radiation of high spectral purity and a primary detector standard are required.

Fig. 2 shows the spectral responsivity of two different semiconductor photodiodes, calibrated at three different beamlines in the photon energy range from 60 eV to 60 keV. While the calibration at the SX 700 [2] and the FCM [3] beamlines in the PTB laboratory was performed against a cryogenic electrical substitution radiometer [4], a free-air ionization chamber [5] of the PTB department for dosimetry has been used at the double-crystal monochromator of the BAM*line* as primary detector standard.
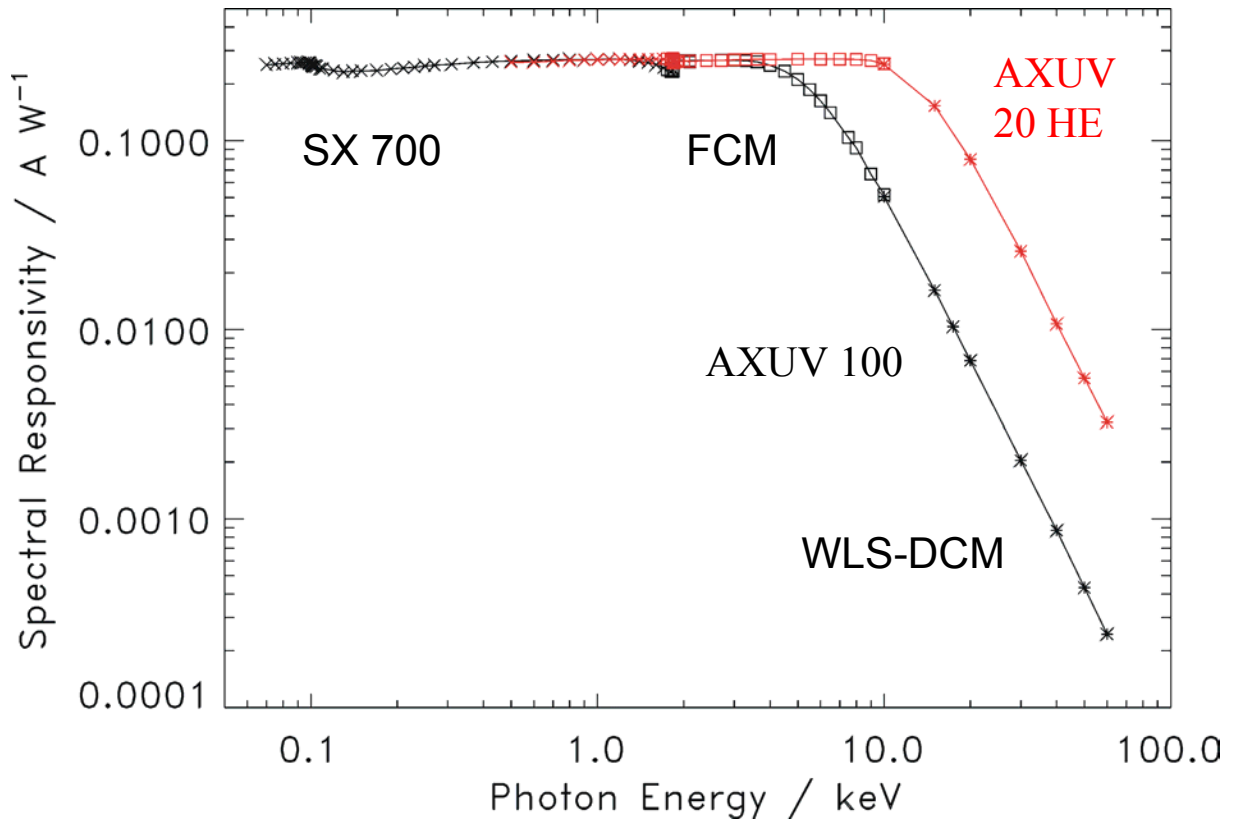
Figure 2: Spectral responsivity of two semiconductor photodiodes: IRD AXUV 100 (black) and IRD AXUV 20 HE (red), determined at three different monochromators: SX 700 (x), FCM (ɘ) and WLS-DCM (∗), by comparison to two different PTB primary detector standards: cryogenic radiometer (below 10 keV) and free-air ionization chamber (above 9 keV).

In the overlapping spectral regions of different monochromators and primary detectors, the obtained spectral responsivities agree within 1.5 %. The different behaviour of the diodes at high energies is due to a very different thickness of the sensitive layer.

References
[1]   W. Görner, M.P. Hentschel, B.R. Müller, H. Riesemeier, M. Krumrey, G. Ulm, W. Diete,
       U. Klein and R. Frahm, Nucl. Instr. and Meth. **A 467-468**, 703-706 (2001)
[2]   F. Scholze. B. Beckhoff, G. Brandt, R. Fliegauf, A. Gottwald, R. Klein, B. Meyer, U. Schwarz,
       R. Thornagel, J. Tümmler, K. Vogel, J. Weser and G. Ulm, Proc. SPIE **4344**, 402-413 (2001)
[3]   M. Krumrey and G. Ulm, Nucl. Instr. and Meth. **A 467-468**, 1175-1178 (2001)
[4]   H. Rabus, V. Persch and G. Ulm, Appl. Opt. **36**, 5421-5440 (1997)
[5]   B.-A. Engelke, W. Oetzmann und G. Struppek, PTB-Report Dos-16, Braunschweig (1988)

EUV Optics characterization at the soft x-ray radiometry beamline

J. Tümmler[a], **F. Scholze**[a], **G. Brandt**[a], **B. Meyer**[a], **F. Scholz**[a],
K. Vogel[a], **G. Ulm**[a], **M. Poier**[b], **U. Klein**[b], **and W. Diete**[b]

[a] Physikalisch-Technische Bundesanstalt, Abbestraße 2-12, 10587 Berlin, Germany
[b] ACCEL Instruments GmbH, Friedrich-Ebert-Straße 1, 51429 Bergisch Gladbach, Germany

Since EUVL is one of the most promising candidates for the next-generation lithography, the manufacture of large EUV optical elements has been planned with a surface finish never achieved before. To get accurate information about the at-wavelength performance of such optical elements new measuring tools are necessary. Therefore, PTB has built a new reflectometer which allows mirrors with a diameter as large as 550 mm, a height of 230 mm, and a weight of up to 50 kg to be investigated. Grazing incidence mirrors with dimensions up to 1000 mm by 150 mm and a height of 230 mm can also be characterized. With this new reflectometer system, PTB will be able to characterize the largest samples in the EUV spectral region worldwide. The reflectometer will be set up at the soft X-ray radiometry beamline in PTB's synchrotron radiation laboratory[1] at BESSY II in March 2002.

The sample stage of the new reflectometer system is placed inside a vacuum chamber. The complete sample stage is motor-operated in vacuum. The sample can be translated in the x, y, and z directions (for orientation see Fig. 1). The incident and reflection angle can be adjusted via θ and 2θ, for the sample and the detector, respectively. The incident angle can be smaller than 1° before the detector blocks the incoming beam. The $\theta\,/\,2\theta$ axis is parallel to the electric field vector of the linear polarized
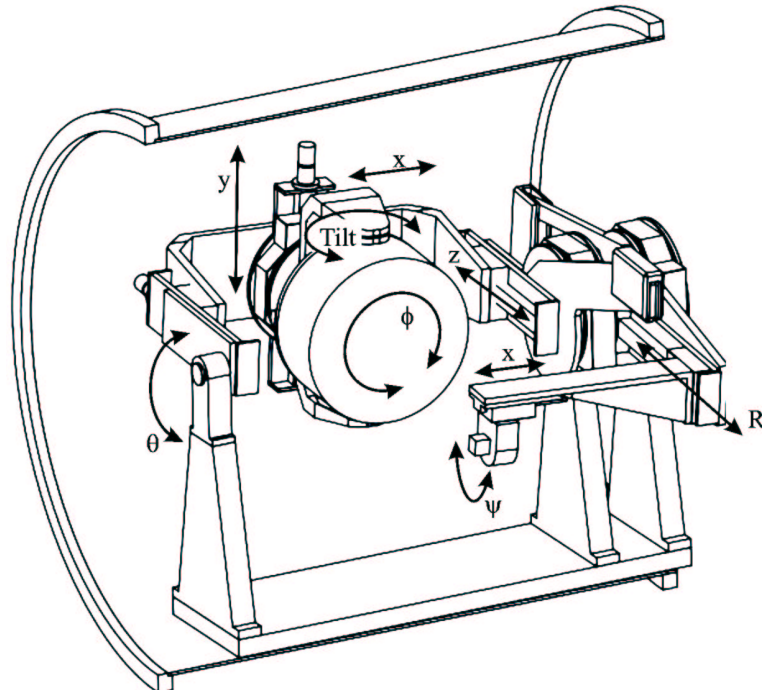
Figure 1. Sketch of the reflectometer system showing all degrees of freedom

	Axis	Range	Accuracy
Sample	x	180 mm	10 μm
	y	310 mm	10 μm
	z	155 mm	10 μm
	ϕ	360°	0.01°
	tilt	20°	0.01°
	θ	125°	0.01°
Detector	2θ	195°	0.01°
	x	120 mm	10 μm
	R	700 mm	100 μm
	ψ	180°	0.01°

**Table 1.** Degrees of freedom with the maximum moving range and the positioning accuracy

synchrotron radiation beam, which is in the horizontal plane. To align the sample and to account for a curved sample surface, tilting about the y-axis is possible. A rotation around the surface normal (ϕ axis) allows a raster scan to be performed in spherical coordinates. With movements in ϕ and y, every point of the sample surface can be positioned into the photon beam. The additional x axis allows to raster the surface of smaller samples in cartesian coordinates, which is a necessary feature for the measurement of e.g. gratings or grazing incidence mirrors.

In addition to the 2θ movement, the detector can be moved in x direction for the measurement of bi-directional scattering. Furthermore, the distance between sample surface and detector can be varied to account for a different beam divergence when reflected from a curved surface. For reference measurements of the direct beam, the detector can be rotated around ψ axis by 180°. This avoids large movements of the sample and the detector.

For stray light suppression a cross slit entrance aperture is installed at the focal plane of the toroidal pre-mirror of our beam-line. This is at a distance of about 0.5 m from the sample surface. The cross slits are fully motor-operated and can be opened in steps of 1 μm.

A summary of all possible movements is given in Tab. 1. A sketch of the reflectometer with all possible degrees of freedom is shown in Fig. 1. The design and manufacture of the reflectometer system was carried out by ACCEL Instruments, Bergisch-Gladbach, Germany. Due to practical weight restrictions it was not possible to strengthen the mechanical drives to a stability of better than 10 μm. Especially a θ-rotation may result in a displacement of the sample by a few ten to a few hundred micrometres. As a solution the mechanical displacement was measured for different sample masses and sample positions. The computer control accounts for the displacement to guarantee an accuracy in the sample position better than 10 μm. The absolute accuracy in the re-positioning of a sample after complete dismounting and remounting on the sample stage should be better than 1 mm.

The large sample weight calls for a handling robot to place the samples into the measuring chamber. The sample is held by a sample holder fitting exactly onto the sample stage inside the reflectometer chamber. The holder is transferred into the reflectometer chamber by a robot. A taper key ensures that the sample holder is centered onto the stage. During the mounting of the sample, the complete front of the reflectometer chamber is opened. A clean room in the front of the reflectometer avoids contamination with dust particles. It allows working conditions of class 1000 or better. In the clean room the samples are unpacked and mounted onto the sample holder. Fig. 2 is a top view of the reflectometer with clean room and robot.
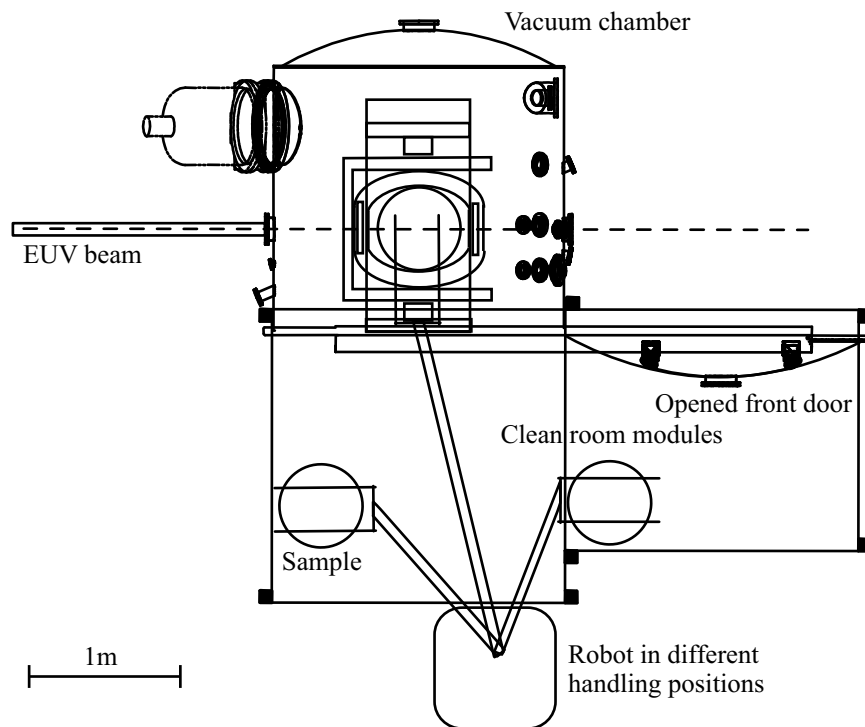
Figure 2. Top view of the reflectometer with attached clean room and handling robot.

The reflectance measurement must be performed in vacuum. A set of four dry compressing vacuum pumps (4 x $48\,\mathrm{m^3/h}$), a turbo pump ($680\,\mathrm{l/s}$ N_2), and a cryo pump ($10000\,\mathrm{l/s}$ N_2) work to evacuate the reflectometer chamber. To prevent the risk of suffocation for the operator, the system is vented with clean and dry air instead of pure N_2.

Due to the missing load lock the sample change will take longer than with the present reflectometer system. The large scanning range, however, allows not only one large sample to be measured but also up to 200 1" samples to be mounted. Therefore, the increased time for a sample change is acceptable compared to the measuring time.

ACKNOWLEDGMENTS

REFERENCES

1. F. Scholze, B. Beckhoff, G. Brandt, R. Fliegauf, A. Gottwald, R. Klein, B. Meyer, U. Schwarz, R. Thornagel, J. Tümmler, K. Vogel, J. Weser, and G. Ulm, "High-accuracy EUV metrology of PTB using synchrotron radiation," *Proc. SPIE* **4344**, pp. 402 – 413, 2001.

Metrology for pulsed VUV radiation

M. Richter, A. Gottwald, U. Kroth, A.A. Sorokin

Physikalisch-Technische Bundesanstalt, Abbestr. 2-12, 10587 Berlin, Germany

I. Tassy, K. Vogler

Lambda Physik AG, Hans-Böckler-Str. 12, 37079 Göttingen, Germany

J. Feldhaus, Ch. Gerth, K. Tiedtke

Deutsches Elektronen-Synchrotron (DESY), Notkestr. 85, 22603 Hamburg, Germany

For a growing number of applications, namely microlithography, radiation in the spectral range of the VUV more and more moves into the centre of interest. High-intense sources, like commercial F_2 lasers or free electron lasers (FEL), emit radiation with strongly pulsed character, in contrast to synchrotron radiation which may be regarded to be almost cw. In this context, there is an urgent need for photodetectors which allow for single-pulse measurements of pulsed VUV radiation. They must be stable and linear and should be suitable for metrology in absolute terms.
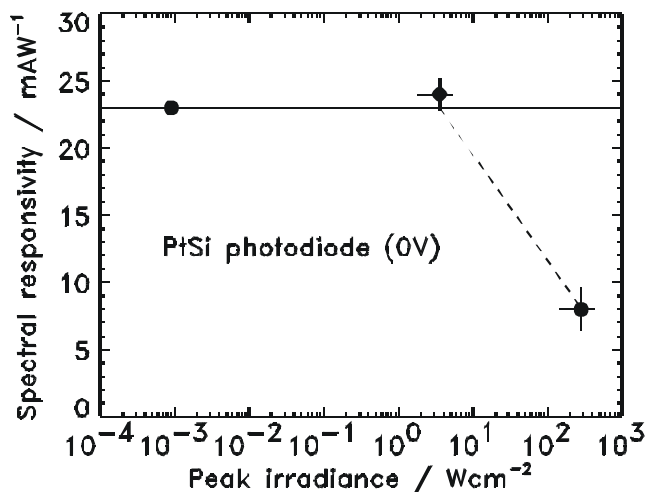

FIG. 1. Spectral responsivity of an ETH-PtSi100 standard detector measured without bias voltage at a wavelength of 157 nm as a function of the peak irradiance, using spectrally dispersed synchrotron radiation and F_2-laser radiation.

Stability measurements on different types of semiconductor photodetectors had been performed in the past by exposure to F_2 laser radiation at a wavelength of 157 nm with total doses up to 350 kJ cm^{-2} between initial calibration and final re-calibration of the detectors using spectrally dispersed synchrotron radiation at the normal-incidence monochromator beamline of PTB at BESSY II [1,2]. Recently, we investigated the linearity of semiconductor photodiodes by determining the spectral responsivity at 157 nm as a function of the peak irradiance. While spectrally dispersed synchrotron radiation was applied on the low-level side, a F_2 laser was used for the high irradiance levels. Fig. 1 shows a corresponding result for a PtSi-nSi Schottky type photodiode (ETH-PtSi100) [3]. The applied peak irradiance was calculated by:

$$peak\ irradiance\ =\ \frac{average\ radiant\ power}{pulse\ frequency\ \times\ pulse\ duration\ \times\ irradiated\ area}$$

Obviously, up to a peak irradiance of 4 W cm^{-2}, the photodiode shows a linear behaviour within the combined uncertainties, whereas saturation occurs somewhere above this level. At a peak irradiance of 200 W cm^{-2}, the spectral responsivity is decreased to about 35% of the initial value.

The result for the linearity was obtained by operating the diode in the short-circuit mode without application of any bias voltage. However, single-pulse readout implies a corresponding current to voltage conversion by a pre-amplifier, and application of a few volts in a high-resistance direction of the photodiode. In this case, it is expected that the linear regime of the photodiode is extended to even higher peak irradiance values, because saturation effects are caused by incomplete charge separation and transfer within the photodiode due to a break-down of the internal electrical field. This occurs when a large number of charges is generated at high photon intensity. An external bias voltage may support the internal electrical field and prevent saturation.

However, a bias voltage also influences the spectral responsivity even in the linear regime as can be seen in Fig. 2. An ETH-PtSi100 photodiode was operated by application of -15 V bias voltage in high-resistance direction and the negative electron current was measured. The upper curve shows the signal normalised to the non-biased case shown at the bottom part of Fig. 2. The observed gain in spectral responsivity of about 30 % in the wavelength regime above 70 nm may be explained by a better charge separation within the PtSi-nSi interface region where recombination losses for this type of
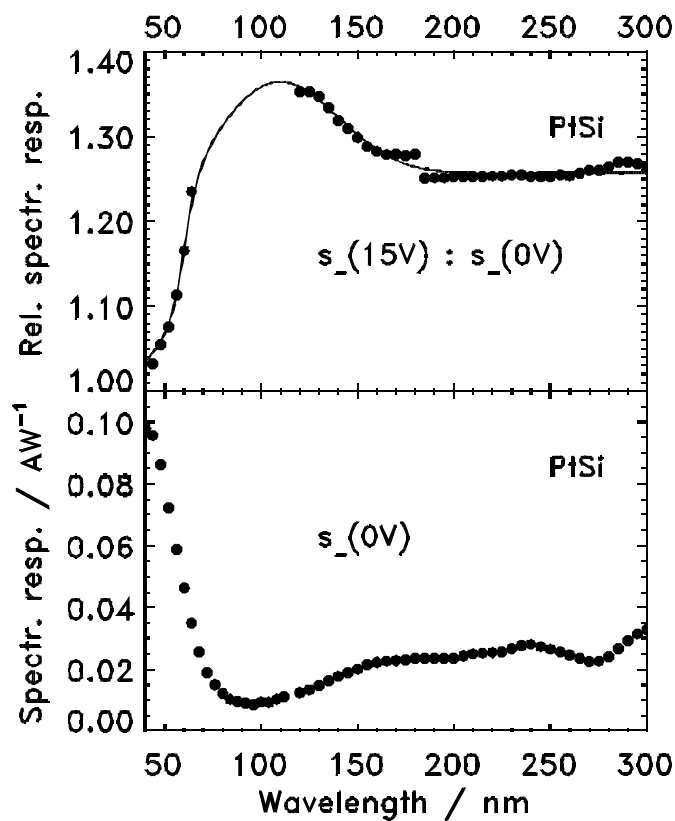

FIG.2. Top: Spectral responsivity of a ETH-PtSi100 photodiode with a bias voltage of -15 V applied, normalised to the spectral responsivity without bias voltage (bottom).

photodiode are known to be considerably high [4]. Below 70 nm, due to the increase of the photoabsorption length in silicon, charge generation within the interface region becomes less important. Hence, the spectral responsivity without bias voltage strongly increases (bottom part of Fig. 2.) and the observed gain effect by application of a bias voltage becomes almost negligible below 50 nm.

However, radiation as emitted from a VUV free electron laser, like the recently installed TTF-FEL at DESY, has an even stronger pulsed character than F_2-laser radiation [5]. At saturation of the FEL, up to about 10^{14} photons are concentrated within a pulse of 100 fs in duration. For metrology of FEL radiation, due to these ra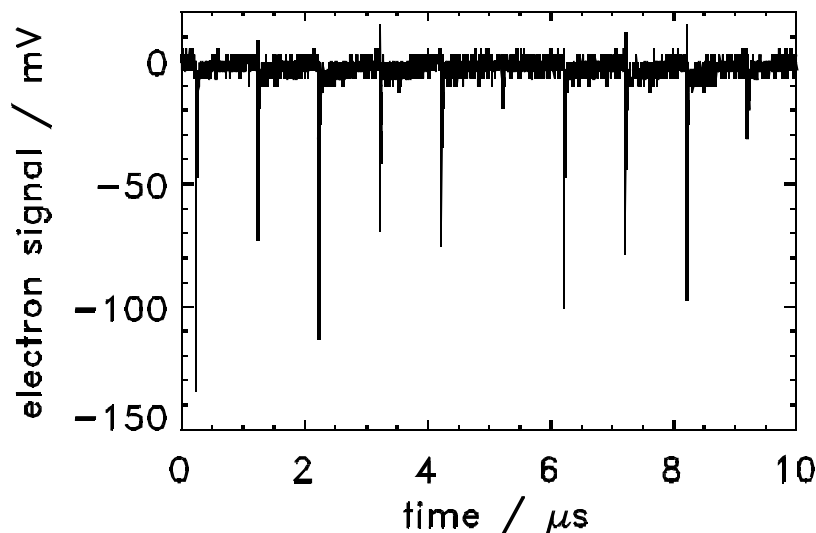ther extreme values, direct measurements with photodiodes would saturate or even destroy these devices. On the other hand, a reliable FEL detector should have an extended dynamic range of high linearity to allow also for calibration of the device at low photon intensity using spectrally dispersed synchrotron radiation with about 10^2 photons within a pulse duration of 30 ps only. First promising results from a recently developed gas-monitor detector based on atomic photoionisation at low target density were obtained at the TTF-FEL at DESY at the end of 2001. Fig. 3 shows an example for a pulse measurement at a wavelength of 87 nm about one order of magnitude below saturation of the FEL. Single pulse readout was realised by photoelectron detection. Limits of the detector are mainly defined by the linearity of the atomic photoionisation process itself and will be studied in detail during phase 2 of the TTF-FEL project.

FIG.3. Electron signal of VUV radiation at 87 nm from a bunch train filled with 10 bunches as measured at the TTF-FEL at DESY with a recently developed gas-monitor detector.

Our investigations in the field of metrology for pulsed VUV radiation will be continued in close co-operation between PTB, the Ioffe-Institute St. Petersburg (S.V. Bobashev), DESY, and industry funded by the German Minister of Education and Research (BMBF) and the Deutsche Forschungsgemeinschaft (DFG).

[1] M. Richter, J. Hollandt, U. Kroth, W. Paustian, H. Rabus, R. Thornagel, G. Ulm, Nucl. Instr. and Meth. **467-468**, 605-608 (2001)

[2] M. Richter, U. Kroth, K. Vogler, E. Bergmann, BESSY Annual Report 2000, 70 (2001)

[3] K. Solt, H. Melchior, U. Kroth, P. Kuschnerus, V. Persch, H. Rabus, M. Richter, G. Ulm, Appl. Phys. Lett. **69**, 3662-3665 (1996)

[4] P. Kuschnerus, PhD Thesis, Technische Universität Berlin, Verlag Dr. Köster, Berlin 2000, ISBN 3-89574-373-9

[5] R. Treusch, Ch. Gerth, T. Lokajczyk, J. Feldhaus, Nucl. Instr. and Meth. A **467-468**, 30 (2001)

Calibration of Lyman-**a** detectors for the NASA satellites TWINS

M. Richter, U. Kroth, R. Thornagel

Physikalisch-Technische Bundesanstalt, Abbestraße 2-12, 10587 Berlin, Germany

H.J. Fahr, G. Lay, H.U. Naß

Institut für Astrophysik und Extraterrestrische Forschung, Rheinische Friedrich-Wilhelms-Universität Bonn, Auf dem Hügel 71, 53121 Bonn, Germany

Photon counting devices like photomultiplier tubes (PMT) or microchannel plate (MCP) detectors equipped with specific photocathode materials are widely used for many years as highly sensitive detectors in the spectral range of UV and VUV radiation. In particular, they are often part of telescope systems or other space-based instruments to investigate solar or extraterrestric radiation. However, accurate calibration of such detectors is not easy to carry out because primary detector standards established like cryogenic radiometers [1] in general are many orders of magnitude less sensitive.

At the former storage ring BESSY I, the Physikalisch-Technische Bundesanstalt (PTB) had established a procedure to transfer the absolute spectral responsivity scale of photodetectors in the UV and VUV from the radiant power range around 1 µW to the (sub-)pW regime [2]. The method profits from PTB's capability to operate the electron storage rings BESSY I and now BESSY II as a primary source standard [3]. The latter requires, among others, the stored electron current to be accurately adjusted and determined with the help of different electron-beam monitors over a wide dynamic range. In the framework of a scientific co-operation between PTB and the University of Bonn, we recently re-established the method for calibration of highly sensitive photon counting devices at the normal-incidence monochromator (NIM) beamline for detector calibration in the radiometry laboratory of PTB at BESSY II [4] in order to calibrate various Lyman-α detectors for the NASA satellites TWINS [5].

The whole calibration procedure consists in three steps:

I   At a stored electron current I_{BESSY}^{I} between 100 mA and 200 mA, i.e. at normal operation of BESSY II, semiconductor photodiodes of high linearity are calibrated against the primary detector standard SYRES [1].

II   At a stored electron current I_{BESSY}^{II} around 1 mA, i.e. during a PTB main user shift, the ratio between the transmitted radiant power $\Phi(I_{BESSY}^{II})$ available at the NIM beamline, measured with a calibrated photodiode, and the electron current I_{BESSY}^{II}, as read-out from the active electron-beam monitor, is determined.

III   At further reduced electron current I_{BESSY}^{III}, adjusted to the requirements for operation of the photon counting device, e.g. at 1 μA, the calibration is performed calculating the radiant power by:

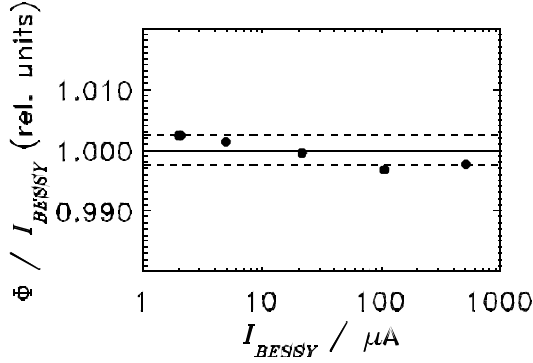$$\Phi\left(I_{BESSY}^{III}\right) \; = \; \frac{\Phi\left(I_{BESSY}^{II}\right)}{I_{BESSY}^{II}} I_{BESSY}^{III} \tag{1}$$

FIG. 1. Radiant power at the NIM-beamline for detector calibration normalised to the beam current of stored electrons, measured in relative units, as a function of the stored electron current. The dashed lines indicate the standard deviation from the mean value of the data points.

Application of equation (1) requires that the ratio between the radiant power and the electron current remains constant while reducing the electron current. It means that quantities that vary with the electron current, like the size of the synchrotron radiation source and the heat load on the optical elements, do not considerably influence the transmission of the NIM beamline. Fig. 1 demonstrates that these requirements are fulfilled within the electron current regime from 1μA to 1mA. The figure shows, measured in zero order of the monochromator and relative units, the signal of a semiconductor photodiode normalised to the electron current and as a function of the electron current. As a result, the radiant power may be regarded, in fact, to be proportional to the stored electron current within a standard uncertainty of ± 0.25 %.

Fig. 2 shows the local distribution of the quantum efficiency h(x,y) of one of the investigated Lyman-α detectors, measured at a wavelength of 121.5 nm by xy-scanning the device under normal incidence across the monochromatised synchrotron radiation beam of about 3 mm x 1 mm in dimension and ± 6 mrad in divergence. The detector consists of a channeltron coated with lead glass, combined with a Lyman-α bandpass filter and a baffle system which reduces the angular acceptance to about ± 50 mrad. The non-uniform geometry of a channeltron explains the rather poor spatial homogeneity of the quantum efficiency as demonstrated by Fig. 2.
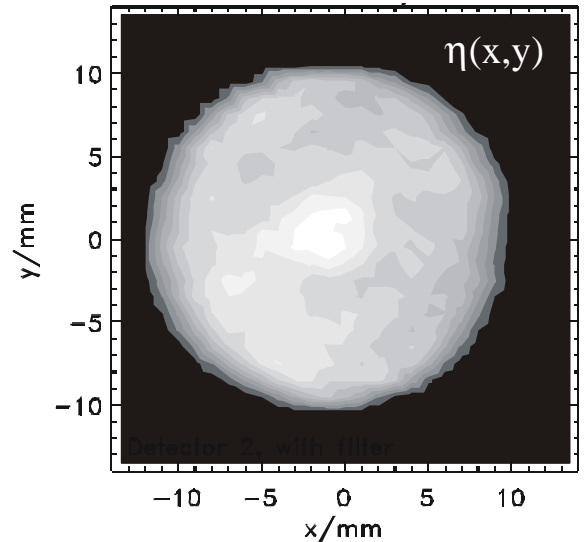

FIG. 2. Local distribution of the quantum efficiency of a Lyman-α detector for the TWINS mission of NASA, measured at 121.5 nm, displayed by grey levels of 10 % in step size.

However, the detector homogeneity is of minor importance since the device was constructed to integrally measure the Lyman-α irradiance E scattered from the geo-corona by:

$$E = \dot{N}\, h_E^{-1} \qquad (2)$$

$\dot{N}$ denotes the measured count rate and h_E the quantum efficiency with respect to irradiance which can be derived by integration of the measured local quantum efficiencies (Fig. 2) over the detector area:

$$h_E = \int_{Detector} h(x, y)\, dx\, dy \qquad (3)$$

Fig. 3a shows the measured h_E of two different Lyman-α detectors investigated. h_E divided by the detector area, as obtained as a further result from the local distribution measurements (Fig. 2), yields the averaged quantum efficiency h_{av} which is shown in Fig. 3b, respectively. The relative standard uncertainties of the calibrations in the spectral range of interest from 115.5 nm to 127.5 nm amount to 5 %. All measurements were repeated also without the respective Lyman-α filters whose peak transmission was found to amount to about 14 % around 119 nm.

Our calibration campaign for the Lyman-α detectors will be finished in May 2002. Launch of the two TWINS satellites is scheduled by NASA for late 2003 and early 2005, respectively. Aim of the experiments is to measure the global hydrogen distribution within the geocorona and its influence on the plasma structure of the magnetosphere.
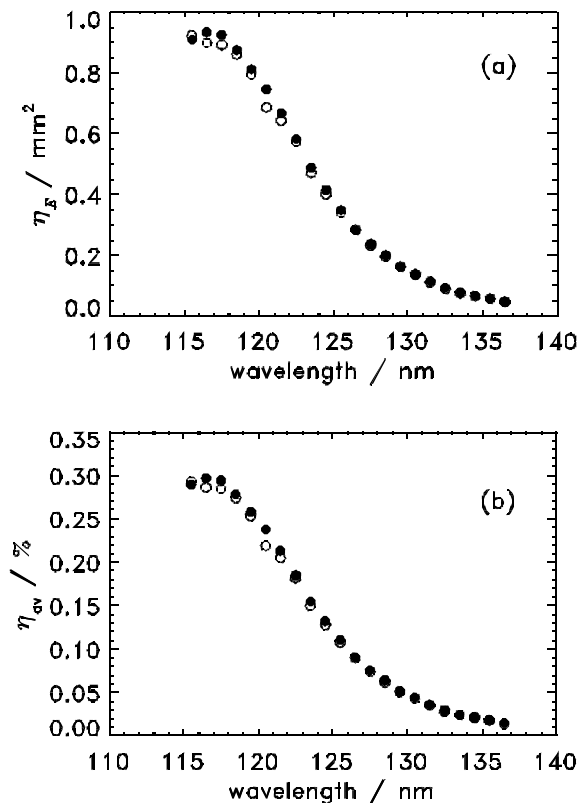

FIG. 3. Quantum efficiency with respect to irradiance (a) and averaged quantum efficiency (b) of two different Lyman-α detectors as measured in June 2001.

[1] H. Rabus, V. Persch, G. Ulm, Appl. Optics **36**, 5421 (1997)

[2] M. Bavdaz, A. van Dordrecht, D. J. Goldie, U. Kroth, P. Kuschnerus, A. Peacock, H. Rabus, N. Rando, M. Richter, G. Ulm, P. Verhoeve, BESSY Annual Report (1997), p. 104

[3] R. Thornagel, R. Klein, G. Ulm, Metrologia **38**, 385 (2001)

[4] M. Richter, J. Hollandt, U. Kroth, W. Paustian, H. Rabus, R. Thornagel, G. Ulm, Nucl. Instr. and Meth. **467-468**, 605-608 (2001)

[5] http://nis-www.lanl.gov/nis-projects/twins/

The new Bending Magnet Beamline DWL20° for EUV Irradiation Experiments

R. Thornagel, R. Klein, F. Scholze, G. Ulm, and M. Wedowski*

Physikalisch-Technische Bundesanstalt, Abbestr. 2-12, 10587 Berlin, Germany
* Carl Zeiss SMT AG, 73446 Oberkochen

In the PTB laboratory at BESSY II [1], a new beamline, called DWL20°, was set up for the irradiation of samples with high EUV power density, mainly for aging experiments of EUV-mirrors [2]. It uses synchrotron radiation from the bending magnet 07-1A, that is deflected by 20° and focussed by an ellipsoidal, Rh-coated Si mirror with an optical area of 1000 x 55 mm², which is placed in a distance of 20.5 m from the source point. The focus lies at 30.5 m. The mirror can be moved out of the beamline for the usage of the existing experimental stations at the white light beamline DWL.

The mirror reflection suppresses the higher photon energies, further suppression can be done by filters, that can be introduced into the optical path behind the mirror. Most importantly, two kinds of Si/Zr filters can be used:
One is a so-called "50% -filter" that roughly has a transmittance of 50 % in the EUV spectral range, the other is a "1%-filter" with roughly 1% EUV transmittance.

The following data are based on:
- Calculated spectral radiant power of the bending magnet for an electron beam current of 100 mA
- Measured reflectance of a sample piece of the Rh-coated mirror
- Measured transmittance of a typical "50%- filter"
- Measured transmittance of a typical "1% -filter "

The spectrum of the radiation available at the beamline is shown in Fig. 1. This is the spectral radiant power, spatially integrated across the photon beam, therefore independent of the location along the optical path. To get an idea on the power levels and EUV in-band power, in table 1 the spectrally integrated power is given for different bandwidths.

	total power (10 eV to 10 keV)	power in 90 eV to 95 eV bandwidth		power in 80 eV to 100 eV bandwidth	
unit	mW	mW	% of total power	mW	% of total power
without filter	461	17	3.7	58	12.6
with 50% filter	71	8	10.9	31	43.8
with 1% filter	0.6	0.16	26.3	0.52	86.9

Table 1: Spectrally integrated power for an electron beam current of 100 mA for different integration bandwidths.
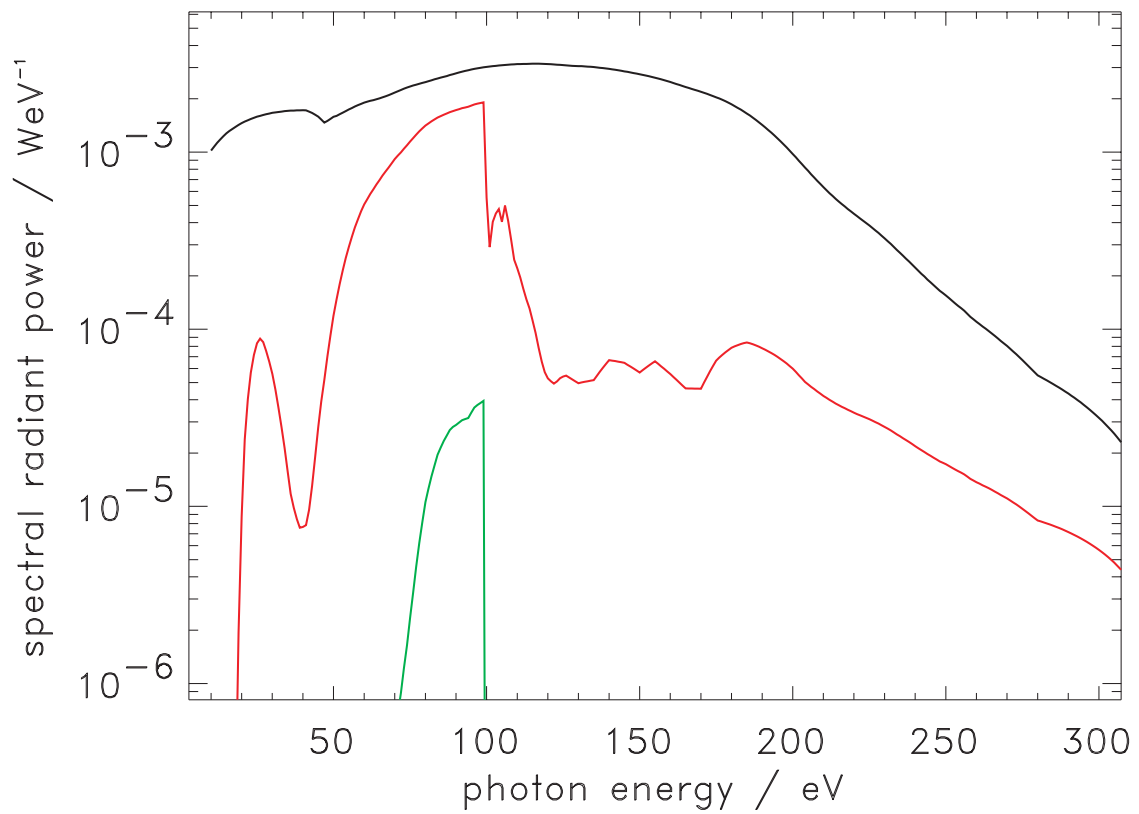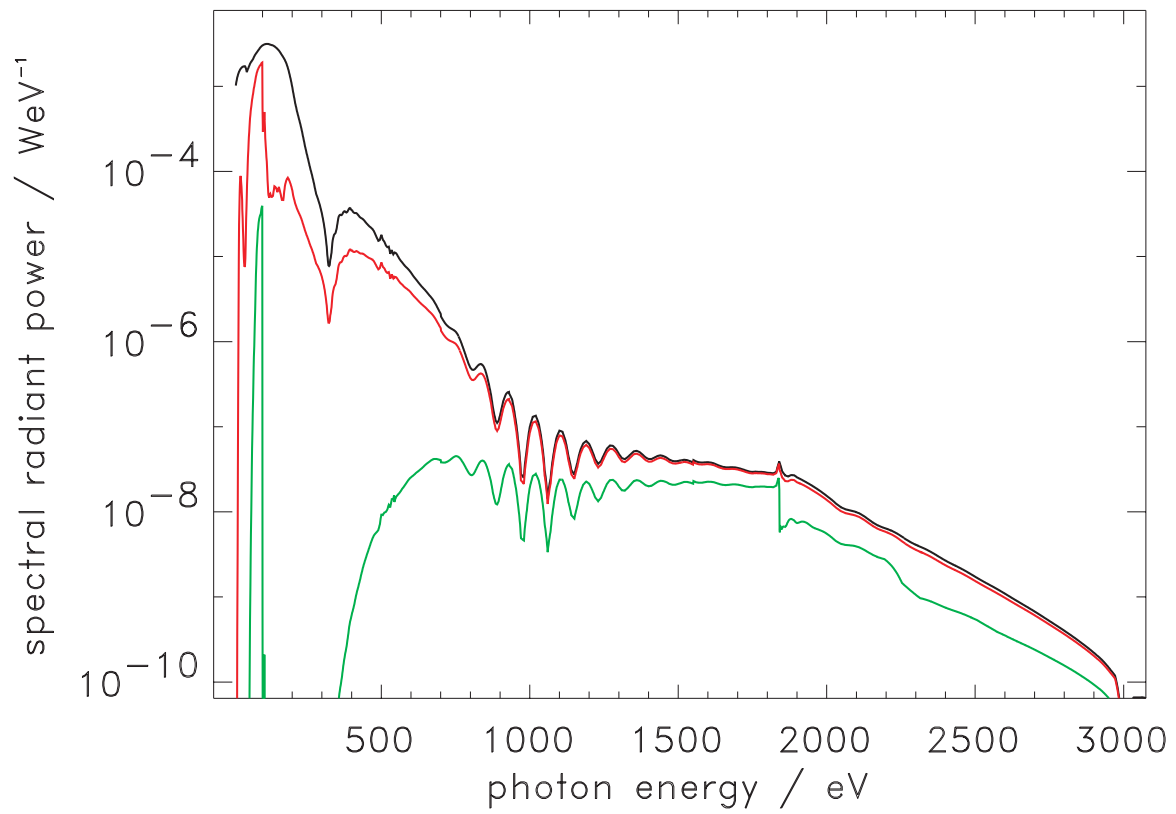
Fig. 1: **Spectral radiant power at the beamline (black: only mirror reflection, no filter; red: 50% filter; green 1% filter)**

Due to the focussing mirror, the spatial shape of the radiation spot changes along the optical path. It was therefore measured at different positions before and behind the focal point. This was done with a thinned, back-illuminated CCD camera with known spectral sensitivity, with no filter in the beamline. At the focal position, the CCD image shows a very sharp focus with about 0.1 mm FWHM with a total power density up to 1000 W/cm^2 at 100 mA storage ring current, surrounded by some halo.

This is much too high a power density in too small a spot for later characterization. Therefore the position of the sample to be irradiated is located 350 mm behind the focus. Fig. 2 shows the power density distribution for a measurement that was taken close to the sample position. One horizontal, and two vertical cuts are shown in Fig. 3 at positions, indicated by the black, green, and blue lines in Fig. 2.

At this position, an illumination chamber with a load lock system is installed, where samples can be irradiated with high EUV power density. This chamber is equipped with a gas inlet system to simulate different environmental conditions. Near the focus, a highly efficient differential pumping stage is installed, so that gas pressures of up to 1×10^{-2} mbar can be handled without influencing the vacuum in the mirror chamber.

The beamline is used in close cooperation with Carl Zeiss, Oberkochen, and TNO-TPD, Delft, The Netherlands, for investigation of contamination processes under EUV illumination, that lead to a reduction of reflectance of Mo/Si multilayer mirrors used in EUV-lithography tools. The goal is to develop strategies for contamination prevention or mitigation in vacuum conditions similar to those in an EUV lithography tool [2].
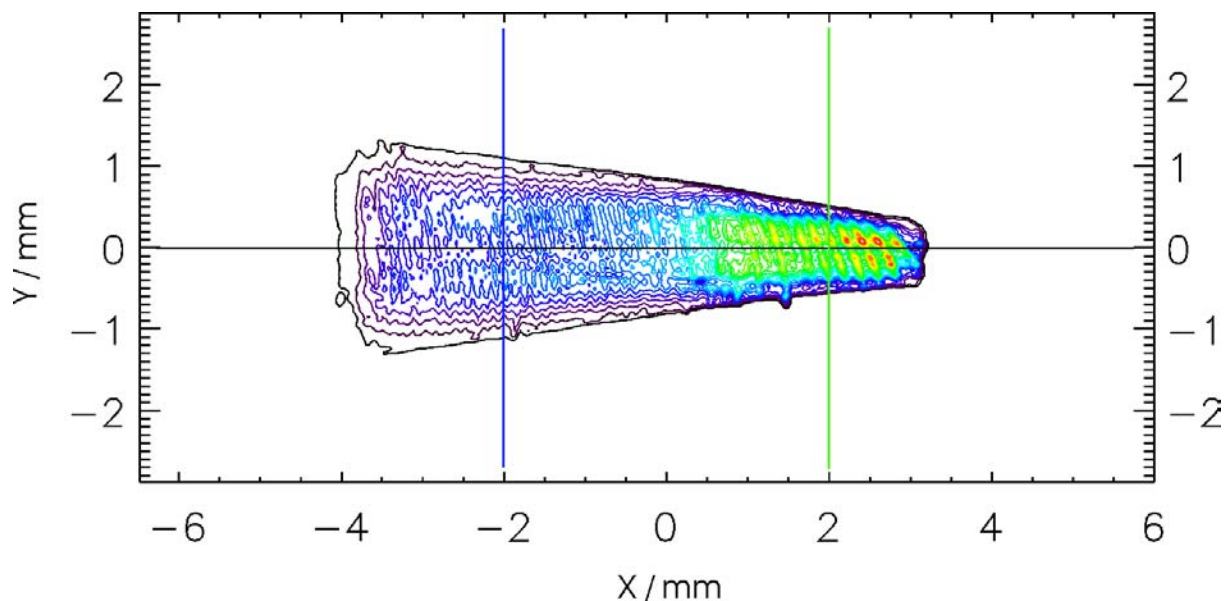
Fig. 2: **Measured power density about 350 mm behind the focus of the DWL20°-beamline at 100 mA storage ring current. The distance between colored lines is 5% of the maximum value of 13 W/cm^2.**
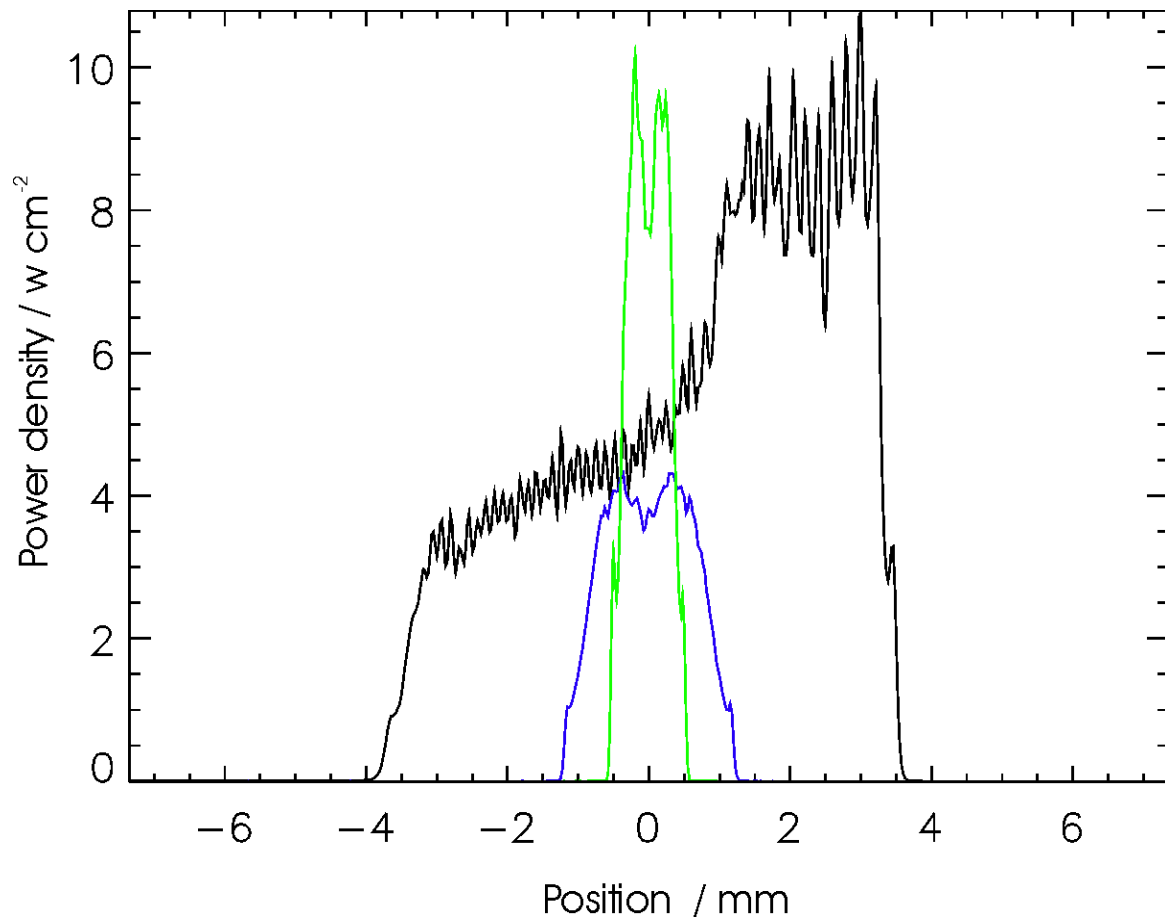
Fig. 3 : **Horizontal (black) and two vertical (green and blue) cuts through the power density image of Fig. 2.**

References

[1] The PTB radiometry laboratory at the BESSY II electron storage ring;
G. Ulm, B. Beckhoff, R. Klein, M. Krumrey, H. Rabus, R. Thornagel;
Proc. SPIE 3444 (1998) 61 –621

[2] Lifetime testing of EUV optics using intense synchrotron radiation at the PTB radiometry laboratory;
R. Klein, A. Gottwald, F. Scholze, R. Thornagel, J. Tümmler, G. Ulm, M. Wedowski, F. Stietz, B. Mertens, N. Koster, J.V. Elp;
Proc. SPIE 4506 (2001) 105-112

INVESTIGATION OF THE CASCADE EFFECT AND SECONDARY PHOTOELECTRON EXCITATION IN X-RAY FLUORESCENCE ANALYSIS OF LIGHT ELEMENTS

N. Kawahara[1], T. Shoji[1], T. Yamada[1], Y. Kataoka[1], B. Beckhoff[2], G. Ulm[2] and M. Mantler[3]

1 Rigaku Corporation, Akaoji 14-8, Takatsuki, Osaka 569-1146, Japan
2 Physikalisch-Technische Bundesanstalt, Abbestraße 2-12, 10587 Berlin, Germany
3 Institut für Angewandte und Technische Physik, Technische Universität Wien,
Wiedner Hauptstraße 8-10, 1040 Wien, Austria

ABSTRACT

We have investigated the cascade effect and the secondary photoelectron excitation effect by means of Cr-L line measurements using monochromatic radiation of high spectral purity and well-known flux provided by two beamlines of the Physikalisch-Technische Bundesanstalt (PTB) at the electron storage ring BESSY II. The plane grating monochromator beamline for undulator radiation covers the energy range from 30 eV to 1.9 keV, and the four-crystal monochromator beamline for synchrotron radiation from 1.75 keV to 10.5 keV. The Cr-L fluorescence intensities show a considerable jump at the Cr-K edge energy as the source photon energy rises, indicating the magnitude of the cascade effect. The fundamental parameter method, including the cascade effect and the secondary photoelectron excitation effect, shows good agreement with the measurement.

INTRODUCTION

Low-energy characteristic X-ray measurements play a key role in X-ray fluorescence (XRF) analysis of light elements and of thin layer materials. Besides primary excitation by incident X-rays and secondary excitation by fluorescent X-rays, there are other secondary processes which contribute to low-energy characteristic X-ray emissions. One of them is the excitation by photoelectrons, which has been introduced into a fundamental parameter method [1] and evaluated experimentally [2]. Another process is the emission of L-series X-rays following radiative and non-radiative relaxations of the K-shell ionization.

This "cascade" effect on L-series X-ray emission occurs when the energy of source X-rays is higher than the K-shell binding energy, i.e. in a measurement of L-lines of low energy using an XRF spectrometer with, for example, a Rh-target end-window tube. The contribution of the cascade effect exceeds that of direct excitation in these situations. Obviously, this effect can contribute also to M-series X-ray emission. Although this cascade effect has been previously studied [3], an experimental evaluation has not been reported to the best of our knowledge. The extension of XRF application, however, requires measurements of L- or M-lines, in which the cascade effect arises.

In this paper, we demonstrate the implementation of the cascade effect into the fluorescent intensity calculation as well as its experimental evaluation using monochromatic radiation provided by two PTB beamlines.

CALCULATION

The implementation formula used for the cascade effect term is shown in Figure 1. Here, the values given by Rao et al.[4] for the total number of holes in an L-subshell after relaxation of the K-shell have been used. Details of the intensity calculation of the secondary photoelectron excitation term are given elsewhere [2].

$$I_{iqs}^{Cascade} = \int_z dz \int_\lambda d\lambda I_0(\lambda) \exp\left(-\rho z\left(\frac{\mu(\lambda)}{\sin\psi_{in}} + \frac{\mu(\lambda_{iqs})}{\sin\psi_{out}}\right)\right) w_i K_{ip} \tau_i(\lambda) n_{i,p\to q} \omega_{iq} R_{iq}^s$$

λ	: Incident X-ray wavelength
$I_0(\lambda)d\lambda$	: Intensity of incident X-rays
$\mu(\lambda)$	: Mass absorption coefficient of the specimen for X-rays of wavelength λ
λ_{iqs}	: Wavelength of iqs line
ρ	: Specimen density
w_i	: Mass fraction of element i in the specimen
$\tau_i(\lambda)$	: Photo-absorption coefficient of element i for X-rays of wavelength λ
K_{ip}	: Fraction of shell p in photo-absorption coefficient; $K_{ip} = (1-1/J_{ip})/\Pi\ J_i$
J_{ip}	: Jump ratio at edge p of element i $\qquad\qquad\qquad\lambda<\lambda_{iq}<\lambda_{ip}$
λ_{ip}	: Wavelength at edge p of element i
ω_{iq}	: Fluorescent yield of shell q of element i
R_{iq}^s	: Relative transition probability of iqs line in iq series
Ψ_{in}	: Incident angle
Ψ_{out}	: Take-off angle
$n_{i,p\text{-}>q}$	: Total number of holes in q shell generated after relaxation of a hole in p shell

Figure 1. The intensity formula for the term of the cascade effect

EXPERIMENTS

The experiments were performed at various photon energies to evaluate the calculation. Hence, tunable synchrotron radiation had to be employed for the specimen excitation [5]. Beside other beamlines intended for radiometric tasks, a plane-grating monochromator (PGM) beamline for undulator radiation and a four-crystal monochromator (FCM) beamline for bending magnet radiation provide monochromatized radiation of high spectral purity[6]. The photon energies available at the PGM ranges from 30 eV to 1.9 keV and at the FCM from 1.75 keV to 10.5 keV. Within the present investi-

Fig. 2. Schematic view of the experimental XRF setup in the PTB laboratory at BESSY

gation requiring photon energies between 300 eV and 8000 eV, the 1200 l/mm Au coated grating at the PGM and the Si(111) crystals at the FCM were employed. At a given photon energy of interest, the radiant power of the incident excitation radiation was adapted to the count-rate capability of the Si(Li) detector used by either varying the trigonometric ratio of the angle of incidence to the angle of diffraction at the PGM or by detuning the second pair of Si crystals at the FCM. The set of experiments was carried out in the ultra-high vacuum XRF irradiation chamber of PTB placed in the focal plane of the PGM and of the FCM beamlines. This chamber allows simultaneous handling and accurate positioning of six samples with an effective diameter of 10 mm that are oriented vertically. The angle at which the exciting radiation is incident on the sample of interest can be varied between 30° and 90°. In this work, both angles of incidence and take-off were set to 45°. The scattered and fluorescence radiation were registered by an energy-dispersive Si(Li) detector with a Si window 0.2μm in thickness placed behind an calibrated aperture spaced 67 mm apart from the sample center. In addition, the efficiency of such a detector was determined in absolute terms with a relative uncertainty ranging from 1.5% to 2% at the photon energies of interest. The schematic configuration is shown in figure 2. The specimen used for this experiment was a chromium layer of 2 μm in thickness on a Si wafer. The spectral region of interest was that of Cr-L radiation.
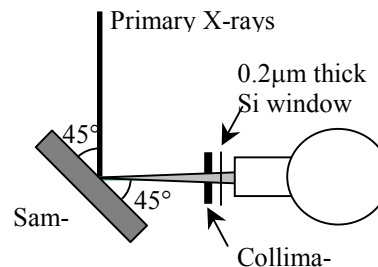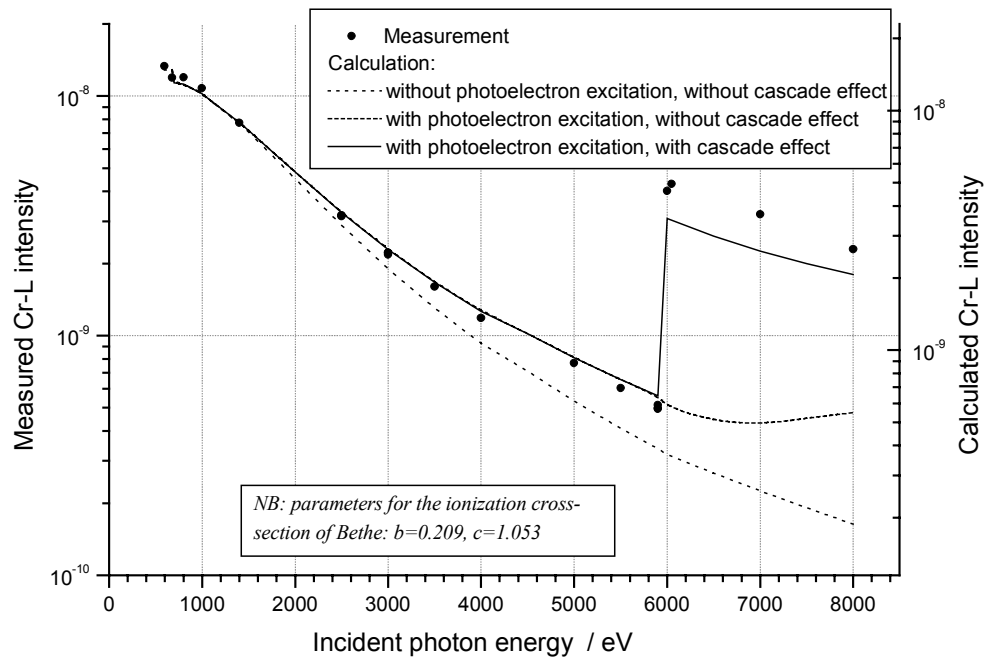
Figure 3. Experimental and calculated results for Cr-L intensities from a 2µm thick chromium layer deposited on a silicon wafer using monochromatized synchrotron radiation. Dots: experimental results. Dotted line: the calculated results obtained by primary and secondary fluorescent X-rays only. Dashed line: the calculated results, which consist of primary and secondary fluorescent X-rays and the secondary photoelectron excitation. Solid line: the results obtained by calculation, which includes primary and secondary fluorescent X-rays, secondary photoelectron excitation and the cascade effect.

RESULTS AND DISCUSSION

Figure 3. presents the comparison between measured and calculated Cr-L intensities. The experimental results obtained by use of monochromatized radiation and three types of calculated results are shown. The three calculations cover (i) the result obtained by primary and secondary fluorescent X-rays only, (ii) by primary and secondary fluorescent X-rays and secondary photoelectron excitation, (iii) the result consisting of primary and secondary fluorescent X-rays, secondary photoelectron excitation and the cascade effect. This figure shows Cr-L intensities in log scale against incident photon energy. The experimental data show a drastic jump at Cr-K edge energy. This jump illustrates the cascade effect very well. Calculations (i) and (ii) show no jump at the Cr-K edge, although calculation (ii) is in line with the experiment below the edge, illustrating the contribution of the secondary photoelectron excitation. In contrast to this, the calculation (iii) reproduces the jump at the Cr-K edge. Part of the remaining difference between the measured data and the calculation above the Cr-K edge would be due to the Coster-Kronig transition, which still must be included into the calculation.

REFERENCES

[1] M. Mantler, Adv. X-ray Anal. 36 (1994) 27
[2] Y. Kataoka et al, Adv. X-ray Anal. 41 (1998) 76
[3] W. Bambynek et al., Rev. Mod. Phys. 44 (1972) 716
[4] P. V. Rao et al. Phys. Rev. A5 (1972) 997
[5] B. Beckhoff et al., Nucl. Instr. and Meth. A 444 (2000) 480
[6] M. Krumrey, G. Ulm, Nucl. Instr. and Meth. A 467-468 (2001) 1175

Start-up of the Application Center for Microtechnique (AZM)

R. Ledworuski, H. Lehr, D. Peters, K. Plückhahn, M. Runge, M. Schmidt, S. Schrader, A. Schütz, J. Theisen, B. Tierock, S. Walter
Technische Universität Berlin, Institut für Konstruktion, Mikro- und Medizintechnik
Keplerstr. 4, 10589 Berlin
Phone: 30/314-23413; Fax: -26610; email: lehr@ifmt.kf.tu-berlin.de

M. Bednarzik, A. Firsov, H. Köhrich, B. Löchel, H.-U. Scheunemann, D. Schondelmeier, T. Wegwerth, I. Wichert
BESSY GmbH
Albert-Einstein-Strasse 15, 12489 Berlin
Phone: 30/6392-2953; FAX: -4682; email: loechel@bessy.de

Finishing Construction

The Technical University of Berlin and BESSY have applied financial support for the construction of an Application Center for Microtechnique (AZM) at BESSY from the Senatsverwaltung für Wissenschaft, Forschung und Kultur of Berlin in 1998. The money was applied from the EU fond for regional development (EFRE). The construction of the AZM started in June 1999 after granting and was finished in December 2001. Beside construction work at the BESSY building, a clean room, chemical laboratories, and laboratories for precision mechanics were build up. Planning and realisation was carried out and controlled by the Clean Room Consulting GmbH, Freiburg. The construction of the AZM was finished in December 2001 as planned.

Parallel to the construction specifications for the equipment were defined and a tendering procedure was done. Finally equipment was installed in the following areas:

X-ray depth lithography: access to three different spectral regions of synchrotron radiation caused by different magnetic fields in a low energy wiggler, standard dipole magnets in the storage ring, and super conducting magnets in a wavelength shifter.

Measurement techniques: measurement and characterisation of micro and nano structures by means of REMs, a Laser scanning microscope, and a multisensor coordinate measurement machine.

Photolithography: fabrication of masks, UV lithography for fabricating micro structures.

Thin layer techniques: deposition of functional layers (PVD, PECVD) and dry etching (IE, RIE).

Wet chemical processes: wet chemical etching, electrodeposition for fabricating microstructures in metal, fabrication of mould inserts.

Chemical lab: development of new chemical processes like electrodeposition and chemical etching.

Material lab: substrate preparation and substrate rework, ultra precision machining

Plastic moulding: hot embossing and micro injection moulding for replication using polymer material, cutting, drilling, and welding by a Nd:YAG Laser.

Metal lab: precision cutting, micro electro discharge machining (wire and die sinking)

Micro assembling: test and development of assembling processes, assembling of hybrid components (under construction).

Packaging lab: development of packaging techniques for mechanical, electromechanical, optical, and electronic components (under construction).
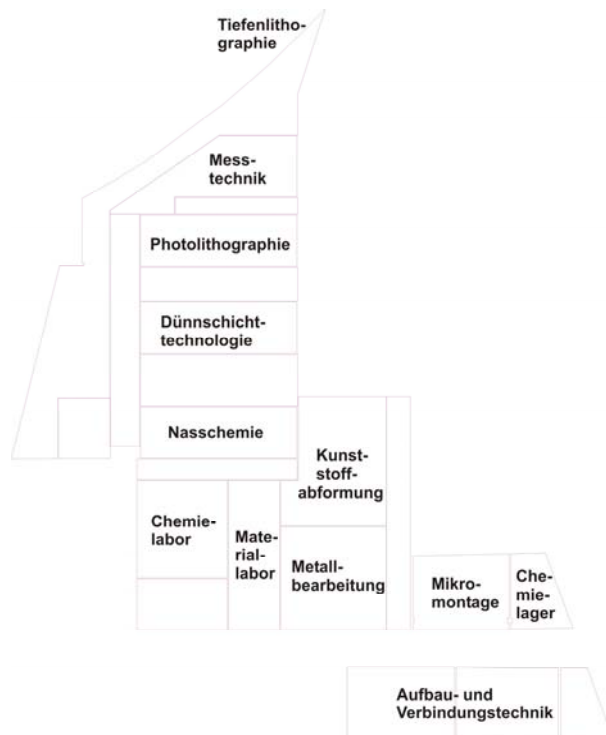
Fig. 1: Footprint of the labs

Tiefenlitho-graphie

Mess-technik

Photolithographie

Dünnschicht-technologie

Nasschemie

Kunst-stoff-abformung

Chemie-labor

Mate-rial-labor

Metall-bearbeitung

Mikro-montage

Che-mie-lager

Aufbau- und Verbindungstechnik

Projects

Depth lithography by using synchrotron radiation for fabricating micro components is one of the main working fields of the AZM. Present work is focussed on the fabrication of primary polymer moulds as well as the replication of these forms in order to generate mould inserts.

Test exposures with new resist materials were used for characterising the achievable resolution, find out the exposure dose, investigating the influence of the secundary radiation caused by the resist, the substrate, or mask material. Additionally stability and pattern fidelity of the micro components depending from the process parameters were investigated.

In a cooperation with the Forschungszentrum Karlsruhe the spectral data for the three different source modes (low energy wiggler, standard dipole magnets, wavelength shifter) were calculated and characterised with respect to the intensity distribution in the X-ray scanners. Test exposures were used for checking the achieved results. A detected misalignment of the low energy wiggler beamline was corrected by moving the whole line for 30 mm at the scanner in order to improve the homogeneity of the synchrotron beam over the exposure field.

Further work concerned with the set-up of the ultra precision mill used for fabricating super planar substrates with roughness values of $R_a < 10$ nm, the substrate treatment by using wire and die sinking electro discharge machining, and tests at the hot embossing machine for replicating micro components in polymer materials.

EUV Lithography

M. Bednarzik, A. Firsov, H. Köhrich, B. Löchel, H.-U. Scheunemann, D. Schondelmeier, T. Wegwerth, I. Wichert
BESSY GmbH
Albert-Einstein-Strasse 15, 12489 Berlin
Phone: 30/6392-2953; FAX: -4682; email: loechel@bessy.de

Progress in microelectronic device fabrication demands further size reduction of components. Especially the lithography as a basic tool of the fabrication process is challenged. In order to overcome physical limits of optical pattern transfer, the wavelength of the applied light must be reduced. Chip factories now apply UV light of 340 nm to generate a minimum feature size of 180 nm. They are prepared to introduce optical steppers using 192 nm for the next chip generation. However, further integration will demand still more size reduction, i.e. a lithography using even shorter wavelength. International investigations in this field are focussed on a wavelength of 13.4 nm, the extreme UV lithography (EUV). Presently all tools and processes for the EUV lithography are under investigation but not available. Therefore, enterprises which are active in this field are looking for partners who could help to increase the development process. The BESSY synchrotron radiation also contains light of 13.4 nm wavelength and is best qualified to serve as a light source for the EUV lithography.

The Infineon AG, Munich, with its branch in Erlangen is developing new photoresists for the EUV lithography. As a subcontractor of Infineon, BESSY built up a special beamline with an exposure tool for the development of EUV resists. Besides a pre-mirror (grazing incidence mode) for cutting off high energy photons, this beamline contains two multilayer mirrors (normal incidence) for selecting the 13.4 nm light and an exposure chamber for carrying out simple open frame exposures of the new photoresists. The pre-mirror acts as an absorber for short wavelengths, which otherwise would heat up the multilayer mirrors and destroy their coatings.

 An ultra thin silicon membrane (0.5 μm thick) separates the vacuum of the exposure tool (10^{-4} mbar) from the ultra high vacuum of the beamline. Using this set-up, a 60 mm wide strip could be exposed on the wafer.

For characterising the new photoresists an exact gradation of the intensity is necessary. Up to 15 different grey levels can be realised simultaneously by using a chopper disc during a single exposure.

The absolute intensity of the 13.4 nm light can be measured by means of a calibrated photodiode.

Clean room conditions and yellow light for the exposures are realised by using a hutch.

First informal experiments were carried out in December 2001.

EUV beam line: pre-mirror chamber on the right, multilayer mirror chamber in the middle, clean room hutch with exposure station on the left
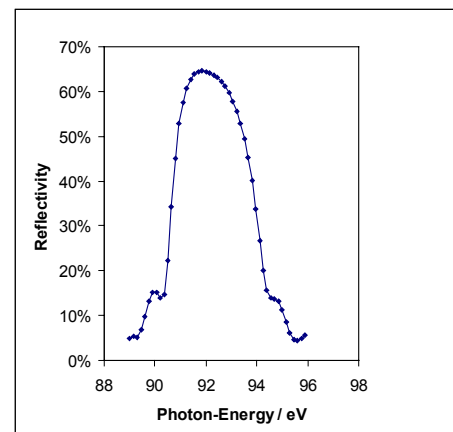
Measured reflectivity of a multilayer mirror

Fabrication of Micro Gears

M. Bednarzik, A. Firsov, H. Köhrich, B. Löchel, H.-U. Scheunemann, D. Schondelmeier, T. Wegwerth, I. Wichert
BESSY GmbH
Albert-Einstein-Strasse 15, 12489 Berlin
Phone: 30/6392-2953; FAX: -4682; email: loechel@bessy.de

Gear technology for microsystems is mainly focussed on planetary type gears. This type of gear contains typically a center wheel (sun) and several orbiting wheels (planets) and is optimised for minimal loss during transfer of torque and rate of revolutions of a micromotor. Aspects like freedom from play, positioning accuracy, and torsional rigidity with main influence on the quality of the gear and the system were not considered in micro gears fabricated until now. Besides having characteristics like small dimension and high precision, micro gears are also be applicable for high precision positioning. The Micro Harmonic Drive[®] is the first micro gear with characteristics like lifelong freedom of play, excellent repetition accuracy in the range of Winkelsekunden, high torque capacity up to 50 mNm, high gear ratio between 160 and 1000:1, consisting of only 6 parts, high efficiency, and minimal loss in torque.

There are two fundamental differences between Micro Harmonic Drive[®] and conventional gears. First is the use of flexible wheels and connected with it, the special kinematics. Second is the gear fabrication by using the LIGA process. Special characteristics of this excellent gear type are its torque per volume and its excellent positioning accuracy.

source: Micromotion GmbH, Mainz
Bee and Micro Harmonic Drive[®]

Basic elements of the Micro Harmonic Drive[®] are the wave generator and the wheels: flexspline, circular spline, and dynamic spline. The wave generator forms an elastic flexspline to an elliptic wheel around the middle axis. The cogs of the flexspline gear into the circular spline and dynamic spline simultanously along the elliptic main axis. Orthogonal to the main axis there is no contact between the cogs of the flexspline and the circular spline.

BESSY and the Mircomotion GmbH Mainz have developed and established a fabrication process for components of a Micro Harmonic Drive gear. The fabrication is based on the

LIGA process and uses modern inexpensive X-ray masks, a special photoresist, and a NiFe plating process. The thickness of the wheels is up to 1000 μm and the minimum feature size is 30 μm. The whole process development was finished in about 5 month. It shows the engagement and high competence of the project partners and the high capacity of synchrotron light for fabricating MEMS components. This efficient cooperation between industrial partners and BESSY will be continued.

3d Photoabsorption of free europium atoms

M. Martins
Universität Hamburg, Institut für Experimentalphysik
Luruper Chaussee 149, D-22761 Hamburg

K. Godehusen,* T. Richter, and P. Zimmermann
Technische Universität Berlin, Institut für atomare Physik
und Fachdidaktik, Hardenbergstraße 36, D-10623 Berlin

The 3d photoabsorption of the rare earth (RE) elements is widely used in solid state physics for the element specific analysis of thin film systems. For the interpretation of the data in general atomic models are used [1], because the 4f electrons should be well localized and can be therefore treated atomic like. Furthermore especially for the lighter elements the question arises, if the 4f wavefunction in the free atoms is collapsed or not and if this
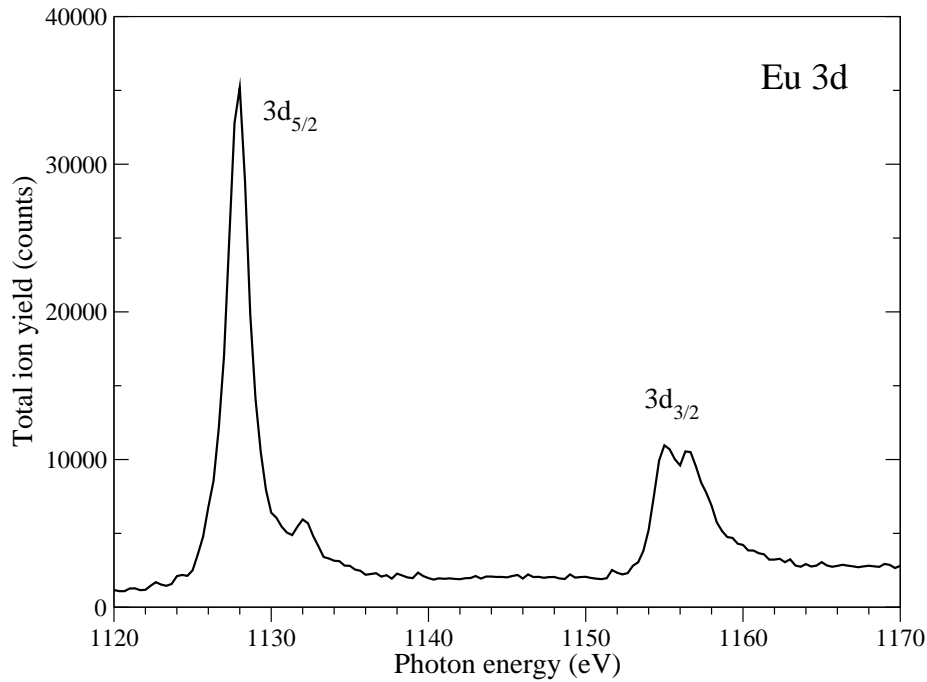
Figure 1: Photoabsorption of free europium atoms in the region of the 3d-4f excitation.

collapse depends on the created core hole. A first photoabsorption experiment by Arp et al. shows [2] shows, that the 4f wavefunction seems to be collapsed already for barium in the case of a 3d core hole, whereas for the 4d core hole the collapse occurs at larger Z. Another interesting aspect of the RE atoms are the strong correlations between the valence electrons

---

*Present address: BESSY GmbH

and the influence of the core hole on the correlations. For the 4f and 5p photoemission of free europium they result in a strong disturbance [3, 4] of the expected simple multiplet structure observed in the solid phase [5].

Up to now no experimental data for the 3d excitation of free RE atoms is known due to the low cross sections and experimental difficulties. However with the high photon flux of the BESSY II undulator beamlines this has now become possible. Therefore the photoabsorption of free europium atoms has been investigated at the U49/2-PGM1 beamline at BESSY. Figure 1 shows the measured photoabsorption signal in the region of the 3d-4f excitation. The absorption spectrum of the free europium atoms with the ground state $4f^7 6s^2\, ^8S_{7/2}$ resembles pretty much the experimental spectrum of solid europium and gadolinium [1] due to the same $4f^7$ core for the divalent europium and the trivalent gadolinium. This shows that for the case of europium due to the well localized 4f electrons the atomic model is completely valid at least in the photoabsorption. Further studies will be made especially on the lighter elements and the 3d photoemission.

The authors would like to thank the BESSY staff for their support during the beamtimes.

References

[1] B. Thole *et al.*, Phys. Rev. B **32**, 5107 (1985).

[2] U. Arp *et al.*, J. Phys. B **32**, 1295 (1999).

[3] A. Verweyen *et al.*, J. Phys. B **32**, 4079 (1999).

[4] M. Martins *et al.*, Phys. Rev. A **in press**, (2002).

[5] B. T. Thole *et al.*, Phys. Rev. B **47**, 9098 (1993).

First test of beamline KMC-2 for X-ray absorption spectroscopy on metalloproteins (BioXAS)

[1*]M. Haumann, [1]M. Grabolle, [1]C. Müller, [2]M. Fieber-Erdmann, [2]A. I. Erko, and [1]H. Dau

[1]*Freie Universität Berlin, FB Physik, Arnimallee 14, D-14195 Berlin, Germany*
[2]*BESSY II, Albert-Einstein-Straße 15, D-12489 Berlin, Germany*
Email: haumann@physik.fu-berlin.de

KMC-2 at BESSY II is a bending-magnet beamline equipped with a monochromator (Si220 crystal). During a first run in August 2001 we set up an experiment for XAS measurements at the manganese K-edge using a photochemically active metalloprotein, photosystem II, which contains a tetra-manganese complex [1]. Due to the relatively low metal concentration of the samples (~1 mM), XAS spectra were measured as fluorescence-detected absorption spectra. Samples were placed in plain air and kept at room temperature. Fig. 1 shows a schematic drawing of the experimental setup. The following results were obtained:

(1) The photon flux was estimated as ~10^8 photons/s in the X-ray energy range 6500-7100 eV (Mn K-edge region). This flux is sufficient to obtain Mn XAS spectra with reasonable signal-to-noise ratio in a scan of ~ 1 h duration.

(2) Testing of the three different types of available fluorescence detectors (scintillation counter, photodiode, single-element energy-resolving detector) revealed that the large-area photodiode in combination with a thin aluminised chromium filter provides the best signal-to-noise ratio.

(3) Using the Si220 crystal, the suppression of the second harmonic was insufficient, resulting in unacceptably large monochromator glitches. The use of a glass capillary for harmonics suppression was impracticable due to the loss of ~80 % of X-ray intensity. To improve the situation, in the future we intend to use a Si111 crystal monochromator.

(4) Measurements of a $KMnO_4$ standard revealed that the X-ray energy was stable (+/- 0.5 eV) as judged by the sharp pre-edge peak (at 6543.3 eV) of the standard.

(5) The XAS measurements on metalloprotein samples are, in principle, possible KMC-2 (Fig. 1). Further improvements of the beamline (xyz-stage for sample positioning, Si111 crystal monochromator) are necessary. A large-area energy-resolving multi-element detector in combination with a He-cryostat would be highly advantageous for BioXAS measurements at KMC-2.
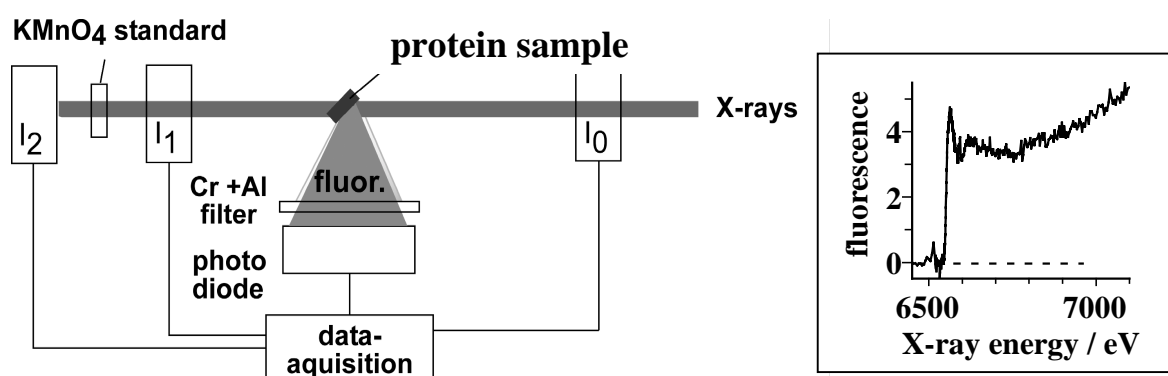
Fig. 1: *Experimental setup for XAS measurements on biological metalloenzymes at KMC-2. Inset: single-scan XAS spectrum of photosystem II at the Mn K-edge.*

[1] Dau, H., Iuzzolino, L. and Dittmer, J. (2001) Biochim. Biophys. Acta 1503, 24-39.

Ultraviolet Photoelectron Spectroscopic Investigations of Aromatic 1,3,4-Oxadiazoles

M. B. Casu, P. Imperia, S. Schrader, B. Schulz, L. Brehmer

Universität Potsdam, Institut für Physik, Am Neuen Palais 10, D-14469 Potsdam, Germany

---

Abstract

The family of substituted 1,3,4-oxadiazole can be used in Organic Light Emitting Diodes acting both as hole blocking and as improved emissive layers. Thin films of aromatic 1,3,4-oxadiazoles, prepared *in-situ* by evaporation from pinhole sources onto freshly deposited gold films on flat silicon wafers, were studied by means of ultraviolet photoelectron spectroscopy (UPS) in order to get detailed information about valence electronic band structure. The UPS measurements were performed at the beam line TGM-2 at BESSY in the energy range between 8 and 80 eV. Furthermore, we determined the vacuum level shift at the interface organic/metal. We used semi-empirical quantum-chemical calculations to evaluate the valence electronic structure of the isolated molecules. This was also the starting point used as input to simulate the UPS spectra obtained from the films. The good agreement between experimental and theoretical curves allows us to assign the different peaks to different molecular eigenstates and it also provides a more quantitative description of the experimental findings.

1. Introduction

Conjugated organic polymers and oligomers as well as low molecular compounds represent an important class of materials for applications in light-emitting devices including non-polarised background illumination in instrumentation, polarised emitters for liquid crystal displays, active low information content displays or multicolour flat panel displays for automotive, telecommunication or consumer electronics. This makes organic electroluminescence a fast developing field of science and technology. At present, many efforts are directed towards optimisation of device performance, in terms of low onset voltage, high efficiency, stable operation, and durability. This implies development of new materials with improved chemical, photochemical and thermal stability, high photoluminescence and electroluminescence efficiency. Emission colour is another important parameter and recently the efforts were focused on blue emitting electron transport materials [1, 2]. From the long experience established in the field of thermally stable polymers it is known that oxadiazoles belong to a class of stable structures in organic chemistry and model compounds based on these moiety show blue emission [3]. In this work we present the results of ultraviolet photoelectron spectroscopy (UPS) measurements on thin films of two different 1,3,4-oxadiazoles.

2. Experimental

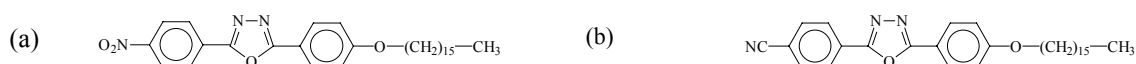We investigated two different aromatic 1,3,4-oxadiazoles: (Fig. 1) [4].

Fig. 1. Chemical structures of (a) 2-(4-hexadecyloxyphenyl)-5-(4-nitrophenyl)-diyl-1,3,4-oxadiazole (HNDO) and (b) 2-(4-hexadecyloxyphenyl)-5-(4-cyanophenyl)-diyl-1,3,4-oxadiazole (HCDO).

The UPS measurements were performed at the beam line TGM-2 in BESSY (Berlin, Germany). This line was characterised by a three gratings monochromator which covered the photon energy range from 8 to 180 eV. The photoelectrons were collected with a Vacuum Generators ADES 400 angle resolving spectrometer system, at room temperature. The base pressure during the experiment was 2×10^{-10} mbar. The resolution of the system monochromator-analyser (80 meV) was determined from the measured Fermi edge of a freshly evaporated gold film. The photoelectron spectra were measured with an angle of incidence of 45° in normal emission for various incident energies. However, because of the amorphous nature of the films, the spectra do not show any dispersion of the peaks with the incident photon energy and this also indicates that no charging effects occurred. The materials were evaporated in-situ from pinhole-sources onto freshly deposited Au films on flat silicon wafers. The film thickness was monitored with a quartz micro-balance (100 nm). During evaporation the pressure increased up to 10^{-7} mbar. The direct transfer from the preparation chamber to the measuring unit was possible, without breaking the vacuum, using a magnetic transfer line. We also directly determined the ionisation potential, I_p, according to the relationship:

$$I_p = E_{inc} - \left[E_k^{max}(org) - E_k^{min}(org) \right]$$

(1)

where E_{inc} is the incident photon energy, E_k^{max} and E_k^{min} are the maximum and the minimum kinetic energy, respectively, of the emitted photoelectrons. Using the shift of the photoemission spectra from the organic layers with respect to that one coming from gold, with special regard to the secondary electrons cut off, the vacuum level shift at the interface organic/gold was also estimated [5].

3. Results and Discussion

Fig. 2 shows the UPS spectra of the two materials. We directly determined the ionisation potential from the UPS spectra obtaining the following values: 6.6 and 7.4 eV for HNDO and HCDO, respectively.

(a)   (b)
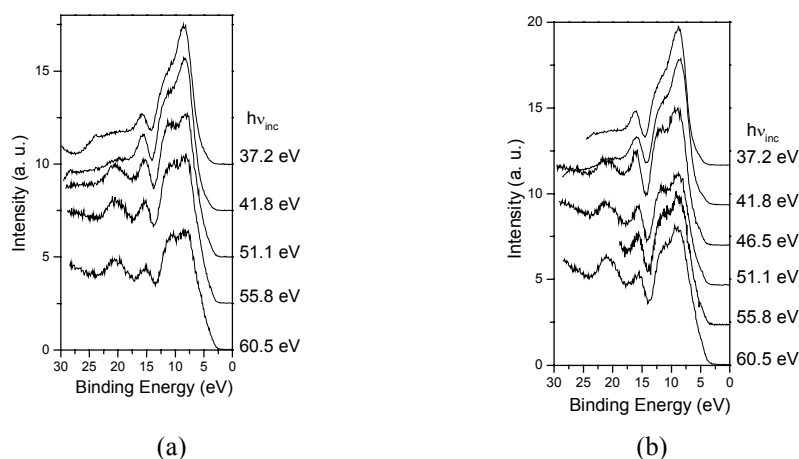
Fig. 2. Valence electronic spectra of HNDO (a) and HCDO (b). The incident photon energy is also indicated. The valence band is given with respect to the vacuum level set at zero. Vertical offsets are used for clarity.

As expected, the values of I_P are quite high for both materials. The reason of this has to be found in the presence of the oxadiazole moiety: the oxadiazole ring is π-deficient and this leads to a high ionisation potential.

Furthermore we estimated the vacuum level (VL) shift at the organic/Au interface, determining the shifts in the UPS spectra of the organic materials in comparison with the spectrum that comes from gold. We obtained -1.2 and -1.4 eV for HNDO and HCDO, respectively. In which the minus stands for the fact that Au-VL is lowered by the deposition of the organics. These values are very close and, in principle, they can be considered as the same when we want to investigate their nature depending on their origin. Moreover they also coincide with the vacuum level shift, -1.4 eV, previously determined for another material belonging to the same family [6]. This shift is an indication of the existence of a dipole layer at the interface. For interpreting the experimental features that characterise the spectra, we performed semi-empirical quantum chemical calculations using the AM1 method. The calculations were performed taking into account a single molecule in vacuum. They gave the complete set of molecular eigenstates. From a superposition of multiple Gaussians (FWHM = 0.5 eV), one for each molecular orbital, we obtained the theoretical valence electronic structure and we shifted the obtained curves to compensate for the solid state polarisation effects. The effect due to Auger electrons was not considered in the simulations. The theoretical curves, compared with the experimental ones, are shown in Figs. 3 (a) and (b) for HNDO and HCDO, respectively. The good agreement between experimental findings and theoretical results allows to relate each UPS peak with the contributions resulting from distinct groups of occupied molecular orbitals. In particular the lowest binding energy peak in the theoretical curve is essentially due to the HOMO for both materials, this contribution is seen as a small shoulder in the experimental spectra at lower binding energies. This emission is characterised mainly by π−orbitals. These states influence the optical properties of the molecule and, also, the electrical properties of the material when it is used in a device. In the spectrum from HNDO, the main contribution to the peak A has a double nature: on one hand, at lower energy, it is due to emission from π−orbitals, on the other hand to σ-states, both contributions are from the whole molecule. Peak B is also related to σ−orbitals from the oxadiazole moiety. The neighbouring peak C is related with the emission from multi-centre σ-states that are strongly localised in the phenyl ring and in the O_2N that is bonded to that ring. The peak at higher energy is related with the emission from multi-centre σ-states that involves the whole molecule. Peak A in HCDO is due to σ-states that involve all the molecule as well as peak B, that is characterised also by multi-centre σ-states. The contribution to peak C is related to multi-centre σ-states from the oxadiazole moiety. The peak at higher energy is related as well as in HNDO with the emission from multi-centre σ-states that involve all the molecule. Following this detailed analysis, the difference in the molecule, due to different donors, is reflected by the different MOs that contribute to the main peaks of the

spectra. But in the higher binding energy range, the spectra in both cases are dominated by the strong contributions linked to the molecular structural properties through the σ-states. Taking into account the overall electronic features of HNDO and HCDO, obtained from UPS studies together with quantum chemical calculations, we can discuss their correlation with the charge transport properties of these materials in a light emitting device. For this discussion we can use as a parameter the ionisation potential as it can give a hint about the behaviour of the materials in a Organic Light Emitting Device (OLED) depending on its value [7]. In principle, the quite high values of ionisation potential, and consequently also the quite high electron affinity [5], makes them materials that can be used as hole blocking/electron transporting layer in emitting devices. In particular, the slightly different values obtained for HNDO and HCDO indicate that the former, characterised by a lower I_p, could be used as emissive material, the latter can also act as hole blocking/electron transporting layer, presumably with very good electron injecting properties [7].
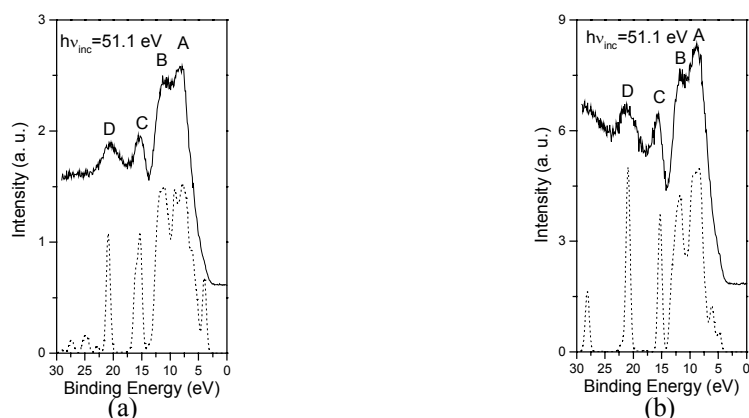
Fig. 3. Valence electronic spectra (full lines) of HNDO (a) and HCDO (b) compared with the simulated ones (AM1, dot lines). The incident photon energy is 51.1 eV. Vertical offsets are used for clarity.

4. Conclusions

The results of quantum chemical calculations shows that the spatial distributions of the HOMO are very similar for both investigated molecules. In particular there exists a high degree of localisation, since the alkyl chain contributes only to a very low percentage to this molecular orbital. On the contrary the same chain always plays a central role in the contribution to the neighbouring peak A. These two aspects together with the particular shape of the spectra can be considered as a fingerprint of the UPS emission in these materials [6].

It is also very interesting to compare the experimental results with the calculated gas phase ionisation potential, I_g. In this way it is possible to get an impression about the degree of interaction between the molecules in the solid state. As a matter of fact we can assume that the difference between I_g and I_P is proportional to the strength of the polarisation effect in the solid state and this difference is 2.5 and 1.3 eV for HNDO and HCDO, respectively. This result means that HNDO molecules interact in the solid state stronger than HCDO. Finally, the VL shift at the interface oxadiazoles/Au is -1.2 and -1.4 eV for HNDO and HCDO, respectively. This shift. It is an indication of the existence of a dipole layer at the interface [5].

5. Acknowledgements

6. References

[1] J. Kido, C. Ohtaki, K. Hongawa, K. Okuyama, K. Nagai, Jpn. J. Appl. Phys. 32 (1993) L917.
[2] A. J. Mäkinen, I. G. Hill, T. Noda, Y, Shirota, Z. H. Kafafi, Appl. Phys. Lett. 78 (2001) 670.
[3] Y. Hamada, C. Adachi, T. Tsutsui, S. Saito, Jpn. J. Appl. Phys. 31 (1992) 1812.
[4] B. Schulz, M. Bruma, L. Brehmer, Adv. Mater. 9 (1997) 601.
[5] H. Ishii, K. Sugiyama, E. Ito, K. Seki, Adv. Mater. 11 (1999) 605.
[6] M.B. Casu, P. Imperia, S. Schrader, B. Schulz, F. Fangmeyer, H. Schürmann, "Electronic Structure of Ordered Langmuir-Blodgett Films of an Amphiphilic Derivative of 2,5-Diphenyl- 1,3,4-Oxadiazole, in "Novel methods to study Interfacial Layers", editors D. Möbius and R. Miller, in the Series "Studies in Interface Science", Vol. 11, page 121, Elsevier, 2001
[7] K. Sugiyama, D. Yoshimura, T. Miyamae, T. Miyazaki, H. Ishii, Y. Ouchi, K. Seki, J. Appl. Phys. 83 (1998) 4928.

The application of synchrotron radiation as a tool for the investigation of self-assembled monolayers

K. Heister[1], S. Frey, M. Zharnikov, and M. Grunze

Lehrstuhl für Angewandte Physikalische Chemie, Universität Heidelberg, Im Neuenheimer Feld 253, 69120 Heidelberg, Germany
[1] *now at Max-Born-Institut, Max-Born-Straße 2a, 12489 Berlin, Germany*

Self-assembled monolayers (SAM) are close-packed 2D arrays of rod-like organic adsorbate molecules. They are chemically bonded to the substrate via their head group while the molecular chain (=spacer) with a certain end group functionality points away from the substrate. Because of this architecture SAMs are an attractive tool to functionalize/passivate a substrate[1] or to laterally structure a surface.[2,3] The structure of a SAM adlayer is governed by the interplay of the intermolecular forces and the substrate-adsorbate-interaction that promote a high degree of order in these films.[4] To evaluate the balance of forces in this system we
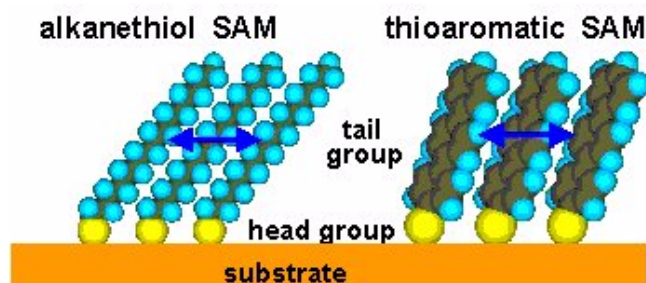
Fig 1: Sketch of aliphatic and aromatic SAMs.

applied synchrotron radiation-based surface analysis techniques, like near-edge x-ray adsorption fine structure (NEXAFS) and high resolution photoelectron spectroscopy (HRXPS), to investigate the properties of SAMs with a thiolate head group for different types of tail groups (see Fig. 1) and substrates. In parallel we studied SAM modification by x-ray and electron irradiation, which can happen non-intentionally during the acquisition of NEXAFS or XPS spectra. We analyzed in detail the consequences of x-ray and electron irradiation to alkanethiolate (AT) SAMs on Au substrates, which is important both for the application of SAMs, e.g. as a resist/template in lithography, and the non-destructive spectroscopic investigation of SAMs.

Fig. 2 shows the Au 4f HRXPS spectra for a clean (22×√3)-reconstructed and a SAM-covered Au substrate with (111) texture at an energy resolution ΔE better than 0.1 eV. Due to the high surface sensitivity at low photon energies the Au 4f components corresponding to the outermost Au layer are clearly perceptible. The Au $4f_{7/2}$ and Au $4f_{5/2}$ surface components (blue) of the clean (111) textured Au substrate are noticeably separated from the bulk doublet components (pink). If this substrate is covered by dodecanethiolates (C12) and biphenylthiolates (BP0) the Au 4f components of the outer Au layer
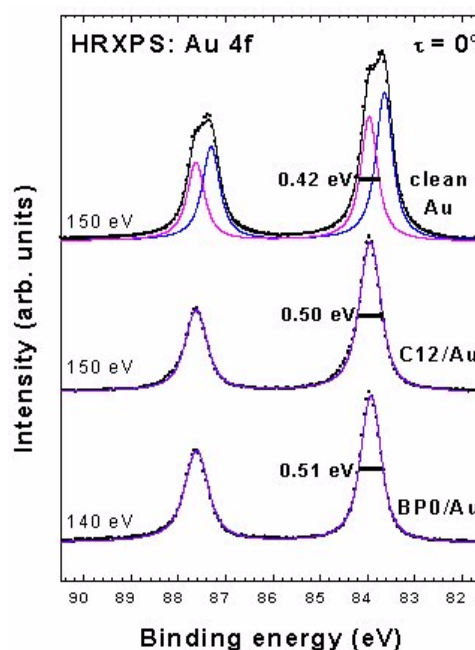

Fig 2: HRXPS Au 4f spectra of clean and SAM-covered Au surface.

shift towards higher binding energies (BE).[5] This indicates a strong adsorbate-substrate bond that lifts the Au surface reconstruction.[6] There is no dif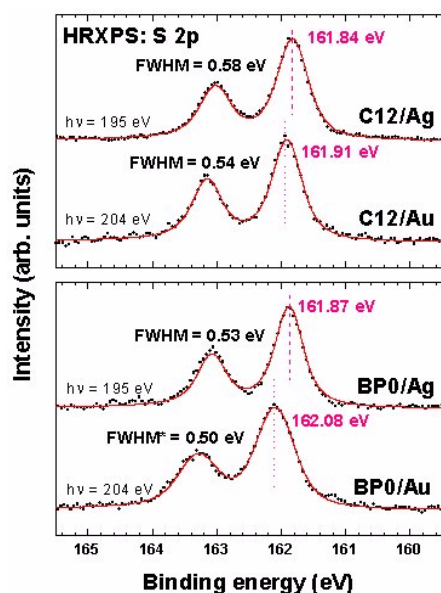ference in the peak position of the surface component between the aliphatic (C12) and aromatic (BP0) adlayer, which shows the insensitivity of the head group-substrate bond to the identity of the spacer. For the Ag substrate, the Ag $3d_{5/2}$ spectra (not shown here) exhibit a small (but noticeable) downward BE shift (by ~0.05 eV) of the component of the outermost Ag atoms upon SAM formation confirming that a strong bonding to the substrate also occurs in the case of Ag.[5]

As to the head group, the S 2p HRXPS spectra in Fig. 3 show a single S 2p doublet (S $2p_{3/2}$ and S $2p_{1/2}$) for both C12 and BP0 on Au and Ag with a peak position at lower BEs on Ag as compared to the Au surface, indicating a larger chemical shift (with respect to unbound thiols) and/or electron relaxation of the S 2p core level on Ag.[5]

Fig 3: HRXPS S 2p spectra of aliphatic and aromatic SAMs on Au and Ag.

We carried out a detailed analysis of the structural properties of the aromatic thiolates in dependence of their molecular length (CH_5SH: TP, CH_5CH_4SH: BPT, $CH_5CH_4CH_5SH$: TPT) and the substrate (Au, Ag)[7] to compare these properties with the characteristics of aliphatic thiolate SAMs.[8] The NEXAFS C 1s spectra in Fig. 4 show a strong linear dichroism of the characteristic resonances for all aromatic SAMs (except for TP/Au) indicating well-ordered monolayers with a nearly upright orientation of
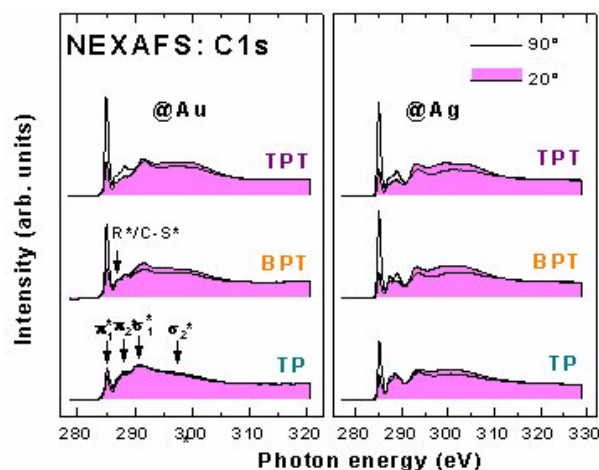
Fig 4: NEXAFS C 1s spectra of aromatic SAMs on Au and Ag at gracing (20°) and normal (90°) x-ray incidence.

the phenyl entities.[7] The data analysis shows clearly that the tilt angle decreases with the chain length, in contrast to the behavior of aliphatic thiolates, indicating an enhanced importance of the intermolecular forces between the spacers in aromatic SAMs. Additionally, the average tilt angle is less dependent on the substrate for the aromatic films (e.g. 16° for TPT@Ag, 20° for TPT@Au)[7] as compared to the aliphatic thiolates, in which the tilt angle is much larger on Au (30-33°) than on Ag (10-12°).[8] This manifests once more the dominated role of the intermolecular interaction in aromatic SAMs.[4] Further differences between the thioaliphatic and thioaromatic systems are reflected in the HRXPS data. The C 1s spectra in Fig. 5 show a quite different substrate dependency for aliphatic and aromatic thiolates.

Fig 5: HRXPS C 1s spectra of aliphatic and aromatic SAMs on Au and Ag.

Whereas the BE of the C 1s emission line is quite similar for BP0 on Ag and Au, the C 1s peak position for aliphatic SAMs (here C12) is significantly different for these both substrates ($\Delta E \approx$ 0.3-0.4 eV). This can only be explained by different molecular arrangements in these systems, as implied also by the NEXAFS data.[7,8]

The irradiation of AT SAMs by X-rays (necessary for an electron spectroscopy experiment) can damage the SAM significantly due to the excitation of secondary and photoelectrons in the substrate.[9] These electrons cause dehydrogenation of the SAM, desorption of molecular fragments, thickness reduction, the appearance of double bonds between adjacent carbon radicals, and the loss of orientational and conformational order as can be seen in the C 1s NEXAFS spectra for electron-irradiated octadecanethiolate on Au in Fig. 6.[10] Furthermore, a new, irradiation-induced sulfur species can be observed in the XPS S 2p spectra at the expense of the pristine thiolate head groups (Fig. 7).
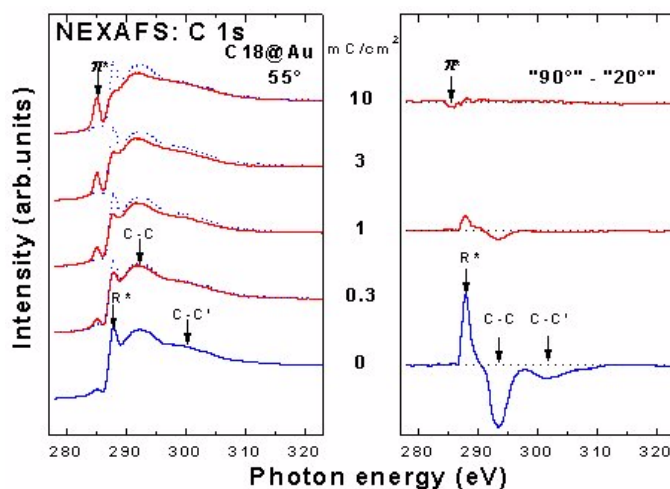
Fig 6: NEXAFS C 1s spectra of aliphatic SAMs in the course of e⁻-irradiation at 55° x-ray incidence and the difference spectra of normal and gracing incidence.
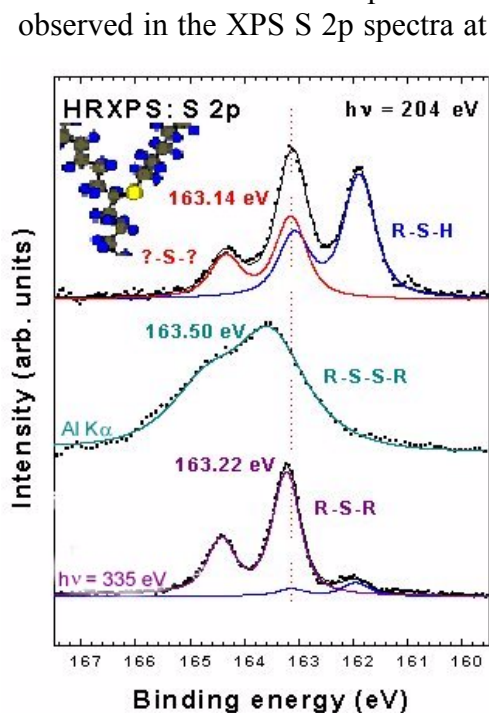
Fig 7: HRXPS S 2p spectra of an x-ray irradiated aliphatic SAM in comparison to reference systems.

The comparison of the BE position of the corresponding S 2p doublet with those of several reference sample (Fig. 7) reveals a chemical equivalence of the irradiation-induced sulfur species to a dialkylsulfide entity.[9] XPS depth profiling by variation of photon energy and emission angle indicates that these species are predominantly located above the head group-substrate interface. This means that the cleavage of the thiolate-substrate bond leaves a mobile sulfur species which easily bonds to an adjacent carbon radical and forms a sulfide bridge as sketched in the inset of Fig. 7.[9] This process contributes to irradiation-caused crosslinking within the adlayer. At the same time, the damage of the S/substrate interface (along with the decrease of the contact angle) makes irradiated areas sensitive to wet etching, which makes aliphatic SAMs suitable for the application as a positive lithographic resist.[11]

These above results show thereby the utility of synchrotron radiation-based techniques for the investigation of thin organic films and, in particular, SAMs.

References

(1) A. Ulman, An Introduction to Ultrathin Organic Films From Langmuir-Blodgett to Self-Assembly (Academic Press, Boston, 1991); Chem. Rev. **96** (1996) 1533.

(2) Y.N. Xia, G.M. Whitesides, Ang. Chem. Int. Edit. **37** (1998) 551.

(3) A. Gölzhäuser, W. Eck, W. Geyer, V. Stadler, T. Weimann, P. Hinze, M. Grunze, Adv. Mater. **13** (2001) 806

(4) M. Zharnikov, S. Frey, H. Rong, Y.J. Yang, K. Heister, M. Buck, M. Grunze, Phys. Chem. Chem. Phys. **2** (2000) 3359.

(5) K. Heister, M. Zharnikov, M. Grunze, L.S.O. Johansson, J. Phys. Chem. B **105** (2001) 4058.

(6) M.S. Yeganeh, S.M. Dougal, R.S. Polizzotti, P. Rabinowitz, Phys. Rev. Lett. **74** (1995) 1811.

(7) S. Frey, V. Stadler, K. Heister, W. Eck, M. Zharnikov, M. Grunze, B. Zeysing, A. Terfort, Langmuir **17** (2001) 2408.

(8) G. Hähner, M. Kinzler, C. Thummler, Ch. Wöll, M. Grunze, J. Vac. Sci. Technol. A **10** (1992) 2758.

(9) K. Heister, M. Zharnikov, M. Grunze, L.S.O. Johansson, A. Ulman, Langmuir **17** (2001) 8.

(10) M. Zharnikov, S. Frey, K. Heister, M. Grunze, Langmuir **16** (2000) 2697.

(11) H.U. Müller, M. Zharnikov, B. Völkel, A. Schertel, P. Harder, M. Grunze, J. Phys. Chem. B **102** (1998) 7949.

Response of biphenyl-substituted alkanethiol self-assembled monolayers to electron irradiation: Damage suppression and odd-even effects

M. Zharnikov, S. Frey, H.-T. Rong, K. Heister, and M. Grunze

Angewandte Physikalische Chemie, Universität Heidelberg, Im Neuenheimer Feld 253, 69120 Heidelberg, Germany

M. Buck

School of Chemistry, St Andrews University, North Haugh, St Andrews, KY16 9ST, United Kingdom

The increasing miniaturization of integrated devices and new areas of biology and medicine demand the development of novel methods for the fabrication of micro- and nanostructures. One of the proposed methods for extending lithography down to nanometer scales, applies electron-beam patterning of a new kind of lithographic resist - self-assembled monolayers (SAMs).The further development of the SAM-based lithography and, in particular, chemical lithography[1] depends on the progress in the technology of electron beam patterning and on the molecular engineering of the SAM resist constituents.

In particular, the reaction of a SAM towards electron irradiation can be affected by the variation of the long chain spacer. In aliphatic thiol-derived SAMs both the alkyl chains and the S-Au interface are affected through the electron-induced dissociation of C–H, C–C, C–S, and substrate-thiolate bonds.[2,3] The most noticeable processes are the loss of orientational and conformational order, partial dehydrogenation with C=C double bond formation, desorption of film fragments, reduction of the pristine thiolate species, and the appearance of a new sulfur species. In contrast to the aliphatic SAMs, almost all irradiation-induced processes resulting in the entire damage of these systems were found to be essentially suppressed in the pure aromatic SAMs.[4] Most important of all, the orientational order in the films and the anchoring to the substrate by substrate-sulfur bond are still retained upon irradiation, even though to a somewhat reduced degree. At the same time, C-H bond scissions in the aromatic matrix occur to a significant extent, which subsequently results in irradiation-induced cross-linking between the neighboring aromatic-chain moieties. Also, the bonds within a functional terminal group are cleaved by electrons, which can result in their modification.

The response of the thioaromatic films to electron irradiation can be affected to a definite extent by the incorporation of a short aliphatic chain between the aromatic moiety and thiolate headgroup.[5] The molecular packing density and orientation of the biphenyl (BP) moieties in such 4,4'-biphenyl-substituted alkanethiols CH_3-$(C_6H_4)_2$-$(CH_2)_nSH$ (BPn) exhibit odd-even variation with the length of the aliphatic chain: A denser molecular packing and a less tilted orientation of the BP moieties occur for an odd number of the CH_2 units in the BPn SAMs on
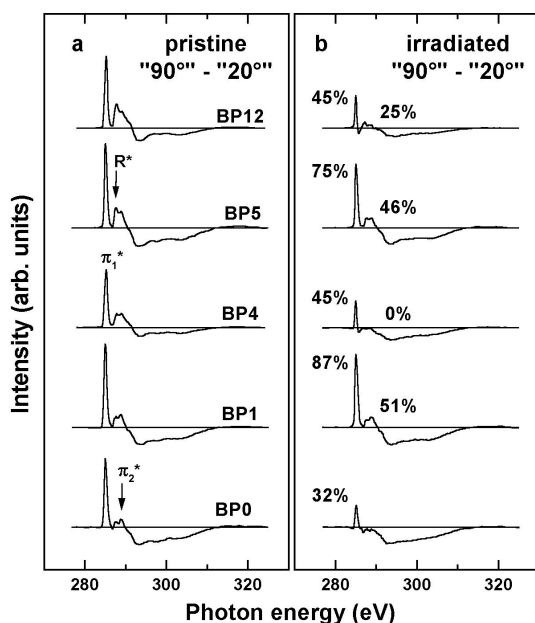

Fig. 1. The differences of the NEXAFS spectra acquired at incident angles of 90° and 20° for the pristine (a) and irradiated (b) BPn films. The π_1^*, π_2^*, and R* anisotropy peaks are indicated. The amplitudes of the π_1^* and R* anisotropy peaks for the irradiated films with respect to the corresponding values for the pristine SAMs are shown at the left and at the right of the curves in (b).

Au, whereas a reduced density and a larger tilt of the BP moieties are observed for an even number of the CH_2 units.[6,7] Whereas BPn SAMs react to electron irradiation in the same manner as pure aromatic SAMs,[4] the odd-even differences in the SAM packing affect the extent of the irradiation-induced changes. The densely packed SAMs are much more stable with respect to electron bombardment than the less densely packed films, as clearly seen from the noticeable differences in the extent of the irradiation-induced processes, such as modification of functional groups, thickness reduction, disordering, reduction of the pristine thiolate species, and the appearance of new irradiation-induced sulfur species.[5] Some of these differences are visualized by Figs. 1 and 2, where the differences of the NEXAFS spectra acquired at incident angles of 90° and 20° (so-called linear dichroism) and the IRRAS spectra in the range containing the characteristic vibration band of the methyl entity at ~1380 cm^{-1} are shown for both the pristine (a) and irradiated (b) BPn SAMs.

The relation between the packing density and the extent of the irradiation-induced changes seems to be a general phenomenon in monomolecular films, which provides a tool to tailor the reaction of these systems towards ionizing radiation for lithographic applications. A possible explanation of this behavior is a larger delocalization and a stronger relaxation of the initial electronic excitation in a better ordered and densely packed monomolecular layer.

The results obtained for the BPn SAMs have an additional aspect. The introduction of an aromatic spacer increases dramatically the stability of these systems with respect to electron irradiation. It is the cross-linking between the adjacent aromatic moieties initiated by the irradiation induced scission of C-H bonds in the aromatic rings which can be accounted for as the major reason responsible for this stability. Even the thiolate-gold interface remains essentially non-damaged because the quasi-polymerization hinders any molecular or atomic shift or movement at and in the vicinity of this interface. A considerable electron-induced damage at the thiolate-gold interface occurs only in the case if the aliphatic part is long enough (BP12), because a long alkyl chain can accommodate conformational defects associated with the cleavage of either S−Au or S−C bond.
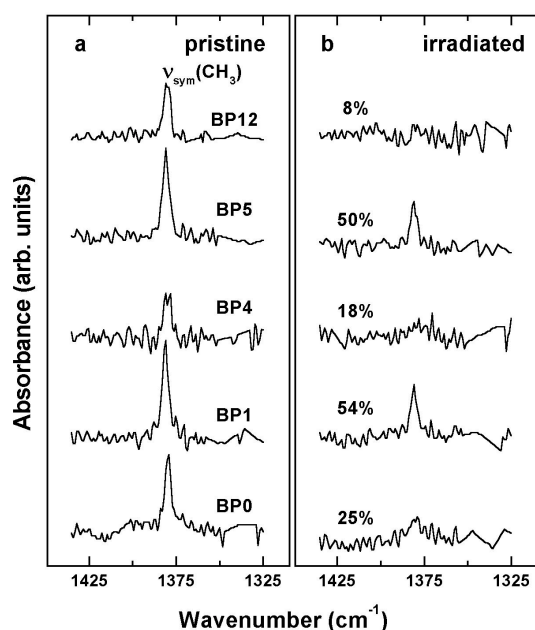
Fig. 2. The IRRAS spectra of the pristine (a) and irradiated (b) BPn SAMs in the range containing the characteristic vibration band of the methyl entity at ~1380 cm^{-1}. The intensity of this mode for the irradiated films with respect to the corresponding values for the pristine SAMs are indicated in (b). Note, that the values for BP12, and BP4 are rather rough estimates, because of the low intensity of the considered mode.

References:

(1) W. Eck, V. Stadler, W. Geyer, M. Zharnikov, A. Gölzhäuser, M. Grunze, Adv. Mater. **12**, 805 (2000).

(2) M. Zharnikov, S. Frey, A. Gölzhäuser, W. Geyer, and M. Grunze, Phys. Chem. Chem. Phys. **1**, 3163 (1999).

(3) M. Zharnikov, S. Frey, K. Heister, and M. Grunze, Langmuir **16**, 2697 (2000).

(4) W. Geyer, V. Stadler, W. Eck, M. Zharnikov, A. Gölzhäuser, and M. Grunze, Appl. Phys. Lett. **75**, 2401 (1999).

(5) S. Frey, H.-T. Rong, K. Heister, Y.-J. Yang, M. Buck, M. Zharnikov, Langmuir, in press.

(6) M. Zharnikov, S. Frey, H. Rong, Y.-J. Yang, K. Heister, M. Buck, M. Grunze, Phys. Chem. Chem. Phys. **2**, 3359 (2000).

(7) H. T. Rong, S. Frey, Y.-J. Yang, M. Zharnikov, M. Buck, M. Wühn, Ch. Wöll, G. Helmchen, Langmuir **17**, 1582 (2001).

Rotational Band Shapes of NO $b^3\Pi_{0,1,2}$ $np\lambda$ $^2\Lambda(v = 0)$ Rydberg States After Dissociation Into Fragments O $(^4S)3s$ $^3S_1$ + N $^4S_{3/2}$

A. Ehresmann, H. Liebel, M. von Kröger, H. Schmoranzer

Fachbereich Physik, Universität Kaiserslautern, D-67653 Kaiserslautern

Motivation. Most of the assignments of vibronic Rydberg states to features in absorption, photoelectron, photoion or fluorescence excitation spectra are based on quantum defect analysis. The quantum defect analysis is adequate to analyse spectra recorded at exciting-photon energy bandwidths of about 10 meV and more. However, such a kind of analysis is getting more and more problematic the narrower the bandwidth of the exciting-photons can be made in experiments. On the other hand, if a bandwidth can be used where single ro-vibronic transitions are observable assignments of the spectral features to transitions are unequivocally possible. At nowadays third generation synchrotron radiation sources (standard beamlines) it is possible to obtain exciting-photon energy bandwidths of about 1 meV for photons with energies of around 20 eV. In fluorescence excitation spectra this small bandwidth is not broadened further by other apparatus effects, in contrast to photoelectron spectroscopy where the bandwidth of the exciting-photons is convolved with the transmission function of the electron spectrometer. A resolution of about 1 meV results in fluorescence excitation spectra which are difficult to analyse by quantum defect theory and where single ro-vibronic transitions are not yet resolved. In this case the comparison of measured rotational band shapes to simulated band shapes may be the tool of choice for an analysis of the spectra.

Experimental. In order to elucidate this task for a particular example, an excitation spectrum for undispersed fluorescence of wavelengths between 115 nm and 200 nm and an absorption spectrum were measured simultaneously after photoexcitation of NO (T = 300K) at exciting-photon energies between 16.00 eV and 16.57 eV at the 3m NIM-2 beamline at BESSY I. In this exciting-photon energy range the undispersed fluorescence intensity signal is proportional to the fragment-state selective photodissociation cross section into fragment pairs O $(^4S)3s$ $^3S_1$ + N $^4S_{3/2}$ (Ehresmann et al. 2001). An exciting-photon energy bandwidth of 1.6 meV as a result of a compromise between a good signal-to-noise ratio during limited beamtime and very narrow bandwidth was achieved. The measured fluorescence excitation and absorption spectra are shown in Figure 1.

Results. Peaks belonging to the NO $b^3\Pi_{0,1,2}$ $np\lambda$ $^2\Lambda(v = 0)$ Rydberg states in the fluorescence excitation spectrum (Erman et al. 1995) were analysed for their fine structure and shape. The fine-structure and shape of these peaks originate either from different rotational bands belonging to the same vibronic state or from the overlap of different electronic states formed by the different ways of electronic coupling of the Rydberg electron to the molecular ion core.

In a certain approximation only the two electronic states NO $b^3\Pi_{0,1,2}$ npπ $^2\Sigma^+$ and NO $b^3\Pi_{0,1,2}$ npσ $^2\Pi$ contribute to the fine-structure of the observed peaks (Ehresmann et al. 2001). The expected intensity distribution among the different ro-vibronic transitions was simulated and the resulting band shapes for the vibronic transitions for both electronic states where calculated by a convolution of the calculated intensity pattern with a Gaussian of 1.6 meV.
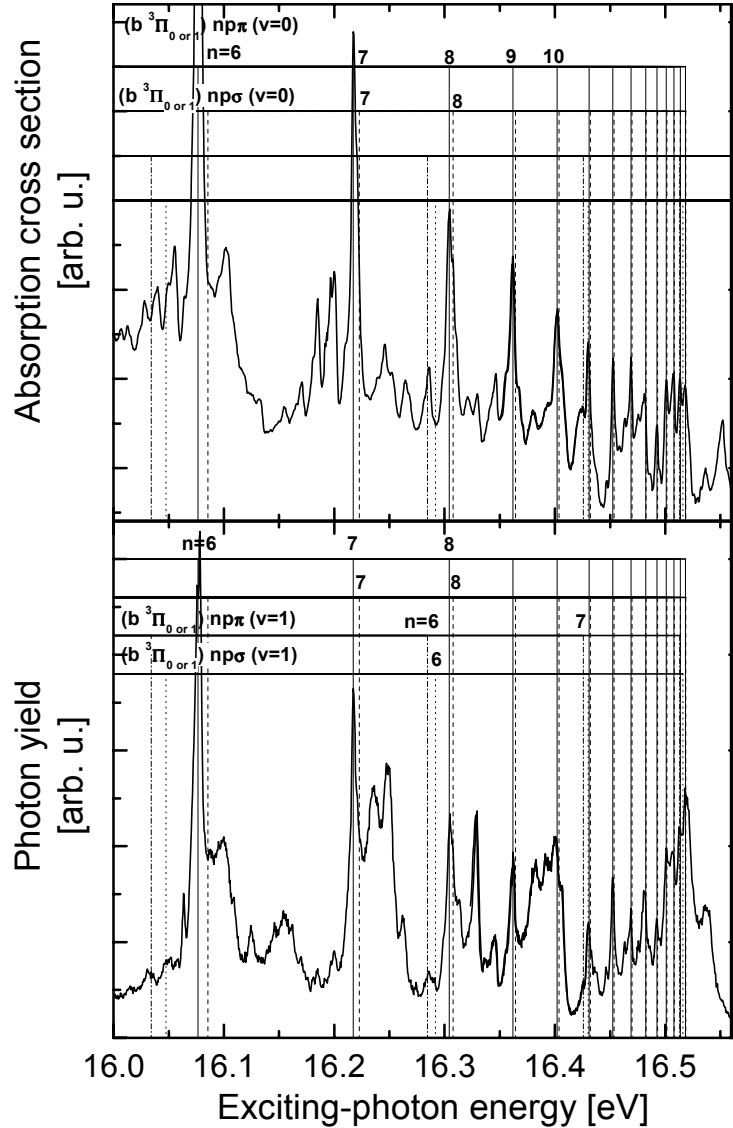

Fig. 1: Measured absorption and VUV-fluorescence excitation spectra.

The simulated band shapes were then used to fit the experimentally observed peak shapes. Fit parameters of this procedure were only the intensity ratio between the bands belonging to the different electronic states and the energy difference between the two respective band heads. The number and shape of the peaks in the recorded spectra could be explained through an overlap of the two different rotational band shapes for the two electronic states (see Fig.2). As a result of the fit it turned out that the two electronic states are populated within the fit accuracy with a branching ratio roughly independent of the Rydberg electron's principal

quantum number (up to n = 13) and that the energetic distance between the two band heads narrows as n increases. The observed fine-structure is therefore caused by overlapping rotational band shapes for two different electronic states.
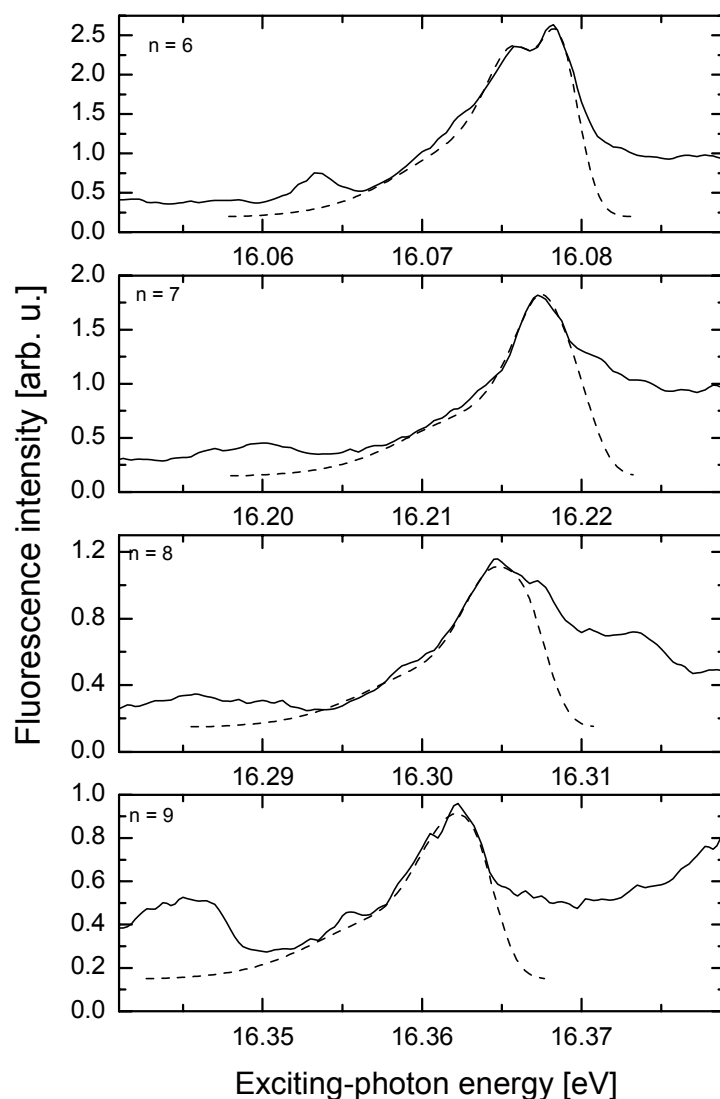
Fig.2: Comparison between the measured band shapes (full curve), seen in fluorescence, and the simulated band shapes (dashed curve) for the NO $b^3\Pi_{0,1,2}$ npπ $^2\Sigma^+$ (v = 0) and NO $b^3\Pi_{0,1,2}$ npσ $^2\Pi$ (v = 0) states (see text).

References

Ehresmann A, Liebel H, von Kröger M, Schmoranzer H, *J. Phys. B: At. Mol. Opt. Phys.* **34**, 2893 (2001)

Erman P, Karawajczyk A, Rachlew-Källne E, Strömholm C, *J. Chem. Phys.* **102**, 3064 (1995)

Branching Ratios of Radiative Transitions from the Decay of the (sp,25-)– and (pd,25)–Doubly Excited He States

S. Mickat, S. Kammer, B. Zimmermann, K.-H.Schartner
I. Physikalisches Institut, Justus-Liebig-Universität, D-35392 Giessen

H. Schmoranzer, A. Ehresmann, H. Liebel
Fachbereich Physik , Universität Kaiserslautern, D-67663 Kaiserslautern

R. Follath, G. Reichardt
BESSY mbH, D-12489 Berlin

The radiative decay of doubly excited He states with the lower energy electron in the N = 2 shell has been shown to be detectable [1], even when dispersive spectrometers are applied [2]. Moreover, calculations of the fluorescence yields of the three (sp,2n+), (sp,2n-) and (pd,2n) series (traditional notation) and of the branching ratios for populating ms and md levels in singly excited He (fig.1) have been carried out recently [3,4]. The doubly excited levels with n = 5 are of special exprimental interest since Zitnik et al. [4] analyzed in detail the population of ms and md levels for m = 2,...,8. The results of the first spectroscopic study of these decay branches using the photon induced fluorescence spectroscopy (PIFS) are presented and compared with the mentioned calculations.

The experiments were carried out at the U125/1–PGM beamline of BESSY II. The linearly polarized undulator radiation with a bandwidth of 4 meV was focussed into a differentially pumped target cell containing He at pressures between 5 mbar and 50 mbar. Typically 10 mbar was used. The photon beam with cross section dimensions of 50 μm x 100 μm replaced the entrance slits of two 1m–normal incidence spectrometers, both equipped with two-dimensional position-sensitive photon detectors for the spectral range of the VUV and the visible, respectively. A small voltage of 10 V was applied to the entrance diaphragm of the target cell in order to attract photoions.
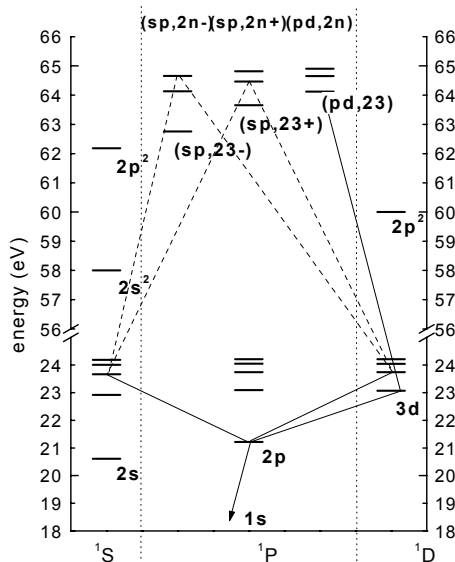

Fig. 1: He** and He* term diagram with decay modes to the ms and nd levels as well as transitions within singly excited He indicated.

In fig. 2 the fluorescence intensities and the ion yield across the (pd,24), the (sp,25-), the (pd,25) and the (sp,26-) resonances are shown. The (pd,2n) resonances preferentially decay into 1snd states showing a dominant 2pnd configuration. 1sms and 1smd states are populated in comparable amount through the decay of the (sp,2n-) states. This indicates their strong (2pnd) contribution. In this case, the decay into levels with m = n -1 is more probable than for levels with m = n. The (sp,2n+) states show a dominating ns contribution.

These features are in qualitative agreement with the predictions by Zitnik et al. [4]. Our quantitative comparison for the n = 5 resonances is so far limited to branching ratios 4d/4s and 5d/5s. The corresponding observed (4d–2p) and (4s–2p), (5d–2p) and (5s–2p) transitions have neighbouring wavelengths, reducing the influence of the relative detection sensitivity which,nevertheless, has been considered. The experimental alignment values of the 4d and 5d levels are in the status of evaluation. A correction of 10 % for the polarization fraction resulting from this alignment has been derived from the calculated ß values [4].

The table shows the comparison between our measured branching ratios and the values according to fig. 3 of Zitnik et al. [4]. The calculated 4d/4s ratio on the (sp,25-) resonance is not confirmed by the experiment while the measured 5d/5s ratio is in good agreement with the calculated one. The 5d/5s ratio measured on the (pd,25) resonance has a large error bar due to the low intensity of the (5s–2p) transition. The dominant 5d contribution of this doubly excited state is, nevertheless, evident. A further evaluation of the measurements aims at the alignment parameter and at the relative population of the md and ms levels for n = 5.
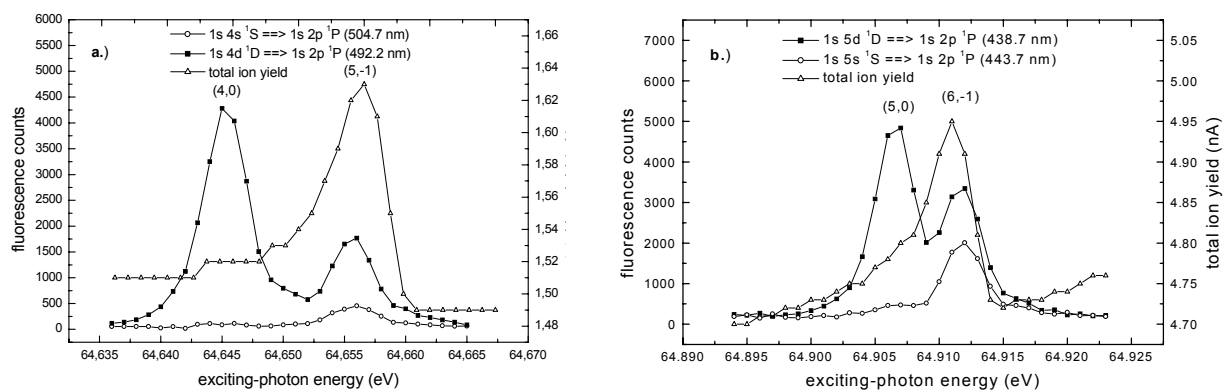
Fig. 2: Fluorescence intensities (and ion yield) of the (a) $(1s4d)^1D$ and $(1s4s)^1S$-$(1s2p)^1P$ transitions on the (4,0) and (5,-1) resonances, (b) $(1s5d)^1D$ and $(1s5s)^1S$-$(1s2p)^1P$ transitions on the (5,0) and (6,-1) resonances as function of the exciting photon energy.

(sp,25-)	Experiment	Calc. [4]
4d/4s	3.0 ± 0.3	1.94
5d/5s	0.6 ± 0.1	0.59
(pd,25)		
5d/5s	16 ± 8	30

References

[1]   J.-E. Rubensson et al., Phys. Rev. Lett. 83 (1999) 947

[2]   K.-H. Schartner et al., Phys. Rev. A 64 (2001) 040501-4 (R)

[3]   C.-N. Liu et al., Phys. Rev. A 64 (2001) 010501 (R)

[4]   M. Zitnik et al. Phys. Rev. A 65/3 (2002)

Circular dichroism of the helium double ionisation

S. Cvejanović, J. Viefhaus, M. Wiedenhöft[1], N. Berrah[1], and U. Becker

Abteilung Oberflächenphysik, Fritz-Haber-Institut der Max-Planck-Gesellschaft,
Faradayweg 4-6, 14195 Berlin, Germany
[1] *Department of Physics, Western Michigan University,*
Kalamazoo, MI 49008, USA

Being a showcase for investigating the electron dynamics within the system of three interacting Coulombic particles, double photoionisation (DPI) of He has over the last 8 years attracted unprecedented experimental and theoretical attention within the atomic and molecular community [1]. In this work we present the analysis of electron triple differential cross sections (TDCS) for circularly polarised light, measured at BESSY at the beamline UE56/2, which complement our previous studies under linear polarisation at this and other excess energies. The apparatus consists of a multi-detectors coincident set-up based on 7 time-of-flight (TOF) analysers and relies on the single-bunch operation mode of the BESSY storage ring.

The data were analysed using the global parametrisation of Cvejanovic and Reddish [2], to derive all amplitude parameters, including their relative phase shift, over a large range of excess energies. The applied parametrization relies on approximating the two ionization amplitudes of Huetz et al.[3] by Gaussian functions of the mutual angle θ_{ab}, with two parameters describing the half widths of the gerade and ungerade amplitudes (Γ_g, Γ_u), and the remaining two giving their relative strengths (η) and the phase angle difference (ϕ). The effects of electron correlations on the amplitude parameters Γ and η are quite well established already, but the role of the phase angle ϕ is presently not well understood.
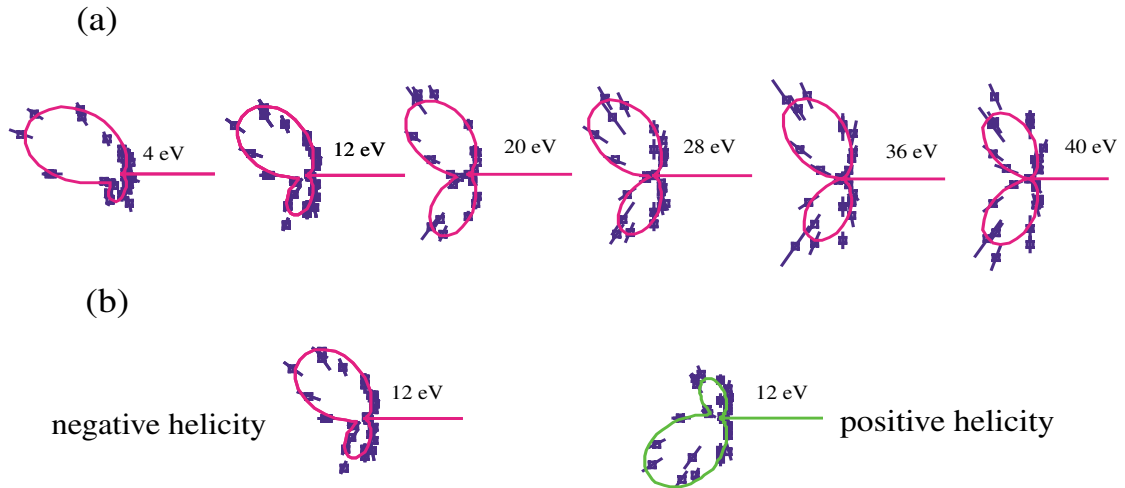
(a)

(b)

Figure 1: Triple differential cross sections of the double photoionization of He for circularly polarised radiation at 80 eV above the double ionisation threshold. (a) Energy sharing effects. The energies and the directions of the reference electron are indicated. (b) Helicity change for the E_{ref} = 12 eV

From the measurements at excess energy E = 80 eV with circularly polarised photons of both handedness, we have constructed the triple differential cross sections (TDCS) for all possible energy sharings between the detected electrons, an example of which is given in Figure 1. In the upper row we presented the variations of the triple differential cross section with energy sharing,

which is indicated by the energy of the reference electron (ejected in the horizontal direction). The form of the distribution has two lobes of slowly varying positions and strongly varying relative sizes, with a very asymmetric distribution corresponding to the largest energy asymmetry between the detected electrons. Beneath is shown the effect of changing the helicity of the light source in a representative case, showing that the lobe asymmetry changes the sign, in the same way as the sign of the lobe asymmetry will change if the two electrons of different energies will swap places under constant polarisation condition.
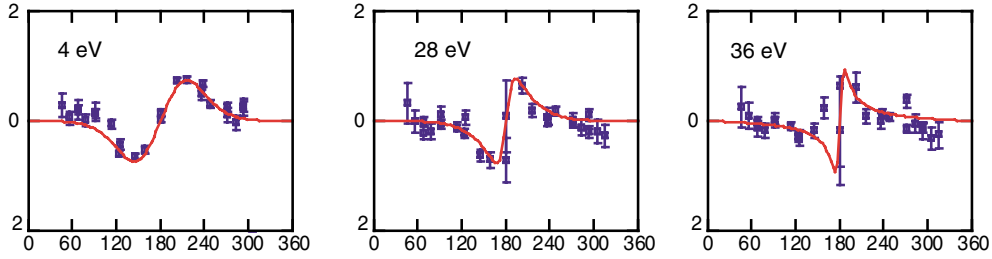
Figure 2: Normalised circular dichroism (CDAD) at E_{exc} = 80 eV. The energies of the reference electron are indicated. The curve represents the parametrisation.

By taking the normalised differences of the TDCS measured at different circular polarisation, presented in Figure 2, we were able to study the evolution (as a function of the energy sharing) of the circular dichroism in the angular distributions, so called CDAD [4, 5]. Those patterns are caused by the interference term between the gerade and the ungerade transition amplitudes, and in combination with the TDCS shown in Fig.1 allow the determination of a complete set of amplitude parameters which fully describe the double photoionisation process. By further reducing the parameter set by requiring that Γ_g and Γ_u are equal, which is a very good approximation at smaller energies, we arrive at a simple parametric curve describing the CDAD in purely geometrical terms, which beside the electron angles include the ratio (η) and the mutual angle (ϕ) between the amplitude vectors, as shown in Fig.3.
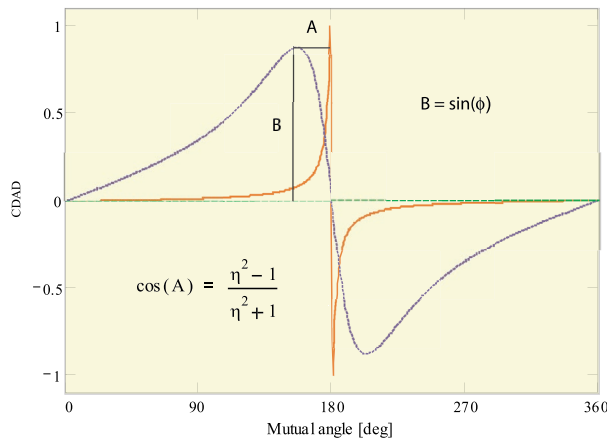

Figure 3: Parametrisation of the CDAD within the restricted amplitude model (see text). Two hypothetical amplitude sets reflect widely different cases of energy asymmetry between the ejected electrons, with the red curve representing the more symmetric distribution. The conspicuous features are the positions and the intensities of the extrema, which parametrise selectively via η and ϕ, as shown.

Both the circular and linear dichroisms in He are different manifestations of the interference effects between the gerade and ungerade amplitudes, which allow the study of the amplitude phase difference ϕ, which is otherwise inaccessible. We have demonstrated that the asymptotic behaviour of this term governs the specific features of the circular and linear dichroisms in a way that one can draw the parallels between understanding the intrinsic handedness for the double ionisation complex in the first case, and the redistribution among the ejected electrons of the energy and angular momentum of the absorbed photon in the latter one. This identifies the electron correlations as the main, if not exclusive, influence on the phase shift ϕ, stressing the overall importance of electron correlations in determining the dynamic features of the TDCS for all energies.

References

[1] J. S. Briggs and V. Schmidt, J. Phys. B 33, R1 (2000)

[2] S. Cvejanovic and T. Reddish, J. Phys. B 33, 4691 (2000)

[3] A. Huetz et al., J. Phys. B 24, 1917 (1991)

[4] J. Viefhaus et al., Phys. Rev. Lett. 77, 3975 (1996)

[5] K. Soejima et al., Phys. Rev. Lett. 83, 1546 (1999)

2p photoionization of atomic Nickel

K. Godehusen[1], T. Richter, P. Zimmermann
Institut für Atomare Physik und Fachdidaktik, Technische Universität Berlin

M. Martins[2]
Institut für Experimentalphysik, Freie Universität Berlin

Nickel in the gas phase exhibits a rather unique property that at the evaporation temperature for the production of an atomic beam (about 1800 K) the lowest states $3d^8 4s^2\ ^3F$ and $3d^9 4s\ ^3D$ of *both configurations $3d^8 4s^2$ and $3d^9 4s$ are populated.*

This offers the possibility for a comparison with corresponding spectra in the solid phase of Ni metal, Ni compounds and molecular Ni complexes where the Ni ground state in many-body $3d$ configuration interaction (CI) calculations employing the Andersen impurity model is described as a mixture of $3d^{10}$, $3d^9$ and $3d^8$ valence configurations [1, 2, 3, 4].

The experiments were carried out at the U49/2-PGM1 undulator beamline at the BESSY II electron storage ring in Berlin. By using electron bombardment the Ni metal was heated to about 1800 K forming an effusive atomic Ni beam. The linearly polarized synchrotron radiation intersected the atomic beam and the resulting photoelectrons were recorded.
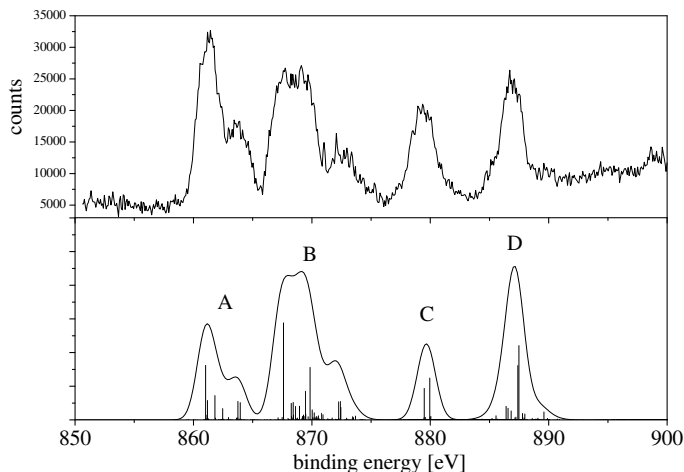
Figure 1: *Ni 2p photoelectron spectrum at hν=940 eV and results of the HF calculation (see text for explaination).*

For the detection of the photoelectrons a Scienta SES 200 hemispherical electron analyzer was used.

The experimental spectrum (see Fig. 1) consists of four main features which have some additional structure. The spectrum is dominated by the spin-orbit interaction of the $2p$ hole (i.e. the splitting between the $2p_{3/2}$ and the $2p_{1/2}$ states) which is in the order of 20 eV (splitting between A+B and C+D). Additionally there are two different populations of the $3d$ shell (i.e. $3d^8$ and $3d^9$) which lead to a binding energy difference for these configurations of about 8 eV in the ionic state (splitting between A and B, C and D). That means that the virtual degeneracy of the ground states is canceled by the core hole. These two splittings ($2p_{3/2} - 2p_{1/2}$ and $3d^8 - 3d^9$) are responsible for the four main features.

The additional structure seen in the experimental spectrum is due to the interaction between the $2p$ and $3d$ shell and the interaction within the $3d$ shell. In the latter case the $3d$ shell does not remain in the $3d^8\ ^3F$ or $3d^9\ ^1D$ state and the recoupling leads to an additional multiplet splitting up to some eV.

---

[1]Present address: BESSY GmbH
[2]Present address: Universität Hamburg

For a more detailed analysis of these interaction we did CI calculations of the atomic Ni $2p$ photoelectron spectrum using the Cowan code [5]. Figure 1 shows that the results of these calculations match very well with the experimental spectrum.
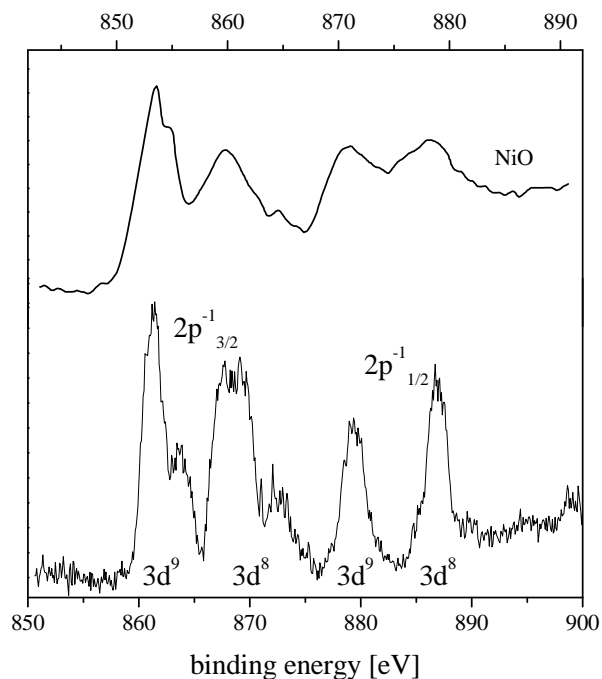

Figure 2: *Ni 2p photoelectron spectrum from Fig. 1 compared to the photoelectron spectrum from a NiO single crystal (from Parmigiani and Sangaletti [6]). The energy scale of the NiO spectrum was shifted by 8 eV to match the spectral features.*

Figure 2 shows the striking similarity between the spectra of atomic Ni and NiO. The spectrum from Parmigiani and Sangaletti [6] was taken from a NiO single crystal at grazing angle. It exhibits the same four main features and some of the additional structure as our spectrum. Here our investigation can give additional information for the solid phase: in our case the population of the $3d$ shell is well known and does not depend on the complicated influence of the crystal structure. It seems that for NiO the population of the $3d$ shell is very similar to the thermally excited Ni atom. This is an evidence for a rather localized character of the $3d$ orbitals in NiO.

A more detailed analysis of the results can be found in our upcoming paper.

References

[1] B. T. Thole and G. van der Laan, Phys. Rev. Lett. **67**, 3306 (1991).

[2] G. van der Laan, M. A. Hoyland, M. Surman, C. F. J. Flipse, and B. T. Thole, Phys. Rev. Lett. **69**, 3827 (1992).

[3] G. van der Laan, M. Surman, M. A. Hoyland, C. F. J. Flipse, B. T. Thole, Y. Seino, H. Ogasawara, and A. Kotani, Phys. Rev. B **46**, 9336 (1992).

[4] A. Tanaka, T. Jo, and G. A. Sawatzky, J. Phys. Soc. Jpn **61**, 2636 (1992).

[5] R. Cowan, *The theory of atomic structure and spectra* (University of California Press, Berkeley, 1981).

[6] F. Parmigiani and L. Sangaletti, J. Electron. Spec. and Rel. Phen. **98-99**, 287 (1999).

Core-level photoemission studies of atomic Ti in the region of the 2p excitation/ionization

T. Richter, K. Godehusen[1], P. Zimmermann
Institut für Atomare Physik und Fachdidaktik, Technische Universität Berlin

M. Martins[2]
Institut für Experimentalphysik, Freie Universität Berlin

$2p$ photoionization studies of Titanium in the gas phase are challenging both to the experiment and theory. The experimental side is confronted with problems of the high evaporation temperatures and the aggressiveness of the molten material. The theoretical side has to deal with the coupling properties of the non-filled $3d$-subshell and the near degeneracy of the $3d$ and the $4s$ orbitals.
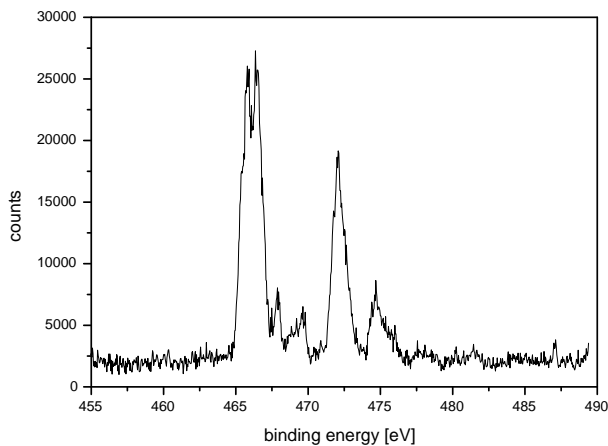
Figure 1: *Ti 2p photoelectron spectrum hν=540 eV*

The experiments were performed at the U49/2-PGM1 beamline. The photoelectrons were detected by a Scienta SES 200 electron analyzer.

Figure 1 shows the $2p$ electron spectrum taken at a photon energy of 540 eV. The spectrum can be divided into two parts corresponding to the fine structure splitting of the $2p$ subshell by the spin-orbit coupling into $2p_{3/2}$ and $2p_{1/2}$ levels. A closer look, however, reveals additional structures. These structures should attributed to several interactions. First one must take into account the electrostatic interaction between the $2p$ core hole and the $3d$ subshell of the valence electrons. This interaction is dominating in the case of the $3p$ core hole spectra with the consequence of a nearly pure LS coupling scheme for the $3p$ core hole spectra. The spin-orbit splitting of the 3p core hole can be neglected. For the $2p$ spectra the spin-orbit splitting is much larger but the many-body electrostatic interaction between the $2p$ core hole an the $3d$ subshell still has to be taken into account. Therefore an intermediate coupling scheme instead of the jj-coupling must be used.

In addition to the electrostatic $2p - 3d$ interaction there is also the electrostatic interaction *within* the $3d$ subshell, giving rise to the recoupling of the $3d$ subshell during the photoionization process. In this case the $3d$ subshell does not stay as a spectator but acts as a participator of the ionsation process. All these interactions must be carefully considered in the analysis of the Ti

---

[1]Present address: BESSY GmbH
[2]Present address: Universität Hamburg

$2p$ spectrum. Therefore we will carry out *ab initio* Hartree-Fock calculations to compare their results with the experimental spectrum.

As the second part of the investigations we measured the absorption spectrum in the region of the $2p$ resonances (about 454 to 467 eV). These resonances are due to the discrete transitions $2p \rightarrow 3d$. The absorption spectrum was obtained by photoion spectroscopy using a conventional time-of-flight analyzer. As in the case of the $2p$ photoelectron spectrum we plan to analyse the absorption spectrum by calculating the resonance structure.

Magnetic Circular Dichroism in the Total Ion Yield of Atomic Iron and Chromium

G. Prümper[1], O. Geßner[1], J. Viefhaus[1], B. Langer[1],
U. Becker[1], and H. Kleinpoppen[2]

[1] Fritz-Haber-Institut der Max-Planck-Gesellschaft, D-14195 Berlin, Germany
[2] University of Stirling, Atomic Physics Unit Stirling FK9 4LA, Scotland

Large non-resonant MCD effects

Magnetic Circular Dichroism (MCD) describes the different response of a magnetized sample to left- and right-handed circularly polarized light. In solid state studies, these effects are large at the 2p-edges of the 3d-transition metals. In the non-resonant region several eV away from absorption edges, MCD vanishes in absorption measurements of thin iron films; i.e. the relative difference in the absorption of left- and right handed radiation differs by less than 10^{-4} [1]. We performed the first experiment for polarized iron in the gas phase and in contrast to that observed a remarkably large polarization dependence of the ion yield of Fe-vapor far away from any absorption edge [3], figure 1. This difference to solid state experiments is easy to understand. The MCD effects are based on the selection rules of the magnetic quantum numbers of the orbital angular momentum. So the main contribution of the MCD asymmetry in the non-resonant region is proportional to the polarization of the orbital angular momentum in the ground state of iron with L=2

Fe: $1s^2\ 2s^2\ 2p^6\ 3s^2\ 3p^6\ 3d^6\ 4s^2\ \ ^5D_{4,3,2,1,0}$

All experiments with iron in the solid state indicate that the expectation value of the ground state orbital magnetic moment is smaller than 0.1 μB per atom as the main contribution to the magnetic moment is caused by the spin [1, 2]. So we explain the absence of non-resonant MCD in the solid state experiments by the absence of polarization in the orbital angular momentum. In order to check this hypothesis we made similar measurements on polarized chromium atoms which do not have any orbital angular momentum in the ground state.

Cr: $1s^2\ 2s^2\ 2p^6\ 3s^2\ 3p^6\ 3d^5\ 4s^1\ \ ^7S_3$

The results of the measurements on chromium are shown in figure 2. As expected below the 2p-threshold, we did not find any MCD.

Unexpected variation of the MCD with photon energy

Even though the existence of the non-resonant MCD is easy to understand, neither its size of several percent nor its variation with photon energy can be understood in the independent particle approximation. If the ionization of all closed sub-shells could be separated from the coupling to the 3d shell in the final ionic state, then their contribution to the MCD must vanish. In this case the measured variation in the ion yield of iron had to be assigned to the 3d shell ionization alone. A Hartree-Fock-calculation shows that the MCD of the 3d-shell cannot vary significantly for kinetic energies of more than 50 eV [5]. The most probable explanation for the observations is a strong coupling of the 3d- and the 3p-continua.
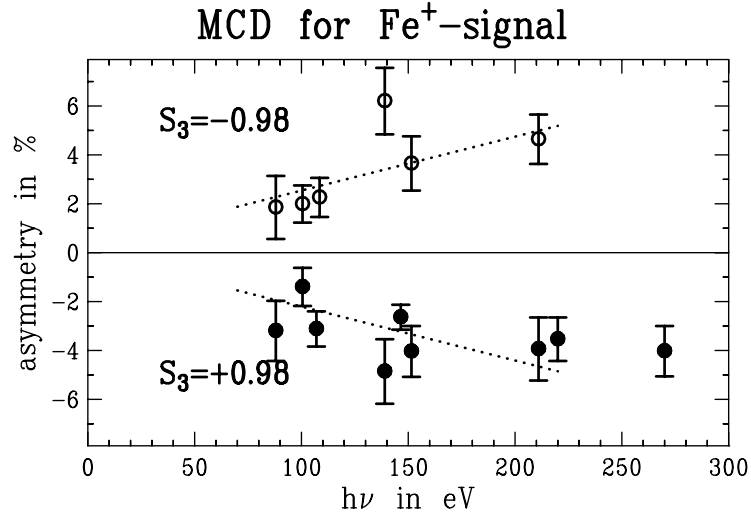
Figure 1: Measurement of the MCD in the ion-yield of singly charged iron ions. To minimize systematic errors, the measurement has been repeated with both helicities of the light. An increase of the MCD with photon energy is illustrated by the straight lines. This observation cannot be understood in the independent electron approximation.
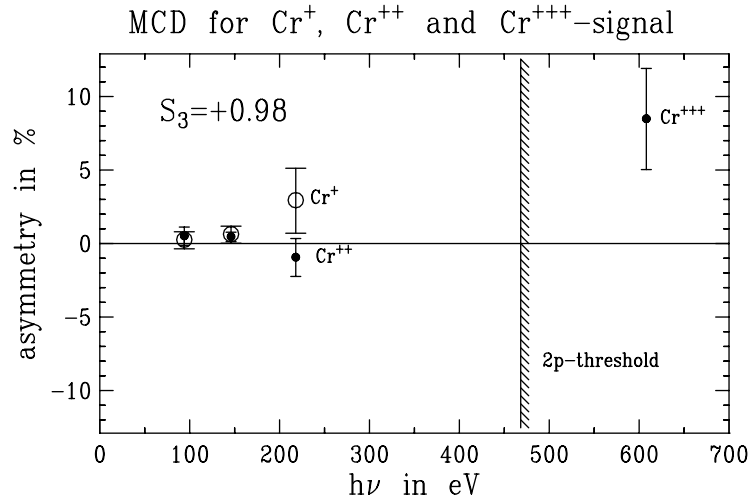

Figure 2: Measurement of the MCD in the ion-yield of polarized chromium atoms. Below the 2p-threshold, we did not find any MCD. This is consistent with non-relativistic models, since the orbital angular momentum in the ground state cannot be polarized. Above the 2p-threshold, relativistic effects may cause MCD. The result of a first measurent above 600eV is shown in the diagram.

The experimental technique:

Iron or chromium is evaporated in a 250 watt electron impact oven from an alsint (Al_2O_3) crucible at 1900 K. After collimation by a water cooled skimmer the iron atoms pass a hexapole magnet with an inner diameter of 7 mm and a pole tips field of 500 mT. The atoms with negative magnetic quantum numbers are deflected to the poles of the magnet while those with positive magnetic quantum numbers are pushed towards the beam axis. Behind a second skimmer the polarized atoms interact with the synchrotron radiation. A magnetic guiding field ($\approx 10\mu T$) was applied defining the direction of atomic polarization $\vec{A}$ at the position where the atomic beam intersects the ionizing radiation. The beam of polarized iron atoms crosses the beam of circularly polarized VUV synchrotron radiation from the UE56-2 PGM1 and PGM2 beamlines at BESSY II Synchrotron Light source [4]. (our typical operation parameters were: $h\nu$=100 to 200 eV, circular polarization $S_3 > 0.98$, flux 10^{14} photons/s).

The ions were detected in a pulsed time-of-flight ion spectrometer. The operation parameters were: pulse high +196V, pulse width 4μs, repetition rate 22 kHz, length of the ion path 10 cm. During the measurement the guiding field was switched with a frequency of 1Hz. In this way the two measurements of the ion count rate were performed at almost the same time and the influence of the varying intensities of the light source and the atomic beam do not need to be taken into account.

References

[1] Chen C T, Idzerda Y U, Lin H J, Smith N V, Meigs G, Chaban E, Ho G H, Pellegrin E and Sette F, Experimental Confirmation of the X-Ray Magnetic Circular Dichroism Sum Rules for Iron and Cobalt, Phys. Rev. Lett. **75**, 152 (1995).

[2] Thole B T, Carra Paolo, Sette F and van der Laan G, X-Ray Circular Dichroism as a Probe of Orbital Magnetization, Phys. Rev. Lett. **68**, 1943 (1992).

[3] Prümper G, Geßner O, Zimmermann B, Viefhaus J, Hentges R, Kleinpoppen H, Becker U, Absorption of Circularly Polarized VUV Radiation in Polarized Iron Vapor J. Phys. B, **34**, 2707 (2001).

[4] Weiss M R, Sawhney K J S, Follath R, Mertins H Ch, Schäfers F, Frentrup W, Gaupp A, Scheer M, Bahrdt J, Senf F and Gudat W First Results Of the Circularly Polarised Undulator Beamline At BESSY II, SRI (1999).

[5] Verner D A, Yakovlev D G, Astronomy and Astrophysics **109**, 125 (1995).

Ultraviolet/Visible-Fluorescence of OClO

R. Flesch, J. Plenge, M. Meyer[*], and E. Rühl

Fachbereich Physik, Universität Osnabrück, Barbarastr. 7, D-49069 Osnabrück, Germany
[*] L.U.R.E., Centre Universitaire Paris-Sud, Bâtiment 209 D, F-91898 Orsay Cedex, France

Chlorine dioxide (OClO) plays an important role as a trace gas in the lower and middle atmosphere, since its occurrence indicates perturbed atmospheric chlorine chemistry that is related to substantial ozone losses in the stratosphere. The electronic structure and ionic fragmentation of OClO have been studied in past, where synchrotron radiation has been applied [1, 2]. Excitation of molecules by vacuum ultraviolet (VUV) radiation leads often to dissociative ionization where excited atomic and molecular photofragments are formed. The subsequent relaxation is accompanied by the emission of light, which occurs often in the ultraviolet/visible (UV/VIS) regime. As a result, fluorescence spectroscopy provides detailed information on the fate of electronically excited states of atoms, molecules, and cations. We have investigated the UV/VIS fluorescence spectrum after photoexcitation of OClO in order to study the quantum states of its photoproducts that occur as a result of primary VUV excitation.

The experiments were carried out at the U49-1-SGM at BESSY, where neat OClO is introduced into a vacuum recipient. Fluorescence light is collected by a spherical mirror and a biconvex lens, finally it is refocused on the entrance slit of a high-resolution spectrograph (Jobin Yvon HR460) which is equipped with a nitrogen-cooled CCD-detector. Two different
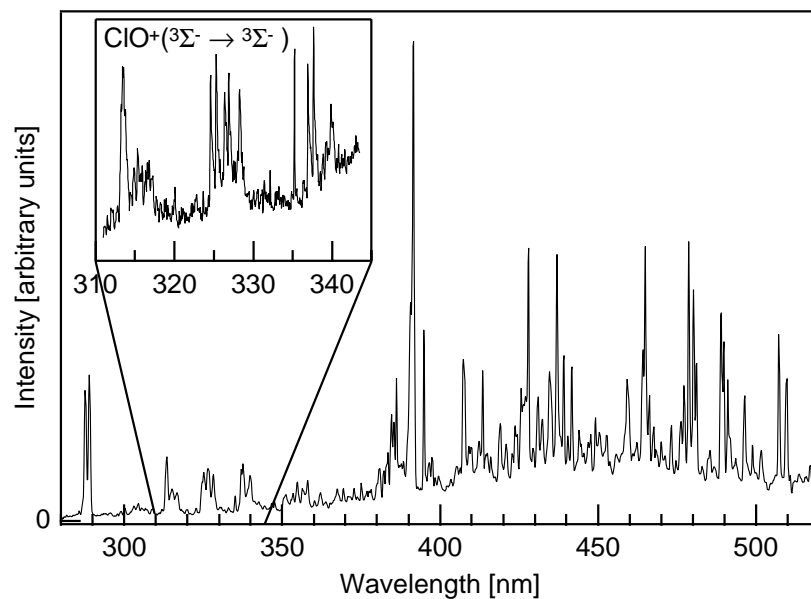
Fig. 1: Dispersed fluorescence spectrum of OClO (photon band width: $\Delta\lambda_{fluo} \approx 0.4$ nm). The spectrum has been recorded using undispersed synchrotron radiation. The inset shows the 310-340 nm regime at an enhanced spectral resolution ($\Delta\lambda_{fluo} \approx 0.1$ nm).

gratings (300 lines/mm and 1800 lines/mm) have been used for overview and high-resolution fluorescence spectra of selected spectral regions [3].

Fig. 1 shows a dispersed fluorescence spectrum of OClO recorded upon excitation with undispersed synchrotron radiation. Various emission lines and bands are observed. They are assigned to a variety of species which occur as a result of photofragmentation of OClO and subsequent radiative relaxation. The most prominent lines are due to the fluorescence of neutral and singly charged atomic species, such as O, O^+, Cl, and Cl^+ [4]. The formation of excited cations is a result of dissociative ionization, which is in agreement with earlier results from photoionization mass spectrometry [2].

In the wavelength regime between 310 nm and 340 nm occurs a variety of fluorescence lines which cannot be assigned to the above mentioned atomic species. These features were also recorded with enhanced spectral resolution, as shown in the inset of Fig. 1. The spectral shape of the structures gives clear evidence for molecular transitions, since they are characteristically shaded to the red, as a result of rotational fine structure. The lines are grouped in sequences, corresponding to vibrational transitions. We assign these features to the emission of ClO^+ for the following reasons: The photoelectron spectrum of ClO has revealed a variety of excited electronic states of ClO^+, where $^3\Sigma^-$ is the cation ground state [5]. Among the excited states, an electronically excited $^3\Sigma^-$ state is known to occur about 4 eV above the cation ground state [5]. Transitions between both states are optically allowed. Consequently, the structures that are observed between 310 nm and 340 nm are assigned to the $^3\Sigma^- \rightarrow {}^3\Sigma^-$ transition. A detailed analysis of the sequences and rotational fine structure is currently in progress.

Fluorescence spectra were also recorded after excitation with dispersed undulator radiation. The experiments indicate that the molecular features disappear in the Cl 2p-continuum (E>202 eV). It is assumed that the formation of electronically excited ClO^{+*} below this threshold is due to the process: $OClO + h\nu \rightarrow ClO^{+*} + O + e^-$. The lack of molecular fluorescence in the Cl 2p continuum can be rationalized in terms of efficient fission of the doubly charged molecule, so that atomic products are formed. Moreover, the population of different electronically excited states of ClO^+ may occur. This is consistent with results from multicoincidence experiments, where correlated atomic fragments as well as fission into the correlated cation pair $ClO^+ + O^+$ are observed in the Cl 2p-continuum.

References
1   R. Flesch, E. Rühl, K. Hottmann, and H. Baumgärtel, J. Phys. Chem. **97**, 837 (1993).
2   U. Rockland, H. Baumgärtel, E. Rühl, O. Lösking, H.S.P. Müller, and H. Willner, Ber. Bunsenges. Phys. Chem. **99**, 969 (1995).
3   A. Marquette, M. Gisselbrecht, W. Benten, and M. Meyer, Phys. Rev. A **62**, 22513 (2000).
4   http://physics.nist.gov/PhysRefData/IonEnergy/tblNew.html
5   D.K. Bulgin, J. M. Dyke, N. Jonathan, and A. Morris, J. Chem. Soc. Faraday Trans. II, **75**, 456 (1979).

Measuring the time-of-flight distribution of a hemispherical electron analyser in BESSY single bunch mode

O. Kugeler [1,2], S. Marburger [1]. U. Hergenhahn [1,2]

[1] Fritz-Haber-Institut der Max-Planck-Gesellschaft, D-14195 Berlin, Germany
[2] Max-Planck-Institut für Plasmaphysik, D-85748 Garching, Germany

Introduction

We have modified the electron detection system of a Scienta SES 200 hemispherical analyser [1]. Originally, this instrument is equipped with a fluorescent screen in the electron focal position, which is read out by a CCD camera. Since this integrating detection method is not suitable for electron-electron coincidence spectroscopy, we are now using a position-sensitive delay-line anode, as provided by Roentdek [2], that allows for a time-resolved measurement of every incoming electron.

The primary aim of the measurements presented here was to determine whether the time-of-flight differences between trajectories pertaining to equal kinetic energy in the hemispherical analyser were sufficiently small for its usage in coincidence sprectoscopy.

Experimental setup

Measurements were carried out at the U49/1-SGM beamline during the first single bunch beamtime in September 2001. The electron analyser was positioned in the dipole plane under an angle of 54.7° to the orbit plane of the storage ring. We have operated the lens in the position resolving mode with a magnification factor of 3. All spectra were recorded using a gas cell as target. Electrons were allowed to enter into the analyser through a thin slit in the gas cell, that was aligned along the photon beam. Thus events created in a linear interaction zone of about 15 mm could be imaged onto the detector. For the spectra shown here a 200 μm curved slit was applied between the retarding lens section and analyser electron lens. The anode was mounted such, that the position of the front microchannelplate exactly matched the electron focal position. The required anode voltages were delivered by a resistor cascade, powered by an ISEG HV supply. The whole anode system was electrically floating on the retarding voltage (RV) of the hemispherical detector. An acceleration voltage of 300 V was applied before the first MCP. Timing signals of the two Lecher wires and the upper MCP were amplified and discriminated with a DLATR6 differential amplifier and used as start signal for the time-measurement with a LeCroy TDC8/ISA PC-card. A delayed MCP pulse was used as common stop signal. The bunchmarker was recorded in an additional channel of the card. The time resolution of the system was limited by the intrinsic resolution of 500 ps of the PC-card.

Results

We have demonstrated the operation of a hemispherical electron analyser with a fast position sensitive readout based on the delay line principle. By that we were able to record the spread of transit times in our electron analyser, see figures 1 and 2. For pass energies of 75 eV or larger, the total time spread is less than 4 ns. From comparison of the experimental values for the time-of-flight with analytical calculations it becomes apparent, that the main influence on the spread is from the length differences of the Kepler orbits through the analyser itself, and not from the lens system. The analytical
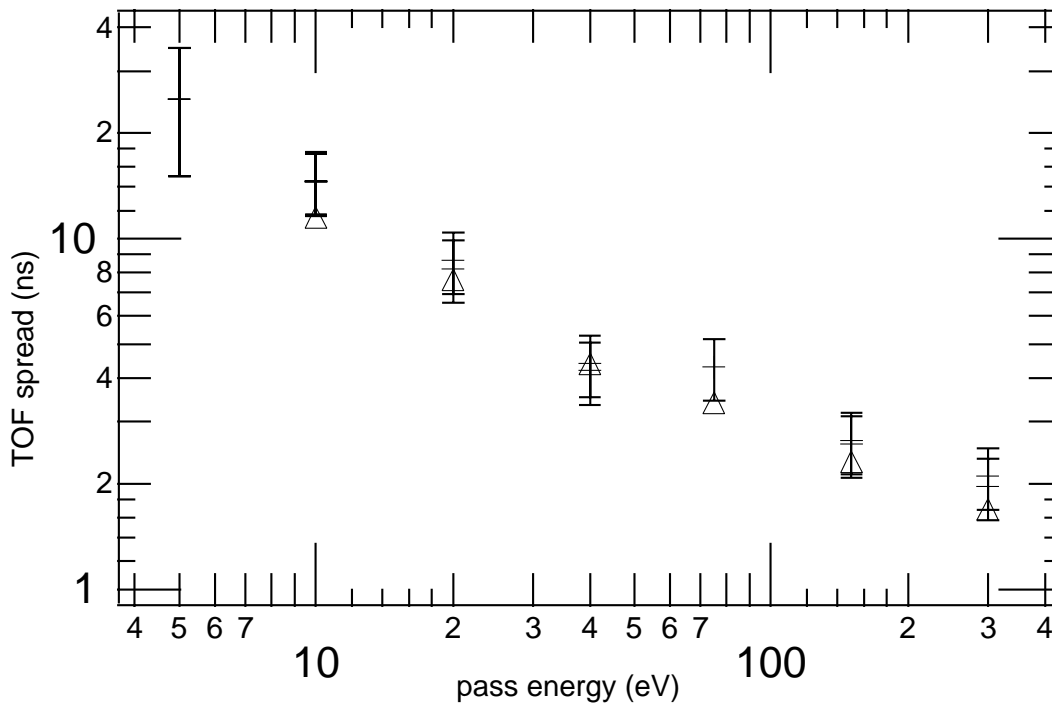
Figure 1: The time-of-flight spread of electrons from an Argon $3p^{3/2}$ photoelectron line, derived as the FWHM of a Gaussian fit to the event-histogram. The vertical lines represent the overall spread due to the finite energy resolution and due to the time-of-flight differences of trajectories pertaining to equal kinetic energy. The triangles represent values, from which the contribution of the finite energy resolution has been removed. The spread drops with increasing pass energy. At 300 eV pass energy it is smaller than the bunch distance in BESSY multibunch mode of operation. Thus the times of electron arrival can then be determined with the same precision as in single bunch mode of operation. This can enable experiments in which the events are referred to the electron arrival times.

calculations reveal that the time-of-flight spread is essentially proportional to the analyser radius, thus increasing the analyser size would reduce the time-of-flight resolution. The main drawback of the current configuration of the system is the low time resolution (500 ps/channel) of the time-to-digital converter (TDC) that was used to read out the delay line signals. TDCs with time resolutions down to 60 ps/channel are now available, which according to our estimates will give the same position and energy resolution as the original readout system of our analyser via a CCD camera.

References

[1] N. Martensson, P. Baltzer, J. Electron Spectr. **70** (1994) 2, p. 117-128

[2] I. Ali, R. Dörner, Nucl. Instr. Meth. Phys. B **149** (1999) 4, p. 490-500
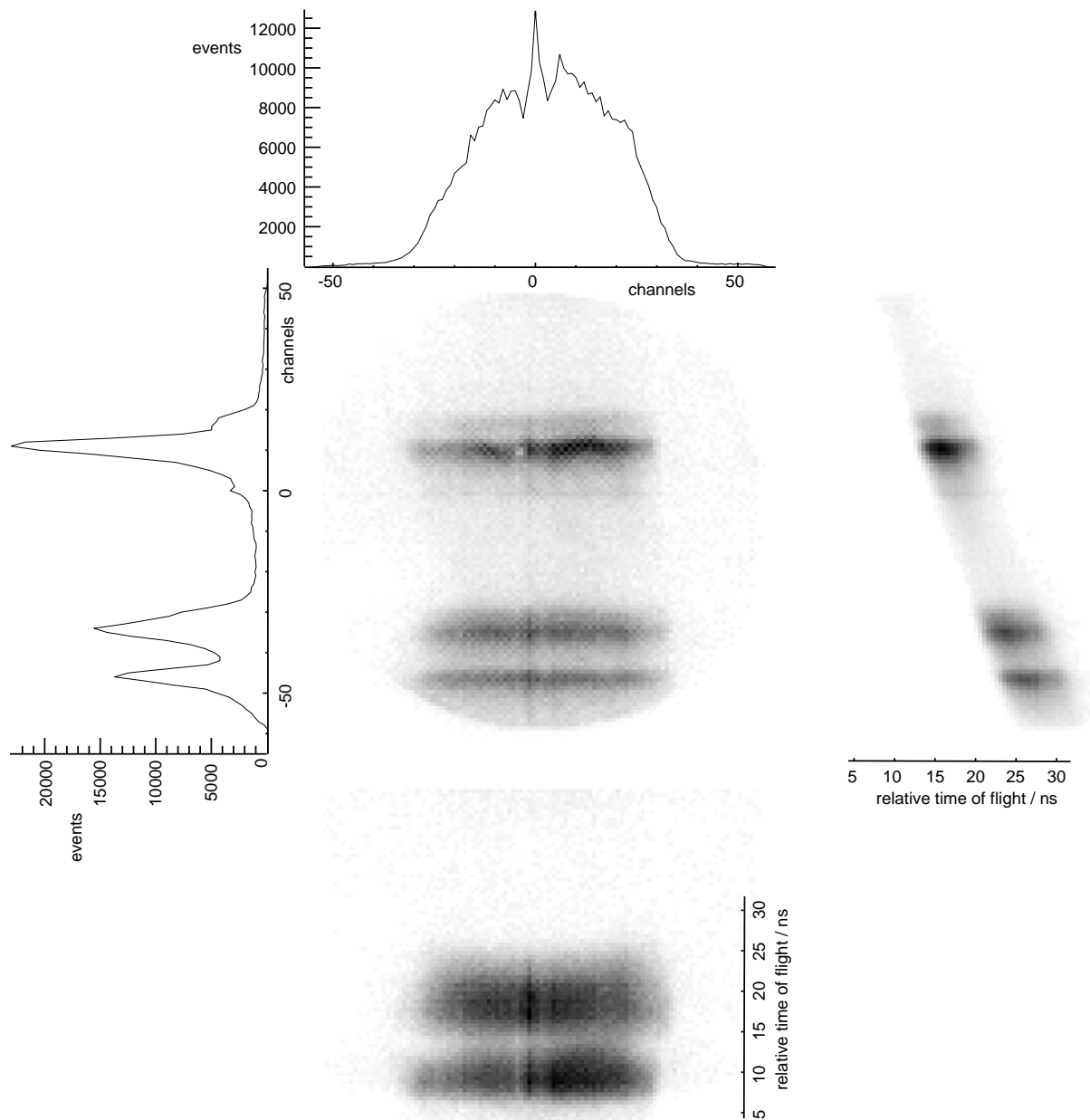
Figure 2: Argon LMM Auger spectrum taken at 40 eV pass energy. The central picture is a histogram of all electrons that hit the anode and their respective positions. Integrating the information in energy-dispersive direction yields the spectrum plotted to the left. The top diagram contains the distribution of electrons integrated along the axis of the entrance slit. The peak apparent at channel number 0 is caused by the pulse-pair dead time of the detector. The right image shows a histogram of of electron positions in the dispersive direction against the relative time-of-flight. The absolute time-of-flight could not be determined due to fluctuations in the phase of the bunchmarker signal. It can be seen that electrons of higher energies take shorter times to reach the detector and vice versa. The time-of-flight spread of 5 ns also becomes apparent. The bottom image shows a histogram of the electron positions in the non-dispersive direction against the time-of-flight. There is a slight hint that those lines are bent towards longer traveling times for off-center trajectories. This effect is caused by the small path differences between the trajectories and becomes larger for smaller pass energies.

Online measurement of photochemical reaction rates with a quartz microbalance.

V. Dietz, I. Twesten, N. Schwentner
Institut für Experimentalphysik, Freie Universität Berlin, Arnimallee 14, D14195 Berlin

Light induced reactions at surfaces and in bulk material represent a broad field of photochemistry. With selected short wavelengths in the spectral range from 200 to 50 nm essentially all chemical bonds can be broken specifically and thus a large variety of reactions can be initiated. Optimized reactions may find application in direct microstructuring [1] as an alternative to the standard resist lithography used nowadays in chip production. By light induced formation of volatile products on the surface material can be removed (etching) and by initiating bonds at the surface with gas phase molecules structures can be built up (deposition). In fact with experiments at BESSYI extremely efficient etching of the most important semiconductors (GaAs/Cl_2 [2], Si/XeF_2 [3]) as well as the reaction of Cu with Cl_2 [4] was demonstrated with quantum efficiencies around 50 in the spectral range between 130 and 110 nm. These short wavelengths support also the trend to a higher spatial resolution [5]. So far the underlying reaction rates had to be determined with an atomic force microscope (AFM) by measuring the reaction depth from individual exposures point by point. The method is indirect with respect to the rates and very time consuming.
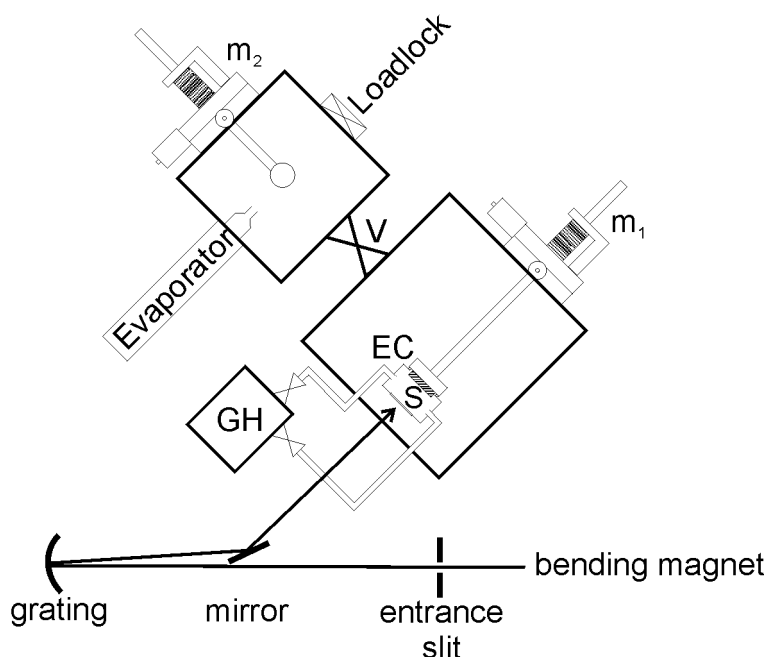
Fig. 1. Scheme of etching set up with sample S, etching cell EC, gas handling GH and manipulator m_1 for cell opening. m_2 represents manipulator for sample transfer to evaporation unit, which is separated by valve V from irradiation unit. Dispersed light (3m-NIM-1 beamline) is focused via grating on the sample.

An improved technique which allows in situ and online a determination of the amount of removed, deposited or reacted material during irradiation is illustrated in Fig. 1. The sample material is evaporated on a gold coated surface of a quartz crystal (Fig. 2). The quartz is then electrically contacted and the frequency is measured in a microbalance device |6| in the gascell. The sample is placed in the focal spot of the beamline monochromator which is operated in a spectrograph mode without exit slit. The cell is connected to the beamline by a window (LiF cutoff 105 nm, MgF_2 cutoff 118 nm) or alternatively by a differential pumping unit. The gas (typically halogen containing mixture) which is to be activated, flows via two tubes through the cell and is handled by an UHV system for reactive gases. The cell is contained in an UHV system and the sealed bottom of the cell can be opened in situ with manipulator m_1 in Fig. 1. The crystal can be transferred with manipulator m_2 to the evaporation chamber which is separated by a valve V. The setup was successfully operated in the first available beamtime of an appropriate VUV beamline (3m-NIM-1) at BESSYII in December 2001 / January 2002.

The first experiments were carried out with the light induced reaction of Cu with Cl_2 |4| for typical Cl_2 partial pressures between 10^{-2} and 10^{-6} mbar and an Ar carrier gas pressure of 0.2 mbar. A Cu layer (thickness 10-500 nm) with a diameter d_2 of 2 or 5 mm is deposited on the gold coated quartz (d_3 = 14 mm) as illustrated in Fig. 2a. The setup is aligned with zeroth order light which generates $CuCl_x$ products in a spot of diameter d_1. The structure of the spot, inspected with an AFM, serves together with the frequency reading as a calibration. The spot size d_1 represents directly the image of the SR light at the entrance slit and the measured values between 1-2 mm indicate that the alignment of the mirrors in the beamline can be improved.
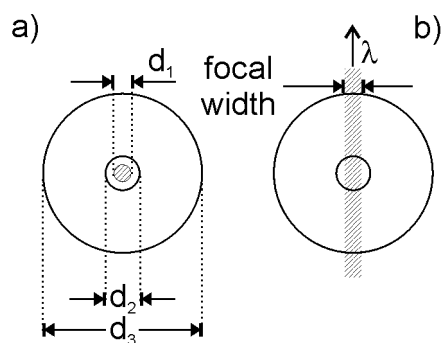

Fig. 2. a) Quartz substrate (diameter d_3) with sample material (diameter d_2) and irradiated spot in zeroth order (diameter d_1). b) Irradiated stripe with dispersed light showing central wavelength λ and wavelength interval $\Delta\lambda = d_2 \cdot d$ for grating dispersion d.

In first order a stripe of dispersed light is imaged on the crystals (Fig. 2b). A variable central wavelength λ and an interval $\Delta\lambda = d_2 \cdot d$ of typical 1 nm is recorded by the crystal with a 600 lines/mm grating of dispersion d = 0.6 nm/mm. Three types of reaction, a dark reaction (DR), a selective reaction (SR) and a non selective reaction (NR) usually compete with each other and can be separated with this device. DR corresponds to the built up of $CuCl_x$ without light and the frequency change due to the increase of mass by the Cl_x intake is displayed in Fig. 3a versus exposure time to Cl_2. The DR has to be minimized. It increases strongly with roughness and contamination, for example by O_2. Therefore only highly polished quartz has to be used and in situ evaporation is essential. The light induced reactions are superimposed

to DR in the central part of Fig. 3a. The light induced reaction rates k are demonstrated in Fig. 3b by differentiating the frequency f versus time t while scanning the central wavelength λ. A large rate causes a large change in frequency and therefore $\Delta f/\Delta t$ is shown.
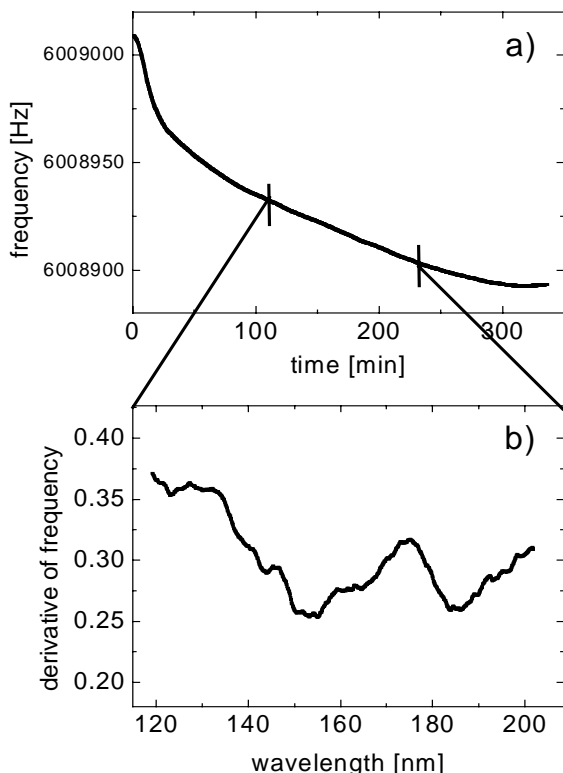
Fig. 3.
a) Quartz frequency f versus time t for a Cu sample due to dark reaction with a Cl_2 partial pressure of 10^{-4} mbar.

b) Reaction rate $k = \Delta f/\Delta t$ versus irradiation wavelength λ taken in a scan of 2 hours for a Cl_2 partial pressure of 10^{-4} mbar.

The band at $\lambda = 175$ nm corresponds to a region of enhanced selective reaction. In this case excitation of adsorbed Cl_2 indicates the reaction. Non selective reaction due to dissociation of Cl_2 in the gas phase takes place at shorter wavelength and causes the rise in k from 140 nm on. The products of NR cover the whole Cu area d_2 because of diffusion of the fragments while SR covers only the directly illuminated stripe of width d_1. The sensitivity for NR is increased with the size of d_2 and in this way NR and SR can be separated.

References:
|1| D. Bäuerle: "Laser Processing and Chemistry" Springer, Berlin 1996
|2| M.V. Dobrotvorskaya, V. Stepanenko, U. Streller, H. Raaf, N. Schwentner: Appl. Surf. Science **136** , 331-337 (1998)
|3| U. Streller, A. Krabbe and N. Schwentner: Appl. Surf. Science **106**, 341-346 (1996)
|4| H. Raaf, N. Schwentner: Applied Surf. Science. **174** , 13-34 (2001)
|5| U. Streller, B. Li, H. Raaf, N. Schwentner: Synchrotron Radiation News **10**, 27-36 (1997)
|6| G. Hayderer, M. Schmid, P. Verga, H.P. Winter, F. Aumayr: Rev. Scint. Instr. **70**, 3696 (1999)

Iodide solvation in liquid water:
effect of counter cation

R. Weber [a], B. Winter [a], M. Dittmar [b], M. Faubel [b]

[a] Max−Born−Institut, Max−Born−Str. 2a, D−12489 Berlin
[b] Max−Planck−Institut für Strömungsforschung, Bunsenstr. 10, D−37073 Göttingen

Photoemission experiments were performed from aqueous salt solutions aiming to a deeper understanding of iodide solvation by water molecules in the presence of different counter cations. In order to make photoelectron spectroscopy applicable to highly volatile liquids we have generated a very thin liquid micron−sized jet (6 μm diameter) in a high−vacuum environment (see fig. 1). The small beam size results in nearly collisionless evaporation, and hence photoelectrons escaping the liquid surface can travel over some appreciable distance to the electron analyzer. The experiments were performed at the MBI−BESSY beamline in the 20−120 eV photon energy range.
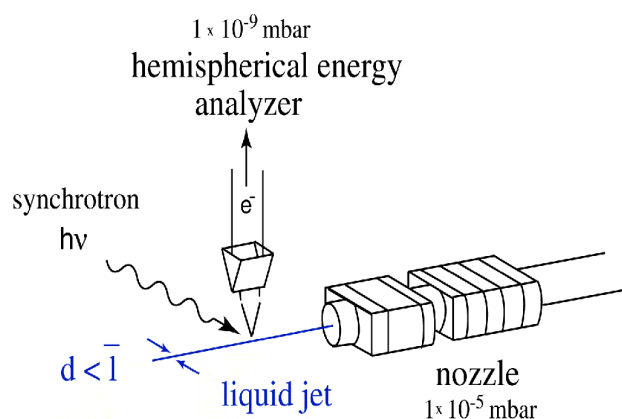
Fig. 1 Setup of the liquid microjet photoemission experiment at the MBI−BESSY beamline

Focus of the present study is on the surface−active tetrabutylammoniumiodide (TBAI) dissolved in water. The interest in such systems is to identify the nature of surface activity, for instance thickness and composition of the segregation layer, and finally the driving force to segregation. These aspects not only depend on the hydrophobicity of the cation but also crucially on the ion−pairing character between cation and anion [1]. In a simple picture the anion is expected to be less likely solvated in the case of stronger coupling [1]. Furthermore, the solvation shell configuration, and consequently energies, are not constant.

The importance of dehydration effects as a function of concentration has been addressed in ref. [2]. The advantage of studying such aspects of surface activity by photoemission is the surface sensitivity of the technique. In addition, using photon energies near 100 eV particularly increases the detection threshold of surface iodide due to the strong $I^-(4d)$ resonance [3]. In this contribution we show results pointing to the possibility that for the fully segregated surface, which corresponds to 0.02 molal TBAI, the large iodide I^- may be exchanged by the smaller Br^- anion, which seems rather surprising [1].

The top spectrum in fig. 2 shows a photoemission spectrum of 0.02 molal TBAI in water obtained for 100 eV photon energy. At this concentration we have found TBAI saturation within the immediate surface region (not further discussed here). The low binding energy features in the spectrum, labeled $1b_1$, $3a_1$, $1b_2$, $2a_1$, arise from the emission of the four liquid water valence orbitals, which are shifted by ca. 1.4 to lower binding energies as compared to the gas phase. The iodide $5p_{1/2}$, $5p_{3/2}$ and $4d_{3/2}$, $4d_{5/2}$ emission are at 7.67 eV, 8.90 eV and 53.63 eV, 55.45 eV, respectively. We note that the iodide binding energies depend on the salt concentration and differ from the respective energies observed in alkali iodides solutions, as

found in ref. [2]. The broad doublet features near 68 eV is assigned to I^- Auger electron emission as this peak shifts proportional to the excitation photon energy used.
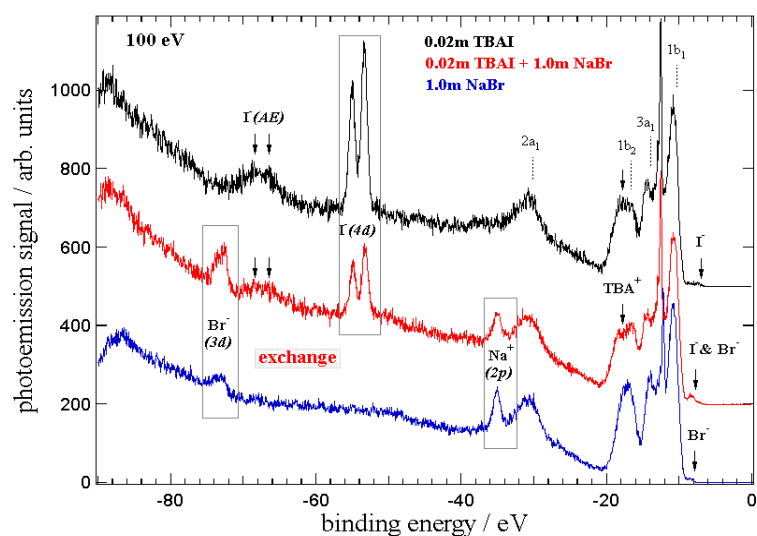
Fig. 2 Photoemission spectra from 0.02m TBAI (top), mixed 0.02m TBAI & 1.0m NaBr (center), and 1.0m NaBr aqueous solutions (bottom) obtained for hν = 100 eV. Spectra are normalized to constant photon intensities.

The bottom spectrum displays the photoemission spectrum from 1.0 molal NaBr dissolved in water. Note that this concentration is 50 times larger than for the TBAI case (top spectrum) but it is just sufficiently high to result in reasonably intense Br^- and Na^+ features (no surface activity and no resonance). The new peaks near 73.51 eV, 74.64 eV, 35.40 and 8.90 eV are assigned to the, $Br^-(3d_{3/2}, 3d_{5/2})$, $Na^+(2p)$ and $Br^-(4p)$ emission, respectively.

Their intensities have been found to increase linearly as a function of concentration below ca. 1 molal concentration. As opposed to aqueous TBAI, in aqueous NaBr solutions the ions are completely dissolved. The center spectrum has been obtained for 0.02 molal TBAI, this time dissolved in 1 molal aqueous NaBr. Hence, this solution contains the identical amount of NaBr species as compared to the aqueous solution (bottom). The most striking result is an increase of the Br^-/Na^+ intensity ratio, which is accompanied by an absolute decrease of the iodide intensity in the mixed salt, as well as by an attenuation of the Na^+ signal relative to the water intensities. Note that in fact the absolute intensity of the Br^- peak is increased. Our preliminary interpretation of these observations is that the iodide anion is being exchanged by the smaller Br^- anion as this would readily account for the changed intensity ratio. The smaller Na^+ intensity would be consistent with the presence of a TBAI segregation surface layer screening the electrons originating from inside the bulk. Note that the three spectra in fig. 2 have been obtained for identical photon intensities, thus the observed intensity changes are correctly scaled with respect to each other. We are aware that the interpretation of the proposed anion exchange may be not very obvious. Experiments to further detail this aspect are underway. Nonetheless, the present results demonstrate the principle potential of a liquid jet experiment, in combination with XUV photoemission, to investigate dynamic phenomena at liquid/vacuum interfaces.

References

[1]   S. Holmberg, Z. C. Yuan, R. Moberg, H. Siegbahn, J. Electron Spectrosc. Relat. Phenom.**47**, 27–38 (1988)
[2]   I. Watanabe, N. Takahashi, H. Tanida, Chem. Phys. Lett. **287,** 714–718 (1998)
[3]   M. Ya. Amusia, N. A. Cherepkov, L. V. Chernysheva, S. T. Manson, Phys. Rev. A, Vol. **61**, 021701 (2000)

Experimental Evidence for a Nondipole Contribution
to the Xe-4p Photoelectron Spin-Polarization

T. Khalil, M. Drescher, B. Schmidtke, N. Müller, and U. Heinzmann

Universität Bielefeld, Fakultät für Physik, Universitätsstr. 25, 33615 Bielefeld

In the photoionization of xenon atoms close to the 4p ionization threshold quadrupole contributions to the spin polarization of the emitted electrons have been predicted [1] to be resonantly enhanced due to a double-well shaped effective potential of the outgoing εf-wave [2] – essentially the same phenomenon leading to the well known (dipole) shape-resonance in the Xe-4d photoionization cross section. These nondipole terms should result in a significant spin polarization component P_{long} along the electron momentum. In order to test the theoretical prediction, we have measured this spin polarization component using circularly polarized light from beamlines UE56/1-PGM and UE56/2-PGM.

Measurement of such effect requires efficient separation from dipole contributions as well as careful control of apparative asymmetries and spectral background. Our particular choice of an electron extraction perpendicularly to the photon momentum completely suppresses any
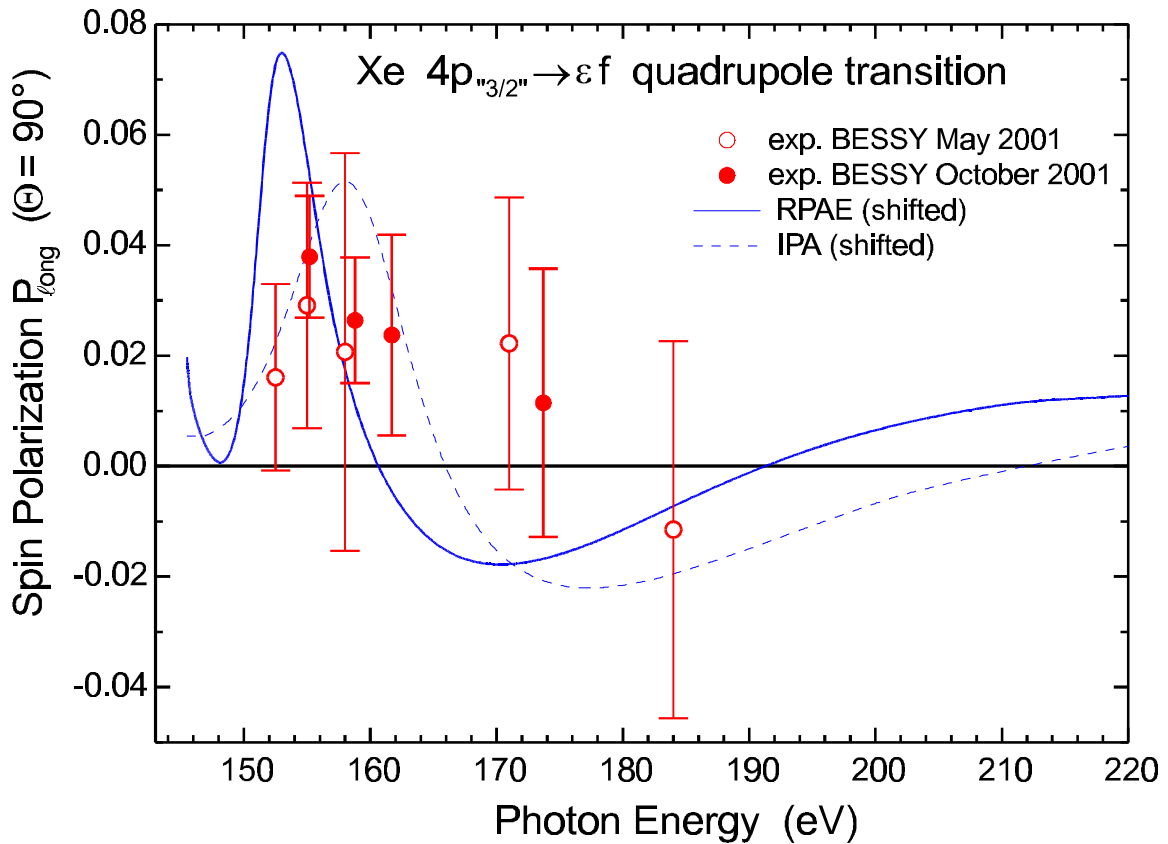
Fig.1: Longitudinal spin polarization component measured in two independent beamtimes in comparison with adapted RPAE [1] and IPA [3] calculations of the quadrupole-contribution close to the Xe-4p ionization threshold.

direct dipole contributions to P_{long}. However, dipole excitation results in a strong transversal spin polarization, which may be rotated by residual magnetic fields along the electron path into a longitudinal one. Therefore we sensitively compensated magnetic fields with 3 Helmholtz-coils by minimizing the dipole signal in P_{long} for the Xe-4$d_{3/2}$ photoline shifted to the same kinetic energy by choosing the photon energy appropriately. Measurements were performed during two independent beamtimes in May (UE56/2) and October (UE56/1) 2001 using different methods for consideration of the spectral background: in May extra kinetic energy data were acquired to the left and right of the 4p-peak at fixed photon energy; in October the photoline was shifted using a slightly smaller excitation energy so as to allow a background determination at the kinetic energy of the (unshiftet) 4p-peak, additionally a higher photon flux was accomplished by coupling of both undulator segments. Interestingly, in the used energy range an abdication of the coupling modulator was accompanied by a loss of flux of less than 20%.

The results of both beamtimes are summarized in Fig.1 clearly revealing a significant nondipole contribution in both data sets. The improved experimental uncertainty for the October data can be attributed to the higher available light intensity. The results of RPAE [1] and IPA [3] calculations for a Xe 4$p_{1/2}$ photoline, plotted for comparison, were shifted according to the deviation of the theoretical ionization threshold from the experimental one. The investigated photoline is known to be subject to strong mixing with double excitations of the 4d-subshells leading to a broadened and asymmetric intensity profile [4]. In order to achieve qualitative agreement, the calculated curves had additionally to be multiplied with - 0.5. Our data therefore support an assignment of the observed line as Xe 4p"$_{3/2}$".

This first experimental verification of quadrupole-contributions to observables other than the intensity angular distribution underlines that higher order multipoles must be considered for a correct description of the photoionization process even at photon energies much below 1 keV. This work was supported by the Deutsche Forschungsgemeinschaft (HE1049/7-2). The support from the BESSY staff is highly acknowledged.

References:
[1]   N.A. Cherepkov and S. Semenov, J. Phys. B 34, L211 (2001)
[2]   N.A. Cherepkov and S. Semenov, J. Phys. B 34, L495 (2001)
[3]   A. Derevianko, W. Johnson, and K. Cheng,
        At. Data & Nucl. Data Tables 73, 153 (1999)
[4]   G. Wendin and M. Ohno, Physica Scripta 14, 148 (1976)

Study of the dynamics of the doubly excited states of H_2

M. Glass-Maujean,, A.Ehresmann* and H. Schmoranzer*
Laboratoire de Dynamique des Ions Atomes et Molécules, Université P. et M. Curie /CNRS, 4, pl Jussieu, F-75252 Paris Cedex 05, France
* Fachbereich Physik, Universität Kaiserslautern, D-67653 Kaiserslautern, Germany

Energies and dynamics of doubly excited states in molecular systems are now accessible to calculations. Most of these calculations are focused on H_2 because it is the simplest molecule [1]. The dynamics of these states is specially diverse: they may autoionize yielding $H_2^+ + e^-$, $H + H^+ + e^-$ or dissociate into neutral ground and /or excited H atoms [2] as well as into $H^+ + H^-$ ions.

We are interested in the process of dissociation into neutrals. Such dissociation leads to excited fragments which may radiate. The radiation wavelength is characteristic of the principal quantum number of the excited state, and its decay times are characteristic of the orbital momentum states.

The doubly excited states were populated through photon absorption in the 25-40eV energy range. The photon excitation out of the ground state of these doubly excited states is allowed only through electron correlations, so their absorption cross sections are very low (10^{-19} cm^2). The dissociation yield is of a few percent. Fluorescence radiation of the atomic fragments was detected: through Lyman$-\alpha$ (121 nm) for the H(n=2) states and through Balmer$-\alpha$ (656 nm) for the H(n=3) states. Time analysis of such fluorescence decay was performed using the single-photon technique. The decay times of the various orbital momentum states are well known and differ enough to be used as a signature [3, 4].

In the 25-40eV energy range, the doubly excited states excited by photons out of the ground state belong to the configurations (in the Franck-Condon region) 2snℓ (Q_1 states) or 2pnℓ (Q_2 states). The excitation threshold of the Q_2 states lies by 3eV higher than the Q_1 state threshold so that we can distinguish the relative contributions.

The H(n=2) states are of 2s or 2p configuration where the 2s atoms, being metastable, may radiate only by collisions so that the 2s fluorescence has to be slow and pressure-dependent.
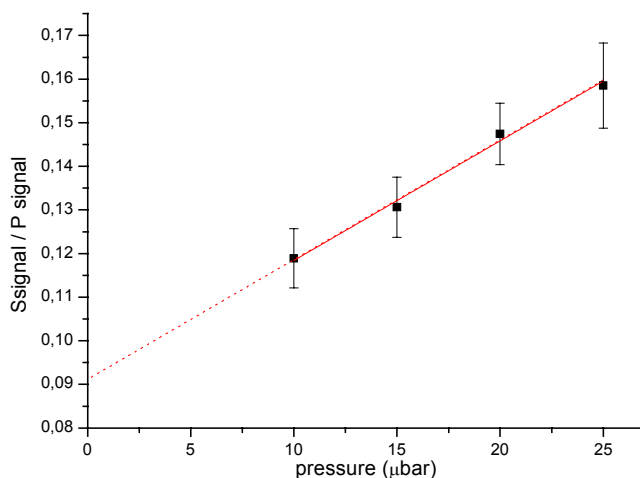
Figure 1: S/P signal ratio for 34eV incident energy.

Each Ly$-\alpha$ decay was analyzed as a double-exponential function; the fast one is assigned to the P signal, the low one to the S one. The population ratio of the orbital momentum states is equal to the exponentials' area ratio. The variations of this ratio versus the pressure values are used as the signature of the H 2^2S state. The experimental set-up did not allow us to measure the pressure dependence of the 2^2S nor the 2^2P lifetime.

The principal result we could obtain is the evidence of 2^2S state population following Q_2 dissociation only whilst the 2^2P state can be populated via Q_2 or Q_1 dissociation.

The Q_1 states, with $2sn\ell$ configuration, are theoretically correlated to H(1sσ)+H(n'ℓ'λ), the process we see through this experiment is therefore the dissociation of a Q_1 $^1\Sigma_u$ or $^1\Pi_u$ state to H(1sσ)+H(2pπ or σ). The Q_2 states, with $2pn\ell$ configuration, are theoretically correlated to H(2pπ)+H(n'ℓ' λ), the process observed through this experiment is therefore the dissociation of the Q_2(1) $^1\Pi_u$ state to H(2pπ)+H(2sσ) [2].

References:

[1] F. Martin J. Phys. B, 32 (1999) R197; I Sanchez and F. Martin J. Chem. Phys. 160 (1977) 7720; I Sanchez and F. Martin J. Phys. Rev. A 60 (1999) 2200

[2] M. Glass-Maujean J. Chem. Phys. 85 (1986) 4830 and J. Chem. Phys. 89 (1988) 2839

[3] M. Glass-Maujean, S. Lauer, H. Liebel and H. Schmoranzer J. Phys. B 33 (2000) 4593

[4] S. Lauer, H. Liebel, H. Schmoranzer and M. Glass-Maujean J.Phys.B 34 (2001) 5121.

Photoelectron Spectroscopy on Camphor.

E. E. Rennie,[1,2] I. Powis,[3] U. Hergenhahn,[1,2] G. Garcia,[3] O. Kugeler,[1,2] T. Lischke,[1] and S. Marburger[1]

1. Fritz-Haber-Institut der Max-Planck-Gesellschaft, Faradayweg 4-6, 14195 Berlin, Germany
2. Max-Planck-Institut für Plasmaphysik, Boltzmannstr. 2, 85748 Garching, Germany
3. School of Chemistry, University of Nottingham, Nottingham NG7 2RD, UK.

In the year 2001 three weeks of beamtime at the UE56/2-PGM1 monochromator were available for this project. In this time, we have recorded a number of photoelectron spectra of camphor comprising the valence and inner-valence region, and have continued our search for chirality effects in the core level photoelectron spectra of enantiomeric pure camphor vapours.

Experimental

Commercial samples of camphor ($C_{10}H_{16}O$, Aldrich >95% enantiomeric purity), which is a solid at room temperature, were admitted into the chamber via a heated gas line at ~80° C. The vapour then entered a gas cell inside the main vacuum chamber where photoionisation occurred. The gas cell contained apertures for the synchrotron radiation and photoelectrons, as well as a photoelectron dump to prevent backscattered electrons from entering the analyser.

Photoelectron spectra were recorded by an SES-200 hemispherical analyser mounted at an angle of 54.7° forward scattering with respect to the photon beam. In the measurements aiming at the detection of chirality effects it was of importance to optimise the speed of data acquisition. Therefore, these were made in the fixed analyser mode, in which the multichannel detector of the spectrometer is readout without scanning the analyser voltages.

Valence photoelectron spectrum of Camphor

The ultraviolet photoelectron spectra of camphor (Fig. 1) has been reported by a number of authors, most recently see Ref. [1], in each case using He I radiation (hν=21.2 eV). Limited assignments and interpretations of the valence bands of camphor have been made on the basis of such comparisons. The low vapour pressure of camphor necessitates using a heated source for such studies and, perhaps as a consequence of ensuing experimental difficulties, these existing spectra are of modest resolution. Moreover there are some significant, unexplained differences in the band intensities in spectra recorded under very similar nominal conditions.

We have recorded the photoelectron spectrum of camphor at hν=95 eV, thus spanning ionisation energies up to 41 eV. The outer valence region is shown in Figure 1 along with an earlier He I spectrum [1]. The extended energy range of the current work allows the observation of a number of distinct additional bands in the 20-24 eV region of the spectrum, with two further broad, diffuse structures centred around 26.5 eV and 32.5 eV. There are also differences in relative band intensity below 20 eV, the most marked of which is the greatly enhanced relative intensity of the outermost band at 8.7 eV in the hν=95 eV spectrum. Such an increase is fully consistent with the assignment of this lowest energy band to the carbonyl oxygen lone pair orbital (nO), since it is empirically established that orbitals with a large atomic O $2p$ character are expected to gain in intensity relative to skeletal C–C bonds with increasing photon energy.

To aid in interpreting the spectrum we have performed calculations using the Gaussian 98 and GAMESS (UK) packages. Optimised geometrical parameters for the camphor molecule were obtained from a density functional calculation performed using a B3LYP functional and a 6-31G** basis set. Estimates of the vertical ionisation energies were calculated using an outer-valence Green's function (OVGF) method and a cc-pVDZ basis. These ionisation energies

agree quite well with the positions of lines in the experimental spectrum, up to ionisation energies of about 16 eV.

In this spectrum, no differences between excitation with left- and right-handed circularly polarized light were found.

Circular Dichroism in the photoelectron angular distribution

We have reported first evidence for a forward/backward asymmetry in the angular distribution of C $1s$ photoelectrons from enantiomeric pure camphor, ionised with circularly polarized light, in the year 2000. The possible appearance of such effect by symmetry selection rules has been worked out by Ritchie [2]. In the dipole approximation, for photoionization of a chiral molecule by circularly polarized light the angular distribution function takes the form

$$I(\theta) = \sigma/(4\pi) \, [1 - (1/2)\beta P_2(\cos\theta) \pm D \cos\theta].$$

The angle θ is referred to the light propagation axis. Since the $(\cos\theta)$-term changes sign with the helicity of the light, from measurements with both helicities a circular dichroism in the angular distribution (CDAD) can be defined by

$$A(\theta) = (I_+(\theta) - I_-(\theta))/(I_+(\theta) + I_-(\theta)),$$

where I_+ and I_- denotes intensities recorded with opposite helicity of the ionising light. Finite values of A in valence photoionisation of bromocamphor molecules have been reported [3].

We have measured this asymmetry at 54.7° in the core level photoionisation of camphor. By our electronic structure calculations reported above we only find the $1s$ line of one carbon atom near to the chiral centre of the molecule with a notable chemical shift, where the pertaining carbon site is of carbonyl character. The other carbon sites in this molecule are chemically similar, and of methyl character.

To analyse our C $1s$ spectra we have assumed that the bulk of C $1s$ electrons from the methyl sites have vanishing asymmetry. Under this assumption, the carbonyl C $1s$ photoelectron line shows asymmetries A up to approx. 0.05, which change sign when the camphor enantiomer of opposite handedness is ionised (Fig. 2). Compared to last year we have greatly extended the energy range of our measurements, and were able to show that even at kinetic energies as high as 20 eV some effect remains to be seen. The pronounced energy dependence of the magnitude and even the sign of the asymmetry indicates, that this asymmetry is of a dynamical rather than a statical origin. In other words, scattering of the outgoing electron at the remaining ionic core should at least play a role in the production of asymmetry.

MS X-α Calculations

To verify these assumptions, we have carried out calculations of the asymmetry parameters by the MS-Xα method. The angular basis used for the calculation of photoionisation matrix elements was $l=4$ for the C and O atoms, and $l=2$ for the H atoms, with the asymptotic partial waves truncated at $l=7$. It was confirmed that, as assumed for the analysis of experimental data, the mean (unresolved) asymmetry of the methyl- C $1s$ electrons is at least an order of magnitude smaller than that of the CO C $1s$ electron, across the energy range examined. The calculated $A(54.7°)$ asymmetry for CO C $1s$ reproduces our measured values quite well (see Fig. 2), and therefore give a first idea that indeed a scattering mechanism is causing the asymmetry observed by us, and by Böwering *et al.* [3] in valence photoionisation.

Future measurements we hope to carry out with a greatly lowered detection limit by employing chopped beams of opposite helicity from both UE-56/2 undulators.
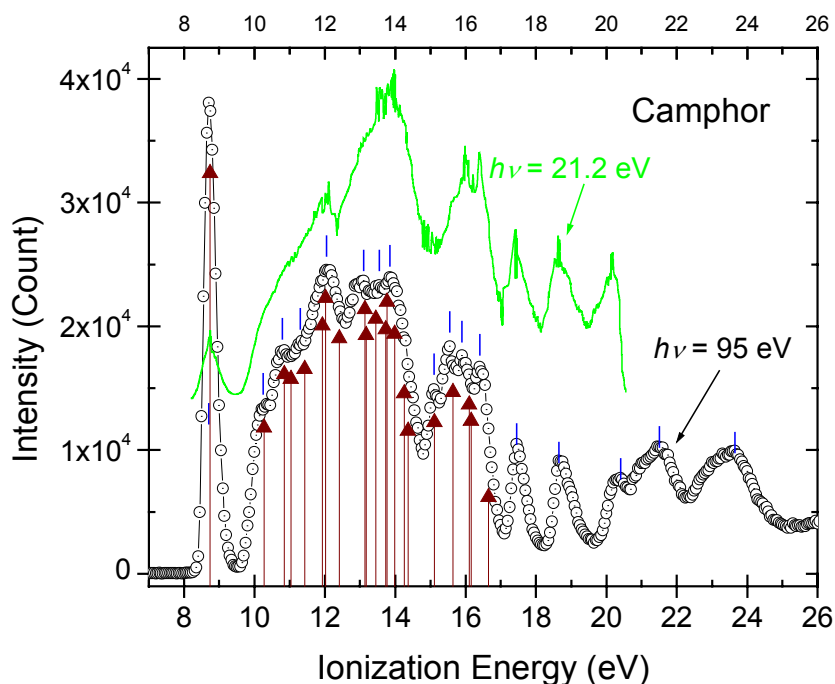
Fig.1:
Camphor $h\nu$ = 95 eV photoelectron spectrum. Experimental peak positions are marked with a tick, while calculated OVGF cc-pVDZ I_{vert} values are indicated by arrows drawn from the axis. The length of the arrows is chosen to guide the eye. A He I spectrum (green) from Ref. [1] is included for comparison

Fig. 2: Normalised photoelectron intensity difference for carbonyl C 1s ionisation of gaseous, unoriented camphor with circularly polarised light for a 54.7° forward scattering geometry. Pairs of spectra with left and right-handed circularly polarized light were repeated two-four times at all photon energies. The experimental uncertainty results mostly from peak/background separation, and can be approximated by the difference between the results obtained from different measurements at the same photon energies
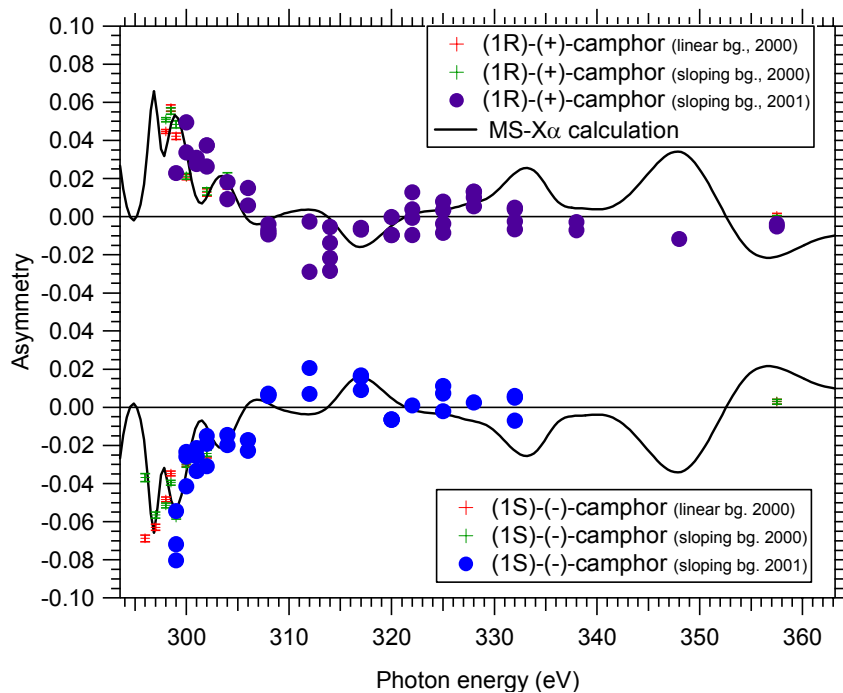
References

[1]   M. Getzlaff and G. Schönhense, J. Electron Spectrosc. Relat. Phenom. **95**, 225 (1998).
[2]   B. Ritchie, Phys. Rev. A **13**, 1411 (1976), Phys. Rev. A **14**, 359 (1976).
[3]   N. Böwering, T. Lischke, B. Schmidtke, N. Müller, T. Khalil, and U. Heinzmann,
Phys. Rev. Lett. **86**, 1187 (2001).

High-resolution studies of doubly excited ${}^1P^o$ states in helium

R. Püttner[1], M. Martins[1,2], Y. Jiang[1,3], D. V. Vyalikh[1], S. L. Molodtsov[4], D. Delande[5], B. Grémaud[5], and G. Kaindl[1]

[1]*Freie Universität Berlin, Institut für Experimentalphysik, D-14195 Berlin*
[2]*Universität Hamburg, Institut für Experimentalphysik, Luruper Chaussee 149, 22761 Hamburg*
[3]*Max-Planck Institut für Physik komplexer Systeme, Nöthnitzer Strasse 38, 01187 Dresden*
[4]*Institut für Oberflächen- und Mikrostrukturphysik, Technische Universität Dresden, 01062 Dresden*
[5]*Laboratoire Kastler-Brossel T12 E1, Université Pierre et Marie Currie, 4 Place Jussieu, 75005 Paris, France*

Photoionization spectra of helium in the double excitation regime were measured at very high resolution using the beamlines UE56-2/PGM2 and the Russian-German Beamline (RGBL). At both beamlines a resolution of better than $\Delta E = 1$ meV was achieved at $h\nu$ = 64 eV. The double excitation states can be assigned using the classification scheme N,K_n [1] with N(n) being the quantum number of the inner (outer) electron and K the angular correlation quantum number. $2N-1$ different Rydberg series converge towards the ionization threshold I_N. These series can be distinguished by the angular correlation quantum number K, with $K = N - 1, N - 2, ..., -|N - 1|$. The most intense series in $N,N-2_n$ followed by $N,N-4_n$ and $N,N-6_n$. Up to now below most of the ionization thresholds only the two most intense series were observed.
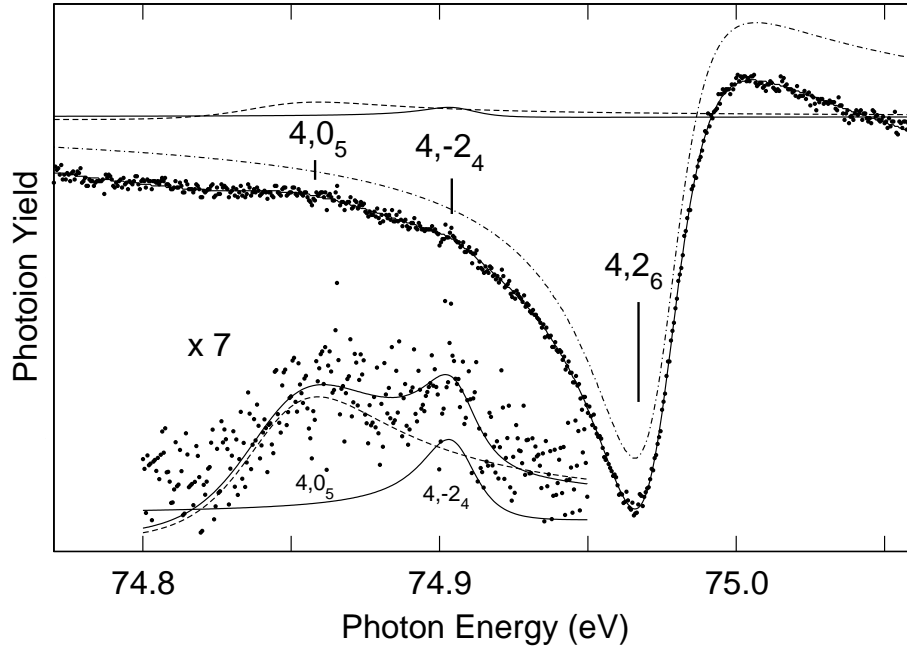
Figure 1: Spectrum of the resonance $4,2_6$ (dash-dotted subspectrum), together with the resonances $4,0_5$ (dashed subspectrum) and $4,-2_4$ (solid subspectrum). The solid line through the data points represents the fit result.

The experiments performed at the RGBL focused on the observation of a previously unobserved Rydberg series below the ionization threshold I_4 and the experiments at the UE56-2/PGM2 focused on measuring the photoionization cross section in the energy region between 78 and 79 eV, i.e. directly below the double ionization threshold.

Up to now below the I_4 ionization threshold the principal series $4,2_n$ and one secondary series, namely $4,0_n$, were observed. Fig. 1 shows the photoionization cross section in the vicinity of the resonance $4,2_6$ measured at the RGBL with a resolution of $\Delta E = 5.5$ meV. In addition to the most intense resonance $4,2_6$, the resonance $4,0_5$ and the previously unobserved resonance $4,-2_4$ can be seen. A least-squares fit analysis of the spectrum was performed. The solid line through the data points represent the result of the fit analysis and it turned out that all free parameters of the fit agree well with the theoretical predictions (see Table 1).

Table 1: The experimental and theoretical energy positions E, relative energy shift ΔE, relative intensities I, linewidth Γ, and Fano parameter q.

resonance	$4,0_5$	$4,-2_4$	$4,2_6$
E (eV)	74.8475	74.9067	74.9749
ΔE_{theo} (meV)	-127.4	-68.2	0
ΔE_{exp} (meV)	$-132.4(8.0)$	$-67.5(6.0)$	0
I_{theo}	0.78588	0.16057	100
I_{exp}	0.83(3)	0.17(3)	100
Γ_{theo} (meV)	61.5917	21.2695	38.2723
q_{theo}	2.28909	-4.07988	0.486666
q_{exp}	$-$	$-$	0.51(2)

The studies of the photoionization cross section between $h\nu = 78$ and 79 eV focus on signatures of quantum chaos. It is well known that the underlaying classical three-body Coulomb problem shows a chaotic behavior and it is expected that this will influence the quantum mechanical system in the semiclassical limit, i.e. close to the ionization threshold. Previous studies in the energy range up to 78.25 eV show clearly a transition towards a quantum chaotic behavior [2]. In very recent experiments at beamline UE56-2/PGM2 we were able to obtain the experimental cross section up to $h\nu \cong 78.6$ eV with a very good signal-to-noise ratio. These results are shown in Fig. 2 together with preliminary theoretical results and reveal an excellent agreement. However, for a better understanding of the spectrum and an analysis with respect to more distinct signatures of quantum chaos more detailed calculations are necessary, which are currently under way.
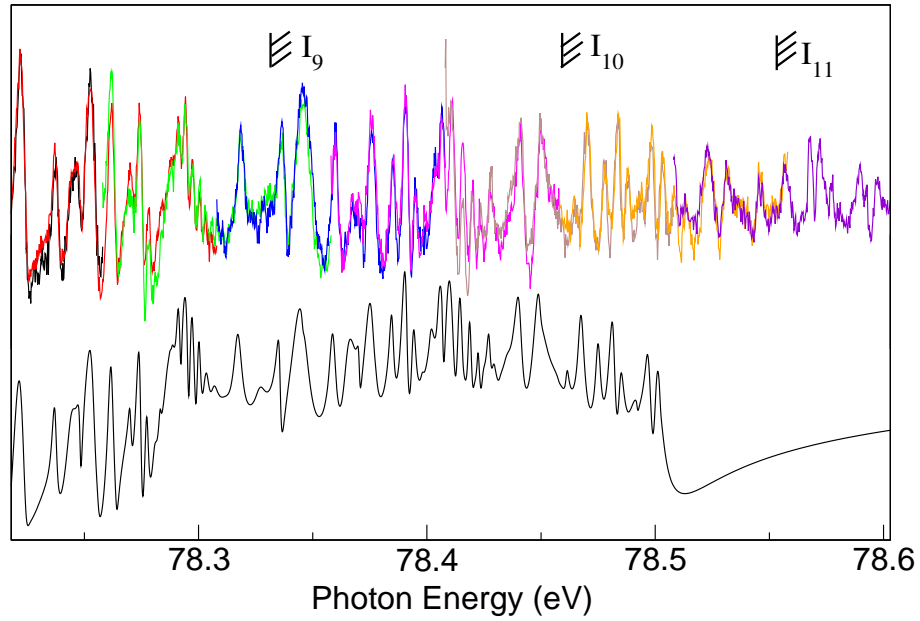
Figure 2: Spectrum of doubly excited helium below the ionization thresholds I = 9 to I = 12. Upper part: experimental photoionization yield. Lower part: calculated cross section.

References

[1] C. D. Lin, Phys. Rev. A **29**, 1029 (1984).

[2] R. Püttner, B. Grémaud, D. Delande, M. Domke, M. Martins, A. S. Schlachter, and G. Kaindl, Phys. Rev. Lett. **86**, 3747 (2001).

Resonant Inelastic Scattering Study of Polycyclic Hydrocarbons

R. Scherer, S. Cramm, S. Eisebitt*, M. Lörgen*, M. Freiwald and W. Eberhardt*

Institut für Festkörperforschung des Forschungszentrums Jülich
*BESSY GmbH, Albert-Einstein-Str.15, 12489 Berlin

We present a detailed study of the electronic structure of thick layers of the polycylic hydrocarbon molecules tetracene, perylene and coronene. These large molecules consist of a assembly of several benzene rings. The samples have been prepared under high vacuum through evaporation onto silicon wafers. Layer thicknesses of up to several hundred nm were studied. The unoccupied states have been studied with NEXAFS-spectroscopy and the occupied states with resonant inelastic x-ray scattering (RIXS). In Fig.1 the NEXAFS-spectra are shown for each sample. The excitation energy was scanned through the C1s-absorption edge with an energy resolution of 0.1eV. The NEXAFS-spectra were recorded by measuring the total electron yield (TEY). The spectra in Fig.1 show sharp resonances in the discrete part followed by a broad band around 288eV. Upon comparison with NEXAFS-simulations, carried out by H. Ågren et al. [1] and H. Oji et al. [2], the sharp resonances could be identified as C1s-π* transitions into the LUMO and LUMO+1. Note that the LUMO is splitted in two resonances. The simulations in [1] and [2] state that these splits are due to chemical shifts (final state relaxation shifts) between the different C-atoms in the molecule (cf. Fig.1). The bars in Fig.1 indicate the calculated chemical shifted C1s-π* transitions into the LUMO. The third resonance in each spectrum corresponds to C1s-π* transitions into the LUMO+1. Only in the coronene spectrum a fourth

resonance could be indentified, which corresponds also to transitions into the LUMO+1, but from a type of C-atoms (2) different from the third resonance (3). Due to resonant excitation on the resonances different C-atoms can be selectively excited. This was done in the RIXS measurements. The resonant excitations with an energy resolution of 0.2eV (beamline) were set to the maximum of each resonance. An additional excitation energy was choosen at the onset of the C1s absorption.

The scattered fluorescence for all excitation energies is shown in Fig.2. Basically all resonant excited spectra show a strong excitation energy dependence. The topmost spectra were nonresonant excited with hv=314eV and reveal the total local partial density of states (LPDOS). The emission spectra (a) and (b) show very sharp emission bands, whereas the spectra (c) and (d) expose much more broadend emission bands. In order to understand these effects in dependence of the excitation energy, Hartree-Fock MO-calculations have been performed and scattering theory was applied. The informations we got from the NEXAFS-measurements were used to carry out the RIXS-simulations. For instance, the information about the chemical shifted C1s-π* transitions. This means , in the simulations it was accounted that for an excitation on a single resonance only a certain group of C-atoms was excited. Additionally, symmetry

Fig.1: NEXAFS-spectra of tetracene, perylene and coronene, recorded with an energy resolution of 0.1eV. The bars indicate calculated C1s-π* transitions taken from Ref. [1] and [2].

selection rules have been applied for the dipole transitions from the valence band states into the inner shell states. The results of the simulations are shown in Fig. 3 and are compared with only the coherent fractions of the RIXS-spectra shown in Fig.2. These coherent fractions have been obtained by subtracting the nonresonant emission spectrum, as it contains all incoherent contributions, times a factor, from each resonant spectrum. Next to each spectrum the excited C-atoms are marked inside the MO-plots in Fig.3. Furthermore the unoccupied state into which the inner shell electrons are excited
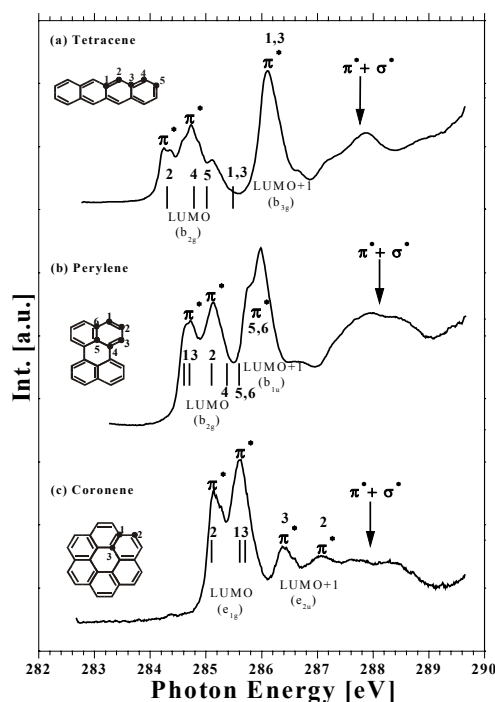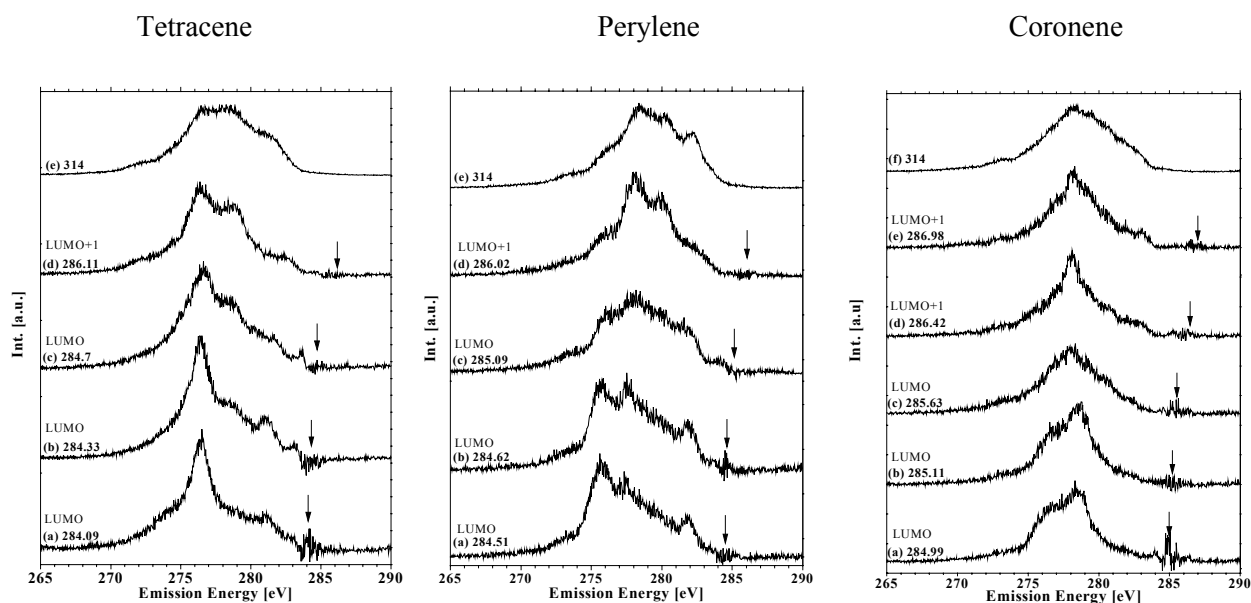
Fig. 2: Tetracene, perylene and coronene RIXS-spectra. The excitation energies are given on the left side next to each spectrum and additionally the molecular orbital into which the electron has been excited is depicted. The topmost spectra are nonresonant emission spectra, excited at 314eV, far above the absorption threshold. The arrows indicate the position of the elastic scattered photons. This peak was fitted and subtracted by a Voigt-curve, in order to identify valence band emission close to the valence band maximum better.

are labeled on the left side. On the right the symmetry of the calculated valence band states is depicted and the fraction of the coherent intensity related to the measured spectrum. Basically, the simulations show good agreement with the experimental data for the excitation at the onset of the absorption (a). Sharp emission bands can be observed for each molecule.

We attribute to these sharp emission lines strong coherent interference effects. Excitation on the first resonance (b) provides in the case of coronene still good agreement, however, in the case of tetracene and perylene strong deviations between simulation and experiment. Vibronic coupling effects are responsible for these deviations, since vibronic coupling leads to the effect that the former equal C-atoms become unequal due to asymmetric vibrations. Thus, the incoherent contribution is increased.
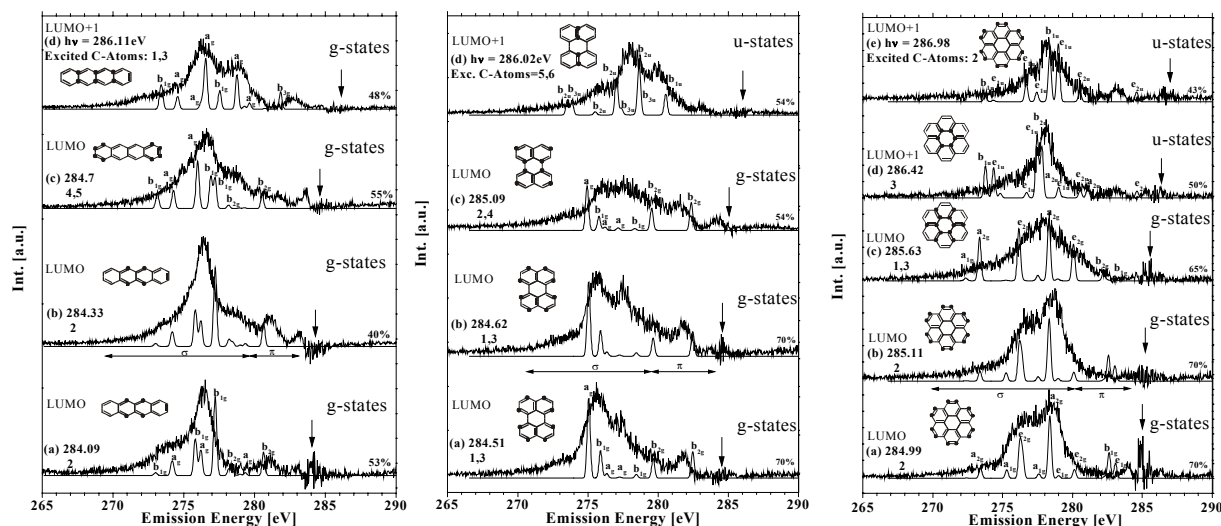
Fig.3: Coherent fractions of the RIXS-spectra compared with RIXS-simulations. On the left side the excitation energy and the MO in which the C1s electrons were excited to are depicted. On the right side the coherent fractions and the symmetry of the calculated valence band states are shown. Inside the molecule pictures excited C-atoms are marked.

Within the incoherent contribution symmetry forbidden transitions are involved. The RIXS-spectra excited on the second peak (c) show for perylene no and for tetracene and coronene weak agreement between simulation and experiment. The RIXS-spectra (c) in Fig.3 show very broad emission bands, compared to the spectra (a) and (b), which suggest also excitation of strong vibrational effects on this second resonance. Excitation on the third resonance (d) yield again more pronounced features in the emission spectra. On the third resonance the C1s excitation is into the LUMO+1. For perylene and coronene the parity changes going from the LUMO to the LUMO+1, whereas for tetracene the parity is unchanged. The emission spectra look totally different to the spectra (a)-(c). For coronene a very sharp emission line at 288eV can be seen, which suggests strong coherent interference effects. As figured out from the NEXAFS-results, only the innermost C-atoms of the coronene molecule are excited on the third resonance. The simulation shows good agreement with the experiment. For perylene only the four C-atoms oriented inside the symmetry axis are excited on the third resonance. Three emission bands can be identified for perylene (d), which are well reproduced by the simulation. For tetracene two strong emission bands are observed in (d), which show also good agreement with the simulation. Hence, for excitations into the LUMO+1 the symmetry selections rules are again very strictly fullfilled and the incoherent contribution is much less than for excitation on the second resonance (c). In the coronene NEXAFS-spectrum additionally a fourth resonance is visible (e). The C1s transition is still into the LUMO+1, however, now the outermost C-atoms are excited. The emission spectrum (e) looks similar to (d), however, more broadend.

To summarize, strong coherent interference effects can be observed in polycyclic hydrocarbon RIXS-spectra. Due to resonant excitation on a π^*-resonance a certain group of equal C-atoms can be excited. This can be attributed to the chemical shift between unequal C-atoms in the molecule. The emission channels are also localized on the excited C-atoms. The emitted coherent light from these excited C-atoms can now interfere constructively and destructively, which leads to very sharp emission lines in the spectra. Confirmation of this statement was given by RIXS-simulations, which have been carried out under the demand of strict symmetry selection rules and the locality of the excitations. These simulations show good agreement with the experimental data. Emission intensities, which cannot be explained by coherent interference and symmetry selection rules are attributed to contributions from incoherent processes. We assume that excitation of a vast number of vibrations lead to vibronic coupling between symmetry forbidden states. Another explaination is, that, due to asymmetric vibrations the C-atoms become unequal, which leads to an increased incoherent contribution.

References

[1] H.Ågren et al. *Chem. Phys.* **196,** 47 (1995).
[2] H. Oji et al. *J. Chem. Phys.* **109,** 10409 (1998).

Separation of final and initial state XPS shifts for cobalt clusters on Al$_2$O$_3$/NiAl(110)

B. Richter, H. Kuhlenbeck, H.-J. Freund

Fritz Haber Institute of the Max Planck Society, Chemical Physics Department

Faradayweg 4-6, D-14195 Berlin

A thin aluminum oxide film grown on NiAl(110) may be used as substrate for the preparation of model catalysts. Metal clusters may be deposited as active components and studied with different techniques. The oxide film is about 5 Å thick and its conductivity is high enough for the application of all kinds of electron spectroscopy. Charging has not yet been observed.

In the final state of a photoemission experiment the electronic structure of the ionized atom and its surrounding is usually relaxed due to a redistribution of electronic charge in the course of the screening of the positively charged hole by surrounding electrons. The energy gained in this process is transferred to the photoelectron. Such a rearrangement process also involves the electrons in the substrate which rearrange to screen the hole. If the substrate is an oxide the contribution is significantly smaller than for a metal since the mobility of electrons in a metal is higher. In first approximation it may be assumed that the oxide does not take part in the relaxation process. On the short timescale of the photoionization experiment it will not be possible to transfer charge from the NiAl(110) substrate through the oxide to the cluster so that electronic relaxation involving the metal substrate may also be neglected. Thus, in first approximation only the electrons within the cluster contribute to the relaxation process. This means that the amount of charge available for hole-screening and thus the final state relaxation energy depend on the cluster size. This effect hampers the study of cluster-size dependent changes of the electronic structure of clusters since it adds to the shift due to changes of the electronic structure in the ground state. The latter one is the more interesting shift since it carries information on the electronic structure of the clusters.

A way to separate initial state and final state effects in photoemission has been described by Hohlneicher et al [1]. This method makes use of the different sizes of initial and final state
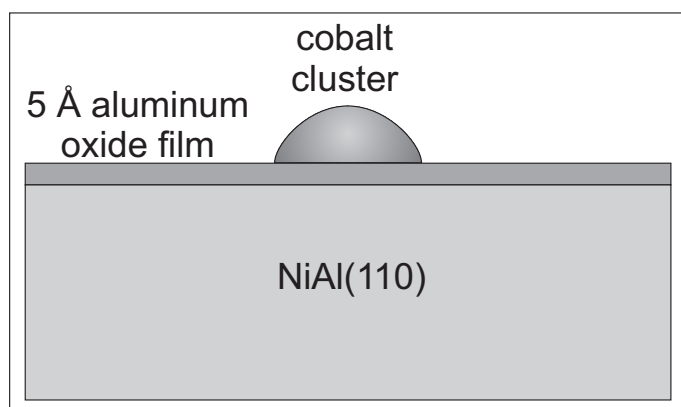
Figure 1: Schematic illustration of a cobalt cluster deposited on Al$_2$O$_3$/NiAl(110).
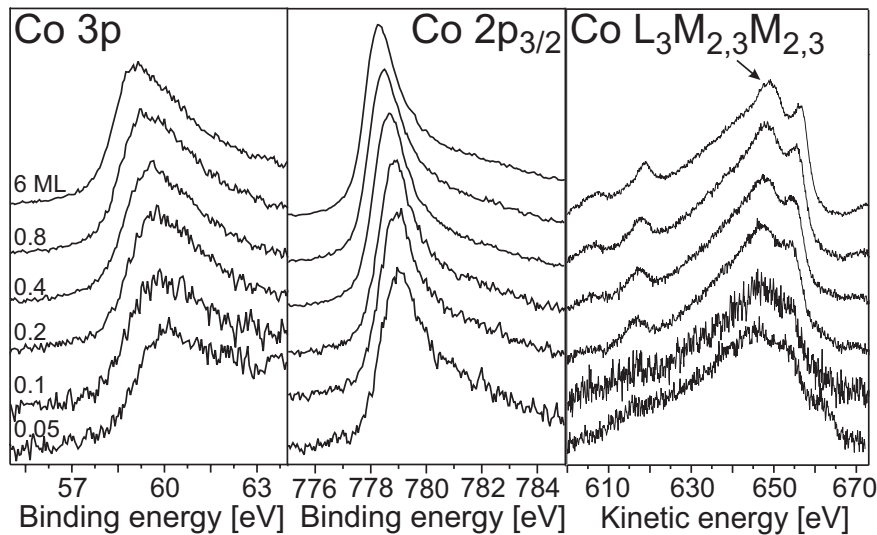
Figure 2: Co 2p, Co 3p and Co $L_3M_{2,3}M_{2,3}$ spectra for Co/Al$_2$O$_3$/NiAl(100) as a function of the amount of deposited cobalt. $E_{Photon} = 1100\,eV$.

effects in Photoemission and Auger processes. The initial and final state shifts may be calculated by a linear combination of the shifts of an Auger peak and two corelevels contributing to the Auger state. The final state of the Auger transition should have two holes in the same level. In order to avoid problems with band structure effects participation of valence levels should be avoided.

For the present study cobalt clusters deposited onto Al$_2$O$_3$/NiAl(110) have been chosen. The 2p and 3p levels and the corresponding $L_3M_{2,3}M_{2,3}$ transition can readily be studied with photon energies available at BESSY II. The measured data are displayed in Fig. 2. In order to suppress structures from the substrate (especially the nickel $L_3M_{2,3}M_{2,3}$ Auger peak) the spectra have been recorded at an angle of 85° with respect to the surface normal. Cluster-size dependent shifts of about 0.8 and 1 eV have been obtained for the corelevels and 2.5 eV for the Auger state (see Fig. 3). From these energy shifts the initial and final state energy shifts of the Co 3p level have been calculated according to the equations given in the figure at the left as discussed by Hohlneicher et al [1]. The shifts are given with respect to the corresponding energies of the 3p level of a layer with a nominal thickness of 6 Å (see Fig. 4).
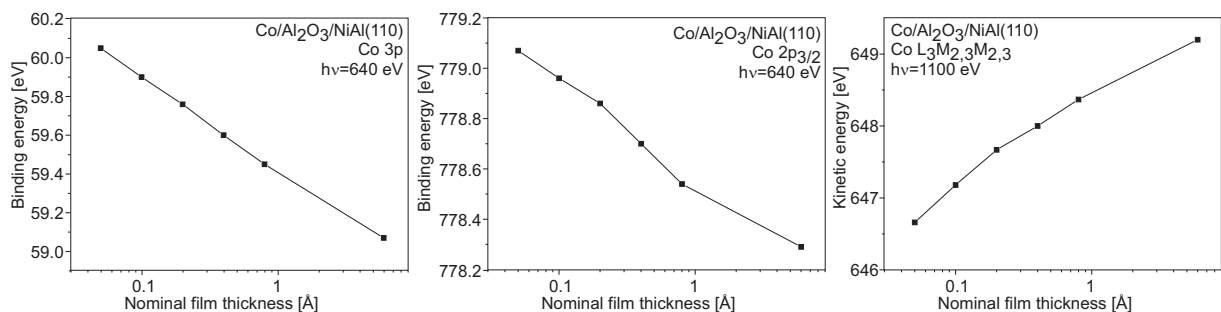
Figure 3: Co 2p and Co 3p binding energies and Co $L_3M_{2,3}M_{2,3}$ kinetic energy for Co/Al$_2$O$_3$/NiAl(100) as a function of the amount of deposited cobalt. $E_{Photon} = 1100\,eV$.
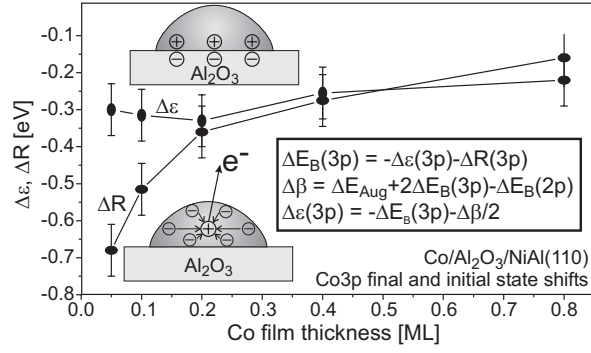
Figure 4: Cluster-size dependent final- (ΔR) and initial-state ($\Delta\epsilon$) shifts of the Co 3p level as a function of the deposited amount of cobalt.
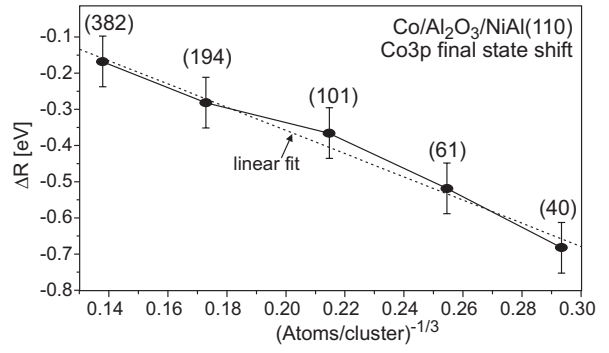
Figure 5: Cluster-size dependent Co 3p final state shift as a function of (number of atoms per cluster)$^{-1/3}$.

Morphological data for the system have been obtained with STM by M. Heemeier et al (M. Heemeier, M. Bäumer and H.-J. Freund, to be published). From these data the average number of atoms per cluster could be calculated. Estimates show that the final state energy should depend on the cluster size approximately according to (atoms/cluster)$^{-1/3}$ which is well fulfilled as judged from Fig. 5.

For the initial state energy a shift of $0.3\,$eV was calculated, depending only weakly on Co coverage. One may argue that the shift is due to the chemical interaction between the cluster and the oxide. However, modifications due to this effect will take place only in the first layer at the interface. In the STM studies it was found that the height of the clusters is about $11\,$Å, depending only weakly on coverage. Since the experimental geometry was such that the clusters have been seen approximately from the side by the analyzer, the contribution of the interface layer to the total signal may be estimated to be about $20\,\%$ which corresponds to the thickness of one layer relative to the cluster height. The direction of the initial state shift would be compatible with a charge transfer from the clusters to the oxide as indicated in Fig. 4.

For Ta, Pd and Pt on Al_2O_3/NiAl(110) and other systems cluster-size dependent variations of the lattice constants have been observed (see for instance [2]). Such variations may also be expected for cobalt clusters and may be responsible for part of the initial state shift.

References

[1] G. Hohlneicher, H. Pulm, and H.-J. Freund, J. Electron Spectrosc. **37**, 209 (1985).

[2] M. Klimenkov, S. Nepijko, H. Kuhlenbeck, M. Bäumer, R. Schlögl, and H.-J. Freund, Surf. Sci. **391**, 27 (1997).

Size Dependent Magnetism of Deposited Small Iron Clusters studied by X-ray Magnetic Circular Dichroism

J. T. Lau, A. Föhlisch, R. Nietubyc, M. Reif, and W. Wurth

Universität Hamburg, Institut für Experimentalphysik,
Luruper Chaussee 149, D-22761 Hamburg

Transition metal clusters are important model systems to study the evolution of magnetic and electronic properties from single atoms to bulk metals. In Stern-Gerlach experiments on cluster beams [1], small clusters have been shown to exhibit superparamagnetic behaviour. Their magnetic moments are enhanced over the respective bulk values and show significant size dependent variations. The bulk values of the magnetic moments are only approached for clusters of several hundred atoms.

To investigate magnetic properties of mass selected deposited clusters, soft X-ray magnetic circular dichroism (XMCD) is a valuable tool because of its element specificity and submonolayer sensitivity. Within the theoretical framework of XMCD sum rules [2], the spin and orbital contributions to the magnetic moments of the cluster atoms can be determined separately, which is an advantage over other techniques

To study the size dependent magnetic properties of small iron clusters, we have performed XMCD measurements on well defined samples of size selected Fe_n clusters (n=2–9), deposited in UHV onto a Ni/Cu(100) substrate magnetised perpendicular to the sample surface. Detailed information on the experiment is given in Ref [3, 4]. In brief, small Fe_n clusters are generated by a sputter source and deposited onto a Ni/Cu(100) substrate under *soft landing* conditions after mass separation. The Ni/Cu(100) substrate was prepared and characterised in situ under UHV conditions. XMCD spectra were taken at BESSY II beamline UE56/1-PGM. Polarisation dependent X-ray absorption spectra were recorded in total and partial electron yield detection mode simultaneously.
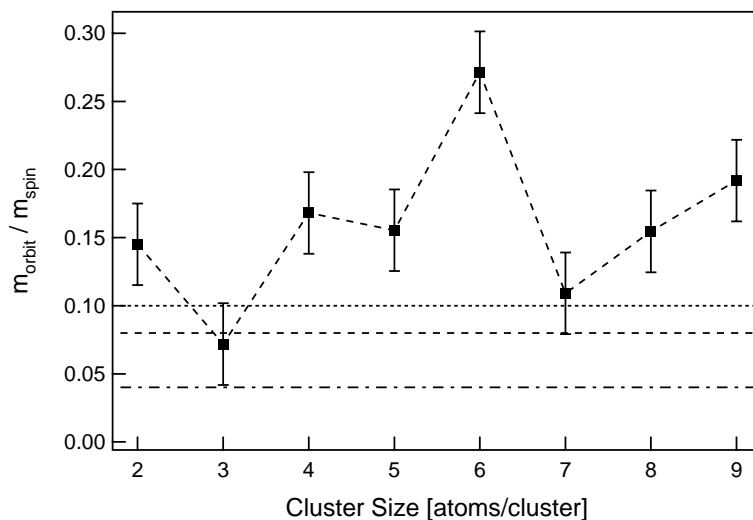
Figure 1: Ratio of Fe_n orbital to spin magnetic moments vs. cluster size as compared to bulk iron (dash-dotted line)[5], ultrathin films (dashed line) [6], and iron nanoclusters with an average cluster size of ≈ 400 (dotted line) [7].

For XMCD measurements, the photon polarisation was reversed while the orientation of sample magnetisation remained fixed. The spectra were cross checked for systematic errors by reversing the magnetisation axis of the nickel layer. XMCD scans were taken at the iron and nickel $L_{2,3}$

edges to characterise Fe_n clusters as well as the nickel underlayer.

The results of an XMCD sum rule analysis of Fe_n XMCD spectra are displayed in Fig 1 and 2. Here, the ratios of m_l to m_s are plotted as a function of cluster size for Fe_2 through Fe_9. These ratios range from 0.11 to 0.27, and in general are larger than those observed for bulk iron [5], iron ultrathin films [6], and iron nanocluster films [7]. An increasing ratio of m_l to m_s is expected with decreasing dimensionality or coordination of a system, and this trend is visible in Fig 1 when going from bulk iron (dash-dotted line) to small iron clusters (markers). In addition to this more general observation, there is also a nonmonotonous variation in the data displayed in Fig 1, with the lowest ratio of m_l to m_s observed for Fe_3, and the highest ratio for Fe_6. This variation reflects the strong dependence of electronic and magnetic properties on cluster size and geometry in the small size regime. In addition, the large changes observed in going from n to n±1 atoms per cluster is further evidence that the sample preparation procedure yields well defined deposited clusters of a single size.

From calculations for small iron clusters on Ag(001) it is expected that the spin magnetic moment is enhanced over the bulk value, and is constant within 10% for small clusters supported on a substrate [8]. Furthermore, for iron atoms on Ag(100) strongly enhanced orbital moments are predicted by theory [9]. Applying these findings to Fe_n on Ni/Cu(001), we tentatively conclude that the large values of m_l to m_s plotted in Fig 1 are due to strongly enhanced orbital magnetic moments in Fe_n on Ni/Cu(001) rather than due to reduced values of m_s. To test this, we have
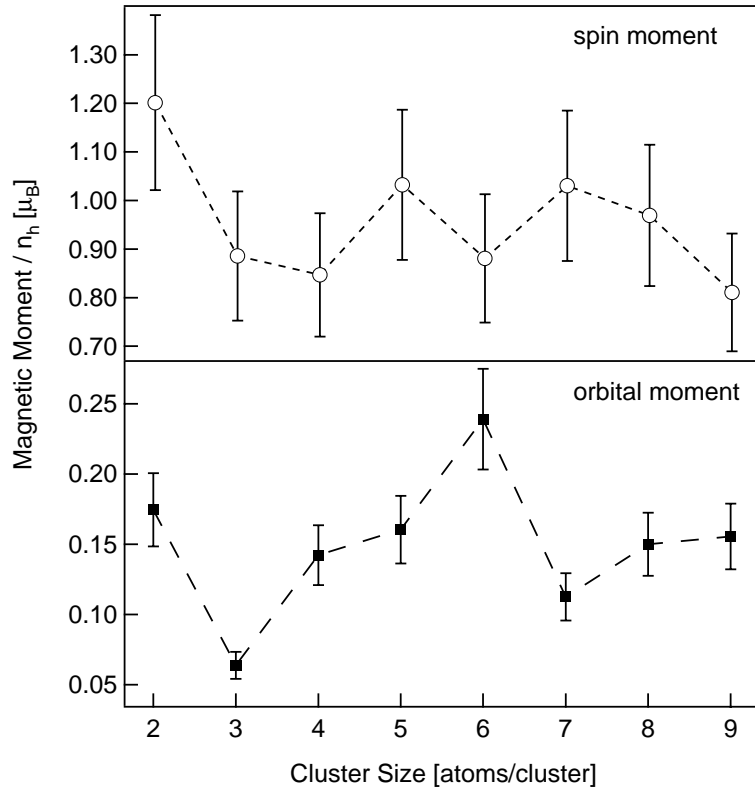
Figure 2: Comparison of spin $\left(\langle S_z \rangle + \frac{7}{2} \langle T_z \rangle \right) / n_h$ and orbital $\langle L_z \rangle / n_h$ magnetic moments *per 3d hole* of Fe_n clusters on Ni/Cu(100).

evaluated Fe_n magnetic moments *per 3d hole*, which are shown in Fig 2. Indeed, the upper panel in Fig 2 shows that with the exception of Fe_2, the spin magnetic moments of the Fe_n clusters are fairly large (approx. 1 μ_B per 3d-hole) and vary only within 15–20 %. The lower panel in Fig 2, on the other hand, shows that orbital moments per d-hole are strongly enhanced compared to $m_l \approx 0,025 \mu_B/n_h$ [6] for bulk and surface iron and that there is a much larger variation of

these moment, e.g. for Fe_6 and Fe_3, which is responsible for the observed strong variation in the ratio of m_l to m_s.

In the upper panel of Fig 2, spin magnetic moments in excess of 1 μ_B are due to contributions from a dipolar term to the spin sum rule [2]. This dipolar term $\langle T_z \rangle$ is a rough measure for the deviation from a spherical spin distribution [2], and therefore is very likely to be dependent on cluster geometry. Since $\langle T_z \rangle$ is included in the spin sum rule, a non negligible contribution of $\langle T_z \rangle$ will result in a larger value of m_s. In the case of Fe_2, where we observe $m_s/n_h > 1$, a large contribution of $\langle T_z \rangle$ to m_s is deduced.

It is not obvious why Fe_2, Fe_3, and Fe_6 should be special with respect to their magnetic properties. Although there is no direct information on the geometric structure of the supported clusters we expect two-dimensional configurations where the iron atoms are located on the nickel sites (pseudomorphic arrangement). Based on this assumption one could speculate that, due to symmetry, clusters with an odd number of atoms should show different geometric arrangements and therefore different magnetic properties than even-numbered clusters, possibly leading to strongly different magnetic properties. Further experimental and theoretical investigations are needed to elucidate this finding.

In summary, we have measured orbital and spin magnetic moments as a function of cluster size for small size selected iron clusters deposited onto Ni/Cu(001). The ratios of m_l to m_s are generally larger than those observed for bulk iron, iron ultrathin films, and iron nanocluster films. There is a strong, nonmonotonous variation particularly in m_l, with strongly enhanced orbital magnetism for the clusters.

References

[1] I. M. L. Billas, A. Châtelain, and W. A. de Heer, Science **265**, 1682 (1994).

[2] see e.g. J. Stöhr, J. Magn. Magn. Mater. **200**, 470 (1999) and references therein.

[3] J. T. Lau, Dissertation, Universität Hamburg (2002 [in Vorbereitung]).

[4] J. T. Lau, A. Föhlisch, R. Nietubyč, M. Reif and W. Wurth, submitted for publication.

[5] P. Söderlind, O. Eriksson, B. Johansson, R. C. Albers, and A. M. Boring, Phys. Rev. B **45**, 12911 (1992).

[6] C. T. Chen, Y. U. Idzerda, H.-J. Lin, N. V. Smith, G. Meigs, E. Chaban, G. H. Ho, E. Pellegrin, and F. Sette, Phys. Rev. Lett. **75**, 152 (1995).

[7] K. W. Edmonds, C. Binns, S. H. Baker, S. C. Thornton, C. Norris, J. B. Goedkopp, M. Finazzi, and N. Brookes, Phys. Rev. B **60**, 472 (1999).

[8] J. Izquierdo, A. Vega, L. C. Balbás, D. Sánchez-Portal, J. Junquera, E. Artacho, J. M. Soler, and P. Ordejón, Phys. Rev. B **61**, 13639 (2000).

[9] B. Nonas, I. Cabria, R. Zeller, P. H. Dederichs, T. Huhne, and H. Ebert, Phys. Rev. Lett. **86**, 2146 (2001).

High-Resolution Spectroscopy of Core-Excited Benzene Clusters

R. Flesch, A. A. Pavlychev[*], and E. Rühl

Fachbereich Physik, Universität Osnabrück,
Barbarastr. 7, 49069 Osnabrück

[*] St. Petersburg State University, St. Petersburg 198904, Russian Federation

High resolution core level excitation of free Van der Waals clusters containing diatomic molecules has been the subject of recent studies [1, 2]. This approach has been shown to be a suitable tool to investigate structural and dynamic properties of free element- and site-selectively excited clusters. Free molecules, variable size clusters, and the condensed phase shows often vibrationally resolved core-to-valence bands in the pre-edge regime. However, there are small, but distinct changes in energy position and spectral shape by going from the gas to the condensed phase of matter. These spectral changes occur already upon the formation of small clusters, so that intermolecular interactions of site-selectively excited molecular clusters can be investigated. Specifically, it has been shown that small spectral shifts, homogeneous and inhomogeneous line broadening as well as variations of the Franck-Condon structure occur as a result of cluster formation [1, 2].

However, no experimental studies on clusters of large polyatomic organic molecules have been performed with high spectral resolution in the inner-shell excitation regime. Benzene (C_6H_6) serves as a suitable model system for such studies. We present in this report an experimental study on the C $1s \rightarrow \pi^*$-transition in benzene clusters. The experiments have been carried out at the U-49-1-SGM beamline at BESSY at an energy resolution of $E/\Delta E \approx 5000$. Benzene clusters are produced by seeding benzene in argon at room temperature. The mixture is expanded at $p_0 = 1$ bar through a nozzle (d=50 μm). This leads to the formation of homogeneous and heterogeneous benzene clusters [3]. The skimmed jet is transferred into the ionization region of a time-of-flight (TOF) mass spectrometer, where it is crossed by monochromatic undulator radiation. Cations are separated and detected in the TOF mass spectrometer. Photoion yields of isolated molecules and clusters are recorded simultaneously so that small spectral changes and energy shifts of spectral features are revealed. Fig. 1 shows the photoion yields of molecular
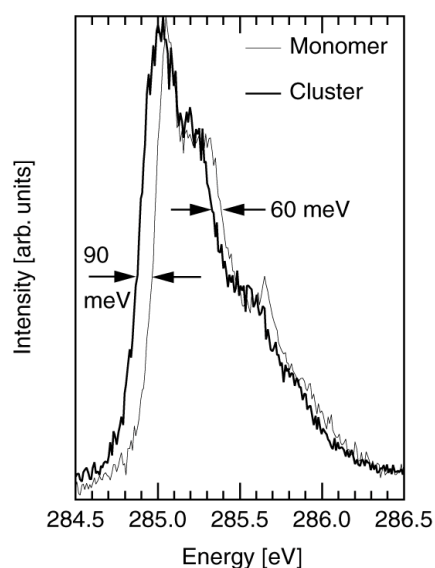
Fig. 1: Comparison of the C $1 \rightarrow \pi^*$-transition of benzene ($C_4H_4^+$-yield) and benzene clusters (($C_6H_6)_2^+$-yield).

benzene ($C_4H_4^+$) and benzene clusters (($C_6H_6)_2^+$) in the regime of the C $1s \to \pi^*$-transition. The overall shape of this transition is similar in both cases, where the spectrum of the bare molecule is in good accordance with recently published high-resolution absorption spectra [4]. However, significant changes are observed between the molecular and cluster spectrum: (i) The onset of the transition is redshifted by 90 ± 5 meV for clusters relative to isolated molecules; (ii) a broadening of the spectral profile by 30 ± 5 meV is found; and (iii) the vibrational fine structure at the high-energy side of the transition is less distinct in the case of clusters. This is unlike previous work on clusters of diatomic molecules which has shown that there are only minor spectral shifts of the order of a few meV [1, 2].

Species	$\alpha/10^{-40}$ Fm^2	$(\alpha_{zz}-\alpha_{xx})/10^{-40}$ Fm^2
Ar	1.83	0
N_2	1.97	0.77
C_6H_6	11.60	-6.20

Tab. 1: Mean polarizability α and polarizability anisotropy $\alpha_{zz}-\alpha_{xx}$ of Ar, N_2, and C_6H_6 [5].

These shifts are conditioned by dynamic stabilization of core-excited species in Van der Waals clusters [1, 2]. The large redshift in homogeneous or heterogeneous benzene clusters compared to previous work is rationalized by considering the following: (i) the mean polarizability of aromatic molecules is significantly enhanced compared to small diatomic molecules, as shown in Tab. 1; and (ii) core-hole localization increases in benzene clusters due to vibronic coupling. In the simplified Z+1 core analogy picture, C 1s-excited benzene is equivalent to pyridine (C_5H_5N). The induction of an electric dipole moment in the neighboring benzene molecules leads to stronger intermolecular interactions. This enhances the stabilization in core-excited benzene clusters compared to clusters of diatomic molecules, so that a more substantial redshift is observed. The broadening in the ($C_6H_6)_2^+$-yield is rationalized predominantly by the considerable polarizability anisotropy of benzene. The orientation of molecules in the cluster is likely different from that of the solid, which is assumed to be a result of the fast condensation process in the cluster beam. The structural disorder results in a variety of spectral shifts as a result of different induced dipole moments. Further investigations on clusters of organic molecules are in progress. These will lead to more specific information on the correlation of molecular properties to spectral shifts in high resolution near-edge spectra and core-to-valence transitions.

References

1 R. Flesch, A.A. Pavylchev, J. J. Neville, J. Blumberg, M. Kuhlmann, W. Tappe, F. Senf, O. Schwarzkopf, A.P. Hitchcock, and E. Rühl, Phys. Rev. Lett. **86**, 3767 (2001).
2 E. Rühl, R. Flesch, W. Tappe, and A.A. Pavlychev, J. Synchrotron Radiat. **8**, 154 (2001).
3 E. Rühl, B. Brutschy, and H. Baumgärtel, Chem. Phys. Lett. **157**, 379 (1989).
4 E. E. Rennie, B. Kempgens, H.M. Köppe, U. Hergenhahn, J. Feldhaus, B.S. Itchkawitz, A.L.D. Kilcoyne, A. Kivimäki, K. Maier, M.N. Piancastelli, M. Polcik, A. Rüdel, and A.M. Bradshaw, J. Chem. Phys. **113**, 7362 (2000).
5 A. Hinchcliffe and R.W. Munn, 'Molecular Electromagnetism', Wiley, New York, 1985.

High-Resolution Spectroscopy of N 1s-Excited Heterogeneous Nitrogen/Argon Clusters

R. Flesch, W. Tappe, A. A. Pavlychev[*], and E. Rühl

Fachbereich Physik, Universität Osnabrück
Barbarastr. 7, 49069 Osnabrück

[*] St. Petersburg State University, St. Petersburg 198904, Russian Federation

Free clusters have received considerable attention in the past since they are known to bridge the gap between the gas and condensed phases of matter. Inner-shell excitation has been shown to be a suitable tool to investigate properties of clusters, because it provides size-, element-, and site-specific information on the geometric and electronic structure of variable size matter [1].

High-resolution core excitation spectra of homogeneous nitrogen clusters have been studied earlier in the N 1s pre-edge regime, where the vibrationally resolved fine structure of the N 1s$\rightarrow\pi^*$-transition was investigated in detail [2]. A redshift of $\Delta E \approx 6$ meV of the vibronic progression is observed in clusters relative to the bare molecule. This has been rationalized in terms of dynamic stabilization arising from the dynamic dipole moment generated by core-hole localization in the low-symmetry cluster field. We extend in this study the investigation to heterogeneous nitrogen/argon clusters (($N_2)_n \cdot Ar_m$), so that structural changes as a function of cluster composition can be investigated. This work also extends previous low resolution work on N_2/Ar-heteroclusters [3].

The experiments were performed at the U-49-1-SGM beamline at BESSY at an energy resolution of $E/\Delta E \approx 10,000$. Heterogeneous nitrogen/argon clusters were produced by expanding the pre-mixed gases (typically 90 % N_2; 10 % Ar) through a nozzle. The supersonic jet is skimmed and crossed by monochromatic undulator radiation. Cations are mass separated and detected by time-of-flight mass spectrometry. Photoion yields are recorded in the N 1s-regime, where the N^+-yield, corresponding to properties of the isolated molecule, and the $N_2 \cdot Ar^+$-yield, corresponding to properties of heteroclusters, were measured simultaneously. As a result, small spectral changes in line profiles and spectral shifts are resolved.

Fig. 1 shows a comparison of the photoion yields of isolated molecules and clusters in the regime of the N 1s$\rightarrow\pi^*$-transition. The spectra are found to be remarkably similar to each other, which is unlike previous results on homogeneous nitrogen clusters [2]. However, small and distinct differences between the spectra are observed: (i) The maxima of the vibrationally resolved band in Ar/N_2-heteroclusters are slightly redshifted by 3±1 meV relative to the bare molecule; (ii) The widths (FWHM) of these features increases from $\Delta E = 122$ meV in the isolated molecules to $\Delta E = 130$ meV in heteroclusters.
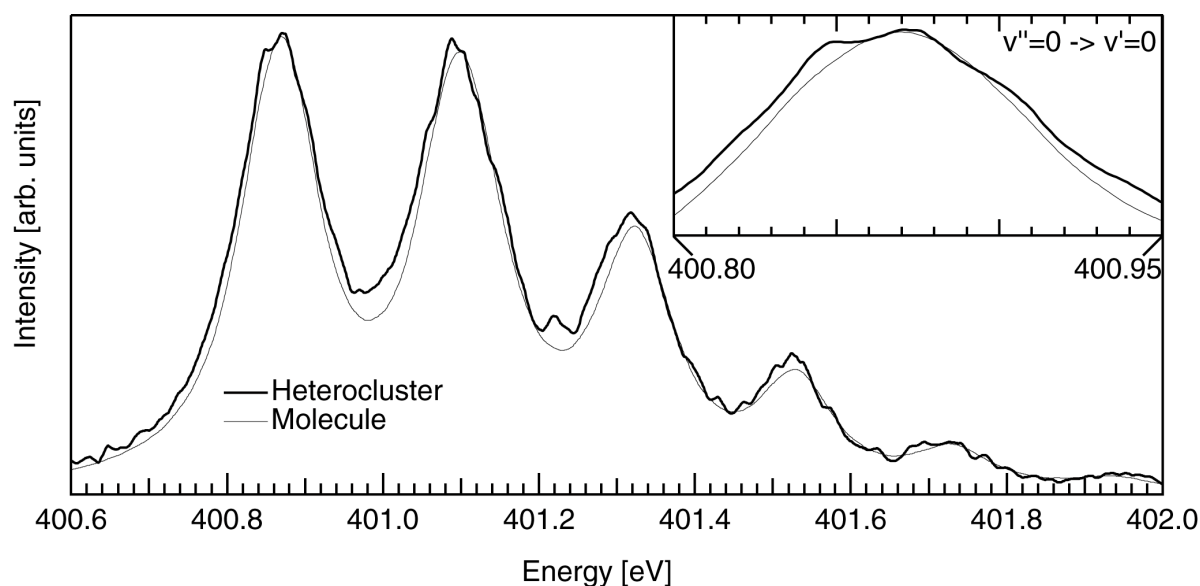
Fig. 1: Comparison of the N $1s \rightarrow \pi^*$-transition of isolated nitrogen and heterogeneous Ar/N_2-clusters. The intense L-continuum of argon has been subtracted in the case of heteroclusters. The inset shows the v''=0 →v'=0-transition in greater detail.

This cannot be attributed to differences in the spectral resolution, since both spectra are recorded simultaneously under entirely identical conditions. No such broadening was observed earlier for homogeneous N_2-clusters under comparable experimental conditions [2]. The de-convolution of the spectral features reveals that a Voigt-fit does not perfectly match the experimental line profiles. Therefore, the experimental results cannot be simply assigned to an increase in linewidth of the Lorentzian and Gaussian contributions. Specifically, it is expected that the band width of the N $1s \rightarrow \pi^*$-progression is efficiently affected by: (i) fast cluster decay dynamics of the final states, which are accessed in clusters as a result of the intermolecular coordinate, and (ii) the presence of intermolecular librations. As the number of clustered atoms and molecules increases, the conventional picture of Gaussian broadening of X-ray transitions in solids is approached, with the standard deviation $\sigma = [S(\omega) \cot(\omega/kT)]^{1/2}$. The coupling constant S is equal to mean number of phonons created in the transition, k is the Boltzmann constant, and T is the temperature. This provides an increase of the Gaussian width as a result of phonon-like broadening in clusters. The present results are currently modeled with respect to possible origins of the spectral shifts and peak shapes, where different compositions of the local surroundings are considered.

References
1   E. Rühl in '*Progress in Experimental and Theoretical Studies of Clusters*', Eds.: T. Kondow and F. Mafuné, World Scientific, Singapore, in press (2002).
2   R. Flesch, A.A. Pavylchev, J. J. Neville, J. Blumberg, M. Kuhlmann, W. Tappe, F. Senf, O. Schwarzkopf, A.P. Hitchcock, and E. Rühl, Phys. Rev. Lett. **86**, 3767 (2001).
3   E. Rühl, A.P. Hitchcock, P. Morin, M. Lavollée, J. Chim. Phys. **92**, 521 (1995).

Magnetic Studies on Mass-Selected Iron Clusters Using the X-Ray Magneto-optical Kerr Effect

V. Senz, R.-P. Methling, A. Kleibert, J. Bansmann, and K.-H. Meiwes-Broer

Universität Rostock, Fachbereich Physik, D-18051 Rostock

The magnetic properties of mass-selected iron clusters have been probed by measuring the x-ray absorption and reflectivity using *linearly polarized light* in the energy range of the Fe $2p$ levels in dependence of the magnetization state.

The iron clusters have been created in a recently developed, continuously working cluster source combining a hollow cathode arc discharge with a gas aggregation [1]. Fig. 1 shows a TEM micrograph of iron clusters with a mean diameter of about 5 nm deposited on a carbon grid.
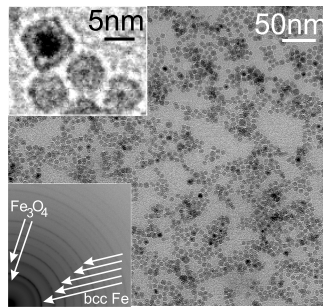
Fig. 1: Transmission Electron Microscopy micrograph of mass-selected iron clusters with a mean diameter of 5 nm. (Bottom inset: Beside the bcc iron diffraction pattern additional rings resulting from iron oxides, e.g. Fe_3O_4, can be observed.)

Prior to the experiments at the storage ring the magnetic hysteresis curves of different cluster samples have been recorded by means of conventional magneto-optical Kerr effect (MOKE) using a HeNe laser as light source. Two samples have been prepared with (24000 ± 2000) and (72000 ± 6000) atoms per cluster embedded in a silver matrix on a Si (111) substrate. Supposing spherical shape and iron bulk lattice constant, this corresponds to $D = (8.1\pm0.2)$ nm and (11.7 ± 0.3) nm, respectively. Fig. 2 shows the measured normalized magnetization M/M_S versus the applied field H at room temperature and 77 K for both cluster samples. Depending on the cluster size and temperature, respectively, these hysteresis curves reveal the transition from the ferromagnetic ordered state to the superparamagnetic state, in which the magnetization of small clusters can fluctuate in space due to thermal activation over the magnetic anisotropy barrier. This state is indicated by vanishing remanence and coercivity, as observed for the 8.1 nm clusters at room temperature. Increasing cluster size (11.7 nm) as well as decreasing temperature (77 K) leads again to locked moments, i.e. the ferromagnetic state.

For further chemical and magnetic characterization the cluster samples have been investigated by x-ray absorption and reflectivity at the Fe $2p$ levels. The x-ray absorption spectrum of the 11.7 nm cluster sample is shown in fig. 3. Whereas the $2p_{3/2}$ level exhibits a shoulder at the low energy side at about 708 eV, two distinct maxima in the $2p_{1/2}$ level at 722 eV and 723 eV are resolved and an additional shoulder at about 721 eV. The threefold splitting is interpreted as chemical shift of the oxidized fraction to higher binding energies. In order to estimate the relative fractions of different oxides three asymmetric Doniach-Šunjić line profiles have been fitted to the $2p_{3/2}$ level (with binding energies $E_{B,1} = 708.30$ eV, $E_{B,2} = 709.45$ eV, $E_{B,3} = 710.40$ eV) and the $2p_{1/2}$ ($E_{B,4} = 721.35$ eV,
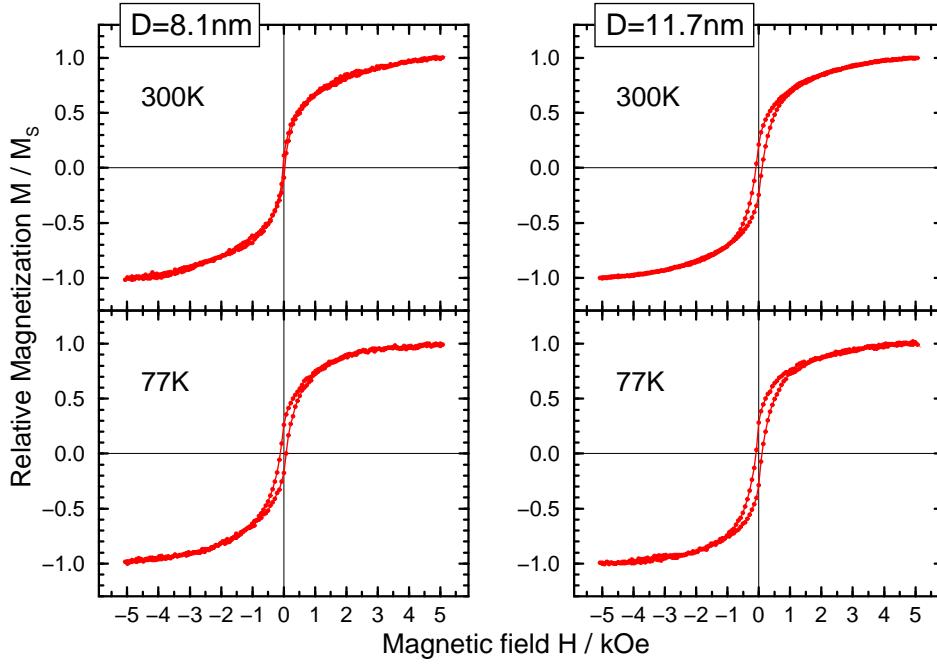
Fig. 2 : Magnetic hysteresis curves of mass-selected Fe clusters in Ag matrix as measured by (conventional) Magneto-optical Kerr effect using a HeNe-laser as light source.

$E_{B,5} = 722.85\,\text{eV}$, $E_{B,6} = 724.00\,\text{eV}$). By comparision with tabulated binding energies (e.g. [2]) the different lines can be most propably attributed to the most stable oxide configurations magnetite Fe_3O_4 and haematite $\alpha\text{-Fe}_2\text{O}_3$.

The investigation of the magnetization dependent reflectivity, i.e. the magneto-optical Kerr effect in transverse scattering geometry, has been the main interest of the experiments using soft x-rays. In fig. 4 the reflectivity spectra of the 11.7 nm cluster sample under the applied field $H\pm$ and after external magnetization are compared. Qualitatively the reflectivity spectra of the clusters can be understood in a similar way as the spectra of the closed iron or cobalt films or islands [3-5]. The reflectivity is determined by both the absorptive as well as the dispersive part of the complex index of refraction. The resonant enhancement sets in at lower binding energies than the absorption and due to the pronounced asymmetry of the absorptive part the reflectivity decreases smoother compared to a symmetric Lorentz like absorption. The magnetic asymmetry is quite remarkable
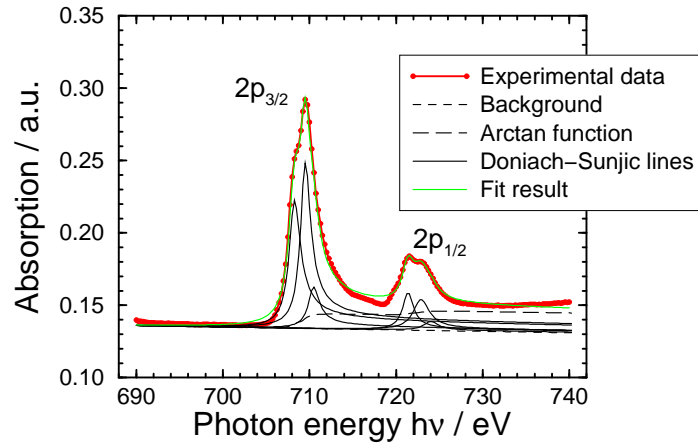
Fig. 3 : Experimental x-ray absorption and quantitative evaluation of the clean and oxdized iron fraction using Doniach-Šunjić line profiles.

for the spectra measured under applied field, but does not reach the noise level in the remanent state. Although the three different chemical components are not really distinguishable in the reflectivity it should be noted that the magnetic asymmetry seems to be restricted to the low energetic peak, i.e. to the clean iron fraction.
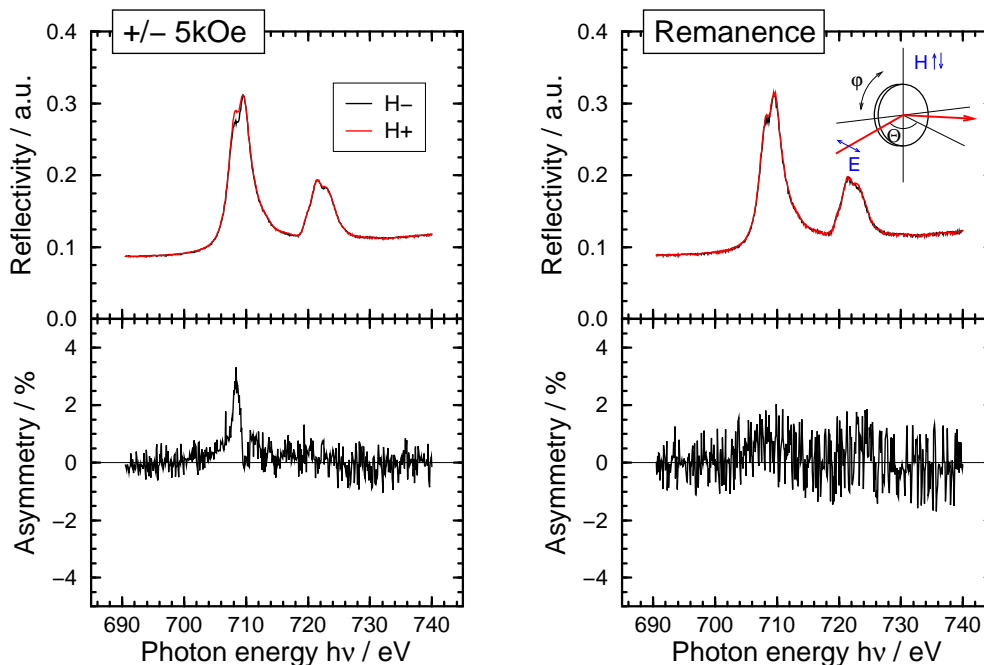
Fig. 4: X-ray reflectivity of Fe clusters ($D = 11.7\,\text{nm}$) embedded in Ag matrix under applied field ($\pm 5\,\text{kOe}$) and in the remanent state measured with linearly polarized light in transverse geometry (see inset).

In summary, although the experimental results presented here are still influenced by remarkable oxidation of the iron clusters, we succeeded to follow the transition from the ferromagnetic ordered spin state to the superparamagnetic relaxed state. By using soft x-rays we could evaluate the chemical nature of the clusters in more detail. After precursory experiments on iron and cobalt films and islands [3-5] we could also observe the x-ray magneto-optical Kerr effect on cluster samples. For the near future this opens the possibility for recording element-specific hysteresis curves on heterogenuous cluster samples, as e.g. alloy clusters.

[1] R.-P. Methling, V. Senz, E.-D. Klinkenberg, Th. Diederich, J. Tiggesbäumker, G. Holzhüter, J. Bansmann, and K.-H. Meiwes-Broer, Eur. Phys. J. D **16**, 173 (2001)
[2] X-ray Photoelectron Spectroscopy Database (NIST), http://srdata.nist.gov/xps/
[3] V. Senz, A. Kleibert, K.-H. Meiwes-Broer, and J. Bansmann, BESSY Annual Report 2000
[4] V. Senz, A. Kleibert, and J. Bansmann, Surf. Rev. Lett., in press
[5] A. Kleibert, V. Senz, K.-H. Meiwes-Broer, and J. Bansmann, BESSY Annual Report 2001

High Resolution Photoelectron Spectroscopy of Small Ne Clusters

S. Marburger[1], O.Kugeler[1,2], S. Adam[3], T. Möller[3], U. Hergenhahn[1,2]

[1] Fritz-Haber-Institut der Max-Planck-Gesellschaft, Faradayweg 4-6, 14195 Berlin, Germany
[2] Max-Planck-Institut für Plasmaphysik, Boltzmannstr. 2, 85748 Garching, Germany
[3] Hasylab am DESY, Notkestr. 85, 22603 Hamburg, Germany

Cold molecular beams produced by supersonic expansion have been studied by a number of groups in the past decades. Nowadays, it is possible to obtain van der Waals clusters of a variable size distribution with these techniques. It is well known that spectroscopic studies on small clusters with up to some hundreds of atoms yield information on cluster atoms from bulk as well as from surface sites. However, little work in the field of photoelectron spectroscopy on free cluster beams has been done in the past [1]. One reason for the lack of results in this field might be that the energy differences of the bulk and surface sites, and the signal from the monomer fraction of the beam, are rather small and with second generation light sources it was difficult to obtain well resolved spectra.

To obtain electron spectroscopic data from neutral van der Waals clusters we have designed a new experimental setup to be used at BESSY II. It combines a supersonic jet source with a high resolution electron analyser.

Experimental

The measurements were carried out at the U-125/1-PGM beamline. A Scienta SES 200 hemispherical electron analyser was positioned in the dipole plane under an angle of 54,7 ° ('magic angle') with respect to the orbit plane of the storage ring. Ne and Ar clusters were produced by a supersonic adiabatic expansion. The jet source was oriented perpendicular to the synchrotron beam as well as to the entrance trajectory of the electron analyser. The source was equipped with a copper nozzle of 0,2 mm diameter and a half opening angle of 15°. To obtain stable low temperatures necessary for clustering the nozzle was cooled with LHe or LN_2 as well as heated when necessary by a commercially available temperature controller . Details on the cluster source can be found in Ref. [2]. The supersonic beam was skimmed once allowing only the central, mostly supersonic part of it to propagate to the interaction region. Ne clusters were produced at temperatures around 43K and Ne gas pressures about 100 mbar. This lead to a pressure in the range of 10^{-3} mbar in the expansion chamber, and of 10^{-6} mbar in the main chamber.

Results

The spectra were recorded in the swept operation mode of the electron analyser at pass energies of 20 eV and 5 eV. An energy calibration was performed by comparing Xe NOO reference Auger spectra with the peak positions found by Aksela *et al.* [3].

Photoelectron spectra of the Ne 2s and 2p photoelectron lines, as well as of some 2p correlation satellites, are displayed in Figures 1a and 1b. Different than in earlier work [4], the 2s photoelectron line is clearly resolved into three components. While the sharp line from the monomer can be seen at highest binding energy, two broader components at lower binding energies result from surface and bulk sites of the cluster. Their shift towards lower binding energy, resulting from polarization of the surroundings of the vacancy left by the photoelectron, has been determined here for the first time, and was found as 0.30 and 0.49 eV. For the 2p photoelectron line the picture is less clear, since the splitting into the two fine-structure components is in the same order of energies as the cluster-monomer separation. The separation into monomer and cluster component is nevertheless clearly seen.
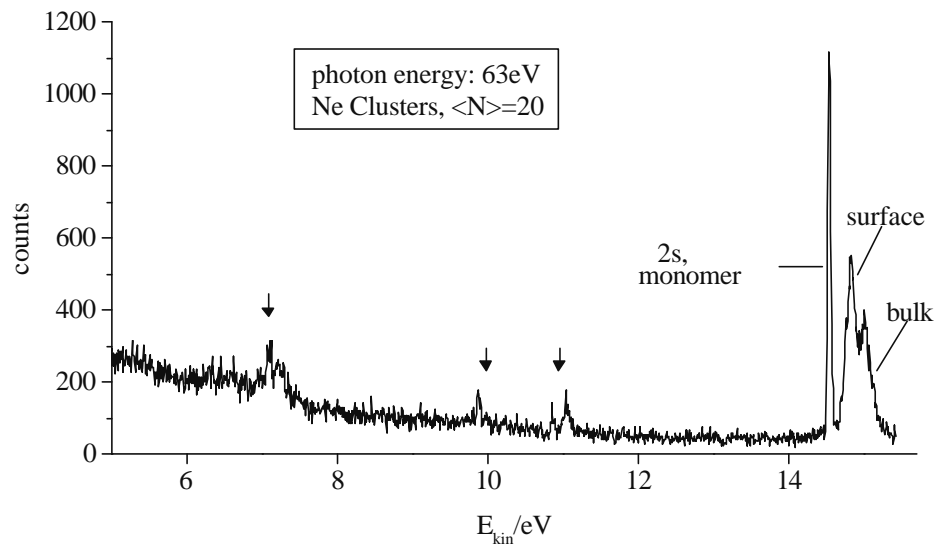
1a) Inner valence photoelectron spectrum of a Ne cluster beam. The satellite lines at 7,10, 9,88, 10,85 and 11,05eV kinetic energy are probably of atomic origin. Positions of atomic Ne $2s^2 2p^4 nl$ correlation satellites are indicated by arrows [5].
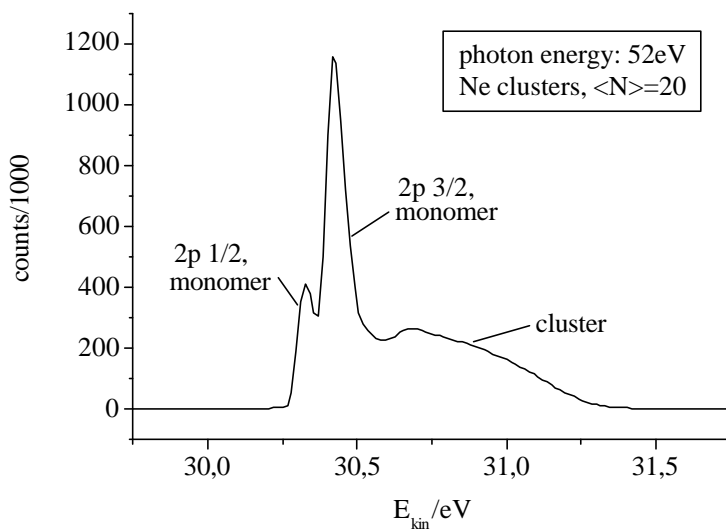
1b) Valence photoelectron spectrum of Ne cluster beam.

Literature

[1]   O. Björneholm, F. Federmann, F. Fössing, and T. Möller,
        Phys. Rev. Lett. 74, 3017-20 (1995).

[2]   R. Karnbach, M. Joppien, J. Stapelfeldt, J. Wörmer, and T. Möller,
        Rev. Sci. Instrum. 64, 2838-49 (1993).

[3]   H. Aksela, S. Aksela, and H. Pulkkinen,
        Phys. Rev. A 30, 865 (1984).

[4]   U. Hergenhahn, A. Kolmakov, M. Riedler, A. R. B. d. Castro, O. Löfken, and T. Möller,
        Chem. Phys. Lett. 351, 235-41 (2002).

[5]   G. Kutluk, T. Takaku, M. Kanno, T. Nagata, E. Shigemasa, A. Yagishita, F. Koike
        J. Phys. B 27 (1994) 5637 and references therein.

Cu - like Ni Clusters on the Graphite Surface

B. Wiesner[1], M. Heßler[1], N. Schneider[1], K. Fauth[1] and G. Schütz[2]

[1]Physikalisches Institut der Universität Würzburg, D-97074 Würzburg, Germany
[2]MPI für Metallforschung, Heisenbergstr. 1, 70569 Stuttgart

The physics involved in the interaction of metallic clusters to supporting surfaces and the changes in the cluster properties as a result thereof is of importance in several contexts of cluster research such as heterogenous catalysis [1,2] or nanoscale magnetism [3-6]. From early on photoelectron spectroscopy was used to characterize small particles grown at or deposited onto surfaces. [7-9]. However, the analysis of binding energy shifts bears some ambiguities as to whether they characterize the ground state electronic structure of the adsorbed species or whether they are more characteristic of the final state produced in the excitation process [7,9,10]. The nature of substrate also needs to be suitably accounted for in order to correctly interpret photoemission results based on electron binding energies and their (size dependent) shifts [11].

In the case of magnetic clusters, the magnetic properties themselves constitute a sensitive probe of interface induced changes to the clusters' electronic structure. However, it is only recently, that magnetic properties of cluster quantities significantly below the monolayer have become accessible to experimental exploration [12,3,4]. In this respect, x-ray circular magnetic dichroism (XMCD) has proven an extremely valuable tool, since it combines some key advantages such as element specificity, surface sensitivity and the possibility to be carried out in applied magnetc fields that make it almost ideally suited for the investigation of adsorbate systems on surfaces.

Recently, we have found that small Fe clusters, while strongly magnetized when embedded in an argon matrix, are forced into a nonmagnetic ground state when being in contact with the graphite surface [4]. Here, we show that the same is true for Ni clusters and explore the change in their electronic ground state upon exposition to the graphite surface by (resonant) valence photoemission using photon energies around the Ni 3p edge.

Cluster cations were generated and deposited *in situ* at low kinetic energies using a portable, UHV compatible laser vaporization and cluster deposition setup. A cluster ion beam is formed that travels through a combination of a quadrupole mass filter and an octopole ion guide before reaching the deposition spot. This setup allows us to mass select the clusters up to 9000 amu either atom by atom or to form larger mass distributions by operating the quadrupole and octopole as high and low pass mass filters, respectively. Soft landing conditions are established by covering freshly cleaved HOPG surfaces with 10-15 monolayers of Ar prior to deposition. Cluster coverages are kept below 5% of the atomic monolayer equivalent. The interaction to the underlying substrate is switched on by gently evaporating the rare gas layer at $\approx$50K. We note that within the cluster size range considered here (6 $\leq$ N $\leq$ 50), experiments on atomically mass selected cluster samples did not differ significantly from those obtained on broader mass distributions. Thus, our results reveal a general behaviour of small Ni clusters on graphite.

XMCD measurements were carried out with the cluster source and a superconducting split coil magnet system (B $\leq$ $\pm$2 T) attached to the UE56/2-PGM2 ellliptical undulator beamline at BESSY II. The photoemission experiments around the Ni 3p absorption threshold were carried out with the same cluster apparatus at the low energy photoemission beamline U125/1-SGM.

Fig. 1 displays absorption spectra measured in TEY mode at the Ni 2p edge of Ni clusters interacting with the graphite surface. No circular dichroism is visible at the applied field of $\pm$0.5T, showing that their ground state is indeed nonmagnetic, as was already the case with Fe clusters.
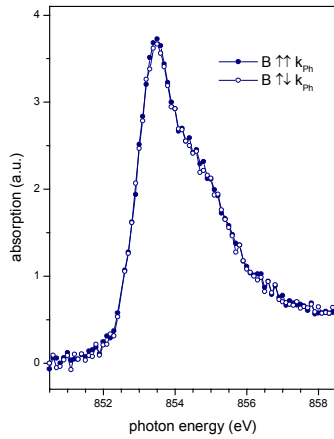
Fig. 1: Ni L_3 absorption spectra with the magnetic field parallel and antiparallel to the light helicity, respectively.

More information on the nature of this nonmagnetic state is contained in the energy dependent relative 3d photoionization cross section reported in Fig. 2. At every photon energy, four valence electron EDC curves were recorded, corresponding to the different stages of the sample preparation. These are the spectra of a) the clean HOPG surface, b) the Ar covered HOPG, c) same as b) but now with Ni clusters deposited and finally d) the bare Ni clusters on the HOPG surface after evaporation of the Ar layer. At the low coverages employed here, a change in the spectra is only observed within a few eV of the Fermi level, where we expect photoemission from the Ni clusters. The difference spectra (with / without clusters), normalized with respect to the incoming photon flux, are integrated over 2 eV below the Fermi level yielding the data points shown in Fig. 2.

The rare gas isolated clusters display a behavior remarkably similar to that of bulk Ni, the data of which [13] are included in Fig. 2. This resemblance shows, that the electronic configuration in the clusters is similar to the one of bulk Ni, i.e. $3d^9$.

As a result of the interaction to the HOPG substrate, the Fano antiresonance profile is largely suppressed. The almost monotonous behavior of the PI cross section is very much reminiscent of the Cu 3p edge, where no resonance occurs due to the filled 3d shell. We thus interpret our results as evidence for the formation of a $3d^{10}$ configuration in Ni clusters when adsorbed on graphite. This interpretation is largely in line with recent

Fig. 2: Ni 3d photoionization cross section close to E_F in bulk Ni [13], Ni clusters in an Ar matrix and the clus-ters on the HOPG substrate.

calculations [14] which predict precisely such a transition to occur for Ni monomers and dimers on graphene. We also note, that our results can be viewed as the inversion of a recent experiment by Verweyen et al. [15], who formed Ni-like metastable Cu atoms by laser excitation, which do, as a consequence, exhibit a Fano resonance profile at the 3p edge.

References

[1]   A. Sanchez et al.: J. Phys. Chem. A 103 (1999), 9573
[2]   H. Freund, Surf. Sci., in press
[3]   J. T. Lau et al.: Verhandl. DPG (VI) 36 (2001), 366
[4]   K. Fauth et al.: submitted to Phys. Rev. Lett.
[5]   G. C. Hadjipanayis, J. Magn. Magn. Mater. 200, 373
[6]   R. H. Kodama, J. Magn. Magn. Mater. 200 (1999), 359
[7]   M. G. Mason, Phys. Rev. B 27 (1983), 748
[8]   S. B. DiCenzo et al.: Phys. Rev. B 38 (1988), 8465
[9]   G. K. Wertheim and S. B. DiCenzo, Phys. Rev. B 37 (1988), 844
[10]   G. Faraci et al.: Z. Phys. D 23 (1992), 263
[11]   S. L. Qiu et al.: Phys. Rev. B 36 (1987), 1292
[12]   O. Rader et al.: Europhys. Lett. 46 (2) (1999), 231
[13]   M. R. Thuler et al.: Phys. Rev. B 27 (1983), 2082
[14]   D. M. Duffy and J. A. Blackman, Phys. Rev. B 58 (1998), 7443
[15]   A. Verweyen et al.: Phys. Rev. A 60 (1999), 737

Formation of a novel ohmic contact on silicon studied using photoelectron spectroscopy with large probing depth

M. Wanke, T. Kalka, S. Vandré, W. Busse, S.K. Becker, C. Preinesberger, and M. Dähne

Institut für Festkörperphysik, Technische Universität Berlin,
Hardenbergstraße 36, D-10623 Berlin, Germany

In a recent photoemission study, performed at the PM-2 and PM-5 beamlines at BESSY-I, we observed flatband conditions for rare-earth silicide monolayers on n-type Si(111) [1-3]. Metal contacts used in current device applications typically show barrier heights around 0.4 eV. Thus, the extremely low barrier heights of rare-earth silicide monolayers are promising for future device applications, e.g. for low-resistivity ohmic contacts on n-type Si in the very large scale integration technology (VLSI). For this purpose, however, a passivation of the monolayer against the ambient is required, without destroying the flatband conditions.

Si overgrowth on top of the monolayer is an interesting opportunity in this respect. In contrast to metal overlayers, Si is expected to conserve the flatband conditions, since the same interface structure is just introduced into the system a second time. This would enable e.g. the design of a low-resistivity ohmic contact, as shown in Fig. 1(a). In this design, a thin epitaxial Si overlayer is grown on top of the silicide monolayer without destroying the flatband conditions. The silicon layer is then contacted by a thick metal film with a much higher Schottky barrier. The resulting potential difference is accomplished by a strong electric field in the Si layer.

The different conductance paths in this device are shown in Fig. 1(b). Tunneling through the Si film will result in a good contact provided that the Si layer is this enough, i.e. in the order of 10 Å. If pinholes are present in the film, the conductance will even be further improved, since in this case a direct contact is formed between the metal overlayer and the monolayer.

Such a device requires that the initial flatband conditions are not modified upon Si overgrowth, Indeed, preliminary Si-2p core-level photoemission studies performed at the PM-2 beamline at BESSY-I did not indicate any shift of the substrate signal upon Si overgrowth, so that the flatband conditions were assumed to be conserved at moderate Si coverages [3-5]. However, the maximum photon energies from this dipole beamline that were useable in view of sufficient flux and resolution resulted in a limited probing depth, so that the band bending could be monitored only up to rather thin Si layers.

In order to investigate this effect in more detail and for higher Si coverages, photoemission experiments at the U41-PGM beamline at BESSY-II were performed. Exemplary results are shown in Fig. 2. The availability of higher photon energies around 400 eV at sufficient resolution and photon flux leads to a much higher bulk sensitivity at this undulator beamline. With these conditions we can clearly monitor the kinetic energy of the Si-2p substrate signal (indicated by the vertical line) up to Si-overlayer thicknesses exceeding 20 Å. Since no significant shift of this
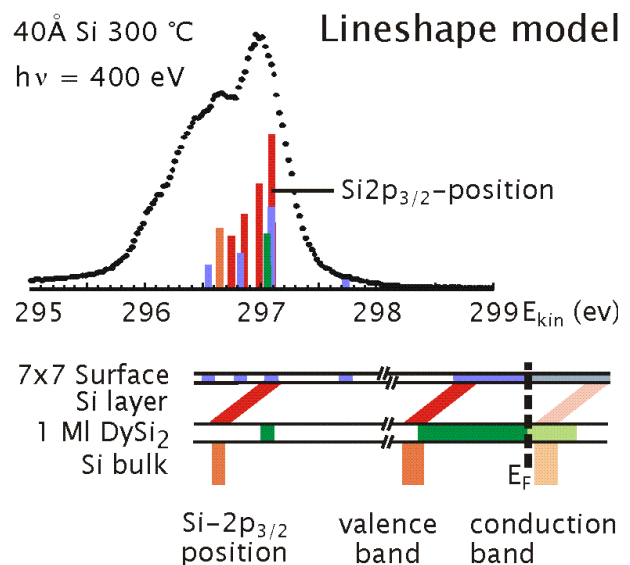

Figure 1

Figure 2

Figure 3

line is observed in Fig. 2 except for a minute variation below 0.1 eV, it is demonstrated that the flatband conditions are conserved to a very high degree upon Si deposition.

The best results in terms of the crystallinity of the Si films were obtained upon subsequent annealing at 300–350 °C, where typical surface-state features of the Si(111)7×7 surface appeared as a fingerprint in the valence-band spectra. At higher annealing temperatures, the increasing Dy-4f signal indicates the onset of Dy diffusion to the surface.

The Si-2p spectrum of such a layered structure consist of a variety of components, which are assigned to the substrate, the silicide monolayer, the thin Si overlayer with a weighted distribution of kinetic energies due to the built-in electric field, and finally the 7×7 reconstructed surface. This is shown schematically in Fig. 3. Preliminary least-squares fit results demonstrate a nice agreement with the experimental spectra, supporting the conservation of the flatband conditions and underlining the validity of the model of the band alignment shown in Fig. 1(a).

[1]   S. Vandré, T. Kalka, C. Preinesberger, and M. Dähne-Prietsch, Phys. Rev. Lett. **82**, 1927 (1999); *ibid.*, Phys. Rev. Lett. **82**, 4370 (1999).
[2]   S. Vandré, C. Preinesberger, T. Kalka, and M. Dähne-Prietsch, J. Vac. Sci. Technol. B **17**, 1682 (1999).
[3]   BESSY-Jahresbericht 1999, p. 336.
[4]   M. Dähne, S. Vandré, C. Preinesberger, S.K. Becker, W. Busse, and T. Kalka, Adv. Solid State Phys. **41**, 227 (2001).
[5]   S. Vandré, C. Preinesberger, W. Busse, and M. Dähne, Appl. Phys. Lett. **78**, 2012 (2001).

High-resolution photoelectron spectra of Si(111) terminated by a GaSe van der Waals layer

R. Fritsche, E. Wisotzki, A. Thißen, A.B.M.O. Islam, A. Klein, W. Jaegermann
Darmstadt University of Technology, Institute of Materials Science, D-64287 Darmstadt
D. Tonti, R. Rudolph, C. Pettenkofer
Hahn-Meitner Institut, Solar Energy Research, D-14109 Berlin

The structure of the Si(111):GaSe system is characterized by a layer of Ga on top of the silicon surface atoms and an outermost hexagonally close-packed Se layer [1]. Each Si atom bounds to one Ga atom and to three Si back bonds, while each Ga has one Si and three Se bonding partners and each Se atom binds to three Ga atoms leading to a saturation of the Si dangling bonds. We have prepared the Si(111):GaSe surface termination by selenization of a monolayer of Ga, which has been deposited onto Si(111)-7×7 at 550°C substrate temperature. The deposition chamber was directly attached to a photoelectron spectrometer system connected to the U49-2/PGM2 beamline of the BTU Cottbus/HMI/TU Darmstadt CRG.

During deposition of Gallium a number of surface structures evolve showing characteristic superstructures in LEED [2-4]. After 40 minutes of Ga deposition at 1Å/min we observe a 6.3√3×6.3√3 superstructure, which has been related to monolayer coverage where a monolayer corresponds to one Ga atom per Si surface atom [2]. The atomic structure of the Si(111)-6.3√3×6.3√3:Ga surface is, however, still unresolved. Si $2p$ and Ga $3d$ core-level photoelectron spectra taken after different Ga deposition times are shown in Fig. 1. The characteristic shape of the Si $2p$ level for the Si(111)-7×7 surface disappears and is replaced by a two component emission structure with a high intensity emission attributed to bulk Si atoms and a low intensity shoulder at lower binding energy. For deposition times below 20 minutes, a single component Ga $3d$ emission is observed. At this coverage we expect the surface to be covered mainly with two-dimensional Si-Ga bilayer islands [5]. These are described in the literature as the atomic structure for the 6.3x6.3 reconstruction for coverages of approximately 0.6-0.7 monolayers [2,5]. At lower substrate temperatures (~400°C) this is the saturation coverage of Si(111):Ga [2]. For the preparation of the Si(111):GaSe termination 1 monolayer Ga coverage is required, which can be achieved only at higher temperatures. With the evolution of the 6.3√3×6.3√3 superstructure, which starts after approx. 20 minutes of deposition, a second component appears in the Ga $3d$ level. Its binding energy corresponds to metallic Ga. Because of the absence of a metallic Fermi edge in the valence bands this second Ga species is attributed to two-dimensional Ga islands adsorbed on the Si-Ga bilayer surface structure rather than to the growth of three-dimensional metallic Ga islands [3]. A modification of the Si-Ga bilayer structure is also not expected as there is no change in the Si $2p$ emission. The changes in binding energy, which are paralleled by those of the Ga 3d emission are due to different band bending in the Si substrate. After 40 min of Ga deposition the binding energy corresponds to a surface Fermi level position of $E_F-E_{VB} = 0.39$ eV, which agrees with the Ga/p-Si Schottky barrier height.
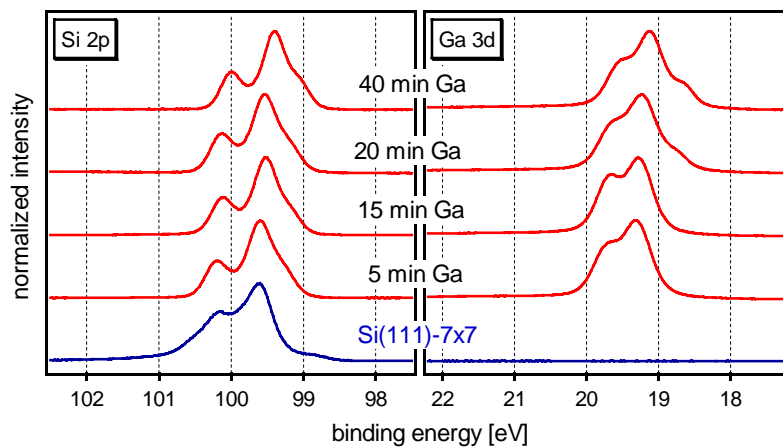

Fig. 1 Photoelectron spectra of Si(111)-7x7 with increasing Ga deposition at 550°C.

Photoelectron spectra of the Si(111)-6.3√3×6.3√3:Ga surface after different times of selenization are shown in Fig. 2. With the evaporation of Se the shape and position of the Si 2*p* core level spectra changes. After the first selenization step of 5 min a very sharp Si 2*p* emission line is observed. The spectral shape of the line is mainly represented by a single component, which is attributed to bulk Si emission. The absence of a surface core-level shift on Si(111) is unique to the Si(111)-1×1:GaSe van der Waals surface and indicates a non-polar Si-Ga bond of this termination [4]. The Ga 3*d* emission shows clearly two components, where the intense high binding energy component can be attributed to emission from Ga atoms bonded in the Si(111):GaSe surface termination. The smaller low binding energy component corresponds to metallic Ga. Obviously the amount of Se deposited was not sufficient. After 10 min of selenization the metallic Ga component disappeared. All three levels are shifted to higher binding energy which can be attributed to reduced band bending in the n-type Si substrate indicating electronic passivation of the surface [4]. A shoulder at low binding energies can be identified in the Si 2*p* emission after 10 min selenization. The intensity of the shoulder increases for longer selenization times and the Si 2*p* spectra obtained becomes closer to those observed for the different Si(111):Ga surfaces. It is evident from the very sharp Si 2*p* emission that after 5 min of selenization most of the Si surface atoms are terminated by the GaSe layer, but there is still metallic Ga on the surface. With longer selenization times the excess Ga is removed from the surface. However, increasing selenization time also removes the Ga atoms from the Si-Ga bonds and therefore the termination of Si surface atoms. This is indicated by the shoulder in the Si 2*p* spectra, which reappears after 10 min. The occurrence of √3×√3 fractional order diffraction spots in LEED, which corresponds to a Si(111) surface covered by 1/3 monolayer of Ga, after 20 min of selenization further supports this conclusion. Surprisingly, higher selenium exposure leads to selective removal of selenium from the surface and leaves 1/3 monolayer of Ga. This indicates a high thermodynamic stability of the Si(111)-√3×√3:Ga surface.
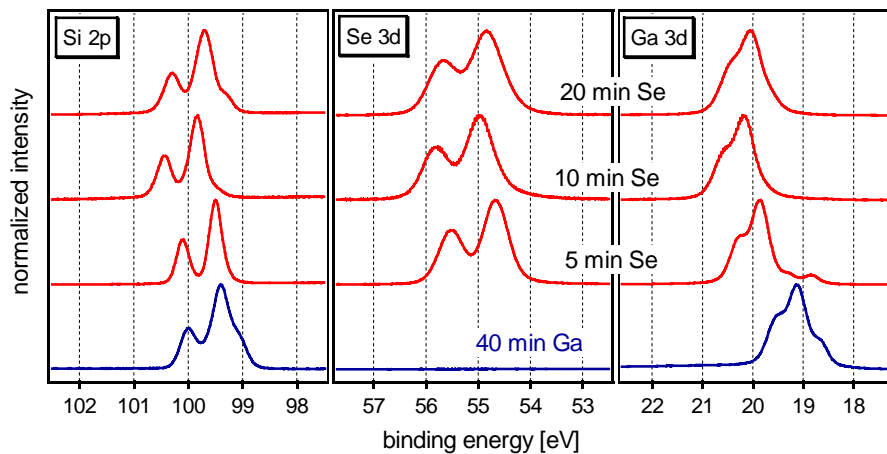
Fig. 3: Si 2p, Ga 3d and Se 3d core-level photoelectron spectra of the Si(111)-6.3√3x6.3√3:Ga surface after selenization for different times.

[1] Jedrecy et al., Phys. Rev. B **56**, 9583 (1997); Köebel et al., Phys. Rev. B **56**, 12296 (1997). Meng et al., Phys. Rev. B **64**, 235314 (2001).
[2] V.G. Lifshits, A.A. Saranin and A.V. Zotov, *Surface Phases on Silicon* (John Wiley & Sons, Chichester, 1994).
[3] R. Fritsche, E. Wisotzki, A. B. M. O. Islam, A. Thißen, A. Klein, W. Jaegermann, R. Rudolph, D. Tonti and C. Pettenkofer, Surf. Sci. (submitted).
[4] R. Fritsche, E. Wisotzki, A. B. M. O. Islam, A. Thißen, A. Klein, W. Jaegermann, R. Rudolph, D. Tonti and C. Pettenkofer, Appl. Phys. Lett. (in press).
[5] M. Y. Lai and Y. L. Wang, Phys. Rev. Lett. **81**, 164 (1998); Phys. Rev. B **60**, 1764 (1999); S.-F. Tsay, M.-H. Tsai, M. Y. Lai and Y. L. Wang, Phys. Rev. B **61**, 2699 (2000).

X-ray absorption studies on $Bi_2Sr_{2-x}La_xCuO_{6+\delta}$

M. Schneider, R. Müller, R. Mitdank, R.-St. Unger, R. Bartmann, T. Stemmler,
A. Krapf, C. Janowitz, R. Manzke

Humboldt-Universität zu Berlin, Institut für Physik, Invalidenstraße 110, 10115 Berlin

In the cuprates the electronic states near the Fermi energy E_F, which are involved in the low lying excitations leading to superconductivity, are mainly due to holes in the CuO_2 planes. Over the last years, soft x-ray-absorption spectroscopy (XAS) has been utilized to obtain information about unoccupied states at both the O and Cu sites [1]. Complementary from photoemission (PES) measurements we can derive information of the occupied density of states.

Here we report the current status of our investigations on the electronic structure of the bismuth-based cuprates by x-ray absorption and photoemission spectroscopy. The aim of the investigations is to understand the influences of doping on the number of holes, T_C, and the electronic structure of the Bi-based cuprates.

We present XAS and PES data from $Bi_2Sr_{2-x}La_xCuO_{6+\delta}$ samples. The advantage of the Bi-n=1 material in comparison to n=2 should be the simple fact that for both, the superconducting and the normal state properties, only one CuO_2 layer is responsible. Therefore the n=1 material seems to be a prototype for the cuprates. It is now well established that Lanthanum free samples are

Fig. 1. Transition temperature T_C as a function of La content x.

strongly hole overdoped with a T_c of about 7 K. In order to reach optimal T_c part of the Sr^{2+} is replaced by La^{3+} what reduces the hole concentrations in the Cu-O plane. The dependence of T_c on x is strongly parabolic (see Fig. 1). The optimum T_c of about 18 K and the sharpest transition ΔT of 2 K is found for a La content of x=0.33 controlled by measuring the ac susceptibility [2].

All samples are sintered pellets prepared by standard powder metallurgical methods from mixtures of Bi_2O_3, La_2O_3, CuO und SrCO with a composition chosen to give a stoichiometric weight of $Bi_2Sr_{2-x}La_xCuO_{6+\delta}$. The content of La was accurately determined by energy dispersive x-ray analysis (EDX).

The x-ray absorption measurements have been carried out in the fluorescence mode at the VLS-PGM beamline. The overall energy resolution at the O 1s absorption edge was 0.3 eV, the sample temperature was 300 K. The fluorescence light was detected at an angle of 45° with respect to the photonbeam using a Ge detector. The vacuum in the chamber was better than 10^{-9} mbar during the measurements. The PES-experiments were performed in HASYLAB, Hamburg by the use of linearly polarized radiation emitted from the high resolution 3m normal-incidence monochromator HONORMI at beamline W3.2. For the measurements discussed here 18 eV photon energy was used. The energy distribution curves (EDC) were recorded with a hemispherical deflection analyser with a total acceptance angle of 1° [3]. Our measurements were performed with an energy resolution of 50 meV as measured from an Au Fermi edge.

In Fig. 2 the photoemission spectrum is shown for samples with a variation of La from x = 0 to x = 78. In the metallic regime the intensity at E_F and simultaneously the emission maximum at 1.5 eV binding energy decrease continuously. In the insulating regime a new state appears at 2.5 eV binding energy. Upon La doping the whole valence band shifts by 400 meV to higher binding energies (observe the dashed line denoting the emission maximum of the La=0 spectrum). In Fig. 3 the samples reveal a Fermi-Dirac distribution at the Fermi level E_F and are thus metallic up to La < 0.7, and there is almost no emission at E_F for La > 0.7. This means that the samples are insulating under these conditions. In conclusion PES probes the spectral weight of the occupied density of states The results can be described within the framework of elaborated models based on a Hubbard Hamiltonian [4].
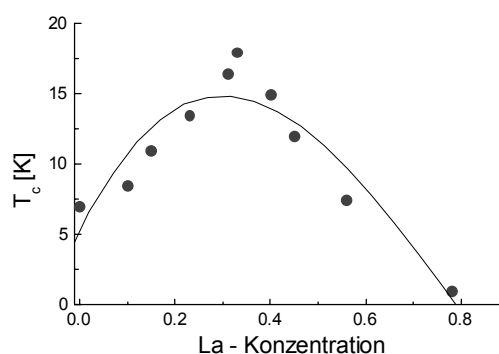
In the XAS spectrum in Fig. 3 the intensity of the pre-peak is highest for optimal La doping ($x \approx 0.33$, $T_c = 18K$). With increasing La content, the height of the pre-peak decreases. With decreasing La content, the height of the pre-peak also decreases. For the material $Bi_2Sr_{2-x}La_xCuO_{6+\delta}$ the spectral weight of the pre-peak scales with Tc and not with the hole density in the CuO-planes. These results are similar to previous findings from XAS measurements on $Bi_2Sr_{2-x}La_xCuO_{6+\delta}$ single crystals [5].

So the XAS measurements on the $Bi_2Sr_{2-x}La_xCuO_{6+\delta}$ system give a reason to put the established view of the origin of the O 1s pre-peak in high-T_c materials into question [1].
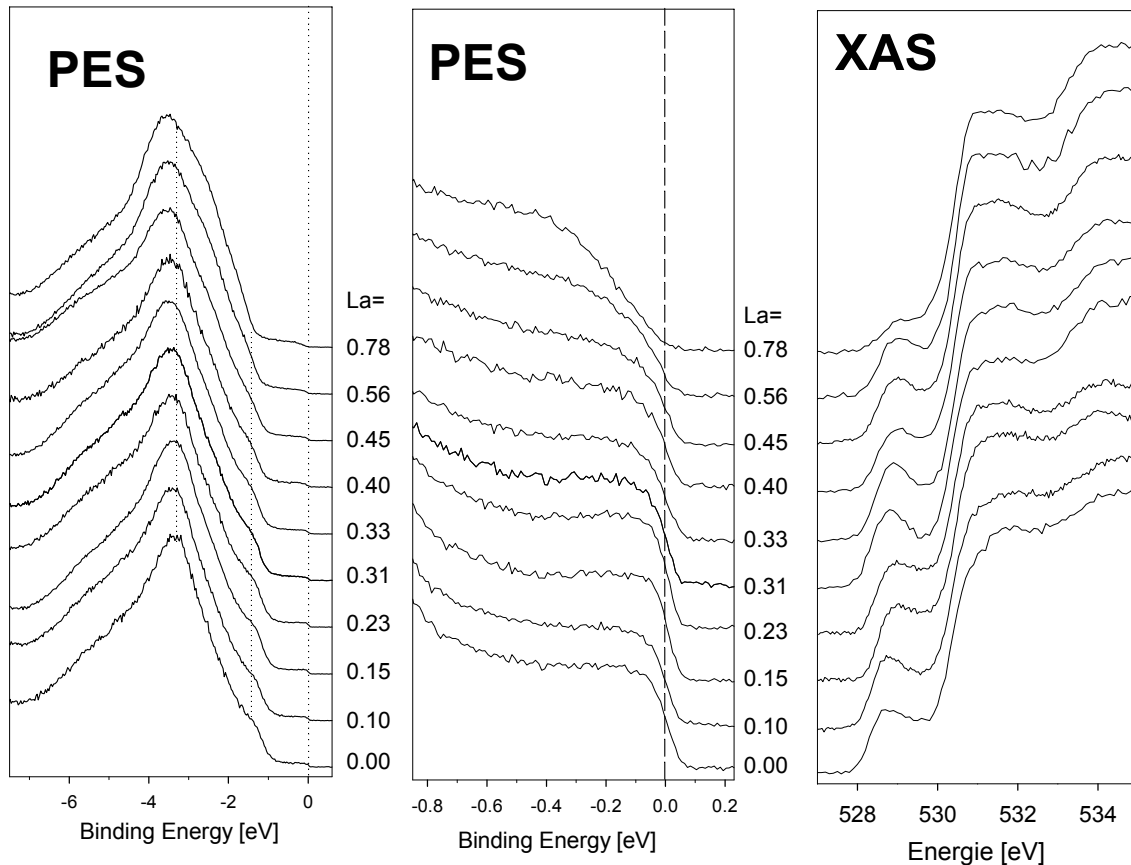
Fig. 2. PES of $Bi_2Sr_{2-x}La_xCuO_{6+\delta}$ (hν=18eV, T=50 K) for samples with various La content (x= 0…0.78)

Fig. 3. Same results like in Fig. 2., only the region near the Fermi-edge

Fig. 4. X-ray absorption spectrum (XAS) of the O 1s prepeak of $Bi_2Sr_{2-x}La_xCuO_{6+\delta}$ of the same samples. The spectra are normalized at 600 eV photon energy.

REFERENCES

[1] J. Fink et al., J. Electron Spectroscopy Rel. Phen. **66** (1994) 395
[2] A. Krapf et al., to be published
[3] K. Roßnagel et al., Nucl. Instrum. Methods Phys. Res. A **467-8**, 1485 (2001)
[4] J. Wagner et al. Phys. Rev. B **43**, 10517 (1991)
[5] R. Müller et al, Physica B (2002), in press, and cond-mat/0110522

Resonant photoemission on iron oxides

Yu. S. Dedkov[1], J. O. Hauch[1], R. Calarco[1], O. Rader[2],
U. Rüdiger[1], G. Güntherodt[1]

[1]*II. Physikalisches Institut, RWTH Aachen, 52056 Aachen, Germany*
[2]*BESSY G.m.b.H. Albert-Einstein-Straße 15, 12489 Berlin, Germany*

The materials class of half-metallic ferromagnets (HMF) has attracted large interest recently in the search for efficient spin-polarizers in spin-electronics. The intriguing feature of metallic conductivity for one spin component and semiconducting behavior for the other was theoretically predicted on the basis of electron band structure calculations for, e .g. magnetite (Fe_3O_4) [1]. The recent studies of Fe_3O_4 by means of spin-resolved photoemission spectroscopy (PES) have shown a high spin polarization near E_F [2] and demonstrate a clear fine structure of photoelectron spectra that make this oxide a promising material for spintronics.

The electronic structure and the Verwey transition (sharp decrease in the conductivity near $T_V \sim 120K$) of Fe_3O_4 have been intensively studied in the past theoretically and experimentally [1-7]. However, the interpretation of the valence-band photoemission spectra of Fe_3O_4 and the other iron oxides has long been a matter of debate. Earlier studies interpret the properties of magnetite by ligand-field theory (3d cation levels split by the oxygen ligand field) [4]. In the next step the configuration interaction within the 3d multiplet and the charge transfer between the 3d and the ligand orbitals was taken into account. In contrast, recent O K-edge x-ray

Fig. 1. Resonance PES spectra for FeO(111)/Fe(110)/W(110) system near 3p-3d resonance.

absorption and emission experiments on Fe_3O_4 suggested that the states on both sides of the band gap are of 3d origin and Fe_3O_4 should therefore be considered as a Mott-Hubbard insulator [5]. The present investigation was dedicated to the investigation of the electronic

structure of the iron oxides (FeO and Fe_3O_4) by resonant photoemission measurements at the 3p-3d resonance.

All experiments were carried out in an UHV chamber with a base pressure of $1\cdot10^{-10}$ mbar that was connected to the U125/1-PGM beamline of BESSY II. The photoemission spectra were collected in the normal emission geometry with 30° off-normal incident light using a VG Escalab analyzer. The electric field vector of the light was parallel to the [001] direction of the bcc lattice of W(110) or Fe(110)) and to the [$1\bar{1}0$] direction of fcc lattice of Fe_3O_4(111).

The mechanism of resonant photoemission in 3d metals and their compounds is well known. From the localized-electron point of view it is caused by the final-state interference between direct photoemission and Auger electron emission. For iron oxides and other late transition-metal oxides it is generally believed that the 3p-3d exitations are quite localized and involve only 3d-derived final states. Therefore, an approach has been used in which the difference between the valence-band electron distribution curves (EDCs) measured just above (on) and below (off) the resonance is used to remove the nonresonant O 2p contributions. The resulting features reflect the 3d-derived final states.

In Fig. 1 the series of the photoemission spectra for the FeO(111)/Fe(110)/W(110) system around the 3p-3d resonance is presented. In the case of FeO, which contains only Fe^{2+} ions, the on-resonance energy of photons corresponds to 57eV and the off-resonance one to 52eV. It is obvious, from the charge transfer point of view, that the photon energies corresponding to on- and off-resonance depend slightly on the valency of the Fe ions in the oxides. Such an example is shown in Fig. 2. In this case for magnetite the on-resonance energy of photons is 58eV and the off-resonance at 53eV. In this Figure the photoemission spectra (a) and the dependencies of the intensity of pronounced features in (a)
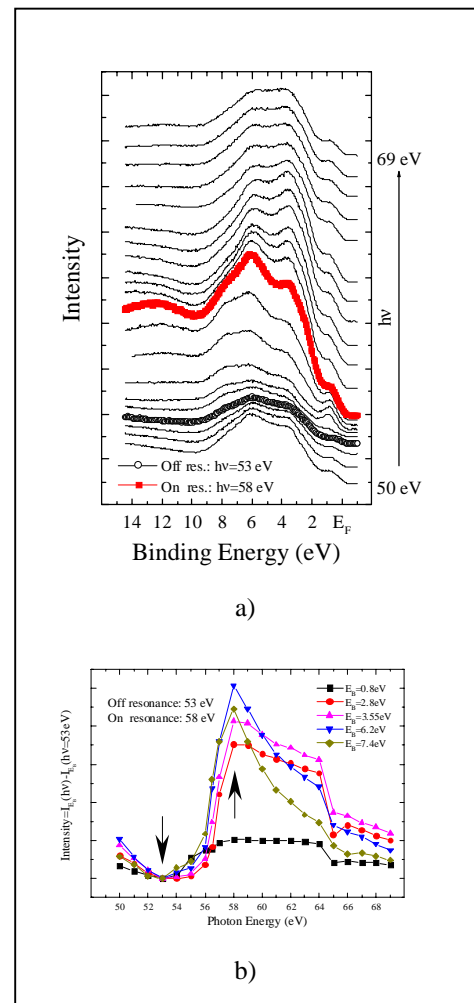
Fig. 2. Resonance PES spectra for different photon energies (a) and intensity of the main features of the resonance spectra as a function of the photon energy (b) for the Fe_3O_4(111)/Fe(110)/W(110) system near the 3p-3d resonance.

at selected binding energies (E_B) on the photon energy (b) are shown for the $Fe_3O_4(111)/Fe(110)/W(110)$ system. As it was found before [6], it may be possible to partially separate the contributions to the resonant photoemission of Fe_3O_4 from Fe^{2+} and Fe^{3+} ions by taking difference curves between EDCs measured at the on- and off-resonance photon energies of the corresponding iron valencies.

From such an analysis of the resonant photoemission spectra of Fe_3O_4 and from comparing such spectra for magnetite and FeO (Fig. 1) we conclude that features at $E_B=0.8eV$ can be related only to final states of the Fe^{2+} ions. In fact, this feature has been assigned in earlier studies to a state of the $d^6\underline{L}$ ($\underline{L}$ presents a ligand hole) final-state multiplet involving charge transfer between the cation 3d and the ligand 2p orbitals [6,7]. Experimentally it appears only when there are Fe^{2+} ions in the oxides (FeO and Fe_3O_4).

Our assignments of the above 3d-derived final states are in essential agreement with previous resonant photoemission studies of Fe_3O_4 [6,7]. The binding energies of the resonanting states in the present work were found at: 0.8, 2.8, 3.55, 6.2 and 7.4eV, somewhat different from the values found in other experiments for (110) oriented single crystal [6] and for epitaxial (111) oriented films of Fe_3O_4 on Pt(111) [7].

The same analysis as for the feature at $E_B=0.8eV$ was carried out for other features in the PES spectra and does not indicate a simple situation in this case. We therefore conclude that in most cases the characteristics of resonant photoemission observed in FeO cannot be used straightforwardly to separate contributions from the Fe^{2+} and Fe^{3+} ions in Fe_3O_4.

[1]. Z. Zhang and S. Satpathy, Phys. Rev. B **44**, 13319 (1991).

[2]. Yu. S. Dedkov, U. Rüdiger, G. Güntherodt, Phys. Rev. B **65**, 064417 (2002).

[3]. W. E. Pickett and J. S. Moodera, Physics Today **54**, 39 (2001).

[4]. S. F. Alvarado et al., Phys. Rev. B **14**, 2740 (1976).

[5]. Y. Ma et al., Phys. Rev. B **48**, 2109 (1993).

[6]. R. J. Lad and V. E. Henrich, Phys. Rev. B **39**, 13478 (1989).

[7]. Y. Q. Cai et al., Phys. Rev. B **58**, 5043 (1998).

A STATISTICAL CROSS-LINKING MODEL FOR THE CHEMICAL STRUCTURE OF THE SiO$_2$/Si(100) INTERFACE

S. Dreiner [1], M. Schürmann [1], C. Westphal [1], and H. Zacharias [2]
[1] Universität Dortmund, Lehrstuhl für Exp. Physik I,Otto-Hahn-Str.4,44221 Dortmund
[2] Universität Münster, Physikalisches Institut, Wilhelm-Klemm-Str.10, 48149 Münster

The thermally grown SiO$_2$/Si-interface has been studied extensively during the last years because of the significant role of SiO$_2$/Si-interfaces in semiconductor devices (for instance in MOSFETs). From previous studies it is known that the intermediate oxidation states of silicon play a central role in the transition from the perfect crystalline structure of the Si substrate to the amorphous silicon oxide [1],

A very powerful experimental tool to investigate the structure of the SiO$_2$/Si interface is high-resolution core-level photoemission spectroscopy. Si 2p photoemission spectra (Fig. 1) show chemically shifted components derived from individual oxidation states. Polar-angle and oxidation-state resolved photoemission investigations of the SiO$_2$/Si(111) system [2] established the statistical cross-linking model. The essence of this model is an abrupt transition from Si to SiO$_2$, with the dangling bonds from the two sides of the interface plane stitched together. The population of each suboxide species at the interface is derived from a statistical analysis. The polar-angle dependence of the Si 2p oxidation states of SiO$_2$/Si(100) system was investigated by Oh et al. [3] .   The result from their observations is a graded interface consisting of three layers. They found an identical polar-angle dependence of silicon suboxides with one bond and suboxides with two bonds to oxygen (Si^{1+}, Si^{2+}). The polar-angle dependence of the Si^{3+} component (three bonds to O) exhibits a steeper increase of the photoemission signal than the two previously discussed suboxides at grazing emission directions. This is explained by a wider depth distribution of the Si^{3+} species than the Si^{1+} and Si^{2+}. They concluded that the Si^{1+} and Si^{2+} exist just at the first layer of the interface, while the Si^{3+} species is distributed over second and the third layer of the interface. In this Report we show that the photoemission polar-angle dependence of Si suboxides at SiO$_2$/Si(100) interface can be explained by a simple statistical model for the atomic populations and depth distributions of the Si^{x+}.

Thin SiO$_2$ films were grown in-situ by thermal oxidation, the oxygen pressure was kept at 5x10^{-6} mbar for 10 minutes while the crystal was at a temperature of 650^0 C. The electron energy resolution was about 50 meV and the photon energy resolution was set to 90 meV. At a fixed polar angle, photoemission spectra were recorded at the BESSY II U-41 PGM beamline over 360^0 azimuth range with an increment of $\Delta\Phi=2°$. Subsequently, a new polar angle was set with an increment of $\Delta\Theta=2°$ and a new azimuth-scan was recorded. This was repeated until the full polar and azimuth range were covered (0°<Θ<84°, 0°<Φ<360°). In order to eliminate photoelectron diffraction effects at a given polar angle all spectra at this polar angle are added up.

Figure 1 shows a typical photoemission spectrum of the oxidized surface after the secondary background has been subtracted. The line-shape consists of seven resolved components, which correspond to the electron signals of Si^0 (B + α + β), Si^{1+}, Si^{2+}, Si^{3+}, and Si^{4+}.   The Si^0-signal was composed of the bulk signal (B) and two extra components (α, β). These components are assumed to be due to strained interfacial Si without any Si-O bonds [3]. Each measured spectrum was decomposed by least squares fitting into seven components, each of which consisting of a pair of spin-orbit split Gaussian peaks. Peak positions agree well within a few percent to previously published results [3].

Figure 1: Typical photoelectron spectrum of the oxidized Si(100) surface. Decomposition into different silicon oxide states is obtained from a least squares fit.

In our model the interface consists of three layers (Fig. 2a). The upper layer is connected with the SiO_2 film and the lower layer is connected with the silicon crystal. A silicon atom within the middle layer may be bond to silicon and oxygen in both directions (upper and the lower layer). In Figure 2b all possible bonding configurations of Si atoms at the interface are displayed. In the easiest configuration the silicon atom in the center of the cluster is bond to silicon neighbours only (Fig. 2b, Si^0-cluster). Each silicon bond can be replaced with a oxygen bond so that all Si oxidation states are possible. Since oxidation of the Si surface is considered to be a relatively random and local process, we derive the probability of each configuration from a statistical analysis. Taking into account the symmetry-equivalent configurations and assuming that each bond to oxygen is as twice as likely as a bond to silicon, the probability p of the suboxides is obtained as displayed in Fig. 2. This assumption can be put down to the fact that the number of O atoms is twice the number of Si atoms in SiO_2. The probabilities of Si in the upper layer are calculated with all bonds to the layer above Si being bonds to oxygen. In the case of Si in the lower layer all bonds to the layer below Si are bonds to silicon. Due to the different Si densities of crystalline silicon and SiO_2 we allow a change of the Si density in the various interface layers.
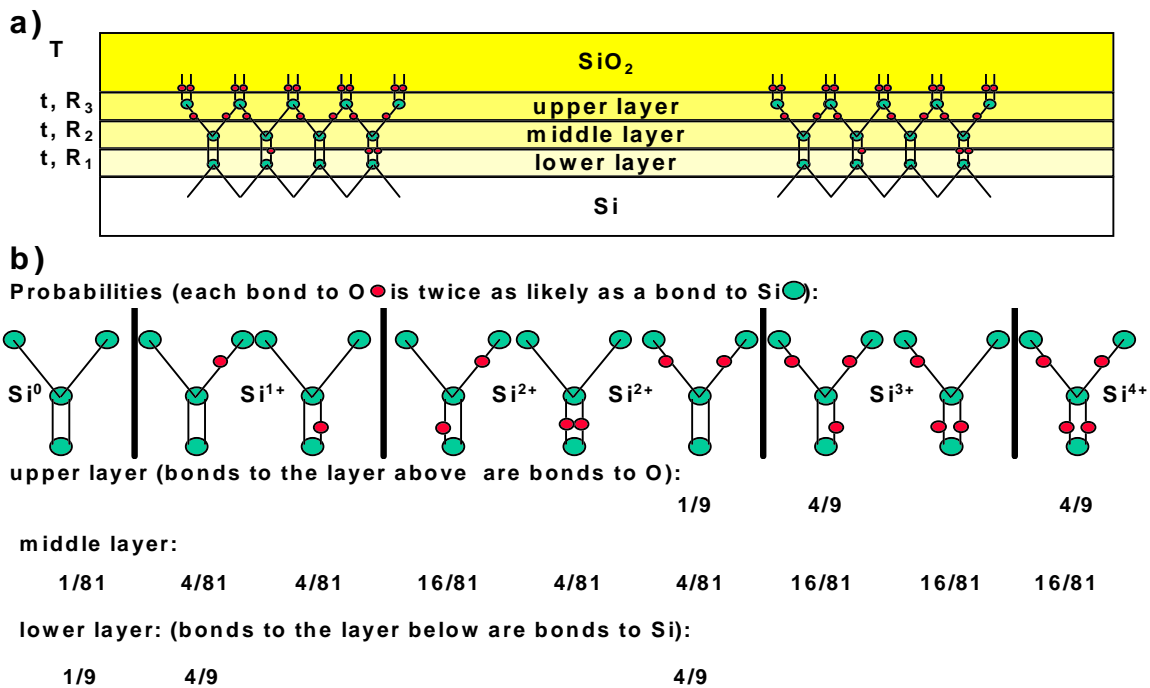
Figure 2: Three layer interface model (a) with all possible local bonding configurations and their probalities (b).

The Si 2p intensity variation as a function of polar angle of each oxidation component ($I_0, ..., I_4$) can be calculated using a simple electron damping scheme, including the probabilities obtained from our model

$$I_0 = n_{Si} \left[e^{\frac{-3t}{\lambda z}} + \left(R_1 \frac{1}{9} e^{\frac{-t}{\lambda z}} + R_2 \frac{1}{81} \right) e^{\frac{-t}{\lambda z}} \left(1 - e^{\frac{-t}{\lambda z}} \right) \right] e^{\frac{-T}{\lambda z}}$$

$$I_1 = n_{Si} \left[\left(R_1 \frac{4}{9} e^{\frac{-t}{\lambda z}} + R_2 \frac{8}{81} \right) e^{\frac{-t}{\lambda z}} \left(1 - e^{\frac{-t}{\lambda z}} \right) \right] e^{\frac{-T}{\lambda z}}$$

$$I_2 = n_{Si} \left[\left(R_1 \frac{4}{9} e^{\frac{-2t}{\lambda z}} + R_2 \frac{24}{81} e^{\frac{-t}{\lambda z}} + R_3 \frac{1}{9} \right) \left(1 - e^{\frac{-t}{\lambda z}} \right) \right] e^{\frac{-T}{\lambda z}}$$

$$I_3 = n_{Si} \left[\left(R_2 \frac{32}{81} e^{\frac{-t}{\lambda z}} + R_3 \frac{4}{9} \right) \left(1 - e^{\frac{-t}{\lambda z}} \right) \right] e^{\frac{-T}{\lambda z}}$$

$$I_4 = n_{Si} \left[\left(R_2 \frac{16}{81} e^{\frac{-t}{\lambda z}} + R_3 \frac{4}{9} \right) \left(1 - e^{\frac{-t}{\lambda z}} \right) \right] e^{\frac{-T}{\lambda z}} + n_{SiO_2} \left(1 - e^{\frac{-T}{\lambda z}} \right)$$

where $\lambda_z = \lambda\cos\Theta$ with the electron mean free path λ=4.2 Å, and Θ is the internal angle which is related by the simple inner potential refraction rule to the observed external angle [2], n is the surface atom density of pure Si (n=6.8x10^{14}cm^{-2}), t=1.37Å, and n_{SiO}=3.4x10^{14}cm^{-2}. The factor R_x describes the change of the Si density in each interface layer x.

Fig. 3 displays the intensity ratios between each suboxide and the Si-bulk intensity as a function of polar angle. The intensity ratios determined from our model show excellent agreement with the experimental data. The fitting parameters are T=1.37 Å , R_1 = 0.77, R_2 =0.45, R_3 =0.93, and the inner potential was set to 19 eV. The reduction of the Si density in the second interface layer to a value of R_x~0.5 can be explained by the bridge-bonded interface structure which was found by theoretical investigations of Tu and Tersoff [4].
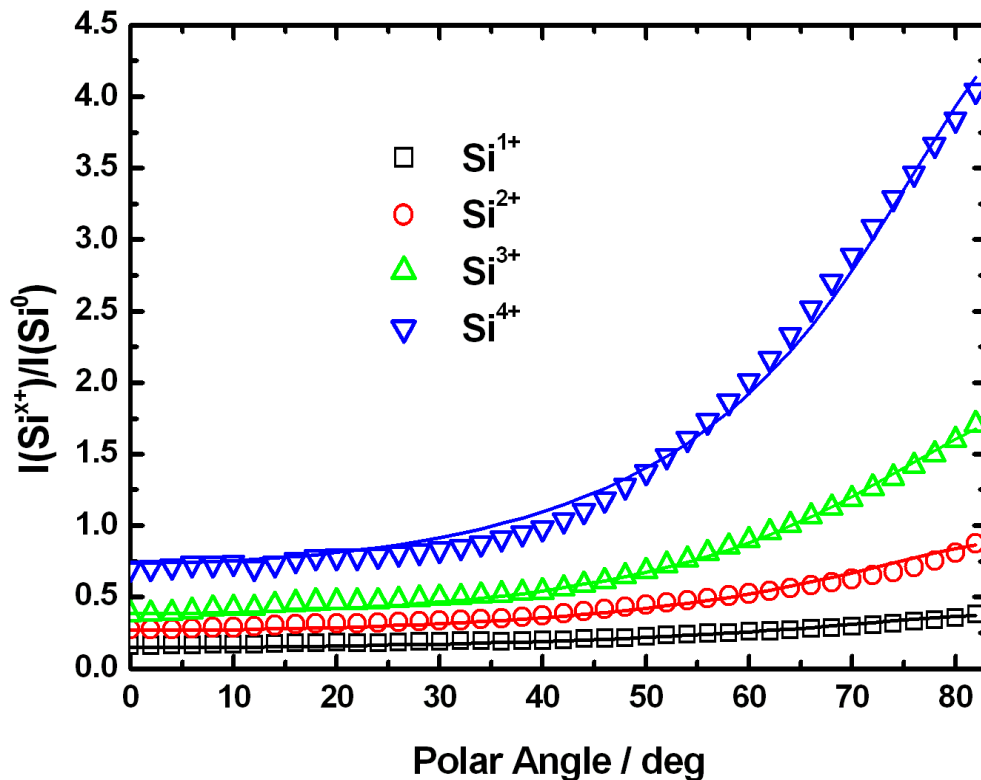
Figure 3: Intensity ratios of Si^{1+}, Si^{2+}, Si^{3+}, and Si^{4+} components normalized to the bulk component as a function of polar emission angle. The symbols represent data points, and the solid lines are obtained fits using the model displayed in Fig. 2.

In conclusion, we derived a simple model for the Si suboxide distribution in the SiO$_2$/Si(100) interface region. This model is based on statistical arguments and describes quantitatively the experimental photoelectron intensity ratios of the Si suboxides. The obtained fitting parameters indicate a bridge-bonded interface structure. A photoelectron diffraction analysis of the obtained data is still in progress and will reveal more detailed information about the interface structure.

References:
[1]   T. Hattori, Critical Reviews in Solid State and Material Science, 20(4) 339-382   (1995)   and references therein
[2]   D.-A. Luh, T. Miller, and T.-C. Chiang, Phys. Rev. Lett. **79**, 3014 (1997)
[3]   Yuhai Tu, and J. Tersoff, Phys. Rev. Lett. **84**, 4393 (2000)
[4]   J.H. Oh, H.W. Yeom, Y. Hagimoto, K. Ono, M. Oshima, N. Hirashita, M. Nywa, and A. Toriumi,   Phys. Rev. B **63**, 205310 (2001)

Photoemission investigation of nitrided III-V semiconductor surfaces – Resonant photoemission and time-dependent effects

J.-D. Hecht[1], L. Zhang[2], F. Frost[1], and T. Chassé[1,2]

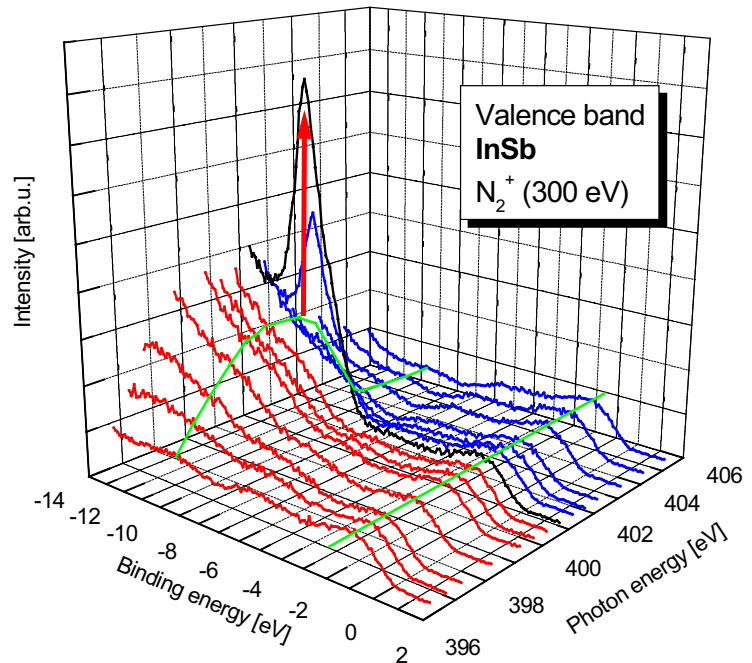[1]Institut für Oberflächenmodifizierung, Permoserstr. 15, D-04318 Leipzig, Germany
[2]Wilhelm-Ostwald-Institut für Physikal. u. Theoret. Chemie, Univ. Leipzig, Linnéstr. 2, D-04103 Leipzig, Germany

The nitridation of III-V semiconductors has attracted much attention due to the importance of epitaxial nitride growth on well-established substrates and of semiconductor surface passivation by nitridation. But in contrast to numerous investigations of plasma- or ion beam nitridation of GaAs, there exist only very few reports on the process of nitridation of the In-based III-V semiconductors InP, InAs, and InSb. The surface nitridation of In-based III-Vs by bombardment with low-energy N_2^+ ions at room temperature has been investigated in comparison to GaAs using X-ray absorption and photoemission spectroscopy [1,2]. Here we focus on our recent experiments on valence and core level photoemission spectra.

Commercially available GaAs, InAs and InSb (100) substrates were nitrided *in situ* in a stainless steel preparation chamber (base pressure 7×10^{-10} mbar) using 300 eV N_2^+ ions provided by a Kaufman-type broad beam ion source. Photoemission spectra of core and valence levels were recorded using an OMICRON EA-125 electron energy analyser at the U49/2-PGM2 beamline in an angle-integrating mode. The energy resolution was better than 0.2 eV at 400 eV. The energy scale was calibrated using gaseous N_2 and metallic Ag.

Fig. 1 shows valence electron spectra recorded on a N_2^+ ion (300 eV) bombarded InSb sample using photon energies near 400 eV. The spectra taken at the high and the low energies exhibit the typical three peak structure displayed by angle-integrated III-V valence spectra [3]. But close to 400 eV photon energy the spectra reveal a striking resonance behavior of a valence feature at a binding energy of about 10.3 eV. The corresponding excitation energy of

Fig. 1: PES valence electron spectra of nitrided InSb recorded at different excitation energies.

401 eV coincides with the $1s$-$1\pi_g^*$ excitation energy of molecular nitrogen, exactly [4]. Further, the binding energy of the resonant energy level falls close to an occupied π-MO of N_2. Therefore, these results strongly support our previous assignment of a high binding energy peak in the N 1s

core level spectra (see feature N_i in Fig. 2) and a striking nitrogen K-edge NEXAFS feature to N_2 in the semiconductor matrix. This correlation of different spectral features is additionally supported by the time-dependence reported below.

Fig. 2 presents a set of N 1s spectra sequentially recorded on a N_2^+ ion bombarded InSb sample. Despite the general decrease of intensity due to the uncorrected ring current a much stronger decrease is observed for the high energy peak N_i. Fig. 3 displays a similar sequence of valence level spectra taken at resonant excitation conditions. The resonance-enhancement fades away within an hour. In striking contrast, there is no similar time-dependence in the nonresonant valence spectra [3]. At present we attribute the observed time-dependences to a photon-flux-related N_2 redistribution, tentatively.

In summary, valence photoemission spectra of low-energy nitrogen bombarded III-V semiconductor surfaces exhibit striking resonance and time-dependent behavior, which may be used to analyse the state of nitrogen in the ion-bombarded samples. It provides further evidence for interstitial molecular nitrogen in addition to the nitride formation by the ions.

Fig. 2: Time-dependent evolution of the N 1s core level spectra of nitrided InAs for an excitation energy of 600 eV.
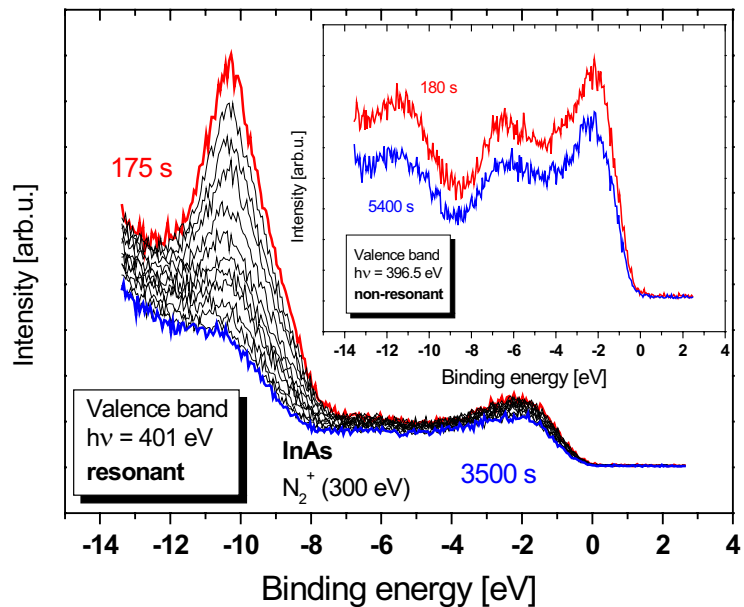
Fig. 3: Time-dependent evolution of the valence band spectra of a nitrided InAs surface at 401 eV and 396.5 eV (inset).

[1] J-D. Hecht et al., Appl. Surf. Sci , **179**, 196 (2000)
[2] J-D. Hecht et al., J. Appl. Phys. **90**, 6066 (2001)
[3] L.Ö. Olsson et al., Phys. Rev. B **53**, 4734 (1996)
[4] C.T. Chen et al., Phys. Rev. A **40**, 6737 (1989)

Investigation of the ligand exchange behaviour of Ni(II)-complexes by XANES and EXAFS spectroscopy

M.P. Feth[1][*], M. Kreitmeir[1], M.A. Seiler[1], H. Bertagnolli[1],
A. Erko[2], M. Fieber-Erdmann[2] and A. Klein[3]

[1]Institut f. Phys. Chemie, Univ. Stuttgart, Pfaffenwaldring 55, 70569 Stuttgart
[2]Berliner Elektronenspeicherring-Gesellschaft für Synchrotronstrahlung m.b.H. (BESSY),
Albert-Einstein-Straße 15, 12489 Berlin
[3]Institut f. Anorg. Chemie, Univ. Stuttgart, Pfaffenwaldring 55, 70569 Stuttgart

* correspondig author. e-mail: m.feth@ipc.uni-stuttgart.de

The nickel and bromine local structure of the square planar nickel(II)-complexes 2,2'-Bipyridylbromomesitylnickel(II) ([(Bpy)Ni(Mes)Br]) and its ligand exchange behaviour towards several solvents has been determined by means of X-Ray Absorption Near Edge Spectroscopy (XANES), Extended X-Ray Absorption Finestructure Spectroscopy (EXAFS) and X-Ray Diffraction (XRD). The results of this study showed that the exchange behaviour strongly depends on the nature of the potential donor ligand (solvent molecule). In some cases a substitution of one or more ligands accompanied with a conservation of the square planar geometry was observed. In other cases a ligand exchange of all ligands by solvent molecules with a change of the goemetry from square planar to octahedral was found. The structural information obtained are important for a further development of such nickel(II)- complexes as catalysts for various applications.

The measurements were performed at the XAFS beamline KMC-2 of BESSY II at the Ni K-(8333.0 eV) and Br K-edge (13473.7 eV). Data were analysed with the program packages described in [1] and [2]. The EXCURV92 module of CERIUS^2 was used for curve fitting.

In square planar Ni(II) complexes two pre-edge peaks can be observed (figure 1). The pre-peak at about 8333 eV can be assigned to a 1s→3d electron transition while the second peak, which occurs at about 8336 eV, is due to a 1s→4p$_z$ transition [3, 4]. In octahedral Ni(II) complexes only the 1s→3d transition is allowed, so that the peak at 8336 eV cannot be observed in these complexes. Furthermore the 1s→3d transition is symmetry forbidden for centrosymmetric pointgroups [3]. This means that high symmetrical octahedral complexes will not show any pre-peaks, while non-symmetric octahedral complexes can be detected by their higher 1s→3d peak-intensity. Therefore the intensity of the 1s→3d peak can be used als an indicator of the geometry in octahedral complexes.

In figure 1 the pre-edge and XANES region of the solid nickel complex [(Bpy)Ni(Mes)Br] is shown in comparison with its solutions in pyridine and methanol. As an octahedral reference compound the XANES spectra of [(1,10-phenantroline)$_2$NiBr$_2$] was also added to the figure.
In the pure, solid square planar complex (solid line) the typical two pre-peaks for the 1s→3d and 1s→4p$_z$ transitions are clearly visible and well resolved. The solution in pyridine (dotted line) also shows these two pre-peaks, indicating that the local structure around the Ni atoms is retained.
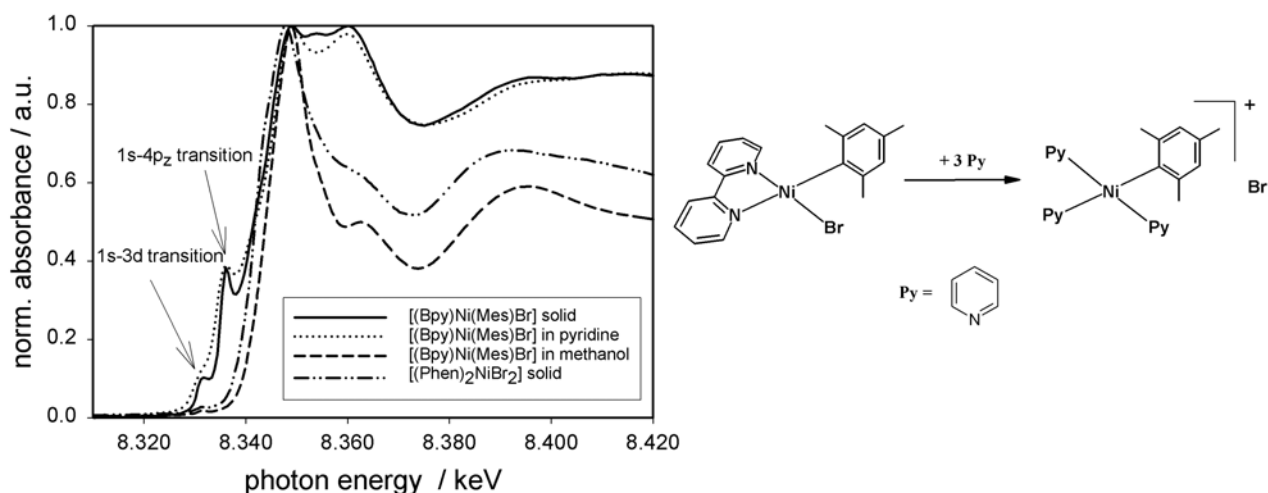
Fig. 1: Comparison of the Ni K-edge XANES regions of solid [(Bpy)Ni(Mes)Br] and its solutions in pyridine and methanol with solid [(1,10-phenantroline)$_2$NiBr$_2$].

In contrast to the pyridine solution the XANES region of the solution in methanol shows only a very weak pre-peak of the 1s→3d-transition. However the XANES spectrum has a similar shape as the spectra of the octahedral complex [(1,10-phenantroline)$_2$NiBr$_2$]. This is a strong hint, that the complex has changed its structure from square planar to octahedral. Furthermore the very weak 1s→3d-transition pre-peak would lead to the conclusion that the local environment of the Ni atoms is highly symmetrical. This can only be the case if complex has exchanged all his ligands by solvent molecules.

The EXAFS results from the nickel and bromine edge are summarized in table 1. The structural parameteres of the pure nickel complex in the solid state determined by EXAFS are in very good agreement with those found from single crystal XRD. Figure 2 shows the experimental EXAFS (a) and its Fouriertransformed EXAFS function of the pure complex in comparison with its solutions.

In THF no structural changes are visible. In pyridine the coordination number of the first coordination sphere around the nickel atom is still 4, but in contrast to THF, the bromine atom is substituded by a pyridine ligand. Futhermore detailed EXAFS investigations of several reference compounds showed that not only the bromine atom was substituted by a pyridine molecule but also the bipyridine ligand, so that in the nickel atom is surrounded by three pyridine molecules and one mesitylene molecule in a square planar geometry.

The solid product of the dissolved complex in methanol shows a complete different structure. The coordination number of the first shell is 6, fitted with oxygen atoms. This means that the nickel atoms is symmetrically surrounded by six methanol molecules. The FT-EXAFS function (figure 2 (b)) shows also a large peak at about 3 Å. This peak can be assigned to nickel backscatterers. In the literature one can find similar octahedral nickel methanol complexes which are arranged to clusters with comparable Ni-Ni distances and coordination numbers [5].

Summarizing the results, the conclusions made from XANES are supported by EXAFS, so that the XANES and EXAFS investigations of this study are in a very good agreement.
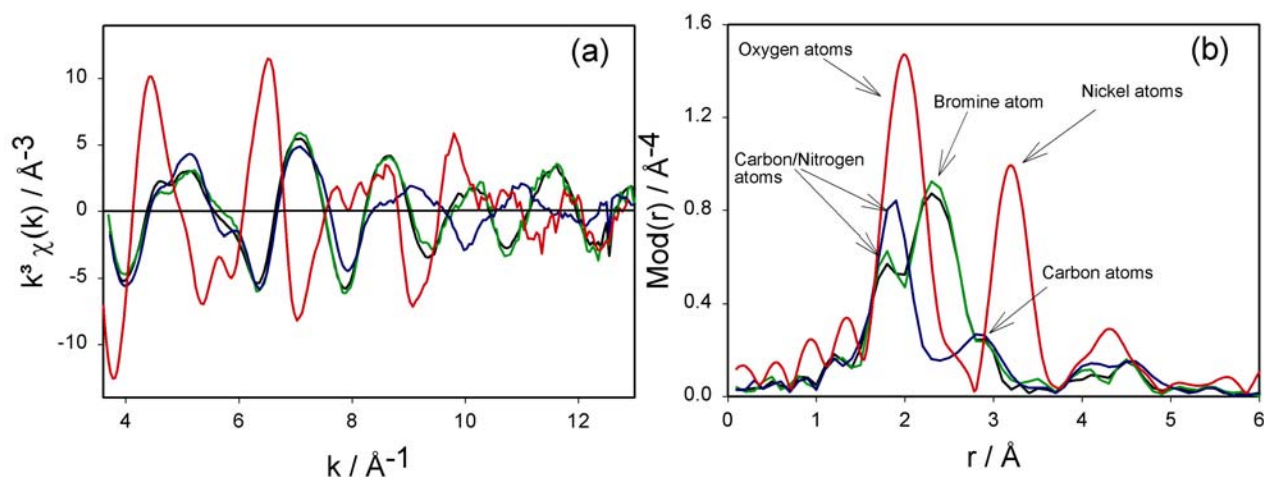
Fig. 2: Comparison of the experimental $k^3 \chi(k)$ functions (a) and their Fourier transforms (b) of solid [(Bpy)Ni(Mes)Br] (black line) and its solutions in THF (green line), pyridine (blue line) and methanol (red line) (Ni K-edge).

Table 1 Structural parameter of solid and dissolved [(Bpy)Ni(Mes)Br] determined from the Ni K- and Br K-edge EXAFS spectrum.

	[a]	r [Å]	N	σ [Å]	ΔE_0 [eV]	k-range [Å⁻¹] Fit-Index / AFAC
pure, solid state EXAFS.	Ni-C/N	1.92 ± 0.02	3.1 ± 0.3	0.081 ± 0.008	28.0	3.60 – 14.90
	Ni-Br	2.30 ± 0.02	1.0 ± 0.2	0.062 ± 0.011		21.8 / 0.8
	Ni-C	2.81 ± 0.03	5.6 ± 1.7	0.110 ± 0.030		
	Br-Ni	2.30 ± 0.02	0.8 ± 0.1	0.060 ± 0.006	14.5	3.60 – 11.30
						23.5 / 0.8
THF, liquid state EXAFS.	Ni-C/N	1.90 ± 0.02	2.7 ± 0.3	0.073 ± 0.008	28.2	3.60 – 13.90
	Ni-Br	2.29 ± 0.02	1.1 ± 0.2	0.065 ± 0.010		21.9 / 0.8
	Ni-C	2.81 ± 0.03	5.5 ± 1.7	0.110 ± 0.030		
pyridine, liquid state EXAFS.	Ni-C/N	1.90 ± 0.02	3.8 ± 0.3	0.072 ± 0.007	28.0	3.80 – 15.00
	Ni-C	2.82 ± 0.03	5.0 ± 1.5	0.087 ± 0.026		21.9 / 0.8
methanol, solid product isolated from a mathanolic solution, solid state EXAFS.	Ni-O	2.05 ± 0.02	6.4 ± 0.3	0.079 ± 0.007	21.3	3.70 – 12.50
	Ni-C	2.95 ± 0.03	6.1 ± 1.5	0.071 ± 0.026		30.3 / 0.8
	Ni-Ni	3.09 ± 0.03	3.5 ± 1.5	0.077 ± 0.026		
pure, single crystal XRD	Ni-C/N	1.93	3			
	Ni-Br	2.30	1			
	Ni-C	2.83	4			
C₃₁H₅₂C₁₄N₄Ni₄O₁₅·Methanol single crystal XRD [5]	Ni-O	2.07	6			
	Ni-Ni	3.09	3			

[a] absorber-backscatterer distance r, coordination number N, Debye-Waller factor σ with their calculated deviation, shift of the energy threshold energy ΔE_0, fit-index R and Amplitude Reduction Factor (AFAC).

References

[1] M. Newville, P. Livins, Y. Yacobi, J. J. Rehr, E. A. Stern, *Phys. Rev. B* **47** (1993), 14126.

[2] T. S. Ertel, H. Bertagnolli, S. Hückmann, U. Kolb, D. Peter, *Appl. Spectrosc.* **46** (1992), 690.

[3] G.J. Colpas, M.J. Maroney, C. Bagyinka, M. Kumar, W.S. Willis, S.L. Suib, N. Baidya, P. K. Mascharak, Inorg. Chem., **30** (1991), 920.

[4] M.W. Renner, L.R. Furenlid, K.M. Barkigia, J. Fajer, J. Phys. IV France **7** (1997), C2-661.

[5] A. Szytula, A. Murasik, M. Balanda, phys. stat. sol, sectio B **43** (1971), 125.

X-ray Resonant Magnetic Reflectometry at a single Pt/Co interface

J. Geissler, E. Goering, S. Gold, and G. Schütz
Max-Planck-Institut für Metallforschung, D-70569 Stuttgart, Germany

D. Schmitz, and H. Maletta
Hahn-Meitner-Institut, D-14109 Berlin, Germany

The Co magnetization depth profile at a single buried Pt/Co interface was investigated by resonant circular x-ray reflectivity measurements. The asymmetry ratio as function of angle of incidence has been measured in the Co L_3-near-edge absorption region at the energy of the strongest XMCD effect. Observed asymmetry ratios in the order of 40 % are described on the basis of a magnetically modified optical approach to determine the depth magnetization profile of the Co layer.

Multilayer systems consisting of magnetic and non-magnetic components have gained steadily growing interest from aspects of fundamental physics as well as for technical applications, since these artificial media exhibit new fascinating properties. Due to the oscillatory exchange coupling in combination with Giant Magneto Resistance (GMR) and Tunneling Magneto Resistance (TMR), multilayer systems are basic components for magnetic sensors and magneto- and spin-electronic devices as used in Magnetic Random Access Memories (MRAMs). Because of strong magnetic contributions in the resonant scattering cross section, it is possible to study also in an element and site-selective manner magnetic characteristics of these structural components by x-ray resonant magnetic scattering (XRMS) using polarized synchrotron radiation in the hard and soft x-ray range [1,2].

We have developed a new method on the basis of the XRMS which gives detailed element-specific quantitative insight into the magnetization profile at a single buried interface [3]. Comparable to non-magnetic specular reflectivity experiments, which yield to well known analysis of layer thickness and interface roughness, specular magnetic measurements provide quantitative information of magnetization profiles perpendicular to the surface related to momentum transfer in this direction.

The method was successfully proven in the hard x-ray regime where the induced magnetic 5d moment of Pt in a Pt/Co bilayer was determined.

To extend this method to the soft x-ray range resonant magnetic reflectometry measurements at the helical undulator beamline UE56/2 at Bessy II have been performed with a new UHV compatible reflectometer. The experimental setup allows specular and off specular reflectivity measurements for depth profiling and lateral magnetic investigations. In addition absorption spectra can be measured simultaneously in total electron yield mode.

The size of the primary photon beam can be reduced by a variable entrance slit system and has been adjusted in our experiment to 0.3mm. For detection of the scattered beam we have used a GaAsP diode from Hamamatsu with 2x2 mm^2 photon sensitive area and a dark current of about 10fA. We could achieve a dynamical range of seven orders of magnitude.
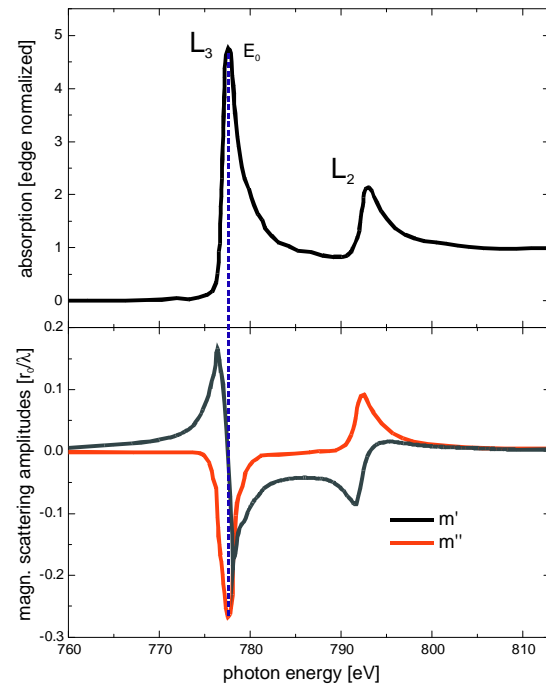

Figure 1: Optical constants of Co at the Co $L_{2,3}$ edge. Top: absorption spectra from [4]. Bottom: Absorptive (m'') and calculated dispersive part (m') of the magnetic scattering amplitude.

The Pt6.2nm/Co2.6nm/Cu2.5nm/Ta4.3nm/Si-substrate thin film was prepared by dc-sputter deposition in a conventional vacuum system on Si (111). Circular polarized light was used and the reflectivity was measured in a theta range from 0.1 to 30 deg by switching the in plane magnetization at

every data point. The sample was magnetized by rotatable liquid nitrogen cooled electromagnet system with a maximum field of 5kOe.
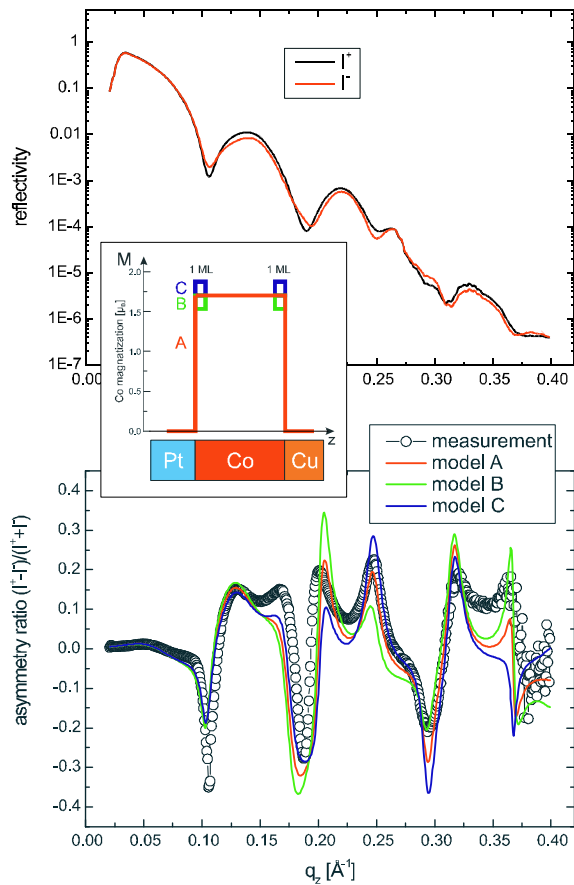
Figure 2: Measured reflectivity (top) and asymmetry ratio together with simulations assuming different simplified magnetization profiles, shown in the inset, of the Co layer (bottom). Inset: Model A: Uniform magnetization of 1.70 μ_B. Model B(C): Reduced (increased) magnetization of 10per cent of 1 ML Co directly at the Pt and Cu interface, respectively.

The asymmetry ratio $(I^+-I^-)/(I^++I^-)$ strongly depends on the energy due to variations of the optical constants in the near edge region which is shown in fig. 1 [6]. The reflectivity was measured at the energy E_0 of the maximum of the dichroic effect, where the dispersive part of the magnetic scattering amplitude m' vanishes and only magnetization induced absorptive changes m'' have to be taken into account. Reflectivities I^+ and I^- were simulated using an optical approach based on Fresnels laws and considering interface roughness by a Nevot-Croce factor [5]. The Co magnetization was considered by modeling the magnetically induced changes of the scattering amplitude.. Absolute magnetic moments of the Co layer were deduced by scaling the changes of the optical constants to the dichroic signal measured in an XMCD experiment at Co $L_{2,3}$ edges [3].
The measured reflectivity and asymmetry ratio are

shown in Fig. 2 (top). To demonstrate the strong dependence of the asymmetry ratio from the assumed magnetization profile of the Co layer, simulations of
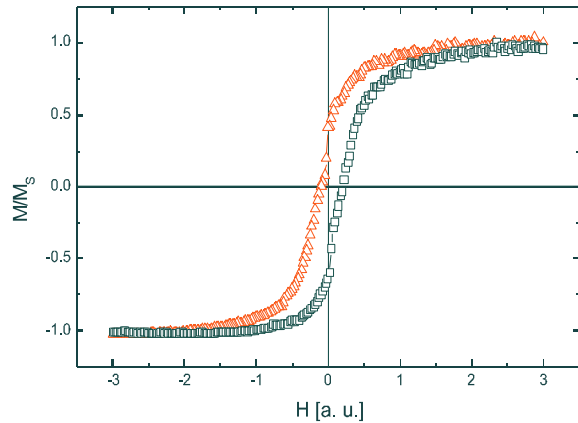
Figure 3: Hysteresis loop measured at the Co L_3 edge at fixed angle of incidence at theta=7.2 deg.

the asymmetry are shown in Fig. 2 (bottom) for three simplified models (inset of Fig 2). Further theoretical work is in progress to extract the "real" Co magnetization profile at each interface.

Additionally we want to mention the possibility of measuring *in situ* element specific hysteresis loops (fig. 3) in less then ten minutes [7].

References:

[1]   D. Gibbs, et al., Phys. Rev. Lett. 61 1241 (1988)
[2]   J. P. Hannon, et al., Phys. Rev. Lett. 61, 1245 (1988)
[3]   J. Geissler, et al., Phys. Rev. B65, (R)020405, (2001)
[4]   C. T. Chen, et al., Phys. Rev. Lett. 78, 152 (1995)
[5]   Parratt32 code, distributed by HMI Berlin
[6]   J. Kunes, et al., Phys. Rev. B64, 174417 (2001)
[7]   K. Starke, et al., Phys. Rev. Lett. 86, 3415 (2001)

High Resolution Photoelectron Spectroscopy on SiC Surfaces

Th. Seyller[1], N. Sieber[1], R. Graupner[1], L. Ley[1],
D. James[2], J. Riley[2], R. Leckey[2], M. Polcik[3], D. Schmeißer[4]

[1] *Institut für Technische Physik, Universität Erlangen-Nürnberg*
[2] *School of Physics, La Trobe University, Bundoora, Vic 3083 Australia*
[3] *Fritz-Haber-Institut der Max-Planck-Gesellschaft, Berlin*
[4] *Angewandte Physik – Sensorik, BTU Cottbus*

Introduction

The electronic and structural properties of SiC surfaces have been subject to a number of studies in the past. In the case of 4H- and 6H-SiC these studies concentrated on the hexagonal (0001)-surface (Si-face) and the ($000\bar{1}$) surface (C-face). Most of these studies were concerned with the Si-rich (3x3) and (√3x√3) reconstructions and the oxygen induced silicate adlayer reconstructions. On all these surface structures surplus silicon and/or oxygen atoms are used for minimizing the number of dangling bonds resulting in a reduced surface energy. Considerably less attention has been paid to hydrogenated surfaces, mainly because of the rather elaborate way this surfaces are prepared. In previous studies, however, we were able to show that hydrogenated SiC surfaces can resist oxidation in air and that they exhibit a very low density of charged interface states (ca. 10^{11} cm^{-1}) [1,2].

Wet-chemical treatment of SiC surfaces is commonly used for cleaning prior to processing and also prior to surface science experiments. Starke et al. [3] studied the surface structure and composition of SiC(0001) after etching in HF and observed a (1x1) surface covered with a monolayer of OH. Hollering et al. [4] proposed a partial H-termination on HF-dipped SiC($000\bar{1}$), but the surface also contained oxygen, which was attributed to oxide in disordered areas of the surface such as scratches. In the light of structural studies on the silicate adlayer reconstructed surfaces it was suggested that the structural elements of the silicate adlayer reconstruction are also present on the HF-prepared SiC($000\bar{1}$) surface, however without long-range order [5].

In this report we will show a few results of our current studies of wet-chemically prepared as well as hydrogen-terminated SiC(0001) and SiC($000\bar{1}$) surfaces using high resolution, surface sensitive photoelectron spectroscopy (SXPS) and LEED. Using beamline UE56/2-PGM2 we have studied the surface core level shifts of hydrogen terminated SiC surfaces and on beamline U49/2-PGM2 we have investigated the effect of a four-step wet-chemical cleaning procedure, which we apply prior to hydrogenation of the samples.

Surface core level shifts on hydrogen terminated SiC surfaces

Fig. 1 shows Si2p and C1s core level spectra taken on the hydrogenated SiC($000\bar{1}$) surface. Thereby photon energies were chosen so that the effective sampling depths λ_{eff} are the same for surface sensitive and bulk sensitive measurements of the two core levels, respectively (see fig. 1). The Si2p spectrum in fig. 1(a) contains a single spin-orbit split doublet from bulk SiC with a spin-orbit splitting of (0.606 ± 0.003) eV and a branching ratio of 0.516 ± 0.004. The C1s spectrum (fig. 1(b)) contains three components, two of which are due to emission from the surface. The surface component with a chemical shift of 2.4 eV with respect to the bulk component can be ascribed to a

Fig. 1: Si2p (a) and C1s (b) spectra of H-terminated SiC($000\bar{1}$). Also shown is a deconvolution of the spectra using Voigt lines.

slight contamination with hydrocarbons, which increases with storage time of the sample. The other surface component is due to the topmost carbon layer in which the carbon atoms are bound to three Si-atoms of the same bilayer and to one hydrogen atom. The binding energy difference with respect to the bulk is (0.47 ± 0.02) eV.
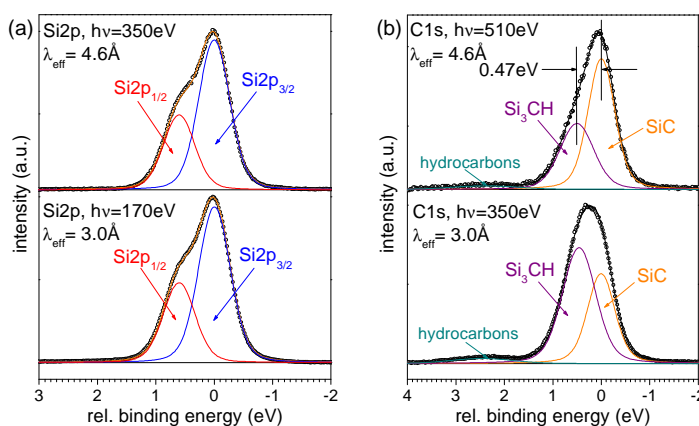
Fig. 2 shows the corresponding spectra of the hydrogenated SiC(0001) surface. Comparing the shape of the Si2p core level in fig. 2(a) with the shape of the Si2p signal in fig. 1(a) it is clear that the spectrum must contain at least two doublets. Because of the surface sensitivity of the measurements the surface to bulk intensity ratio can be taken from the C1s core level spectra of the carbon face. Using this constraint we obtain the fit shown in fig. 2(a) for the Si 2p core level. The surface component is shifted to higher binding energy by (0.22 ± 0.02) eV. However, it is possible to obtain fits of equal quality by changing this assignment such that the higher lying component is the bulk component and the lower one due to emission from the surface, i.e. reverting the intensity ratio. This is due to the intrinsically large Gaussian width of the core levels (around 0.6eV) which are in agreement with previously published results on SiC surfaces (see e.g. [6]) and the small binding energy difference of only 0.22 eV. The assignment made above is supported by comparing the binding energy

difference between the bulk C1s and Si2p core level emission. This value can be determined from bulk sensitive XPS measurements with an accuracy of 50meV. Initial state arguments favor the opposite assignment, since hydrogen is less electronegative than carbon. Further investigations are necessary to clarify this issue.

The C1s core level of hydrogenated 6H-SiC(0001) is shown in fig. 2(b). Although the shape of the main contribution appears much less asymmetric when compared with the C1s core levels of C-terminated 6H-SiC three components are needed to yield satisfactory fitting results. These

Fig. 2: Si2p (a) and C1s (b) spectra of H-terminated SiC(0001).

components can be assigned to emission from the bulk, to small amounts of hydrocarbons and to small amounts of carbon atoms bonded to hydrogen. This is reasonable since epitaxial layers on off-axis cut SiC(0001) surfaces as well as polished on-axis substrate surfaces contain a significant number of steps, where carbon atoms are present at the surface. In view of the small chemical shift of the Si2p core level it is not surprising that no such component was observed in the Si2p spectra of the C-face.

Wet-chemically treated surfaces

The procedure we apply to the samples before hydrogenation consists of step A: 10 minutes in a 4:1 mixture of H_2SO_4 (97%) and H_2O_2 (30%) (Piranha solution) at 180°C; step B: 10 minutes in HF (40%) at room temperature; step C: 10 minutes in a 4:1:1 mixture of H_2O, H_2O_2 (30%), and HCl (37%) at 80°C; step D: 5 minutes in HF (5%) at room temperature. Each step is followed by rinsing in deionized water. Step A of the wet-chemical treatment removes contamination by organic substances. Step B and D are supposed to etch silicon oxide and step C is intended to dissolve inorganics from the surface [7].

The so treated SiC(0001) surface contained considerable amounts of oxygen. No sulfur or chlorine was detected after the steps A and C, but small amounts of fluorine are usually visible in XPS after steps B and D. In addition, the Si2p core level spectra (not shown) revealed the presence of Si in oxidation state 1+ (Si^+) and smaller amounts of Si in oxidation state 4+ (Si^{4+}). No Si^{2+} and Si^{3+} was detected. The

Fig. 3: Si2p spectra taken on (a) SiC(0001) after preparation step A and (b) on a SiC(0001) surface with silicate adlayer reconstruction.

intensity ratios of Si^+ and Si^{4+} to SiC were determined by fitting three doublets to the Si2p spectra as shown in figure 4(a) for the spectrum obtained after step A. They are compiled in table 1. As can be seen from that table, the relative intensity of the Si^+ component is almost constant but the Si^{4+} component has a maximum after Step A. It is smallest after the HF etches (steps B and D) and has an intermediate value after step C, which is also an oxidizing step. As already noted, HF-prepared SiC(0001) surfaces were previously shown to be terminated by OH groups [3]. Therefore we assign the Si^+ signal observed after steps B, C and D to Si-OH units. The fact that the Si^+/SiC ratio is constant is evidence for a monolayer coverage with OH as was also suggested by Starke et al. [3].

The Si^+ signal after step A must be assigned at least partially to a different bonding geometry. The fingerprint of the spectrum is very similar to the one observed on a silicate adlayer-terminated SiC(0001) surface with ($\sqrt{3}\times\sqrt{3}$)R30° periodicity [9]. It was previously shown that silicate adlayer reconstructed SiC(0001) and (000$\bar{1}$) surfaces can be prepared by either etching the surfaces in a hydrogen plasma or by a annealing in hydrogen at elevated temperatures [8-10]. The Si2p spectrum of a plasma prepared silicate adlayer reconstructed SiC(0001) surface is shown for comparison in fig. 4(b). The spectrum

preparation	Si+ / SiC	Si4+ / SiC
Step A	1.30	0.50
Step B	1.52	0.13
Step C	1.33	0.20
Step D	1.45	0.07

Table 1: Relative (to bulk SiC) contributions of the Si^+ and Si^{4+} components of the Si2p spectra measured at 170eV photon energy.

shows a bulk component and two chemically shifted components due to Si^+ and Si^{4+}, in agreement with the structural model shown in figure 5 [8]. In this case a Si^+/SiC ratio of 1.21 is observed, which fits well to the values listed in table 1. However, the Si^{4+}/SiC ratio is 1.39 and thus three times larger than on the wet-chemically prepared surface. This indicates that at best about one third of the surface is covered with the silicate adlayer
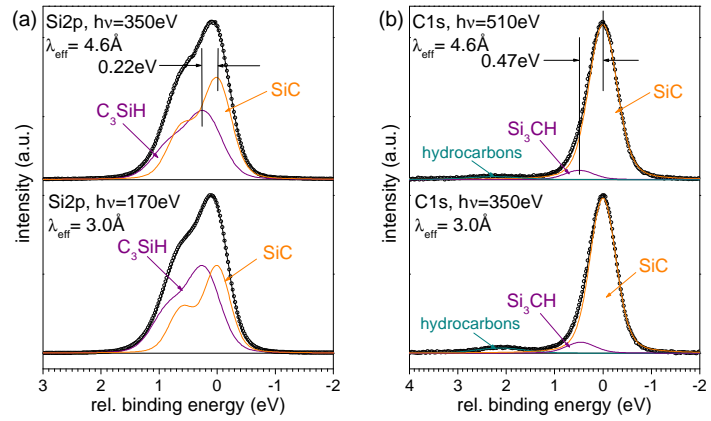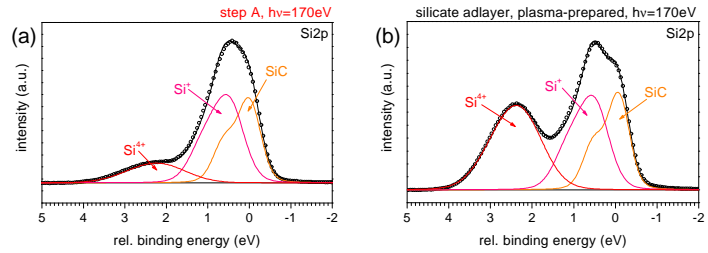
reconstruction after preparation step A. Nevertheless a weak (√3×√3) LEED pattern was observed. A quite sharp (√3×√3) LEED pattern was observed after performing the Piranha etch at 200°C with a mixture of 3:1 (see fig. 5). An increase of the Si^{4+} component and thus of the silicate adlayer reconstructed areas was observed by using pure sulfuric acid at 260°C, but it was always less than 50% of the surface. In this case a sharp (√3×√3) LEED pattern was observed, too.
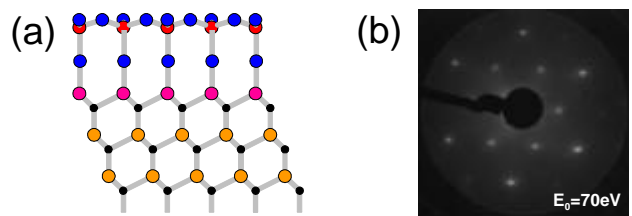

Fig. 5: (a) Side view of the silicate adlayer reconstruction on SiC(0001) [8]. (b) LEED pattern taken at 70eV from a SiC(0001) surface after a modified preparation step A.

The impact of the wet-chemical preparation steps on the carbon face was also studied, but in less detail. We did not observe surface structures other than (1×1) and we shall concentrate on the state of the surface after step B of the procedure. The photoelectron survey scan (not shown) revealed the presence of oxygen on the surface. Figure 6(a) depicts the Si2p spectrum of SiC($000\overline{1}$). It shows a strong tailing towards higher binding energies. This tailing is due to Si in higher oxidation states. Fitting the spectrum using Voigt doublets reveals that Si atoms in different oxidation states Si^+, Si^{2+} and Si^{3+} are present on the surface. The chemical shifts with respect to the bulk

Fig. 6: Si2p (a) and C1s (b) spectra taken on SiC($000\overline{1}$) after preparation step B.

SiC component are 0.54 eV, 1.08 eV and 1.64 eV, respectively. No Si^{4+} component is detected. The Si2p core level spectrum of the silicate adlayer reconstructed SiC($000\overline{1}$) surface contains only the bulk component and a chemically shifted component due to Si^{3+} [10], in agreement with the structural model (see fig. 7) [8]. The observation of Si^+, Si^{2+} and Si^{3+} after HF dip would fit to the above mentioned reconsideration of the structural properties of wet-chemically prepared SiC($000\overline{1}$) [5]. This reconsideration is based on the striking similarity of the LEED-I(E) curves for the integer order diffraction spots of silicate adlayer reconstructed SiC($000\overline{1}$) and wet-chemically prepared SiC($000\overline{1}$) with (1×1) symmetry [5]. It was suggested that the surface contains structural units where the carbon atoms of the topmost bilayer are replaced by

Fig. 7: Side view of the silicate adlayer reconstruction on SiC($000\overline{1}$) [8].

oxygen, which form bridging bonds between two silicon atoms, just as they would do in the silicate adlayer reconstruction, but without long range order.

Finally, in fig. 6(b) the C1s spectrum of the wet-chemically prepared SiC($000\overline{1}$) surface is given. Again, a deconvolution reveals the presence of chemically shifted components, which are located at the surface. The component at 0.5 eV higher binding energy is due to carbon atoms which are bound to three Si atoms and one hydrogen atom. The second component at 1.93 eV with respect to bulk SiC indicates a hydrocarbon contamination of the ex-situ prepared sample. This together with the Si2p core level points to a mixture of hydrogen termination and incomplete silicate adlayer reconstruction at the surface.

Conclusion
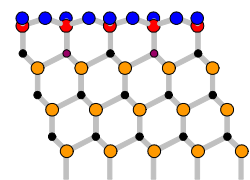
High resolution photoelectron spectroscopy was used to determine surface shifted components in C1s and Si2p spectra of hydrogenated 6H-SiC(0001) and ($000\overline{1}$). On wet-chemically prepared SiC(0001) a monolayer of OH is observed, except after Piranha etch, where the surface is partially covered with the silicate adlayer reconstruction. On HF-dipped SiC($000\overline{1}$) we observed Si in oxidation states up to Si^{3+}, which supports the recent reconsideration of the structure of this surface. In addition, we observed a partial hydrogen termination of this surface.

References
[1]   N. Sieber *et al.*, Mater. Sci. Forum 353-356 (2001) 223.
[2]   N. Sieber *et al.*, Appl. Phys. Lett. 78 (2001) 1216.
[3]   U. Starke *et al.*, Appl. Surf. Sci. 89 (1995) 175.
[4]   M. Hollering *et al.*, Phys. Rev. B 58 (1998) 4992.
[5]   J. Bernhardt, Ph.D. thesis, University of Erlangen-Nürnberg, Germany (2001).
[6]   L.I. Johansson, F. Owman and P. Mårtensson, Phys. Rev. B 53 (1996) 13793.
[7]   W. Kern, ed. *Handbook of semiconductor wafer cleaning technology*. Electronic Materials and Process Technology, ed. R.F. Bunshah, G.E. McGuire and S.M. Rossnagel. 1993, Noyes Publications: Park Ridge.
[8]   J. Bernhardt *et al.*, Appl. Phys. Lett. 74 (1999) 1084.
[9]   N. Sieber *et al.*, Mater. Sci. Forum 338-342 (2000) 391.
[10] M. Hollering *et al.*, Surf. Sci. 442 (1999) 531.

Time-resolved core level photoemission: Surface photovoltage dynamics at the SiO$_2$/Si(100) interface

W. Widdra[1,2], D. Bröcker[1], T. Gießel[1], I.V. Hertel[1], W. Krüger[1], A. Liero[1], F. Noack[1], V. Petrov[1], D. Pop[1], R. Weber[1], I. Will[1], and B. Winter[1]

[1] *Max-Born-Institut für Nichtlineare Optik und Kurzzeitspektroskopie, Max-Born-Strasse 2A, D-12489 Berlin, Germany*
(corresponding author:W. Widdra, e-mail:widdra@mbi-berlin.de)

[2] *Institut für Atomare Physik und Fachdidaktik, Technische Universität Berlin, D-10623 Berlin, Germany*

Localized states at semiconductor surfaces and interfaces are known to modify, e.g. due to potential gradients, the valence- and conduction bands which control many semiconductor phenomena and device properties. This motivated many studies of surface-induced band bending at a great variety of semiconductor surfaces [1,2]. Since the potential gradients depend on the charge carrier densities additional photo-induced charge carriers will alter the band bending and introduce a surface photovoltage (SPV). Based on the assumption that sufficiently strong illumination results in a complete flattening of the surface band bending via screening of the surface charge by free carriers, the SPV under photosaturation conditions is an often used tool to determine the absolute value of the band bending [2].

Here we present a time-resolved SPV study of the SiO$_2$/Si(100) interface with combined Laser synchrotron radiation (SR) photoemission in a pump-probe scheme. The experiments have been performed at the MBI beamline which is located at the U-125/1 undulator of the synchrotron radiation facility BESSY [3]. The pump-probe photoemission experiments in the region of the Si2p core levels have been performed with synchrotron radiation photons of 130 eV and synchronized Laser pulses from a specially designed Nd:YVO$_4$ laser system (200 nJ pulse energy at a photon energy of 1.2 eV, pulse length 12 ps). The laser is operating at a repetition rate of 1.25 MHz which corresponds to the synchrotron radiation repetition rate in the single bunch mode. Via an active piezo control of the laser cavity length the laser repetition rate is synchronized to the storage ring electronic master clock to better than 5 ps. The time delay between the laser and the SR pulses can be controlled electronically and optically between 0 and 800 ns. The successful synchronization has been verified by sum frequency generation (SFG) from the synchrotron radiation (white light) pulses and the Laser pulses in a nonlinear BBO crystal. The resulting cross correlation of the SFG signal as function of the Laser to SR delay shows a full-width at half maximum of about 60 ps which corresponds to the SR pulse width in the single bunch mode and defines the overall experimental time resolution here.

The clean Si(100)-(2x1) surface has been prepared by Ar$^+$ ion sputtering and annealing as described previously [4]. The quality of the surface has been verified using XPS by a well

resolved D_{up} Si 2p surface core level component [5] and by a sharp two-domain (2x1) LEED pattern. The SiO_2/Si(100) interface has been prepared by exposure of the clean surface to 100 L of oxygen at a sample temperature of 870 K which results in a 13 Å thick oxide layer [6]. At room temperature Si 2p photoemission spectra measured with and without additional laser excitations show a rigid shift of all spectral features to higher kinetic energies of up to 300 meV. This shift is
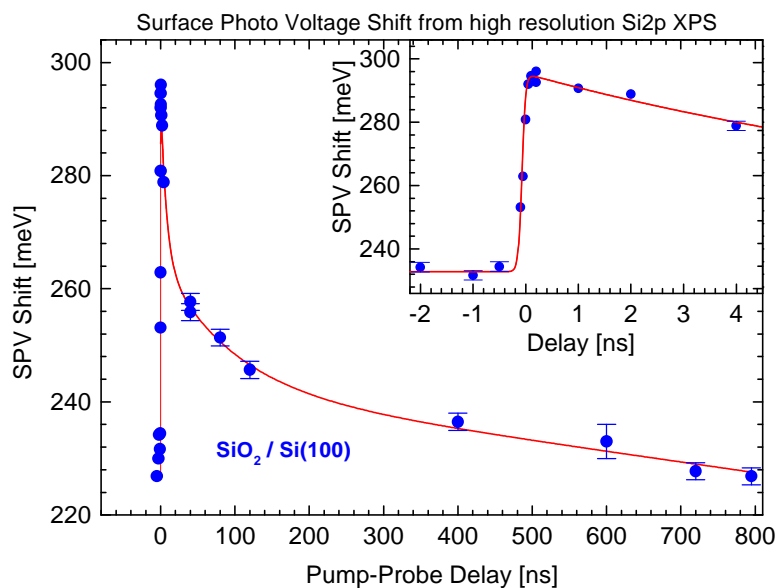

Fig. 1: *Time-resolved surface photovoltage shift at the SiO_2/Si(100) interface as determined from Si2p XPS after laser excitation.*

interpreted as SPV shift and shows as function of the laser to SR pump-probe delay, see Fig. 1, a fast onset which is slightly slower than the experimental time resolution of about 60 ps. The decay can be described by several different time constants as shown by the solid line in Fig. 1. Initially we find a fast decay with a time constant of 6 ns which is followed by a slower decay with about 90 ns. Finally for pump-probe delays longer than 200 ns the remaining SPV shift can by described by a decay with about 11 µs time constant. These results can be compared with the observed SPV shifts for differently prepared silicon surfaces. Similar to the data here, carrier recombination times in the order of 10 - 100 ns (depending on the preparation) have been found for different oxidized Si surfaces [7] whereas decay times below 1 ns have been deduced for clean Si surfaces [8-10].

[1]   W. Mönch, Semiconductor Surfaces and Interfaces, Springer Series in Surface Science, G. Ertl, R. Gomer, and D. L. Mills eds. (Springer, Berlin-Heidelberg, 1993).

[2]   L. Kronik and Y. Shapira; Surf. Sci. Rep. 37, 5-206 (1999).

[3]   T. Quast, R. Bellmann, B. Winter, J. Gatzke, and I. V. Hertel; J. Appl. Phys. 83, 1642-48 (1998).

[4]   A. Fink, W. Widdra, W. Wurth, C. Keller, M.Stichler, A. Achleitner, G. Comelli, S. Lizzit, A. Baraldi, and D. Menzel; Phys. Rev. B 64, 045308 (2001).

[5]   E. Landemark, C. J. Karlsson, Y. C. Chao, and R. I. G. Uhrberg; Phys. Rev. Lett. 69, 1588–91 (1992).

[6]   T. W. Pi, J. F. Wen, C. P. Ouyang, R. T. Wu, and G. K. Wertheim; Surf. Sci. 478, L333-L38 (2001).

[7]   M. Marsi et al.; Phys. Rev. B 61, R5070-R73 (2000).

[8]   N. J. Halas and J. Bokor; Phys. Rev. Lett. 62, 1679–82 (1989).

[9]   T. E. Glover, G. D. Ackermann, A. Belkacem, B. Feinberg, P. A. Heimann, Z. Hussain, H. A. Padmore, C. Ray, R. W. Schoenlein, and W. F. Steele; Nucl. Instrum. Methods A 467, 1438-40 (2001).

[10]   M. Marsi, M. E. Couprie, L. Nahon, D. Garzella, T. Hara, R. Bakker, M. Billardon, A. Delboulbe, G. Indlekofer, and A. Taleb-Ibrahimi; Appl. Phys. Lett. 70, 895-97 (1997).

Copper Satellite Structure in Porphyrazine Compounds

D. Pop[1], B. Winter[1], D. R. Batchelor[2,3], W. Freyer[1],
R. Weber[1], D. Bröcker[1], I. V. Hertel[1], D. Schmeißer[3], W. Widdra[1,4]

[1]*Max-Born-Institut, Max-Born-Str. 2a, D-12489 Berlin, Germany*
[2]*BESSY II, Rudower Chaussee 5, D-12489 Berlin, Germany*
[3]*Brandenburgisch Technische Universität Cottbus, Erich-Weinert-Str. 1, D-03046 Cottbus, Germany*
[4]*Institut für Atomare Physik und Fachdidaktik, Technische Universität Berlin, 10623 Berlin, Germany*

Porphyrazines and phthalocyanines have long been of interest in numerous technological applications such as energy conversion, gas sensors, optical data storage, sensitizers for photodynamic therapy, and many others [1]. They are exceptionally stable and their physicochemical properties can be well adjusted by suitable substitutions. The properties of main interest are their high symmetry, planarity, and electronic delocalization. Here we present photoemission studies on a family of such compounds in order to investigate the interaction between the central metal atom (in this case Cu) and the ligand as a function of the size of the π-electron system. The photoemission experiments were conducted at the MBI-SGM U125 beamline. Additional NEXAFS studies have been performed at the BTUC-PGM beamline.

Photoemission spectra for a thin film of Cu-tetra(tert-butylbenzo) porphyrazine (P1-Cu) and metal-free tetra(tert-butylbenzo) porphyrazine (P1) are shown in Fig. 1.
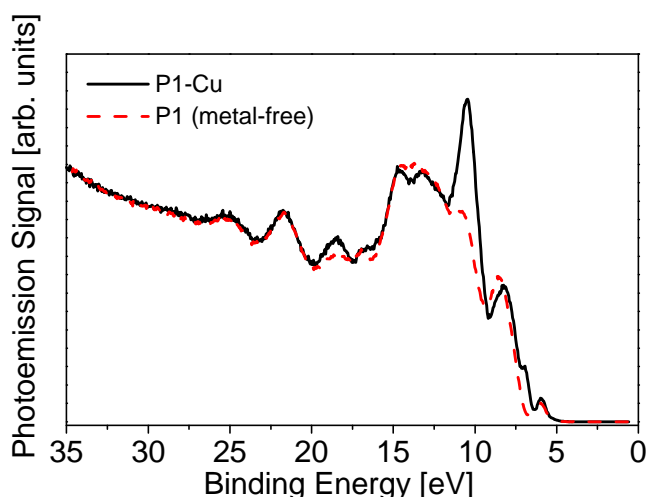
Fig. 1 Photoemission spectra for a thin film of Cu-tetra(tert-butylbenzo) porphyrazine (P1-Cu) and the respective metal-free compound at 70 eV excitation energy.

Roughly, the assignment of the features in the spectra is as follows. The direct emission from Cu3d makes up for the strong peak near 10.5 eV binding energy as inferred from comparison with the metal-free film. Additionally at about 18 eV the Cu satellites are visible. The peaks observed at 25 and 22 eV binding energy are assigned to C2s emission. The features near 14.5, 13.5, and 11.0 eV, respectively, largely arise from C2p orbitals.

Figure 2 displays photoemission spectra for thin (vacuum sublimed on a gold substrate) films of Cu-porphyrazine with different size of the π-electron system. The species were studied were obtained by linear benzoannelation of Cu-porphyrazine. In Fig. 2 pairs of spectra for excitation at 75 and 70 eV are shown from top to bottom for Cu-tetra(tert-butyl) porphyrazine, Cu-tetra(tert-butylbenzo) porphyrazine, Cu-tetra(tert-butylnaphtho) porphyrazine, and Cu-octaphenyl-tetraanthraporphyrazine which are denoted for simplicity P0-Cu, P1-
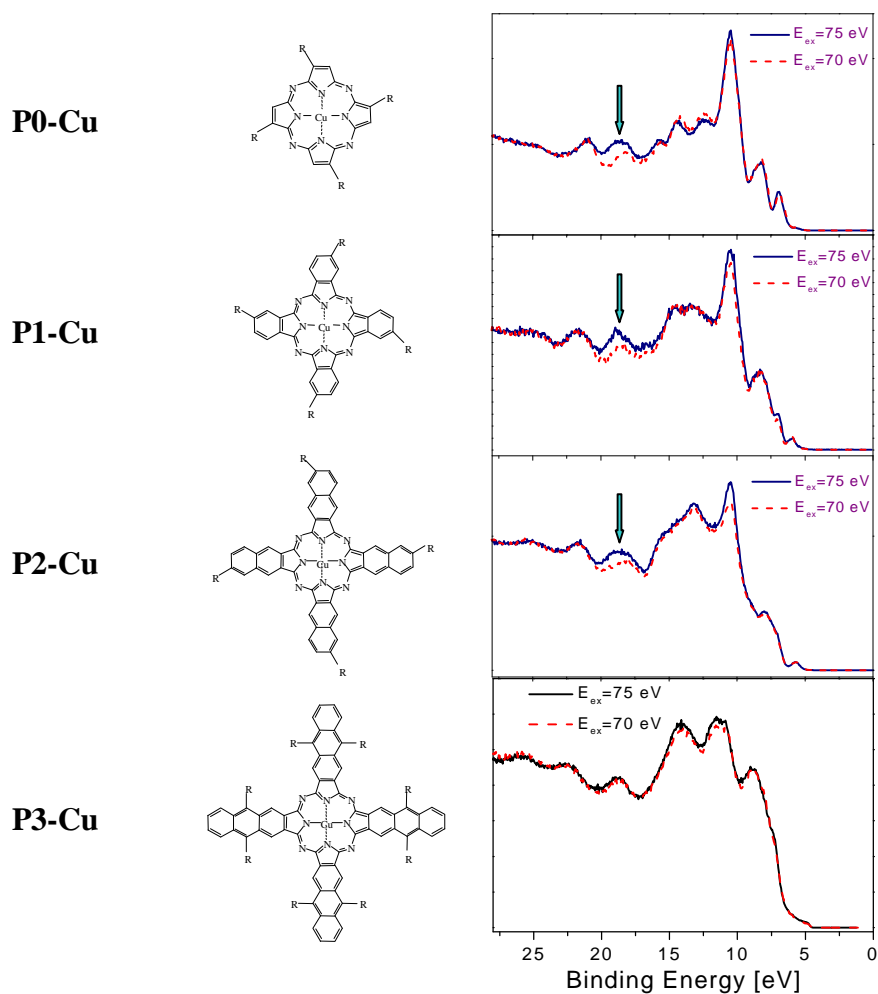
Fig. 2 Photoemission spectra for thin films of Cu porphyrazine compounds obtained for 70 and 75 eV photon energy. The Cu3d satellites positions near 18 eV binding energy are marked by arrows. The molecules are indicated by sketches.

Cu, P2-Cu, and P3-Cu depending on the number of benzo-units attached to the porphyrazine core. Note that the increasing benzoannelation is accompanied by a rise of the characteristic aromatic-type features as can be also observed in Fig. 2. The comparison of spectra at 75 and 70 eV (and for other photon energies, not shown here) indicates a resonance behavior of the copper satellites (marked by arrows) for three compounds. However, no resonance effect is observed for the largest molecule. Note that the satellites are in all three cases also present at off-resonant photon energies. For P1-Cu this is demonstrated in Fig. 1 where the photoemission spectrum for the Cu compound is compared with that of the metal-free compound.

The satellite enhancement at 75 eV is related to the 3p—3d transition in copper. Around this photon energy the direct photoemission is in resonance with the Auger electron emission. Since this Auger process involves excitation into the 3d state it implies the existence of holes in the 3d level. The presence or absence of the satellite enhancement points to an incomplete or filled 3d shell, respectively. Therefore the photoemission data in Fig. 2 indicate that for the first three compounds, P0-Cu, P1-Cu, and P2-Cu, Cu has at least one hole in the 3d shell,

whereas in the largest compound, P3-Cu, Cu is in a 3d^{10} configuration. As an alternative approach to the initial state configuration NEXAFS studies have been carried out. Figure 3 shows the absorption spectra for thin films of the two largest compounds, P2-Cu and P3-Cu. Whereas we find a strong absorption peak at around 932 eV for P2-Cu, this feature is significantly weaker for the larger P3-Cu compound. It is interpreted as the 2p to 3d absorption. The different intensities support the conclusion from the valence spectra that the configuration is different for the two different molecules. In standard Cu-phthalocyanine, a molecule which very similar to the compound P1-Cu, the central Cu atom is divalent having a formal $3d^9 4s^0$ configuration [3]. This configuration was identified by its characteristic sharp 2p—3d peak near 931 eV in NEXAFS. The similarities of the NEXAFS results would indicate here that the configuration of the Cu atom is $3d^9 4s^0$ also for the chemically similar P2-Cu compound. However the absorption edge for the largest molecule, P3-Cu, very much resembles the typical data for Cu^{I} or Cu^{0} compounds with completely filled 3d shells [3].
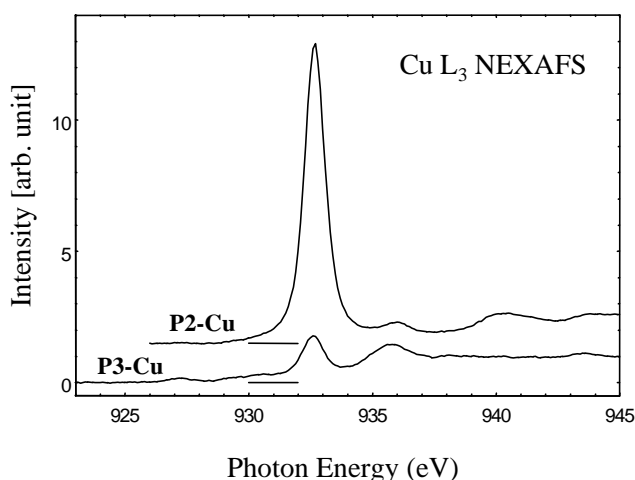
Fig. 3 NEXAFS spectra for the compounds P2-Cu and P3-Cu. The spectra have been vertically translated for clarity.

Further corroboration for the initial state configuration of the central Cu atom in the molecules comes from additional XPS studies (not shown here). It is known that only for an incomplete 3d shell, Cu2p satellites may arise [4]. In this case the satellites have a $\underline{2p}3d^9$ configuration, and the main line arises from $\underline{2p}3d^{10}\underline{L}$. Here, $\underline{2p}$ and $\underline{L}$ indicate that there is a hole in the Cu2p and the ligand valence state, respectively. Thus the main line corresponds to a charge transfer state in which a core hole is screened by the electron transfer from the ligand to Cu3d. This is consistent with our data showing satellites in the XPS spectra for the molecules P0-Cu, P1-Cu, P2-Cu but not for the largest one. From the comparison of the UPS, XPS, and NEXAFS data different final states and their charge transfer characteristics might be inferred.

References

[1] C. C. Leznoff, A. B. P. Lever, Phthalocyanines, Properties and Applications, Vol. **3**, VCH Publishers, Inc., New York, 1993
[2] M. S. Liao, S. Scheiner, Jounal of Chemical Physics, 114 (2001) 9780
[3] M. Grioni et al. , Phys. Rev. B, 39 (1989) 1541
[4] G. van der Laan, C. Westra, C. Haas, G. A. Sawatzky, Phys Rev. B, 23 (1981), 4369
[5] M. Ohno, Journal of Electronic Spectroscopy and Related Phenomena, 113 (2001) 109-115

# Detection of ferromagnetic spin structure of Manganese in a exchange biased IrMn/CoFe Bilayer

D. Schondelmaier[*], J. Morenzin[†], S. Cramm[†], H.A. Dürr[*] and W. Eberhardt[*]

[*] *BESSY GmbH,Albert- Einstein-Str.15, D - 12489 Berlin*
[†] *Forschungszentrum Jülich, IFF/IEE, D - 52425 Jülich*

More than 40 years ago Meikeljohn and Bean[1] discovered the exchange bias phenomenon, i.e. as a shift of the hysteresis loop by a bias field H_e of a ferromagnetic (FM) layer brought in contact with an antiferromagnetic (AF) layer. The effect is ascribed to an uncompensated amount of ferromagnetic spins at the interface layer in the AF. However, even after a large amount of work a microscopic basis of the effect is not yet established. Experimentally this may be due to the fact that most of the observation methods can not distinguish the small signal of less than a monolayer of uncompensated spins from the magnetic background due to the FM layer. Using x-ray magnetic circular dichroism (XMCD) at high-brilliance 3rd generation synchrotron light sources such as BESSY we show that it is now possible to obtain element specific information on the magnetic moments and to detect even minute magnetic effects at the interface layers of exchange biased samples.

We have measured the XMCD of Manganese and Cobalt in an exchange biased IrMn/CoFe bilayer. The measurements were performed at the CRG beamline UE56/1-SGM (FZ Jülich) using circular polarized light with an energy resolution of 0.3 eV.

MOKE hysteresis loop

H_E = 43,9 Oe
H_C = 36,0 Oe
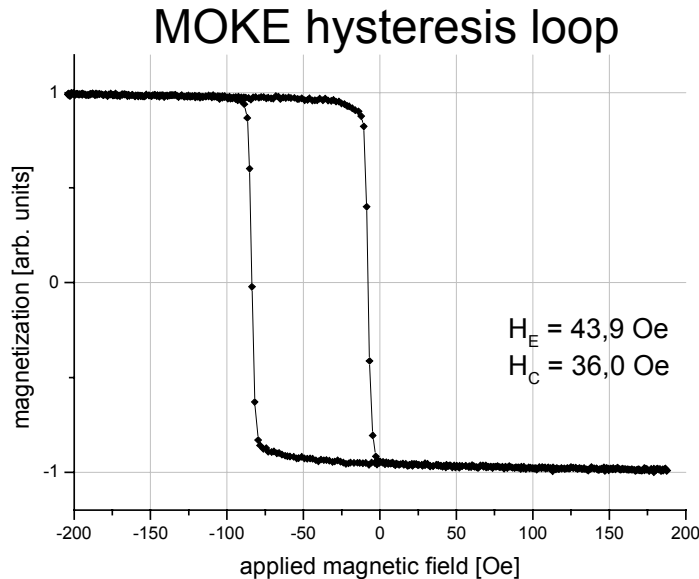
Fig. 1 Hysterese loop of the easy axis of the exchange biased sample.

For this study a 200 Å Cu / 85 Å IrMn / 150 Å CoFe /50 Å Cu. sample was prepared on a 1000Å thick SiN membrane by magnetron sputter deposition. The Cu seed layer was needed to cause an appreciable exchange biasing of the FM CoFe layer after the whole structure was deposited in an applied magnetic field. The Cu capping layer served as a contamination protection of the sample. A hysteresis loop of the sample obtained using the magneto-optic Kerr effect (MOKE) is shown in Fig. 1. The magnetic field was applied along the easy magnetization direction. We obtain an exchange field of H_e = 43 Oe.

The coercivity was to H_c = 36 Oe.

[1] W.H. Meikeljohn and C.P. Bean, *Phys. Rev..* **102**, 1413 (1956)

XMCD spectra were obtained by switching a static magnetic field generated by a pair of permanent magnetis mounted in the high-vacuum chamber parallel/antiparallel to the easy axis of the sample during each energy step. The sample normal was aligned with a fixed angle of 45° relative to the incident x-rays. The transmitted x-ray intensity, I, was measured with a GaAsP diode mounted behind the sample. The x-ray intensity, I_0, before the sample was measured as the total electron yield of a gold mesh.
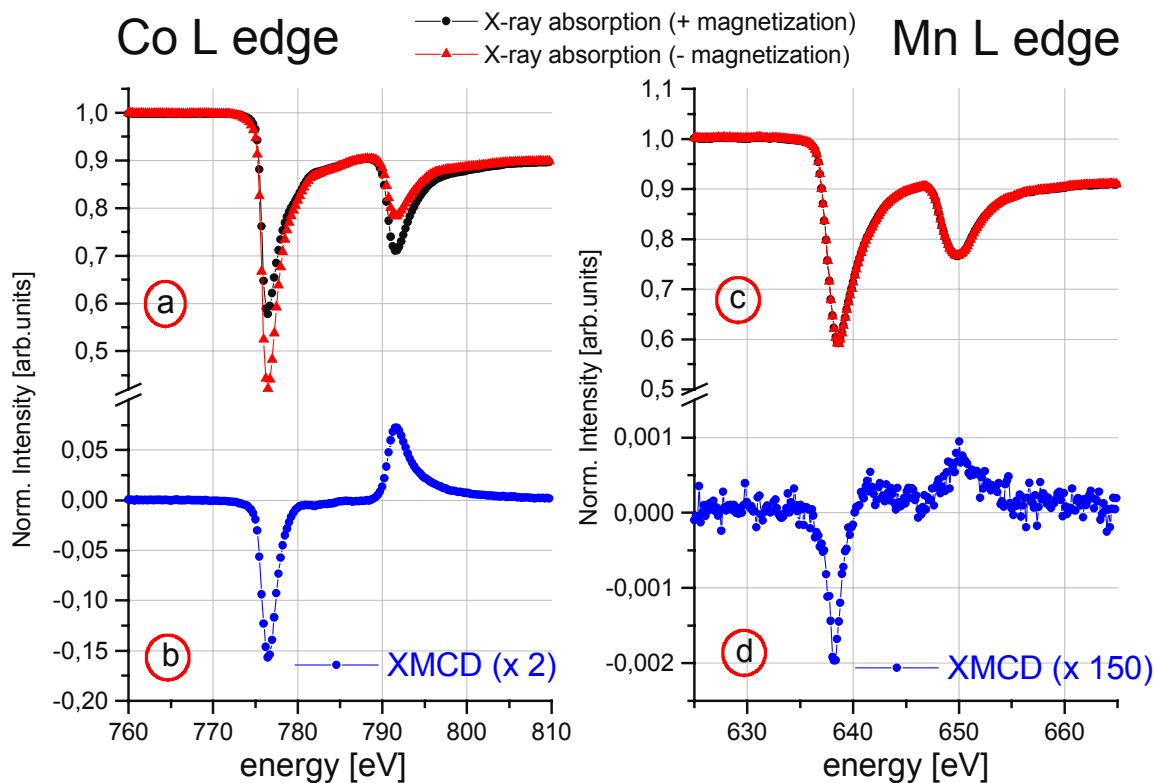
Fig. 2 X-ray absorption (a) & (c) and XMCD (b) & (d) spectra versus photon energy at the $L_{2,3}$ edges of Co and Mn. The XMCD spectra were taken by flipping the magnetization of the sample with help of an applied external field.

The normalized absorption spectra at the $L_{2,3}$ edges of Mn and Co are shown in Fig. 2a and Fig. 2c. The spectra obtained for each magnetization were subtracted from each other to get the XMCD spectra the Mn and Co L edge respectively. The XMCD spectra are shown in Fig. 2b and Fig. 2d. We found a strong dichroism of 31% at the Co edge and a dichroism of 0.48% at the Mn edge. In AF IrMn the XMCD signal should be zero. We can estimate the number of uncompensated Mn spins assuming that the dichroism is similar on both Mn and Co $L_{2,3}$ edges. Taking into account the thickness of 85 Å of the IrMn and assuming that 3 Å IrMn correspond to one monolayer, the total XMCD signal at the Mn L edge originates from about 13% of a monolayer of IrMn. The data in Fig. 2d clearly show the existence of uncompensated Mn spins at the CoFe/IrMn interface. Uncompensated spins are recently discussed to play a key role in the AF/FM coupling in exchange biased systems[2,3].

[2] K. Takano et. al., *Phys. Rev. Lett.* **79**, 1130 (1997)
[3] W.J. Antel, Jr., F. Perjeru, and G. R. Harp ., *Phys. Rev. Lett.* **83**, 1439 (1999)

ELECTRON-PHONON COUPLING IN *2H*-NBSE$_2$ AS PROBED BY PHOTOEMISSION SPECTROSCOPY

M. Sing, B. Lax, R. Claessen, M. Klemm, S. Horn

Experimentalphysik II, Universität Augsburg, D-86135 Augsburg, Germany

Recently, renewed interest was attracted to the effects of electron-phonon coupling on the electronic structure of solids [1-6]. As a prominent example, in the case of the high-temperature superconductors it was claimed on the ground of measurements by angle resolved photoemission spectroscopy (ARPES) performed on a set of various cuprate systems that electron-phonon coupling may be of more importance for superconductivity in these materials than believed until then. The coupling of the electron system to the lattice degrees of freedom plays an important role also in the formation of other phases, particularly the CDW phase in low-dimensional systems. Against this background the layered, electronically two-dimensional dichalcogenide *2H*-NbSe$_2$ offers the possibility to study the effects of electron-phonon coupling in a system showing both a CDW transition at about 35 K and superconductivity below 7.2 K. In this report we focus on the electronic structure just above the CDW transition temperature.

Fig. 1: *Grey scale plot of the second derivative of the photoemission intensity along the $\overline{\Gamma}\,\overline{M}$ -direction. The straight lines are intended as a guide to the eye visualizing the sudden change in slope of the quasiparticle excitations.*

2H-NbSe$_2$ single crystals were grown by an iodine-assisted chemical transport method as described elsewhere [7]. Clean surfaces were achieved by *in situ* cleavage exposing the (0001) surface. The ARPES experiments were carried out using an OMICRON AR65-spectrometer [8] at the U125/1-PGM-beamline with a photon energy of 35 eV. The energy resolution was 23 meV, the angle acceptance amounted to ±0.5°.

In Fig. 1 we show a grey scale plot of the photoemission intensity in an *E* vs. $k_{\parallel}$- map along the high-symmetry direction $\overline{\Gamma}\,\overline{M}$ in reciprocal space. We concentrate on an energy and momentum region where an electronic band approaches and finally crosses the Fermi level E_F. Going from high to low $k_{\parallel}$-values one clearly sees a sharp step in the *E* vs. $k_{\parallel}$ dispersion with a considerable smaller slope at lower $k_{\parallel}$. This behaviour matches the simplest picture of the effect of a phonon mode coupling to an electron where the electron velocity is abruptly reduced on the energy scale of the phonon mode since the electron is dressed by virtual emission and absorption of the phonon. For real systems this energy scale is given by the Debye energy $\hbar\omega_D$ which for NbSe$_2$ is reported to be about 19 meV [9]. The lines in Fig. 1 indicate the bare (blue) and dressed (red) electron dispersion in the $k_{\parallel}$-regions where notable

spectral weight is seen (solid lines) or only weak intensity is recorded (dashed line). From the band width of the renormalized branch we deduce a Debye energy of about 30 meV. In addition, the change in the slopes between the two branches as indicated by the solid lines, i.e. the change in electron velocity, is a measure for the strength of the electron-phonon coupling as expressed in the dimensionless coupling constant λ according to $v_\mathbf{k}^* = v_\mathbf{k}/(1+\lambda)$. Our measurements yield a value $\lambda \approx 1.4$ which falls well within the range of values reported in the literature [10].
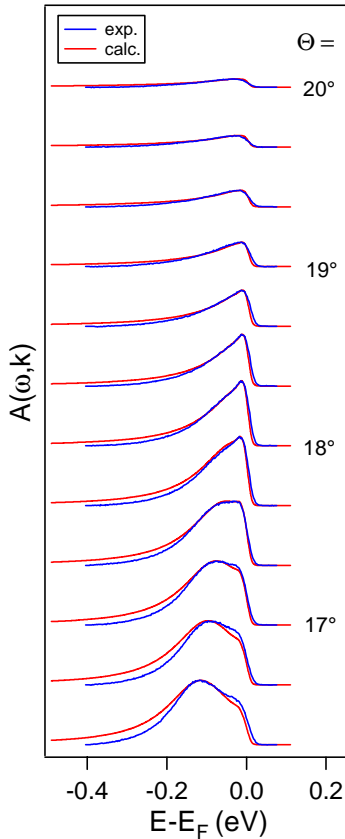
That the agreement of our data with theoretical expectations goes far beyond the gross features of a simple text-book treatment as discussed so far is visualized in Fig. 2. There we show energy distribution curves taken along another high symmetry line, $\overline{\Gamma}\overline{K}$, together with calculated spectra. These were obtained within a real many-particle approach evaluating the spectral function for the case where a single electronic band is coupled to phonons in the framework of a zero temperature isotropic Debye model [11]. Assuming constant electron-phonon matrix elements there are – besides a constant contribution to the imaginary part of the self-energy due to impurity scattering – only two parameters left to reproduce the experimental data, the Debye frequency and the electron-phonon coupling constant λ. The qualitative agreement between model and experiment is remarkably well. Again we find a Debye energy of about 30 meV. However, the value for λ comes out too low while the contribution due to impurity scattering seems to be rather high. Partly this may be attributed to the different situation at the surface which is seen by PES, partly it may be related to the shortcomings of the used model.

In any case experiment and theory clearly show that indeed in *2H*-NbSe$_2$ a many-particle description of the electronic structure close to E_F is needed as is reflected in the complex evolution of the spectral function being comprised out of two peaks with a relative shift of spectral weight from the high binding energy structure (the remnant of the unrenormalized quasi-particle excitation) to the low binding energy peak (corresponding to the screened excitation).

Fig. 2: Modelling of PES-spectra along $\overline{\Gamma}\overline{K}$. For details see the text.

[1] T. Valla, A. V. Fedorov, P. D. Johnson, S. L. Hulbert, Phys. Rev. Lett. **83**, 2085 (1999).
[2] T. Valla, A. V. Fedorov, P. D. Johnson, J. Xue, K. E. Smith, F. J. DiSalvo, Phys. Rev. Lett. **85**, 4759 (2000).
[3] Th. Pillo, J. Hayoz, H. Berger, R. Fasel, L. Schlapbach, P. Aebi, Phys. Rev. Lett. **62**, 4277 (2000).
[4] S. LaShell, E. Jensen, Phys. Rev. B **61**, 2371 (2000).
[5] A. H. Castro Neto, Phys. Rev. Lett. **86**, 4382 (2001).
[6] A. Lanzara, P. V. Bogdanov, X. J. Zhou, S. A. Kellar, D. L. Feng, E. D. Lu, T. Yoshida, H. Eisaki, A. Fujimori, K. Kishio, J.-I. Shimoyama, T. Noda, S. Uchida, Z. Hussain, Z.-X. Shen, Nature **412**, 510 (2001).
[7] M. Nohara, M. Isshiki, F. Sakai, H. Takagi, J. Phys. Soc. Jpn. **68**, 1078 (1999).

[8] C. Janowitz, R. Müller, T. Plake, Th. Böker, R. Manzke, J. Electron Spectrosc. Relat. Phenom. **105**, 43 (1999).

[9] J. M. E. Harper, T. H. Geballe, F. J. DiSalvo, Phys. Rev. B **15**, 2943 (1977).

[10] R. Corcoran, P. Meeson, Y. Onuki, P.-A. Probst, M. Springford, K. Takita, H. Harima, G. Y. Guo, B. L. Gyorffy, J. Phys. :Condens. Matter **6**, 4479 (1994).

[11] G. Grimvall, *The electron-phonon interaction in metals*, (North-Holland, Amsterdam, 1981).

The X-Ray Magneto-Optical Voigt Effect at the Co 2p Edge

H.-Ch. Mertins, P.M. Oppeneer*, J. Kunes*, D. Abramsohn, A. Gaupp, F. Schäfers, W. Gudat

BESSY, Albert-Einstein-Strasse 15, D-12489 Berlin, Germany

* IFW-Dresden, P.O. Box 270016, D-01171 Dresden, Germany

X-ray magneto-optical (MO) spectroscopies like the magnetic circular dichroism (XMCD) /1/ are widely used for the investigation of new magnetic materials /2/. A new X-ray MO phenomenon that is quadratic in the magnetization M is the Voigt effect. X-ray MO spectroscopies that are sensitive to $<M^2>$ hold great potential for the future investigation of anti-ferromagnetic materials, something which is not possible with X-ray spectroscopies that are linear in M like the XMCD. Technologically important materials of broad current interest, as magnetoresistive, spin-valve and exchange-bias materials /2/ can be investigated by such new type of X-ray spectroscopies on an element selective level.

The Voigt effect is detected in the geometry shown in Fig. 1. The incident light beam is normal to the surface, and is linearly polarized at an angle α with respect to the magnetization. Upon transmission, the polarization plane becomes rotated over the Voigt angle θ_V, and, in addition, the light becomes elliptically polarized by an amount ε_V. The two refractive indices of the material are $n_\parallel$ and $n_\perp$, corresponding to the propagation of linear modes which have the electrical field vector parallel and perpendicular, respectively, to the magnetization. For $\alpha=\pi/4$ the incident light is decomposed into two equal components, one parallel and one normal to the magnetization. When the two refractive indices are unequal, which happens in an isotropic material only because of the magnetization, the Voigt effect occurs upon transmission.

In our experiment we used a 200 nm amorphous Co film, grown on a 100 nm thick Si_3N_4 membrane. The X-ray polarization analysis (see Fig. 1) was performed with the BESSY polarimeter /3, 4/. The measured soft X-ray Voigt rotation spectrum is shown in Fig. 2. Each data point for θ_V is the result of a polarization analysis for fixed photon energy. Due to the resonant excitation from 2p to 3d levels the rotation data display resonant maxima immediately below and above the absorption edge /4/. The maximum values of up to 7.5 deg./µm are almost an order of magnitude larger than those observed in the visible. To verify the quadratic dependence on the magneti-
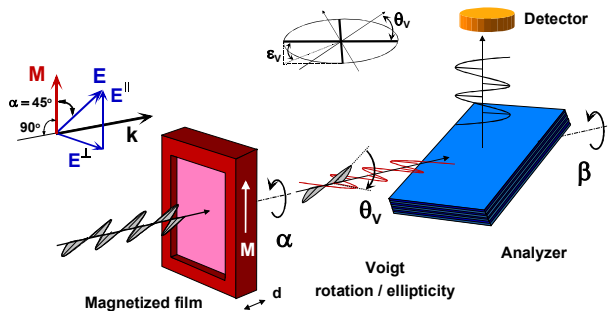
Fig. 1 Experimental set-up for the X-ray Voigt effect on magnetic films. The polarization plane of the transmitted light is tilted over an angle, which is the Voigt rotation, and also the transmitted light has become elliptically polarized.

zation we measured the Voigt rotation under inverted magnetic field, which we found to be independent of the magnetization direction, as expected /4/. For comparison we determined experimentally the XMLD asymmetry which is also sensitive to $<M^2>$. It is detected by an intensity measurement, recording the transmission spectra $T_{||}$ and $T_\perp$. The result is shown in Fig. 2. As expected, the two quantities agree well, except for the high-energy side of the $2p_{3/2}$ absorption edge /4/. Here the XMLD experiment is disturbed by fluorescence back-ground,

which is excited at this energy, diminishing the XMLD asymmetry. The measurement of the Voigt rotation is less sensitive to fluorescence disturbances, because the analyzer is energy selective and set to select the incident light, while the fluorescence light with its different wavelength is suppressed.
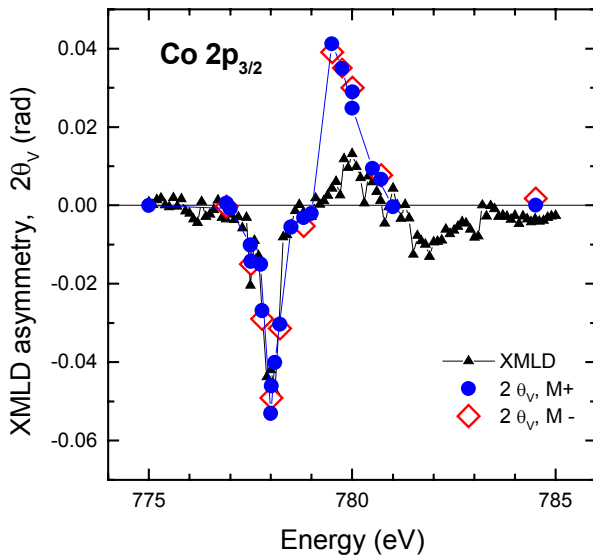
Fig. 2 The X-ray Voigt rotation measured at the Co L_3-edge with 2 antiparallel directions of the magnetization M. Their equivalence shows the quadratic dependence of the Voigt rotation on M. For comparison the XMLD asymmetry is shown. Both spectra ought to agree according theory, but do not around 780 eV because the XMLD is diminished by fluorescence.
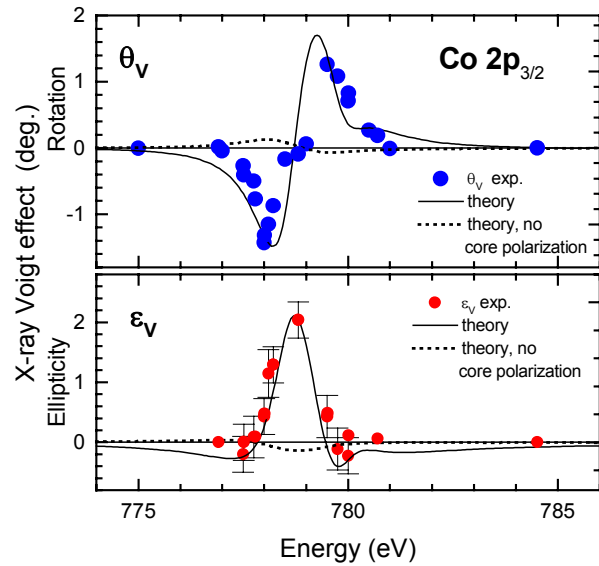
Fig. 3 Calculated and measured X-ray Voigt effect at the L_3-edge of 200 nm Co. Top: experimental Voigt rotation and calculated spectrum. Full curve gives the Voigt rotation computed with spin polarization of the $2p_{3/2}$ core states, the dashed curve is obtained without core polarization. Bottom: likewise, but for the Voigt ellipticity ε_V.

Further information follows from our ab-initio calculations /4/. They revealed an unprecedented sensitivity of the X-ray Voigt effect to the spin polarization of the core states. This is shown in Fig. 3 where we plot the experimental Voigt spectra together with the calculated spectra of fcc Co, that were computed both with and without the core spin polarization. Obviously, the Voigt rotation predicted with the $2p_{3/2}$ spin polarization included and the measured spectrum are in excellent agreement. Conversely, the Voigt effect calculated without core spin polarization, but with exchange-split valence states, is practically zero and bears no correspondence to the experiment. This demonstrates that the X-ray Voigt effect depends critically on the core spin splitting, which is unexpected, since the spin splitting of the 3/2, -3/2 sublevels of Co is only 0.79 eV.

1 C.T. Chen et al., Phys. Rev. Lett. **75**, 152 (1995).

2 G.A. Prinz, Science **282**, 1660 (1998).

3 F. Schäfers et al., Appl. Opt. **38**, 4074 (1999).

4 H.-Ch. Mertins et al., Phys. Rev. Lett. **87**, 047401-1 (2001).

Short-range V spin-polarization in Fe/V/Fe(110) trilayers

A. Scherz[1], P. Poulopoulos[1], H. Wende[1], F. Wilhelm[2], G. Ceballos[1] and K. Baberschke[1]

[1]*Freie Universität Berlin, Institut für Experimentalphysik, Arnimallee 14,*
D-14195 Berlin-Dahlem, Germany
[2]*European Synchrotron Radiation Facility (ESRF), B.P.220, 38043 Grenoble, France*

Fe/V superlattices (SL) are excellent systems with high quality single-crystalline epitaxial metallic structure [1,2]. They are used as prototype systems to investigate the rich variety of phenomena in multilayer magnetism [2-4]. However, the layer-dependent distribution of the V induced magnetic moments in the Fe/V SL's appeared to be controversial in literature [2,5,6]. Large V magnetic moments extending more than 4 atomic layers (ML) away from the Fe/V interface were reported [2]. In contrast to that the theory found much smaller V magnetic moments, by a factor 2-4 depending on the crystallographic direction, mainly localized at the interface, i.e. the V reveals a short-range spin polarization [5,6]. The discrepancies between theory and experiment on the Fe/V SL's may be related to roughness and interdiffusion at the Fe/V interfaces [2,4-6].

We report on thickness-dependent XMCD measurements on Fe/V_n/Fe(110) trilayers at the UE56/1-PGM beam line [7]. The selection of the trilayers offers us the possibility to manage the growth step-by-step and moreover, to perform the entire experiment *in situ*. The V films with thicknesses ranging from n=1-8 ML were deposited at room temperature on a thick Fe(110) buffer layer on Cu(100) single crystal and capped by a 5 ML Fe film, successively. A certain growth recipe, proven by a STM study, allow us to minimalize the roughness and interdiffusion in our system, for details see [7].

In Fig. 1 on the left the x-ray absorption spectra (XAS) and the XMCD in the near edge region at the $L_{2,3}$ edges of V and Fe are presented after normalization of the edge jump to unity. Although the V dichroism effect is small (enlarged by a factor 'x15'), the reproducibility of the absorption spectra in the ultrathin V films is excellent (free of noise). This is due to the use of an undulator beamline of the third generation synchrotron source in Berlin (BESSY II). Moreover, since we work *in situ* we do not need protective layers which damp the absorption signals. In addition, *ex situ* samples have the drawback of oxygen contamination leading to strong absorption at the O K edge (~530 eV) and consequently, the analysis of the V spectra is
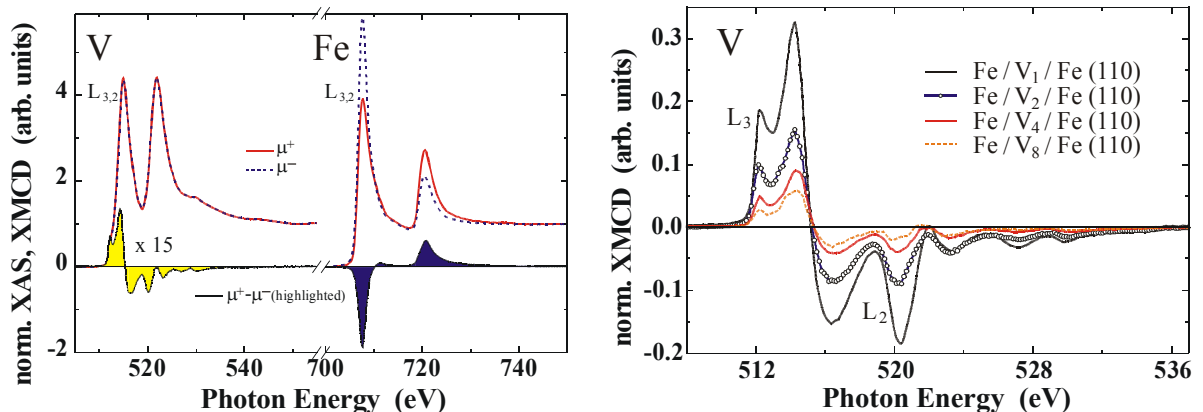
Fig 1: Left) Normalized XAS for left (dashed line) and right (solid line) circularly polarized light and the XMCD (highlighted) at the $L_{2,3}$ edges of V and Fe for a Fe/V_4/Fe(110) trilayer. Right) Series of normalized XMCD spectra of V for 1,2,4 and 8 ML film thickness as indicated.

$$\overline{\mu}_{av} \cdot n = \sum_{i=1}^{n} \mu_i = 2\,\mu_{Int} + \sum_{i=2}^{n-1} \mu_i = 2\,\mu_{Int} + (n-2)\,\overline{\mu}_{Vol}$$
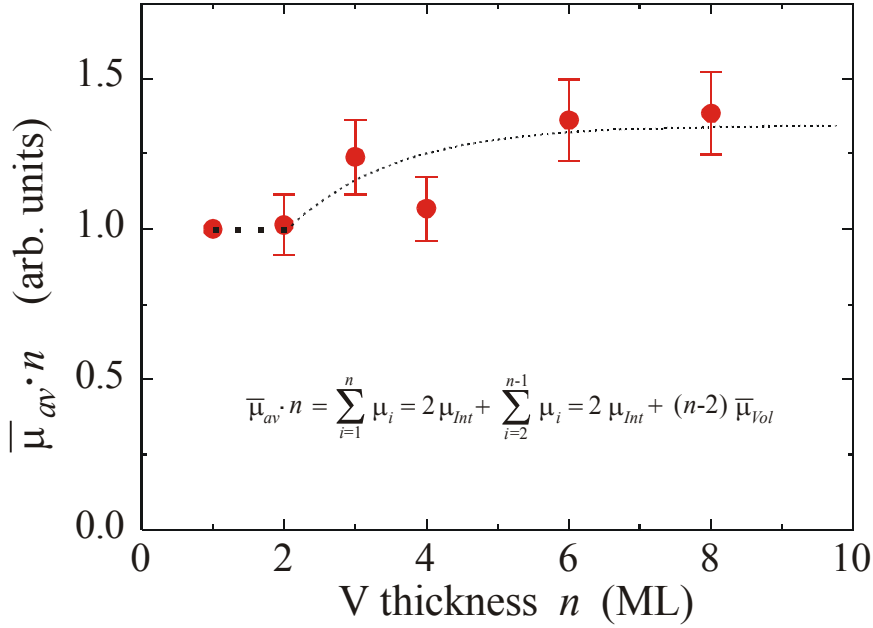
Fig 2: The average magnetic moment $\mu_{av} \cdot n$ (normalized with respect to the magnetic moment of one layer) times the thickness n (see equation) is shown as a function of n. The signal starts saturating above $n=3$ ML, indicating a short range polarization.

complicated due to the normalization of V with respect to the background. The high purity of our samples is reflected in the negligible O K edge. Opposite onsets in sign of the V and Fe dichroism indicate an antiferromagnetic coupling of the Fe and the induced V magnetic moments in agreement with theory and previous experiments[2,4-6].

The Fe spectra for all the trilayers reveal no thickness dependence, i.e. the measured XAS and XMCD intensities are identical to a Fe bulk reference sample taken in the same beam time. This result is due to the use of a Fe buffer layer for the trilayer preparation. The conventional 'sum rules' analysis to the Fe spectra using a value of 3.4 d-holes per atom yields a Fe magnetic moment which equals within 5% the bulk value of 2.22 μ_B per atom. Since we measure at remanence and detect the full Fe magnetic moment we conclude that the in-plane remanent magnetization is equal to the saturation magnetization, i.e. the hysteresis loops are square-like. Moreover, the Curie temperature of the samples is bulk-like as one expects for thick Fe layers.

A series of V XMCD spectra normalized to a constant edge jump are shown in Fig. 1 on the right. Due to the small spin-orbit splitting in the core levels the $L_{3,2}$ edges partially overlap. Therefore, the spin sum rule is not applicable to the experimental data. Moreover, the results of the sum rules for 3d elements at the beginning of the series is questionable, since core hole effects are present. Here, in good approximation, we take use of the proportionality between the measured XMCD amplitudes and the relative change of the V magnetization. The V magnetic moment for the trilayer with $n=1$ was set to unity. Since XMCD is not a layer-resolved technique the measured amplitudes represent the average V magnetization and the average induced magnetic moment μ_{av}, respectively. One can deduce that the sample with $n=1$ exhibits a magnetic moment which is twice as large as the one for $n=2$. Moreover, it has two interfaces to Fe and consequently double Fe nearest neighbors. This means accordingly that the V moment depends linearly on the number of Fe neighbors and confirms *ab initio* calculations for Fe/V interfaces [5].

By increasing the number of V layers the strong reduction of the XMCD signal suggests that μ_{av} decays rapidly. In Fig. 2 the product of $\mu_{av} \cdot n$ is plotted over n. This product provides the sum over the magnetic moments of each V layer (see equation in Fig. 2, where μ_{Int} is the interface V magnetic moment and μ_{Vol} the average volume contribution). The product remains nearly constant beyond the second ML from the interface. This demonstrates that the interface and the volume contributions are constant and no more magnetic moments comes from the inner V layers. The outcome is a saturation curve which is the dashed line in Fig. 2. The present data are in good agreement with *ab initio* theory for sharp interfaces [5,6] while diffused interfaces show a $\mu_{av} \cdot n$ curve without saturation [2]. One may visualize the V spin-polariza-

Fig 3: The layer-resolved magnetic moment profile of V for Fe/V$_n$/Fe(110) with n=1,2,3,4,6 and 8 ML is shown. The profile is deduced from the saturation curve in Fig.2 which implies that the induced V magnetic moment depend only on the distance from the Fe interface. The range of the V spin-polarization is in good agreement to theory (solid circles).

tion by deducing a magnetic moment profile for V (shown in Fig. 3) from μ_{av}. Therefore, one assumes that the induced V magnetic moment depends only on the distance from the Fe interface for all samples which is justified from calculations [6]. However, experimentally one approximates that the Fe/V interfaces in all samples are equal. The profile reveals that the induced V magnetic moment is mainly located at the interface. This is the first experimental support to recent *ab initio* calculations [5,6].

In summary, in the present experiment we show V XMCD spectra at the L$_{2,3}$ edges free of noise. By means of *in situ* XMCD measurements on prototype Fe/V/Fe trilayers with high purity, we probed a strong thickness dependence for the induced V magnetic moments. Our results are in agreement with *ab initio* theoretical predictions for superlattices with sharp interfaces. Therefore, we can lift off some previous inconsistencies between experiment and theory on the problem of short- or long-range induced V polarization in Fe/V layered systems.

References:
[1] A.N. Anisimov *et al.*, J. Phys.: Condens. Matter **9**, 10581 (1997) and references therein.
[2] M. M. Schwickert *et al.*, Phys. Rev. B, **57**, 13681, (1998) ; M. A. Tomaz *et al.* , J. Phys.: Condens. Matter, **9**, L179-184, (1997).
[3] B. Hjörvarsson *et al.*, Phys. Rev. Lett. **79**, 901 (1997); M. Sacchi *et al.*, *ibid.* **81**,1521 (1998); A.N. Anisimov *et al.*, *ibid.* **82**, 2390 (1999).
[4] A. Scherz *et al.*, Phys. Rev. B **64**, 180407(R) (2001).
[5] R. Coehoorn, J. Magn. Magn. Mater. **151**, 341 (1995).
[6] J. Izquierdo *et al.* , Phys. Rev. B, **59**, 14510, (1999).
[7] A. Scherz *et al.*, to appear in J. Appl. Phys. **91**,(May 2002).

Epitaxial NiO layers on Ag(100) studied by X-ray fluorescence and photoemission spectroscopy

S.A. Krasnikov, A.B. Preobrajenski, T. Chassé, R. Szargan

Wilhelm-Ostwald-Institut für Physikalische und Theoretische Chemie, Universität Leipzig, Linnéstr. 2, D-04103 Leipzig, Germany

Investigation of electronic structure of transition metal (TM) oxides has been an active field of research for several decades arising from many puzzling issues such as the nature and origin of the insulating state in partially filled 3d systems, like NiO and the existence of metal-insulator transitions [1]. In the last years, ultra-thin films and multi-layers have become very popular because of their interesting and novel physical properties. One of the interesting aspects of the electronic structure of thin NiO films is the influence of the film thickness on the antiferromagnetic order. Indeed, a strong thickness dependence of magnetic moments has been found in ultrathin epitaxial NiO films studied by X-ray magnetic linear dichroism in the Ni $L_{2,3}$-absorption [2]. In particular, even for the 20 ML thick films the Néel temperature was reported to be strongly reduced from the bulk value, and the 5 ML thick layers were even supposed to be paramagnetic at room temperature.

The electronic structure of thin NiO layers can be probed by X-ray fluorescence spectroscopy (XF) due to its elemental selectivity and dipole selection rules, which allow the Ni 3d component in the valence band of these oxides to be studied separately from other states. Nowadays XF becomes more and more popular due to the advent of high-brilliance synchrotron radiation (SR) sources (for review see, e.g., [3]). Because of its photon-in and photon-out nature XF also allows to study insulators, which is a crucial point for the TM monoxides. In this work we study the electronic structure of thin epitaxial NiO layers using X-ray fluorescence spectroscopy and X-ray photoemission

spectroscopy (XPS) expecting a thickness dependence of spectra due to reduced dimensionality.

The X-ray fluorescence measurements on epitaxially grown NiO films with different thicknesses on Ag(100) substrate were performed *in situ* using the X-ray monochromator XES 300 (mounted on the end station ROSA) and synchrotron radiation at the U41-PGM beam-line at BESSY II. The axis of X-ray monochromator was set perpendicular to the beamline axis in the plane of polarization of incident radiation in order to avoid the elastically scattered peak. The angle between the sample normal and the monochromator axis was 30°. The X-ray photoemission measurements were carried out with monochromatized Al K_α radiation in a VG ESCALAB 220i-XL spectrometer. All samples were prepared by thermal evaporation of metallic nickel onto cleaned Ag(100) substrates at 350 °C in an oxygen atmosphere with 8.0 x 10^{-6} mbar pressure. The Ag(100) substrate was cleaned in the usual way by cycles of Ar^+-ion bombardment and annealing until the low-energy electron diffraction (LEED) pattern was of sufficient quality. The amount of deposited NiO was monitored with a quartz microbalance and then confirmed by comparative analysis of intensities of the XPS Ni 2p, Ag 3d and O 1s core-lines. The surface structure of NiO films was verified by LEED.

Figures 1 and 2 show the measured Ni $L_{\alpha, \beta}$ emission spectra for the studied 2 ML and 6 ML NiO thin films on Ag(100), respectively. The relative intensities of the spectra have been normalized to the intensity of Ni L_α emission line. The spectra
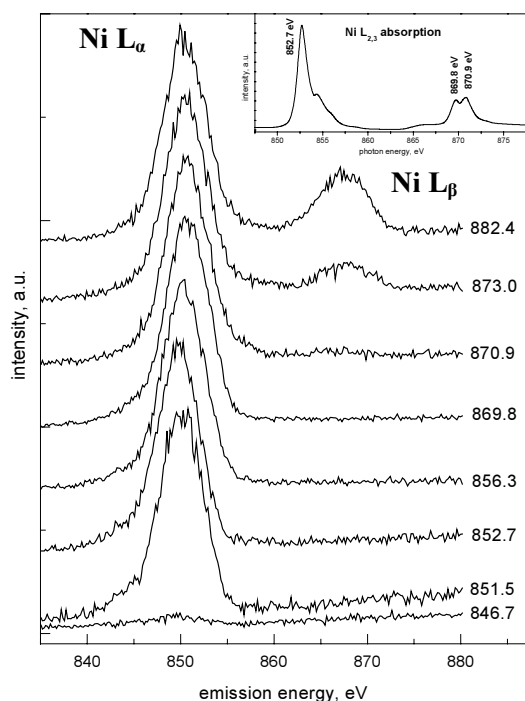
Fig. 1. *Ni L$_{\alpha,\beta}$ emission spectra of NiO (2ML) on Ag(100). At the right part excitation energies are shown. The inset shows Ni L$_{2,3}$ XANES spectrum of NiO single-crystal [4].*


Fig. 2. *Ni L$_{\alpha,\beta}$ emission spectra of NiO (6ML) on Ag(100). At the right part excitation energies are shown.*

were excited with a band of photon energies (FWHM ≈ 20 eV) varying the band edge from 846.7 eV to 882.4 eV covering the Ni L$_{2,3}$ XANES region (see Fig. 1, inset). Because of the large band width of exciting radiation (we used fully opened exit slit to obtain the maximum intensity of incoming radiation) the resonant behavior of the recorded spectra could not be resolved. In these sets of spectra we will pay attention on relative intensities of Ni L$_\alpha$ (3d→2p$_{3/2}$ transition) and Ni L$_\beta$ (3d→2p$_{1/2}$ transition) at different excitation energies and different thicknesses of NiO thin film. One can see that the Ni L$_\beta$ emission line undergoes significant changes in its relative intensity in going from 2 ML to 6 ML NiO thin film. For the case of 882.4 eV excitation energy the ratio between Ni L$_\beta$ and L$_\alpha$ emission lines equals to 0.3 and 0.4 for 2 ML and 6 ML of deposited NiO, respectively. This effect is related to the delayed appearance of the Ni L$_\beta$ band. At the 870.9 eV excitation energy the Ni L$_\beta$ band is only present in the case of 6 ML NiO sample. The origin of these features may be related

to the binding energy shift and valence band (VB) structure as well as final state effects.

Figure 3 shows a comparison of the Ni L$_\alpha$ and L$_\beta$ emission bands recorded at the excitation energy 882.4 eV, O K$_\alpha$ emission band recorded at the excitation energy 550.0 eV, XPS VB (all spectra measured on 6 ML NiO) and the XPS VB spectrum measured on 2 ML and 12 ML NiO. XPS VB spectra were obtained by subtraction of the Ag 4d signal from measured VB spectra from NiO on Ag(100). Ni L$_\alpha$, L$_\beta$ and O K$_\alpha$ emission spectra were aligned on the binding energy scale using our measured XPS binding energies of core levels: E$_{BE}$(Ni2p$_{3/2}$) = 854.2 eV, E$_{BE}$(Ni2p$_{1/2}$) = 871.7 eV, E$_{BE}$(O1s) = 529.7 eV. From the figure 3 it is clearly seen that the main band A-B is dominated by Ni 3d states. The position of O K$_\alpha$ emission band corresponds to the O 2p states. The VB spectrum from 12 ML NiO film is in good agreement with the VB spectrum from the bulk material [5]. The difference between the spectra from thin film and bulk materials is a change of
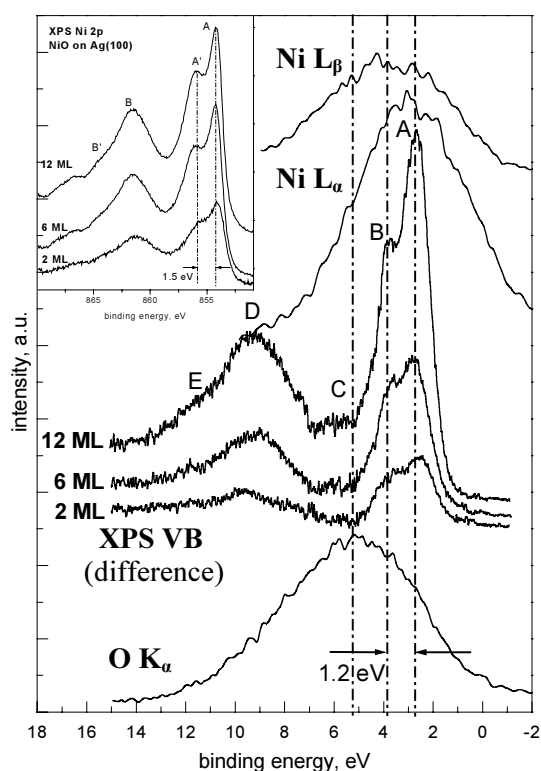
Fig. 3. *Comparison of Ni L_α -, Ni L_β -, O K_α – emission, XPS VB of NiO (6ML) on Ag(100) and XPS VB of NiO (2ML and 12ML) on Ag(100). The inset shows Ni 2p XPS of NiO (2ML, 6ML and 12ML) on Ag(100).*

the intensity ratio between bands A and B. It is clearly seen that band B becomes more intensive with respect to band A as the thickness decreases. In the case of Ni 2p XPS (see Fig. 3, inset) we also observed the relative intensity change of band A´ with respect to band A during change of the NiO thickness, which is influenced by a competition between transitions of screening electrons coming from the surrounding ligands (O-ligands inside of one NiO_6 cluster) and electrons coming from ligands around a neighboring Ni^{2+}-ion (O-ligands inside of a neighboring NiO_6 cluster). This experimental fact was confirmed by calculations on clusters,

involving more than one Ni^{2+}-ion (for taking into account these so called nonlocal screening effects one has to study the cluster Ni_7O_{36}) [6]. In the case of VB XPS we have a mixing of the nonlocal screening effects and effects of the $d(e_g)$-$d(t_{2g})$ splitting of the valence band caused by symmetry reduction at the surface sites which play a significant role in a thin film.

In conclusion, the epitaxially grown and well ordered NiO films exhibit thickness dependent spectra of X-ray fluorescence and photoemission. For the final explanation more detailed high-resolution resonant XF investigations are planned.

Acknowledgements:

References:

[1] N. F. Mott, *Metal Insulator Transitions*, 2nd ed. (Taylor & Francis, London, 1990).

[2] D. Alders et al., *Phys. Rev. B* **57** (1998) 11623.

[3] A. Kotani, S. Shin, *Rev. Mod. Phys.* **73** (2001) 203; J. Nordgren, E. Z. Kurmaev, *J. Electr. Spectr. Rel. Phen. Special Issue* **110-111** (2000).

[4] H. Ishii et al., *J. Phys. Soc. Jap.* **70** (2001) 1813.

[5] F. Parmigiani, L. Sangaletti, *J. Electr. Spectr. Rel. Phen.* **98-99** (1999) 287.

[6] M. A. van Veenendal, G. A. Sawatzky, *Phys. Rev. Lett.* **70** (1993) 2459; D. Alders et al., *Phys. Rev. B* **54** (1996) 7716.

Chemical bonding effects in iron compounds studied by X-ray absorption.

A.S. Vinogradov [a], A.B. Preobrajenski [a,b], S.A. Krasnikov [a,b], A. Knop-Gericke [c],
O. Timpe [c], P.R. Bressler [d], T. Chassé [b], R. Szargan [b], R. Schlögl [c]

[a] *V.A. Fock Institute of Physics, St. Petersburg State University, 198504 St. Petersburg, Russia;*
[b] *W.-Ostwald-Institut für Physikalische und Theoretische Chemie, Universität Leipzig, Linnéstr. 2,D-04103Leipzig, Germany;* [c] *Fritz-Haber-Institut der Max-Planck-Gesellschaft Faradayweg 4-6,D-14195 Berlin, Germany;* [d] *BESSY GmbH, A.-Einstein-Straße 15, D-12489 Berlin, Germany*

The 2p absorption spectra of metal atoms in the 3rd-period transition metal (TM) compounds is the best probe of the unoccupied 3d electronic configurations, which determine many technologically important properties of these compounds. A strong correlation between the localized 3d electrons makes a single-particle description of these spectra unrealistic. It is a standard practice to assume that the metal 2p absorption and the electronic structure of the first-row TM compounds can be understood in the framework of an atomic-like multiplet approach. This implies in particular that the 2p excitations of Fe(II) and Fe(III) atoms in compounds are considered as *intra-atomic* excitations of the ions Fe^{2+} ([Ar]$3d^6$ ground-state configuration) and Fe^{3+} ([Ar]$3d^5$), respectively. Thus, these excitations are widely described in various ionic multiplet approaches [1] neglecting effects of chemical bonding completely or taking them into account in part and implicitly. Obviously such a treatment of the 2p absorption spectra restricts the applicability of X-ray absorption spectroscopy for obtaining information on the chemical bonding effects in the electronic structure of the 3d TM compounds. It should be also noted that *no systematic experimental studies of these effects in 2p absorption spectra of iron compounds are available up to now* and, as a consequence, the role of chemical bonding is still not clearly understood.

In our previous work [2] we have observed a ligand effect on the Fe $2p_{3/2}$ excitations in iron compounds as the low- or high-energy shift of their center of gravity and associated it with the 4s or 3d electron transfer between the iron and ligand atoms. Here we continue to discuss the near-edge structure in the high-resolution Fe $2p_{3/2}$ absorption spectra of various iron compounds in order to reveal and to understand those features in the spectral profiles, which originate from chemical bonding effects. For this purpose, we have measured and uniformly calibrated the absorption spectra in some TM compounds with a higher energy resolution and with a much better counting statistics than the spectra reported earlier. For the most ionic iron compounds, the fluorides, the F 1s absorption spectra were measured for the first time.

The X-ray absorption measurements on iron compounds were performed at the VLS-PGM beam-line at BESSY II in the total electron yield detection mode. All the samples were in powder form and were prepared by rubbing of the powder in a scratched copper plate. The estimated photon-energy resolution at the Fe $2p_{3/2}$ edge (~710 eV) was better than 0.2 eV. Absorption structures in the vicinity of the F 1s threshold (~690 eV) were taken only with energy resolution of ~0.4 eV because of a lower intensity for the fluorine spectra. The spectra were normalized monitoring the incident photon flux by means of the I_0-signal of a gold mesh. The photon energy was calibrated using the known position of the first resonance at 683.9 eV in the F 1s absorption spectrum of K_2TiF_6 [3].
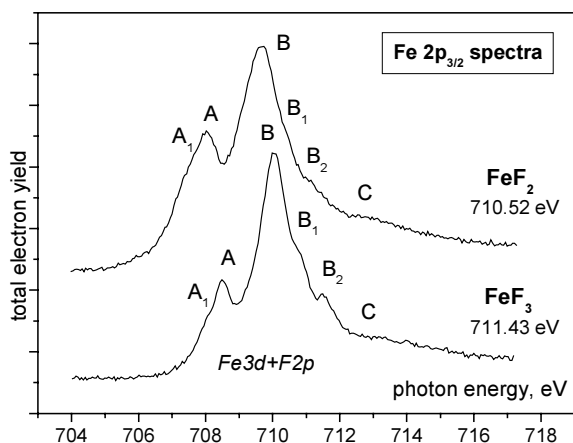
Figure 1 shows the Fe $2p_{3/2}$ absorption spectra of the iron fluorides, FeF_2 and FeF_3. These spectra exhibit very similar spectral profiles with a small low-energy shift (~0.3 eV for the main absorption band B; ~0.9 eV for the center of gravity), with somewhat different relative
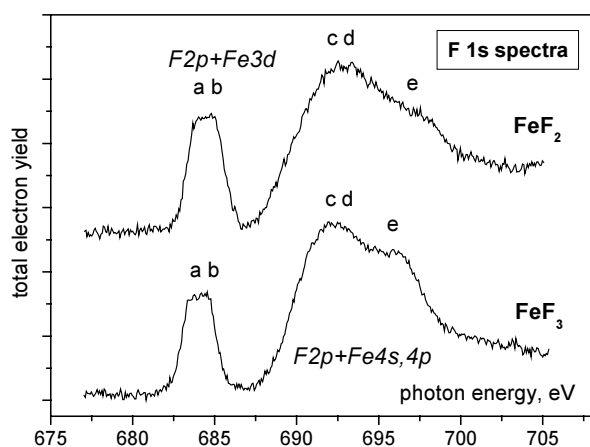

Fig. 1. *Fe $2p_{3/2}$ absorption spectra of iron fluorides.*

Fig. 2. *F 1s absorption spectra of iron fluorides.*

intensities for absorption structures and with their marked broadening in going from FeF$_3$ to FeF$_2$. The observed similarity of these spectra is very surprising because the strongly ionic iron compounds FeF$_2$ and FeF$_3$ have to show very different 2p absorption spectra in the ionic multiplet approach: the 2p excitations for the Fe(II) and Fe(III) atoms with the most well defined [Ar]3d^6 and [Ar]3d^5 ground-state electronic configurations and with similar octahedral fluorine surroundings [4] result in different final-state electronic configurations 2p^{5}3d^7 and 2p^{5}3d^6 [5], respectively. It is interesting that the F 1s absorption spectra of the iron fluorides are also very similar in absorption structures and their energy positions and are broadened in going from the Fe(III) fluoride to the Fe(II) one (Fig. 2). The low-energy band consists of two poorly resolved subbands **a** and **b** that are clearly separated in the spectra measured with a higher resolution during commissioning at the Russian-German beam-line [6]. Clearly the observed similarity of the iron (fluorine) absorption spectra reflects *a very similar spectrum of unfilled electronic states for both fluorides*, which can be easily understood within the framework of a *quasimolecular* (FeF$_6$) approach to the electronic structure of FeF$_2$ and FeF$_3$. The important point of this approach is the inclusion of the covalent mixing between the iron and fluorine valence electronic states. It should be emphasized that the very occurrence of the F 1s spectra, even though of low intensity, is already indicative of a covalent mixing between the Fe 3d and F 2p electronic states because in a purely ionic model all the F 2p electronic states are filled, and no dipole allowed F 1s→2p transitions are available. Within the framework of our quasimolecular approach, the similarity of the absorption spectra for FeF$_2$ and FeF$_3$ is explained by the same order of unfilled *molecular orbitals* (MOs) for the FeF$_6$ quasimolecule. The differences in spectra can be associated with the somewhat different energy position and atomic character of these MOs due to the considerable increase and distortion of the F$_6$ octahedron in FeF$_2$ (interatomic distances d$_{Fe-F}$ are 1.92 Å for FeF$_3$ and 1.99 Å (2 bonds) and 2.12 Å (4 bonds) for FeF$_2$ [4]), as well as due to the different coupling between the octahedra in FeF$_2$ and FeF$_3$.

Based on the above discussion, we consider further the Fe 2p$_{3/2}$ absorption spectra for iron compounds with the metal atom coordinated octahedrally to oxygen atoms in comparison with the spectrum of FeF$_3$ (Fig.3). The observed structural similarity of the spectra for α-Fe$_2$O$_3$ and FeF$_3$ is evident within the framework of the quasimolecular approach: the FeO$_6$ and FeF$_6$ quasimolecules contain the ligand atoms, oxygen and fluorine, that are closely related to each other in chemical properties and differ little in size (d$_{Fe-F}$ =1.92 Å ; mean d$_{Fe-O}$=2.03 Å) and, therefore, they have the same order of unfilled MOs. A small structure smearing for the spectrum of α-Fe$_2$O$_3$ results from the trigonal distortion of the FeO$_6$ octahedron. In going from α-Fe$_2$O$_3$ (d$_{Fe-O}$=2.03 Å) to Fe(acac)$_3$ (d$_{Fe-O}$=1.99 Å), the absorption spectrum varies only slightly. This means that an acetylacetonate anion is linked to the iron atom like two bridge oxygen atoms in the oxide and there is no marked π-interaction between the metal 3d and ligand valence electronic states which we have observed for

Fig. 3. *Fe 2p$_{3/2}$ absorption spectra for compounds of iron coordinated octahedrally to oxygen atoms as compared to the spectrum of FeF$_3$.*

hexacyano complexes of 3d atoms [2]. In our opinion, this additional interaction is responsible for drastic changes in the absorption spectrum in going from the oxides to $FeCO_3$, FeS and FeS_2 (Fig. 4):

these findings probably reflect changes in the order of unfilled MOs due to the hybridization between Fe 3d atomic orbitals (AOs) and low-lying empty π^*-MO of the anion CO_3^{2-} ($FeCO_3$) and between Fe 3d and S 3d AOs (FeS, FeS_2).

One more evidence of the important role of the covalent mixing in the iron compounds we obtain from a direct comparison between the high-resolution metal $2p_{3/2}$ absorption spectra for $[Mn(CN)_6]^{4-}$ and $[Fe(CN)_6]^{3-}$ that have the same ground-state electronic configuration, $...3d2t_{2g}^5$ (Fig.5). These spectra aligned in energy at the position of the peak t (MO $2t_{2g}$ [2]) should look the same in a rigorous ionic multiplet approach. The spectra compared show the similar absorption structures but with very different intensities because of changes in the covalent mixing in going from the manganese complex to the iron one.

Fig. 4. *Comparison between Fe $2p_{3/2}$ absorption spectra of iron compounds with the metal atom coordinated octahedrally to oxygen and sulphur atoms.*
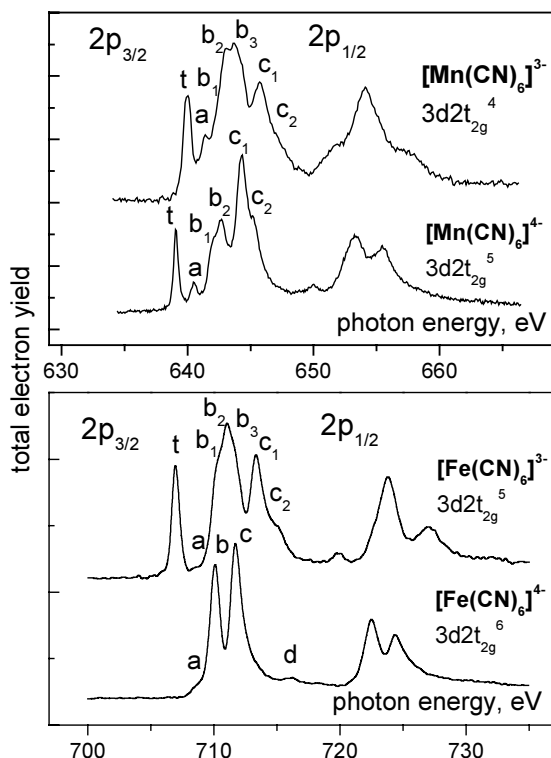
Fig. 5. *Metal $2p_{3/2}$ absorption spectra for hexacyano complexes of iron and manganese with the same ground-state electronic configuration $...3d2t_{2g}^5$.*

References:

[1] T. Yamaguchi, S. Shibuya, S. Suga, S. Shin, *J. Phys. C: Solid State Phys.* **15** *(1982) 2641;* B.T. Thole, R.D. Cowan, G.A. Sawatzky, J. Fink, J.C. Fuggle, *Phys. Rev. B* **31** *(1985) 6856;* F.M.F. de Groot, J.C. Fuggle, B.T. Thole, G.A. Sawatzky, *Phys. Rev. B* **41** *(1990) 928;* **42** *(1990) 5459;* G. van der Laan, I.W. Kirkman, *J. Phys.: Condens. Matter* **4** *(1992) 4189.*

[2] A.S. Vinogradov, A.B. Preobrajenski, S.A. Krasnikov, A. Knop-Gericke, P.R. Bressler, T. Chassé, R. Szargan, R. Schlögl, *BESSY Annual Report 2000, p.160; Surf. Rev. Lett. 2002, in print.*

[3] A.S. Vinogradov, A.Yu. Dukhnyakov, V.M. Ipatov, et al., *Sov. Phys. Solid State* **24** *(1982) 803.*

[4] A.F. Wells, *Structural Inorganic Chemistry, 5th Edition (Oxford University Press, Oxford, 1986).*

[5] S. Gota, F. Jollet, J.P. Crocombette, Z.Y. Wu, M. Pollak, N. Thromat, M. Gautier-Soyer, C.R. Natoli, *J. Phys. IV France* **7** *(1997) C2-507.*

[6] A.S. Vinogradov, S.I. Fedoseenko, S.L. Molodtsov, D. Vyalikh, V.K. Adamchuk, C. Laubschat, G. Kaindl, *BESSY Annual Report 2001.*

Strong anisotropy of projected Cr 3d and O 2p moments of epitaxial grown CrO$_2$-films

E. Goering, A. Bayer, S. Gold and G. Schütz

MPI für Metallforschung, Heisenbergstrasse 1, 70569 Stuttgart - Germany

Abstract

Soft X-ray magnetic circular dichroism (XMCD) spectra along different crystallographic projections of CrO$_2$ have been investigated. Strong anisotropic magnetic behavior and orbital Cr 3d contributions are observed and attributed to t$_{2g}$-majority states near the Fermi level. In addition, spin sum rules have been applied even for the light transition metal Chromium by so called moment analysis, which also exhibits strong anisotropic behavior in projected spin contributions attributed to a huge magnetic dipole term T$_z$. A reduced projected isotropic Cr 3d spin moment has been interpreted in terms of hybridization with oxygen. Oxygen K edge absorption reflects O 2p orbital moment projections and shows similar behavior compared to Cr 3d orbital moments. A band structure related description of the 3d magnetism seems to be more appropriate compared to a localized ionic picture of CrO$_2$.

Introduction

In the last few years CrO$_2$ has attracted revived interest due to its remarkable high spin polarization at the Fermi energy, theoretically predicted to be 100% [1; 2] and recently verified by superconducting tunneling spectroscopy at T = 18K [3] and spin-polarized photoemission spectroscopy at T = 293K [4]. The reason for this revival is mainly related to promising future technological applications on the basis of CrO$_2$-electrodes such as magnetic tunneling and spin injection devices. The oxygen mediated coupling and its half metallic nature are a challenging problem for theoretical investigations, originated by the presence of oxygen-hybridization, double exchange, self doping, and correlation effects [1]. The quantitative influence of orbital moments [5], inner 3d shell spin-orbit-coupling, and the T$_z$-term [6] to magneto-crystalline-anisotropy (MCA) is still unknown but very important and of fundamental interest towards satisfying understanding of the magnetic properties of CrO$_2$.

Experimental and Discussion

CrO$_2$ crystallizes in a rutile structure with two equivalent a-axes (0.4421nm) and a shorter c-axis (0.2916nm). CrO$_2$ -films investigated have been epitaxially grown on isostructural TiO$_2$ -substrate by a recent chemical vapor deposition technique (CVD) with a sample thickness of 100nm. CrO$_2$-films are (100) orientated and have a Curie-temperature of approximately 385K. All spectra were recorded in total electron yield mode at the bending-magnet-beamline PM I at BESSY II with an energy resolution E/ΔE = 2000 in an applied magnetic field of ±5kOe (flipped at each data point). The degree of circular polarization was about 95%. All spectra have been measured at 80K, carefully background subtracted and edge normalized using the same background and normalization factor for parallel and antiparallel orientation of the photon beam $\vec{k}$ -vector with respect to the sample magnetization. The experimental geometry is schematically shown in the inset of fig. 1a. XMCD-spectra were taken with fixed grazing incidence (ϕ = 60deg) and the sample was rotated by the azimuthal angle ϑ around the
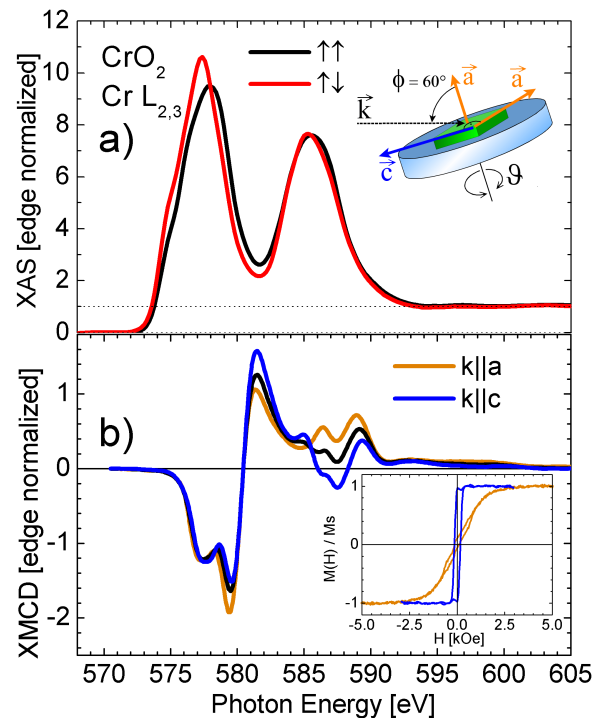

FIG. 1: a) CrO$_2$ XAS for parallel and antiparallel alignment of the photon beam to the sample magnetization; inset shows the experimental geometry of the crystallographic axes of the sample relative to the incoming photon beam; b) XMCD signal at 5kOe applied magnetic field for different azimuthal angles ϑ and fixed ϕ = 60deg for enhanced a- (orange line), c- (blue line) and intermediate (black line) axis projections; the inset shows *in situ* Cr 3d related XMCD magnetization loops.

surface normal probing a- and c- axis projected magnetism.

Figure 1a shows normalized XAS spectra for ϑ = 7deg and fig. 1b the corresponding XMCD signals for nearly a-axis (7deg), c-axis (86deg) and intermediate (40deg) projected azimuthal sample orientations. Compared to other 3d metal XMCD spectra, very strong and pronounced changes are present, which culminates in a directly observable and unexpected change of sign at

587eV. This negative XMCD intensity suggests a strong increase of the projected orbital moment for increased c-axis projections. In contrast only very small changes in the averaged Cr $L_{2,3}$ XAS are present and therefore not shown. We have measured at various different angles ϑ partially omitted in fig. 1b for enhanced clarity, but considered in the following data analysis. In addition *in situ* element specific magnetization curves [7] have been measured at each ϑ, shown in the inset of fig. 1b for a-axis and c-axis enhanced projections. From these hysteresis loops, verified by *ex situ* SQUID measurements, we have extracted a strong uniaxial anisotropy energy of $K_1=(5.8\pm0.5)\ 10^4\ J/m^3$. This clearly exhibits a magnetic easy axis along the crystallographic c-axis, which is consistent to previously published thin film data, which also shows easy c-axis behavior for thick and unstrained CrO_2 thin films [8].
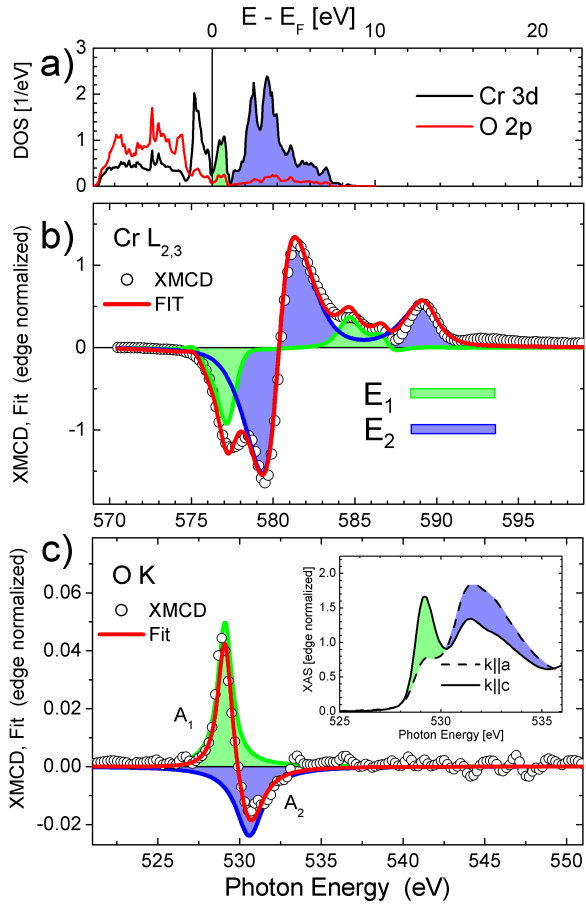
FIG. 2: a) Cr 3d (black line) and O 2p (red line) DOS from ref. [1]; The narrow green shaded area is related to t_{2g}-majority and the blue shaded area to e_g-majority ($t_{2g}e_g$) -minority states; b) Cr $L_{2,3}$ –XMCD (circles) and moment analysis fit result (red line) corresponding to two different energy contributions (green and blue); c) O K-edge XMCD (circles) and Lorentzian fit result (red line) corresponding to two different energy contributions (green and blue); Inset shows ϑ dependence of the O K edge XAS.

For a detailed analysis of experimental data we have reproduced a recent LSDA+U calculation performed by Korotin *et al.* [1]. Figure 2a shows the DOS for Cr 3d and O 2p states. Two general features are directly ob-

servable, a narrow (1eV wide) full spin polarized unoccupied band feature at 0.5eV above the Fermi level (green) and a broader feature 3eV above (blue). For interpretation of the angular dependent XMCD spectra we take the DOS into account as a simple superposition of only two sets of ground state moments which are separated by 3.5eV and broadened by 1.4eV and 2.7eV, respectively. Conventional sum rule analysis [9; 10] can unambiguously yield to the total projected 3d orbital moment but not to the Cr 3d spin moment, which is related to the small 2p spin-orbit splitting ($E_{SO} = 9.3eV$). Therefore, XMCD data has been fitted by a superposition of so called ground-state-moments $<w^{xyz}>$ introduced by van der Laan [11]. Those moments represent several *one particle* contributions to the 2p 3d XMCD signal, for example the moments $<w^{000}> = n_h$, $<w^{101}> = L_z/2$, $<w^{011}> = 2S_z$, $<w^{110}> = -LS$, and $<w^{211}> = 7\ T_z$, corresponding to the number of holes in the 3d-band, orbital moment, spin moment, spin-orbit-coupling, and the magnetic dipole term, respectively. This method has been previously proven for iron-garnets [12]. By application of this fitting procedure the spectral overlap of L_3 and L_2 edges could be separated. Figure 2b shows an intermediate spectrum at $\vartheta = 40deg$ (open circles) and a moment analysis fit (red line) using a sum over two different sets at energies $E_1 = 577.0eV$ (green), $E_2 = 580.5eV$ (blue) corresponding to the DOS in fig. 2a.

All spectral features could be reproduced nearly perfectly by this fitting procedure. Associated fit results are presented in fig. 3a. Data points in the polar plot were mirrored at the horizontal and vertical axes to complete a full polar diagram. Figure 3a shows the absolute angular dependency of the total projected spin moment (black diamonds) and extracted projected orbital contributions for the two energy separated regions (green circles and blue squares). The Cr 3d related spin part exhibits a pronounced angular dependency, which we attribute to a very strong magnetic dipole term T_z corresponding to a quadrupolar spin distribution at the Cr site [6; 13]. This observed T_z related "spin"-anisotropy is extremely high compared to previously published 3d transition metal results. An isotropic Cr 3d spin moment of $1.20\mu_B$ could be extracted and assuming a simplified hybridization picture an effective correction factor of 1.53 yield to a total XMCD related spin moment of $(1.9\pm 0.1)\mu_B$, quite near to the expected Cr $3d^2$ configuration high spin and experimental values (for details [14; 15]). This is strong evidence that hybridization is a dominating effect of the XMCD related spin reduction, and not the small $L_{3,2}$ - edge separation with related mixing effects.

Fitted orbital projections L_1 and L_2 (fig.3a) exhibit increased absolute orbital projections along the magnetic easy axis, while the L_1 orbital moment has positive and the L_2 moment a negative sign [14; 15], and the total magnetic orbital moment is negative and consistent to Hund's rules. The total change of the orbital moment by rotation of 90deg is $\Delta L = (0.065\pm 0.005)\mu_B$, but the observed change of the narrow (green) part of the unoccupied DOS near the Fermi level dominates the angular dependency (fig. 3a green circles). Considering Bruno's model of the MCA [5], which is a second order perturba-

tion approach for a filled majority spin system, one would expect an enhanced absolute orbital projection along the easy axis, which is not in agreement with our experimental observation. Van der Laan has recently modified the Bruno-model [6] considering orbital contributions of majority spin-up and minority spin-down electrons separately. In the case of CrO_2 the minority band is empty and the orbital part of the minority band vanishes. Thus the orbital part to the MCA reduces to $\delta E = +\frac{1}{4} \cdot S \cdot \langle L^{\downarrow} \rangle$, which has opposite sign compared to Bruno's model. Therefore, the total orbital moment should favors a-a-plane easy axis behavior. We believe that the T_z term dominates the anisotropy of CrO_2 which will be discussed in a forthcoming paper [14].

the O K edge areas with the fitted Cr 3d orbital projections, the same behavior could be observed. Considering that O 1s XMCD spectroscopy reflects O 2p orbital contributions, a clear one-by-one correspondence of O 2p and Cr 3d orbital moments is present. In this context delocalized electrons are responsible for the magnetism in CrO_2. Delocalized wavefunctions with O 2p and Cr 3d contributions are eigenfunctions of the total Hamiltonian and have the same set of eigenvalues, reflecting the spin-orbit-coupling induced energy splitting, which is the proposed origin of residual non quenched orbital moments [5; 6].

Summary

An unexpected strong anisotropic behavior of the Cr $L_{2,3}$ XMCD spectra has been observed. Moment analysis in combination with band structure calculated energy positions and line widths results in a quantitative and qualitative description of XMCD spectra. Due to this analysis a consistent description of the absolute spin value in terms of hybridization has been discussed. The application of sum rules in conjunction with moment analysis gives reasonable absolute values for light transition metal ions. The intrinsic magnetic easy axis behavior along the rutile c-axis could be quantitatively associated to orbital properties of the majority Cr t_{2g} conduction band. The angular dependency of O 2p orbital projections is quantitatively comparable to Cr 3d orbital projections. This is strong evidence that recent band-structure calculations are an appropriate description of CrO_2 ground state properties.

FIG. 3: Azimuthal angular dependencies of the fitted a) XMCD related effective spin moments **S** (black diamond) and the two antiparallel orbital Cr 3d projections $\mathbf{L_1}$ (green circle) and $\mathbf{L_2}$ (blue square) and b) the oxygen XMCD areas A_1 (green circle) and A_2 (blue square).

In addition we have performed O K-edge absorption spectroscopy (see inset in fig. 2c) and corresponding XMCD spectroscopy (fig. 2c hollow circles) performed in the same way as for the Cr $L_{2,3}$ edges (see above). Only *one* (see ref. [16]) O K edge spectrum at intermediate angle ϑ is shown. Again, a narrow feature near the threshold and a broad feature approximately 3eV above could be observed, which is consistent to the DOS in fig.2a. For a quantitative analysis we have fitted the O K edge XMCD with a narrow Lorentzian line near threshold (fig. 2c green line) and a broader one above (fig. 2c blue line). The corresponding areas A_1 and A_2 as a function of ϑ are shown in fig. 3b. Comparing the changes in

[1] Korotin, M. A. et al.; Phys.Rev.Lett. 80 (1998) 4305
[2] Schwarz, K.; J.Phys.F: Met.Phys. 16 (1986) L211
[3] Soulen, R. J. et al.; Science 282 (1999) 85
[4] Dedkov, Yu. S. et al.; Appl.Phys.Lett. accepted
[5] Bruno, P.; Phys.Rev.B 39 (1989) 865
[6] Van Der Laan, G.; J.Phys.: Condens.Matter 10 (1998) 3229
[7] Goering, E. et al.; J.Appl.Phys. 88 (2000) 5920
[8] Li, X. W. et al.; Appl.Phys.Lett. 75 (1999) 713
[9] Carra, P. et al.; Phys.Rev.Lett. 70 (1993) 694
[10] Thole, B. T. et al.; Phys.Rev.Lett. 68 (1992) 1943
[11] Van Der Laan, G.; Phys.Rev.B 55 (1997) 8086
[12] Goering, E. et al.; J.Sync.Rad. 8 (2001) 422
[13] Stöhr, J. et al.; Phys.Rev.Lett. 75 (1995) 3748
[14] Goering, E. et al.; Phys.Rev.Lett. submitted
[15] Goering, E. et al.; Appl. Phys. A accepted
[16] Goering, E. et al.; Europhys. Lett. submitted

Structure and Interface Composition of Cobalt on the As-rich GaAs(001) c(4x4) surface

Kathy Lüdge[1], Patrick Vogt[1], Brian D. Schultz[3], Oliver Rader[2], Andreas Wange[1], Walter Braun[2], Chris J. Palmstrøm[3], Wolfgang Richter[1] and Norbert Esser[1]

[1] Technische Universität Berlin, Institut für Festkörperphysik, PN 6-1, Hardenbergstrasse 36, 10623 Berlin,
[2] BESSY GmbH, Albert-Einstein-Straße 15, 12489 Berlin,
[3] University of Minnesota, 151 Amundson Hall, 421 Washington Avenue, Minneapolis, MN 55455, USA

The initial growth of cobalt on the GaAs(001) c(4x4) surface has been studied using soft X-ray photoemission spectroscopy (SXPS), scanning tunneling microscopy (STM) and low energy electron diffraction (LEED). The structure and chemical reactivity of the Co layer are studied as a function of the substrate temperature and Co coverage.

Spin randomized scattering at ferromagnetic metal/semiconductor interfaces is believed to be the limiting factor in realizing spin polarized injection needed for spintronic devices. Especially for novel spin sensitive devices that use the controlled injection of spin polarized carriers into a semiconductor. Detailed knowledge of the interface structure and chemistry is required in order to determine the origin of the spin scattering. The growth is complicated by significant interfacial reactions between the Co overlayer and the GaAs substrate. The primary objective of this work is to systematically clarify the impact of growth temperature on the structural and chemical properties of the interface.

Soft X-ray photoemission spectroscopy (SXPS) measurements were performed at the U125/1 PGM beamline at the BESSY II synchrotron with a total instrumental resolution (beamline plus analyzer) of 90meV. For these experiments, molecular beam epitaxy (MBE) grown GaAs samples, which were capped by an amorphous As layer
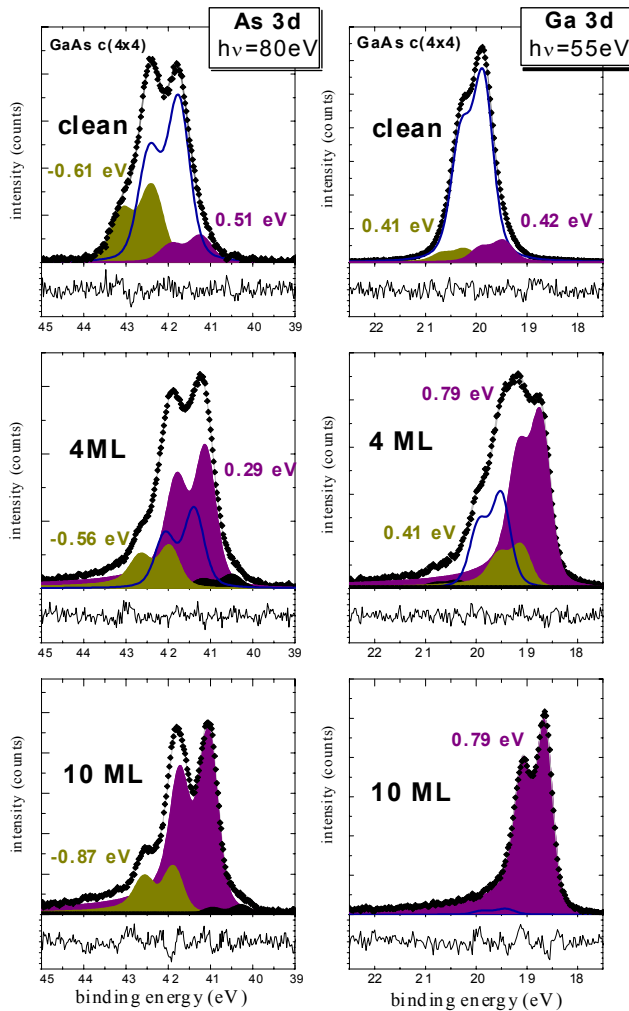
Fig. 1: *As3d and Ga3d core level spectra for growth of Co on GaAs(001) c(4x4) at 150°C; solid lines are the bulk components and filled curves represent the surface/interface components. The bottom lines represent the residuum.*

directly after the buffer layer growth, were used. In the UHV analysis vessel the amorphous protection layer was thermally desorbed at 350°C to yield a GaAs(001) c(4x4) As-rich surface, and Co was grown under UHV conditions directly on these surface. For additional studies, GaAs(001) surfaces were prepared and analyzed *in situ* in an UHV interconnected MBE growth and analysis system, where STM, LEED and XPS with an Al-Kα X-ray source at an emission angle of 55° were used. XPS yields a total resolution of 700meV.

XPS and SXPS studies were performed after the Co growth to determine the chemical composition of the deposited layers following the deposition of Co on GaAs(001) c(4x4) surfaces at a substrate temperature of 150°C. The As3d and Ga3d core level spectra, taken at photon energies of 80eV and 55eV at BESSY II, respectively, are plotted in Fig.1. The spectra were analyzed by numerical deconvolution into pairs of spin orbit-split doublets.

With deposition of the first monolayer the surface related components vanish and both the Ga and the As core level spectra show new reacted components that cause the line shapes of the spectra to change with increasing Co thickness. The Ga3d core level spectra contain two new components shifted to lower binding energy, whereas there are three reacted components found in the As3d emission line. The predominant reacted component (shown as filled purple curves) of As3d and Ga3d are shifted by -0.4eV and -0.8eV, respectively (with respect to the binding energy of the bulk component). They are attributed to CoAs and CoGa compounds, after comparison of the binding energies with core level spectra taken on thick CoAs and
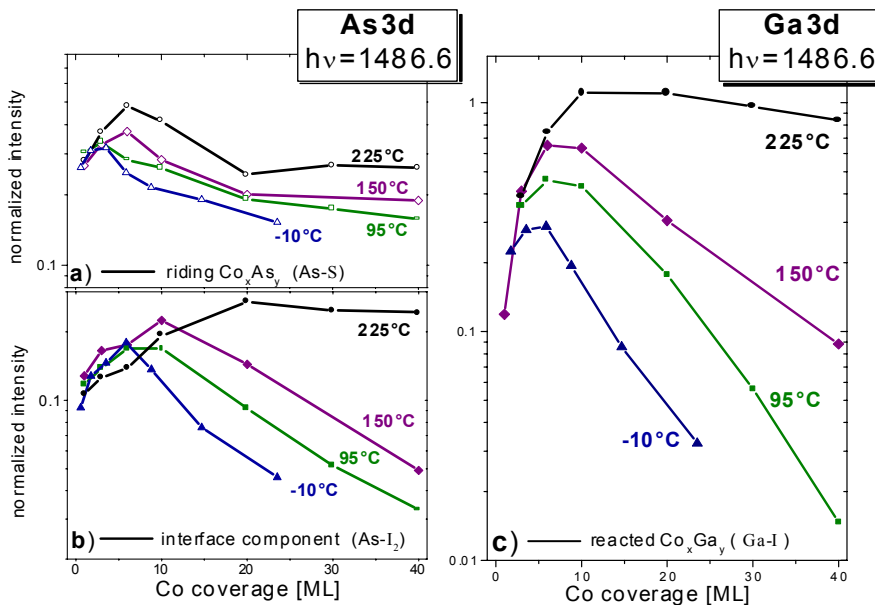
Fig. 2: *Coverage and temperature dependence of the normalised XPS-intensity of the reacted components in the As3d and Ga3d core level spectra.*

CoGa. The components displayed as filled yellow curves in Fig.1 are referred to as elemental As and a thin elemental Ga layer, based on the Pauling electronegativity differences of Co, Ga, and As.

To quantify the thickness and the composition of the interface layer that forms during deposition, attenuation curves of the XPS intensities in dependence of the Co coverage were measured. The components obtained from the deconvolution of the SXPS spectra were used to deconvolute the lower resolution spectra obtained from the *in situ* XPS. The intensity of the reacted Ga component (sum of both reacted interface components, Fig.2c) initially increases

before reaching a maximum and then decreases as the Co coverage is increased. These changes are due to the formation of a reacted layer at the interface, whereby the thickness of the layer increases as the growth temperature is increased. Furthermore, the attenuation of the Ga component becomes slower as the growth temperature is increased at Co coverages exceeding 10ML. This behavior requires there to be diffusion of Co, As and Ga across the reacted interface. The intensity of the dominating reacted As component (Fig.2a) is not strongly attenuated for any of the growth temperatures indicating that a fixed amount of As must be segregating to the surface during growth.
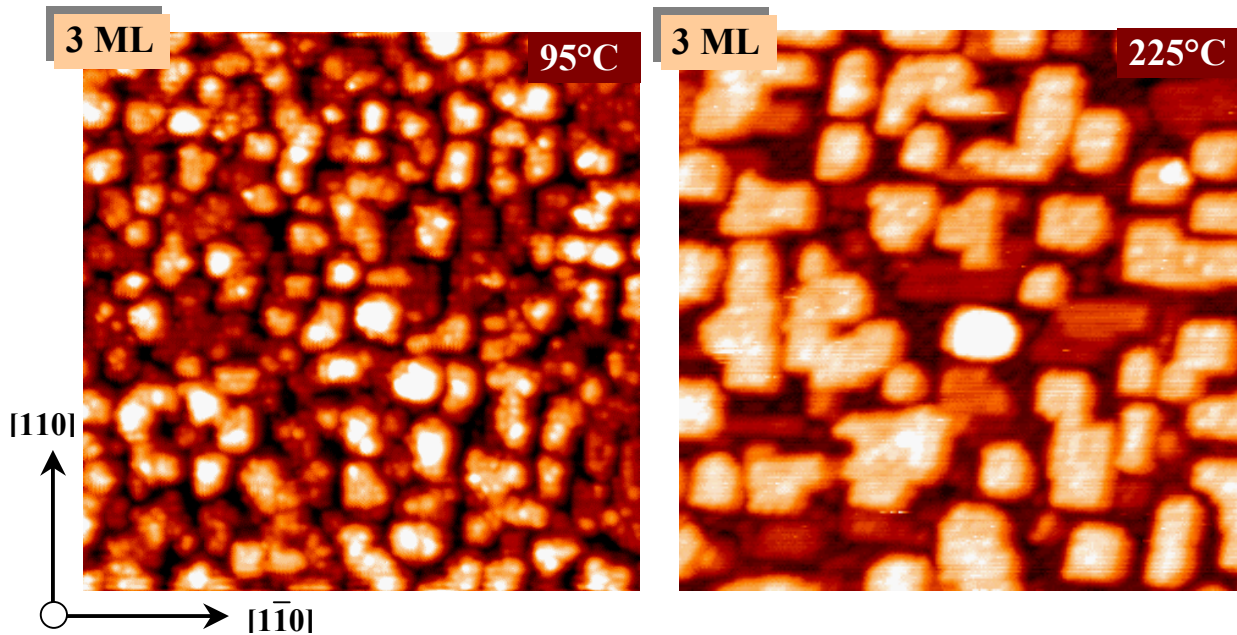
Fig. 3 *Filled state STM image of 3 ML of Co on GaAs(001) c(4x4) deposited at 95°C and 225°C, image size 45nm x45nm*

Fig.3 shows filled state STM images taken after deposition of 3ML of Co at 95°C and 225°C. It can be seen, that the growth temperature has a strong impact on the surface morphology, as expected. According to the SXPS/XPS results the rectangular shaped islands may consist of CoGa. The small white structures on top of the islands are interpreted as As that is acting as a surfactant during growth. The surface after 3ML of Co growth at 95°C is nearly completely covered and consists of both, rectangular shaped islands and irregular clusters. Compared to that, the surface after growth at 225°C contains only CoGa like islands that cover less of the GaAs substrate, since there are still As-dimers visible in between the islands. The irregular shaped clusters, that are seen after growth at 95°C are interpreted as the beginning of pure bcc Co growth that already forms on top of the reacted interface layer.

In conclusion we have shown that the Co growth on GaAs(001) c(4x4) is accompanied by interface reactions even at lower deposition temperatures (-10°C). The epitaxial islands, that are observed during growth at higher temperature, are found to consist of CoGa compounds with about one monolayer of riding CoAs on top.

For more detailes see:

[1] K.Lüdge, B.D.Schultz, P.Vogt, M.M.Evans, W.Braun, C.J.Palmstrom, W.Richter and N.Esser, J. Vac. Sci. Tech. B (2002), PCSI 29 proceedings, *to be published*

A NEW 2π SPECTROMETER FOR DOUBLE PHOTO EMISSION PROCESSES FROM SURFACES

[1]M.Hattaß, [1]A.Czasch, [1]S.Schößler, [1]T.Jahnke, [1]Th.Weber, [1]O.Hohn, [2]A.Morozov, [2]F.U.Hillebrecht, [2]J.Kirschner, [1]R.Dörner, [1]H.Schmidt-Böcking

Institut für Kernphysik,Universität Frankfurt, August-Euler-Str.6, 60486 Frankfurt
Max-Planck-Institut für Mikrostrukturphysik, Weinberg 2, 06120 Halle

The double photo emission process is a very important tool to probe electron correlation in atomic systems as the excitation and ejection of more than one electron in a direct photo absorption event is forbidden in a single particle picture. Double photo emission from single atoms and simple molecules (e.g. He and H_2 [1,2,3]) has been studied in great detail in the recent years but only very few experiments on this process have been performed on solid targets [4,5]. Nevertheless solids are supposed to be very interesting targets as many effects in solid state physics rely on electron correlation e.g. superconductivity.

The experimental problem in investigating the ejection of more than one electron is to detect the electrons in coincidence with a reasonable event rate. The event rate depends on the acceptance angle Ω of the spectrometer hence the event rate for a N-particle coincidence scales with Ω^N. Ω is very small in traditional electron spectrometers (e.g. spherical analyzers). Consequently the expected true coincidence rate will be extremely low.
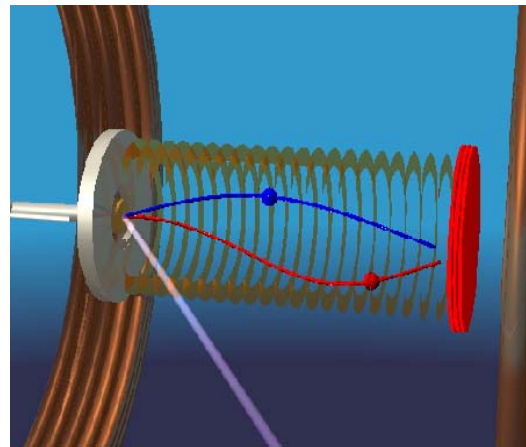
Figure 1 Schematic view of the time of flight spectrometer

To avoid this problem we have used a spectrometer of the "COLTRIMS"-type known from gas target studies (e.g. [6]). This spectrometer is based on the time-of-flight technique in combination with a position sensitive detector. The electrons are extracted from the target region by a weak electric field (~3 V/cm) and guided onto a position sensitive detector by a magnetic field (~10 Gauß). By measuring the time-of-flight and the electron impact position on the detector we can reconstruct the initial momentum. The position read out of the detector is done by a hexagonal delay line anode which is capable to accept multiple hits with an almost vanishing dead time. To allow for a time-of-flight measurement the synchrotron has to be run in Single Bunch mode. As no pre selection of angles and energies is done by this setup we are able to detect all possible combinations of emitted electrons at once. Therefore this setup is able to map the
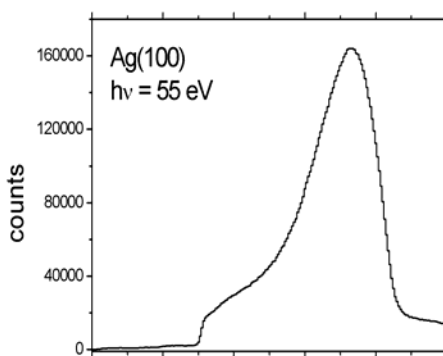

Figure 2 Time of flight spectrum, integrated over all emission angles

complete two electron final state (except the spin) for the double photo emission process at surfaces.

Figure 1 shows an image of the setup. The sample can be inserted in the spectrometer through the hole in the end plate where it is being intersected with the photon beam under an angle of 60° to the surface normal. The copper ring electrodes generate the homogeneous electric field to extract the electrons while the magnetic field is produced by a pair of Helmholtz coils outside the vacuum chamber. An energy resolution of $\sim\Delta E/E = 1/15$ is currently achieved with this setup.

First photoemission measurements with this setup have been performed during the Single Bunch mode at BESSY II at the U49/2 PGM-1 beamline. The target was a clean Ag(100) surface. The photon energy has been varied in the range 40 eV to 55 eV. An angle integrated time-of-flight spectrum for 55 eV photons is shown in figure 2. Due to the maximum electron energy, defined by the incoming photon, the spectrum shows a minimum flight time for electrons emitted along the surface normal. Furthermore the electric field extracts also 0 eV electrons onto the detector which defines a maximum flight time of 110 ns.
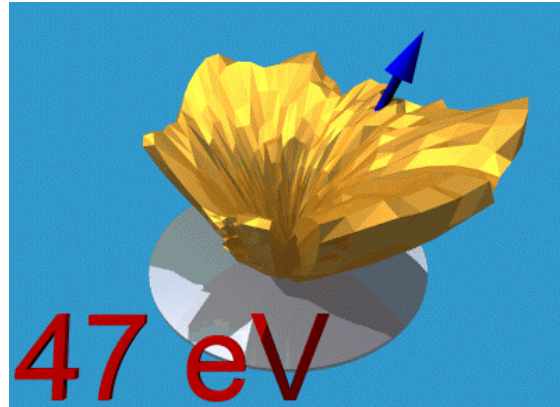
Figure 3 Angular distribution of photo electrons from a Ag(100) surface. Blue : polarization

An angular distribution of photo electrons emitted from the Ag 4d-band obtained with our setup is shown in figure 3. The electron energy is 47 eV and the photon energy 55 ev. The blue arrow denotes the direction of the polarization vector which is under an angle of 30° to the surface normal.

To find true coincidentally emitted electron pairs the angle integrated "single" electron emission rate has been decreased to ~1/1000 of the repetition rate of the synchrotron bunches (1.25 Mhz). This is necessary to make sure that the two detected electrons are released by only *one* photon.
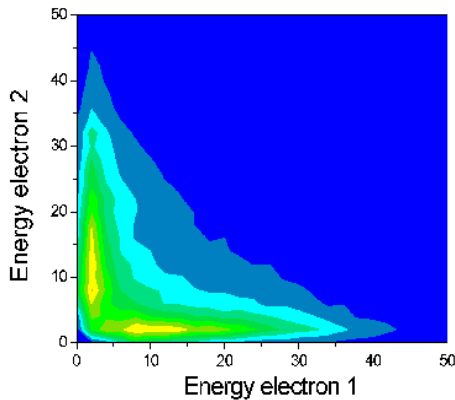
Figure 4 Energy correlation diagram of the photo electron pairs, integrated over all emission angles.

A first sign of electron pairs emitted in coincidence is shown in figure 4. Plotted is the energy of the first electron against the energy of the second for 55eV photons on the Ag(100) target. The spectrum is integrated over all emission angle combinations. Clearly visible is the triangle shape which is due to energy conservation : the photon defines the upper limit for the sum of the electron energies ($E_1 + E_2 < E_{phot}$).

A first angle resolved double photo emission spectrum is shown in figure 5. Plotted is the energy sharing of the two emitted electrons for different angular combinations. Figure 5a is for the case of emission in the cone +/- 40° around the polarization axis while figure 5b show the energy sharing in the case of emission in the cone +/- 40° around the surface normal. The spectra can be understood by considering the scaling factor

$\hat{e} \bullet (k_1 + k_2)$ ($\hat{e}$ polarization vector, $k_{1,2}$ electron momenta) for the double photo emission process at a surface [7]. Consequently equal photo electron energies are suppressed if one electron is emitted in the direction close to the polarization axis (right side of figure 5) while equal energies can occur when the electrons are emitted symmetrically around the polarization axis (left side of figure 5).
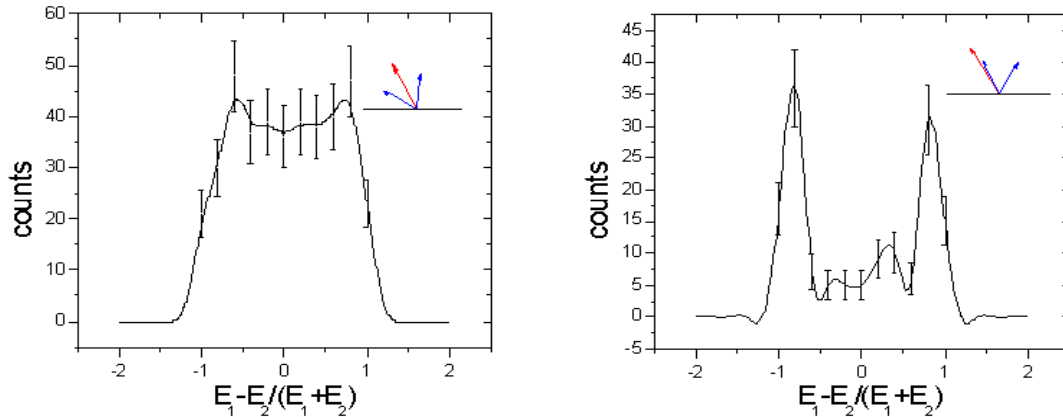
Figure 5 Enegry sharing of the electron pairs for different emission geometries. Left : emission symmetric +/- 40° around the polarization axis, right : symmetric emission +/- 40° around surface normal (one electron es emitted close to the polarization axis). The lines are fit throught the data to guide the eye.

[1] O.Schwarzkopf *et al.* Phys. Rev. Lett. **70**, 3008 (1993)
[2] R.Dörner *et al.* Phys. Rev. Lett. **77**, 1024 (1996)
[3] R.Dörner *et al.* Phys. Rev. Lett. **81**, 5776 (1998)
[4] H.W.Biester *et al.* Phys. Rev. Lett. **59**, 1277 (1987)
[5] R.Herrmann *et al.* Phys.Rev.Lett. **81**, 2148 (1998)
[6] R.Moshammer *et al.* Nucl. Instr. Meth. B **108** 425 (1996)
[7] J.Berakdar, Phys.Rev. B **58**, 9808 (1998)

Electronic structure of Sr_2FeMoO_6: Resonant Inelastic X-ray Scattering (RIXS)

K. Küpper[1], C. Heske[2], O. Fuchs[2], M. Matteucci[3], D. D. Sarma[4],
R. Szargan[5], and M. Neumann[1]

[1]University of Osnabrück, Department of Physics, Barbarastr. 7, D-49069 Osnabrück,
Germany
[2]University of Würzburg, Experimentelle Physik II, Germany
[3]Institute of Condensed Matter, National Research Council c/o Sincrotone Trieste,
Padriciano 99, 1-34012 Trieste, Italy
[4]Solid State and Structural Chemistry Unit, Indian Institute of Science,
Bangalore 560012, India
[5]Wilhelm-Ostwald-Institut, University of Leipzig, Germany

The ordered double perovskites with the general formula $A_2BB'O_6$ are known for several decades [1]. The discovery of the CMR effect in a double perovskite system, Sr_2FeMoO_6 by Kobayashi [2], has lead to a rapidly increasing interest in this class of material rapidly. Sr_2FeMoO_6 shows a strong effect at low magnetic fields and a high ferromagnetic transition temperature ($T_c \approx 420K$) and a half metallic behaviour as predicted on the basis of band structure calculations. Because of these features this material is an outstanding candidate for technological applications.

In this work we investigate the partial density of iron states in this compound. We therefore performed Resonant Inelastic X-ray Scattering (RIXS) at the Fe L-edge. RIXS is known as element selective and surface independent method. The spectra have been taken with the ROSA endstation at beamline U41-PGM at BESSY II.

Figure 1 shows the Fe L-emission spectra taken at indicated excitation energies. L_2 emission can be observed at 707 eV, and L_3 emission is detected around 717 eV. At excitation energies between 707,5 eV to 712,8 eV the resonant excitation of the L_2 emission can be observed. The variation in spectral lineshape is due to an additional contribution from the superimposed elastically-scattered peak. The energy position of this peak is marked by arrows. Note that the elastically-scattered peak exhibits a resonance near the L_2 absorption edge, but is very small at higher excitation energies.

At $E_{exc} = 717,6$ eV and above, we observe L_3 emission as well. At $E_{exc} = 722,0$ eV a strong resonance can be detected. At higher excitation energies, non-resonant X-ray emission takes place. A detailed analysis of the data and a comparison with theoretical results are in progress. In addition measurements at the Mo M-edge and the O K-ede are necessary for a deeper understanding of the electronic structure of this compound.

In contrast to Sr_2FeMoO_6, Sr_2FeWO_6 is an antiferromagnetic insulator [3]. Because of the different transport properties of these two materials, it is predicted that an alloy $Sr_2FeMo_xW_{1-x}O_6$ will show a metal-insulator transition (MIT) as a function of x. Ray *et. al.* found $x_c \approx 0.25$ [4].

It would be interesting to perform RXES measurements on such alloys to get information about the influence of the MIT due to the electronic structure of this class of material.
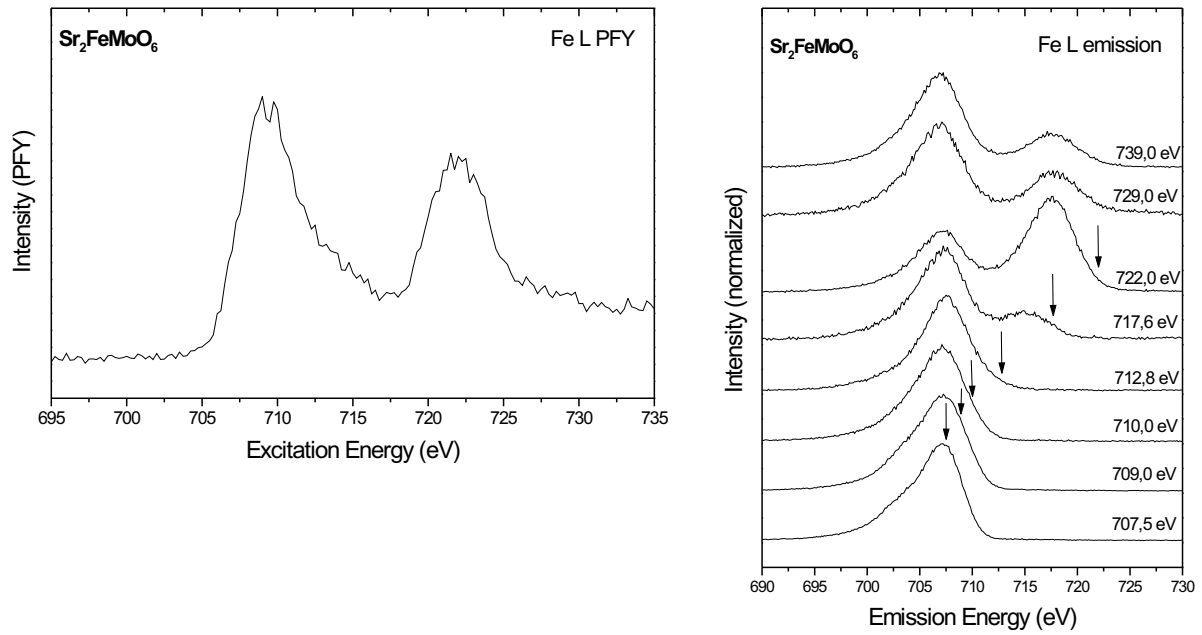
Figure 1: Fe Lα emission spectra of Sr_2FeMoO_6

References

[1] T. Nakagawa, K. Yoshikawa, and S. Nomura, J. Phys. Japan, 1969, **27**, 880

[2] K.-I. Kobayashi, T. Kimura, H. Sawada, K. Tekura, and Y. Tokura, Nature, 1998, **395**, 677

[3] H. Kawanaka, I. Hase, S. Toyama, and Y. Nishihara, Physica B, 2000, **281+282**, 518

[4] S. Ray, A. Kumar, S. Majumdar, E. V. Sampathkumaran, and D. D. Sarma, J. Phys. Cond. Mat., 2001, **13**, 607

XAS Study of Vanadium Oxide Growth on SiO$_2$ and Gold

M. Sánchez-Agudo, L. Soriano, J. Bareño, G.G. Fuentes, P. R. Bressler[a], J.M. Sanz

Departamento de Física Aplicada, Instituto de Materiales Nicolás Cabrera,
Universidad Autónoma de Madrid, Cantoblanco, E-28049 Madrid, Spain.
[a]*BESSY, Albert Einstein Strasse 15, D-12489 Berlin-Adlershof, Germany.*

Oxides like VO$_x$ are of great importance in the industry of catalysis and other technological fields. Therefore, the study of the growth of vanadium oxide on different substrates and their interfaces is an interesting research topic. In this work we present preliminary x-ray absorption (XAS) data on the growth of vanadium oxides (VO$_x$) on two different substrates: SiO$_2$ and Au. VO$_x$ thin films have been simultaneously grown on both substrates by reactive evaporation of 99,8% vanadium in an oxygen atmosphere (2×10^{-6} Torr) at room temperature. The evaporation rate (11.5 Amps) was low enough to allow the deposition of a sub-monolayer, as the early stages of growth, to study possible interfacial effects. For large coverages, the evaporation current and oxygen pressure were increased (15 Amps, 1x10^{-5} Torr) to obtain a larger deposition rate. The SiO$_2$ substrate was grown by dry oxidation of a Si(111) wafer, giving a 800 Å film of amorphous SiO$_2$. A 99.99% purity polycrystalline gold sample was also used as substrate. The V 2p XAS spectra were measured *in situ* as a function of the evaporation time. The spectra were measured at the VLS-PGM beam-line of BESSY in the total electron yield detection mode.

The V 2p XAS spectra represent transitions from [2$p^6$3d^n] initial states to [2$p^5$3d^{n+1}] final states. Vanadium oxides have been studied previously by XAS [1,2]. Fig. 1 shows, as fingerprints, the V 2p XAS spectra of V$_2$O$_3$, VO$_2$ and V$_2$O$_5$ taken from Ref. [1]. The series of spectra show two main bands corresponding to transitions from V 2$p_{3/2}$ and V 2$p_{1/2}$ states. It is seen that the spectral weight throughout the series shifts towards higher photon energies as the formal oxidation state of vanadium increases. Although no absolute energy calibration of the Fermi level is achieved in XAS, this is related to the XPS binding energy chemical shift for these oxides. The spectra show similar shapes and structures although their different relative intensities make possible to distinguish one oxide from the other. On the other hand, it is important to note that the weak peak in between the two main bands in V$_2$O$_3$ is characteristic of this oxide.
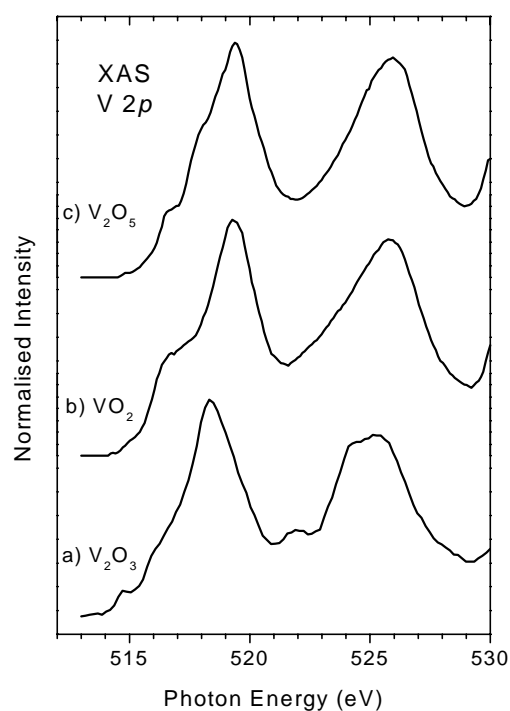

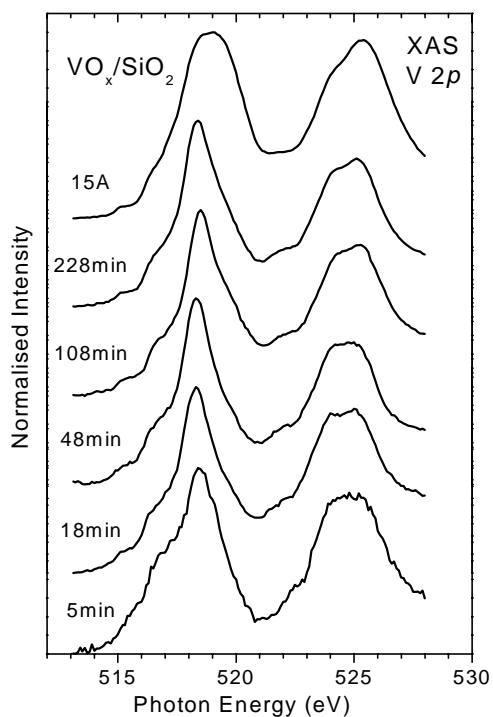Fig.1: Reference V 2p XAS spectra from [1]

Fig. 2: V2*p* XAS spectra of VO$_x$ overlayers overlayers grown on SiO$_2$
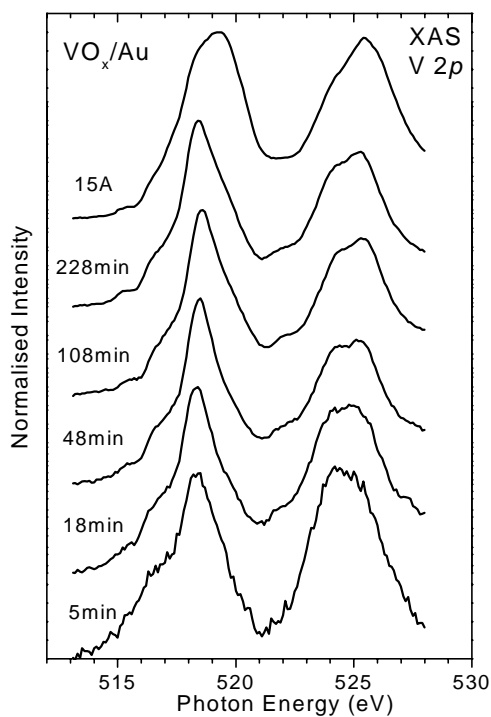
Fig.3: V2*p* XAS spectra of VO$_x$ overlayers grown on gold.

The V 2*p* XAS spectra of VO$_x$ deposited on SiO$_2$ and gold as a function of the evaporation time are shown in Figs 2 and 3 respectively. The spectrum labelled as 15A corresponds to large coverages obtained with the evaporator working at 15 Amps. The V 2*p* XAS spectra corresponding to the VO$_x$/SiO$_2$ system are similar except for low coverages (5 min) and large coverages (15 A). These spectra completely agree in shape and energy with the V$_2$O$_3$ spectrum reported by Abbate *et al.* [1]. Also, the small structure at about 522 eV, characteristic of V$_2$O$_3$, is present.

For low coverages (5min.), the V 2*p* spectrum clearly differs from the others. The small shoulder at the low energy side is more intense in this spectrum. The small structure between the two main features of the spectrum changes too, and appears slightly shifted to higher energies. According to the reference spectra shown in Fig. 1, this spectrum cannot be explained in terms of higher oxidation state of vanadium, as otherwise it should be shifted to higher photon energies. As this spectrum corresponds to the sub-monolayer regime, the VO$_x$ overlayer could be influenced by the substrate. However, to understand the origin of such changes more work should be done. For large coverages (15 A) the spectral weight shifts to higher energies and the structure at 522eV becomes hidden. This can be attributed to the formation of vanadium species with higher oxidation states, i.e. V^{4+} or V^{5+}.

On the other hand, the spectra corresponding to VO$_x$ overlayers grown on gold are identical show exactly the same behaviour as the spectra of the VO$_x$ overlayers grown on SiO$_2$. From this comparison it can be inferred that the growth of these overlayers is not dependent on the substrate. This is in contrast with the growth of TiO$_2$ overlayers which have been found to strongly depend on the nature of the bonding of the substrate.

References:

[1] M. Abbate, H. Pen, M.T. Czyzk, F.M. de Groot, J.C. Fuggle, Y.J. Ma, C.T. Chen, F. Sette, A. Fujimori, Y. Ueda, K. Kosuge. *J. Electron Spectrosc. Relat. Phenom.* **62** (1993) 185.
[2] H. F. Pen, in *High energy spectroscopy on vanadium oxides: electronic structure and phase transitions*, PhD thesis, University of Nijmegen, 1997.

Influence of structure and interface on magnetic properties of ultrathin Co films on W(110)

A. Kleibert, V. Senz, K.-H. Meiwes-Broer, and J. Bansmann

Fachbereich Physik, Universität Rostock, Universitätsplatz 3, D-18051 Rostock

Here, we report on investigations on the magnetic behavior of ultrathin cobalt films focussing on the geometric structure of the film and the interface to the substrate. Tungsten single crystals offer the possibility to modify the surface by oxygen adsorption (e.g. p(2×1)-superstructure) or by creating a carbon-induced R(15×3) reconstruction on the (110) surface. Therefore, we prepared cobalt layer on these W(110) surfaces in order to gain films with a different structure or a different interface. Earlier studies showed a modification in the growth mode of cobalt from the hcp(0001) for clean surfaces to the fcc(001) in case of a carbon R(15×3) reconstruction [1].

For determining the magnetic properties of such films we used the transverse magneto-optical Kerr-effect (MOKE) which is well known in the visible regime. Here, the magnetization gives rise to small intensity differences in the reflected light. These effects are extremely small for ultrathin films (thickness t ≪ wavelength λ) [2]. Thus, we were using the advantage of transverse MOKE in the soft x-ray regime, where the intensity differences upon reflection is enhanced by several orders of magnitude [3]. The experimental setup is shown in the left part of fig. 1.
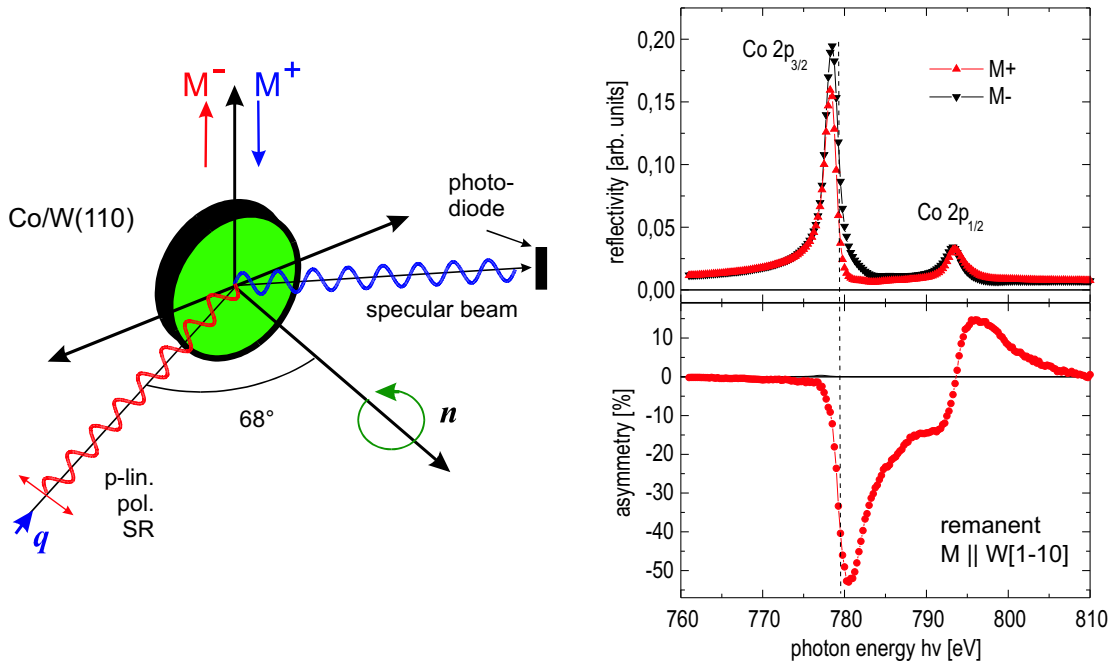
Figure 1: Left: experimental setup; right: X-ray reflectivity and related asymmetry spectra for opposite remanent magnetization of a 8 ML hcp(0001)Co film on clean W(110).

In general, the reflectivity of metals in the soft x-ray regime is very small, but resonantly enhanced near the absorption edges. This is illustrated in the upper right part of fig. 1, where the reflectivity of a 8 ML hcp(0001)Co film is shown near the 2p core levels for opposite magnetization directions. Close to the Co absorption edges at 778eV and 793eV one can observe a strongly enhanced reflectivity. The lower right part of fig. 1 shows the corresponding asymmetry with values up to 50%. The magnitude of the asymmetry is caused by scattering into strongly
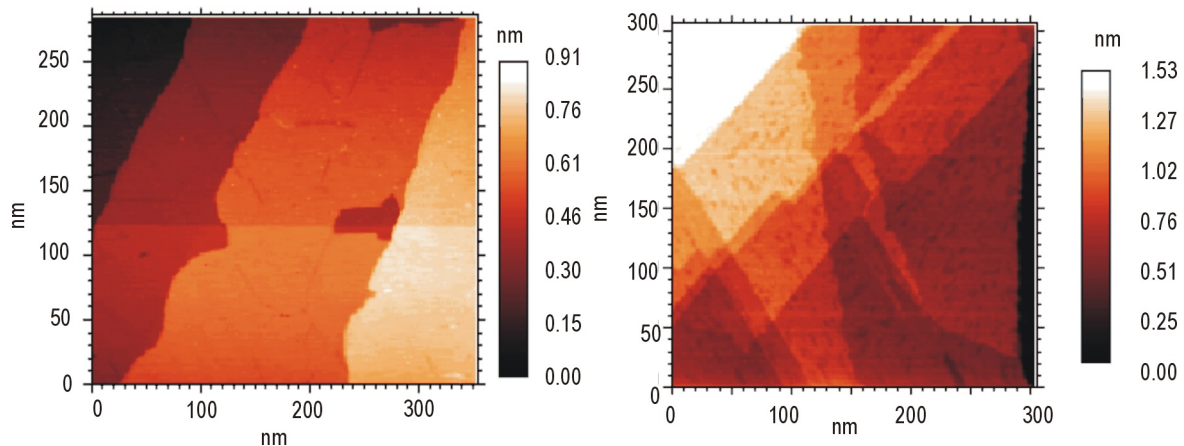
Figure 2: Left: STM image from a hcp Co film on the clean W(110) surface showing atomically flat terrasses over more than 100nm. Right: STM image from a similarly prepared fcc(001) Co film in two domains on the carbon-induced reconstrution [5] yielding in a much higher roughness).

spin-polarized states near the Fermi level and by the spin-orbit interaction at the Co 2p edges ($\Delta E_{so} \approx 15\,\text{eV}$) and can be used for recording hysteresis loops.

We prepared in-situ epitaxially ordered Co films on clean W(110), on the carbon R(15×3), and the oxygen p(2×1)-reconstruction of W(110) (see fig. 2). On clean W(110) cobalt grows in hcp(0001) structure in Nishiyama-Wassermann orientation. In this case it is well known that the lattice mismatch between tungsten and cobalt leads to a constant strain of about 3% in the W[1$\bar{1}$0] direction up to 10 monolayers [1,4]. Also on the oxygen-reconstructed W(110) surface cobalt grows in hcp structure. In contrast to this one will find cobalt in two domains in fcc(001) structures on the carbon-induced reconstruction of W(110)[1]. The STM images in fig. 2 show that hcp Co films are smooth after annealling, whereas the fcc films stay significantly rough [5].

In fig. 3 three sets of hysteresis loops of a 6 ML Co film on the different modifications of the W(110) surface are shown where the azimuthal angle between the W[1$\bar{1}$0]-direction and the external field was altered. In all three cases one can see square hysteresis loops when applying magnetic field parallel to W[1$\bar{1}$0] direction indicating the magnetic easy axis. When rotating the sample around the surface normal a transition to the hard axes (parallel to W[001]) was observed. This behavior can be explained by assuming a magnetic uniaxial in-plane anisotropy. Earlier measurements of the anisotropy of cobalt films on W(110) from Fritzsche et al. showed that the in-plane contribution for films up to 10 monolayers is mainly due to the constant strain along the W[1$\bar{1}$0] direction [2].

In order to determine the anisotropy constant from hysteresis loops the saturation field H_S of the hard-axis loop (M ∥ W[001]) is required. For hcp(0001) cobalt films on clean W(110) with a thickness between 4 and 12ML we found a good agreement between our measurements [6] and data from ref. [2]. A Comparison of the saturation fields of 6 ML Co films on different prepared W(110) surfaces shows a decreased field H_S for Co on the oxygen-induced reconstruction of W(110) and a significantly increased field H_S for Co on the carbon (15×3)-reconstruction. Assuming that the magnetic moments of Co films on the different modifications of the W(110) surface do not change significantly one can see that the structure of film and the surface prop-
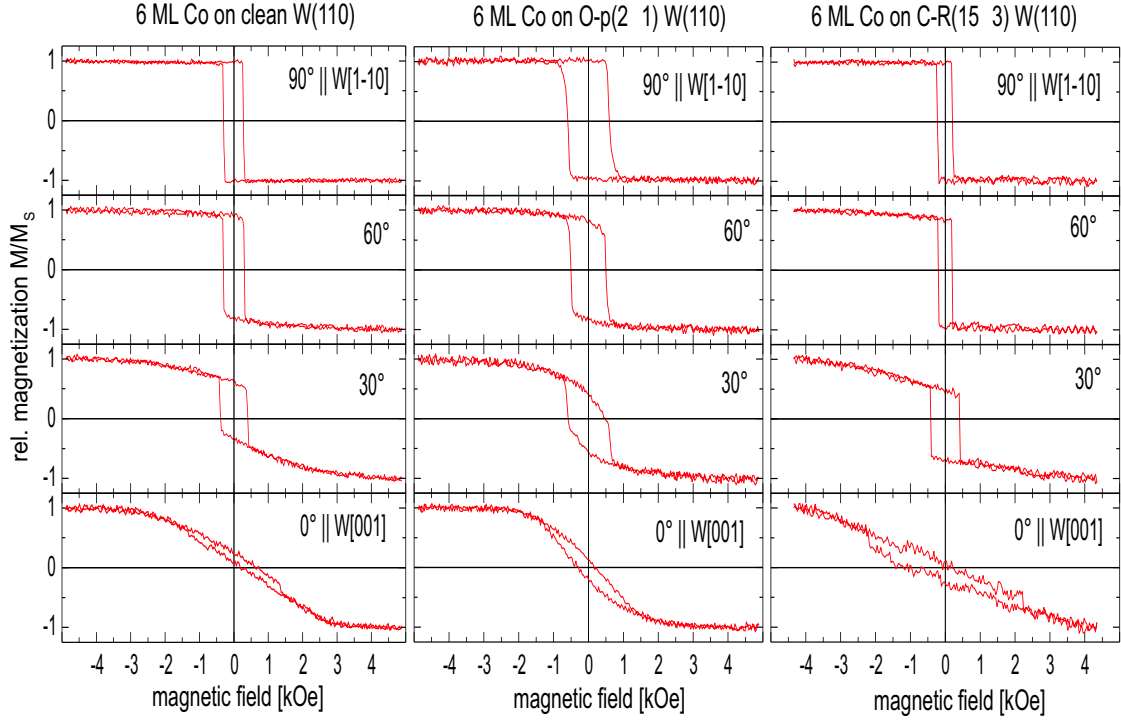
Figure 3: Hysteresis loops of 6 ML Co on different modifications of the W(110) surface.

erties have a remarkable influence on the magnetic anisotropy.

Moreover, it is instructive to compare the coercive forces H_C in the case of magnetization along the easy axes. The coercive force is not an intrinsic physical quantity but is very sensitive to microstructure, e.g. roughness and defects, and anisotropy. We found a larger coercive force for the cobalt film on the oxygen-induced reconstruction of W(110) compared to the one of Co on the clean W(110) surface. For the fcc cobalt films on the carbon(15×3)-reconstruction one can see a significantly smaller coercive force. This is an interesting fact because one would expect an increased value due to the higher anisotropy of this film. However, this behavior reflects the roughness of the cobalt film in the fcc(001) structure leading to an easier nucleation of domain walls which supports the process of magnetization reversal.

In conclusion, we have shown that both the interface as well as the structure of the cobalt films do not have a strong influence on the magnetic anisotropy. The easy magnetization axis is always pointing along the W[1$\bar{1}$0] direction of the underlying substrate. However, the individual hysteresis loops and thus, the coercive forces, the switching fields and the saturation fields change slightly with, e.g., the structure and the roughness.

[1] H. Pinkvos, H. Poppa, E. Bauer, and J. Hurst, Ultramicroscopy **47**, 339 (1992).
[2] E. R. Moog, C. Liu, S. D. Bader and J. Zak, Phys. Rev. B **39**, 6949 (1989).
[3] C. Kao et al., Phys. Rev. Lett. **65**, 373 (1990).
[4] H. Fritzsche, J. Kohlhepp and U. Gradmann, Phys. Rev. B **51**, 15933 (1995).
[5] A. Bettac et al., Surface Sci. **454-456**, 936 (2000).
[6] A. Kleibert, diploma thesis, Universität Rostock (2001).

Unusual hybridisation of Cr–Pt alloys probed by angular resolved photoemission (ARUPS)

A. Borgschulte[1], D. Zur[1], D. Menzel[1], U. Barkow[1], J. Schoenes[1],
P. M. Oppeneer[2]

[1]Institut für Halbleiterphysik und Optik, TU Braunschweig, Mendelssohnstrasse 3,
D-38106 Braunschweig
[2]Institute of Solid State and Materials Research, P.O. Box 270016, D-01171
Dresden

Over the last decades the combination of $3d$ transition elements with noble metals has opened various exciting fields of research and applications. Intermetallic compounds of $3d$ transition metals and the noble element Pt exhibit a multitude of magnetic properties, making some of them potential candidates for magneto-optical recording media due to their high magneto-optical Kerr rotation and magnetic anisotropy. Recent experiments have shown a strong dependence of the magnetic properties on the crystalline long-range order of $CrPt_3$. Ordered $CrPt_3$ (111) films have a large perpendicular anisotropy, which scales with the degree of chemical order. Such a system is of great scientific interest since it allows the exploration
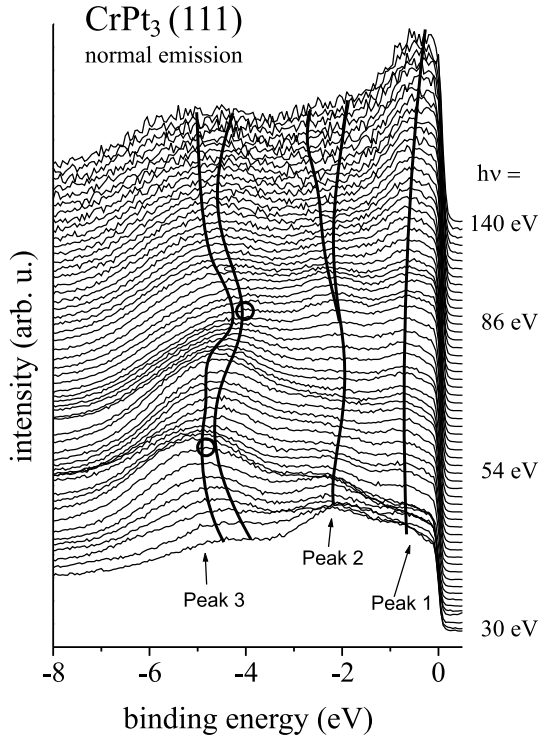
Figure 1: Electron energy distribution curves (EDCs) from $CrPt_3$ (111) in normal emission collected for photon energies between 30 and 140 eV in 2 eV steps. Solid lines serve as guides to the eye marking the dispersion of main emission features. Circles represent the suggested Γ and R point in k-space at the photon energies of 54 eV and 86 eV, respectively.

of one of the most important yet still poorly understood magnetic phenomenon, namely the origin of magneto-crystalline anisotropy (MCA). A particularly strong hybridization of Cr and Pt states in ordered $CrPt_3$ was predicted by electronic structure calculations on the basis of density-functional theory in the local spin-density approximation (LSDA) and was attributed to be the physical origin of the high magnetic anisotropy.[1]

---

[1]I. Galanakis et al., Phys. Rev. B **63**, 172405 (2001)

Here, we report on ARUPS measurements of epitaxial Cr_xPt_{1-x} films. The variation of the intensity of a photoemission transition with photon energy can be used to assign the transition to a particular element in the alloy. The measurements were performed with the BESSY HIRES equipment using the U125/1PGM beamline providing a resolution of 25 meV. In Fig. 1 various electron EDC's obtained from $CrPt_3$ (111) in normal emission are shown for photon energies between 30 and 140 eV. The valence d band of $CrPt_3$ extends to around 7 eV below the Fermi level which is in qualitative agreement with the calculated bandwidth. The binding energy and relative intensity vary both with the photon energy and emission angle (see Figs. 2). The angular dependence can be explained by the momentum conservation of the electrons and will be discussed later. The energy dependence of the intensity, on the other hand, is a consequence of both momentum and energy conservation and photoionization cross-section. In Fig. 2 the intensity of the marked maxima in Fig. 1 are shown for photon energies between 30 and 140 eV. The intensities are normalized to the total area of the photoemission spectrum. The inset in Fig. 2 gives the normalized photoionization cross-section as calculated by Yeh.[2] From a comparison of the experimental and theoretical curves, we attribute the electronic states near the Fermi edge (peak 1) to mainly Cr-derived states, and peak 3 to mainly Pt-derived states. The intensity of peak 2 as a function of the photon energy follows that of peak 3 at higher energies, while it is nearer to peak 1 at lower energies. Not included in the calculation are threshold transitions and Cooper minima.
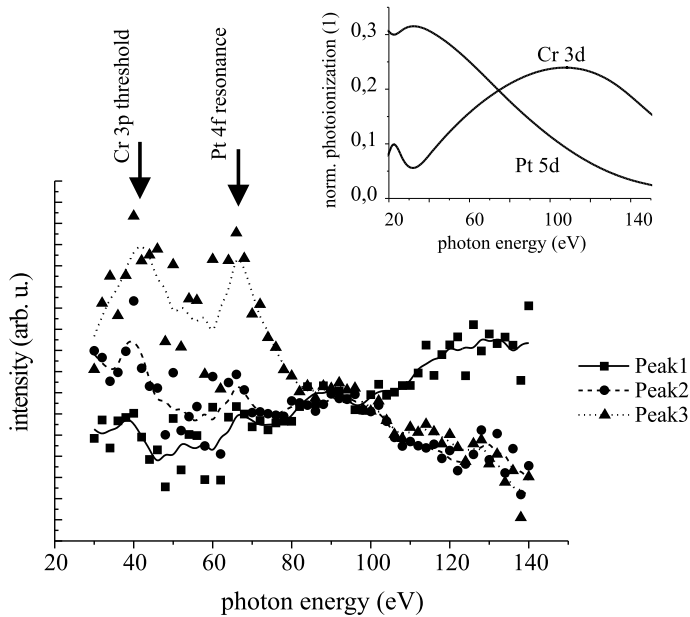
Figure 2: Intensity of the marked maxima in Fig. 1 from $CrPt_3$ (111) in normal emission for photon energies between 30 and 140 eV. The intensities are normalized to the total area of the photoemission spectrum. The lines serve as guide to the eye. The inset shows the normalized photoionization cross-section as calculated by Yeh and Lindau. The arrows indicate the energy positions that are attributed to the Cr $3p$ threshold and the resonant excitations from the Pt $4f$ levels.

Thus, the peak in the experimental spectrum at 40 eV can be attributed to the Cr $3p$ threshold. The maximum around 70 eV is considered to be due to a resonant enhancement caused by excitations from the Pt $4f$ levels. The additional intensity modulation is a consequence of the dipole selection rules ($k-$ and $E-$ dependence).

[2]J. J. Yeh and I. Lindau, *At. Data Nucl. Data Tables* **32**, 1 (1985)

The observed peak energies in Fig. 1 are assigned to energy bands of ordered $CrPt_3$. The strongest minimum (at 54 eV) and maximum (at 86 eV) are attributed to the Γ and R point in reciprocal space, respectively. These points are marked in Fig. 1, where additional angle-dependent photoemission measurements were performed.

In order to compare the measured spectra with our theoretical calculations we assume a free-electron-like final state for the excited photoelectron. In Figs. 3a and 3b we compare our calculated and measured energy dispersions along the $\Gamma - M - \Gamma$ and $R - X - R$ directions, respectively. The calculated band structure consists of many bands, which can obviously not all be resolved in the ARUPS measurements. Therefore we chose to indicate regions of dense bands by a brighter gray level. As can be recognized in Fig. 3, there exists an overall reasonable correspondence between the measured and calculated dispersions. The lowest bands at Γ and X, contain mainly Pt s character, as do also to a lesser extent the lowest bands at R and M. The bands with mainly s character are not detected in the ARUPS measurements. One of the most striking result is the intensity modulation at the Fermi level. The
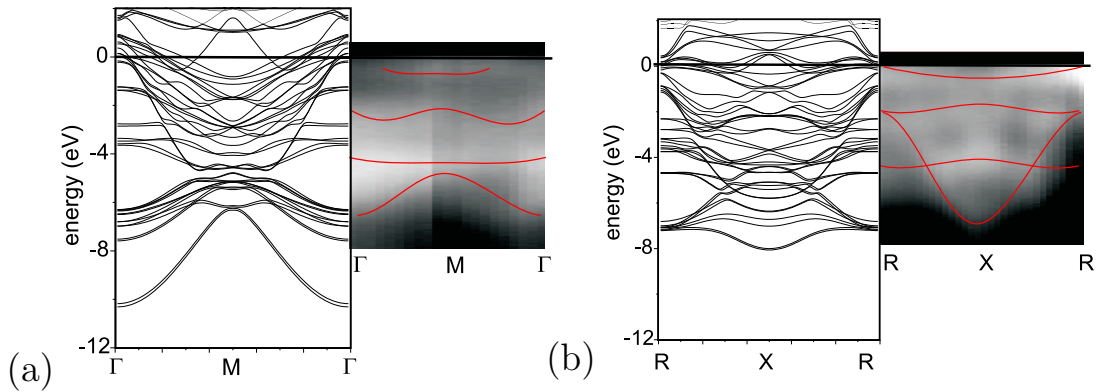
Figure 3: Comparison of the experimental and calculated band structure of ordered $CrPt_3$, for the $\Gamma - M - \Gamma$ (a) and $R - X - R$ (b) symmetry directions in the simple cubic BZ. The LSDA calculated energy dispersions are shown by the solid lines. The bright regions represent high photoemission intensities. Lines in the photoemission intensities are guides to the eyes.

intensity at the Fermi energy is determined by character, the $E(k)$ dispersion and the degeneracy of the bands near E_F. High intensities are found at the M and R points in Fig. 3 (a) and (b), respectively. While the high intensity at the R point can be explained by the crossing of E_F by several bands, no Fermi level crossing can be found at the M point. From a comparison with Fig. 3 we conclude that the high PDOS of Cr derived states (with a high photoionisation probability) at the M point is the origin for this intensity maximum. This is another hint for the unusual hybridisation of Cr and Pt states.

Resonant Photoemissión in Cr Silicides at the Cr 2p absorption energy

L.Galán[1], M.García[1], J.M.Ripalda[1], I.Montero[2], E.Román[2], D.R.Batchelor[3], P.R.Bressler[3]

[1]*Departamento de Física Aplicada, Universidad Autónoma de Madrid, E-28049, Madrid, Spain.*
[2]*Instituto de Ciencia de Materiales de Madrid, CSIC, E-28049, Madrid, Spain.*
[3]*BESSY, Albert Einstein Strasse 15, D-12489, Berlin, Germany.*

In a long-term research on surface coating materials to prevent multipactor effect in high-power RF in communication and surveying equipment in spacecraft, we have been guided to study Cr silicides because of their low secondary electron emission yield and its reluctance to deterioration upon air exposure. In order to study the electronic structure of these thin films in relation with those properties, we have performed valence band photoemission spectroscopy near the high-energy Cr $2p_{3/2} \rightarrow$ 3d adsorption threshold, that is known to produce interesting resonance effects in the pure metal [1].

Very thin silicide films were prepared in nearly UHV (10^{-9}mb range) by sublimation of Cr onto Si (100) substrates and posterior rapid annealing in the preparation chamber of the experimental station. Cr-Si reaction was indicated by valence band structures [2] and Si 2p chemical shifts. Photoemission spectroscopy was performed *in situ* at the PM-1 beam line of BESSY, with the SX-700-I monochromator and a SPECS large angle-resolved electron energy analyzer. The resolution of the monochromator at the high energies of interest (~ 580 eV) was ~1.7 eV. Photoemission spectroscopy was recorded in the EDC, but also CIS and CFS modes. Thus, a well-normalized map as a function of photoelectron and photon energy could be computed.

Some results of the analysis of the experimental data are shown now. Resonance enhancement of the Cr 3d valence levels appeared at 575.8 eV photon energy (PE), while Cr L_3 XAS absorption peak is at 576.3 eV PE [1] and Cr $2p_{3/2}$ XPS core level at 574.3 eV binding energy (BE) as in the pure metal. However, enhancement was not so pronounced, ×2.5, as in pure metal, ×20 [1]. Before resonance the valence band spectra, all with line shape like that for hv = 571 eV (PE) in Fig.1, show structures due to Cr 3d, Si 2s and O 2s (contamination) orbitals. The O 2p band should have about one fourth of the intensity in a broader band and should not affect to following. A typical spectrum above resonance (hv = 579 eV) is also in Fig.1. Besides those structures, it shows also two Auger peaks easily identified because they appear at constant kinetic energy (KE) of 570.3 and 549.5 eV, respectively. The first one is the Cr L_3VV Auger emission. The Auger spectrum was fitted with the computed line shape shown at the bottom of Fig.1, corresponding to threshold when it is slightly narrower. To fit experimental data, it was only necessary to adjust its intensity and to modify slightly its position and its width. The values of these parameters are shown in Fig.2 and 3. For decreasing PE, the Cr Auger emission converges towards the 3d band until 2.3 eV PE passed the resonance and 2.8 eV PE passed the absorption peak, when it reaches a
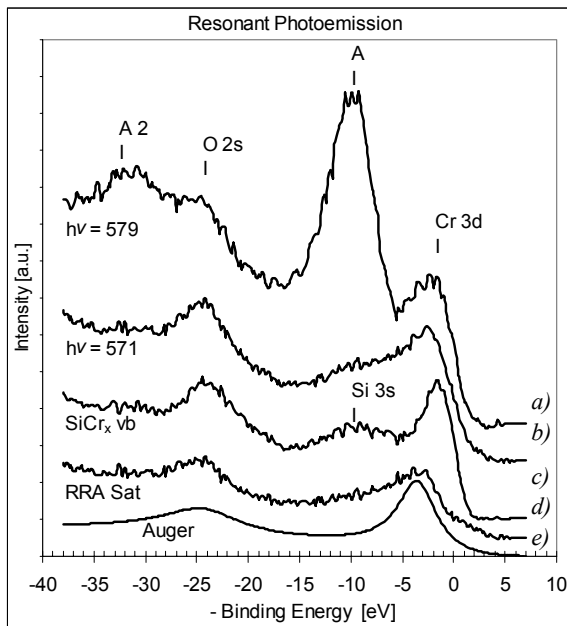
Fig.1 EDC for Resonant Photoemission in CrSi$_x$
Spectra for above *(a)*and below *(b)* resonance photon energies, *(c)* valence band without Auger signal, *(d)* resonant Raman satellite, and (d) Auger theoretical spectrum.
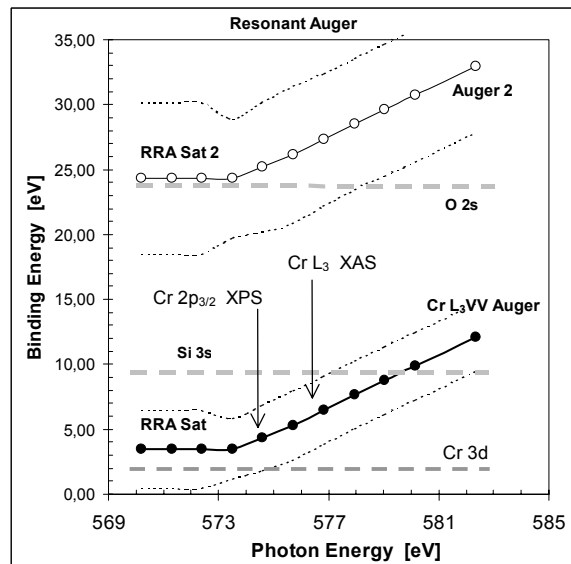
Fig.2 Map of the Photoemission Structures
The position of main structures are represented as well as the width (dotted lines) of Auger signal. The position of the absorption peak and the core level binding energy are also marked.

threshold at 3.5 eV BE, while Cr 3d band peaks at 1.8 eV BE. It should be noticed that this abnormal behavior is maintained nearly 1 eV PE further than in the pure metal. This is because the Cr Auger is ~ 0.5 eV KE less than in the pure metal, indicating some less metallic character for the silicide.

The result of subtracting the Auger emission to spectra above resonance is shown in Fig.1 as SiCr$_x$ vb. This line shape is in agreement with spectra taken at 206 eV PE, far from resonance and with much better resolution and statistics. This line shape is clearly different from spectra below resonance. The difference spectrum is shown in Fig.1 as RRA satellite, that is clearly identified as the resonant Raman Auger or two-hole satellite since it has the same line shape as the Auger emission but appears at constant 3.5 eV BE. The appearance of the radiationless resonance Raman phenomenon is clear indication of genuine photoemission resonance. One more thing should be checked: that the intensity enhancement of the 3d band at resonance is not due to addition of the overlapping Auger signal. That is demonstrated in Fig.4, where a CIS spectrum for 0.5($\pm$5) eV BE is shown as measured, together to that resulting after subtraction of the Auger signal. The 3d resonance occurs at the absorption peak. However, no destructive interference (Fano line shape) was observed before the resonance peak (the dip in the lower spectrum of Fig.4 is due to the RRA satellite not being subtracted for the first three points) contrary to the case for the low-energy Cr 3p absorption threshold in the pure metal [3].

Thus, the final picture is drawn in the PE-BE map of the photoemission structures of Fig.2. The intensity along the Auger and the 3d lines can be read in Fig.3 and 4 (second

spectrum), respectively. These intensities of the Auger and 3d lines should be convoluted with the third and the last spectra of Fig.1, respectively, in order to get the complete picture.
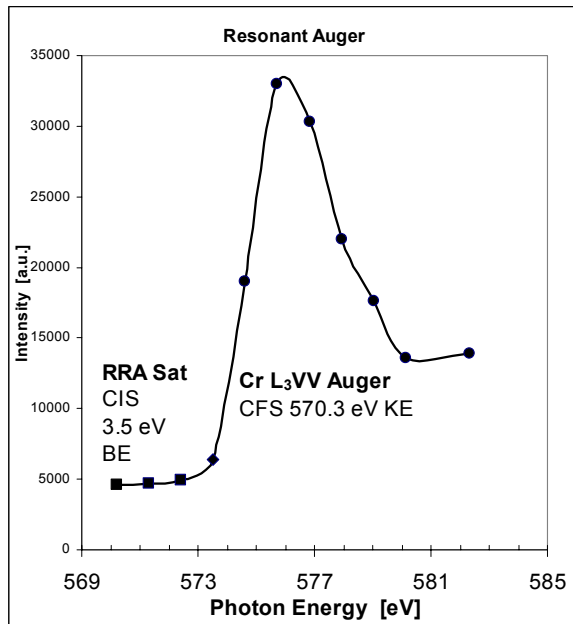
Fig.3 Intensity of the normal Auger and resonant Raman Auger.
The intensity values correspond to the Cr Auger line of the map in Fig.2.
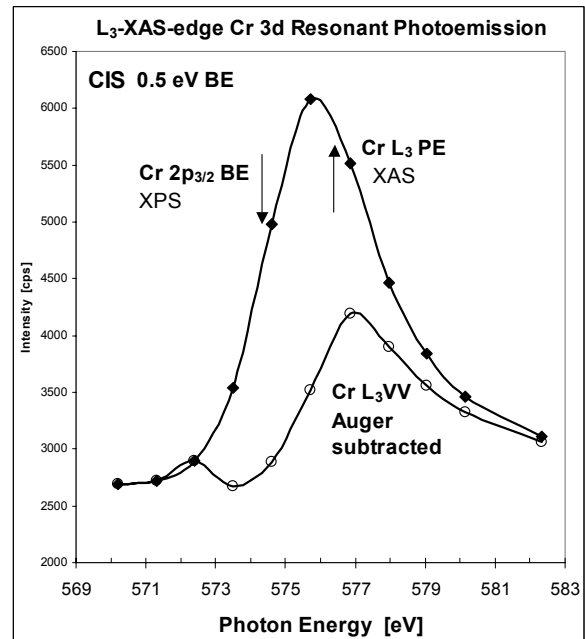
Fig.4 Constant Initial State spectra of Cr 3d.
The contribution of the Cr Auger signal has been subtracted in the lower spectrum.

It should be pointed out that it is generally assumed that the resolution in the photon energy should be very good compared to the absorption line width for the resonant Raman Auger satellite to occur [1, 4]. In this case, the resolution of the photon channel (~1.7 eV) was probably in the limit (~3 eV for the absorption), because they were not easily observable but all the characteristics of the phenomenon were there.

References

1.   S.Hüfner et al, Phys. Rev. B, **61** 12582 (2000)
2.   J.H.Weaver et al, Phys. Rev. B, **29** 3293 (1984)
3.   T.Kaurila et al, J. Phys.: Condens. Matter, **9** 6533 (1997)
4.   M.Finazzi et al, Phys. Rev. B, **59** 9933 (1999)

PEEM AND µ-NEXAFS OF Cu-In-S-SURFACES

K. Müller, P. Hoffmann, S. Milko, Y. Burkov, D. Schmeißer, Brandenburgische Technische Universität Cottbus, Angewandte Physik-Sensorik, 03013 Cottbus, P.O.Box 101344, Germany

Introduction

The composition of $CuInS_2$–films tends to differ from the ideal ratio of 1:1:2. A molecularly variation of $\delta m=[Cu]/[In]-1\neq0$ occurs due to the formation of binary phases as segregation's at the surface, as crystallites in the bulk of the film or at the surface of grains [1]. Furthermore, the range of homogeneity of the phase $CuInS_2$ is relatively large caused by a low enthalpy of formation of defects like Cu-vacancies [2]. Segregation's at surfaces can be removed by KCN etching or by an electrochemical process [3, 4] We investigated the effect of an in-situ-heat-treatment of samples, prepared in the Cu-rich regime with additional amounts of copper, deposited on the surface of the Cu-In-S-films.

We used Cu-In-S-films on molybdenum, prepared from precursors of Cu/In and a following reactive annealing-process in a sulphur–atmosphere. The experiments were performed as follows: The surface of the films was cleaned in situ to remove CuS-Phases by Argon-bombardment. The thin layers of additional Copper were prepared by evaporation of copper metal in Knudsen-cells. The thickness of this copper-films is in the range of monolayers, revealed by a calibration with copper on iron-substrates. After this deposition the samples were heated up to several temperatures (up to 550^0C) for ten minutes, respectively. Here the molybdenum back-contact was used as electrical heater.

Results and discussion:

The elementary ratios of Cu/In, Cu/S and In/S, determinated by photoelectron spectroscopy (XPS, UPS) tends to become more, but not completely stoichiometric due to the pure annealing process without any additional copper (Cu/In from high values of 10 before and a stable value of 5 after the treatment, independent of temperature). Deposited Copper and a following heating leads to ratios of Cu/In, Cu/S (and In/S) near stoichiometry (eg. $Cu(2p)/In(3d) = 1,5$ at 400^0C).

To confirm this results, we investigate the development of topology, the change of lateral element distribution and chemical reactions upon the above described process. The surfaces were characterised by PEEM, µ-NEXAFS and µ-PES.

In Figure 1 – above - we show PEEM images, taken at 120eV before and after a thermal treatment with additional copper up to temperatures of 550^0C. They shows a reduction of the average grain size of the CIS particles due to the thermal treatment. Beneath, we show difference-images of PEEM, taken around the absorption edge of copper at 925 and 933eV. Inhomogeneities in the Cu-distribution
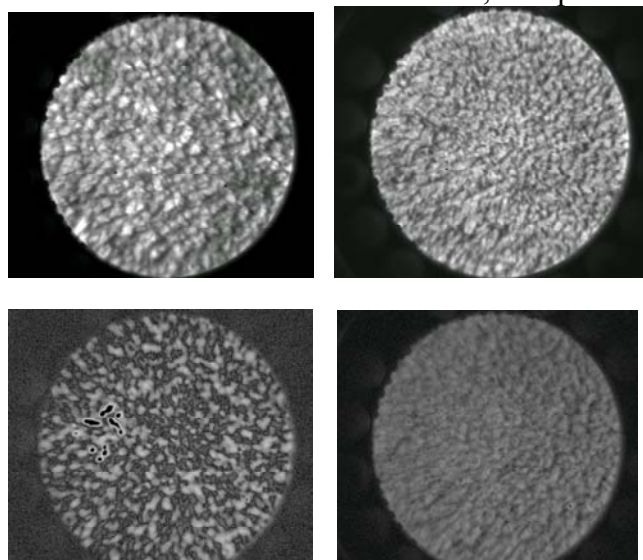

Figure 1, top: PEEM images, taken at 120eV before (left hand side) and after thermal treatment (right hand side); bottom: Difference-images around the absorption edge of copper before and after thermal treatment (Diameter: 110µm)

were observed and thermal treatment leads to more homogeneous distributions of copper. This development is obviously due to the deposition of copper, but this tendency was confirmed in difference images of sulphur, too. To confirm a surface reaction into more stoichiometric Cu-In-S, we show the µ-NEXAFS spectra taken during the annealing process (Figure 2).
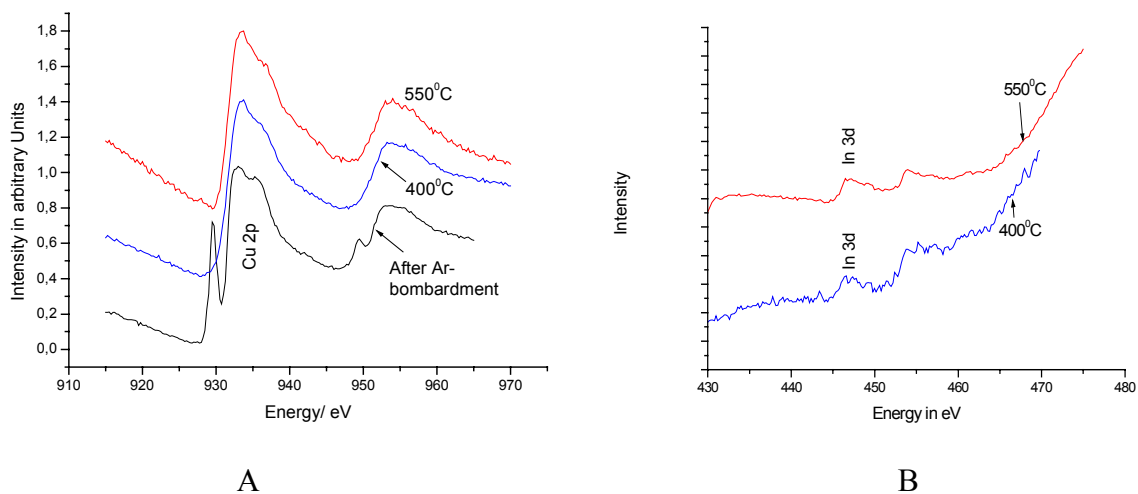

A   B

Figure 2: µ-NEXAFS-Spectra of Cu-In-S-Films A: Spectra taken at the Cu 2p absorption edge and normalised to the rise of the Cu2p-absorption edge; B: Spectra taken at the In3d absorption edge (black: after argon-bombardment; blue: with additional copper and annealed at 400^0C for 10min; red: annealed at 550^0C, 10 min).

Before annealing, the Cu2p-spectrum shows a resonance at 929,5eV, the signal at 949,5eV reflect its spin-orbit-component. Band structure calculations for $CuInS_2$ shows no distinct density of electronic states above the Fermi-energy, which could explain this additional resonance near the real absorption edge [5]. This resonance could belong to the binary phase-segregation's, which were removed by the thermal treatment.
The measurements shows, that an annealing-process with an additional deposition of copper could lead to the formation of stoichiometric $CuInS_2$ at the surface of thin Cu-In-S-films.

Literature:
[1] V. Nadenau, D. Hariskos, H. Schock, M. Krejci, F. HaugA. Tiwari, H. Zogg, G. Kostorz, J. Appl. Phys. 85 (1999), 534
[2] J. Binsma, L. Giling, J. Bloem, J. Cryst. Growth 50 (1980), 127
[3] M. Aggour, H.J. Lewerenz, J. Klaer, U. Störkel, Electrochemincal and Solid State Letters, 3, (9), (2000), LETTERS ONLINE
[4] M. Aggour, U. Störkel, C. Murrell, S.A. Campbell, H. Jungblut, P. Hoffmann, R. Mikalo, D. Schmeißer, H.J. Lewerenz, Thin Solid Films, 2002, Strasbourg 2001 contribution Symp. P
[5] T.Yamamoto, H.Katayama-Yoshida, Jpn. J. Appl.Phys. 35, L1562

Characterisation of the PrO$_x$/Si(001) Interface by Photoelectron Spectroscopy

D.Schmeißer, P.Hoffmann

BTU Cottbus / Lehrstuhl Angewandte Physik-Sensorik / Universitätsplatz 3-4 / 03044 Cottbus

Praseodymium oxide on Silicon is recently investigated as a high-k gate material for substituting SiO$_2$ [1]. To investigate Praseodymium oxide on Si we first remove the native oxide on Si(001) by flashing (heating shortly above 1200°C). Then we evaporate Pr$_6$O$_{11}$ from a Ta crucible. In this contribution we first show he valence band features of the PrO$_x$/Si(001) system and then focus on the Pr4d / Si2p emission range.

In Fig.1a we show the valence band emission in the range between 50eV binding energy and Fermi energy (E$_F$). The spectrum is taken at a photon energy of 660eV, the Praseodymium oxide film has a thickness of about 2nm. In the spectrum we identify emission from Pr(5s, Pr5p, Pr4f) and O(2s, 2p) states. The Pr5s is located at a binding energy of -37.5eV, the Pr5p appears at -18.5eV. The Pr4f states show a rather sharp (FWHM

Figure 1: Valence band emissions of Praseodymium oxide taken at a photon energy of 660eV.

~1eV) feature which peaks at a binding energy of -3eV. The Valence Band Maximum (VBM) is found at –1.5eV.

The range of the upper valence band states is shown in more detail in Fig.1b. The emissions at a binding energy of -10.0eV and -7.8eV can be assigned to contribution from O2p sates [2]. The Si valence states do not show up because of their low photoionisation cross section.

The emissions from Pr4d states is shown in Fig.2, again taken at hν=660eV. The Pr4d states are split and form a band which is almost 25eV wide. The lowest Pr4d state have a negligible intensity while the upper states appear very strong with a maximum at a binding energy of -117eV (binding en-

Figure 2: Emissions from Pr4d and Si2p taken at hν=660eV.

ergy 17.7eV higher relative to $Si2p^{\pm0}$ emission), the band starts at a binding energy of –108eV.

The emissions from the Si2p levels are shown in more detail in Fig.3. The evaporation of the Praseodymium oxide causes a chemical shift in the Si2p emission (indicated by $Si2p^+$ in Fig.2 and Fig.3) which differs from that of SiO_2 (3.6eV shifted to higher binding energy relative to $Si2p^{\pm0}$). These data demonstrate that the Si substrate reacts with the Praseodymium oxide as the Si2p line is shifted by about 2.0eV, indicative of an oxidation state between +2 and +3. The large contribution of the $Si2p^+$-emission compared to the $Si^{\pm0}$ emission from the underlying Si(001) substrate should be emphasised here. Together with the chemical shift of 2.0eV - typical for Silicates – this gives rise to the assumption of

Figure 3: Detailed view of the Si2p emission. Spectra taken at 3 different photon energies representing surface sensitivity (hν=135eV, red and hν=220eV, green) and bulk sensitivity (hν=660eV, blue).

the growth of a Pr-Silicate on the Si(001) rather then the forming of such a large amount of Si^{+2} or Si^{+3} suboxides.

Additional to the $Si2p^+$ peak an emission shifted 0.6eV toward lower binding energy could be observed. Due to its shift towards lower binding energy this emission can be assigned to Pr-Silicides. From the rise of this emission in surface sensitive spectra (hν=220eV and hν=135eV, see Fig.3) it can be concluded that this Pr-Silicide must be located somewhere between the Si substrate and the Pr-Silicate.

Nevertheless the mixed Si-Pr-oxide (Pr-Silicate) has a significant contribution of PrO_2 because of the strong Pr4f emission in the valence band data. These conclusions are confirmed by our comperative studies of Praseodymium oxide on SiO_2 and Pr-Silicides [3].

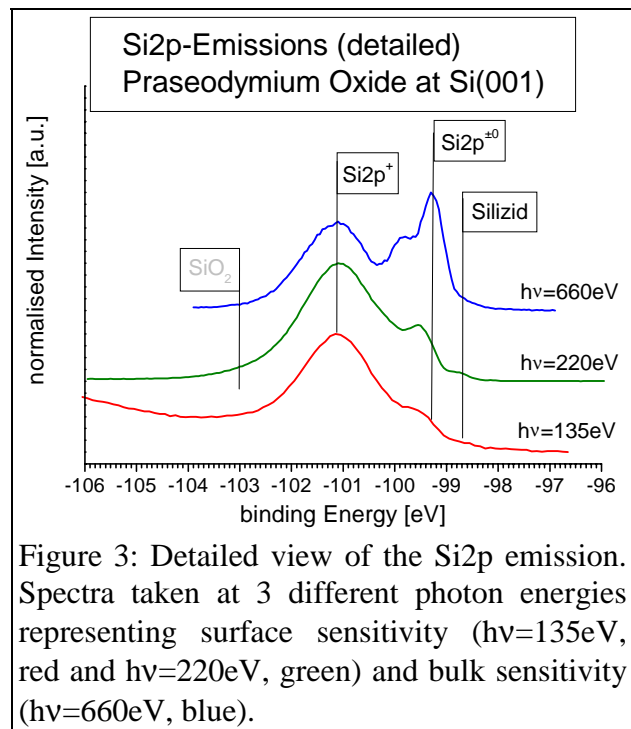[1]   H.-J.Müssig, J.Dabrowski, K.Ignatovich, et al.: Sol.St.Phen. **82-84** (2002) 783-788.
[2]   S.Lütkehoff, M.Neumann, A.Slebarski: Phys.Rev. B **52** (1995) 13808.
[3]   D.Schmeißer, P.Hoffmann, H.-J.Müssig: to be published

Evidence for short range orbital order in paramagnetic insulating $(Al,V)_2O_3$

P. Pfalzer, J. Will, A. Nateprov jr., M. Klemm, and S. Horn

Institut für Physik, Universtität Augsburg, Universitätsstraße 1, 86159 Augsburg, Germany

M. L. denBoer

Department of Physics, Hunter College, City University of New York,
695 Park Avenue, New York, New York 10021

We have investigated the local structure of $(Al_{0.06}V_{0.94})_2O_3$ in the paramagnetic insulating (PI) and antiferromagnetically insulating (AFI) phase using soft and hard x-ray absorption techniques. We show that the vanadium $3d$ - oxygen $2p$ hybridization, as gauged by the oxygen $1s$ absorption edge, is the same for both phases, but distinctly different from the paramagnetic metallic phase of pure V_2O_3 and that, on a local scale, the symmetry of the vanadium sites in both the PI and the AFI phase is the same. These findings can be understood in the context of a recently proposed model which relates the long range monoclinic distortion of the antiferromagnetically ordered state to orbital ordering, if orbital short range order in the PI phase is assumed.

The metal-insulator transition (MIT) in V_2O_3 has been intensively investigated and discussed for many years as an example of a classical Mott transition. However, such a picture is blurred by the complexity of the V_2O_3 phase diagram[1] which involves magnetic and structural transitions coinciding with the MIT, as a function of temperature, doping (Cr, Al, Ti), pressure, and oxygen stoichiometry. At room temperature pure V_2O_3 is in a paramagnetic metallic (PM) phase which x-ray diffraction (XRD) shows to be trigonal. At about 180 K there occurs a transition to an antiferromagnetically insulating (AFI) monoclinic phase. Doping with Cr or Al results in the formation of a paramagnetic insulating (PI) phase. The lattice parameters change but long-range trigonal symmetry is preserved, as indicated by XRD.[2,3] The role of electronic correlations in the interplay between changes in the physical structure, the magnetic properties, and the electronic structure at the various transitions needs further investigation. It is still not certain whether the electronic transition is driven by structural changes or vice-versa. Although recent LDA + DMFT calculations[4] show the importance of electronic correlations in a description of the electronic structure, a description of the MIT in V_2O_3 must take into account the relationship between physical structure and the electronic and magnetic properties of the system.

Here we show using EXAFS and NEXAFS techniques that, on a local scale, the structural and electronic properties of the AFI and PI phase are the same. This fact is attributed to short range orbital order in the PI phase, consistent with recent model calculations[5,6] and the characteristics of magnetic short range order observed by neutron scattering.[7]

NEXAFS measurements on the O $1s$ edge were performed under ultra high vacuum at the U41-1/PGM beamline at the BESSY 2 storage ring. EXAFS measurements were performed at beam line X23B at the National Synchrotron Light Source at Brookhaven National Laboratory using the same crystal in the same geometry as for the NEXAFS measurements.

NEXAFS spectra of the O $1s$ absorption edge in the PI and AFI phase of an Al-doped V_2O_3 crystal grown by chemical transport are presented in Fig. 1 (a) and (b), respectively. Large changes in the spectra are apparent as the sample is rotated from a geometry with $\vec{E}$ parallel to $\vec{c}_{hex}$ ($\vartheta = 0°$) to one with $\vec{E}$ perpendicular to $\vec{c}_{hex}$ ($\vartheta = 90°$). It is evident that cooling from the PI to the AFI phase has no significant effect on the spectra or their dependence on angle. These spectra and their angular dependence are similar to those of pure V_2O_3 in its low temperature AFI phase,[8] but different from those of pure V_2O_3 in its high temperature PM phase, which has a much weaker angular dependence [Fig. 1(c)].

The similarity of the PI and the AFI phase is confirmed by an EXAFS investigation, which shows that a monoclinic distortion of the crystal structure already exists on a short range scale in the PI phase. Shiina[6] attributed the monoclinic lattice distortion in the AFI phase to orbital ordering which would make the three originally equivalent magnetic bonds in the *ab*-plane inequivalent and cause a monoclinic lattice distortion. Evidence for orbital fluctuations in the PI phase was provided by neutron scattering measurements,[7] which showed that magnetic short range order was limited to nearest neighbor distances, resulting in a first order transition from the PI to the AFI phase. Given the results of Ref. 6, orbital fluctuations in the PI phase could cause a dynamic monoclinic distortion. Assuming the time scale for such fluctuations is long compared to the time scale of the x-ray absorption process, EXAFS and soft
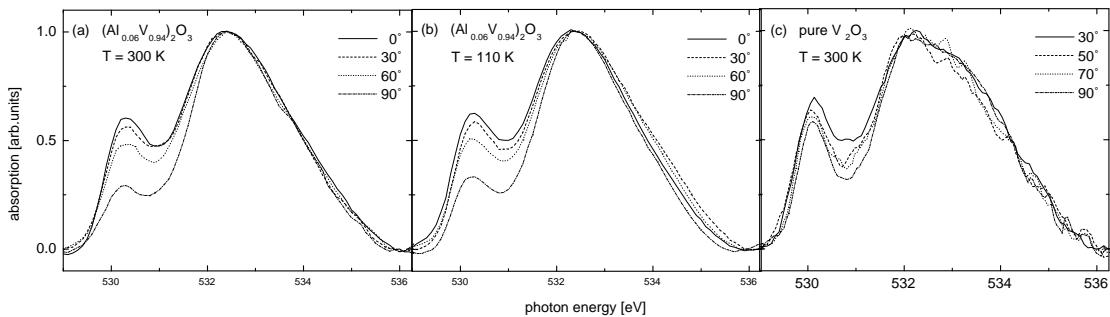
FIG. 1: NEXAFS spectra of the O $1s$ edge of $(Al_{0.06}V_{0.94})_2O_3$ as a function of angle between $\vec{E}$ and the c_{hex} axis, showing large but identical angular anisotropy for (a) the PI and (b) the AFI phase. For comparison, this angular dependence almost vanishes for pure V_2O_3 in its metallic state (c) (from Ref. 8, energy-shifted to facilitate comparison). All spectra were normalized to the large maximum at about 532 eV.

x-ray absorption would measure an instantaneous structure and the PI phase would appear monoclinic, while XRD, which measures on a much longer time scale, would see a trigonal lattice. In the AFI phase the monoclinic distorton might become static although, on a local scale, still having the same magnitude as in the PI phase. This model would account for the fact that neither EXAFS nor soft x-ray absorption observe differences between the PI and the AFI phase, in contrast to XRD. The spectroscopic results are, however, also consistent with static short range orbital order in the PI phase, which would, accordingly, be an orbital glass, with an disorder-order transition to the ordered AFI phase.

The x-ray absorption measurements presented here lead to the following conclusion: both the paramagnetic and antiferromagnetic insulating phases of V_2O_3 are distinguished from the PM phase by: (i) the presence of local or long range distortion of the lattice (probably connected to short or long range orbital order, respectively) and (ii) differences in the V $3d$ - O $2p$ hybridization, accompanied by corresponding band shifts. Both the distortion and the hybridization appear to be independent of the presence of antiferromagnetic correlations, which are present in all phases.[7] The similarity of the PI and the AFI phases, at least on a local scale, suggests a common route from their insulating behavior to the metallic behavior of the PM phase. Interactions between orbital degrees of freedom, which lead to an orbitally ordered state in the AFI phase and orbital short range order in the PI phase, appear to be an an important fingerprint of the MIT.

Acknowledgments

---

[1] D. B. McWhan, A. Menth, J. P. Rameika, W. F. Brinkmann, and T. Rice, Phys. Rev. B **7**, 1920 (1973).

[2] D. B. McWhan, J. P. Rameika, and T. M. Rice, Phys. Rev. Lett. **23**, 1384 (1969).

[3] J. Spalek, J. Solid State Chem. **88**, 70 (1990).

[4] K. Held, G. Keller, V. Eyert, D. Vollhardt, and V. I. Anisimov, Phys. Rev. Lett. **86**, 5345 (2001).

[5] F. Mila, R. Shiina, F.-C. Zhang, A. Joshi, M. Ma, V. I. Anisimov, and T. M. Rice, Phys. Rev. Lett. **85**, 1714 (2000).

[6] R. Shiina, F. Mila, F.-C. Zhang, and T. M. Rice, Phys. Rev. B **63**, 144422 (2001).

[7] W. Bao, C. Broholm, G. Aeppli, S. A. Carter, P. Dai, T. F. Rosenbaum, J. M. Honig, P. Metcalf, and S. F. Trevino, Phys. Rev. B **58**, 12727 (1998).

[8] O. Müller, J. P. Urbach, E. Goering, T. Weber, R. Barth, H. Schuler, M. Klemm, S. Horn, and M. L. denBoer, Phys. Rev. B **56**, 15056 (1997).

F 1s absorption study of hybridization and collapse of 3d electronic states of first-row transition-metal fluorides

A.S. Vinogradov,[a] S.I. Fedoseenko,[a] D. Vyalikh,[b] S.L. Molodtsov,[a,c]
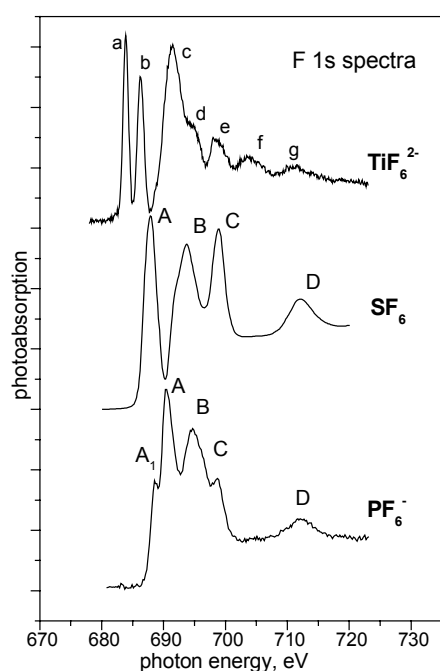V.K. Adamchuk,[a] C. Laubschat,[c] and G. Kaindl [b]

[a] *V.A. Fock Institute of Physics, St.Petersburg State University, 198504 St.Petersburg, Russia*
[b] *Institut für Experimentalphysik, Freie Universität Berlin, 14195 Berlin, Germany*
[c] *Institut für Oberflächen- und Mikrostrukturphysik, TU Dresden, 01062 Dresden, Germany*

The 3d transition-metal compounds reveal interesting magnetic and electric properties arising from their incompletely filled 3d shells. For decades, near-edge X-ray absorption spectroscopy was used to study electronic structure of these compounds. Nevertheless, a lot remains to learn: Hybridization between the metal 3d states and the valence states of nearest-neighbor atoms and its role in formation of the electronic structure of transition-metal compounds remain nowadays among other central problems of X-ray absorption and photoemission spectroscopies. Within a simple ionic model, one believes that the valence band of the most ionic transition-metal compounds, fluorides, is built up only by the fluorine 2p electrons and, thus, no 3d-2p hybridization occurs. In this paper we present high-resolution F 1s absorption spectra of some 3d transition-metal fluorides with the metal site coordinated octahedrally (or nearly octahedrally) to the fluorine sites. Analyzing the data with respect to possible structures reflecting the 3d-2p hybridization between the metal and fluorine atoms we used as references F 1s spectra of the gas-phase molecule SF_6 and the molecular anion PF_6^- in solid KPF_6.

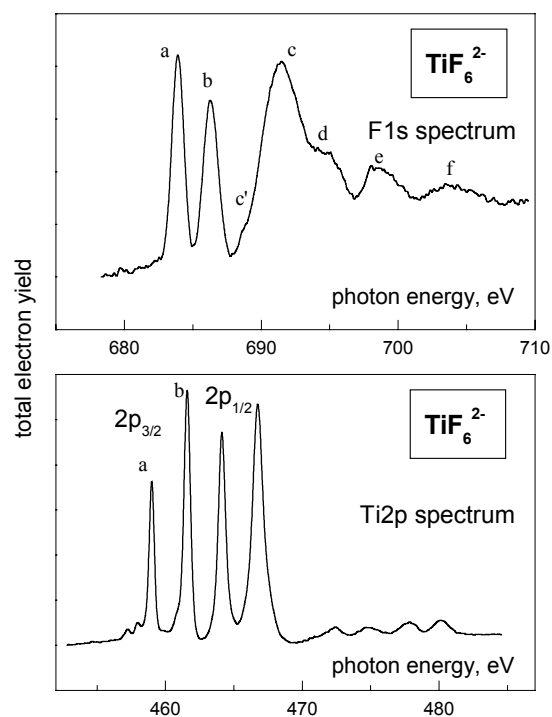The X-ray absorption measurements on transition-metal fluorides, SF_6, and KPF_6 were performed in December 2001 during commissioning of the Russian-German beamline at BESSY [1]. The spectra of solids were taken detecting the total electron yield from respective powders fixed onto a scratched copper plate, the spectrum of SF_6 was measured with the ionization chamber. The estimated photon-energy resolution at the F 1s edge (~690 eV) was better than 0.2 eV. The spectra were normalized to the photocurrent acquired from a gold mesh. The photon energy was calibrated using the known position of the first resonance at 683.9 eV in the F 1s absorption spectrum of K_2TiF_6 [2].

Fig. 1. *F 1s absorption spectra of solid K_2TiF_6, KPF_6 and gas-phase SF_6.*

Figure 1 shows near-edge absorption spectra in the vicinity of the F 1s ionization threshold for covalent molecular anions PF_6^- and TiF_6^{2-} as well as for the gas-phase molecule SF_6. The well-known spectrum of the latter exhibits rich fine structures containing intense absorption bands C and D in the continuum that are associated with core-electron transitions into virtual MOs t_{2g} and e_g [3]. These empty molecular states originate from the mixing (hybridization) of the sulfur 3d and fluorine 2p states and are, therefore, observed in absorption spectra of both atoms of this molecule. Similar interpretation of the corresponding absorption spectrum of the molecular anion PF_6^- was given in Ref. [4].

In contrast to that, the F 1s spectrum undergoes considerable changes when going from SF_6 and PF_6^- to the anion TiF_6^{2-}: Two narrow intense peaks a and b emerge in front of the onset of the absorption edge. Note that these lowest-energy peaks in the spectrum of solid K_2TiF_6 are narrower than lo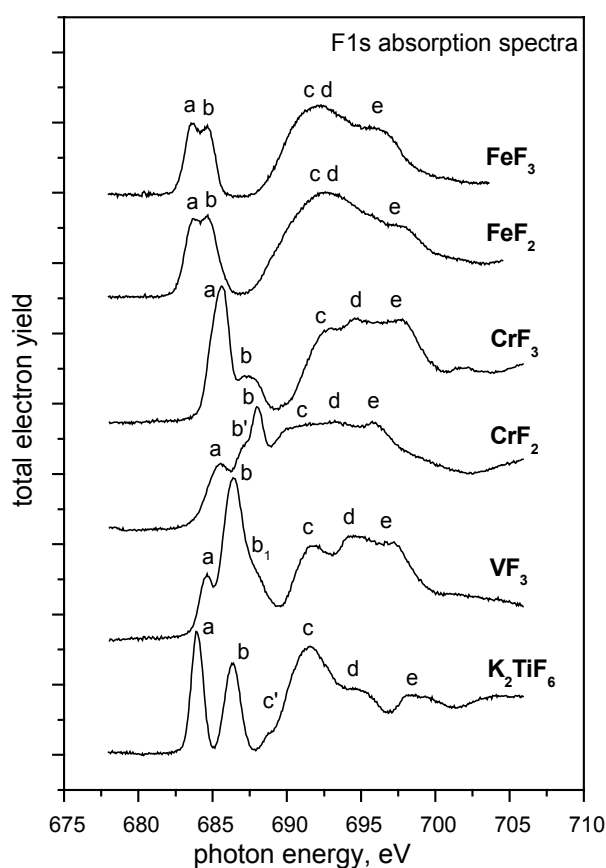w-energy absorption band A in the spectrum of the gas-phase molecule SF_6. To gain insight into the origin of these F 2p character resonances, in Fig. 2 we compare the F 1s and Ti $2p_{3/2}$ spectra of the molecular anion TiF_6^{2-}. The data are aligned using obtained with photoemission energy separation (222.9 eV) between the F 1s and Ti $2p_{3/2}$ core levels. The corresponding spectra of K_2TiF_6 have previously been measured with, however, much lower resolution exploiting bremsstrahlung excitation [2]. The Ti $2p_{3/2}$ spectrum is dominated by two sharp peaks a and b that reflect the core-electron transitions into unoccupied electronic states with the $3dt_{2g}$ and $3de_g$ character, respectively. Direct comparison between the energetically aligned spectra shows that absorption peaks a and b have similar energy positions in both cases. The observed small deviations in energy locations of these resonances (~1 eV) can be understood by different final-state interactions between the F 1s and Ti $2p_{3/2}$ holes and excited electrons. The a-b energy splittings therewith are essentially the same in both spectra: 2.41 eV (F 1s), 2.60 eV (Ti $2p_{3/2}$) and 2.64 (Ti $2p_{1/2}$). By this reason we believe that resonances a and b in spectra of TiF_6^{2-} result from the core electron transitions into the virtual MOs t_{2g} and e_g, which have hybridized Ti $3dt_{2g}$ – F 2p and Ti $3de_g$ – F 2p origin, respectively. In this case, the change in energy position of the t_{2g} and e_g resonances relative to the F 1s ionization threshold when going from SF_6 to TiF_6^{2-} should be regarded as due to a collapse of the 3d wave functions in the first-row transition-metal atoms.

Fig. 2. F 1s and Ti 2p absorption spectra of molecular anion TiF_6^{2-} in solid K_2TiF_6.

Figure 3 shows F 1s absorption spectra of some 3d transition-metal fluorides. The lineshape differs from one spectrum to another. One can distinguish, however, two spectral regions with structures similar for all spectra presented. The first region contains narrow resonances a and b in front of the onset of the main F 1s absorption edge (~690 eV). In some cases peak b reveals additional shoulder b' or b_1. The second region involves broad absorption bands c, d, and e that are located above the absorption edge and significantly overlap with each other. It should be noted that the F 1s spectrum of ScF_3 [5] measured with a lower energy resolution (~0.5 eV) can also be characterized by two similar absorption regions. These regions exhibit perceptible changes of absorption structures with increasing atomic number of the transition-metal atom from Ti to Fe. The changes of the width, the energy positions as well as the relative intensities of resonances a-b observed along the TiF_6^{2-} - FeF_3 series are particularly interesting, since they reflect characteristic details of the metal 3d – F 2p covalent mixing (hybridization) in the transition-metal fluorides. The first evidence for partly covalent bonding in binary 3d metal fluorides is the observation of the F 1s absorption edges itself: In a

purely ionic model the F 2p final states, which are only allowed for dipole transitions of the F 1s electrons, are fully occupied.

Fig. 3. F 1s absorption spectra of molecular anion TiF$_6^{2-}$ and transition-metal fluorides.

A comparison between the absorption spectra for the covalent molecular anion TiF$_6^{2-}$ and the binary fluorides allows us to assign resonances a-b to the hybridized metal 3d – F 2p states. The compounds under study have the metal atom coordinated in the similar way (octahedrally or nearly octahedrally) to the fluorine atoms. Therefore the hybridization here can be regarded within the framework of the MF$_6$ octahedron involving the metal atom M and its nearest neighbor atoms F. We can assume that the observed changes of structures a-b are caused by the decreasing number of the 3d electrons, octahedron distortion and different coupling between the MF$_6$ octahedra in various solids.

References:
[1] S.A. Gorovikov, S.L. Molodtsov, R. Follath, *Nucl. Instr. and Meth. A* **411** (1998) 506; S.A. Gorovikov, R. Follath, S.L. Molodtsov, G. Kaindl, *Nucl. Instr. and Meth. A* **467-468** (2001) 565; S.I. Fedoseenko, I.E. Iossifov, S.A. Gorovikov, J.-S. Schmidt, R. Follath, S.L. Molodtsov, V.K. Adamchuk, G. Kaindl, *Nucl. Instr. and Meth. A* **470** (2001) 84.
[2] A.S. Vinogradov, A.Yu. Dukhnyakov, V.M. Ipatov et al. Sov. Phys. Solid State **24** (1982) 803.
[3] T.M. Zimkina, A.S. Vinogradov, *J. de Physique 32 (1971) C4-3*; J.L. Dehmer, *J. Chem. Phys. 56 (1972) 4496*; E. Hudson, D.A. Shirley, M. Domke, G. Remmers, A. Puschman, T. Mandel, C. Xue, G. Kaindl, *Phys. Rev. A 47 (1993) 361*; J.T. Francis, C.C. Turci, T. Tyliszczak, G.G.B. de Souza, N.Kosugi, A.P. Hitchcock, *Phys. Rev. A 52 (1995) 4665*.
[4] A.S. Vinogradov, A. Yu. Dukhnyakov, T.M. Zimkina, et al. *Sov. Phys. Solid State 22 (1980) 1517*.
[5] M. Ueda, Y.Tezuka, S. Shin, A. Yagishita, *Phys. Rev. B 53 (1996) 1783*.

The Pr_2O_3/Si(001) interface:
a mixed Si-Pr oxide

D.Schmeißer, P.Hoffmann, and H.-J.Müssig*,
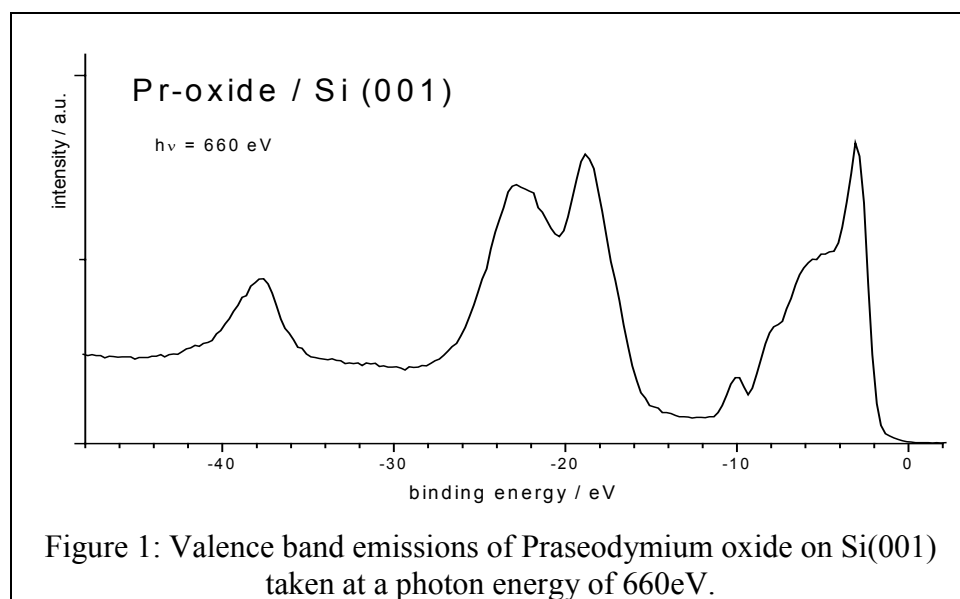Angewandte Physik-Sensorik, BTU Cottbus, Postfach 10 13 44, 03013 Cottbus,
*IHP, Im Technologiepark 25, 15236 Frankfurt (Oder), Germany

Praseodymium oxide (Pr_2O_3) is a candidate to replace SiO_2 as the gate dielectric material for sub-0.1μm CMOS technology. In order to maintain a high-quality interface and channel mobility, it will be important to have no metal oxide or silicide phases present at or near the channel interface [1, 2].

We studied the Pr_2O_3/Si(001) interface by a non-destructive depth profiling using Photo-Electron Spectroscopy at the undulator beam line U49/2-PGM2. Our data provide evidence that there is no silicide formation at the interface. Pr_2O_3 films are prepared in-situ by electron beam evaporation of Pr_6O_{11} at a deposition rate of 0.1nm/min. During deposition, the Si(001) sample was kept at 600°C to enable the hetero-epitaxial growth of Pr_2O_3 [1,2].

In this contribution we first show he valence band features of the PrO_x/Si(001) system and then focus on the Pr4d / Si2p emission range. All the spectra shown in this contribution are taken at a photon energy of 660eV.

In Fig.1 the valence band emission is displayed in the range between 50eV binding energy and the Fermi energy (E_F). The Praseodymium oxide film has a thickness of about 2nm. In the spectrum we identify emission from Pr(5s, Pr5p, Pr5d, Pr4f) and O(2s, 2p) states. The Pr5s is located at a binding energy of -37.5eV, the Pr5p appears at -18.5eV. In the

Figure 1: Valence band emissions of Praseodymium oxide on Si(001) taken at a photon energy of 660eV.

range of the upper valence band states the Pr5d features with the highest binding energy appear at a b.e. of -10.0eV. There are shoulders at –7.8eV and at -6eV. In that range we also expect the contributions of the O2p states. The Pr4f states show a rather sharp (FWHM ~1eV) feature which peaks at a binding energy of -3eV. These features in the valence band region and their assignment is in line with previous studies on the oxidation of Pr [4]. Si valence states do not show up because of their low photo-ionisation cross section. An analysis of the band line up between the Si(001) substrate and the Pr-oxide layer is topic of our current interest. At this point we like to mention that interface dipoles do exist which complicate the data analysis.

The emission pattern from the Pr4d and Si2p states is shown in Fig.2, again taken at hν=660eV. The Pr4d states are split and form a band which in total is about 25eV wide. The

lowest Pr4d states (probably shake up contributions due to multiplet splitting in the final state) have a negligible intensity (in contrast to data from Pr-oxide on a non reactive SiO_2 substrate) while the upper Pr4d states (see Fig.2) appear very strong with a maximum intensity at a binding energy of around -117eV (energy 18eV above the $Si2p^0$ emission of the Si(001) sub-

Figure 2: Emission from Pr4d and Si2p taken at hν=660eV.
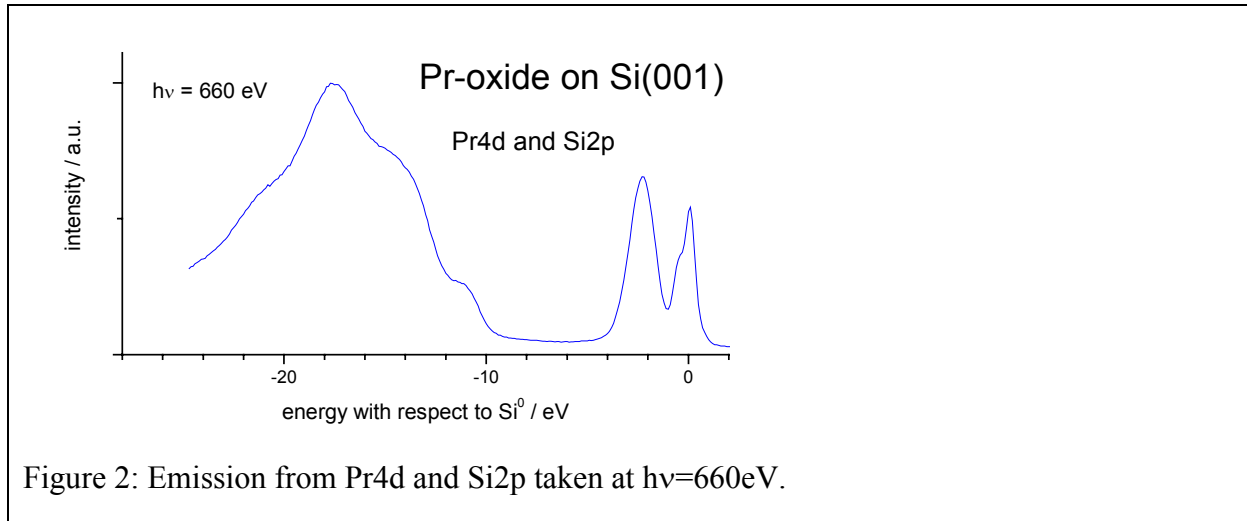
strate), the band starts at a binding energy of –108eV.

The Si2p levels are shown in more detail in Fig.3. The epitactic grown Pr-oxide layer causes a chemical shift in the Si2p emission of about 2eV which differs from that of SiO_2 (4.0eV shifted to higher binding energy relative to $Si2p^0$). These data demonstrate that the Si substrate reacts with the Praseodymium oxide. The shift of the Si2p line indicates an oxidation state between +2 and +3 which is characteristic for Silicates. The large contribution of the

Figure 3: Detailed view of the Si2p emission taken at 660eV.
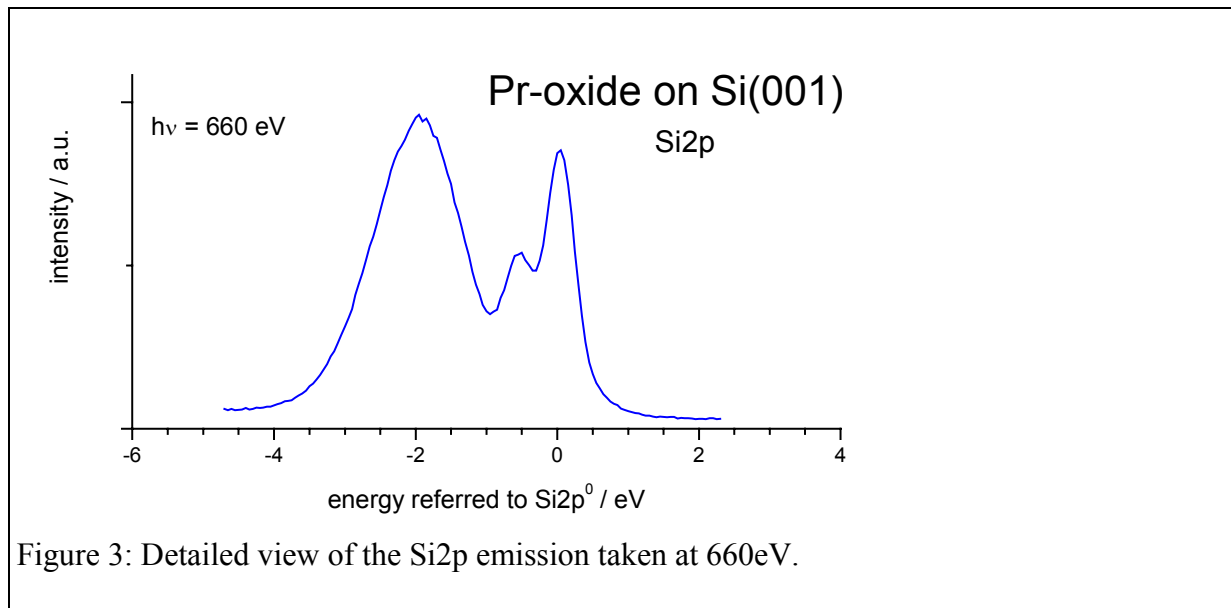
chemically shifted Si2p emission leads us to conclude that the growth of a Pr-Silicate on the Si(001) occurs. We find that the composition of the interface is not dependent on the thickness of the Pr-oxide film. Even at lowest coverage, the specific Pr and Si features are developed. We conclude that a chemical reactive interface exists, consisting of a mixed Si-Pr-oxide such as $(PrO_2)_x(SiO_2)_{1-x}$, typically in non-stoichiometric composition.

The mixed Si-Pr-oxide (Pr-Silicate) has a significant contribution of PrO_2 because of the strong Pr4f emission in the valence band data. Further experimental evidence of the PrO_2 phase comes from the binding energy of the O1s core level and the intensity of the satellite structure in the Pr3d levels. These results are based on our comparative studies of Praseo

dymium oxide films on the reactive Si(001) as well as the non reactive SiO_2 substrate and of Pr-Silicides [5].

[1]   H.J. Osten et al., IEDM Technical Digest (2000) 653.
[2]   H.-J. Müssig, J. Dąbrowski, K.Ignatovich, J.P.Liu, V.Zavodinsky, H.J.Osten, Surface Science, in press.
[3]   D.Schmeißer, H.-J.Müssig, E-MRS 2002, to be published.
[4]   S.Lütkehoff, M.Neumann, A.Slebarski, Phys.Rev. B **52** (1995) 13808.
[5]   D.Schmeißer, P.Hoffmann, H.-J.Müssig, to be published.

Finite-size effect in an antiferromagnet: Resonant magnetic scattering from ultrathin Ho-metal films

E. Schierle, H. Ott, C. Schüßler-Langeheine, D. V. Vyalikh, A. Starodubov, G. Kaindl, E. Weschke

Institut für Experimentalphysik, Freie Universität Berlin, Arnimallee 14, D-14195 Berlin, Germany

V. Leiner, H. Zabel

Institut Für Experimentalphysik IV, Ruhr-Universität Bochum, 44780 Bochum, Germany

Properties of systems with reduced spatial dimensions may differ strongly from those of the respective bulk material. Such effects have to be taken into account if, for the sake of miniaturization, spatial dimensions are reduced but bulk-like properties should be preserved, or, on the other hand, can be utilized to create systems with special properties. Thin magnetic films are of quite some interest because they are used in magnetic storage media and novel devices like GMR sensors. Besides ferromagnetic layers, which are usually the main components of such devices, antiferromagnets have attracted considerable interest because their magnetic structure is comparably insensitive to external magnetic fields. Therefore they can be used to define the magnetic orientation of an adjacent ferromagnetic layer. Besides structural differences between bulk samples and thin films caused by strain and relaxations, one further has to consider effects of the shape anisotropy of the film and such that simply result from the small number of atoms in directions of the film normal. Of the latter kind is the finite-size effect, *i.e.*, the decrease of the magnetic ordering temperature with decreasing film thickness. This effect is rather well known for ferromagnets and the observed data agree well with mean-field considerations predicting a power-law relation [1]:

$$\frac{T^*(\infty) - T^*(d)}{T^*(\infty)} = Cd^{-\frac{1}{\nu}}.$$ (1)

$T^*(\infty)$ is the ordering temperature of the bulk system, $T^*(d)$ that of a film of thickness d, C a constant. ν is the critical exponent, which governs the temperature dependence of the magnetic correlation length in the vicinity of the bulk ordering temperature.

We investigated how the reduced thickness is reflected in the magnetic properties of antiferromagnetic Ho films. Resonant magnetic x-ray scattering in the soft x-ray range at the lanthanide M_5 resonances had proven to be a powerful tool for the investigation of ultrathin magnetic films [2], especially for those with 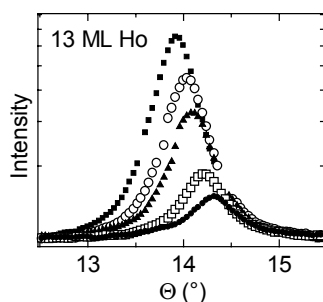antiferromagnetic order, where the diffraction pattern is clearly separated from the charge scattering pattern. We studied Ho films with thicknesses of 80 monolayers (ML), 19 ML, and 13 ML, respectively. Ho films were grown by the method of molecular beam epitaxy on sapphire with a Nb buffer layer, sandwiched between two Y layers [3]. The multilayer system was covered by a top Nb layer to prevent oxidation. The experiments were performed at the U49/1-SGM beamline using a home-built UHV-compatible ($\Theta/2\Theta$) diffractometer. As example, Fig. 1 displays transversal scans across the magnetic (00τ)-satellite taken from the thinnest film at a photon energy corresponding to the maximum of the M_5

Fig. 1: Transversal (rocking) scans across the magnetic (00τ) satellite from a 13-ML-thick Ho film at various temperatures between 49 and 70 K.
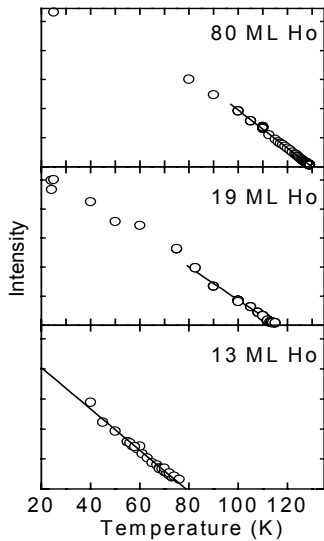
Fig. 2: Intensity of the magnetic satellite versus temperature plotted for the three different films. The thickness dependence of the ordering temperature is clearly visible.
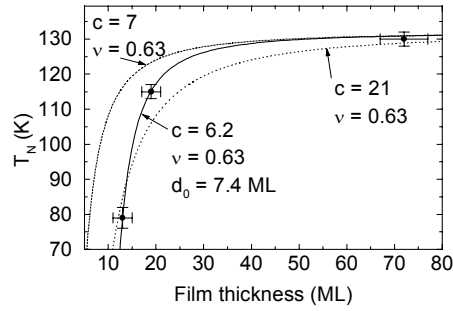

Fig. 3: Néel temperature versus film thickness compared to three different power-law models.

absorption edge. The presence of the magnetic super-structure satellites demonstrates the persistence of the helical antiferromagnetic structure down to Ho thicknesses of 13 ML in these particular samples, probably due to the presence of the Y layers.

The integrated peak intensity is proportional to the square of the antiferromagnetic order parameter and hence decreases with increasing temperature; the shift of the peak position reflects the temperature dependence of the magnetic period. The sample scans of Fig. 1 illustrate the high data quality that can be obtained even from a film as thin as 13 ML. The temperature dependences of these integrated intensities for the three films studied are summarized in Fig. 2. It turns out that in the vicinity of the ordering temperature, the intensities can be well described by linear functions (solid lines). The extracted Néel temperatures as a function of Ho film thickness are shown in Fig. 3. The dashed line represents the behavior of Gd [1], which differs significantly from that found here for Ho. The best fit of the data using Eq. (1) is given by the dotted line, which is not at all adequate and moreover results in an unreasonably large C value. A very satisfactory description, however, can be found if equation (1) is modified by introducing a 'zero thickness' d_0 [4]:

$$\frac{T*(\infty) - T*(d)}{T*(\infty)} = C(d - d_0)^{-\frac{1}{\nu}}.$$

Such a behavior was found for antiferromagnetic Cr metal [4], with d_0 representing the minimum thickness required to develop the incommensurate spin-density wave, even though a deeper understanding is still missing. The analysis of the present data yields $d_0 \approx 7$ ML, which in fact corresponds to the stability limit of the antiferromagnetic helix in Ho [5]. On the other hand, the adjacent Y layers might as well play a role, since the period corresponding to the Fermi-surface nesting vector in Y is approximately 7 ML. The role of Y will be elucidated by corresponding experiments from uncapped Ho films, grown *in situ* on W(110).

References:
[1] M. Farle *et al.*, Phys. Rev. B **47**, 11571 (1993).
[2] C. Schüßler-Langeheine *et al.*, J. Electr. Spectrosc. Relat. Phenom. **114-116**, 953 (2001).
[3] V. Leiner *et al.*, Physica B **283**, 167 (2000).
[4] E. E. Fullerton *et al.*, Phys. Rev. Lett. **75**, 330 (1995).
[5] N. Bohr and D. M. Moncton, Physica B **159**, 93 (1989).

XAS investigation of texture development in TiO_2 thin films prepared by IBICVD

F.Gracia, A.I.Martin-Concepcion, A.Barranco, J.P.Holgado, J.P.Espinos, F.Yubero, D.R.Batchelor[1], D.Schmeißser[2], and A.R.Gonzalez-Elipe

ICMSE C/ Americo Vespucio s/n 41092 Sevilla, Spain
[1] BESSY GmbH, Albert-Einstein-Str. 15, D-12489 Berlin, Germany
LS Angewandte Physik – Sensorik, BTU Cottbus, 03044 Cottbus, Germany

We have performed an XAS investigation of thin film samples of TiO_2 (~100 nm thick) prepared by ion beam induced chemical vapour deposition (IBICVD). The method of preparation consists in the decomposition of a volatile precursor by bombardment of O_2^+ ion beams of 400 eV. The thin film deposition takes place at room temperature. The thin films prepared with this method are flat, dense, and in general amorphous due to the ion beam assistance. Details about the experimental preparation conditions can be found in ref.[1].

Due to the fact that the thin film growth takes place under ion bombardment (ion ranges ~2 nm) disorder is favoured during growth. In fact, characterization of the as deposited thin films by conventional X-ray diffraction (XRD) shows absence of well defined diffraction reflections, indicating that the film either is amorphous or that there is no the long range (~10 nm) crystalline order [2]. However post-annealing at 700K of these TiO_2 thin films induces crystallization to anatase phase as it is clearly evidenced by XRD. Besides, texturization of the film is evidenced by the preferential orientation of several crystallographic planes parallel to the thin film surface [2].

With the beamtime allocated to our project at the beamline U49/2-PGM2, we wanted to investigate the local crystal field around the atoms of the films. In particular, it is well know that the e_g and t_{2g} components of the crystal field splitting show up in the O K absorption edge.

The experiment consists in the acquisition of the Ti $L_{2,3}$ and O K absorption edges in two different experimental geometries: with normal and grazing incidence of the X-ray photons with respect to the thin film surface. By measuring normal to the surface, the electric field of the radiation is parallel to the thin film surface while it interacts with the atoms of the sample. On the other hand, using grazing incidence (70º in our case) an important component of the electric field of the radiation normal to the surface interacts with the sample atoms. Note that if all the bonds between the atoms in the film are randomly oriented in space, both measurements (normal and grazing) must show the same spectra. However, if there is a preferential orientation of the bonds in the film, this asymmetry will show up as differences in the normal and grazing absorption spectra.
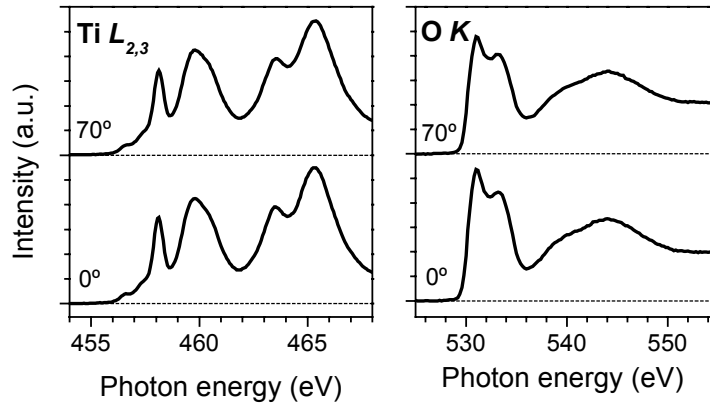
Figure 1. Ti $L_{2,3}$ and O K absorption spectra measured at normal (0°) and grazing (70°) incidence of thin film of TiO_2 as prepared at room temperature by IBICVD

Figure 1 shows the Ti $L_{2,3}$ (left) and O K (right) absorption edges measured with normal (0°) and grazing (70°) incidence of the radiation of a thin film of TiO_2 as prepared at room temperature.

The Ti $L_{2,3}$ absorption spectra are characterised by the spin-orbit splitted L_3 (456-462 eV) and L_2 (462-468) edges. These bands split due to the crystal field interaction. The intensity of the crystal field is related to the crystal field parameter 10Dq so that the shape of the Ti $L_{2,3}$ spectra in our sample is coherent with a 10Dq value of ~1.9 eV [3]. On the other hand, two main regions can be identified in the O K spectra. The first two-peak structure between 529 and 535 eV is due to the oxygen 2p empty states hybridized with the Ti3d band. The structure between 538-548 eV is due to the O 2p states hybridized with Ti 4s and 4p states. Moreover, in the first 3d band the t_{2g} (~531 eV) and the e_g (~ 533 eV) symmetry bands separated by the ligand field splitting $\Delta d = E(e_g) - E(t_{2g})$ can be identified [4]. In this case it is found $\Delta d = 2.1$ eV. This value is a bit small compared with the observed ligand field splitting in well crystallize anatase TiO_2 materials. On the other hand, the relative intensity between these two subbands reproduces well the expected degeneration degree of d levels for d^0 electronic structure.

It is observed that the Ti $L_{2,3}$ and O K spectra of this sample do not show any dependence on the angle between the propagation vector of the light and the surface normal, thus confirming that the Ti-O bonds are randomly oriented without any preferential orientation.

Figure 2 shows the Ti $L_{2,3}$ (left) and O K (right) absorption edges measured with normal (0°) and grazing (70°) incidence of the radiation of a thin film of TiO_2 after annealing to 700 K. The assignment of the different structures of the two absorption edges is the same described above. In this case it is observed that the crystal field parameter from the $L_{2,3}$ spectra 10Dq is ~2.2 eV. The ligand field splitting deduced from the O K edge is $\Delta d = 2.5$ eV characteristic value of well crystallise TiO_2 anatase. However, the main difference with the situation presented in figure 1 (as deposited samples) is the strong geometry dependence of
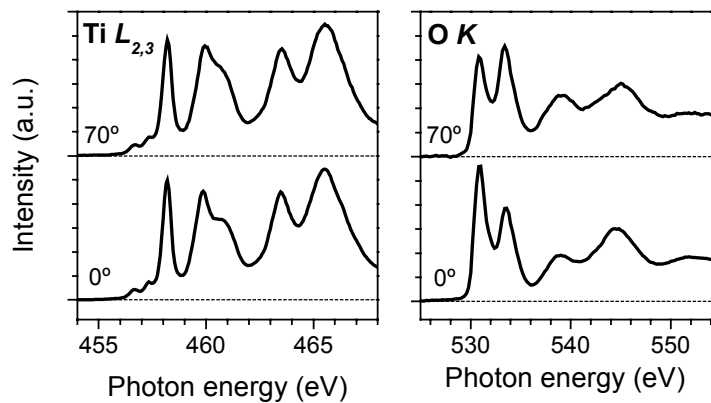
Figure 2. Ti $L_{2,3}$ and O K absorption spectra measured at normal (0º) and grazing (70º) incidence of thin film of TiO_2 prepared by IBICVD after annealing to 700K.

the O *K* edge. We assume that this effect must be correlated with the textured growth observed by XRD [2].

The preliminary analysis of this set of results suggests an increase of the intensity of the crystal field when the TiO_2 samples are well crystallised. Besides, the obtained results appear as a way to estimate by means of XAS the texture in thin films grown with preferential orientation of certain family of planes.

References:

[1] A.R.Gonzalez-Elipe, J.P.Espinos, A.Barranco, F.Yubero, A.Caballero, J.Phys. IV France 9 (1999) Pr8-699

[2] F. Gracia, S. Rath, J.P.Holgado, F.Yubero, A.R.Gonzalez-Elipe (to be published)

[3] M.F.M. de Groot, J.C.Fuggle, B.T.Thole, G.A.Sawatsky, Phys. Rev. B 41 (1990) 929 .

[4] M.F.M. de Groot, M.Grioni, J.C.Fuggle, J.Ghijsen, G.A.Sawatsky, H.Petersen, Phys. Rev. B40 (1989) 5715.

NEXAFS and photoemission investigation of electrochemically deposited organic layers on p-Si(111)

D.R. Batchelor [1], P.R. Bressler [1], P. Hartig [2], J. Rappich [2], and Th. Dittrich [3]

[1] BESSY GmbH, Albert-Einstein-Str. 15, D-12489 Berlin, Germany
[2] Hahn-Meitner-Institut, Abteilung Silizium-Photovoltaik, Kekuléstrasse 5, D-12489 Berlin, Germany
[3] Technische Universität München, Physik Department E16, D-85748 Garching, Germany

Introduction

Solid state and semiconductor principles predict intriguing new properties for structured layers of organic molecules on metal and semiconductor surfaces. The structural and electronic properties give rise to unique applications such as nanopatterning with self-assembled monolayers [1,2]. Controlled interfacing organic molecules with semiconductor surfaces has the fundamental benefit that individual electronic properties can be tailored. The well-developed state of silicon-based device technology and the general bio-compatibility of silicon make silicon surfaces of particular interest for applications in biotechnology. Determining the bonding of organic molecules to a silicon surface is the initial step in describing the processes of organic layer deposition.

A relatively simple - and therefore technologically interesting - method of grafting organic layers on silicon is by electrochemical deposition. The method has the advantage over more traditional techniques such as Langmuir-Blodgett in that the electrochemistry is utilised to control the reaction and ordering at the surface. The BESSY HMI TUM cooperation carried out first trial experiments to prepare and characterise such silicon-organic compound systems.

Experiment and Results

The films were produced using a new and improved technique similar to that described by Allongue et al [3]. The wafer samples were transferred to the SIFES experimental station via a fast entry load lock. Partial yield NEXAFS and photoelectron spectroscopy (Specs PHOIBOS 150 analyser) were performed at 5×10^{-10} mbar on the PM-1 beam line. NEXAFS was measured at the carbon, nitrogen and oxygen edges over a range of angles from normal to grazing incidence (0-75^0). Photoemission spectra were recorded at various photon energies to probe the surface sensitivity. A hydrogen terminated silicon wafer was used as a reference for the NEXAFS measurements.
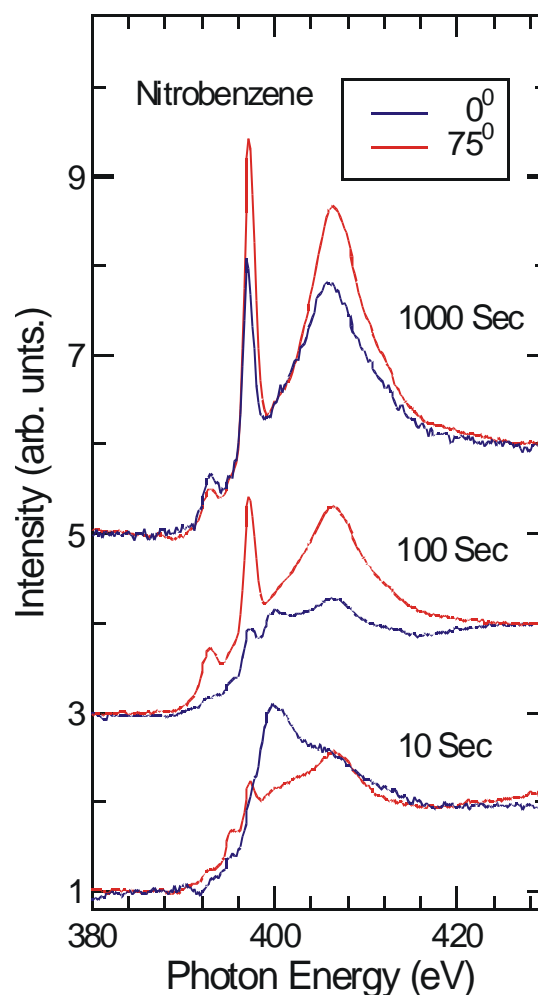
Figure 1.: Nitrogen partial yield NEXAFS from Nitrobenzene normal (0^0 blue) and glancing incidence (75^0 red) for deposition time 10, 100, and 1000 seconds. The spectra have been normalised after the edge.

Figure 1 shows the NEXAFS nitrogen edge spectra as a function of deposition time for Nitrobenzene at normal and glancing inci-
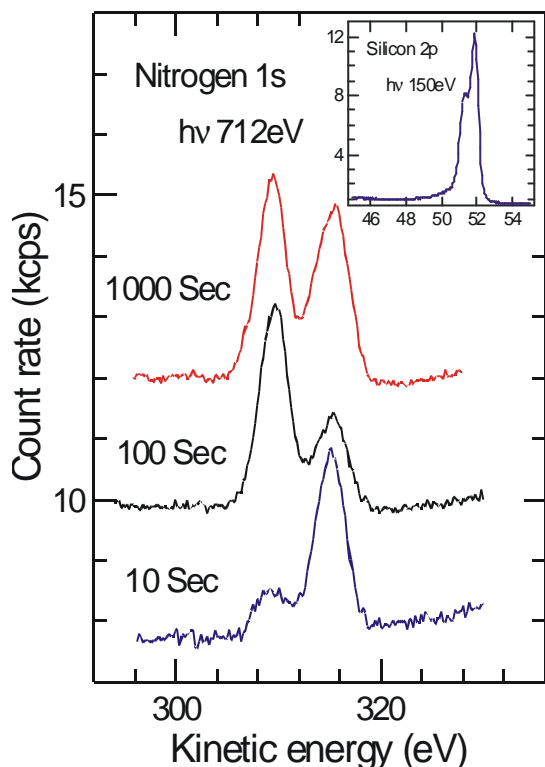
Figure 2.: Nitrogen photoelectron spectra taken at glancing incidence for the three Nitrobenzene films. The spectra from the 100 and 1000 sec films have been displaced by 2 and 4kcps respectively. The insert shows a Silicon 2p core level for a photon energy of 150eV.

dence. As the film thickness increases three peaks, two sharp π^* resonant like peaks and a broad σ^* like peak, dominate the spectrum the angular dependence of which is weak but correlated. The 10 second film shows a very different spectrum with some features in the glancing incidence reminiscent of the thick film. Figure 2 shows the N 1s core level in photoemission for the nitrobenzene films. Two species separated by 5eV can be seen. The relative ratios of the peaks is not a linear function of the deposition time and indicates the occurrence of different chemical reactions. The insert to Figure 2 shows the hydrogen terminated silicon (111) surface which is used as the substrate. The silicon 2p splitting is clearly seen and the spectra shows no evi-

dence of a Si^{4+} oxide state. A weak tail attributed to submonolayer fractions of the suboxides can be seen however. At this kinetic energy the spectrum is surface sensitive and the suboxide contribution is estimated <0.1ML. For comparison a methoxy benzene film was investigated as well. Figure 3 shows the carbon edge NEXAFS for the 10 second, 1000 second nitrobenzene and 100 second methoxy films.
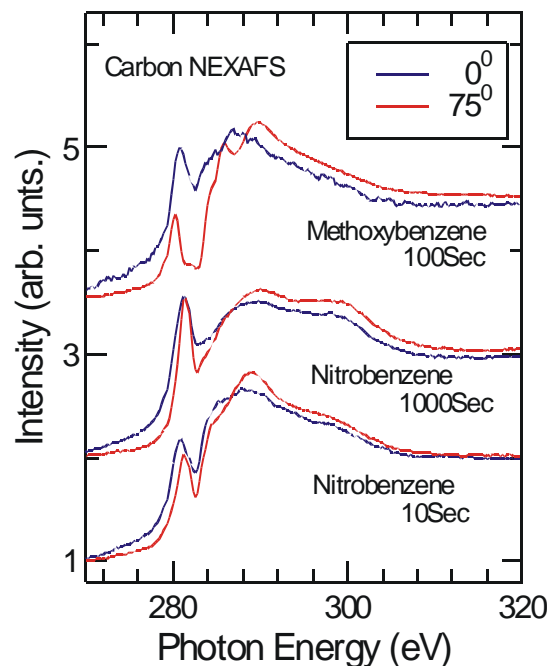
Figure 3.: Carbon partial yield NEXAFS spectra taken for the the 10 and 1000 second nitrobenzene films and a 100 second methoxybenzene film. The spectra have been normalised after the edge.

Further investigations and a comparison of these compounds are in process.

Summary
These first results demonstrate the feasibility of investigating electrochemically grafted films ex-situ by NEXAFS and PES. The spectra show orientation and growth mode dependent features Further investigations will help describe and optimise the growth process.

References
1. A.Ulman, Chem.Rev. 96:1533 (1996).
2. W.Geyer et.al. Appl.Phys.Lett.75:2401(1999)
3.P.Allongue, Electrochim. Acta 43:2791 (1998).

Intermolecular coupling and band dispersion in ultrathin organic films

Ying Zou, R. Fink, D. Gador, C. Buchberger, E. Umbach

Experimentelle Physik II, Universität Würzburg, Am Hubland, D-97074 Würzburg, Germany

Organic molecular thin films have attracted considerable attention due to their promising prospectives as electronic devices. For applications such as field-effect transistors (OFET) or optoelectronic devices like organic light-emitting devices(OLED), charge mobility is one of the key parameters to be increased in order to enhance the device performance. Depending on the electron transport mechanism, hopping or band-like, and on the density of defects and inhomogeneities the charge mobility can vary several orders of magnitude. For such molecular solids, which are usually regarded as Van-der-Waals crystals, the interactions between the molecules might be too weak to enable band formation, which makes coherent (band) transport rather unlikely in such systems [1]. However, in favourable systems the wave functions overlap via the π-orbitals and may even favour the formation of a 1D band.

In order to study possible band formation we investigated epitaxial films of 3,4,9,10-perylene-tetracarboxylicacid-dianhydride (PTCDA) which have been in-situ grown on a Ag(111) substrate by k-resolved photoemission at the BESSY TGM1-beamline. PTCDA grows quasi-epitaxial in its β-modification with the molecular planes parallel to the Ag substrate. Due to limitations in the experimental setup we used normal emission geometry; the photon energy was varied from 25 eV to 70 eV to cover the whole Brioullin zone. Energy calibration was performed with an experimental error of ±25 meV.
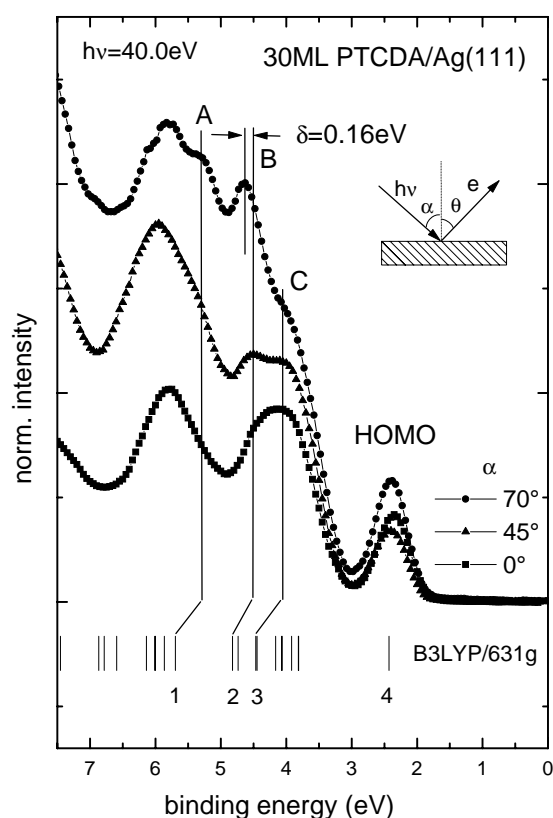
Fig. 1: Normal emission UPS spectra of a 30 ML thick PTCDA film adsorbed on Ag(111). The definition of polar angle α is shown in the insert. Bottom: results of DFT calculations (see text).

Fig.1 shows normal emission UPS spectra of a 30 ML thick PTCDA films recorded with photon energy hν = 40 eV under three polar angles, α = 70°, 45°, and 0°. On the bottom of Fig. 1 the results of a density functional theory (DFT) calculation are displayed. They were , carried out utilizing the Gaussian98 program with a 631g basis set whereby three hybrid functionals which include a mixture of Hartree-Fock exchange and DFT exchange-correlation (B3LYP) are adopted. The calculations agree well with features in the experimental spectra. The small shift of 0.16 eV of peak B between the polar angles 70° and 45° may not yet be uniquely ascribed to band dispersion, since cross section or matrix element effects may also influence the spectra. Furthermore, the features A and B around 5eV show the same polar dependence as the HOMO, indicating their π-orbital origin.

In Fig. 2 a series of normal emission UPS spectra for excitations in the photon energy range from 26 eV to 70 eV is shown. The features have been labelled as in Fig. 1. One can easily trace distinct shifts of feature B around 4.7eV. Feature A around binding energy 5.3 eV also shows a subtle but discernible energy shift

in „anti-phase" relative to feature B. Since within a three-step model of photoemission, the final continuum state is a parabolic free-electron like band in a constant inner potential V_0 the wave vector component of the photoexcited electron along the surface normal $k_\perp$ can be calculated. Assuming a (reasonable) value of 3 eV for V_0 the peak shifts in Fig. 2 are plotted as a function of $k_\perp$ (Fig. 3). The dispersion clearly demonstrates a cosine-like behaviour with distinct periodicities. We have also illustrated bands B' and C', which we attribute to localized bands and the „anti-phase" dispersing band A. The deduced lattice spacing ($a_\perp = 3.58 \pm 0.1$Å) approximately corresponds to the distance between the PTCDA layers. Thus, we may speculate that quasi 1D-bands are formed along the molecular stacks. The determined band width is ≈ 0.2 eV, from which the charge mobility can estimated as 0.27 cm^2/Vs [2] in reasonable agreement with transport measurements [3]. Thus, we found first experimental evidence for band dispersion in ultrathin PTCDA films. The band width of ≈ 0.2 eV is rather large supporting a band-like transport perpendicular to molecular plane at least at low temperatures.
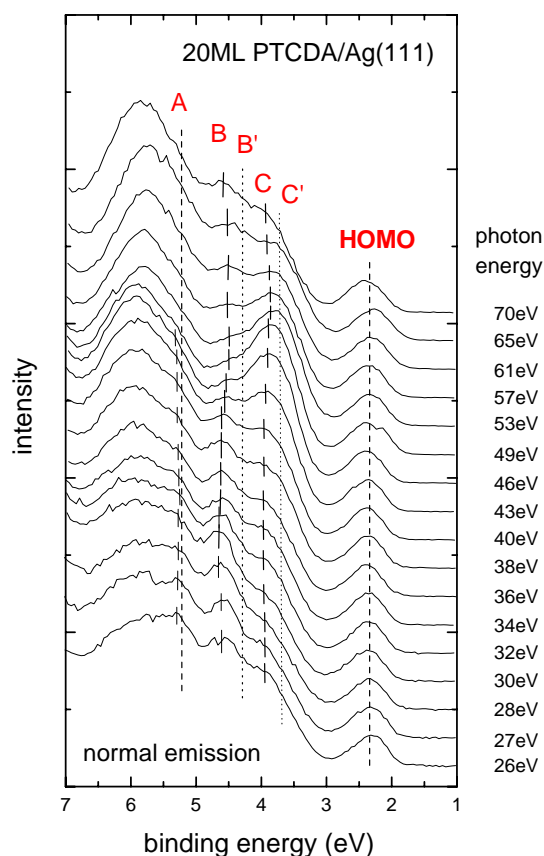

Fig. 2: *Valence-band photoemission spectra of 20 ML PTCDA/Ag(111) recorded in normal emission for $26\ eV \leq h\nu \leq 70\ eV$. The peak positions labelled with tick marks and dash lines for guiding the eyes. The spectra are normalized to the HOMO intensity.*
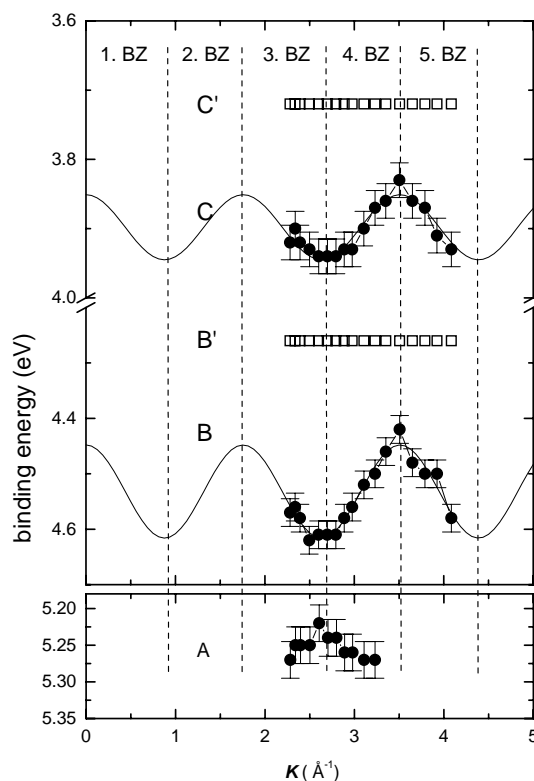
Fig. 3: *Dispersion of the bands A,B,B',C,C' in an extended zone scheme and the best fit (dotted line) in a tight binding model for bands B, C. The non-dispersing bands B' and C' are displayed as hollow squares. The weakly dispersing band A is illustrated at the bottom.*

References:

[1]   G. Horowitz, Adv. Mat. 10 (1998) 365.
[2]   W. Warta, N. Karl, Phys. Rev. B 32 (1985) 1172.
[3]   S. Forrest, M. Kaplan, P. Schmidt, J. Appl. Phys. 55 (1984) 1492.

High-resolution NEXAFS gives new insight into the properties of condensed organic thin films

A. Schöll, Y. Zou, D. Hübner, Th. Schmidt, R. Fink, and E. Umbach

Experimentelle Physik II, Universität Würzburg, Am Hubland,D-97074 Würzburg, Germany

High brilliance third-generation synchrotron sources provide new opportunities, for instance by drastically enhanced spectral resolution and photon fluxes. These improvements can be utilized to get new insight with spectroscopic techniques. A class of materials that has recently attracted enormous interest due to their outstanding optical and transport properties and their applicability as active components in commercial devices are organic thin films. These consist either of polymers or of evaporable medium-size organic molecules. A technique that is ideally suited to study such organic systems is *near-edge x-ray absorption fine structure (NEXAFS)*. This technique can distinguish between chemical states, is (semi)quantitative, can be applied as microscopic probe with a spatial resolution of a few (presently few tens of) nanometers, and provides information about molecular orientation and unoccupied electronic orbitals.

In previous studies of ultrathin films of NTCDA (1,4,5,8-naphthalene-tetracarboxylicacid dianhydride) we could demonstrate that high-resolution NEXAFS spectra of organic thin films reveal a wealth of fine structures that allow the identification of strong electron-vibron coupling and of additional electronic transitions hitherto undiscovered. In particular, NEXAFS resonances corresponding to excitations into molecular orbitals mainly localized on the anhydride groups exhibited very narrow line widths. We therefore decided to start a
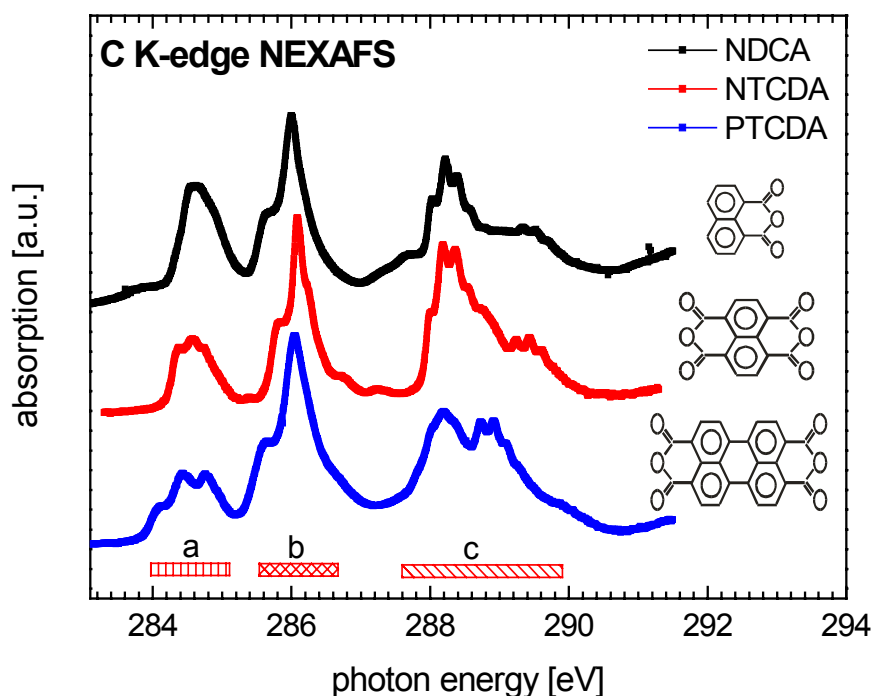

Fig. 1: Comparison of the π^*-regimes of the high-resolution C K-NEXAFS spectra of NDCA (top), NTCDA (center) and PTCDA (bottom) multilayers. The molecular structure of these anhydrides is shown on the right-hand side.

systematic analysis of various anhydrides, e.g., NDCA (1,8-naphthalene dicarboxylicacid anhydride), NTCDA and PTCDA (3,4,9,10-perylene-tetracarboxylicacid dianhydride). Multilayer films of these substances were grown in-situ by vacuum sublimation onto well characterized Ag(111) single crystal substrates. The substrate temperatures during film growth were chosen slightly below the multilayer desorption temperature in order to achieve structural properties close to equilibrium growth, i.e., the structural conformations of the respective single crystals.

Fig. 1 compares high-resolution NEXAFS spectra of NDCA (top), NTCDA (center) and PTCDA (bottom) multilayers. For clarity we have only plotted the regime of the π^*-resonances. Distinct fine structures are discernible for all three molecules. As in the case of NTCDA the fine structure can easily be identified as electron-vibron coupling. However, the astonishing result is that – although the molecules are quite similar – the fine structures strongly differ from substance to substance. The regime around 286 eV (*regime b*), however, is quite similar for all substances. According to ab-initio calculations for NTCDA using the GSF3 program package developed by Kosugi, the resonances around 286 eV stem from excitations into orbitals localized on the aromatic core. The same holds for *regime a*, however, where we detect significant differences. *Regime c* is prominently a fingerprint of the anhydride group.

What do we learn from such high resolution spectra? First, we now get all electronic transitions with very accurate relative intensities and energies (absolute energy accuracy ~0.1 eV, depending on calibration; relative energy accuracy ~10 meV) which, of course, requires some data evaluation (curve fitting). Thus all calculated transitions can be discovered in the experimental data and determined with high accuracy - which has successfully been demonstrated for NTCDA. Since each transition reflects the local properties around one sort of equivalent atoms within the molecule one is now able to distinguish the changes that occur within the molecule due to interactions, e.g. due to the involvement of a certain functional group in a reaction or bonding process.

Secondly, one can easily identify the fine structure as strong electron-vibron coupling. Although expected, such fine structure was not observable in NEXAFS data of organic materials until now. It was usually argued that inhomogeneous broadening and the coupling of too many, partly low-energy vibrations would prevent the observation of electron-vibron coupling in NEXAFS which apparently is not true. Now it is possible to identify vibrations that couple preferably to certain electronic transitions. Since the latter are atom-specific one gets information about local vibronic properties within the molecule.

And thirdly, it is possible to monitor changes of subtle electronic energy shifts, or of vibrational energies and coupling strengths as a function of geometric structure, order within the film, and interaction with other molecules or with the substrate. Some of these effects might be responsible for the differences observed for the three anhydrides of Fig. 1, since the electrostatic moments and the sizes of the aromatic parts, and thus the structural properties and mutual interactions differ. However, this effect has to be investigated in more detail by, e.g., manipulating the structural parameters.

Resonant soft X-ray scattering of amino acid powders: first experiments with the ROSA apparatus

C. Heske[1], O. Fuchs[1], L. Weinhardt[1], E. Umbach[1], K.-H. Hallmeier[2], S.A. Krasnikov[2], L. Zhang[2], R. Szargan[2], M. Grunze[3], and C. Jung[4]

[1]*Experimentelle Physik II, Universität Würzburg, Am Hubland, D-97074 Würzburg*
[2]*Wilhelm-Ostwald-Institut für Phys. und Theor. Chemie, Universität Leipzig*
[3]*Angewandte Physikalische Chemie, Universität Heidelberg*
[4]*BESSY GmbH, Berlin*

Soft X-ray emission spectroscopy (XES) and its resonant counterpart (resonant inelastic X-ray scattering - RIXS) are uniquely suited tools for studying the chemical and electronic structure of a wide variety of materials, including insulators and powders. The nature of a "photon-in-photon-out" technique opens up a completely new window of opportunity for studying the electronic properties of *buried* systems. One particularly intriguing "buried" system is the study of liquids and liquid solutions, for which suitable wet cells with liquid-vacuum windows are necessary. As a starting point on the roadmap towards an understanding of biologically relevant molecules in liquid solutions (or immobilized at surfaces in a liquid environment), we have used the Rotatable Spectroscopy Apparatus (ROSA) and the U41-PGM beamline to study the electronic structure of selected amino acids. Amino acids constitute important building blocks of larger biological molecules (e.g., proteins) and hence a detailed understanding of their electronic and chemical properties is of fundamental importance. ROSA is equipped with a commercially available X-ray emission spectrometer, which, after substantial optimization [1], was commissioned during a beamtime in October/November of 2001.

Fig. 1 presents schematic diagrams of the amino acids cysteine and methionine. Among the 20 most common amino acids, cysteine and methionine are the only ones containing a sulfur atom, which allows an investigation utilizing S $L_{2,3}$ X-ray emission spectra. Such spectra give a wealth of information about the local chemical and electronic environment of the sulfur atoms [2]. It can be envisioned that such atoms can be used as "markers" in substantially larger molecules than probed here. The S $L_{2,3}$ XES spectra obtained for cysteine and methionine powders are shown in Fig. 2. By illuminating the sample with an excitation energy of 200 eV, we collected a non-resonant superposition of electronic transitions involving valence electrons and a S $2p_{1/2}$ or S $2p_{3/2}$ core hole. Due to the spin-orbit splitting of the S 2p levels (1.2 eV), all spectral features are observed in duplicate. Two main features can be distinguished in the spectra of Fig. 2, between 148 and 152 eV (pertaining to 3s states in S atoms bound in a molecular environment) and between 154 and 158 eV. The latter feature most likely arises from a surface oxidation of the amino acid powders. Quite apparently, the emission from the molecular sulfur atoms differs between cysteine and methionine, which is probably due to the fact that in cysteine

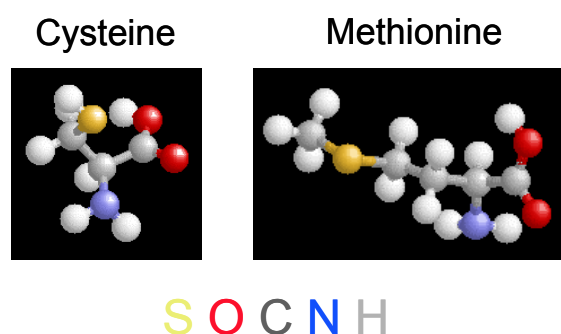### Cysteine   Methionine

S O C N H

Fig. 1: Schematic representation of cysteine and methionine amino acids. The color code represents the different atomic species.

the sulfur atom is bound to one carbon and one hydrogen atom, while in methionine it is bound to two carbon atoms (see Fig. 1). These results hence give a first impression of an experimental approach for investigating the electronic structure of biological systems. Future experiments will aim at a systematic study of selected relevant amino acids, both in powder form and in liquid solution.

A complementary aspect of studying the electronic structure is made possible by using resonant excitation, as demonstrated in Fig. 3 for carbon K emission. In this case, we recorded a series of emission spectra with varying excitation energy. The fundamental process has to be described by the Kramers-Heisenberg-formalism and should hence be regarded as an electronic X-ray Raman scattering process (RIXS). In the case of molecules, a well-defined monochromatic excitation is able to probe specific functional groups of the molecule by selectively exciting certain molecular orbitals. In the case of cysteine in Fig. 3, excitation well above threshold (300 eV) leads to an averaged emission involving all possible occupied states. The shoulder with highest emission energy is associated with the highest occupied molecular orbital (HOMO), as marked. As can be clearly seen in Fig. 3, this shoulder vanishes for near-threshold excitation (286 eV), i.e., for excitation into the lowest unoccupied molecular orbital (LUMO). We ascribe this to the localized nature of the LUMO excitation in a specific functional group of the molecule, which results in a reduced HOMO emission intensity. This finding gives an example of the potential of the RIXS technique for studying large organic molecules.

[1] O. Fuchs, Diplomarbeit, Würzburg 2001.
[2] C. Heske, U. Groh, O. Fuchs, E. Umbach, N. Franco, C. Bostedt, L.J. Terminello, R.C.C. Perera, K.H. Hallmeier, A. Preobrajenski, R. Szargan, S. Zweigart, W. Riedl und F. Karg, phys.stat.sol. (a) **187**, 13 (2001).
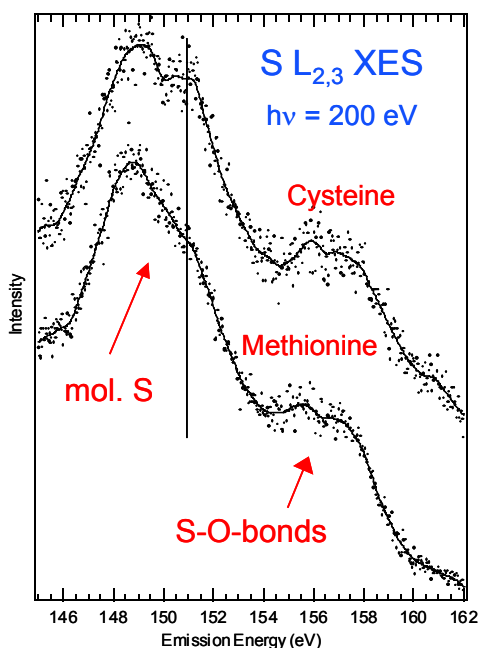
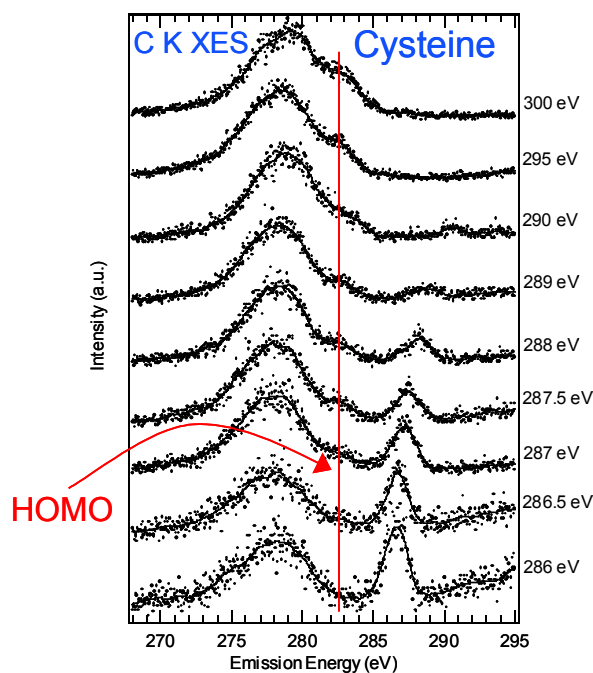Fig. 2: S $L_{2,3}$ X-ray emission spectra of cysteine (top spectrum) and methionine powder (bottom spectrum).

Fig. 3: Series of RIXS spectra for C K emission of cysteine powder. The nominal excitation energy is given on the right hand side.

Effects of lateral quantization in a step-decoration system: Au/W(331)

A. M. Shikin[1,2], O. Rader[1], A. Varykhalov[1,2], V. Mozhaiskii[2], G. V. Prudnikova[2], V. Adamchuk[2], and W. Gudat[1]

[1]) BESSY ⸺ [2]) St. Petersburg State University, St. Petersburg 198904, Russia

Angle-resolved photoelectron spectroscopy has in recent years revealed the effect of quantization on the electronic structure in various systems. In thin films, typically the reflectivity at the film surface and at the film-substrate interface is utilized and, consequently, confinement of electrons and formation of standing waves can be achieved along the direction normal to the film plane [1].

Basically the same physics should govern *lateral* quantization of electronic states, the recipe for which is to take a two-dimensional electronic structure (at a surface or interface) and further confine the electrons by introducing additional one-dimensional barriers. In order to be detected by angle-resolved photoemission, a certain number of atoms needs to participate which, in atomic dimensions, generally requires a periodic arragement of these structures. One good possibility to form such laterally periodic systems is to "decorate" by adsorbed metal atoms the periodically arranged steps that are present at surfaces with a certain miscut relative to a low-index crystal plane. The distance between such self-organized stripes or wires is then determined by the terrace width of the substrate. Lateral quantization at vicinal surfaces, i. e., quantum-well-state formation in the direction perpendicular to the steps, has been demonstrated for surface states on a clean Au(778) surface [2], but for wires or stripes formed by step-decoration no study by angle-dependent photoemission or inverse photoemission has been reported as yet. We have therefore deposited Au on the W(331) surface which is a vicinal W(110) surface at 13° miscut angle, i. e., it consists of (110) microsurfaces (terraces) of ~9.5 Å width with the steps running along the [1-10] direction. We have chosen this system because we can directly compare to the behavior of Au quantum-well states on flat W(110) [3]. The experiment was done at the UE56/1 PGM beamline with linearly polarized light of 62 eV.

Fig. 1 shows series of angle-dependent photoemission spectra for 0.4 monolayer Au on W(331), deposited at room temperature and annealed at about 500°C (a, b) and clean W(331) for comparison (c). The emission angle θ was varied parallel (a) and perpendicular (b,c) to the step direction with the surface projection of the **E** vector lying along the same direction in which θ was varied. Corresponding dispersions are displayed in Figs. 2 and 3. As is seen from Fig. 1a, an intense peak is observed at 1.1 eV for angles close to the terrace normal ($\theta=0°$). Fig. 2a compares its dispersion (filled circles) to the one of a prominent surface resonance (see Ref. 4 and refs.) on flat W(110) (crosses) and a similar peak on pure W(331) (open circles) indicating that these features are related. These peaks as well as other features at 0.5 and 1.5 eV all show energy extrema and maximum intensity close to 0°, i. e., the surface normal of the (110) microsurface.

Spectra measured *perpendicular* to the steps show a very different behavior: Fig. 1b displays a very pronounced peak at 0.6 eV. This feature is Au-induced as it is not present for pure W(331) (Fig. 1c) and does not disperse with photon energy up to at least 80 eV (not shown). Its intensity (Fig. 3b, filled circles) varies strongly with θ. We determine an intensity maximum at $\theta=4°$ (uphill) and almost no intensity at 0°, the (110) normal. This constrasts the surface resonance on W(331) which is centered around the (110) normal (Figs. 1c and 3a). We relate this observation to the formation of Au nanowires at the W terraces. The dispersion of the Au-induced state which likely is a Au-W interface state is influenced by the new periodicity imposed by the step structure. There is further support for the assumption that the angle dependence of the 0.6 eV peak for Au/W(331) is not a singular case: The feature at 1.1 eV also varies strongly in intensity with θ. Fig. 3b (open circles) displays its maxima at $\theta=0°$ and 8°, i. e. it is symmetric around $\theta=4°$. As this peak is intense for $\theta=0°$, it is not surprising that it also appears in the "parallel" geometry in Fig. 1a. Altogether, the 1.1 eV peak disperses substantially parallel to the steps whereas it has a fixed energy when θ is varied perpendicular to the steps, possibly even with stepwise energy changes (e. g., between -1° and -4° in Fig. 1b). This is the behavior of a lateral quantum-well state formed as a result of electron confinement at the step edges. A similar behavior has recently been observed for a surface state on a pure stepped surface [2].

It should be noted that a consequence of our data is that the surface resonance on clean W(331) behaves (110)-terrace-centered while the Au-W interface state behaves according to the superlattice periodicity. This is an interesting observation that is possibly related either to a modification of the potential due to the Au adsorption. Generally, it appears promising to further explore interface states on W to probe the electronic structure of a step decoration system, provided observed peaks are thoroughly characterized since W presents an abundance of bulk transitions that may easily be mistaken for surface or interface ones.

1. See T. C. Chiang, Surf. Sci. Rep. 39, 183 (2000) and F. J. Himpsel et al., Adv. Phys. 47, 511 (1998).
2. Mugarza et al., Phys. Rev. Lett. 87, 107601 (2001).
3. A. M. Shikin, O. Rader, G. V. Prudnikova, V. K. Adamchuk, W. Gudat, Phys. Rev. B 65, 075403 (2002); BESSY Report 2000, p. 195.
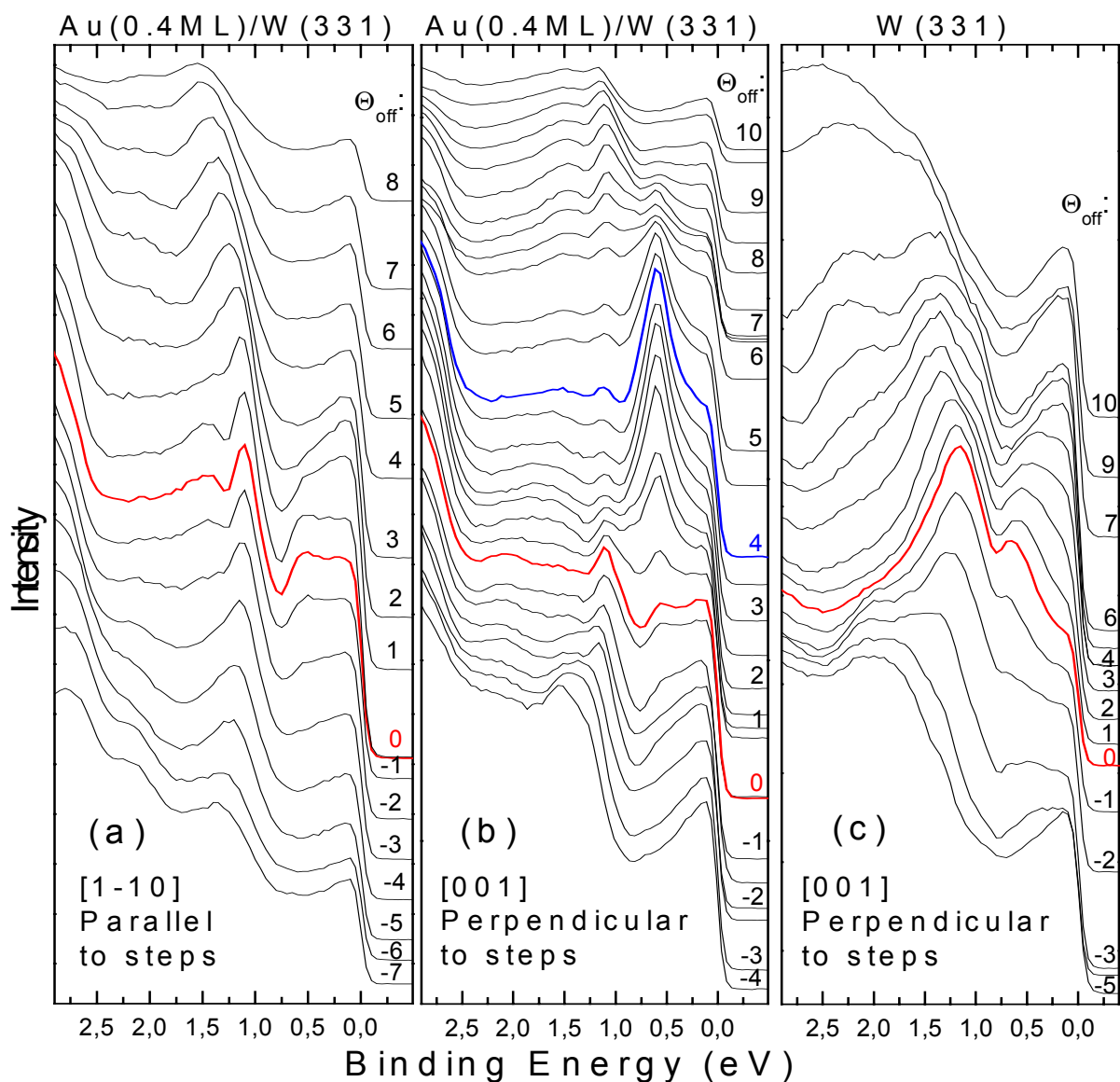
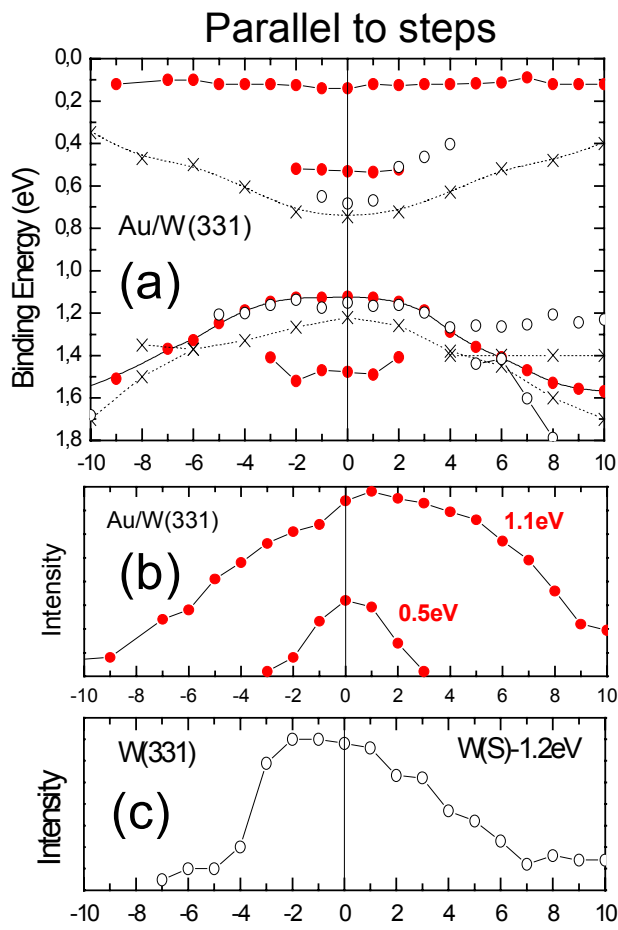Fig. 1. Angle-resolved photoemission from 0.4 ML Au/W(331). Au-induced state appears for 0.6 eV in panel (b).

Parallel to steps

Perpendicular to steps

Binding Energy (eV)

0,0 0,2 0,4 0,6 0,8 1,0 1,2 1,4 1,6 1,8

Au/W(331)

(a)

-10 -8 -6 -4 -2 0 2 4 6 8 10

0,0 0,2 0,4 0,6 0,8 1,0 1,2 1,4 1,6 1,8

Au/W(331)

(a)

-8 -6 -4 -2 0 2 4 6 8 10 12

Intensity

Au/W(331)

(b)

1.1eV

0.5eV

-10 -8 -6 -4 -2 0 2 4 6 8 10

Au/W(331)

(b)

1.1eV

x1.5

x0.5

0.6eV

-8 -6 -4 -2 0 2 4 6 8 10 12

Intensity

W(331)

(c)

W(S)-1.2eV

-10 -8 -6 -4 -2 0 2 4 6 8 10

W(331)

(c)

W(S) - 1.2eV

-8 -6 -4 -2 0 2 4 6 8 10 12

Polar Angle relative to the terrace normal

Fig. 2. Angle dependence parallel to steps of energy and intensity of selected peaks. a: Comparison between Au/W(331) (filled circles), W(331) (open circles), and W(110) (crosses). b and c: Selected intensity variations.
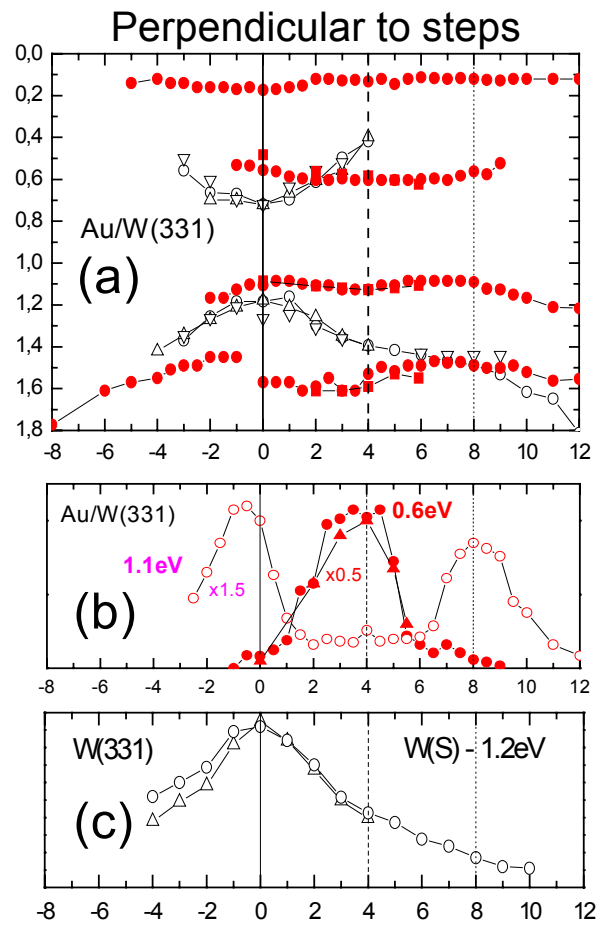
Fig. 3. Same as Fig. 3 for the perpendicular direction. The Au-induced state behaves differently from the surface resonance. Angles with respect to terrace normal.

Observation of lateral superlattice effects in graphene stripes on stepped Ni(771)

A. M. Shikin[1,3], S. A. Gorovikov[2,3], V. K. Adamchuk[3], W. Gudat[1], O. Rader[1]

[1]) BESSY —[2]) MAXlab, Lund —[3]) St. Petersburg State University

A number of interesting phenomena has recently been observed examining the electronic structure of stepped pure crystals by direct, two-photon and inverse photoemission. Typically, a crystal-induced or image-potential induced surface state is picked in order to probe the laterally structured surface by electron spectroscopy or scanning tunneling microscopy [1-4]. In this way it is made sure that electrons are confined to the surface, however, this holds only in a certain part of phase space due to the limited extent of the confining band gap in k-space and the limited energy range, in particular in the occupied part of the valence band accessible in photoelectron spectroscopy. The L-centered Shockley surface state, e. g., extends from E_F down to only -0.4 eV for Cu and Au. Therefore, our aim is to overcome this constraint and try to impose the lateral superstructure of a stepped substrate onto the whole valence band range of a monoatomic overlayer.

Our present work is devoted to step-induced lateral effects in stripes of graphene (i. e., monolayer graphite) formed at Ni(771), i. e., a vicinal Ni(110) surface, which are studied by angle-dependent photoemission in the directions parallel and perpendicular to the stripes. The system was chosen because π and σ states of graphite are strongly dispersive and can very easily be distinguished from the electronic structure of the Ni substrate. The graphene stripes were formed by cracking of propylene at T=500 ^{o}C and a pressure of 1×10^{-6} mbar using a procedure elaborated previously for graphene on Ni(111) [5,6]. Propylene cracking is a self-limited reaction: as soon as the Ni surface is covered with a full graphene sheet, the reaction stops because it can only take place at a pure Ni surface. After additional annealing at 450-500 ^{o}C in ultra-high vacuum the system consists (as shown by STM [7]) of graphene stripes along the Ni terraces with finite width in the perpendicular direction due to the limited size of the Ni(110)-oriented terraces (~12.3Å). Angle-resolved photoemission stectra have been measured at the undulator beamlines I311 at MAXlab and U-125 at BESSY.

Figure 1a shows the polar angle dispersion for π and σ states from photoemission spectra parallel to the stripes. The dispersions resemble almost fully the ones obtained from graphene on flat Ni(111) and can be assigned according to Ref. 5. Compared to monocrystalline bulk graphite, the π and σ branches are shifted towards higher binding energies due to strong interaction of the graphene sheet with the Ni substrate.

The dispersion observed perpendicular to the stripes, shown in Fig. 1b, is very different. First of all, *two instead of one* π and σ band structures can be recognized, and they appear to be interwoven. Both of them lead to photoemission peaks of high intensity with the left-hand-side one somewhat more intense. Secondly, the right-hand-side band structure shows *pronounced gaps* which have no counterpart neither in the parallel dispersion data (Fig. 1a) nor for graphene on flat Ni(111) or in bulk graphite [5]. A third striking observation is that the right-hand-side band structure is *shifted upwards* in energy with respect to the left-hand-side one. This is seen for π as well as for σ branches for the bottom and the top of the branches.

Having established these experimental results, we want to discuss them in greater detail: The left-hand-side branches of π and σ states are shifted relative to the macrosurface normal [771] by –6 to –7°. This value is identical to the miscut angle between the Ni(771) macrosurface and the Ni(110) terrace [6,7]. It allows us to ascribe the left-hand-side branches of π and σ states as (110)-terrace centered. The angle shift of the right-hand-side branches, which are characterized by less intense photoemission peaks, with respect to the left-hand-side branches correlates with the terrace width L=12.3Å. E. g., considering the σ_3 branch we obtain $\Delta k_{||}=2\pi/L$. For the π and σ branches at lower binding energy the situation is more complex possibly because of a modification of the π-σ hybridization due to the influence of the lateral superlattice. A similar situation exists with the opening of band gaps: They do not appear symmetrically around the bottom of the right-hand-side branch, instead they are centered almost exactly around the macrosurface normal. Note that the perturbation due to the superlattice is symmetric along the macrosurface (although there is no strict mirror symmetry about the surface normal) and that this means that the electrons in the right-hand-side

branch feel the influence of the lateral superlattice (as opposed to, e. g., being confined to one terrace by reflection). The left-hand-side branch, centered around the microsurface normal, does not show clear gaps because the electrons are mainly travelling on the terrace. The shifted right-hand-side branch describes electrons affected by the step barrier in the [-1-17] (downhill) direction. The fact that the shifted branch is not due to a simple umklapp process is evidenced by (i) the presence of the band gaps and (ii) by the energy shift of the whole branches which amounts to 0.4-0.5 eV and 0.3-0.4 eV for π and σ_3 branches, respectively. Note that another intensive branch uphill from the terraces is not observed in our experiment.

In conclusion, we have thoroughly characterized the electronic structure of a step-decoration system for the first time and observe that the overlayer electronic structure can very strongly be modified by the choice of the stepped substrate.

1. M.F. Crommie et al., Nature 363, 524 (1993).
2. X.Y. Wang et al, Phys.Rev.B 56, 7665 (1997).
3. J.E. Ortega et al, Phys. Rev. Lett. 84, 6110 (2000).
4. A. Mugarza et al, Phys. Rev. Lett. 87, 107601 (2001).
5. A.M. Shikin et al, Phys. Rev B 62, 13202 (2000); A.M.Shikin et al., Phys.Solid State 42,173 (2000).
6. W.-H. Soe et al, Phys. Rev.B 64, 235404 (2001).
7. R. Koch et al, Phys. Rev B 45, 1525 (1992).
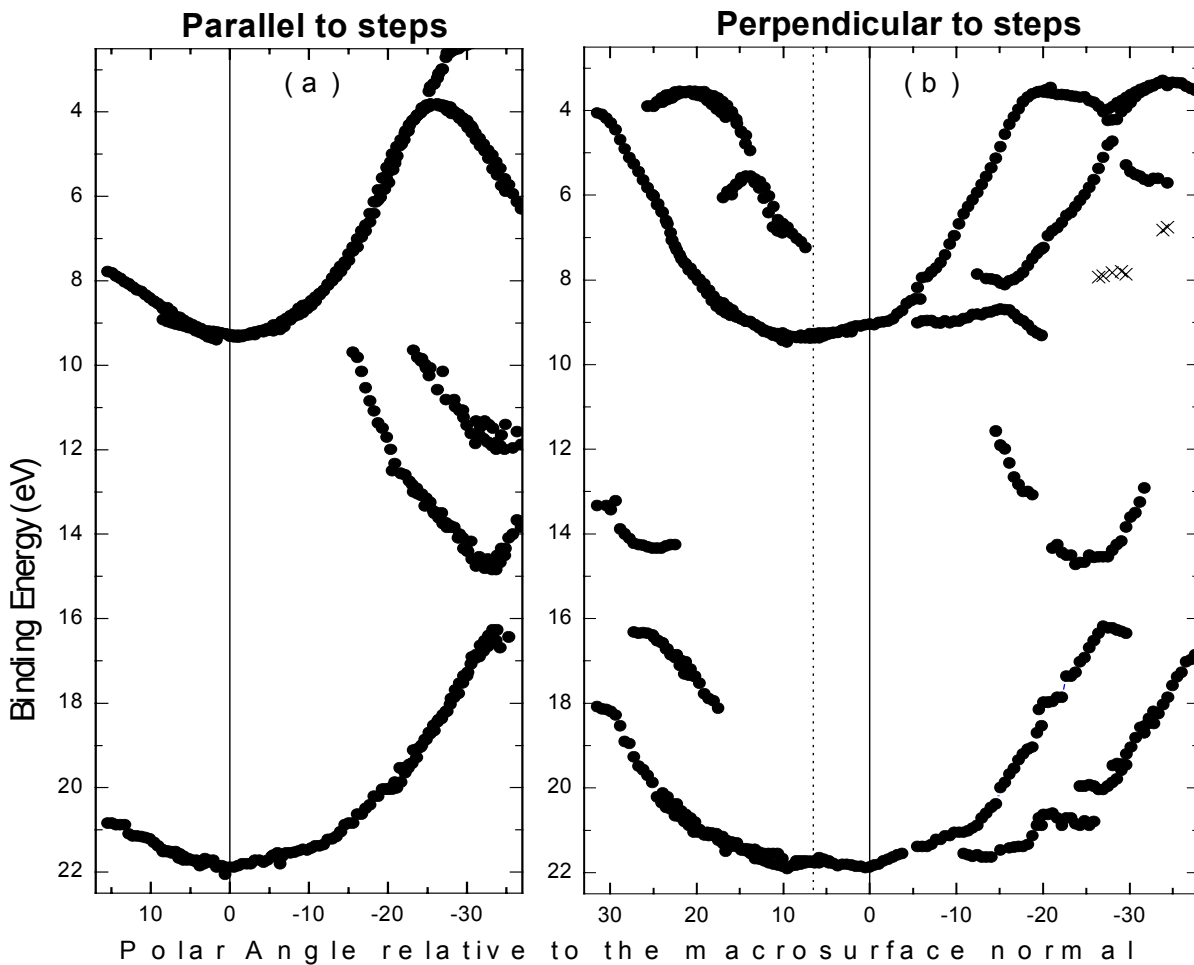
Fig. 1. Angle dispersion from graphene stripes on Ni(771) for emission angles parallel to the stripes, i. e., along [1-10] (a) and perpendicular (b). In (b), uphill, i. e., [-1-17], is to the left, and downhill, , i. e., [-1-17], is to the right.

Resonant photoemission at the Mn 2p threshold of $Ga_{1-x}Mn_xAs$

O. Rader[1], C. Pampuch[1], A. M. Shikin[1], W. Gudat[1], J. Okabayashi[2], T. Mizokawa[2], A. Fujimori[2]
T. Hayashi[2], M. Tanaka[2]

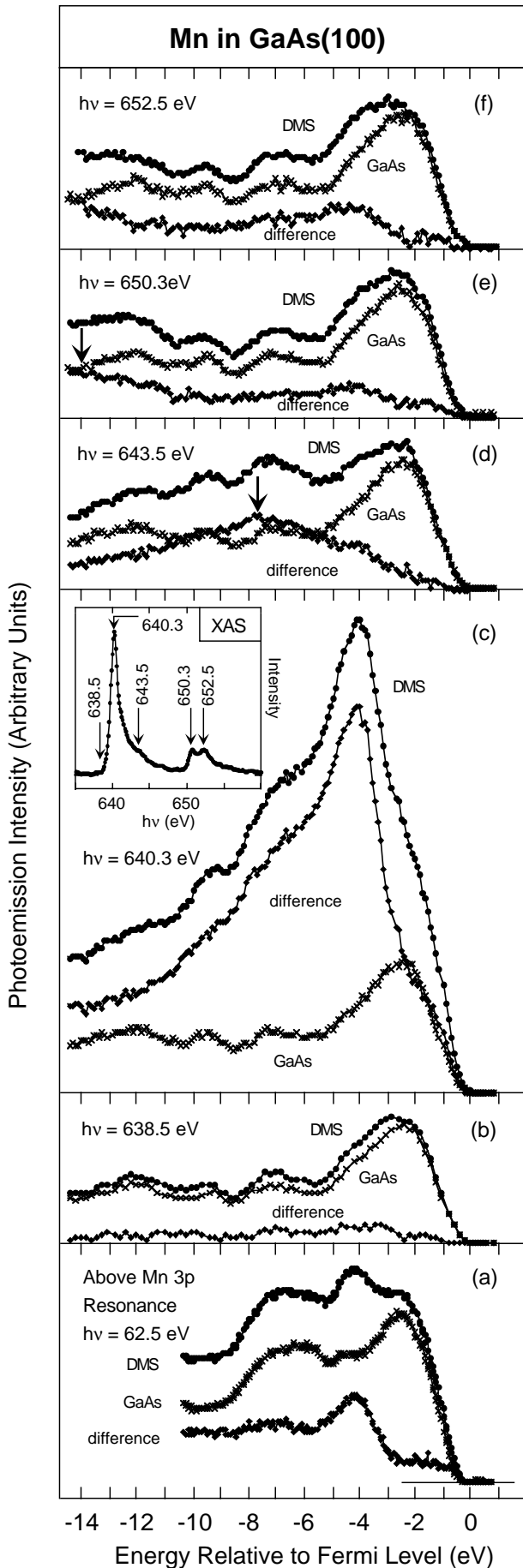[1]) BESSY — [2]) University of Tokyo, Bunkyo-ku, Tokyo 113-0033, Japan

Diluted magnetic II-VI semiconductors have extensively been studied in the past because of their optical properties [1]. Recently, scientific interest has strongly focused on diluted magnetic III-V semiconductors since it has been achieved to dope Mn in molecular beam epitaxy of InAs and GaAs to such concentrations that a spontaneous magnetization occurs [2,3].

It is undisputed that ferromagnetism in these systems is caused by carriers created through Mn doping, but which electron configuration causes the long-range ferromagnetic interaction remains unclear. Progress in this situation can be achieved by a determination of the electronic structure in a photoemission experiment. To decide on the sign of the magnetic exchange interaction between the Mn and its host, the Mn 3d electron configuration needs to be determined. From Mn 2p core level spectra of $Ga_{1-x}Mn_xAs$ we have previously determined the d electron number to be 5 via a configuration interaction analysis [4]. This means that in case Mn forms a neutral impurity of $3d^4$ configuration in the ground state it will be accompanied by a bound As 4p hole in the valence band. Otherwise Mn $3d^5$ with a delocalized As 4p hole will form. Direct measurements of the Mn 3d partial density of states by resonant photoemission at the Mn 3p excitation threshold off resonance (48 eV), on resonance (50 eV), and well above resonance (70 eV) supported this result [5]. In angle resolved, photon energy dependent spectra, the Δ_1 band of GaAs shifts by 0.1 to 0.2 eV to higher binding energy and states induced by Mn doping below E_F are observable for photon energies in the range up to 40 eV [6]. For doping-induced states near E_F there are different predictions from theory: band structure calculations using *FLAPW* for $Ga_{1-x}Mn_xAs$, x=0.5, and a supercell geometry [7] and *LDA+U* [8] find low Mn 3d density of states near E_F while a coherent-potential-approximation calculation for a Mn impurity in InAs and GaAs finds Mn 3d character dominating near E_F [9]. The aforementioned resonant photoemission at and above the Mn 3p threshold has only discerned moderate enhancement of intensity near E_F indicating that 3d character may not be dominating.

Maximum intensity enhancement of Mn 3d as compared to As 4p occurs at photon energies (50 to 70 eV) where probing depth for electrons near E_F assumes a minimum. Therefore, surface disorder, deviation from bulk concentration, or simply surface-induced modification of the electronic structure at a perfectly bulk truncated surface may in principle affect resonant photoemission spectra. For this reason, we have measured resonant photoemission spectra across the Mn 2p threshold (640.3 eV) as well with the aim to compare the more bulk sensitive data to the previous results. The surface preparation of the MBE grown films has been done by sputtering and annealing as described before [4-6]. Precise intensity normalization has been done via equal Ga3d intensity and E_F has been determined from a Mo foil in contact with the sample.

Figure 1 shows spectra taken at the UE56/2 beamline for $Ga_{1-x}Mn_xAs$, x=0.043, (dots), GaAs (crosses), and the difference representing Mn-derived emission (diamonds). Figure 1a displays spectra at 62.5 eV, i. e., above the Mn 3p threshold. The spectral shape changes strongly with concentration and for $Ga_{1-x}Mn_xAs$, x=0.043, it is intermediate between the ones for x=0.035 and x=0.069 in Ref. 5 indicating that the Mn concentration in the near surface region is close to the one in the bulk. Moreover, the difference spectrum shows a maximum at 4.2 eV below E_F which is also consistent with the data of Ref. 5. For each energy, $Ga_{1-x}Mn_xAs$ and GaAs are compared in Fig. 1, and a very small Mn-derived intensity is seen off resonance (b: 638.5 eV), but on resonance (c: 640.3 eV) the enhancement is huge (higher by a factor of 20). The Mn-derived spectral shape is very similar to the one determined at 62.5 eV photon energy with a maximum at 4.2 eV and only moderate enhancement near E_F, e. g, at 1 eV below E_F it is 6 times smaller than at 4.2 eV. The overall shape appears broader than for 62.5 eV. For spectra above the Mn $2p_{3/2}$ threshold (d-f), the intensity enhancement is small. This is different from the 3p threshold where photoemission cross sections for Mn 3d (as compared to those of As and Ga 4p) remain high even 20 eV above threshold. However, the shape of spectra d-f appears to change strongly with photon energy. In order to interpret these changes, expected $2p_{3/2}3d3d$ Auger emission from Mn has been marked by arrows in Fig. 1, and these arrows coincide with broad intensity enhancements. It is concluded that the photon energy dependence above the Mn $2p_{3/2}$ threshold is mainly determined by Auger emission and that therefore a strong Auger contribution possibly causes also the broadened shape of the on-resonance spectrum at 640.3 eV. However, as shown in Ref. 10 for Ni metal, there is substantial (coherent) resonant photoemission intensity at the $2p_{3/2}$ threshold and the 3d density of states can therefore be derived from the on-resonance spectrum. Resonant photoemission calculations based on a configuration-interaction cluster model for Mn in GaAs are on the way to further support our conclusions [11].

In summary, we find that strong photoemission enhancement effects at the Mn 2p threshold can be used to determine the Mn 3d derived emission in a bulk sensitive way. The good agreement between results obtained at low photon energy (around the Mn 3p threshold) and at high photon energy indicate that surface derived

Mn in GaAs(100)

(f) hν = 652.5 eV — DMS, GaAs, difference

(e) hν = 650.3eV — DMS, GaAs, difference

(d) hν = 643.5 eV — DMS, GaAs, difference

(c) hν = 640.3 eV — DMS, difference, GaAs

Inset: XAS, Intensity, 638.5, 640.3, 643.5, 650.3, 652.5, hν (eV), 640, 650

(b) hν = 638.5 eV — DMS, GaAs, difference

(a) Above Mn 3p Resonance hν = 62.5 eV — DMS, GaAs, difference

Photoemission Intensity (Arbitrary Units)

Energy Relative to Fermi Level (eV)
-14 -12 -10 -8 -6 -4 -2 0

features are small for this systems and both methods can be used, at least for the present samples where special effort has been made to reprepare crystalline surfaces.

1. J. K. Furdya and J. Kossut (eds.), Diluted magnetic semiconductors, Academic Press, Boston, 1986.
2. H. Ohno, H. Munekata, T. Penny, S. von Molnar, A. Segmüller, L. L. Chang, Phys. Rev. Lett. 68, 2664 (1992).
3. H. Ohno, A. Shen, F. Matsukura, A. Oiwa, A. Endo, S. Katsumoto, Y. Iye, Appl. Phys. Lett. 69, 363 (1996).
4. J. Okabayashi, A. Kimura, O. Rader, T. Mizokawa, A. Fujimori, T. Hayashi, M. Tanaka, Phys. Rev. B 58, R4211 (1998).
5. J. Okabayashi, A. Kimura, T. Mizokawa, A. Fujimori, T. Hayashi, M. Tanaka, Phys. Rev. B 59, R2986 (1999).
6. J. Okabayashi, A. Kimura, O. Rader, T. Mizokawa, A. Fujimori, T. Hayashi, M. Tanaka, Phys. Rev. B 64, 125304 (2001).
7. M. Shirai, T. Ogawa, I. Kitagawa, N. Suzuki, J. Magn. Magn. Mater. 177-181, 1383 (1998).
8. J. H. Park, S. K. Kwon, B. I. Min, Physica B 281-282, 703 (2000).
9. H. Akai, Phys. Rev. Lett. 81, 3002 (1998) and private commun.
10. M. Weinelt, A. Nilsson, M. Magnuson, T. Wiell, N. Wassdahl, O. Karis, A. Föhlisch, N. Martensson, J. Stöhr, M. Samant, Phys. Rev. Lett. 78, 967 (1997).
11. A. Kimura, A. Tanaka, unpublished.

Fig. 1. Resonant photoemission of GaAs4.3%Mn above the Mn 3p threshold and across the Mn 2p threshold. GaAs4.3%Mn (dots), GaAs (crosses) and the difference (diamonds). The inset shows the absorption spectrum.

Identifying atomic chains: Large surface-state and core-level splittings in Gd/W(110)

O. Rader[1], A. M. Shikin[1,2], C. Pampuch[1], G. V. Prudnikova[2], W. Gudat[1]

[1]) BESSY — [2]) St. Petersburg State University, St. Petersburg 198904, Russia

There is huge interest in the electronic structure of one-dimensional atomic arrangements at surfaces: This holds on the one hand side from the point of view of application because ideally one is able to produce large numbers of quantum-well units with taylored electronic properties at the same instance without the need to manufacture three-dimensional multilayers by stacking layer upon layer. From the other side there is the wish to experimentally test fundamental theoretical predictions concerning the electronic structure like the occurrance of Luttinger-liquid behavior.

Two methods have been explored to fabricate such structures: step decoration of vicinal surfaces and self-organized growth on flat, i. e., low-Miller-index, substrates. We have previously succeeded in showing that the electronic structure of self-organized Au chains on Ni(110) is one-dimensional [1]. A first-principles calculation has shown that formation of the one-dimensional electronic structure in this metal-on-metal system is enabled by band gaps in the substrate [1,2].

Another self-organized metal-on-metal system is Gd/W(110), where a number of one-dimensional structures are observed in the thickness range below one monolayer (ML) [3,4]. The Gd atoms arrange in chains along the [1-10] direction, and with increasing Gd coverage the distance between chains decreases leaving the interatomic distance along the chains unaffected [3,4]. This peculiar behavior is due to dipole formation upon adsorption of Gd on W and concomitant repulsive dipole-dipole interaction between Gd atoms at the W surface. The electronic structure of the W(110) surface, on the other hand, is characterized by large band gaps and an abundance of surface-localized states. A band gap of even symmetry extends from 6.3 to 2.0 eV binding energy along the Γ-N direction (the [110]-direction), and it could be shown that this band gap supports the formation of quantum-well states in Gd films up to 4 ML thickness [5]. Among the aforementioned surface-localized states there is a surface resonance in a spin-orbit induced band gap at 1.2 eV binding energy for normal emission [6]. For this reason, the system Gd/W(110) appears well suited for the observation of effects of the reduced dimensionality of atomic chains in valence-band photoemission. Experiments have been done at the UE56 and U125 beamlines with linearly polarized light at 2×10^{-8} Pa with a VG Escalab hemispherical analyzer. Gd chains and overlayers have been produced by room-temperature deposition and postannealing.

The valence-band spectrum of clean W(110) at the bottom of Fig. 1 shows intense surface-resonance emission at 1.2 eV and W s,p-derived emission at 6.2 eV binding energy. At 0.33 ML, Gd growth can be seen from the Gd 4f peak at 8.3 eV binding energy. At the same time, the surface resonance at 1.2 eV is strongly damped. For 0.47 ML, the former surface-resonance peak shifts to higher binding energy (1.25 eV) and a new peak appears at lower binding energy (0.9 eV). At 1.05 ML, the Gd 4f starts shifting to lower binding energy, and in the former surface-resonance region a new peak at 1.0 eV replaces the features at 1.25 and 0.9 eV.

A very good probe of the electronic structure at the W(110) surface or interface is the large surface core level shift of clean W(110). Figure 2 displays the W 4f (7/2) core level measured together with the valence band. It is seen that the surface component ("S", "S1") stays at rather fixed energy separation from the bulk component ("B") up to 0.54 ML. From 0.40 ML on, a new component ("S2") with very large core level shift starts growing. At the same coverage for which the Gd 4f shifts and the 1.0 eV peak appears in the valence band, the components S1 and S2 are replaced by a new interface core level ("I"). The fit in Fig. 3 locates B at 31.463 eV and S at 31.142 eV in agreement with the literature. At 0.69 ML, the two core level shifts amount to -256 meV (S1) and -562 meV (S2). (The splitting of S2 is thus much larger than the one of 1 ML Gd/W(110) (390 meV) which has been the largest surface or interface shift of W(110) according to Ref. 7.) The splitting between S1 and S2 is thus of the same size as between the two valence-band peaks in the same thickness region.

Based on the structure characterization of Refs. 3 and 4 (see insets in Fig. 3) we identify the split valence band peaks and the split core levels with chain and interchain sites. Although the appearance of three core levels and the size of the shift are unprecedented, the trend is in line with other strongly covalent adsorption systems like alkali or alkaline earth metals on W. The intensity behavior in Fig. 2 tells us that peak S2 (which grows with increasing Gd coverage) must correspond to W sites in contact with the Gd chains and S1 which stays close to the energy of the clean W(110) surface relates to the interchain W atoms. Upon approching 1 ML, the difference between the sites vanishes and a new interface state and interface-core-level shift appear.

Returning to Fig. 1, we observe that between 0.47 ML and 0.92 ML the spectral shape changes also strongly in the range between 6 and 2 eV binding energy. Intense peaks appear and disappear for very small changes in Gd coverage. Due to the W bulk band gap these peaks must be related to either the Gd or the W surface layer. As our resonant photoemission study indicates that they are not Gd derived, we assign these peaks to the confinement of W surface electrons by the repulsive forces of the atomic Gd chains with each spectrum correpoinding to a certain quantum-well width given by the varying interchain distance.
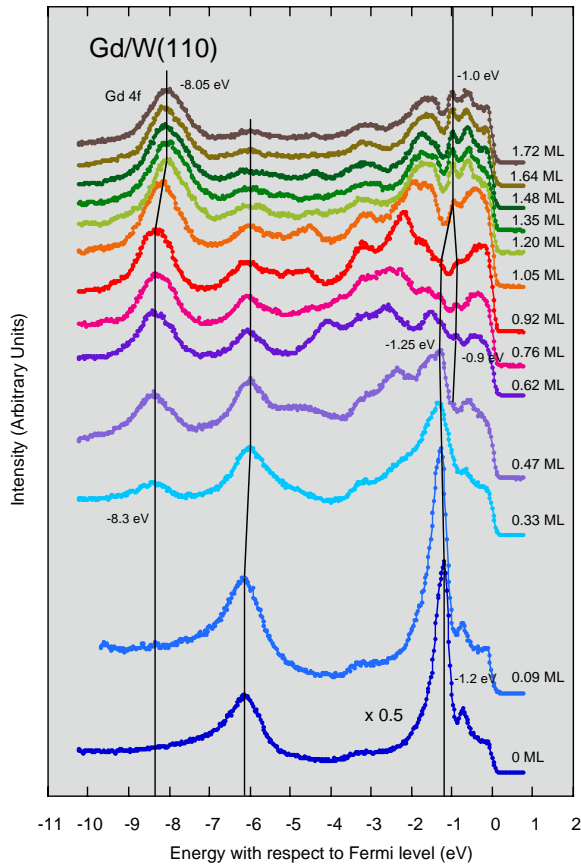
Fig. 1. Photoemission spectra of Gd/W(110) for various Gd coverages at 62.5 eV photon energy.
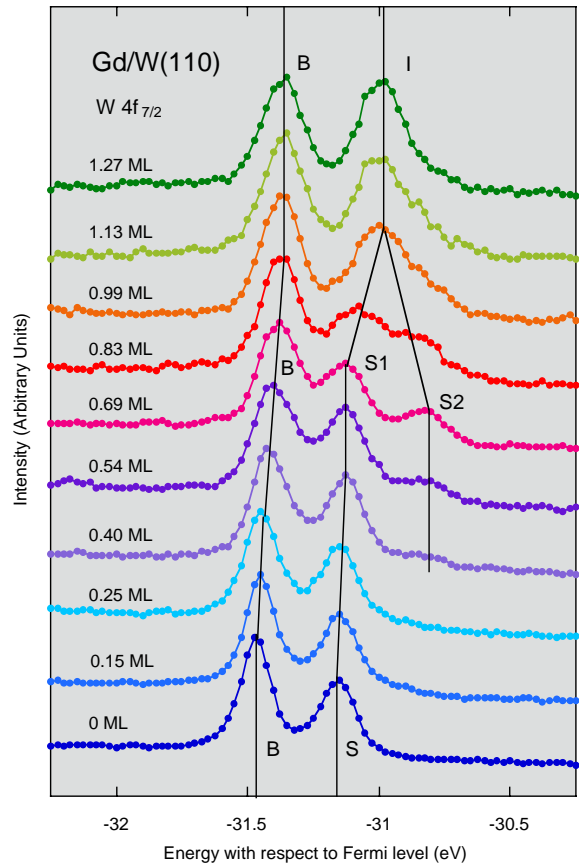

Fig. 2. W 4f (7/2) core-level spectra at 62.5 eV photon energy for Gd coverages corresponding to those of Fig. 1.
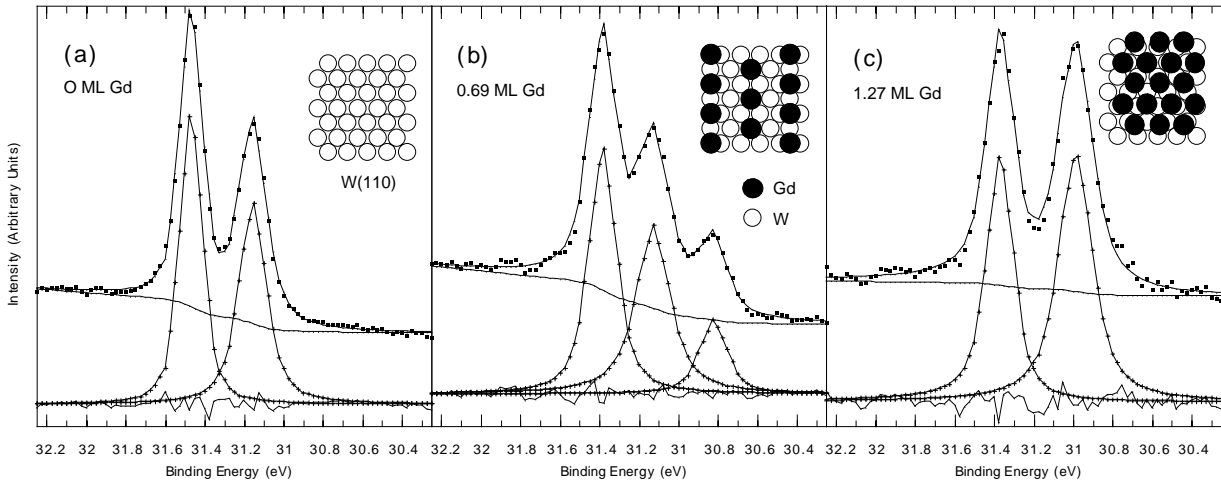

Fig. 3. Results of a least-squares fit to selected spectra of Fig. 2 together with structure models derived from the STM work of Ref. 4.
a: clean W(110), b: 0.9 ML Gd, c: 1.66 ML Gd.

1. C. Pampuch, O. Rader, T. Kachel, W. Gudat, C. Carbone, R. Kläsges, G. Bihlmayer, Blügel, W. Eberhardt, Phys. Rev. Lett. 85, 2561 (2000).
2. Band gaps of the Ni substrate are also believed to cause the spin polarization observed in Ref. 1.
3. J. Kolaczkiewicz, E. Bauer, Surf. Sci. 175, 487 (1986).
4. R. Pascal, Ch. Zarnitz, M. Bode, R. Wiesendanger, Phys. Rev. B 56, 3636 (1997).
5. O. Rader, A. M. Shikin, Phys. Rev. B 64, 201406 (2001); BESSY Annual Report 2000, p. 252.
6. J. Feydt, A. Elbe, H. Engelhard, G. Meister, Ch. Jung, A. Goldmann, Phys. Rev. B 58, 14007 (1998).
7. E. D. Tober, R. X. Ynzunza, F. J. Palomares, Z. Wang, Z. Hussain, M. A. Van Hove, C. S. Fadley, Phys. Rev. Lett. 79, 2085 (1997).

The ammonia oxidation over copper: First experiments with copper clusters investigated by means of in situ NEXAFS

R.W. Mayer, M. Hävecker, H. Bluhm, A. Knop-Gericke, M. Melzer, J. Urban, and R. Schlögl

Fritz-Haber-Institut der Max-Planck-Gesellschaft, Faradayweg 4-6, 14195 Berlin, Germany

Introduction

The partial oxidation of ammonia to nitrogen and water according to

$$4NH_3 + 3O_2 \rightarrow 2N_2 + 6H_2O \qquad (1)$$
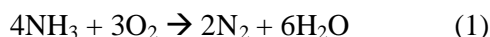
is relevant for a wide range of applications [1] and the subject of this investigation. In addition to reaction (1) the total oxidation

$$4NH_3 + 5O_2 \rightarrow 4NO + 6H_2O \qquad (2)$$

is also preferred in oxygen containing feed gas. Copper and its oxides were found to be potential catalysts for these reactions [1,2]. The aim of our investigation is to reveal the catalytically active surface species. We have found that copper(II)oxide (CuO) catalyzes the total oxidation to NO, whereas copper(I)oxide (Cu_2O) is absolutely necessary for the desired partial oxidation to nitrogen [3]. These results were obtained using a copper foil as model catalyst. However, since real catalysts usually consist of oxide or zeolite supported small copper particles (like Cu-ZSM-5 or Cu/Al_2O_3), the question arises whether these results are transferable to real catalyst systems. To answer this question we have performed experiments using small copper particles that are deposited on a gold grid covered with amorphous carbon.

Experimental

All experiments were carried out in a double chamber UHV system. The first chamber (base pressure 3×10^{-9} mbar) was connected to beamline UE 56/2 at BESSY II. The second chamber is used as reactor and is separated from the first by a 100 nm thick silicon nitride window (Ø 4 mm aperture), withstanding a pressure of at least 100 mbar in the reaction chamber. The detector system is described in detail elsewhere [4,5].

The sample was prepared using the inert gas aggregation method [6], where copper clusters with a mean particle size of 2.8 nm are produced by aggregation of supersaturated copper vapor [7]. For the experiments with the copper clusters we applied the same reaction conditions like in our previous studies with copper foil, i.e. 1.2 mbar absolute pressure, 0.38 ml/min NH_3, and 4.5 ml/min O_2. The pressure in the reaction chamber (p_{abs}) was

adjusted with a valve at the reactor outlet to a foreline pump, and the gas flows were provided by calibrated mass-flow-controllers. Since the clusters were expected to react at lower temperatures than the (bulk) copper foil and to prevent sintering, the clusters were heated from room temperature up to not more than 470K in steps of 50 degrees (in difference to the mentioned studies with copper foil). A quadrupole mass spectrometer is connected to the reaction chamber to analyze the product gas, which allows a correlation of the products with the state of the catalyst's surface.

Results

Fig. 1 shows the NEXAFS spectra of the Cu L_3-edge at different temperatures and time.
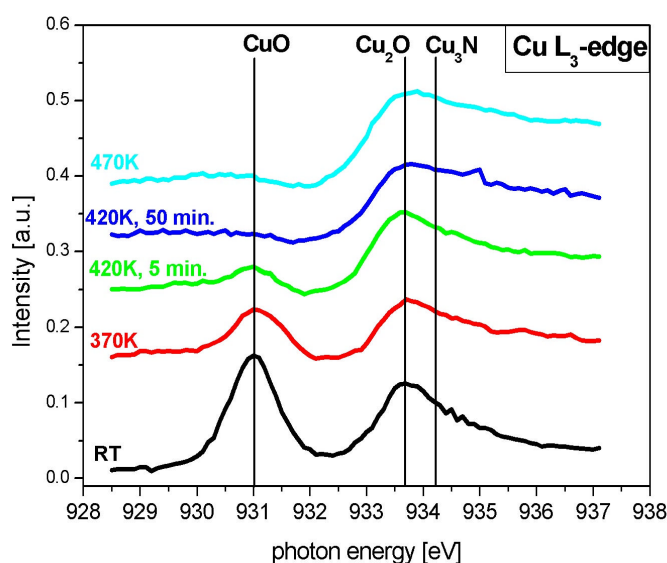
Fig. 1: NEXAFS spectra of the copper clusters at the Cu L $_3$-edge at different temperatures

At room temperature the clusters consist mainly of CuO and Cu_2O, as indicated by the two resonances at 931.0 eV and 933.6 eV. After heating to 370 K a slight reduction of the CuO is visible. This effect is intensified by further heating to 420 K. After 5 min at this temperature only small contributions of CuO are found, and after 50 min no CuO is detectable anymore. Instead, an additional resonance at 934.2 eV appears as shoulder of the Cu_2O resonance. This resonance can be identified as copper(I)nitride (Cu_3N) which is present also after further heating to 470K. Therefore, it can be concluded that the formation of Cu_3N, which is well known from our former experiments with copper foil, also takes place with copper clusters, but – as expected – at lower temperatures. Unfortunately, no ammonia conversion could be detected by mass spectrometry, what is ascribed to the very low total copper content of about 100 µmol in the sample. In addition to in situ NEXAFS, the sample was investigated by TEM

before and after the reaction. The size distributions of the copper clusters determined by the TEM images are shown in Fig. 2.
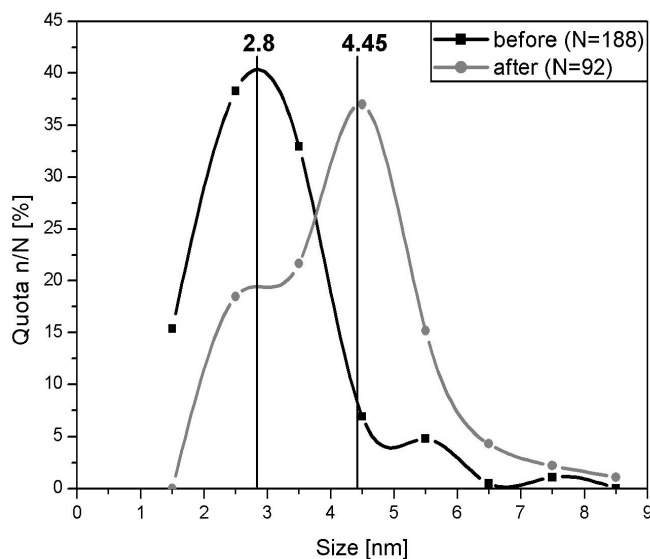
Fig. 2: Size distributions of the copper clusters before and after the reaction

The increased mean size and reduced number of clusters after the reaction indicates a slight sintering of the clusters during the reaction. However, a film formation by spreading of the clusters can be excluded. Thus, the NEXAFS spectra (Fig. 1) are actually obtained from the copper clusters, which have reacted with the gas phase. Since the conversion of ammonia could not be determined by mass spectrometry, further experiments using different gas flows are necessary to provide a longer residence time of the reactants and therefore a higher conversion. We will also investigate if the clusters have reached their equilibrium size with 4.45 nm or if they will sinter even more to form bigger clusters.

References

[1] T. Curtin, F. O'Regan, C. Deconinck, N. Knüttle, and B.K. Hodnett, Catal. Today 55 (2000) 189

[2] H. Bosch and F.J.J.G. Janssen, Catal. Today 2 (1988) 369

[3] R.W. Mayer, M. Hävecker, A. Knop-Gericke, and R. Schlögl, Catal. Lett. 74 (2001) 115

[4] M. Hävecker, A. Knop-Gericke, T. Schedel-Niedrig, and R. Schlögl, Angew. Chem. Int. Ed. 37 (1998) 1939

[5] A. Knop-Gericke, M. Hävecker, T. Schedel-Niedrig, and R. Schlögl, Topics in Catalysis 10 (2000) 187

[6] F.Frank, W.Schulze, B.Tesche, J.Urban, and B.Winter, Surface Science 156 (1985) 90

[7] J.Urban, H.Sack-Kongehl, and K.Weiss, Zeitschrift für Physik D 36 (1996) 73

Quantitative structural determination of the high coverage phase of the benzoate species on Cu(110)

M. Pascal, C.L.A. Lamont
Centre for Applied Catalysis, University of Huddersfield, Queensgate, Huddersfield HD1 3DH, UK

M. Kittel, J.T. Hoeft, R. Terborg, M. Polcik
Fritz-Haber-Institut der Max-Planck-Gesellschaft, Faradayweg 4-6, 14195 Berlin, Germany

J.H. Kang, R.Toomes and D.P. Woodruff
Physics Department, University of Warwick, Coventry CV4 7AL, UK

The benzoate species is a good example of an organic molecule which is complex enough to be chemically interesting, yet at the same time simple enough to be studied using surface science techniques. In recent years there has been a growth in the number of surface science studies of larger organic molecules due to the considerable interest in thin organic films which have potential applications as sensors, optoelectronic devices, etc. For these systems the crystalline structure of the film, i.e. the orientation of the molecules and the long range order within the film, is of key importance as this will determine its optical and electronic properties. Benzoate is an interesting species as it contains two functional groups – the carboxylate group and the aromatic phenyl ring – both of which are known to interact strongly with surfaces. In this paper we describe the results of applying scanned-energy mode photoelectron diffraction (PhD) to provide an independent quantitative determination of the structure of the benzoate species in the higher coverage phase on Cu(110), reported by Frederick et al. [1].

The PhD measurements were performed using light from the HE-TGM1 beamline at the BESSY 1 synchrotron radiation source. The saturated benzoate layer was prepared by exposing the Cu(110) sample to ~ 1.2 x 10^{-4} mbar.s benzoic acid at 330 K, via a pinhole doser terminating ~ 2 cm in front of the sample.

The analysis of the experimental data is based on comparison with the results of full multiple scattering spherical wave simulations for model adsorption geometries using our established methodology [2]. The best agreement between the experimental and calculated spectra for O 1s spectra (fig.1) was achieved for the structural model shown in fig. 2. The benzoate has been found to adsorb, via the carboxylate group, on the short bridge sites. The molecular plane is oriented perpendicular to the surface and along the [$\bar{1}$10] azimuth. Best agreement between experiment and theory was found for a small, but marginally significant twist of the molecule (5° ± 5°) about an axis perpendicular to the surface and through the centre of the

molecule. The O atoms were found to adsorb in atop sites (at a height of 1.91 ± 0.02 Å above the topmost layer of Cu atoms) with a small displacement of 0.07 ± 0.07 Å towards the short bridge site. The intramolecular O-O separation was 2.42 ± 0.14 Å, which is larger than reported for adsorbed acetate and formate species on Cu surfaces [3, 4].

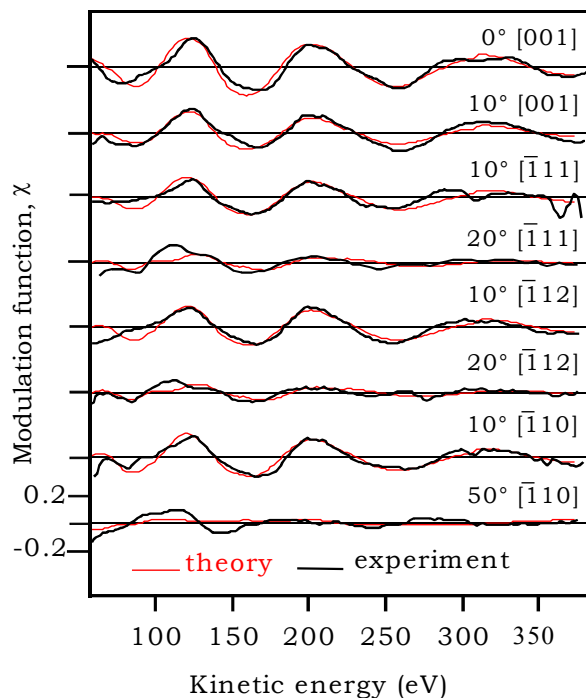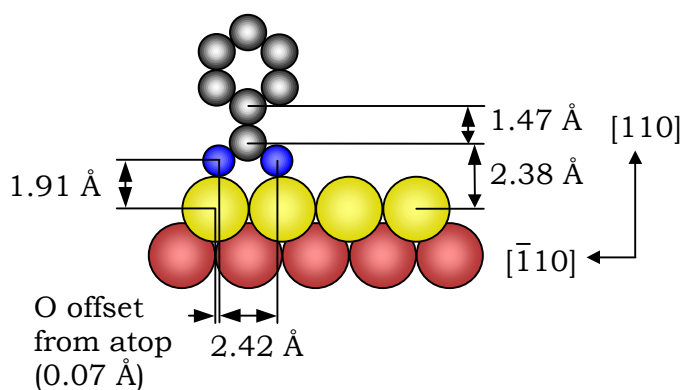*Fig. 1. Comparison of the experimental O 1s PhD modulation functions with the 'best-fit' calculated curves.*

Fig. 2. Side view of the benzoate species on Cu(110) showing the parameters obtained from the multiple scattering analysis.

1. B.G. Frederick, Q. Chen, F.M. Leibsle, M.B. Lee, K.J. Kitching, N.V. Richardson, Surf. Sci. 394 (1997) 1.
2. D.P. Woodruff and A.M. Bradshaw, Rep. Prog. Phys. 57 (1994) 1029.
3. K.U. Weiss, R. Dippel, M. Schindler, P. Gardner, V. Fritzsche, A.M. Bradshaw, A.L.D. Kilcoyne and D.P. Woodruff, Phys. Rev. Lett. 69 (1992) 3196.
4. D.P. Woodruff, C.F. McConville, A.L.D. Kilcoyne, Th. Lindner, J. Somers, M. Surman, G. Paolucci and A.M. Bradshaw, Surf. Sci. 201 (1998) 228.

First SEXAFS measurements using the gap-scan technique
in the extended energy range at BESSY II

Ch. Litwinski[1], H. Wende[1], T. Gleitsmann[1], A. Scherz[1], Z. Li[1],
K. Baberschke[1], and Ch. Jung[2]

[1]Freie Universität Berlin, Institut für Experimentalphysik, Arnimallee 14, D-14195 Berlin-Dahlem, Germany
[2]BESSY GmbH, Albert-Einstein-Str. 15, D-12489 Berlin, Germany
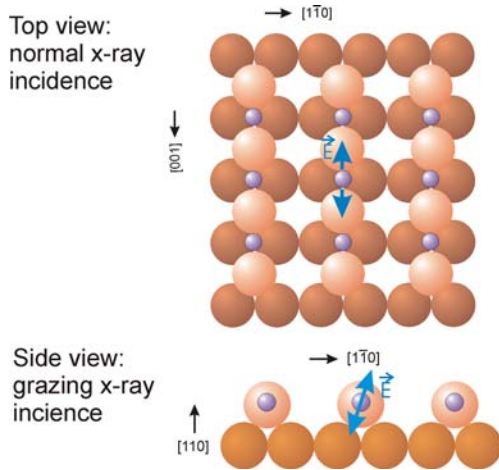
Fig.1: Schematic picture of the adsorption geometry for the (2x1)O/Cu(110) system.

The purpose of this study for the reconstructed (2x1)O/Cu(110) system is a further insight into the atomic EXAFS (AXAFS) effect. Recently in our group, the presence of the controversially discussed AXAFS for the systems (2x3)N/Cu(110) and ($\sqrt{2}$x2$\sqrt{2}$) R 45° O/Cu(100) was definitively evidenced [1]. The lack of attention to the AXAFS effect over years was due to the non-availability of high quality Surface-EXAFS (SEXAFS) data. The use of the U41-PGM beamline in the present work enables us to present SEXAFS data with the required high signal to noise ratio. For those data the AXAFS contribution can be identified unambiguously. The AXAFS contribution can be described as the scattering of the photoelectron at charge densities placed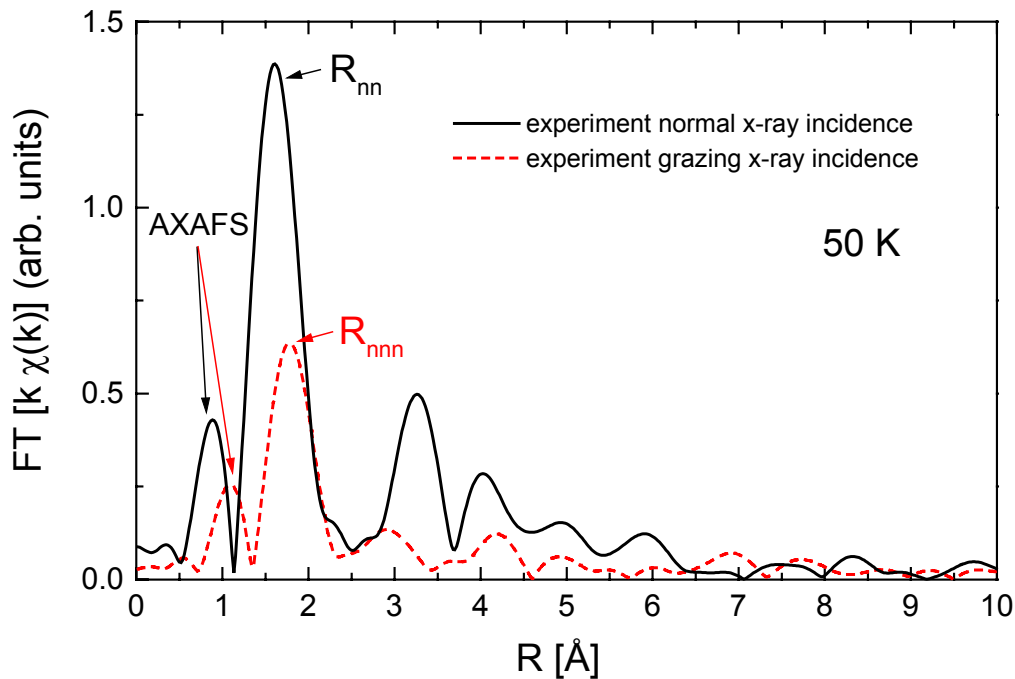 between the nuclei. The adsorbate induced reconstructed systems mentioned above show a strong AXAFS contribution since they are characterized by very directional bonding. Light adsorbates on metal surfaces are established as model systems for this kind of investigations since no multi-electron excitations can mimic the long-range oscillatory fine structure in the x-ray absorption coefficient [1]. It is well known from the literature and prior works in our group that the chemisorption of oxygen on the Cu(110) surface leads to an adsorbate induced missing row reconstruction [2,3]. There is general agreement that the O is located in a long-bridge position along the [001] rows and the O-Cu bond is highly directional along this direction (see Fig. 1). Therefore, in this reconstruction the azimuthal arrangement of the oxygen nearest neighbors is anisotropic with respect to the crystallographic orientation of the substrate. This particular oxygen adsorption site represents a fortunate situation for studying the angular dependence of the atomic EXAFS since one expects a strong anisotropic behavior of the AXAFS contribution.

Fig. 2: X-ray absorption coefficient μ(E) for O/Cu(110) for normal x-ray incidence (**E**‖[001]) and 3rd harmonic versus gap settings. In addition the spline function which was used to extract the SEXAFS oscillations is shown.
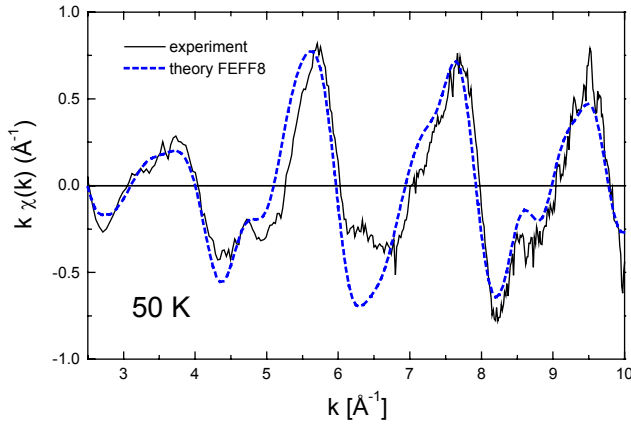
Fig. 3: SEXAFS oscillations k χ(k) (solid line) extracted from the x-ray absorption coefficient given in Fig. 1 for normal x-ray incidence at 50 K together with the result for an *ab initio* calculation using the FEFF8 code (dotted line).

The reconstructed surface was prepared *in situ* on a clean well characterized Cu(110) single crystal. It is known that a dosage of 12 L oxygen at room temperature on a Cu(110) surface leads to a stable (2x1) missing row reconstructed structure. The angular dependent SEXAFS was measured at the O K-edge in the photon energy range of 500-930 eV. These measurements were carried out at the undulator beamline U41-PGM using the gap- scan technique for the first time in the extended energy range with a scan-range of $\Delta E=430$ eV. Since the photon flux at this beamline is at least two orders of magnitude larger than at comparable dipole beamlines high quality data can be collected. The measurements of the x-ray absorption coefficient $\mu(E)$ were carried out using the quasi total electron yield detection mode. The results are given in Fig. 2 together with the 3rd harmonic versus the gap setting. It can be seen that the full width half maximum of the 3rd harmonic in the photon energy range of 500 eV is about 6.5 eV. At 950 eV the 3rd harmonic broadens to a FWHM of 14.5 eV. Because of this sharpness the gap position was changed parallel to the monochromator at every data point (1 eV steps) to ensure the highest possible photon flux. The x-ray absorption coefficient for the measurements at normal incidence with the E-vector along the O-Cu bonding axis in the surface plane (**E**∥[001]) exhibits huge SEXAFS wiggles due to the shortness of the nearest neighbor distance of $R_{nn}=1.81\pm0.03$ Å with a signal to noise ratio of about 100:1. These oscillations were extracted using a stiff spline function as shown in Fig. 2. The extracted SEXAFS oscillations $\chi(k)$ are presented in Fig. 3. The k-weighted $\chi(k)$ is nearly free of noise and exhibits various fine structures, e.g. in the k-range of 4-5 Å^{-1} and 8-9 Å^{-1}. In order to exclude experimental artifacts due to the gap-scan technique the experimental SEXAFS oscillations are compared to *ab initio* calculations using the FEFF8 code [5] (dashed line in Fig. 3). The experimental oscillations agree in amplitude as well as in phase with the calculation. Even the various fine structures are represented in the calculation. The difference between experiment and calculation in the k-range of 6-7 Å^{-1} is due to the AXAFS effect which is not included in this calculation. For a more detailed analysis of this AXAFS contribution the Fourier transforms $|FT[k\,\chi(k)]|$ of the experimental data are given in Fig. 4. The data are presented for normal and grazing x-ray incidence at 50 K. At normal incidence (**E**∥[001]) the main contribution corresponds to the nearest neighbor bond of the O atoms to the Cu atoms in the surface plane whereas the main contribution at grazing incidence (**E**⊥[001]) represents the next nearest neighbor distance of $R_{nnn}=1.99\pm0.03$ Å. The distances determined in the present SEXAFS investigation are in excellent agreement with recent literature [3,4]. In both cases AXAFS contributions can be identified at about half the nearest neighbor distance (marked in Fig. 4) which are clearly out of the noise level which can be seen at large distances in the Fourier transform. Obviously the AXAFS contribution at grazing incidence is located at a larger distance compared to the normal incidence data. The reduction of the AXAFS contribution and the main peak at grazing incidence can be explained by the reduction of the effective

Fig. 4: Fourier transform [FT[kχ(k)] of the SEXAFS oscillations for normal (solid line) and grazing (dotted line) x-ray incidence.

coordination number for this particular next nearest neighbor backscattering shell. The reduction of the corresponding AXAFS feature underlines the strong directionality of the O-Cu bonds and consequently the anisotropy of the interstitial charges.

In conclusion we find that the gap-scan technique enables us to measure SEXAFS data of high quality because of the high photon flux at the U41-PGM beamline. This ensures that the x-ray absorption coefficient of 0.5 ML oxygen can be measured with the necessary precision. The analysis of the angular dependence yields an obvious anisotropy of so called atomic EXAFS feature. This allows for a more detailed investigation of the backscattering of the photoelectron at interstitial charge densities by means of theoretical full potential calculations in the future. The detailed analysis will provide a profile of the AXAFS contribution depending on the orientation of the E-vector with respect to the crystallographic orientation.

References:

[1]   H. Wende, K. Baberschke, J. Electr. Spectr. Relat. Phenom., **101-103** (1999) 821.
[2]   U. Döbler, K. Baberschke, J. Haase and A. Puschmann, Phys. Rev. Lett., **52** (1984) 1437.
[3]   F. Besenbacher, J. K. Nørskov, Prog. Surf. Sci. **44** (1993) 5.
[4]   W. Liu, K. C. Wong, H. C. Zeng, K. A. R. Mitchell, Prog. Surf. Sci., **50** (1995) 247.
[5]   A. Ankudinov, B. Ravel, J.J. Rehr, S.D. Conradson, Phys. Rev. B **58** (1998) 7565.

In situ characterisation of vanadium-phosphorus-oxide (VPO) catalysts for n-butane oxidation by applying X-ray absorption spectroscopy

M. Hävecker, A. Knop-Gericke, R.W. Mayer, M. Fait, H. Bluhm,
and R. Schlögl

Fritz-Haber-Institut der Max-Planck-Gesellschaft, Faradayweg 4-6, 14195 Berlin, Germany

Introduction

Vanadium phosphorus oxides (VPO) are well known to be efficient catalysts in the selective oxidation of n-butane to maleic anhydride [1]. It is believed that vanadyl pyrophosphate $(VO)_2P_2O_7$ is the active phase in this process [2]. Structural nuances of the catalyst seem to be of great importance for the catalytic performance. The material undergoes strong structural rearrangements during the activation process from the precursor to the equilibrated catalyst. The preparation conditions have a strong influence on the performance of the catalyst. The specific structure of vanadyl pyrophosphate with its chains of V_2O_8 octahedra linked by tetrahedra of pyrophosphate P_2O_7 units was found to be uniquely active and selective for the reaction. This catalyst is especially interesting since there exists no other direct oxidative activation for n-alkane molecules.

Experimental

We used high-pressure X-ray absorption spectroscopy (XAS) in the soft energy range [3,4] to study the electronic structure of VPO catalysts. In combination with mass spectrometry this method allows to obtain spectroscopic information from the catalyst´s surface and to measure the conversion of the gas phase by the catalytic reaction simultaneously.

The XAS experiments were performed with a special reactor cell designed for in situ X-ray absorption investigation. Details about the set-up and the data processing can be found in the literature [3,4]. The experiments were carried out at the undulator beamline U49/1. In our experiments we analysed the near edge X-ray absorption fine structure (NEXAFS), i. e. the strong variations of the absorption coefficient just at the absorption edge.

Spectra were taken ex situ under high vacuum as well as under reaction conditions in a stream of 1.2vol% n-butane, 20vol% oxygen and 78.8vol% helium at temperatures from 300 K up to 673 K at a total pressure of 2 mbar. The activity of the catalyst was monitored by on-line mass spectrometry. The VPO powder sample was prepared by subsequent transformation of

the precursor compound $VOHPO_4 \cdot 0.5H_2O$ under n-butane oxidation conditions (feed gas: 1.5vol% butane in air for 200 h).

Results

Fig. 1 shows the V L_3-NEXAFS of the VPO catalyst. For comparison the spectrum of the reference compound V_2O_5 which possesses a similar local geometric structure is also shown. The spectra are related to the V3d-O2p hybridised unoccupied states. The overall peak position at the V L_3-absorption edge is determined by the formal oxidation state of the absorbing vanadium atom. Details of the absorption fine structure are influenced by the geometric structure of the compound. Empirically, we found a linear relationship between the energy position of several absorption resonances and the V-O bond length of the participating
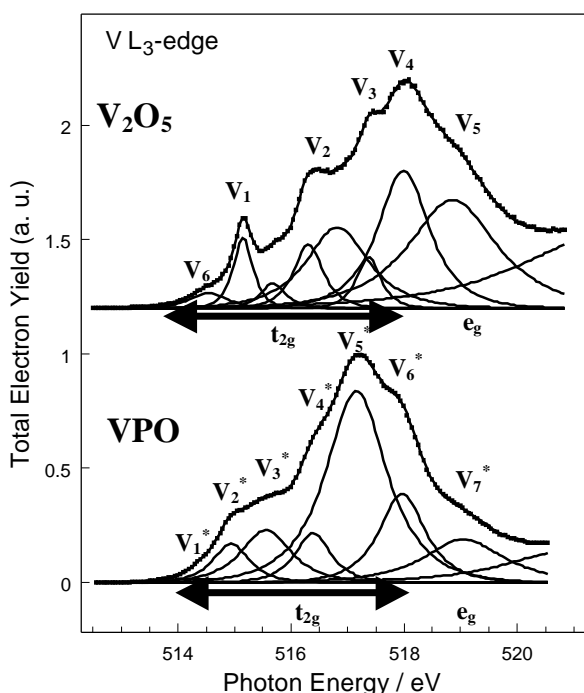
Fig.1: V L_3-NEXAFS of V_2O_5 and VPO

atoms [5]. This allows to identify the contribution of specific V-O bonds to the V L_3-near edge X-ray absorption fine structure. Our analysis points to a deviation of the geometric surface structure of the VPO catalyst from the crystalline bulk structure of $(VO)_2P_2O_7$. This deviation could be caused by disorder or an amorphous layer at the catalyst´s surface, an interpretation which is supported by HRTEM.

A detailed analysis of the V L_3-absorption edge by a least square fit showed defined reversible changes depending on the reaction conditions. An example for the

observed dynamic behaviour of the VPO surface is shown in Fig. 2. The spectral weight of a particular resonance (V_5^*) is decreasing from 50% of the total intensity at the V L_3-edge at 300 K to 43% under n-butane oxidation conditions at 673 K. While cooling down to room temperature the initial state is almost recovered. A decrease in intensity and therefore a change in the electronic structure could be caused by a modification of the geometric structure or the presence of adsorbats on the surface. Simultaneously, the energy position of this resonance shifts by about 90 meV to lower photon energies, an effect which is partially reversible if returning to 300 K. The catalytic activity of the sample under the applied

conditions could be proven by using simultaneously on-line mass spectrometry which showed a decrease of the n-butane abundance in the reactant stream of around 5% at 673 K.

In summary our observations show a significant difference of the electronic structure of the catalyst surface under reaction conditions and its ability to react dynamically on the reaction conditions.
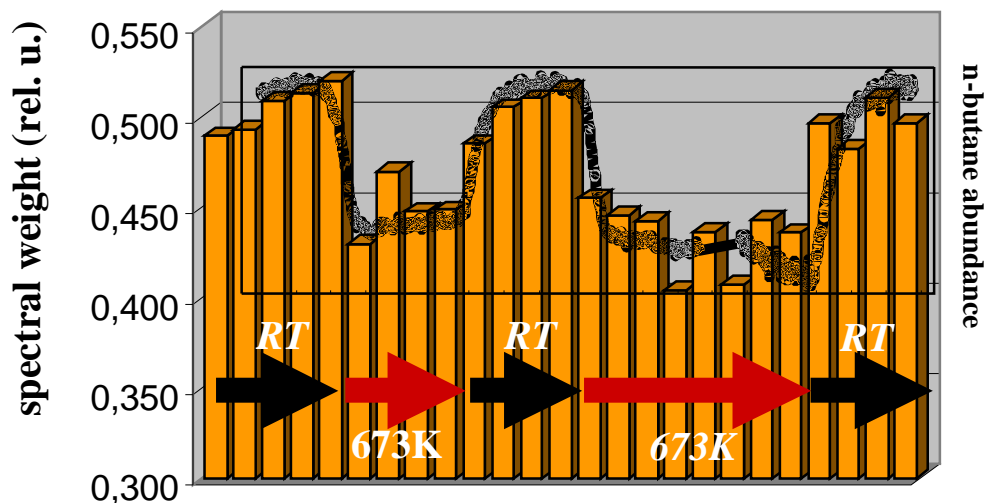
Fig.2: *The relative spectral weight of resonance V_5^* (compare to Fig. 1) while changing temperature from 300 K to 673 K in a stream of n-butane, oxygen and helium is displayed as a bargraph. Additionally, the abundance of n-butane in the gas phase is shown.*

References

[1]   R. L. Bergman, and N. W. Frisch, U.S. Patent, 3,393,368 (1968) assigned to Princeton Chemical Research

[2]   G. Centi, Catal. Today, 16 (1993) 5

[3]   M. Hävecker, A. Knop-Gericke, Th. Schedel-Niedrig, and R. Schlögl, Angew. Chem., 110 (1998) 2049; Int. Ed. 37 (1998) 206

[4]   A. Knop-Gericke, M. Hävecker, Th. Schedel-Niedrig, and R. Schlögl, Topics Catal., 15 (2001) 27

[5]   M. Hävecker, A. Knop-Gericke, R. W. Mayer, M. Fait, H. Bluhm, and R. Schlögl, submitted to J. Electron Spectrosc. Rel. Phenom. (2001)

Investigation of Molecular and Layer-type Products from Di- and Tetravalent Dissolution of Silicon in Dilute Acidic NH$_4$F Solutions

H. Jungblut, C. Murrell, E. Goncalves, M. Kanis, E. Rüthers, H. J. Lewerenz
Hahn-Meitner-Institut Berlin, Interface Engineering Group, 14109 Berlin

Wet surface structuring and conditioning of silicon find many important applications (e.g. sensors, light coupling devices for solar cells, porous silicon and photonic crystals). Many fundamentals of the corresponding structure formation processes, however, are still unclear. There is a general need for further miniaturisation of silicon based microstructures (e.g. photonic crystals). An advanced control of the structuring can result from detailed analyses of the interface electrochemistry in the divalent dissolution regime.
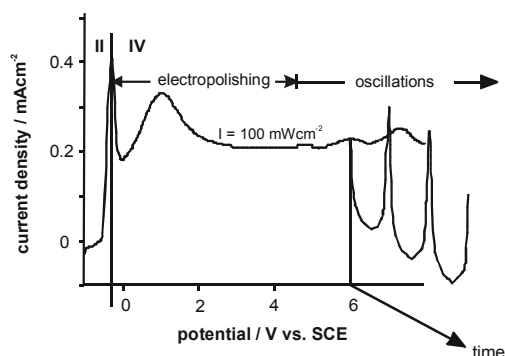
Fig. 1: *Current-potential characteristics of n-Si(111) in dilute acidic ammonium fluoride.*

The I-V characteristic shown in Fig. 1 can be devided into three parts. At low overpotentials, H-termination and por-Si formation prevail (region II, divalent dissolution). Beyond the first photocurrent maximum, electropolishing sets in followed by oscillatory behavior (region IV, tetravalent dissolution). Starting from a H-terminated (111) surface we investigated the initial phases of por-Si formation by PES. The proposed dissolution mechanism is given in Fig. 2 [1]. The corrosion begins at a kink site where a radical is formed by hole capture. Hydrolysis with electron injection into the conduction band takes place at this site. Further steps involve ligand exchange, solvolytic splitting of backbonds and solution reactions.
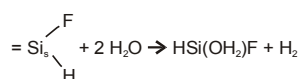

**Fig. 2:** *Flow diagram of divalent Si dissolution and DFT results on solution species.*

We investigate the surface condition after our two-step electrochemical hydrogenation treatment [2] which corresponds to the foot of the I-V characteristic (cf. Fig. 1), showing the Si 2p core level at the photon energy $h\nu$ = 170 eV (Fig. 3a). The deconvolution of the spectrum allows to discern three contributions shifted by 0.23 (signal B) and 0.8 eV (signal C) with respect to the main peak at -99.14 eV (signal A). The respective areas under the curves are related 0.55 and 0.07, respectively, when normalised to the main peak structure. In the binding energy range where higher oxidised Si species are expected (E$_b$ ≤ -101 eV), only a very small signal is found, demonstrating the quality of the preparation.

The corresponding O 1s and F 1s lines (Fig. 3b, c) show signals attributed to OH$^-$ (-532 eV) and molecular water (-532.8 eV) and a fluoride line at E_b = - 687 eV. The signal for oxygen in silicon oxide lies at -533.8 eV and is not observed here.
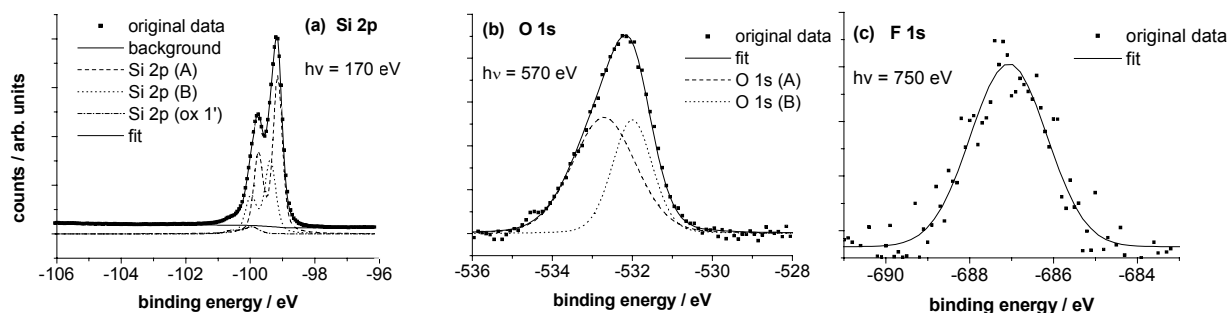
Fig. 3: (a): Si 2p line, (b): O 1s line (c): F 1s line obtained for an electrochemically H-terminated surface; deconvolution has been done using a combined Gauss-Lorentzian fit routine.

The signal shifted by 230 mV in Fig. 3a can be attributed to a surface core level shift due to the Si – H bonds of the topmost Si atoms of the (111) face. In a simple estimate which takes into account the partial charge shift in a microcapacitor model we determine the partial charge transfer using Sanderson electronegativities [3] towards the H atoms of 0.1 resulting in an expected energy shift of 200 meV in good agreement with the experiment. The second contribution in Fig. 3a indicates a higher oxidised species in small amount (~ 10% of a monolayer). From Fig. 3b we know that oxides are not present. We find hydroxide, which must be a surface species from the reaction in this acidic solution, and a small amount of fluoride. From our HREELS experiment on H-terminated surfaces, it is known that even the best surfaces with extremely low surface state density [4] are not ideally terminated by hydrogen [5]. The observed shift of the Si line without Si-O bonds of ~ 800 meV could correspond to a change of ρ of about 0.4 - 0.5, a value obtained for =Si-H-OH species by DFT calculations. Due to the structural formation of terraces, e.g. in $<1\bar{2}1>$ direction [6], a considerable number of reactive kink sites can exist on such surfaces. The signal from OH$^-$ in the O 1s line (Fig. 4b) also shows that the surface binds OH to some extent. The coverage determined from the Si 2p line analysis is in the range of 0.1 ML with ~ 0.2 ML water. Thus we conclude that a part of the surface, probably at kink sites, binds OH anions. The rather little amount of molecular water (~ 0.2 ML) found in the O 1s line is indicative of the hydrophobic H-terminated surface parts and might be related to the small areas with OH termination.
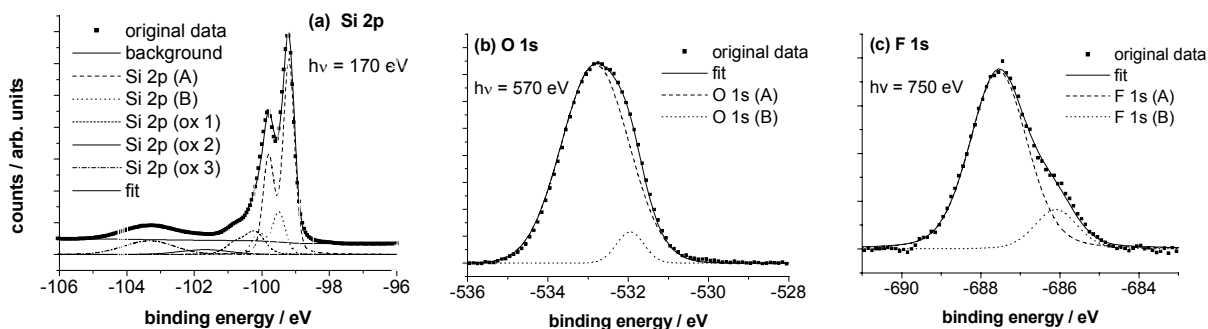
Fig. 4: (a) Si 2p line, (b) O 1s line, (c) F 1s line after sample emersion at the first current maximum in the I-V characteristic (see Fig. 1) including deconvoluted signals.

Fig. 4 displays PES data obtained after emersion close to the first photocurrent maximum (cf. Fig. 1). Five features are discernible in Fig. 4a: the core level signal (signal A), a surface core level shift

indicating residual H-termination (0.35 ML; signal B) and mainly two oxidised species shifted by 1 eV (C) and 4 eV (E). The former is attributed to a =Si-H-F species. DFT calculations yield a Si partial charge of $\rho = 0.54$ for the =Si-H-F species. Signal D is too small for serious evaluation; signal E can only be evaluated under consideration of the O 1s and F 1s lines (Fig. 4b, c). The former shows O in OH⁻ and H_2O but not O in SiO_2. The latter shows predominantly F in $Si-F_x$. In conjunction with DFT calculations we attribute the 4 eV shifted signal to $SiOHF_3$, a precipitate from the dissolution reaction. The presence of species C indicates that solvolytic splitting of back- bonds is possibly rate determining, due to the multistep reaction sequence.

In the tetravalent dissolution regime, oxidic layers of varying thickness and composition are formed. Oxides formed under electropolishing conditions, for instance, are of interest for devices because of their morphology and chemistry (incorporation of fluorine [7]) and their reduced thickness. For improvement of the oxidic layer properties, a depth dependent composition analysis is mandatory. Table 1 shows the evaluation of O 1s and F 1s signals for different photon energies after sample emersion at +4 V in the I-V curve (cf. Fig. 1). From the $Si\ 2p^0/Si^{4+}$ signal ratios obtained for the different photon energies given in table 1, the thickness d of the electropolishing oxide is found to be 3.1 ± 0.4 nm.

Table 1.
Line positions E_B of deconvoluted F 1s(a), F 1s(b), O 1s(a) and O 1s(b) components, corresponding intensity ratios I(b)/I(a) and inelastic mean free paths λ in the oxidic layer for different photon energies hν.

hv/eV	E_B/eV F 1s(a)	F 1s(b)	λ/Å	I(b)/I(a)	E_B/eV O 1s(a)	O 1s(b)	λ/Å	I(b)/I(a)
572	-	-	-	-	-	-534.1	9	only O 1s(b)
761	- 687.5	- 688.5	8	8.4	-	-	-	-
957	- 687.5	- 688.5	12	1.8	-932.3	-533.9	16	17.1

The F 1s line includes two components at -687.5 eV and -688.5 eV which can be attributed to F in $Si-F_x$ and Si-O-F species, respectively [8]. The strong increase of the Si-O-F contribution with decreasing photon energy (higher surface sensitivity) shows that this species is preferentially incorporated into the surface-near region of the electropolishing film. For the highest photon energy, also two components in the O 1s signal are found at –532.3 eV and at -533.9 eV. The former is attributed to oxygen in SiOH, the latter to oxygen in SiO_2. For the lowest photon energy no signal from OH is found suggesting that OH species found for larger escape depths are concentrated near the semiconductor/film interface as would be expected from the oxide formation mechanism. The small shift of the O 1s line towards higher binding energy ($E_B \geq$ 533.8 eV) is attributed to the existence of Si-O-F species in which O is somewhat more oxidised compared to SiO_2.

[1]   P. Allongue, V. Kieling, H. Gerischer, *Electrochim. Acta* **40**, 1353 (1995)
[2]   H. J. Lewerenz, T. Bitzer, M. Gruyters, K. Jacobi, *J. Electrochem. Soc. Lett.* **140**, L44 (1993)
[3]   P. Perfetti, C. Quaresima, C. Coluzza, C. Fortunato, G. Margaritondo, *Phys. Rev. Lett.* **57**, 2065 (1986)
[4]   S. Rauscher, Th. Dittrich, M. Aggour, J. Rappich, H. Flietner, H. J. Lewerenz, *Appl. Phys. Lett.* **66**, 3018 (1995)
[5]   T. Bitzer, M. Gruyters, H. J. Lewerenz, K. Jacobi, *Appl. Phys. Lett.* **63**, 397 (1993)
[6]   O. Nast, S. Rauscher, H. Jungblut, H. J. Lewerenz, *J. Electroanal. Chem.* **422**, 169 (1998)
[7]   H.J. Lewerenz, H. Jungblut, S. Rauscher, *Electrochim. Acta* **45**, 4627 (2000)
[8]   S.R. Kasi, M. Liehr, S. Cohen, *Appl. Phys. Lett.* **58**, 2975 (1991)

In-situ XPS Study of CO Oxidation on a Pt(111) Surface

M. Kinne, R. Denecke, T. Fuhrmann, J. Zhu, C. Whelan, H.-P. Steinrück
Physikalische Chemie II, Universität Erlangen-Nürnberg

In order to study the kinetic behavior of a surface reaction, one could think of basically two approaches: (1) Detection of reaction products desorbing from the surface, e.g., by mass spectroscopy, with the disadvantage of having no information about the species present on the surface during reaction. (2) Identification of adsorbed molecules by spectroscopic methods like HREELS, IR spectroscopy or X-ray core level spectroscopy. Here, the speed of the particular method is the crucial point; in the case of XPS, the use of third generation synchrotron radiation is required to be able to measure on a faster time scale than the one of the studied reactions. In our case a transportable setup (described in detail elsewhere [1,2]) has been used at the U49/2-PGM1 and U49/1-SGM beamlines. Besides an electron energy analyzer this apparatus is equipped with a three-stage supersonic molecular beam source, which allows for relatively high sample pressures (up to 10^{-5} mbar) during measurement.

As the first bimolecular surface reaction to be studied with this new setup we chose CO oxidation, which is probably the most examined surface reaction at all. Here, we restrict ourselves to the reaction of CO dosed onto an ordered (2×2) adlayer of atomic oxygen on Pt(111), which is known to consist of 0.25 ML of three-fold coordinated O-atoms [3]. The reaction product, CO_2, cannot be detected on the surface, since it is known to desorb very rapidly in the temperature range above ~270 K where the reaction is observed [4]. The (2×2)-O layer is prepared by dosing $1 \cdot 10^{-7}$ mbar of O_2 at 100 K for 180 s and subsequent annealing to 300 K [3]; after each preparation the structure is checked by LEED. O1s spectra taken with a photon energy of 650 eV show, in accord with the literature [5], a single peak with a binding energy of 529.90 eV, which can be fitted by an asymmetric peak function (Fig. 1a). For comparison, CO adsorbed on the surface yields two distinct peaks at E_B=532.80 and 531.05 eV (Fig. 1b), which are associated with linearly (on-top) and two-fold (bridge) coordinated molecules, respectively. Photoelectron diffraction effects are probably the reason that the peak areas of different species are not comparable without normalization: A c(4×2) layer of CO, known to consist of 0.25 ML on-top and the same amount of bridge bound CO, gives a spectrum with a considerably smaller bridge- than on-top-related peak.

At a temperature of 100 K CO adsorbs on the (2x2)-O layer, but no reaction takes place at all. In this coadsorbate system the oxygen atoms block the bridge sites for CO adsorption and only the on-top related peak is observed in the spectra which corresponds with literature results [6]. Above T~270 K a reaction is observed. In addition to the sample temperature, the reaction rate can be limited by the coverage of both reactants and by diffusion processes, if the sample is not saturated with adsorbates. The latter effect can be excluded by using a sufficiently high CO pressure (here ~$1 \cdot 10^{-6}$ mbar) during the reaction, so that reaction products leaving the surface are immediately replaced by CO. Fig. 2 shows the time evolution of the peak areas of oxygen (a) and CO on bridge sites (b) in arbitrary units for different sample temperatures. In order to avoid beam damage effects by synchrotron radiation, the beamline valve was closed after each spectrum, if possible. Spectra could be taken as fast as 5 s/spectrum. The beam of CO has been switched on after the first data point in each run. If the maximum values of oxygen and CO bridge intensity are
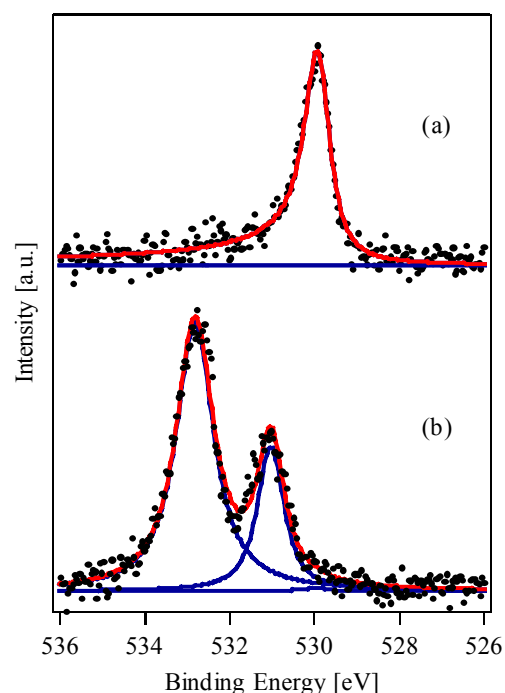
Figure 1: (a) Saturated O-(2x2) layer (b) CO covered surface after reaction ($h\nu$=650eV, T=280K)

normalized to 0.25 ML (which is the amount present in the CO c(4×2) structure), the sum of both values turns out to be a constant during the reaction, indicating that empty sites are indeed immediately filled with CO molecules.

In order to model the kinetic behavior of the reaction the following approach is used: From the data shown in Fig. 2 the reaction rates $d\theta_O/dt$ can be determined by differentiation, after smoothing the curves by smoothing splines. A double logarithmic plot of $d\theta_O/dt$ versus θ_O yields a linear dependance, indicating that the reaction rate can be written as

$$d\theta_O / dt = -k\theta_O^\alpha . \qquad (1)$$

A straight line fit to the data points gives a value of $\alpha \approx 0.5$, which can be explained by island formation of oxygen atoms after reaction start. If the reaction takes place only at the edge of oxygen islands, which has indeed been observed with STM [7] one would expect the exponent to be 0.5. Integrating equation (1) gives the time evolution of θ_O:

$$\theta_O = \left[\theta_O^{1-\alpha}\Big|_{t=0} - (1-\alpha)kt \right]^{\frac{1}{1-\alpha}} \quad (2)$$

Using this equation instead of (1) has the advantage that no smoothing and numerical differentiation of data is required. Eq. (2) can now be fitted to the data of Figure 2 (a) (solid lines in figure), which results in a value of $\alpha = 0.55\pm0.06$ for the exponent, in agreement with recent STM measurements [7]. By again fitting the data, now with α fixed at 0.55, we obtain temperature dependence of k. Assuming an Arrhenius-like behavior

$$k = \nu \exp(- E_a / k_B T),$$

a straight line fit to a plot of $ln(k)$ versus $1/T$ (Figure 3) yields the activation energy and the preexponential factor of the reaction:
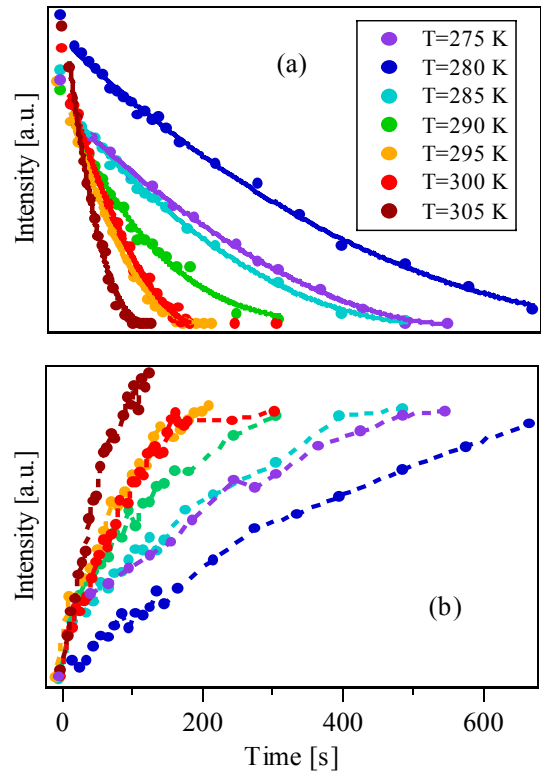
$$E_a = 0.47 \pm 0.07 \text{ eV}$$
$$\nu = 2\cdot10^{(5\pm1)} \text{ s}^{-1}.$$

Figure 2: Relative coverages from O1s spectra during reaction in $\sim 1\cdot10^{-6}$ mbar CO. (a) oxygen; solid lines are fits according to Eq. (2). (b) CO on bridge sites

Figure 3: Arrhenius plot of rate constant

This activation energy is in excellent agreement with observations from STM measurements [7,8], where a value of 0.49 eV was observed; also our findings for the preexponential factor are still comparable with their value of $5\cdot10^7$ s^{-1}.
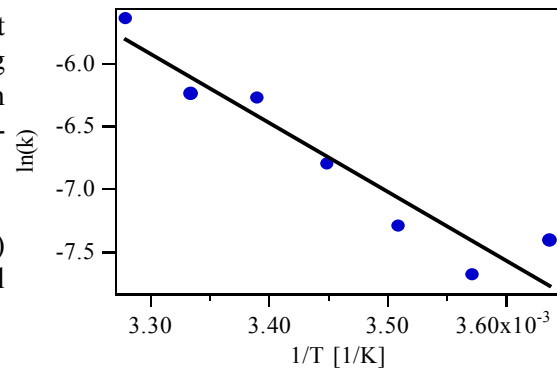
References:
[1] R. Denecke, M. Kinne, C. Whelan, G. Held, J. Pantförder, M. Probst, H.-P. Steinrück, BESSY Jahresbericht (2000) 305
[2] R. Denecke, M. Kinne, C. Whelan, H.-P. Steinrück, Surf. Rev. Lett. (in print)
[3] L. Gland, B. Sexton, G. Fisher, Surf. Sci. 95 (1980) 587
[4] D. Kulginov, M. Persson, C. Åkerlund, I. Zoric, B. Kasemo, J. Vac. Sci. Technol. A 13 (1995) 1511
[5] C. Puglia, A. Nilsson, B. Hernnäs, O. Karis, P. Bennich, N. Mårtensson, Surf. Sci. 342 (1995) 119
[6] J. L. Gland, E. B. Kollin, Surf. Sci. 151 (1985) 260
[7] S. Völkening, J. Wintterlin, J. Chem. Phys., 114 (2001) 6382

[8] J. Wintterlin, S. Völkening, T. Janssens, T. Zambelli, G. Ertl, Science 278 (1997) 1931

Partial Dissociation of Water on Cu(110)

Ch. Ammon[a], A. Bayer[a], H.−P. Steinrück[a], and G. Held[b],

[a]Univ. Erlangen-Nürnberg, Physikal. Chemie II, Egerlandstr. 3, D–91058 Erlangen.
[b] Univ. of Cambridge, Dept. of Chemistry, Lensfield Rd., Cambridge CB2 1EW, UK.

In a recent theoretical study by Feibelman it was suggested that after adsorption of water on Ru(0001) the first chemisorbed layer consisted of equal amounts of water (H_2O) and hydroxyl (OH) [1]. According to the DFT calculations this partially dissociated layer is the most stable one and leads to a structure similar to the one found in an earlier LEED–IV analysis for this system [2]. This finding is somewhat in contradiction to the assumption of most authors made in earlier studies that water does not dissociate on the late transition metal surfaces and forms, instead, a puckered bilayer similar to the layers in ice [3]. The $c(2 \times 2)$ superstructure of water formed on Cu(110) at a coverage of 1 ML (1 adsorbate molecule per surface Cu atom) was also interpreted in such a way [4, 5]. Using high resolution XPS (HRXPS) we study the extent of OD–formation on Cu(110), a surface, which is expected to be less reactive than Ru(0001). HRXPS provides an ideal tool for this kind of investigation as the binding energies (BE's) of the O 1s signals arising from hydroxyl and water, respectively, differ by about 2 eV and can therefore clearly be discriminated and analysed quantitatively. The measurements were carried out at the BESSY–II beamline U49–1/PGM using a Scienta SES-200 analyser with an overall resolution of about 140 meV (at $h\nu = 650$ eV). The spectra were normalized with respect to the background signal and deconvoluted using pseudo Voigt functions and Shirley background subtraction. Water (D_2O) was adsorbed onto the Cu(110) surface through a stainless steel needle doser at a sample temperature of 110 K and a background pressure of 2×10^{-9} mbar. The water coverage was calibrated by comparing the total O 1s intensity in the sub-monolayer range with the intensity of a saturated $p(2 \times 1)$–O–Cu(110) overlayer (0.5 ML). We checked carefully for beam–induced effects (dissociation, desorption) by moving the spot position on the surface and recording fast spectra consecutively at the same position. The only such effect found was beam–induced desorption in the multilayer coverage range, however, no beam–induced dissociation.

The HRXP spectra shown in Figures 1 (a) and (b) were recorded after dosing steps of 10s (0–100s), 20s (120–200s), 50s (250–300s), and 100s (400s), respectively. Note that the spectrum for 0 s already shows some intensity due to adsorption for the background pressure. The time for aquiring each spectrum was about 6 minutes using an excitation energy of 650 eV. Figure 1 (a) shows the spectra up to about 1 ML (140 s). The 140s spectrum (1 ML) at the top of Figure 1(a) shows peaks assinged to D_2O in the first chemisorbed layer (BE 533.4 eV) and OD (BE 531.3 eV) and a small contribution of D_2O adsorbed on top of the first layer (multilayer). Figure 1 (b) shows the spectra for

higher coverages. The spectrum for 400s (2.7 ML) at the top has small contributions from chemisorbed D_2O, OD and a main contribution at BE 534.2 eV from water in the multilayer. After completion of the chemisorbed layer the D_2O peak shifts continuously to higher binding energy, which is most likely due to weaker screening of the core hole by the metal surface and to charging effects. The spectra clearly show the formation of OD on Cu(110) even at low temperatures. As shown in Figure 2 (a), the total area of the OD peak increases with the dosing time up to about 75 s (0.5 ML) while the ratio OD/D_2O decreases from 28% (0.07 ML) to 10% (0.5 ML). Above 0.5 ML water dissociation has almost stopped which is most likely a site blocking effect due to missing adsorption sites for the dissociation product D. For 1.0 ML, where a sharp $c(2 \times 2)$ LEED pattern is observed, we find a OD/D_2O ratio of 6%. Note that this value is significantly smaller than the value of 50% predicted by Feibelman for Ru(0001) [1]. The decrease of the OD signal above 1 ML is due to damping by the multilayer proving that hydroxyl stays at the metal–water interface even when covered by a layer of condensed water.

Figure 2 (b) shows a series of HRXP spectra recorded after successive annealing steps starting with a coverage of about 2 ML. It can clearly be seen that most of the molecular water desorbs from the surface between 165 and 195 K. Above 200 K the remaining D_2O dissociates to OD up to 277 K. Between 303 and 353 K most of this hydroxyl desorbs recombinatively while a small fraction (30%) dissociates further leaving 15% of the saturation coverage of atomic oxygen on the surface. This is somewhat in contradiction with earlier TPD results where no recombinative desorption was found for a pure water layer [4], however the amount of recombinative desorption is relatively small and may have been below the detection limit of these studies.

References

[1] P. Feibelman, Science 295 (2002) 99

[2] G. Held, D. Menzel, Surf. Sci. 316 (1994) 92.

[3] P. A. Thiel, T. E. Madey, Surf. Sci. Rep. 7 (1987) 211.

[4] K. Bange, D. E. Grider, T. E. Madey, J. K. Sass, Surf. Sci. 136 (1984) 38.
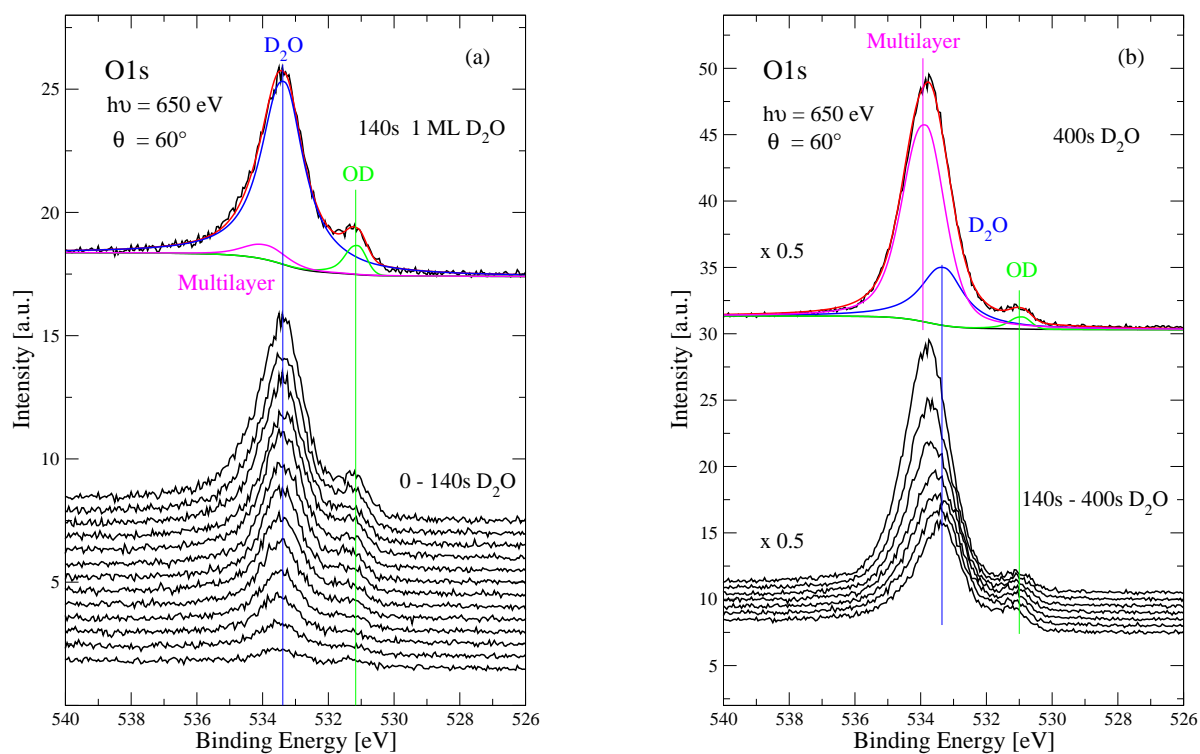
[5] A. Spitzer, H. Lüth, Surf. Sci. 160 (1985) 353.

Figure 1: O 1s uptake spectra for (a) submonolayer (0 − 140s) and (b) multilayer (140 − 400s) coverages of D$_2$O. The spectra at the top represent the highest coverage showing the fitted peaks and the subtracted background together with the raw data. (Photon energy 650 eV, emission angle 60° from the surface normal).
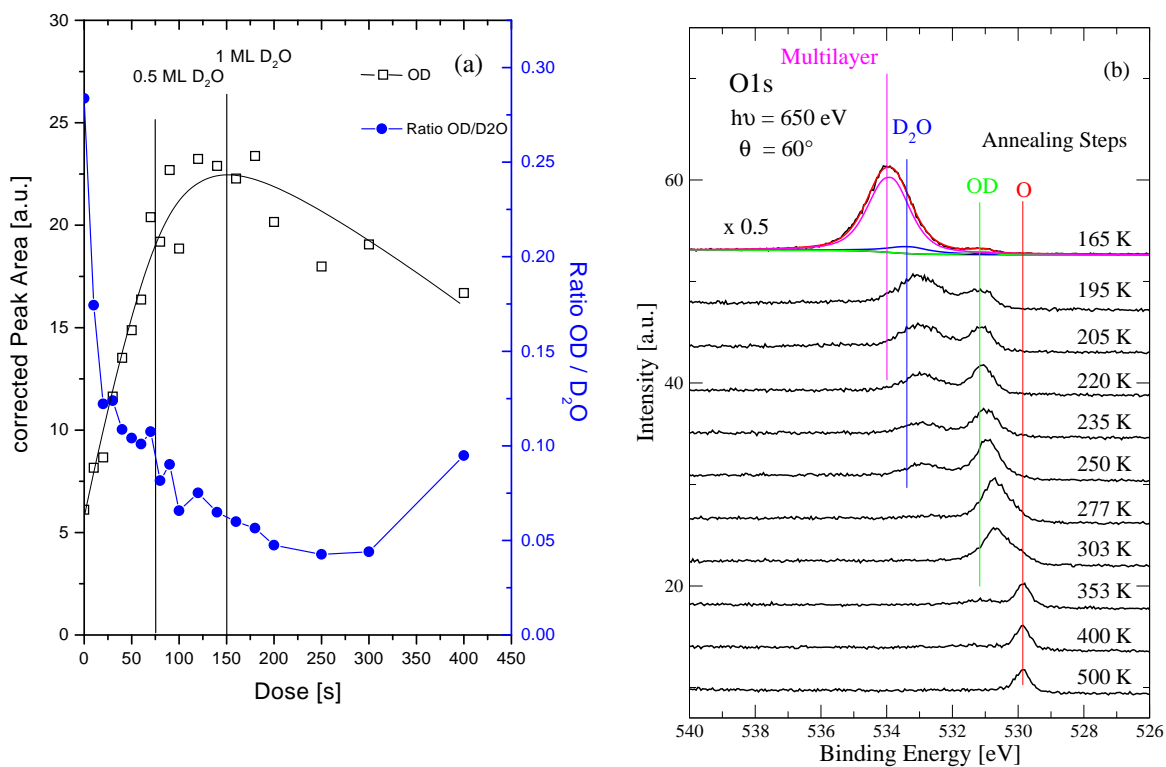

Figure 2: (a) Peak area of the OD signal and OD/D$_2$O ratio from the spectra in Figs 1(a) and (b) vs. dosing time (coverage). (b) O 1s HRXP spectra recorded after annealing the about 2 ML D$_2$O on Cu(110) to the specified temperatures. (Photon energy 650 eV, emission angle 60° from the surface normal).

In-situ high resolution XPS studies of activated adsorption of CH$_4$ on Pt(111) by using molecular beam techniques

T. Fuhrmann, M. Kinne, C. Whelan, J. Zhu, R. Denecke and H.-P. Steinrück
Physikalische Chemie II, Universität Erlangen-Nürnberg

In general, surface science is dealing with adsorption and desorption processes and surface reactions. Only recently efforts have been undertaken to study these phenomena in situ, i.e., while the respective processes take place. In order to do this, existing techniques had to be improved to allow for time-resolved measurements on time scales relevant to these processes. In 2000, we built up an apparatus to do "in-situ" photoelectron spectroscopy experiments with assistance by synchrotron radiation. The integrated supersonic molecular beam system allows for a good time resolution of adsorption processes on surfaces due to fast switching of the sample pressure. We are also able to control adsorption parameters separately. Adding the probe gas to an inert gas with lower molecular weight, e.g. He, leads to higher kinetic energy of the probe molecules due to collisions between the particles in the nozzle, a process called "seeding". Alternatively, by heating the nozzle a variation of the gas temperature at the time of adiabatic expansion yields also different kinetic energies. However, in this case degrees of freedom of vibrational and rotational motion of the molecules are excited in addition, which could change their adsorption behavior. Using these techniques allows to observe the activated adsorption of molecules, which normally only takes place at high reaction pressures or temperatures. Within the scope of our beamtimes in June and December 2001, we performed measurements in this context at the beamline U49/2 PGM-1. The complete apparatus has been described elsewhere [1].

For our first in-situ experiments of activated adsorption, we chose CH$_4$ on Pt (111). This system is well investigated, especially by sticking coefficient measurements [2]. We performed two kinds of measurements: (i) uptake of CH$_4$ at constant T$_{sample}$ and (ii) applying a linear heating ramp to the saturated sample. While the first set of data should give insight in the kinetics of the adsorption process and reveal the identity of the adsorbed species, the second approach is used to monitor temperature-induced reactions and to identify the intermediate species. Here a comparison to other hydrocarbons like C$_2$H$_4$ is made.

A typical uptake experiment is shown in Fig. 1. We record C 1s spectra at 380 eV excitation energy with a combined resolution of 120 meV while the CH$_4$ beam is impinging on the surface. The sample temperature was 110 K, the nozzle temperature of the molecular beam system was 700 °C and the seeding ratio was 1:20 (CH$_4$: He). In good agreement with literature [3], we find a strong dependence of the sticking probability on the angle of incidence with a maximum for normal incidence. Therefore we performed all ex
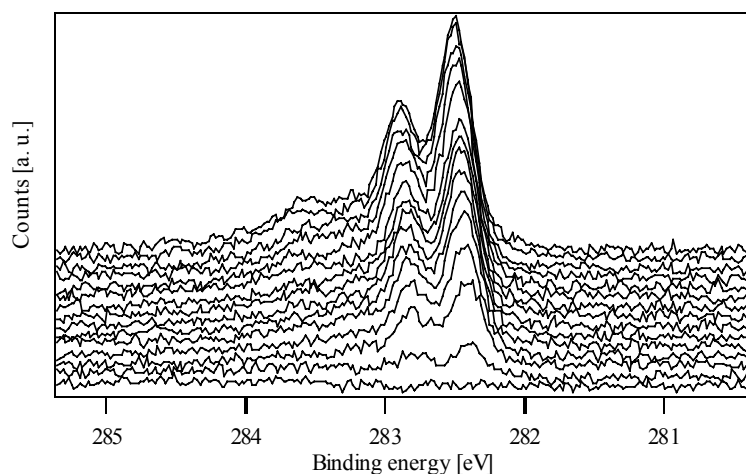
Figure 1: Typical set of C 1s uptake spectra, T$_{nozzle}$=700°C, 5% CH$_4$ in He, T$_{sample}$ =110 K.
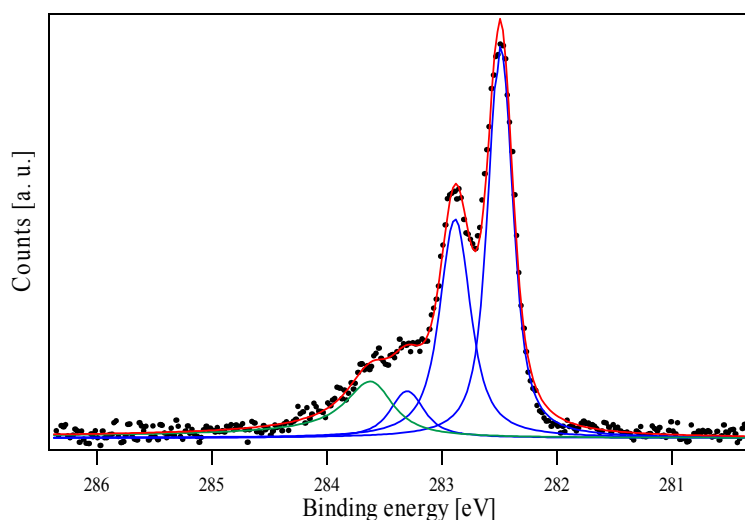
Figure2: Fitted Spectra, at saturation coverage

periments with this geometry. As can be seen in Fig. 2, the spectra can be deconvoluted into four different contributions. At saturation coverage we observe a main peak at 282.47 eV, followed by two peaks at 282.87 and 283.27 eV. During uptake a parallel shift of these three peaks towards higher binding energies can be observed, pointing towards adsorbate-adsorbate interactions. If one follows the intensity evolution of the two largest peaks during the uptake, as is shown in Fig. 3, it becomes clear that they appear with a fixed intensity ratio (right axis in Fig. 3). From this and the observation that the binding energy difference between successive peaks is about 400 meV, we can identify the two smaller peaks as the first and second vibrationally excited states of the main peak. The value of 400 meV correspond to the C-H stretching mode from a comparison with theoretical calculations [3] and measurements in the gas phase [4].

The fourth peak represents the next species in the reaction process. This can be derived from its increasing intensity with increasing substrate temperature during adsorption as well as during temperature-programmed XPS measurements. Interestingly, prolonged irradiation with synchrotron light also causes an increase of the intensity of this peak due to radiation damage. The exposure times have been minimized to reduce this effect. From a comparison with temperature-dependent XPS spectra of C_2H_4 on Pt(111) we hope to be able to identify this species. Other studies suggest ethylidyne (CCH_3) as intermediate in the temperature evolution of both CH_4 and C_2H_4 [5].

Figure3: Time dependence of peak intensity for the peaks at 282.47 and 282.87 eV, as well as the ratio between them.

Variation of the kinetic and internal energy of CH_4 leads to changes in the time dependence of the adsorption process, as expected for activated processes. A quantitative analysis of these data is in progress. From a preliminary screening it seems as if the nature of the adsorbed species is independent of the energy parameters.

[1]   R. Denecke, M. Kinne, C. Whelan, G. Held, J. Pantförder, M. Probst, H.-P. Steinrück, Bessy Annual report (2000), 305; R. Denecke, M. Kinne, C.M. Whelan, and H.-P. Steinrück, Surf. Rev. Lett. (in print).
[2]   A. Luntz, D. Bethune, J. Chem. Phys. 90 (1988) 1274.
[3]   T.D. Thomas, L.J. Saethre, S.L. Sorensen, S. Svensson, J. Chem. Phys. 109 (1998) 1041.
[4]   B. Kempgens, H. Köppel, A. Kivimäki, M. Neeb, L. Cederbaum. A. Bradshaw, Phys. Rev. Lett., 79 (1997) 3617.
[5]   D.J. Oakes, H.E. Newell, F.J.M. Rutten, M.R.S. McCoustra, M.A. Chesters, J. Vac. Sci. Technol. A 14 (1996) 1439.

The adsorption of acenes on rutile $TiO_2(110)$

S. Reiß, A. Niklewski, T. Strunskus, and Ch. Wöll

Lehrstuhl für Physikalische Chemie I, Ruhr-Universität Bochum, 44801 Bochum, Germany

Introduction

The investigation of metal oxides is currently attracting a considerable amount of interest. This interest stems to a large part from the desire to understand the fundamental processes occurring in heterogeneous catalysis using metal-oxide supported metal particles [1-3]. Therefore, the adsorption of molecular compounds on metal oxides is of great interest.

NEXAFS is a powerful tool to study the orientation and electronic properties of adsorbates on surfaces. In the present work the adsorption of benzene, naphthalene and anthracene was studied [4]. A series of quantum-chemical ab initio calculations for the interaction of benzene with the $TiO_2(110)$ surface is used to aid the interpretation of the experimental data.

Experimental

NEXAFS experiments were carried out at BESSY I using beamline HE-TGM2 and at BESSY II using beam-line PM1. All NEXAFS spectra were recorded in the partial electron yield (PEY) mode using a home made electron detector based on a double channel plate (Galileo). For the energy calibration of the NEXAFS spectra the photocurrent of a carbon contaminated gold grid with a characteristic peak at 285 eV was recorded simultaneously with each spectrum. This grid was also used as a radiation flux monitor. The sample could be rotated making measurements for different polar angles possible. The variation of the resonance intensities in the NEXAFS spectra with the photon angle of incidence allows for the calculation of the tilt angle α of the molecule with respect to the surface.

The $TiO_2(110)$ single crystal was cleaned by repeated cycles of argon ion bombardment (1×10^{-4} mbar Ar, sputter voltage 1kV, current density 2 $\mu A/cm^2$) and annealing in an oxygen atmosphere (1×10^{-6} mbar O_2, 850 K surface temperature). This preparation leads to a near stoichiometric (1x1) surface [5]. The cleanliness and stoichiometry of the substrate was controlled by XPS and LEED. Benzene and naphthalene were adsorbed by backfilling the chamber through a leak valve. Anthracene was deposited from a Knudsen cell (deposition temperature: 350 K, deposition rate: 0.4 Å/s) placed in the preparation chamber of the NEXAFS-apparatus.

Results

A. Benzene

Fig. 1 shows NEXAFS spectra recorded for the three different adlayers of benzene. The spectra are dominated by a prominent peak labeled A located at 285 eV. This resonance is unequivocally assigned to an excitation of a C 1s electron into an empty $\pi*$ (e_{2u}) orbital of the aromatic ring. A detailed analysis of the NEXAFS data reveals that the Rydberg resonance X, which is clearly visible for the multilayer (Fig. 1, top), is quenched in the monolayer. At the same time two new resonances labeled A_1 and ξ appear in the monolayer data. Fig. 1(inset) shows an enlarged view of the energy range between 280 and 290 eV of the benzene monolayer NEXAFS spectrum taken under normal incidence (90°) of the X-ray photons.

In the monolayer and submonolayer NEXAFS data there is significant intensity below the $\pi*$ resonance located at 285 eV, which is not present in the corresponding multilayer data. Comparison to data recorded for the substrate prior to adsorption demonstrates that this feature is related to adsorbed benzene molecules. We assign this feature A_1 to an excitation
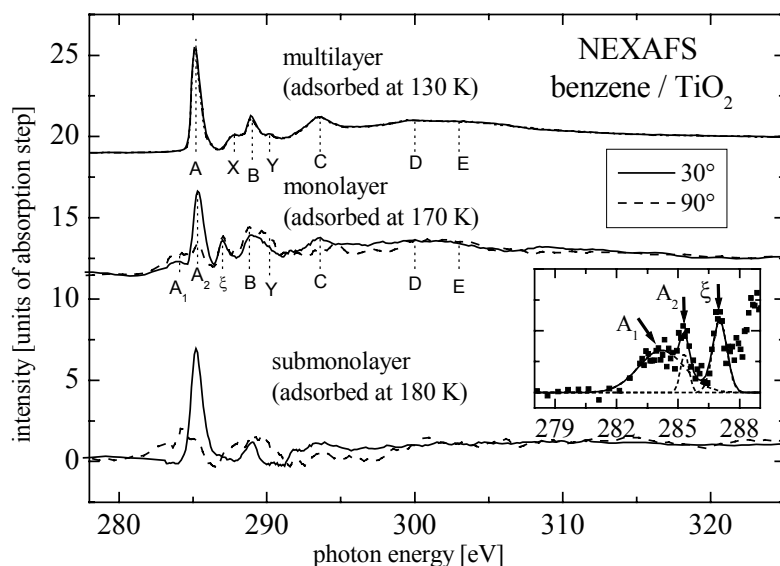
Fig.1: Comparison of NEXAFS spectra recorded for different layers of benzene. The angle of incidence was varied from 30° to 90°. *Inset:* Enlarged view of the pre-edge regime of the NEXAFS spectrum of a benzene monolayer taken under normal incidence (90°).

into a π^* orbital of benzene molecules bound to defect sites at the TiO_2 surface while resonance A_2 corresponds to the π^* resonance of the "regular" monolayer species. The energetic position and the line width of resonance A_2 are identical to those of resonance A in the multilayer spectrum. The monolayer and submonolayer data reveal a pronounced dichroism of the resonance intensities. A detailed quantitative analysis yields a tilt angle between the benzene molecular plane and the surface plane of 24° ($\pm$ 5°) and 19° ($\pm$ 8°) for the monolayer and the submonolayer, respectively. No dichroism was seen in the NEXAFS spectra for the benzene multilayer, indicating the presence of random molecular orientation.

B. Naphthalene, Anthracene

In Fig. 2 we present the NEXAFS spectra for three different layers of anthracene. In contrast to the spectra recorded for benzene, the NEXAFS data for anthracene were measured at beamline PM1 at BESSY II. The resolution of this beamline as well as the signal to noise ratio are inferior to that of the HE-TGM2 beamline. A significant amount of intensity is observed for photon energies below 284 eV. As in the case of benzene, this observation is attributed to the presence of anthracene molecules bound to surface defect sites. A quantitative analysis of the π^* resonance intensity seen in the monolayer spectra taken under normal and grazing incidence yielded an average tilt angle of 28°. Prior to this quantitative analysis, the feature located at energies below 284.0 eV attributed to molecules bound at defect sites had been subtracted. In contrast to the two smaller acenes the multilayer spectra recorded for incident angles of 30° and 90° reveal

Fig.2 Comparison of NEXAFS spectra of anthracene on TiO_2 (110).

a strong dichroism. For the multilayer, the average tilt angle between molecular and surface plane calculated from the variation of the π^* resonance intensity with angle of incidence amounts to 67° ($\pm$ 10°). For the bilayer an average tilt angle of 42° ($\pm$ 12°) is obtained.

Discussion

A. Benzene

The present data indicate that when exposing a $TiO_2(110)$ surface to benzene two different adsorbed species are observed, one of them located at structurally perfect parts of the surface (species A) and a second one bound to defect sites (species B). Benzene adsorbed on a "perfect" adsorption site is characterized by a sharp π^* resonance located at 285.2 eV. The molecules bound to surface defect sites (species B) are characterized by a broader π^* resonance in the NEXAFS spectra located at 284.2 eV, i.e. about 1 eV lower than the position of the π^* resonance assigned to species A. The width of the π^*-resonance (A_2) assigned to species A is virtually the same as that observed for the multilayer, indicating the absence of a strong chemical interaction between the benzene π-system and the substrate.

In the absence of a significant chemical interaction one would assume that the benzene-TiO_2 interaction is controlled by electrostatics leading to an orientation with the molecular plane orientated parallel to the surface. This expectation is fully confirmed by recent ab initio calculations [4] which unequivocally favor a planar orientation of benzene. However, a tilt angle of zero is outside the error bars of the tilt angles determined from the dichroism in the NEXAFS spectra. A detailed analysis suggests the possibility that a significant fraction of the benzene molecules is adsorbed on misaligned micro-facets of the single crystal. The rather high concentration of such defect species is consistant with the fact that the structural quality of the TiO_2 surface is clearly inferior to that what can be reached for metal single crystals where this effect is not observed.

B. Naphthalene and Anthracene

The XPS and NEXAFS data for naphthalene and anthracene do not reveal the presence of an adsorption mechanism different from that seen for benzene. Accordingly, we propose a electrostatic interaction between the larger acenes and TiO_2. As in the case of benzene the presence of a broad feature at energies of around 284 eV in the NEXAFS spectra indicates the existence of a defect species. Also the dichroism in the NEXAFS spectra is similar to benzene.

The anthracene multilayer spectra exhibit a strong dichroism (average tilt angle of 67°) revealing the presence of a high degree of molecular orientation. Similar to naphthalene (not shown) the data would be consistent with the growth of molecular crystallites exhibiting the monoclinic bulk structure of anthracene [6, 7] and with their b-axis orientated normal to the surface plane.

References:

1. J. Evans, B.E. Hayden, and G. Lu, Surf. Sci. **360**, 61-73, (1996).
2. V.E. Henrich and P.A. Cox, *The surface science of metal oxides*. 1994, Cambridge: Cambridge University Press.
3. M.A. Vannice and C. Sudhakar, J. Phys. Chem. **88**, 2429-2432, (1984).
4. S. Reiß, H. Krumm, A. Niklewski, V. Staemmler, Ch. Wöll, J. Chem. Phys., in print.
5. M. Li, W. Hebenstreit, U. Diebold, M.A. Henderson, and D.R. Jennison, Far. Disc. **114**, 1-14, (1999).
6. C. Pratt and J.D. Dunitz, Acta Cryst. B **46**, 795, (1990).
7. A.M. Mathieson, J.M. Robertson, and V.C. Sinclair, Acta Cryst. B **3**, 245, (1950).

Interaction between metals and organic films

S. Park, T. U. Kampen, and D. R. T. Zahn
Institut für Physik, TU Chemnitz, D-09107 Chemnitz, Germany

T. Kachel, P. Bressler and W. Braun
BESSY GmbH, Albert-Einstein-Straße 15, D-12489 Berlin-Adlershof, Germany

The injection of carriers into organic molecular semiconductors is a key to the operation of organic based devices. In most cases, top metal electrodes are fabricated by evaporating metals onto organic films through a shadow mask. The resulting carrier injection is determined by the chemical and electronic properties at metal/organic interfaces. Despite the technological importance, however, only a few investigations have focused on metal-on-organic interfaces. In this study, near-edge x-ray absorption fine structure (NEXAFS) is employed to investigate chemical interaction upon deposition of various metals on organic films of two different perylene derivatives, 3,4,9,10-peryelenetetracarboxylic dianhydride (PTCDA) and dimethyl-3,4,9,10-peryelenetetracarboxylic diimide (DiMe-PTCDI). The molecular structures of PTCDA and DiMe-PTCDI are shown in Figure 1.

Organic films of ~ 20 nm thickness were grown on S-passivated GaAs(100) surfaces via organic molecular beam deposition in an ultrahigh vacuum chamber and serve as substrates for the subsequent metal deposition. Ag and In were evaporated from Knudsen cells while Cs was evaporated from a dispensor. The thickness of the organic films as well as the metal layers was controlled using a quartz microbalance in the vicinity of the sample. During the evaporation the substrate was kept at room temperature. The fine structure in C-K, N-K, and O-K absorption edges was measured using the PM1 monochromator at BESSY II. The spectra were recorded in the total electron yield (TEY) mode. For the normalization spectra of a Ag film of 100 nm thickness were taken and used as reference spectra.

Figure 2 shows NEXAFS spectra of the C K-shell absorption taken for 20 nm PTCDA films and for subsequent metal deposition on the PTCDA films. The spectra were taken at two different angles of incidence with respect to the substrate surface normal. The spectra corresponding to the 20 nm PTCDA film are characterized by sharp structures in the low photon energy region due to transitions from core levels to unoccupied π^* orbitals, followed by broad features due to transition to σ^* orbitals in continuum states. Peak C1 and C2 can be assigned to transitions from the C atoms in the perylene core into the LUMO and LUMO+1 states, respectively, while transitions involving the anhydride group contribute to peak C3 in the C K-edge spectra [1].

The evaporation of Ag on the 20 nm PTCDA film does not change the lineshape, the relative
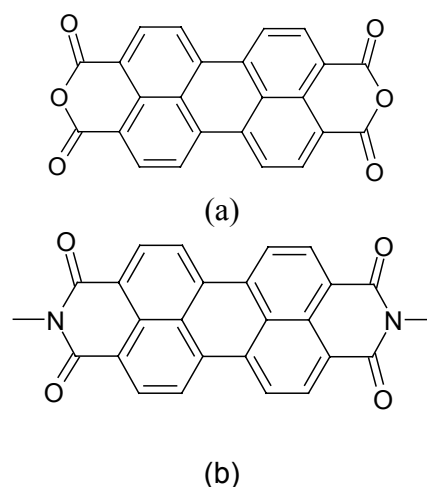

Figure 1. Molecular structure of (a) PTCDA and (b) DiMe-PTCDI.

intensities, as well as the angular dependence. This indicates the formation of an unreactive Ag/PTCDA interface, which is in good agreement with the synchrotron photoemission study by Hirose *et al.* [2].

The situation is different when Cs and In are evaporated on the PTCDA film. Changes in the spectra are apparent in the spectra at 70°, indicating that predominantly transitions to π^* orbitals are influenced by the metal deposition. Upon Cs deposition, all the π^* resonance peaks become broadened, the intensity of C1 and C2 orbitals decreases, the energy position of C3 slightly shifts towards higher photon energy. The spectral change indicates that there is a charge transfer between the Cs atoms and the PTCDA molecules. More dramatic changes are observed upon In deposition. Upon 0.3 nm In deposition, peak C1 completely disappears and a decrease in intensity and a broadening of the peak width are observed. Similar behavior is observed in the O K-edge NEXAFS spectra. Thus, it can be seen that the degree of the charge transfer between the metals and the PTCDA molecules is in the order of Ag (negligible) < Cs < In, and the spectral changes can be understood according to the rate of the charge transfer.

From an element and functional-group analysis of the NEXAFS spectra, the charge transfer mechanism between metals and organic molecules can also be deduced. The survival of the peaks corresponding to the π^* orbitals of the carboxylic C atoms, the absence of strong shifts or new features and the negligible dependence of peak intensities on the metal thickness indicate that the interaction between metals and PTCDA molecules is not accompanied by a covalent bond formation [3]. It is known that a reaction of metals with π^*-conjugated molecules form organometallic-complexes, resulting in cationic metal states, like Cs^+ and In^{3+} [4]. The cationic metal is bound to the entire π^*-electron system of the ring, not forming a covalent bond at a
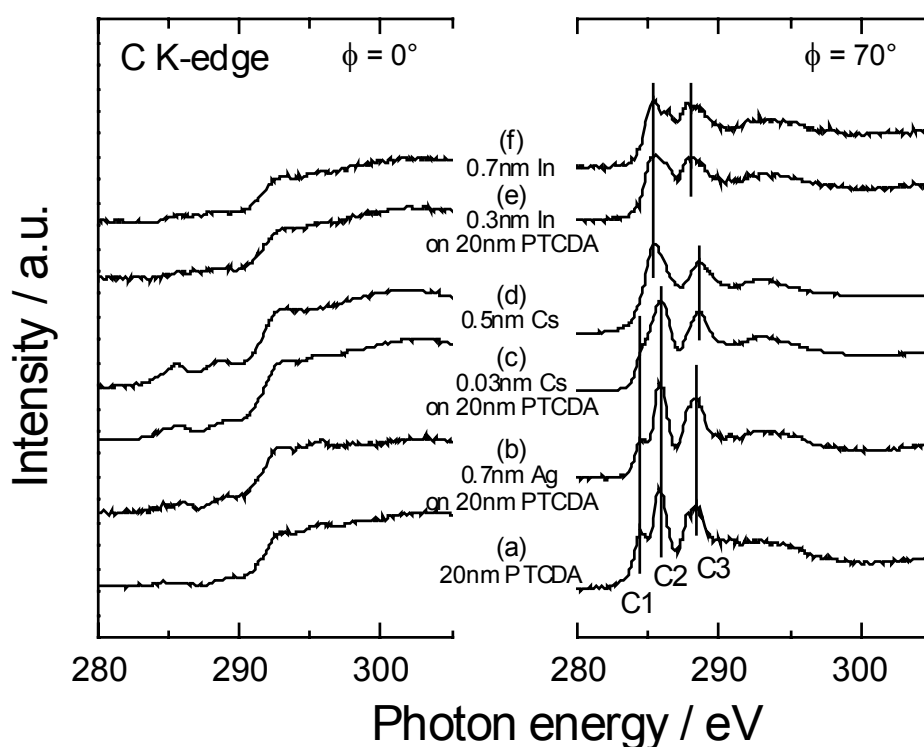

Figure 2. C K-edge NEXAFS spectra at two different (0 and 70°) angles between the incident photon beam and the surface normal for (a) PTCDA film of 20 nm thickness, (b) 0.7 nm Ag deposited on 20 nm PTCDA film, (c) 0.03 nm, (d) 0.5 nm Cs deposited on 20 nm PTCDA film, and (e) 0.3 nm, (f) 0.7 nm In on 20 nm PTCDA film.
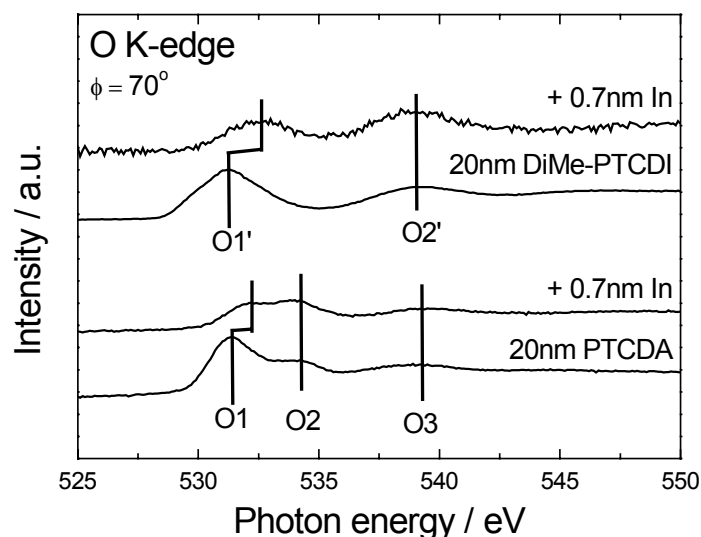
2

Figure 3. O K-edge NEXAFS spectra for 0.7 nm In deposited on PTCDA and DiMe-PTCDI films 20 nm thickness.

certain molecular site. Wherever in the molecule the charge transfer occurs, the charge should consequently be redistributed over the molecules. Since, as in the case of the highest occupied molecular orbital in the photoemission spectra, the low lying π^* orbitals are most susceptible to any charge redistribution, pronounced changes in the spectra occur in peaks corresponding to transition to the π^* orbitals.

Figure 3 shows O K-edge NEXAFS spectra upon deposition of In on the PTCDA and DiMe-PTCDI films. A main feature in the spectra is that the shift of peaks (O1 and O1') which arise from excitation of carboxylic O atoms to LUMO is bigger for In deposition on the DiMe-PTCDI film. This indicates that stronger charge transfer occurs between In and DiMe-PTCDI than between In and PTCDA. Comparing the molecular structure of the two molecules (Figure 1), it can be deduced that an additional charge transfer occurs via the dimethyl pendant group in the DiMe-PTCDI molecule.

In this report, the chemical interaction upon the deposition of various metals on the PTCDA and DiMe-PTCDI films was investigated using NEXAFS. The charge transfer between metal atoms and organic molecules is found to strongly depend on type of metal and organic molecular structure. The results show that NEXAFS is a suitable tool to probe the degree of the charge transfer.

[1] J. Taborski, P. Väterlein, H. Dietz, U. Zimmermann, E. Umbach, J. Electron Spectrosc. Relat. Phenom. 75 (1995) 129.
[2] Y. Hirose, A. Kahn, V. Aristov, P. Soukiassian, V. Bulovic, S.R. Forrest, Phys. Rev. B 54 (19) (1996) 13748.
[3] S. Park, T.U. Kampen, T. Kachel, P. Bressler, W. Braun, D.R.T. Zahn, Appl. Surf. Sci., in print.

Amorphization and defect formation in Si implanted GaN: A NEXAFS study.

M. Katsikini, F. Pinakidou, E. C. Paloura
Aristotle University of Thessaloniki, Department of Physics, 54006 Thessaloniki, Greece.
R. Mitdank, M. Schneider
Humboldt University zu Berlin, Institut für Physik, Invalidenstraße 110, 10115 Berlin, Germany.
A. Markwitz
*Institute of Geological & Nuclear Sciences Ltd., Rafter Laboratory, 30 Gracefield Road
PO Box 31-312, Lower Hutt, New Zealand*

GaN is a direct wide band-gap semiconductor, which finds applications in opto- and micro-electronics in the blue-UV[1]. Doping by ion implantation is attractive because it permits precise control of the dopant profile and concentration. However implantation causes lattice damage which can be recovered by post-implantation annealing, which is also necessary for the implant activation[2]. Here we apply NEXAFS spectroscopy in order to study the effect of lattice damage, due to Si ion implantation, on the density of empty states of GaN.

The GaN samples were grown by molecular beam epitaxy on (0001) Al_2O_3 substrates, using an electron cyclotron resonance plasma source for the activation of nitrogen[3]. The GaN sample was implanted using 90 keV Si ions with doses 1×10^{14}, 1×10^{16} and $1 \times 10^{18} cm^{-2}$. The NEXAFS spectra were recorded at room temperature, at the N-K-edge (395-435eV), using monochromatised light from the VLS-PGM monochromator at the electron storage ring BESSY-II in Berlin (the base pressure during the measurements was 1×10^{-9} mbar). The NEXAFS were recorded with a 60μm exit slit, at $\vartheta = 55^\circ$ (relative to the sample surface), using a high purity Ge fluorescence detector. The information depth of the fluorescence photons is 40nm, i.e. they probe the implanted region.

The N-K-edge NEXAFS spectra of the under study samples are shown in Fig. 1. After normalisation to the primary beam current, the spectra were subjected to linear background subtraction and normalisation to the atomic limit (~ 435eV). It is obvious from the figure that as the implantation dose increases, the NEXAFS resonances become broader due to the implantation-induced increase of the static disorder. At the high dose limit ($1 \times 10^{18} cm^{-2}$) the NEXAFS resonances become very broad and practically disappear, i.e. the spectrum resembles that of an amorphous sample. According to L. A. Bugaev et al[4] the absorption cross-section σ of an atom in a compound is the sum of different photoelectron scattering contributions, i.e.:

$$\sigma = \sigma_{at} \left[1 + \chi_{SS}^{(1)} + \chi_{SS}^{(MRO)} + \chi_{MS} \right] \qquad (1)$$

where σ_{at} is the absorption cross section due to photoionisation, $\chi_{SS}^{(1)}$, $\chi_{SS}^{(MRO)}$ and χ_{MS} are the contributions of single scattering events within the first shell, single scattering from more distant shells (middle range order) and multiple scattering processes (double- and triple-scattering), respectively. To account for the static and thermal disorder every component of σ should
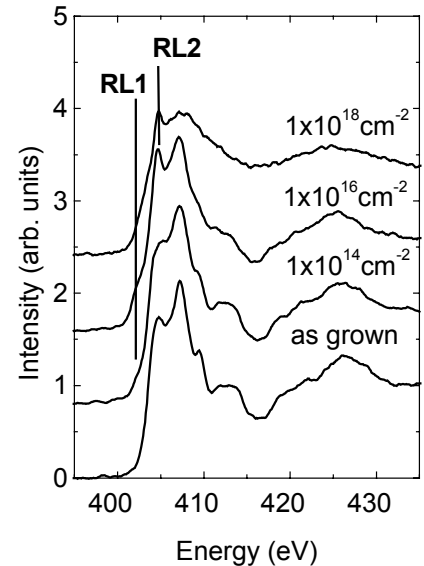
Fig. 1: N-K-edge NEXAFS spectra of the Si implanted GaN samples. The spectrum of the as-grown sample is shown at the bottom of the Figure.

be multiplied by the Debye Waller factor DW_1 for the first shell (i.e. the tetrahedron around N) and DW_2 for the more distant shells and the multiple scattering events. The "fine structure" of the spectrum depends on the ratio (DW_2/DW_1). As the static disorder increases (due to implantation) the value of the ratio (DW_2/DW_1) increases and the component of σ due to the single scattering from the 1st shell dominates the spectrum. Therefore, it can be concluded that the GaN sample which is implanted with the dose 1×10^{18} cm^{-2} becomes amorphous and for that reason the contribution from the more distant shells is minimised.

In addition to the broadening of the NEXAFS resonances, implantation introduces two resonance lines in the spectrum. The first one (denoted RL1) appears below the absorption edge of the implanted samples and the second one (denoted RL2) appears above the absorption edge at high implantation doses. The RL1 was previously detected in MOVPE GaN samples implanted with N and O ions with doses 5×10^{13} and 5×10^{14} cm^{-2}, respectively, and it was attributed to nitrogen interstitials (N_i) and/or nitrogen antisites (N_{Ga})[5]. Between these two defects, N_i is preferentially formed via implantation. According to J. Neugebauer et al[5], the N_i relaxes in the (100) split-interstitial configuration where the two N atoms occupy the same substitutional site and each one forms two bonds with two Ga atoms. The two N atoms give πp-like antibonding midgap states while the N-Ga bond gives bonding states. The N_i-related state is expected to appear at about 1.4-1.9eV above the VBM [5]. The N_{Ga} defect is also expected to give mid-gap states[6]. Therefore, since the NEXAFS peaks correspond to transitions from initial N 1s states to unfilled states of antibonding molecular orbitals, the RL1 could be attributed to either of these defects.

The RL2 appears above the absorption edge when the implantation dose exceeds 1×10^{16} cm^{-2}. According to a theoretical study of amorphous GaN by P. Stumm and D. A. Drabold[7] a significant amount of three-fold coordinated N and Ga atoms exist in GaN. Incompletely coordinated N atoms lead to the formation of N dangling bonds. Although the implanted samples (except from that implanted with the dose 1×10^{18} cm^{-2}) are not completely amorphous, some isolated amorphous nuclei are expected to exist[8] and thus a significant number of Ga and N dangling bonds at relatively high implantation doses is expected to exist. Therefore it is proposed that RL2 in GaN is related to defects that contain N dangling bonds.

In conclusion, we have applied NEXAFS spectroscopy in order to probe to Np density of states in the conduction band of Si implanted GaN samples grown by MBE. It is found that implantation increases the static disorder while the sample which is implanted with 1×10^{18} cm^{-2} Si ions became completely amorphous. Implantation introduces states in the gap, which can be attributed to nitrogen interstitials and/ or nitrogen antisites. At high implantation doses ($\geq 1 \times 10^{16}$ cm^{-2}) an additional resonance line, which can be attributed to N dangling bonds, is observed.

[1] "Gallium Nitride I, Semiconductors and Semimetals", ed. J. I. Pankove, T. D. Moustakas, Academic Press, 1998, S. Nakamura, p. 431-457

[2] S. J. Pearton, J. C. Zolper, R. J. Shul, F. Ren, J. Appl. Phys., **86**, 1 (1999).

[3] T. D. Moustakas, R. J. Molnar, Mat. Res. Soc. Symp. Proc. **281**, 753 (1993).

[4] L. A. Bugaev, A. P. Solonenko, H. V. Dmitrienko, A. -M. Flank, Phys. Rev B., **65**, 24105 (2002).

[5] J. Neugebauer, C. G. van de Walle, Phys. Rev . B, **50**, 8067 (1994).

[6] I. Corczyca, A. Svane, N. E. Christensen, Solid State Communications, **101**, 747 (1997).

[7] P. Stumm and D. A. Drabold, Phys. Rev. Lett., 79, 677 (1997)

[8] C. Liu, B. Mensching, M. Zeitler, K. Volz, B. Rauschenbach, Phys. Rev. B, **57**, 2530 (1998).

N K and O K edge EXAFS characterization of SiO_xN_y samples.

F. Pinakidou, M. Katsikini, E. C. Paloura[*].

*Aristotle Univ. of Thessaloniki, Dept. of Physics, GR54006 Thessaloniki, Greece*

Thin silicon oxynitride films (SiO_xN_y) have been a subject of extensive study because they find applications as gate dielectrics in Si technology. Their superior to SiN_x and SiO_2 properties include high resistance to ionizing radiation, low density of interface defects, high dielectric constant and good masking properties against impurity diffusion[1]. Nitridation by ion implantation[2] is an attractive method to produce oxynitride films because it permits tailoring of the composition and precise control of the layer thickness and profile[3,4,5].

In this report, SiO_xN_y samples, with compositions $SiN_{0.33}O_{0.16}$, $SiNO_{0.5}$ and $SiN_{0.87}O_{0.76}$, are studied using EXAFS measurements at the N- and O-K-edges. The SiO_xN_y layers were produced by implantation of 16 keV N_2O^+ in Si substrates. The EXAFS spectra were recorded using the monochromator SX700-I and a high purity Ge detector. The spectra were normalized for the transmission function of the monochromator using the TEY spectrum of a clean Si sample. The spectra were subjected to subtraction of the atomic absorption using the AUTOBK[6] program and correction for self-absorption effects[7]. The $\chi(k)$ spectra were fitted with the FEFFIT[6] program using a model of crystalline Si_2N_2O constructed with FEFF8.0[6]. In Si_2N_2O every O atom is bonded with two Si atoms, which are sp^3 coordinated with the O atom and other 3 N atoms. The N atoms are sp^2 coordinated with 3 Si atoms. The Fourier transforms of the $\chi(k)$ spectra of the under study samples are shown in Fig. 1(a) and (b), for the N-K and O-K edges, respectively. An amorphous stoichiometric a-Si_3N_4 film is used as a reference.

The results of the fitting of the N-K-edge spectra are listed in Table I. In the samples with $y/x \cong 2$ we detect the presence of a N-enriched a-Si phase (a-Si:N), embedded in the SiO_xN_y matrix. Therefore, an additional N-Si path, between the 1st (N-Si) and the 3rd (N-O) shells, is needed for the fitting of the N-K-edge spectra. The fitting results of the O-K-edge spectra are listed in Table II. In all the under study samples the O atom is found coordinated with two Si atoms. The second neighboring atoms are anions. In the case of the samples with $y/x \cong 2$ the anions are only N atoms while for the $SiN_{0.87}O_{0.76}$ sample, which has higher amount of O, four N atoms are substituted by O atoms. This means that as the O concentration increases, the concentration of the SiN_2O_2 tetrahedra increases at the expense of the SiN_3O_1 tetrahedra.

The O-Si distance is found constant (independent of the composition) and equal to that in SiO_2 while the N-Si distance decreases with the O concentration. Furthermore, the O atom is coordinated with 2 Si atoms, while the coordination of the N atom depends on the composition. In the samples $SiNO_{0.5}$ and $SiN_{0.87}O_{0.76}$ the N atom is undercoordinated due to the presence of N-dangling bonds, as verified by N-K-edge NEXAFS measurements reported earlier[8].

The percentage of N which is bonded in the α-Si:N phase depends on the growth conditions[9] and the stoichiometry of the sample[8]. Among the under study samples, the sample $SiNO_{0.5}$, with the highest N content, has the greatest percentage of N atoms in the a-Si:N phase
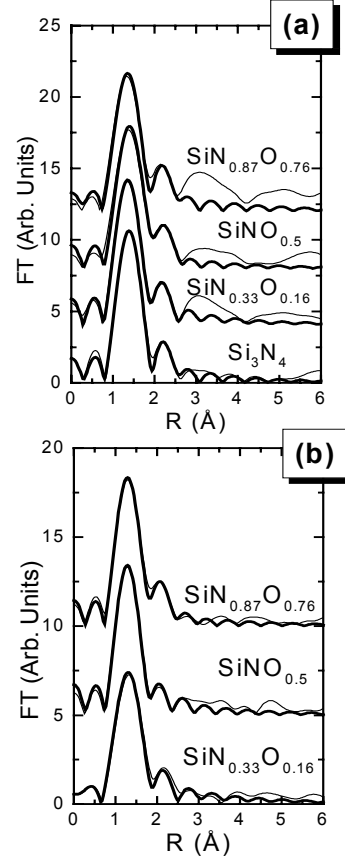
Fig. 1: *Fourier transforms of the $\chi(\kappa)$ spectra recorded at (a) N-K and at (b) O-K-edge respectively. The experimental and the fitting curves are shown in thin and thick solid lines, respectively.*

[*] *e-mail: paloura@ physics.auth.gr*

(the number of the N atoms in the a-Si:N phase is proportional to the N-Si bonds detected in the 2nd nn shell at the N-K-edge). The N-O distance increases with increasing O content while the N-N distance is almost the same for all three samples, independent on the stoichiometry and equal to the corresponding distance in the reference sample.

In conclusion, EXAFS measurements on SiO_xN_y samples show that the microstructure depends on the composition: with increasing O content the bond length N-Si decreases, the N-O distance increases while the bond length Si-O and the distance N-N remain constant. Furthermore, it is demonstrated that EXAFS can detect and identify the existence of a partially reacted a-Si:N phase embedded in the SiN matrix. The a-Si:N phase exists in the SiO_xN_y when $y/x \cong 2$.

Table I: *Fitting results of the EXAFS spectra at the N-K edge. N_i are the coordination numbers, R_i the nn distances and A_i the Debye-Waller factors.*

Sample	Si_3N_4	$SiN_{0.33}O_{0.16}$	$SiNO_{0.5}$	$SiN_{0.87}O_{0.76}$
T_1	Si	Si	Si	Si
N_1	3	2.8	2.5	2.6
R_1(Å)	1.70	1.69	1.68	1.66
$A_1 \times 10^{-3}$(Å^2)	3	2.6	2.6	2.6
T_2 (a-Si:N)		Si	Si	
N_2		0.45	0.9	
R_2 (Å)		2.10	2.20	
$A_2 \times 10^{-3}$(Å^2)		1.5	1.5	
T_3		O	O	O
N_3		2.3	2.6	2.7
R_3 (Å)		2.60	2.64	2.72
$A_3 \times 10^{-3}$(Å^2)		6.5	6.5	6.5
T_4	N	N	N	N
N_4	6	4.1	5.2	3.1
R_4 (Å)	2.79	2.80	2.77	2.78
$A_4 \times 10^{-3}$(Å^2)	13	13	13	13

Table II: *Fitting results of the EXAFS spectra at the O-K edge. N_i are the coordination numbers, R_i the nn distances and A_i the Debye-Waller factors.*

Sample	$SiN_{0.33}O_{0.16}$	$SiNO_{0.5}$	$SiN_{0.87}O_{0.76}$
T_1	Si	Si	Si
N_1	2	2	2
R_1(Å)	1.60	1.61	1.60
$A_1 \times 10^{-3}$(Å^2)	1.15	1.11	1.10
T_2	N	N	O
N_2	6	6	4
R_2 (Å)	2.65	2.68	2.64
$A_2 \times 10^{-3}$(Å^2)	23.8	21.7	3.66
T_3			N
N_3			2
R_3(Å)			2.94
$A_3 \times 10^{-3}$(Å^2)			2.04

[1] P. J. Tobin, Y. Okada, S. A. Ajuria, V. Lakhotia, W. A. Feil and R. I. Hedge, J. Appl. Phys., **75**, 1811 (1994).

[2] J. A. Diniz, P. J. Tasch and M. A. A. Pudenzi, Appl. Phys. Lett., **69**, 2214 (1996).

[3] F. H. P. M. Habraken and A. E. T Kuiper, Mat. Sci. and Engineering, **R12**, 123 (1994).

[4] A. E. T. Kupier, H. G. Pomp, P. M. Asveld, W. Arnoldbik and F. H. P. M. Habraken, Appl. Phys. Lett., **61**, 1031 (1992).

[5] J. C. Riviere, J. A. A. Crossley and B. A. Sexton, J. Appl. Phys., **64**, 4585 (1988).

[6] J. Mustre de Leon, J. J. Rehr, S. I. Zabinsky, R. C. Albers, Phys. Rev. **B 44**, 4146 (1991).

[7] M. Katsikini et al, Phys. Rev. **B56**, 13380(1997).

[8] E. C. Paloura et al, Electrochemical Society Proceedings, **98-22**, 327 (1999).

[9] E. C Paloura et al, J. Appl. Phys., **80**, 5742 (1996).

Interfaces of sputtered ZnO films

F. Säuberlich, J. Fritsche, R. Hunger, and A. Klein

Darmstadt University of Technology, Institute of Materials Science, D-64287 Darmstadt

Interfaces of transparent conducting oxides like ZnO are part of many optoelectronic devices like solar cells. Their application often requires cost-effective and fast deposition techniques, which can be scaled for large area deposition like chemical vapour deposition or magnetron sputtering. We have studied the electronic properties of magnetron sputtered ZnO films with II-VI compounds CdS and CdTe. The deposition chamber was attached to a photoelectron spectrometer system connected to the U49-2/PGM2 beamline of the BTU Cottbus/HMI/TU Darmstadt CRG. ZnO was sputtered from a ceramic target using either pure Argon or Ar/O_2 gas mixtures. CdS and CdTe were deposited from home made effusion cells.

S2p photoelectron spectra of an evaporated CdS film with increasing ZnO thickness are shown in Fig.1(a). The evolution of the valence band maximum determined for CdS from S2p binding energies with BE(S2p)-BE(VBM)=159.97 eV and for ZnO from O1s binding energies with BE(O1s)-BE(VBM)=527.5 eV is shown in Fig.1(b). The valence band offset for the ZnO/CdS interface as determined from the present experiment for sputtered ZnO films on evaporated CdS substrates is given by ΔE_{VB}=0.85±0.1 eV. A resulting energy band diagram is shown Fig.1(c), where conduction band positions are determined with literature values for the band gaps. A previous determination of the band alignment for CdS evaporated on (ex-situ) sputter deposited ZnO films has revealed a significantly different valence band offset of ΔE_{VB}=1.2±0.1 eV [1]. The origin of the differences still have to be resolved. In principle, only small variations of band alignment depending on the atomic interface structure are expected for interfaces between homopolar semiconductors as CdS and ZnO. However, the deposition techniques are strongly different and might lead to considerably different interfaces, induced, e.g., by the momentum impact on the substrate during sputter deposition. Since in Cu(In,Ga)(S,Se)$_2$ solar cells, e.g., the ZnO window layer is deposited by sputter deposition on the CdS layer, it is important to understand such sputter induced interface modifications.
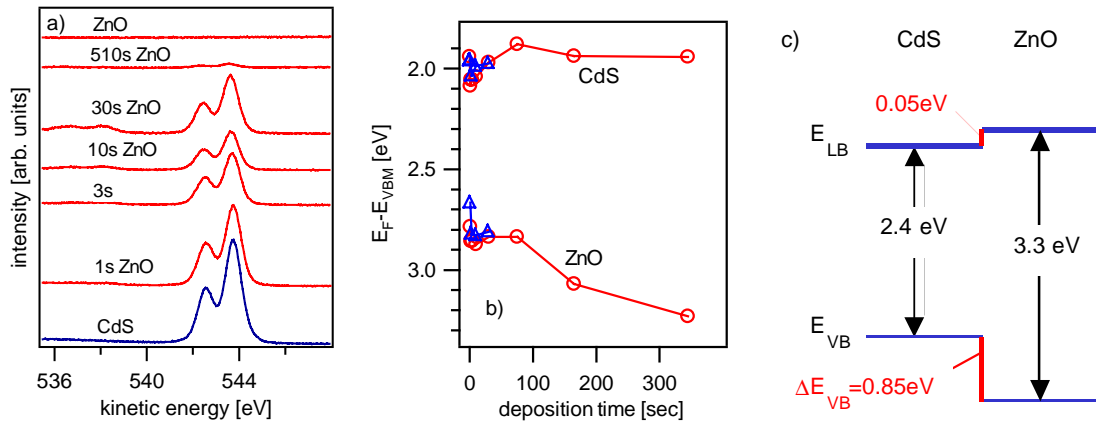

Fig.1: S2p core level photoelectron spectra of evaporated CdS with increasing ZnO thickness excited with hn~700 eV photons (a). The intensities are not normalised to the photon current. Evolution of the valence band maxima of CdS and ZnO with film thickness from two different experiments (b), and band alignment for ZnO/CdS (c).

In the experiment shown in Fig.1 the ZnO films have been sputtered with pure Argon as sputter gas. Nevertheless some oxidation of the substrate occurs with increasing deposition time as evident from the S2p spectra in Fig.1(a). If a few percent O_2 are added to the sputter gas, considerably stronger interface oxidation occurs. In Fig.2. O1s and Te3d core level spectra of evaporated CdTe substrates covered with thin ZnO films are shown. All ZnO films were deposited for 1 min with identical total gas pressures and plasma powers to give approximately the same ZnO film thicknesses. The bottom spectra for sputtering with pure Ar show the typical two-component O1s emission of sputter deposited films and only little substrate oxidation [2]. The oxidation is identified from the emission at kinetic

energies around 129 eV. If the sputter gas contains 10% oxygen much stronger substrate oxidation occurs, evident from both the Te3d and O1s level, which shows an additional third component due to Te and Cd oxides. The two subsequent spectra are again obtained with pure Argon as sputter gas. The degree of oxidation decreases with time, which indicates a modification of the sputter target by oxygen. Stable experimental conditions are therefore only achieved by suitable target pretreatments. The top spectra are deposited with a sputter gas containing 3% oxygen. Again an increase of substrate oxidation is observed.
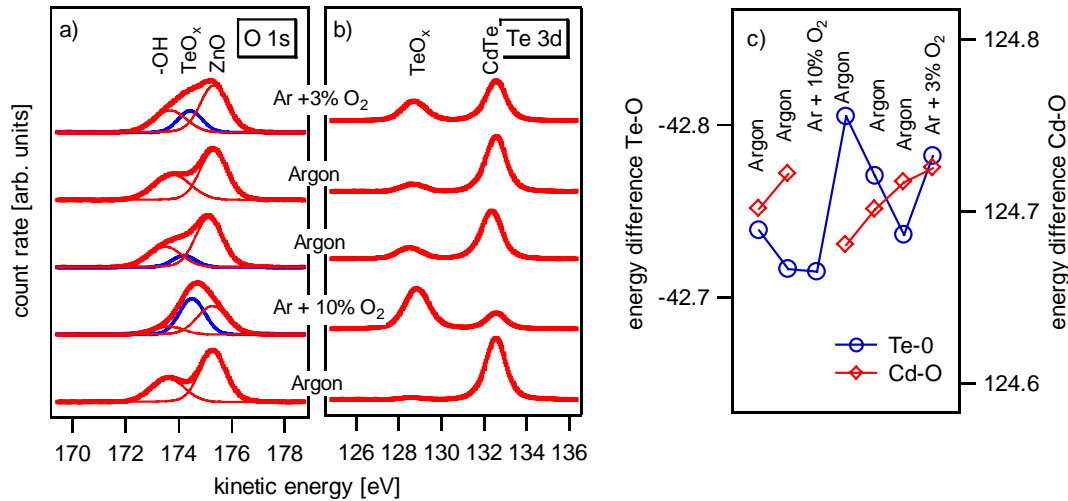
Fig.2: O1s (a) and Te3d (b) core levels excited with 700eV photons. The spectra were taken from ZnO/CdTe samples with similar ZnO thicknesses but different sputter gases. The Te3d-O1s energy difference (c) is a measure for the ZnO/CdTe band alignment.

To identify the influence of substrate oxidation on the band alignment of the interface the binding energy differences between substrate Cd 3d and Te 3d and the ZnO O1s component are determined. The result is given in Fig.2(c). The data point of Cd 3d for the strongest interface oxidation has been omitted since the Cd 3d level is also affected by a chemical shift due to oxidation. The variation of binding energy differences is smaller than 100 meV. This indicates that sputter induced substrate oxidation has no significant influence on the band alignment. To clarify the origin of band lineup modification by sputter deposition further experiments are required. The chemistry and morphology during initial growth are important parameters, which are most likely modified by the sputtering parameters. The surface sensitivity and high energy resolution of synchrotron radiation from undulator beamlines provides a unique tool to understand these technologically important questions.

[1] M. Ruckh, D. Schmid, H. W. Schock, J. Appl. Phys. 76, 5945 (1994).
[2] The high binding energy component (KE=173.5 eV) of the O1s level is due a surface localised species as determined from energy dependent photoemission. Experiments are presently under way to clarify its origin and dependencies.

Vectorial characterization of magnetic domain structure in ultrathin magnetic layered systems by photoemission microscopy

W. Kuch, K. Fukumoto, F. Offi, L. I. Chelaru, and J. Kirschner

*Max-Planck-Institut für Mikrostrukturphysik, Weinberg 2, D-06120 Halle, Germany*

The rapid progress in the field of ultrathin film magnetism and the use of layered magnetic systems with microscopic lateral dimensions in magnetoresistive devices demands for an adequate characterization technique. Photoelectron emission microscopy (PEEM) in connection with x-ray magnetic circular dichroism (XMCD) in the absorption of soft x-rays has already proven its versatility as a technique that allows layer-resolved microscopic magnetic imaging [1] due to the element-specificity of XMCD. In this method, the local intensity of emitted low-energy secondary electrons for excitation at the maxima of elemental absorption edges is imaged by a set of electrostatic lenses. The local secondary electron intensity is a measure for the local x-ray absorption, which depends on the relative orientation of the magnetization direction and the direction of the incoming, circularly polarized x-rays. We demonstrate here that because of this directional dependence the effect can be also used for the vectorial characterization of the local magnetization direction by combining domain images of the same spot on the sample for different incidence directions of the exciting x-rays.

As an example we present the magnetic microstructure at spin-reorientation transitions in an ultrathin Ni layer, epitaxially grown on a Cu(001) single crystal surface and capped by Cu. A spin-reorientation transition is the continuous or discontinuous change of the direction of easy axis of magnetization in an ultrathin magnetic film. Its macroscopic behavior is described by magnetization-direction dependent terms of the free energy, the so-called magnetic anisotropy energy.

Thin Ni films have been deposited on Cu(001) by electron beam assisted thermal evaporation at room temperature as 0–50 atomic monolayers (ML) thick wedges of 200 μm width, and capped by 11 ML Cu. The PEEM measurements have been performed at the UE56-2 PGM 2 beamline, using radiation from the fifth harmonic of the elliptical undulator, and a commercially available PEEM [2]. The incidence angle of radiation was 60° with respect to the surface normal. Images for different azimuthal orientations of the light incidence have been obtained by rotating the sample about its surface normal, adjusting the lateral position in order to keep the same field of view.

Fig. 1 shows domain images of the Ni wedge obtained for two different incidence azimuth angles, as indicated by arrows labeled "hv". The contrast at the Ni L_3 absorption

edge (853 eV photon energy) was used to image the magnetic domains. The Ni thickness increases from bottom to top, as indicated at the left axis. The images show the absorption asymmetry in a grayscale code. The asymmetry is proportional to the projection of the local magnetization direction on the light incidence direction. The two images shown in Fig. 1 represent thus two independent measures of the local magnetization direction projection at each point of the image, which suffice to determine the two degrees of freedom of the magnetization direction in angular space. Comparing the two images it is in particular easy to distinguish magnetization directions parallel to the film plane ("in-plane") and magnetization directions parallel or antiparallel to the surface normal ("out-of-plane"). The former undergo approximately a contrast reversal upon the near-180° change in x-ray incidence azimuth presented in Fig. 1. The asymmetry contrast of the latter, on the other hand, does not change, since the light polarization component perpendicular to the film plane does not change.
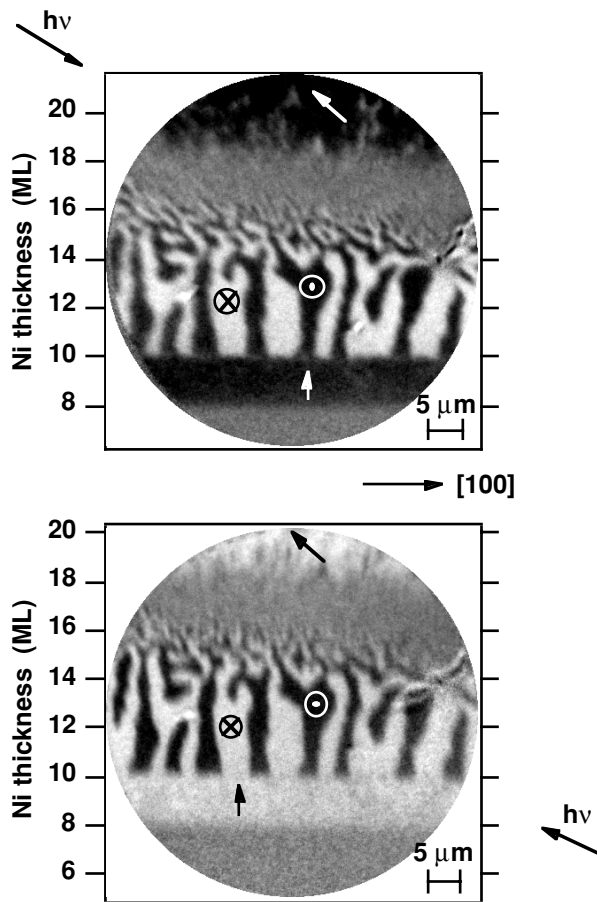
Fig. 1: Magnetic domain images at the Ni L_3 edge of 11 ML Cu/ Ni wedge/Cu(001). The Ni thickness is given at the left axes. The two images show the same region of the sample for different incidence angles, as indicated by arrows labeled "hν". This allows to determine the direction of the local magnetization, as indicated in some domains.

Looking at the images of Fig. 1 one recognizes a large region with out-of-plane magnetization for Ni thicknesses between 10 and 16 ML, characterized by a stripe-like domain pattern. At Ni thicknesses between 8 and 10 ML as well as above 18 ML the magnetization is in the film plane. The local magnetization directions are indicated in the images in some representative domains.

The sign of the magnetic anisotropy consequently changes twice as a function of Ni thickness, at 10 ML and at 18 ML Ni thickness. This is similar to the case of ultrathin Ni/Cu(001) films, which are known to exhibit an out-of-plane anisotropy caused by magneto-elastic energy contributions from tetragonal strain [3]. For uncapped Ni/Cu(001) films this results in a thickness interval of 11–37 ML in which out-of-plane magnetization is observed [4, 5]. In the present case already starting from 18 ML Ni thickness an in-plane magnetization is observed. This has to be attributed to the influence of the Cu cap layer. Since the formation of misfit dislocations in Ni/Cu(001) starts already at 13 ML Ni thickness [4], the upper Ni/Cu interface is not identical to the lower one. The growth of Cu on the partially relaxed surface of the Ni film probably acts to further reduce the strain in the Ni layer, and/or add an interface anisotropy energy favoring in-plane magnetization [6].

There is a characteristic change in the stripe domain pattern as a function of Ni thickness in the out-of-plane region. Starting at about 14 ML Ni thickness an increase in the number of stripes is recognized, which is accomplished by bifurcations in the stripe domains. This leads to a rapidly decreasing domain size. The shrinking of the average domain size can be explained by the competition between the magnetostatic energy on the one hand, and the energy cost for creating domains on the other hand [7]. Closely spaced alternatingly up and down magnetized perpendicular domains have a lower magneto-static energy than a single out-of-plane domain due to partial magnetic flux closure [8]. The formation of such domains can be energetically favorable close to the spin-reorientation transition because at that point the anisotropy energy, and hence the energy for the formation of domain walls (in which an in-plane component of the magnetization occurs) is low. Interestingly in the present sample this is only observed at the second spin reorientation transition at 18 ML Ni thickness, not at the first at 10 ML Ni thickness. The reason for this is not fully clear at the moment. Kinetic barriers for the formation of the stripe domains in the course of film deposition could be responsible.

[1] W. Kuch, Xingyu Gao, and J. Kirschner, Phys. Rev. B **65**, 064406 (2002).

[2] Focus IS PEEM, Omicron.

[3] B. Schulz and K. Baberschke, Phys. Rev. B **50**, 13467 (1994).

[4] W. L. O'Brien, T. Droubay, and B. P. Tonner, Phys. Rev. B **54**, 9297 (1996).

[5] R. Vollmer, T. Gutjahr-Löser, J. Kirschner, S. van Dijken, and B. Poelsema, Phys. Rev. B **60**, 6277 (1999).

[6] K. Fukumoto, H. Daimon, L. I. Chelaru, F. Offi, W. Kuch, and J. Kirschner, Surf. Sci., (to be published).

[7] M. Speckmann, H. P. Oepen, and H. Ibach, Phys. Rev. Lett. **75**, 2035 (1995).

[8] B. Kaplan and G. A. Gehring, J. Magn. Magn. Mater. **128**, 111 (1993).

Non-destructive evaluation of advanced Materials by Synchrotron Radiation Refraction Topography

Bernd R. Müller, Manfred P. Hentschel, Axel Lange

Bundesanstalt für Materialforschung und -prüfung (BAM), D-12200 Berlin, Germany

Introduction

The effect of X-ray refraction provides unconventional small angle X-ray scattering (SAXS) techniques which have been developed and applied in the last decade at our laboratory to meet the actual demand for improved non-destructive characterization of advanced materials. X-ray refraction reveals the inner surface and interface concentrations of nanometre dimensions due to the short X-ray wavelength near 0.1 nm. Sub-micron particle, crack and pore sizes are easily determined by "X-ray refractometry" without destroying the structure by cutting or polishing for microscopic techniques.

Beyond this analytical potential for (integral) analysis, spatial resolution can be achieved, when the sample is scanned across a narrow X-ray beam. In this case we call it "X-ray refraction topography". The X-ray refraction topogram of a probe can be measured within relatively short time, as the scattered intensity at very small angles of few minutes of arc is much higher than in conventional wide angle X-ray scattering (WAXS).

Physics and instrumentation

The physics of X-ray refraction is quite similar to the well-known refraction of the visible light by optical lenses and prisms, which is governed by Snell's law. However a major difference to the visible optics is, that the refractive index n of X-rays in matter is nearly one ($n < 1$) [1]. This causes deflections at very small angles in the order of a few minutes of arc. The refracted intensity distribution of a cylinder without absorption effects can be expressed as $I^*_R(2\theta) = I_R(2\theta) - I_{R0}(2\theta) \cdot I/I_0 = I \cdot k \cdot d \cdot N \cdot R$ [2] where I^*_R depends on the transmitted intensity I, the thickness d and the inner surface density $\Sigma = N \cdot R$ (N is the amount of fibres) of the sample, respectively. R is the radius of the fibre, θ is the scattering angle and I_0 the intensity of the incident beam. The proportional factor k is a specific constant of the used apparatus and can be determined by measuring a probe with a known inner surface density. The proportional factor k and the inner surface density Σ define the refraction value $C = k\cdot\Sigma$, which is a relative measure of the surface density of the sample. For practical measurements the surface density of the sample can be measured according to $C = 1/d \cdot (I_R/I - I_{R0}/I_0)$.
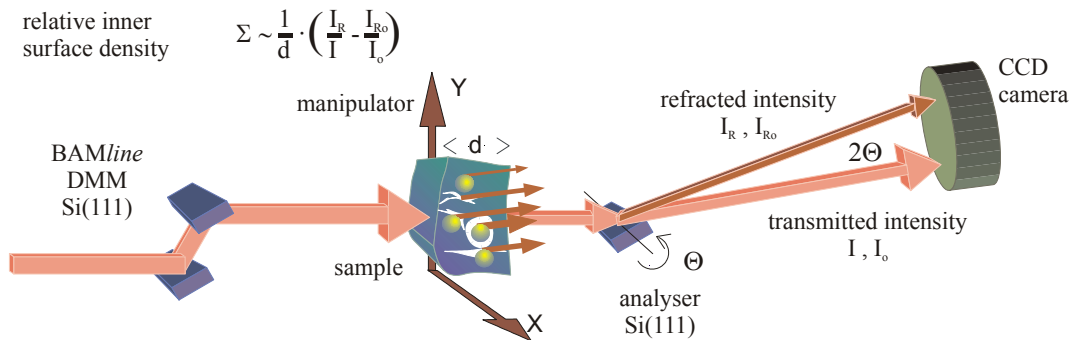

Fig.1: Current SAXS instrumentation at the BAM*line* with a Si(111) DMM (collimated X-ray beam from 5 keV to 40 keV), an x-y-sample manipulator, a Si(111) crystal as analyser and a CCD camera which measures the refracted intensity of the sample (I_R) or if the sample is not in place (I_{R0}) as well as the intensity I_0 (without sample) or I (with sample), respectively.

The current SAXS instrumentation at the BAM*line* is sown in Fig.1. It consists of the Si (111) Double Crystal Monochromator (DMM) of the BAM*line* [3] which delivers a collimated and monochromatised bundle of x-rays from 5 keV to 40 keV photon energy, an x-y-manipulator which scans the sample across the beam, an analysing Si (111) crystal which selects the refracted or the direct beam and an X-ray sensitive CCD-camera which detects the intensity of the refracted (I_R, I_{R0}) or direct (I, I_0) beam, respectively.

Results

Fig. 2 shows the experimental set up and first results from test measurements at the BAM*line*. At top right it images the crack pattern in the bi-directional CFRP sample. The image is made up of six measurements at equally spaced positions along the Y-axis. Each measurement shows the inner surface density distribution of an area of 16×0.6 mm^2. The type of cracks is a mixture of cracks at the fibre-matrix interface (single fibre debonding, vertical structure; red and blue colour) and matrix cracks (horizontal structure; white colour).
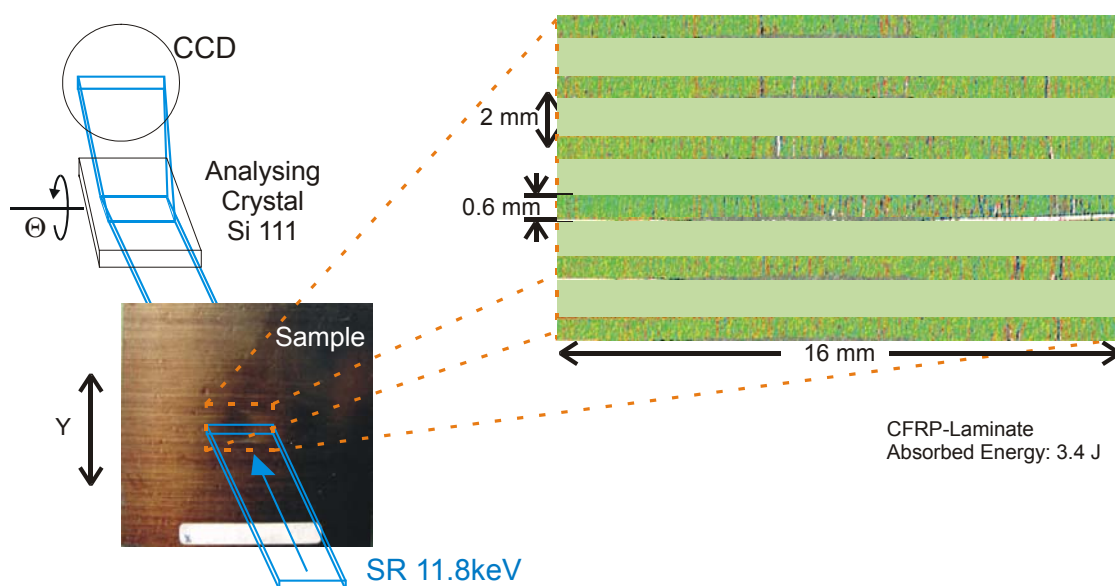
Fig.2: Large area X-ray Refraction Topography of an impact area at 12 μm spatial resolution.

Scanning X-ray refraction localises the projection of inner surface concentrations or individual edges of surfaces and interfaces such as sub-micrometer pores or cracks. The spatial resolution can be better than 10 μm, although this is not the main advantage of refraction techniques, as the signal level itself contains the information about inner surfaces. As an example we investigated carbon fibre reinforced plastic (CFRP) after impact damage. The single fibre debonding area, which develops at lower loads (e.g. 3.4 J absorbed energy in the layers), is only detectable by X-ray refraction topography.

References

[1] A. H. Compton, S.K. Allison: "X-ray in Theory and Experiment", Macmillan and Co. Ltd., London (1935).
[2] M.P. Hentschel, R. Hosemann, A. Lange, B. Uther, R. Brückner: "Röntgenkleinwinkel-brechung an Metalldrähten, Glasfäden und hartelastischem Polypropylen", *Acta Cryst.* A **43** (1987) 506.
[3] W. Görner, M.P. Hentschel, B.R. Müller, H. Riesemeier, M. Krumrey, G. Ulm, W. Diete, U. Klein, R. Frahm; "The first hard X-ray beamline at BESSY II", *Nucl. Instr. and Meth. A* **467-468** (2001) 703-706.

Temperature and time resolved X-ray scattering at thin organic films

Y. Bodenthin[a] J. Grenzer[a] R. Lauter[a] U. Pietsch[a]
P. Lehmann[b] D. G. Kurth[b] and H. Möhwald[b]

[a]Institute of Physics, University of Potsdam, D - 14415 Potsdam, Germany,

and [b]Max-Planck-Institute of Colloids and Interfaces, D - 14476 Golm, Germany

E-mail: upietsch@rz.uni-potsdam.de

At BESSY II a white beam experiment (EDR-beamline) is installed at a bending magnet and is applied for x-ray reflectivity and in-plane diffraction. The experiment exploits the exponentially decaying hard tail of the 1.7 GeV BESSY emission spectrum between $4 < E < 30$ keV [1]. The incident beam is manipulated by different slits only without passing through any further optical element before it strikes the sample aligned on the goniometer. Using a typical slit width of 0.1 x 1 mm² and a beam current of 100mA, the useful incident beam intensity is in the order of 10^{10}cps, which is sufficient to perform time resolved experiments [2].

In 2001 the capability of the set-up could be demonstrated by simultaneous measurement of the in-plane and out-of plane lattice spacing of thin organic films during annealing. In particular, we inspected the phase transition behaviour of Fe-polyelectrolyte-amphiphilie complexes (Fe- PAC) deposited as multilayers by means of the Langmuir-Blodgett (LB) technique.
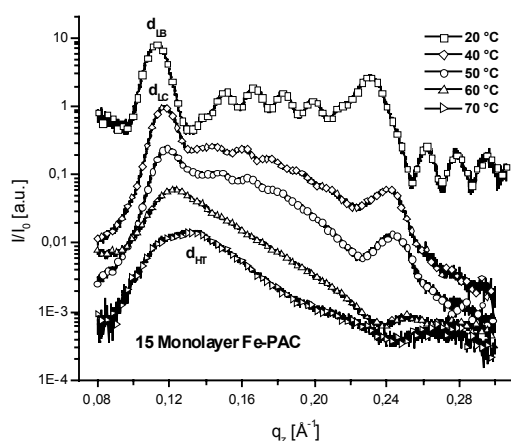
Fig.1 Reflectivity spectra at $\alpha=1°$ Fig.2: In-plane diffraction spectra of Fe-PAC
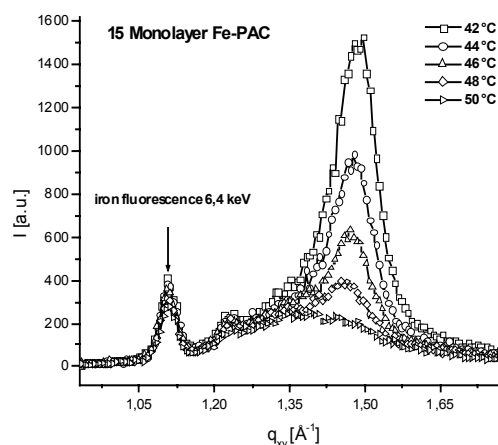
Fig. 1 shows several reflectivity spectra recorded at different temperatures at $\alpha=1°$. They are selected from a series of spectra collected over a temperature ramp of about 120s/°C. The recording time of each spectrum was 60s. Above 45°C the shape of the spectrum changes indicating a phase transition from the LB-phase with $d_{LB}= 56$ Å into a liquid-crystalline (LC) phase with $d_{LC} = 52$ Å. The phase transition is irreversible. The entire film structure remains unchanged. The Kiessig fringes

measure the total thickness, which corresponds to 15 monolayers. Between 45°C and 65°C the lattice spacing continuously changes reversibly to $d_{LC} = 50$ Å . Above 65°C the film completely reorganises it's structure. Kiessig fringes are no more visible, new Bragg peaks appear. The peak widths indicate simultaneous appearance of stacks of different spacing and number of monolayers. At 70°C the layer spacing amounts to $d_{HT} = 46$ Å.

Fig. 2 shows temperature resolved in-plane diffraction spectra. Here the incident beam strikes the sample surface at a shallow angle of incidence $\alpha = 0.2°$. The beam is diffracted at in-plane lattice planes created by the lateral arrangement of amphiphilic molecules.   The large peak at $q_{x,y} = 1.5$ Å^{-1} corresponds to a lattice spacing of $d_{in} = 4.2$ Å. The single peak indicates a hexagonal arrangement of amphiphilic molecules. The peak width measures the correlation length L of laterally molecular order. After correction by the experimental broadening L corresponds to about 18 next neighbour distances. The peak at $q_{x,y} = 1.1$ Å^{-1} reflects the K-fluorescence (E = 6.4 keV) of the Fe(II) atoms in the sample, which allows EXAFS investigations of the Fe(II) next-neighbour co-ordination [3]. As shown in fig.2, the Bragg peak intensity vanishes at about T=45°C. In contrast to reflectivity the in-plane signal reappears at the same energy if the sample is cooled below T=45°C. This can be described by a transition from the ordered LB-multilayer into a liquid-crystalline phase with rotational disorder of the amphiphilic chains. The second phase transition above T=65°C is not accompanied by the appearance of a new in-plane Bragg peak.

The kinetics of both phase transitions were studied by time dependent measurements (not shown here). The plot of the changing integrated intensity of Bragg peaks vs. 1/T gives the activation energies of $E_{C1} = (1.3 \pm 0.2)$ eV for the first phase transition at 45°C and $E_{C2} = 1.2 \pm 0.3$) eV for the second transition at about 65°C.

The present experiment demonstrates the capability of EDR set-up for 3D structure investigation of supramolecular multilayers. The simultaneous recording of the reflected and diffracted intensity guarantees identical conditions for both experiments which is necessary to identify the nature of the indicated phase transitions.

[1] J. Grenzer A. Pucher, Th. Geue, Ch. Symietz, F. Neissendorfer and U. Pietsch,
Bessy Annual Report 2000 , 233-234

[2] U. Pietsch, J. Grenzer, Th. Geue, F. Neissendorfer, G. Brezsesinski, CH. Symietz, H. Möhwald
and W. Gudat ,   Nucl. Instr. & Meth in Phys. Res. A 467-468, 1077-1080 (2001)

[3] Yves Bodenthin et al. BESSY Annual Report 2001

EXAFS measurements of organic films containing Fe(II)-ligand complexes

Y. Bodenthin[1*], U. Pietsch[1],
D. Kurth[2], P. Lehmann[2], H. Möhwald[2]
A. Erko[3], M. Fieber-Erdmann[3]
[1]*Institute of Physics, University of Potsdam, P.O.B. 601553, D-14415 Germany*
[2]*Max-Planck-Institute of Colloids and Interfaces, D-14424 Golm, Germany*
[3]*BESSY GmbH, Albert-Einstein-Straße 15, D-12489 Berlin, Germany*

Thin films of Fe(II) polyelectrolyte amphiphile complexes (PAC) are good candidates for studying molecular magnetism. The Fe(II) ions are surrounded by ligands of 1,4-bis(2,2':6',2''-terpyridin-4'-yl) benzene creating a nearly octahedral crystal field. At room temperature the Fe(II) spins occupy low spin levels only. Magnetic properties are expected at higher temperatures when the octahedral co-ordination becomes distorted [1].
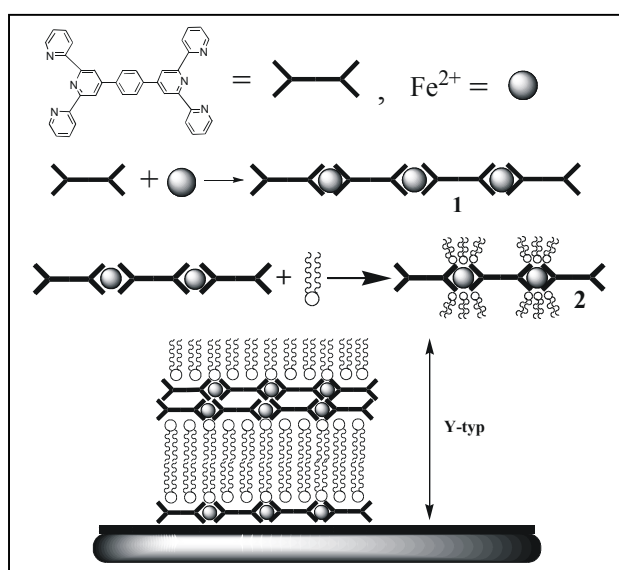
Fig.1 Supra-molecular architecture
of Fe(II)-PAC films

PAC films prepared by the Langmuir-Blodgett technique show an irreversible phase transition into a liquid-crystalline (LC) phase at about T=55°C. Above a temperature of 65°C the film completely reorganise it's structure to a high temperature phase. This structure is stable after cooling down [2]. Therefore we performed temperature dependent Surface Extended X-ray Absorption Fine Structure Spectroscopy measurements of thin film samples at room temperature (RT) and after annealing at 55°C and 77°C. The absorption spectra were performed at KMC2 exploiting the K-fluorescence yield of the few Fe(II) ions within the sample. The 11 and 15 layer thick films were prepared by means of Langmuir Blodgett (LB) technique on silicon support (Fig.1). The detector was a PIN diode with an attached thin manganese foil for background suppression. It was operated under a grazing incident angle of $\alpha = 0.25°$. Figure 2 shows the absorption spectra of a 15 monolayer film at RT. The PAC film shows a sharp iron K-absorption edge at $E_K = 7127$ eV. The chemical shift of about 10 eV compared to that of free Fe(II) ions can be explained by its octahedral ligand environment [3]. The energetic

position of EXAFS oscillations can be used to find changes in the crystal field around the central ion induced by structure changes.

Fig 3 shows the EXAFS function and its theoretical fit of a 15 monolayer film at room temperature before heating. The fit was done in terms of the two core approximation with two different Fe-N distances, R_1=1,692 Å and R_2=2,116 Å. respectively. The complete results of al measurement are given in table 1. There was found changes of ΔR=0,1 Å in the average distance $<R>$. It is obvious that
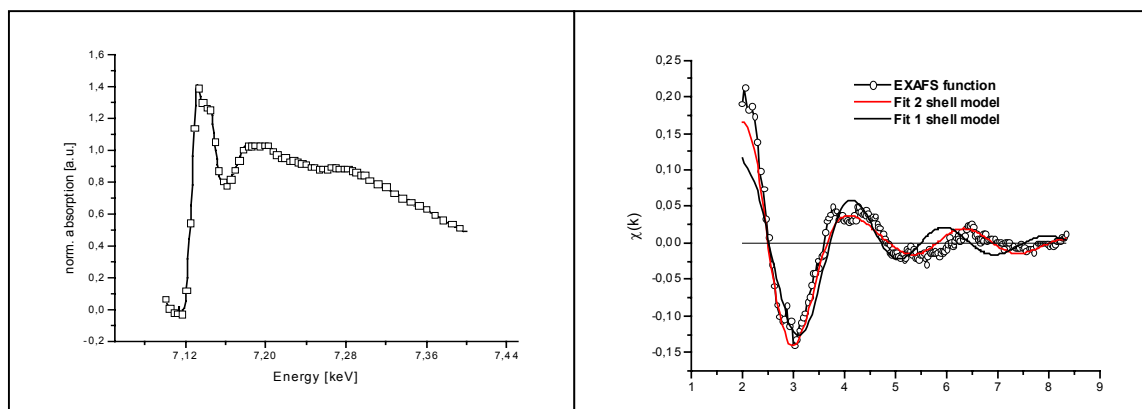
Fig.2: EXAFS spectrum of a 15 monolayer film   Fig.3: Measured and simulated EXAFS function

the EXAFS data cannot be fitted by a single shell model. Already at room temperature the octahedral crystal field is distorted. At higher temperature the deformation is increased, which could initiate a transition from a low spin to a high spin system.

The present experiment demonstrates the possibility to perform EXAFS measurements at supramolecular samples with a low concentration of iron ions. The EXAFS theory gives the possibility to get bond length and co-ordination states of the ligands and helps to understand the magnetically behaviour of Fe(II)PAC films.

The authors thanks BESSY for the possibility to execute the experiments.

Tab.1. Fit parameters used for simulation of the EXAFS function shown in fig.3.

Temp. [°C]	R_1[Å]	R_1[Å]	$<R>$[Å]
T (heating) 32°C	1,692	2,116	1,905
T (heating) 55°C	1,700	2,161	1,931
T (heating) 77°C	1,755	2,188	1,977
T (cooling) 55°C	1,682	2,120	1,902
T (cooling) 32°C	1,695	2,147	1,921

*e-mail: bodenth@rz.uni-potsdam.de
[1] O. Waldmann *Intramolekulare antiferromagnetische Kopplung in supramolekularen Gitterstrukturen* Diss. Universität Erlangen Nürnberg, 1998
[2] Y. Bodenthin et al. J. Synchr. Rad.(2001) submitted
[3] J. E. Huheey, *Anorganische Chemie*, Verlag Walter de Gruyter 1988

Bragg Reflection Measurements of Fe(II)PAC Films at the Fe-L Absorption Edge

Y. Bodenthin[1*]**, U. Pietsch**[1]**,**
D. Kurth[2]**, P. Lehmann**[2]**, H. Möhwald**[2]
F. Schäfers[3]**, I. Packe**[3]
¹Institute of Physics, University of Potsdam, P.O.B. 601553, D-14415 Germany
²Max-Planck-Institute of Colloids and Interfaces, D-14424 Golm, Germany
³BESSY GmbH, Albert-Einstein-Straße 15, D-12489 Berlin, Germany

The detection of the magnetic circular dichroism (MCD) on the iron L absorption edge is a frequently used method to measure very small magnetic moments. Particularly on systems with a very small iron concentration the measured dichrotic function can help to understand the magnetic characteristics of the sample [1]. Thin films of Fe(II)-polyelectrolyte-amphiphile-complexes are good candidates for studying the magnetic behaviour of iron ions in a organic coordination. In the metalpolyelectrolyte (MEPE **1** Fig.1.) the Fe(II) ions are surrounded by ligands of 1,4-bis(2,2':6',2''-terpyridin-4'yl)benzene creating a nearly octahedral crystal field. To build the complex **2** there are added 6 dihexadecylphosphat-amphiphiles (DHP) per molecule unit to the MEPE [2]. At room temperature the iron spins occupy the non-magnetic low-spin states. Small changes of the coordination sphere can induce a transition into a magnetic high-spin state [3].
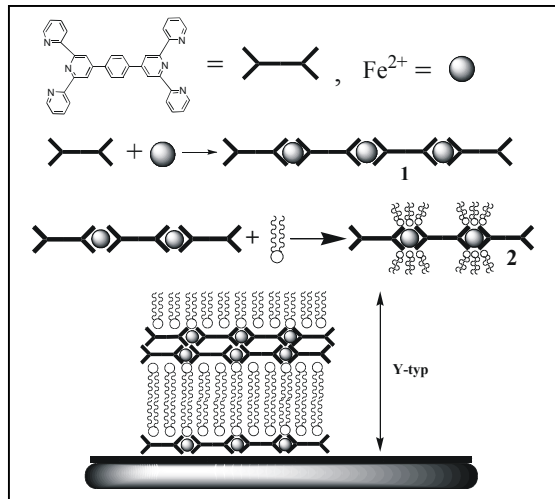
Fig.1: Structure of Fe(II)-PAC films
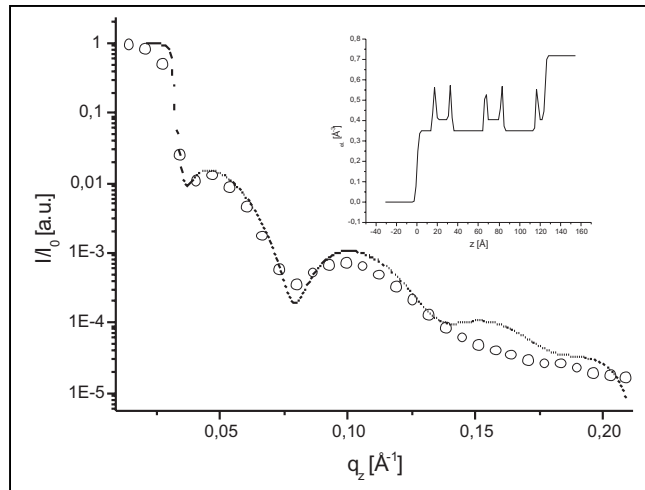
Fig.2: Reflectivity of a 5 ML films at E=783 eV

It can be expected that the magnetic properties of thin films differ from those of bulk material. Therefore it is helpful to establish the method of measuring the MCD at PAC films. The investigated samples were 11 and 15 monolayer thick films prepared by means of the Langmuir-Blodgett (LB) technique on silicon support. Before measurement the vacuum stability of samples was proved. No structural changes appeared after transfer into the experimental chamber. Fig.2. shows a reflection curve of a 5 ML film recorded at E= 783 eV together with a fit curve using the density profile shown as inset. This electron density profile is the same as we obtained from reflectivity curves detected

under normal pressure conditions and at energies in the keV range. The density maxima represents the headgroups of the DHP amphiphiles embedding the MEPE groups.

Fig 3. shows the position of the first Bragg peak of a 15 ML plotted as a function of incident beam energy. It is clearly to see that the few iron ions of the PAC films are sufficient to detect the two iron L-edges. Comparing with critical energies extracted from Henke´s table [4] and using the formalism published by H.Ch. Mertins et al. [5] both edges are shifted by about 4.5 eV to smaller energies. This might be caused by the influence of the ligand field created by MEPE. A detailed analysis of experimental data is under way.
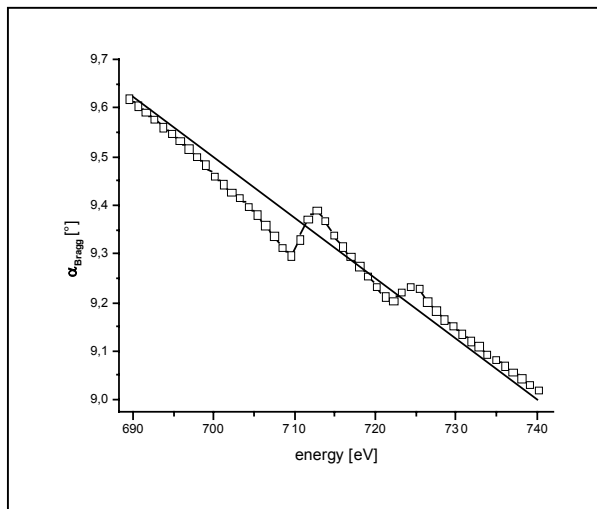
Fig.3: Variation of 1st order Bragg peak vs. E   Fig.4: Comparison of exp. Data with Henke´s table
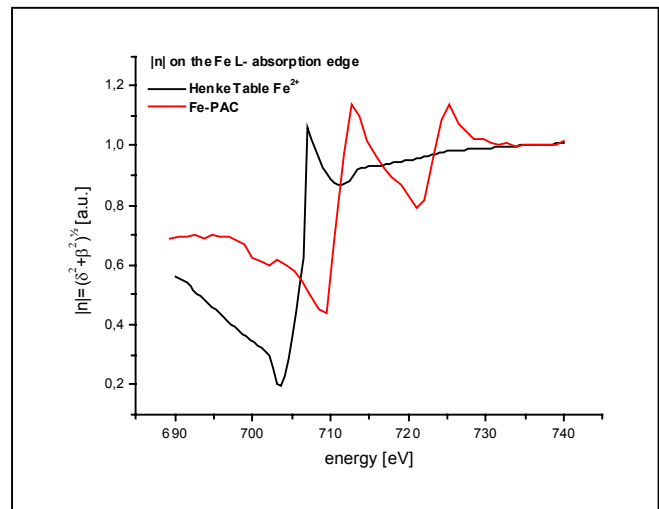
The present experiment is the first step to measure the magnetic circular dichroism of thin Fe(II)PAC films with Bragg scattering. The investigated structure is stable under high vacuum conditions. Despite the small iron concentration the position of the first braggpeak shows a non-linear behaviour at the L absorption edges.

*e-mail: bodenth@rz.uni-potsdam.de

[1] J. Als-Nielsen, D. McMorrow, Elements of Modern X-Ray Physics, John Wiley and Sons Ltd, (2001)
[2] M. Schütte, D.G. Kurth, M.R. Linford, H. Cölfen, H. Möhwald, Angew. Chem. Int. Ed., 37, 2891 (1998)
[3] Y. Bodenthin, U. Pietsch et. al. BESSY annual report 2001, submitted
[4] B. L. Henke, E. M. Gulklikson, J. C. Davis, *http://www-cxro.lbl.gov*
[5] H.-Ch. Mertins et al., Journal of Magnetism and Magnetic Materials, (2001), in press

Wetting behaviour of thin LC films studied by white light SAXS

Stefan Schlagowski, Thomas Pfohl, Stephan Herminghaus, Karin Jacobs
University of Ulm, Department of Applied Physics, 89069 Ulm

Robert Lauter, Ullrich Pietsch
University of Potsdam, Institute of Physics , 14469 Potsdam

Introduction

Thin films (20-200 nm) of liquid crystals from the nCB (4'-n-alkyl-4-cyanobiphenyl) series on silicon substrates show a transient instability in film thickness while changing from the nematic to the isotropic phase (see Fig.1). Although this instability leads to patterns reminiscent of spinodal dewetting [1], we have shown in a recent study [2] that it is actually based on a nucleation mechanism. Above the nematic-isotropic transition, the film dewets into droplets. Studying the instability with optical microscopy and AFM [2] revealed a strong dependence of the emerging patterns on the heating rate. Heating rates vary from 0.1 to 10 K/min. The instability starts to develop 2-6 °C below the nematic-isotropic phase transition temperature (T_{NI} = 41 °C). This leads to changes of the film morphology on a time scale of seconds. For that reason energy disperse small angle X-ray scattering (SAXS) was chosen as a method to observe the change in film thickness quantitatively in real time.
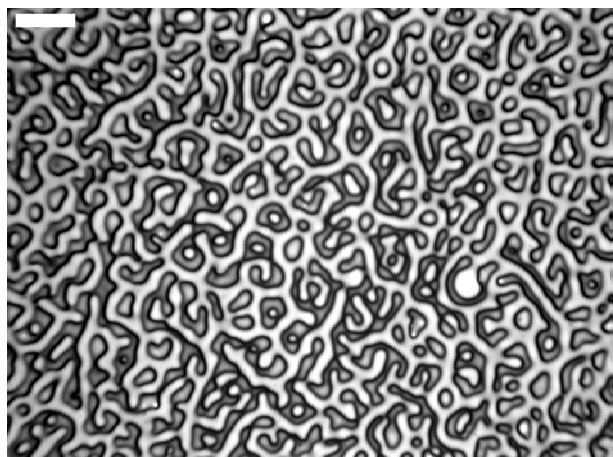
Fig. 1: Optical micrograph of an 86 nm thick 8CB film undergoing an instability at a heating rate of 1 K/min, snapshot taken at 39.9 °C (white bar = 100 µm)

Experiment

Thin films of 8CB were prepared by spincasting the liquid crystal from hexane solution onto silicon wafers (size approx. 2x2 cm^2) at room temperature resulting in films in smectic A phase. The samples were then mounted on a heat stage at the BESSY II EDR beamline in order to record X-ray reflectograms while changing the sample temperature in situ.

With the EDR set-up, we were able to record a reflectogram every 30 seconds, since here a white X-ray beam is used and the reflected intensity is recorded with an energy disperse detector, which allows to record the full q_z range at once ($q_z = (4\pi/\lambda) \sin \Theta$, Θ can be constant since the white beam provides different λ). This allowed us to take series of reflectograms with sufficient time resolution while ramping the sample temperature at rates of 1-2 K/min through the undulation regime up to the onset of dewetting. To reduce beam damage, the lateral position of the 8CB sample was changed after recording each reflectogram.

Results

Fig. 2 shows a typical series of reflectograms taken of an 8CB sample during a heating and cooling cycle.
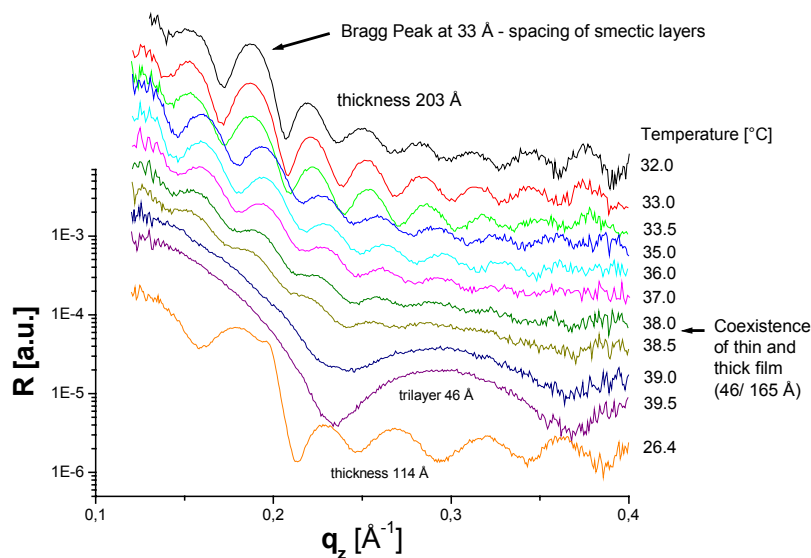
Fig. 2: Series of reflectograms taken while heating an initially 20 nm thick 8CB film (curves shifted to enhance readability). See text for further details.

The topmost curve represents the smectic film as prepared on a Si-wafer, clearly showing a Bragg-peak due to the smectic layering. The film thickness can be determined by the spacing of the Kiessig fringes. The Bragg peak vanishes with increasing temperature, but is still detectable above the bulk smectic-nematic phase transition at 32.5 °C. In the nematic phase, damping of the Kiessig fringes increases with increasing surface roughness. At temperatures around 38 °C, where the surface instability is known to occur, the shape of the reflectivity curve can be attributed to a coexistence of thin and thick film areas. At temperatures above 39 °C the film starts to dewet into droplets and and only a layer of 4.6 nm thickness remains. We identify this residual layer as a trilayer of 8CB next to the substrate, which is known to possess an enhanced stability [3]. The droplets spread again when recooling the sample and a smectic film is formed again, albeit less thick than on the freshly prepared sample lowest curve since the spreading process is not completely homogeneous.

Summary

Energy disperse SAXS has been sucessfully used to follow the morphological changes of thin liquid crystalline films in real time, providing quantitative data on changes in film thickness not acessible by complementing techniques like AFM or optical microscopy. The decay of smectic order in the film can be followed as can the coexistence of areas of different film thickness while the film undergoes its instability.

References

[1] F. Vandenbrouck, M.P. Valignat, A.M. Cazabat, Phys. Rev. Lett. **82**, 2693 (1999)
[2] S. Schlagowski, K. Jacobs, S. Herminghaus, Europhys. Lett. *in print*
[3] S. Bardon, *et. al.*, Phys. Rev. E **59**, 6808 (1999)

Synchrotron X-ray Diffraction during Epitaxy: Reconstruction Dynamics on the Growing GaAs (001) Surface

Wolfgang Braun, Bernd Jenichen, Vladimir M. Kaganer, Alexander G. Shtukenberg
Lutz Däweritz, Carl-Günter Schulz, Klaus H. Ploog
Paul-Drude-Institut für Festkörperelektronik, Hausvogteiplatz 5-7, D-10117 Berlin
Alexei Erko
BESSY GmbH, Albert-Einstein-Straße 15, D-12489 Berlin

The PHARAO beamline of the Paul-Drude Institute started regular measurement operation in September 2001. This beamline is a dedicated setup to study the epitaxy of compound semiconductors and magnetic materials *in situ* using synchrotron x-ray diffraction. The beamline uses the following configuration: The main optical elements are a water-cooled condenser mirror producing a parallel beam, a double-crystal monochromator and a focusing mirror producing a 0.8 mm spot diameter at the sample position. Although operating at the very far end of the wiggler spectrum between 6 and 12 keV, the x-ray intensity is proven to be sufficient for surface diffraction experiments at the straight-through beamline of the U125/2 wiggler source.

The experiment designed for this beamline (Fig. 1) consists of a fully featured molecular beam epitaxy (MBE) system mounted inside a six-circle diffractometer allowing for surface and conventional diffraction experiments. The system is capable of growing epitaxial layers with up to 7 components during a diffraction experiment. In addition, it is equipped with a high-resolution reflection high-energy electron diffraction (RHEED) setup that can be operated simultaneously with growth and x-ray diffraction.

We have started our measurements at this beamline with growth experiments specific for GaAs homoepitaxy. Choosing growth conditions that optimized the $\beta(2{\times}4)$ surface reconstruction before growth and minimized the damping of RHEED oscillations, we have performed growth
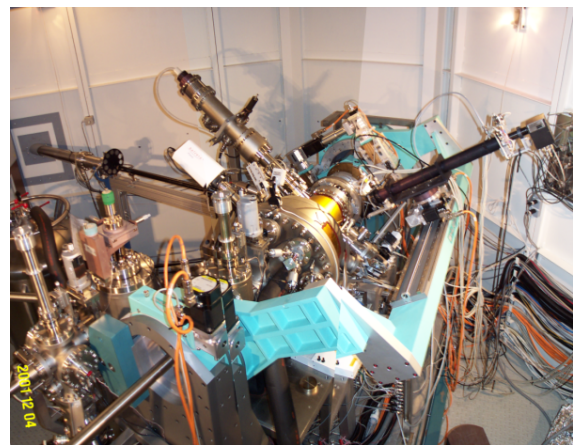

Figure 1: The combined MBE/Diffractometer experimental station at the PHARAO beamline.

runs at various growth rates and measured the resulting x-ray diffraction oscillations on different reciprocal lattice rods.

A typical measurement, taken on the $[\bar{3}\,1\,L]$ rod for small L, is shown in Fig. 2. The bulk-forbidden reflection $[\bar{3}\,1\,0]$ provides destructive interference between successive atomic layers of GaAs(001), which results in strong diffraction oscillations. Layer-by-layer growth in this system proceeds by successive completion of GaAs bilayers with a height of one half of the cubic bulk unit cell. This results in a real-space shift of the atomic coordinates by $[\frac{1}{2}\,0\,\frac{1}{2}]$ from layer to layer with respect to the sides of the cubic bulk unit cell. In terms of the layers exposed at the surface, the surface therefore grows in an A-B-A-B stacking. Any surface reflection $[h\,k\,L]$ with h, k odd and small L is sensitive to this
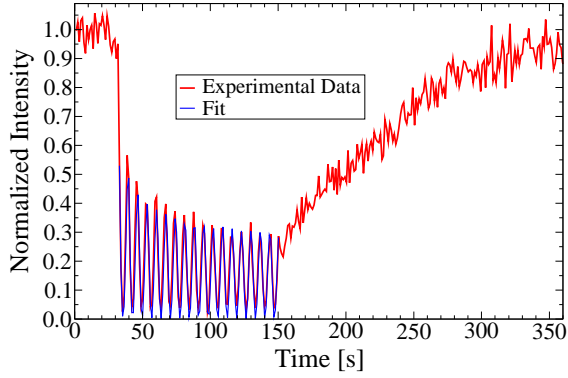
Figure 2: X-ray diffraction oscillations recorded at the reciprocal lattice position $[\bar{3}\,1\,L]$, $L = 0.02$.
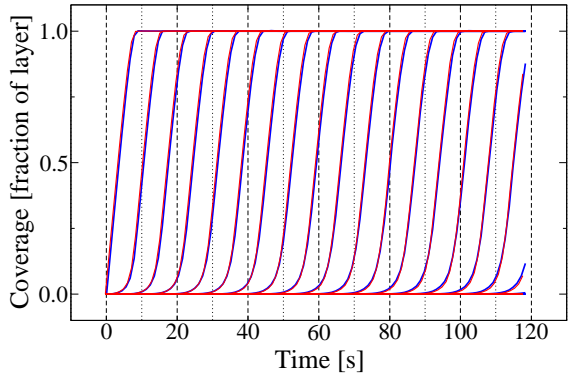

Figure 3: Layer coverage from fit to single diffraction oscillation measurement in Fig. 2 (blue) and full set along the rod in Fig. 5 (red).

Figure 4: Measured vs. calculated intensities during growth for the $[\bar{3}\,1\,L]$ Bragg rod.

phase shift. The strongest oscillations can be observed in an almost in-plane geometry where the surface normal coordinates of the atom positions are irrelevant.

With a pre-growth intensity of 550 counts per second (normalized to 1 in Fig. 2) and full, unattenuated primary beam intensity, we measure a background of 15 counts. Under optimized operation conditions, the diffuse scattering from the Be and Kapton windows are therefore negligible for most experiments.

From a fit of a standard birth-death model [1] to the oscillations (shown in blue in Fig. 2), we obtain the (bi-)layer coverages shown in blue in Fig. 3. As expected from the low damping of the oscillations, the epitaxy is close to ideal layer-by-layer growth, with one layer being al-

most completely finished before the next layer nucleates. Even at the termination of growth at the 17th layer, the growth front has not significantly roughened.

When we repeat the oscillation measurement shown in Fig. 2 for different L, we obtain different values for the static (non-growing) intensities as well as the intensity minimum of the first oscillation. These are plotted, together with theoretical predictions, in Fig. 4. The theoretical curves (red and blue lines) are calculations based on the β(2×4) structure solved ex situ at room temperature using x-ray diffraction [2]. The deviations indicate that the structure at growth temperature differs from the one found on the quenched samples.

The observed β(2 × 4) surface reconstruction is preserved during growth. This can be shown by simultaneously fitting oscillations at different L with the same growth model (Fig. 5). The good fit on all curves throughout the complete growth interval indicates that the structure factor of the surface reconstruction remains unchanged during growth. The layer coverages obtained from the fit are shown in red in Fig. 3. They are practically identical to the fit obtained from the growth shown in Fig. 2, again confirming the good run-to-run reproducibility of our setup.

Note that these measurements are not sensitive to the positional disorder of the surface reconstruction units, since all eight possible positions of the 2×4 unit cell on the underlying
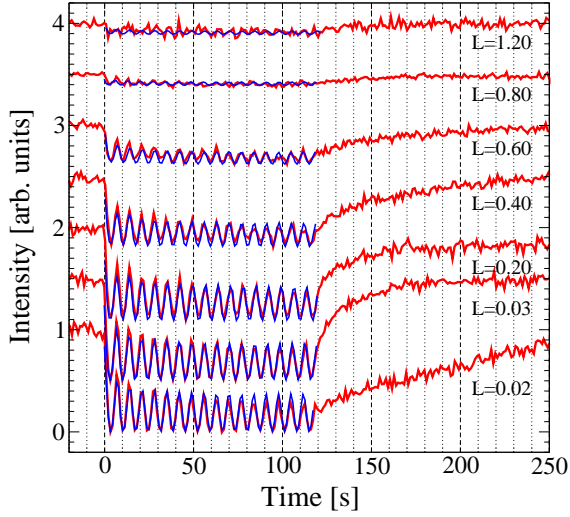
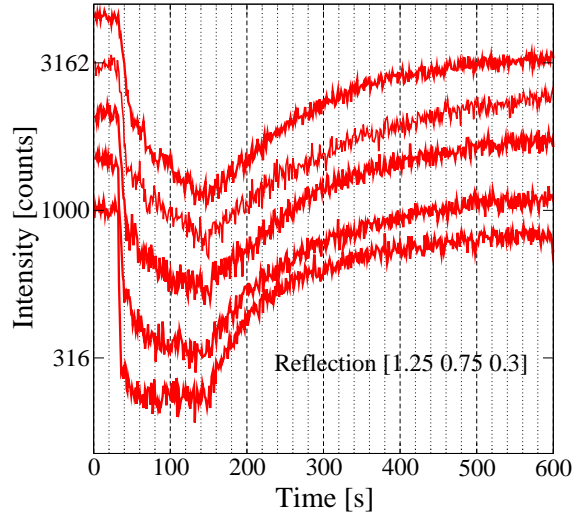Figure 5: Diffraction oscillations for different L on the Bragg rod $[\bar{3}\,1\,L]$.

Figure 6: Diffraction oscillations from a fractional-order reflection [1.25 0.75 0.3] for different growth rates.

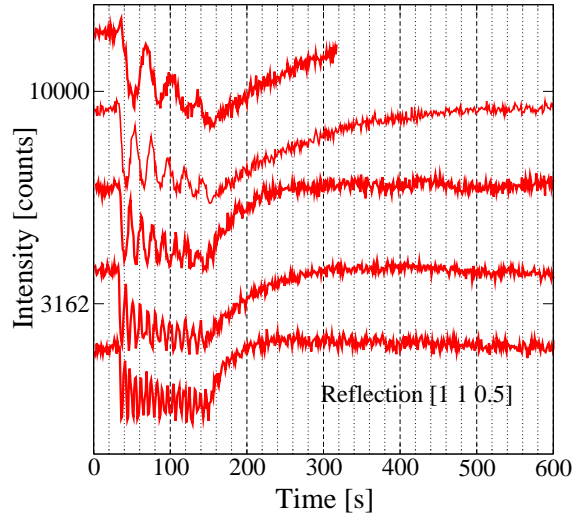Figure 7: Reference oscillations on an integer-order rod insensitive to reconstruction domains.

bulk 1×1 mesh of the (001) plane contribute in phase to the measured intensities. The signal therefore monitors the terrace evolution on the surface. The dynamics of the reconstruction on these growing terraces can be probed by measuring the diffraction oscillations of a fractional-order reflection, like in Fig. 6. Such a measurement is sensitive to the relative positions of the reconstructed surface unit cells within a terrace and can therefore be used to monitor the ordering dynamics of the reconstruction. The reference integer order measurements recorded directly afterwards are shown in Fig. 7. In both figures, the growth rate is increasing from top to bottom in the figures. Whereas clear growth oscillations with small damping are observed throughout in Fig. 7 for the terraces, the intensity rapidly decays to the background level on the fractional order rod.

This can be explained by the fact that the 2×4 surface reconstruction can nucleate in eight different relative positions, thus forming many small domains during growth if they nucleate randomly. This is expected especially at high growth rates, when initially a large number of small, independent islands nucleate and then coalesce into larger terraces as the layer completes. The integer-order Bragg rods are insensitive to the relative shifts of the 2×4 units, since the shift is always an integer multiple of the bulk unit cell.
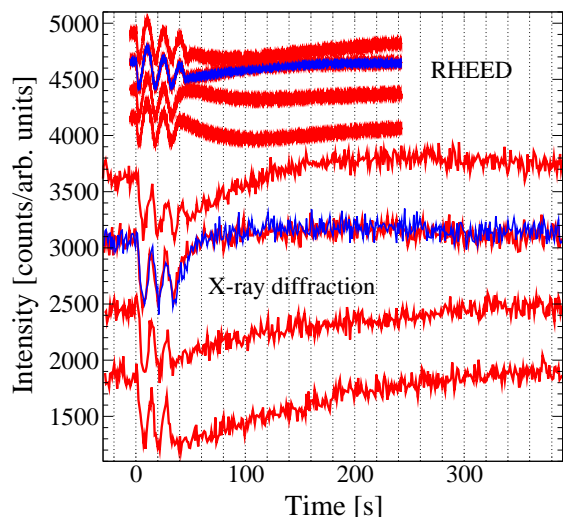
Figure 8: Comparison of RHEED and x-ray diffraction curves (reflection [1 1 0.5]) measured simultaneously on the same sample.

Hence, the reference measurements of Fig. 7 directly provide the terrace dynamics.

For the surface reconstruction to cover large areas with a single domain, the small domains need to grow by domain wall movement. The recovery for the reconstruction measurements shown in Fig. 6 is slower than on the corresponding reference integer-order reflection of Fig. 7. The difference is especially strong if the growth is terminated at an integer layer coverage. The terrace signal then recovers quickly and the reconstruction recovery is slow, as can be seen on the third curve from the top. The second curve from the top represents the other extreme: growth termination at half-layer coverage leads to slow recovery of the terrace signal, since significant material transport is required to recover large terraces. In this case, the reconstruction domains grow at a rate similar to the terraces. The reconstruction recovery seems to be faster after growth with high growth rate. This may be due to the smaller scale roughness produced by growth at higher rates, followed by mass transport on short length scales that may favor surface structure domain growth.

Figure 8 compares RHEED and x-ray diffraction oscillations measured simultaneously. Our capability of performing both types of

surface diffraction from the same growing surface opens up new ways of comparing the different scattering mechanisms of x-ray and electron diffraction. Figure 8 shows a series of experiments with constant growth rate in which the growth was terminated at different coverages between 2.5 and 3.25 layers. The blue curves represent repetitions of the measurements shown in red to check for reproducibility. In all x-ray measurements, the intensity during growth is lower than before. This is independent of the reciprocal lattice rod and the position L along the rod, as may be verified from Figs. 2 and 5–7. Also, all x-ray oscillations have maxima at integer coverages and minima at half-filled layers. When L is varied, the amplitude of the oscillations varies. In RHEED, a variation of L, in addition to changing the amplitude of the oscillations, also affects their phase. Consequently, oscillations with intensities higher than the pre-growth intensity are observed. Both phenomena can clearly be seen when comparing the RHEED and x-ray diffraction traces in Fig. 8. Note again that with the second curves from the top in each group, the terrace signal in the x-ray oscillations recovers faster than the RHEED signal. This confirms our previous findings that RHEED oscillations mainly sample the surface reconstruction and are less sensitive to the terraces [3].

References

[1] P. I. Cohen, G. S. Petrich, P. R. Pukite, G. J. Whaley, A. S. Arrott, *Birth-death models of epitaxy*, Surf. Sci. **216** (1989) 222-248.

[2] Y. Garreau, M. Sauvage-Simkin, N. Jedrecy, R. Pinchaux, M. B. Veron, *Atomic structure and faulted boundaries in the GaAs(001) β(2x4) surface as derived from x-ray diffraction and line-shape analysis*, Phys. Rev. B **54** (1996) 17638.

[3] W. Braun, L. Däweritz, K. H. Ploog, *Origin of Electron Diffraction Oscillations during Crystal Growth*, Phys. Rev. Lett. **80** (1998) 4935.

NEXAFS investigation of nitrided III-V semiconductor surfaces – effects of elevated substrate temperatures

J.-D. Hecht[1], S. Krasnikov[2], L. Zhang[2], A. Sidorenko[1], F. Frost[1], and T. Chassé[1,2]

[1]Institut für Oberflächenmodifizierung, Permoserstr. 15, D-04318 Leipzig, Germany
[2]Wilhelm-Ostwald-Institut für Physikal. u. Theoret. Chemie, Univ. Leipzig, Linnéstr. 2, D-04103 Leipzig, Germany

The nitridation of III-V semiconductors has attracted much attention due to the importance of epitaxial nitride growth on well-established substrates and of semiconductor surface passivation. The nitridation of III-V surfaces by bombardment with low-energy N_2^+ ions at room temperature has been investigated using X-ray absorption and photoemission spectroscopy, recently [1,2].

Here we report on NEXAFS studies on the influence of the preparation parameters like annealing and nitridation temperature of In-based III-V compounds. Commercially available (100) InP, InAs, InSb, and GaAs substrates were nitrided *in situ* in a stainless steel preparation chamber using 300eV N_2^+ ions provided by a Kaufman-type broad beam ion source. NEXAFS measurements were performed at the nitrogen (and oxygen) K-edge in total electron yield (TEY) mode at the VLS-PGM beamline. The energy resolution was better than 0.2 eV. The energy scale was calibrated using peak positions of K_2TiF_6. The spectra were normalized to the photon flux curves as measured by a gold mesh.

Fig.1 shows TEY spectra of the N K-edge recorded at III-V(100) surfaces following N_2^+ ion bombardment in comparison to epitaxial α-GaN layers on SiC(0001). The TEY-spectrum of the GaN layer exhibits all the fine structures previously reported for wurtzite GaN. While this fine structure is completely absent in the spectra of e.g. GaAs, the major absorption features nevertheless indicate the formation of a disordered surface nitride layer. However, all the spectra of the bombarded surfaces exhibit a very sharp feature at an energy of 401 eV, which is particularly prominent for the In-based substrates. It coincides with the 1s-π* excitation of molecular nitrogen, and therefore it has been attributed to incorporated N_2 [2].

Fig. 1: NEXAFS of the N K-edge at different ion-bombarded (N_2^+, 300 eV) III-V(100) semiconductors.

The influence of the nitridation temperature is reflected by the spectral changes of the nitrogen NEXAFS as shown in Fig. 2. At elevated temperatures the peak at 401 eV decreases significantly, indicating disappearence of the molecular nitrogen from the bombarded region. Additionally, above 200°C some fine structure starts to develop, which might reflect an im
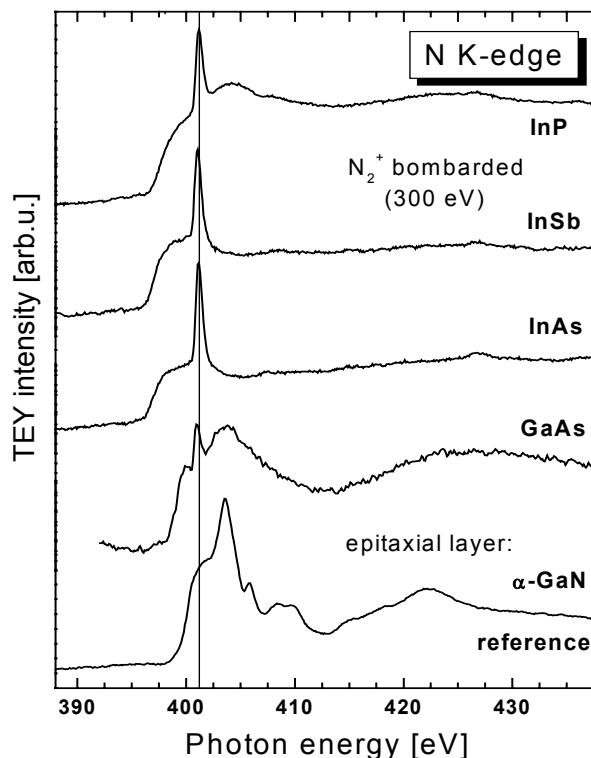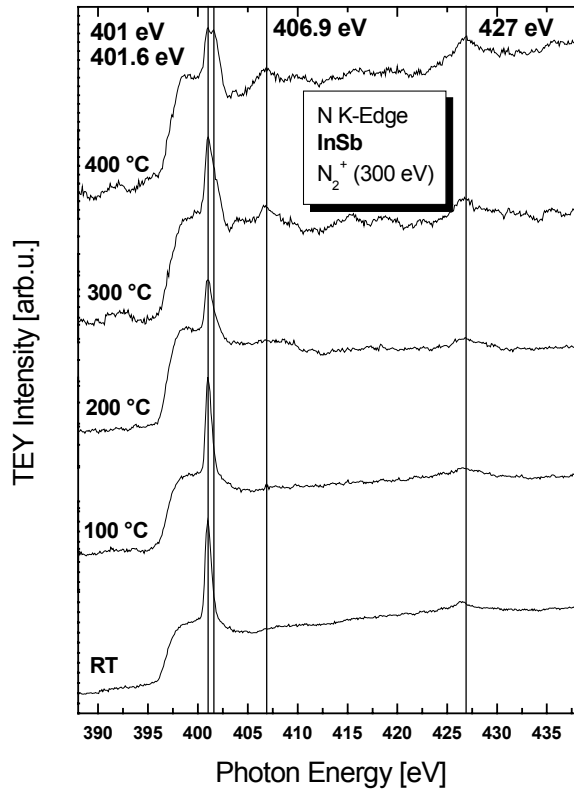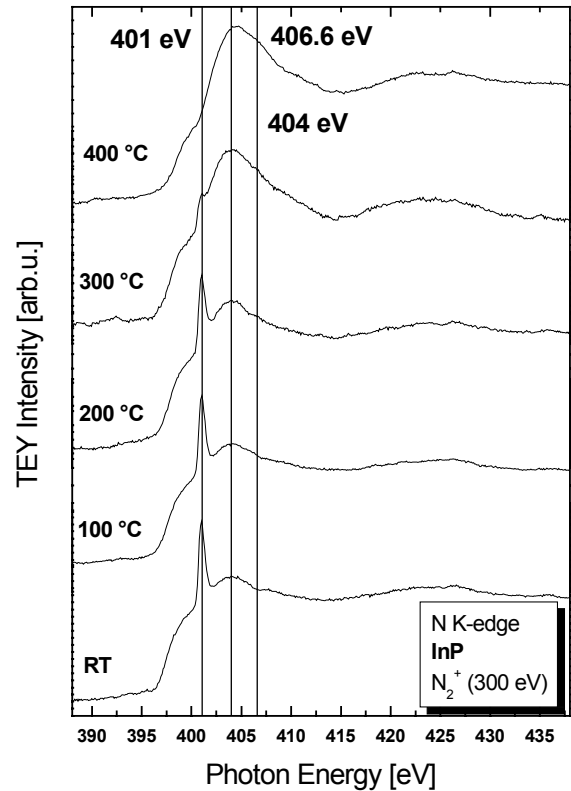
Fig. 2: NEXAFS of the N K-edge taken at different substrate temperatures during N_2^+ (300 eV) ion beam bombardment of InSb(100).

Fig. 3: NEXAFS of the N K-edge for different annealing temperatures following N_2^+ (300 eV) ion beam bombardment of InP(100).

proved ordering of the local environment of the absorbing nitrogen atoms in the near surface region.

Fig. 3 presents TEY spectra of InP following N_2^+ ion bombardment at room temperature and subsequent annealing for one hour. At higher temperatures again a decrease of the peak at 401 eV and thus a removal of the interstitial nitrogen may be observed. In case of InP both In-N and P-N bonding contribute to the broader spectral features. The slight shift of spectral weight to 404 eV and the decrease of the low energy shoulder at 398.5 eV point to an increasing relative amount of P-N contributions due to highly coordinated phosphorous after high temperature annealing [3,4]. But in contrast to the nitridation of InP at elevated substrate temperatures (not shown) there is no significant change in the ratio of In-N to P-N contributions observed.

Thus, tuning of the temperature in an appropriate manner offers several opportunities to affect composition and also ordering of the ion-beam nitrided III-V semiconductor surfaces.

[1] J.-D. Hecht et al., Appl. Surf. Sci. **179**, 196 (2001)
[2] J.-D. Hecht et al., J. Appl. Phys. **90**, 6066 (2001)
[3] L. Soriano et al., J. Electron Spectrosc. Relat. Phenom. **62**, 197 (1992).
[4] A. Markwitz et al., Appl. Phys. A **59**, 435 (1994)

First computed tomography experiments at BAM*line*

G. Weidemann, J. Goebbels, Th. Wolk, H. Riesemeier
Bundesanstalt für Materialforschung und –prüfung (BAM), 12200 Berlin, Germany

At 15th and 17th of May 2001 the first experiments on computed tomography were performed at BAM*line* (BESSY II) [1-3]. Fig. 1 shows the set-up with the four-stage manipulator system (two translation, one rotation and one elevator axis) together with the detector system. The latter consists of a 1340 x 1300 cooled back illuminated CCD camera coupled by an optical lens system to the scintillator screen (GdOS, thickness 20 μm). The resulting pixel size of the detector is 11 μm.
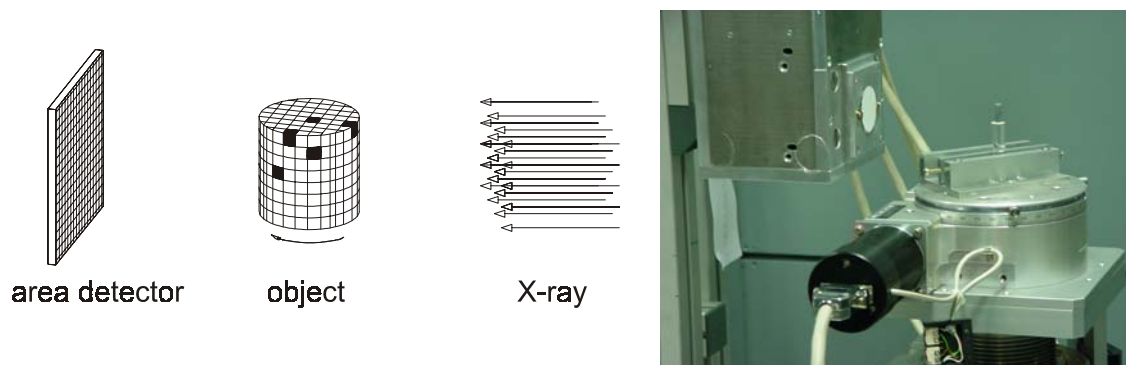
Fig. 1: Principle of parallel beam geometry for CT and experimental set-up of CT system at BAMline.

The principle of parallel beam CT is also shown in fig. 1. Projections of the object have to be recorded for a sufficient number of angles in a range of 0 to 180 degree, i.e. the object has to be rotated by 180 degree during the CT-measurement. From all digital radiographies a three dimensional image data set can be reconstructed. Due to the parallel beam geometry a conventional filtered back projection algorithm is used. According to the inhomogeneous illumination and the different sensitivity of single CCD camera pixels a dark and flat field correction has to be performed.

The first experiments suffered from instabilities of the source point caused by changes in the magnetic field of the 7T-WLS. Additional instabilities were induced by thermal drift of the double crystal monochromator. Therefore, the CT-software was modified to measure the flat field changes repeatedly during the CT-measurement. Consequently the flat field corrections are performed at the beginning of measurement and than repeated after a fix number (30 to 60) of CT-projections. This resulted in an increased image quality, however more frequent flat field corrections would be necessary for full compensation of the instabilities.

The main applications are the characterization of density variations in ceramic parts and the determination of geometrical features like pore size distribution. Fig. 2 shows as an example an Al_2O_3 micro structural element, measured in the green state and after sintering. These samples were investigated in collaboration with FZ Karlsruhe and Hydraulik Nord Parchim. The image shows a comparison between conventional CT (X-ray tube) and CT with synchrotron radiation. The advantage of synchrotron CT is the absence of the beam hardening (i.e. ostensibly higher density at the outer edge of the sample) which is often a problem at laboratory equipment where the X-ray beam couldn't be monochromatised with sufficient

intensity. The measurement was performed with the double crystal monochromator at 20 keV. The aim was the detection of density variations and flaws like cracks and small pores.
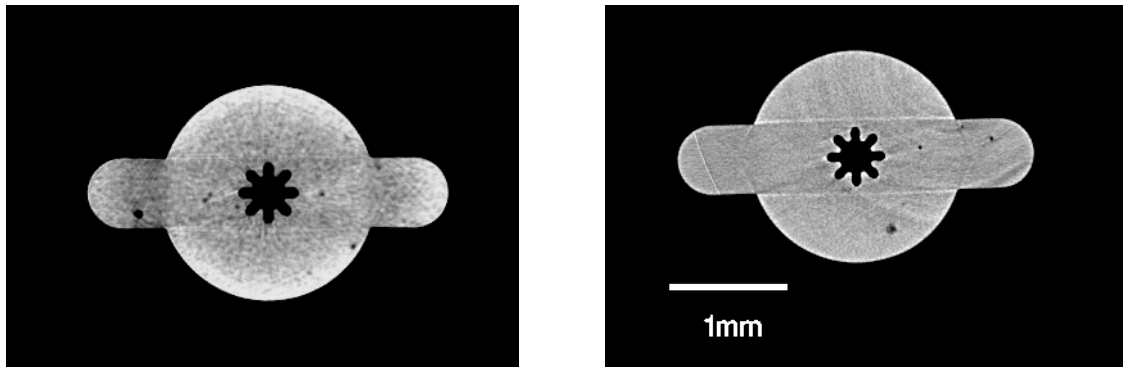

Fig. 2: Al$_2$O$_3$ sample in the green state. Comparison between laboratory result (left image) which shows the beam hardening artefact and CT with monochromatic synchrotron radiation (right image).
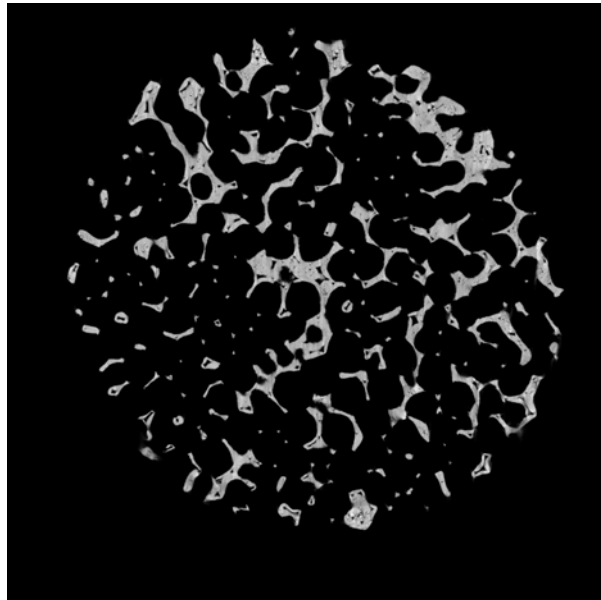

Fig. 3: Ceramic foam samples with different pore size distribution

The spatial structure of small complex samples was determined for ceramic foam samples from the project "Bio materials and Implantation" of BAM, project leader G. Berger. Fig. 3 shows a cross section of a sample with a nominal porosity of 30 ppi (pores per inch). For an automatic determination of the pore size distribution with image analysis the homogenous density due to the monochromatic radiation is of great advantage.

References
[1] J.Goebbels, H. Riesemeier, R. Rudert, T. Rabe, Green Body Characterization by Computed Tomography with Synchrotron Radiation, *DKG, 8. Keramiktag der BAM, Symposium Grünkörpercharakterisierung, Berlin, 28.-29. Mai 2001,* to be published.
[2] H. Riesemeier, *BAMline - Status und Zukunft, 2. Seminar zur Nutzung des Wellenlängenschieber-Meßplatzes bei BESSY II, Berlin, 8.-9. November 2001.*
[3] J. Goebbels, *Bestimmung der Dichteverteilung in keramischen Bauteilen mit Computertomographie an der BAMline, 2. Seminar zur Nutzung des Wellenlängenschieber-Meßplatzes bei BESSY II, Berlin, 8.-9. November 2001.*

SYNCHROTRON RADIATION STUDY
ON THE OXIDATION BEHAVIOUR OF NEW TI ALLOYS

M. F. López and F. J. Palomares
Instituto de Ciencia de Materiales de Madrid, CSIC, Cantoblanco, E-28049 Madrid, Spain

L. Soriano, M. Sánchez- Agudo, G. G. Fuentes and A. Gutiérrez
Departamento de Física Aplicada, Insituto de Materiales Nicolás Cabrera, Universidad Autónoma de Madrid, Cantoblanco, E-28049 Madrid, Spain

J. A. Jiménez
Centro Nacional de Investigaciones Metalúrgicas, CSIC,
Avda. Gregorio del Amo 8, E-28040 Madrid, Spain

Titanium alloys are very interesting because they have one of the highest strength/weight ratio among the metallic materials. The spontaneous formation of a protective native oxide layer on its surface, named passive layer, leads to a high corrosion resistance which makes these alloys good materials for different technological applications [1,2]. However, for some applications, the protection against the environment can be improved by generating an oxide layer by heat treatment.

The aim of the present work is to investigate the oxidation behaviour of three Ti alloys, Ti-13Nb-13Zr, Ti-15Zr-4Nb and Ti-7Nb-6Al, using soft X-ray absorption spectroscopy (XAS). The main contributions to the chemical composition of the oxide layers formed on these alloys at room and at high temperature were determined.
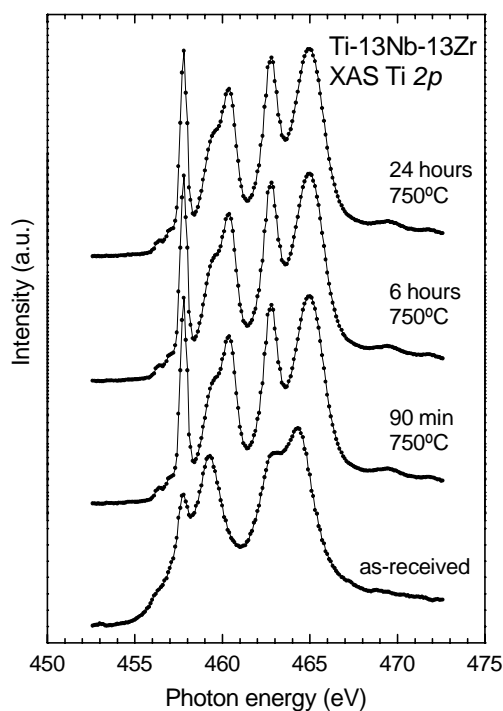
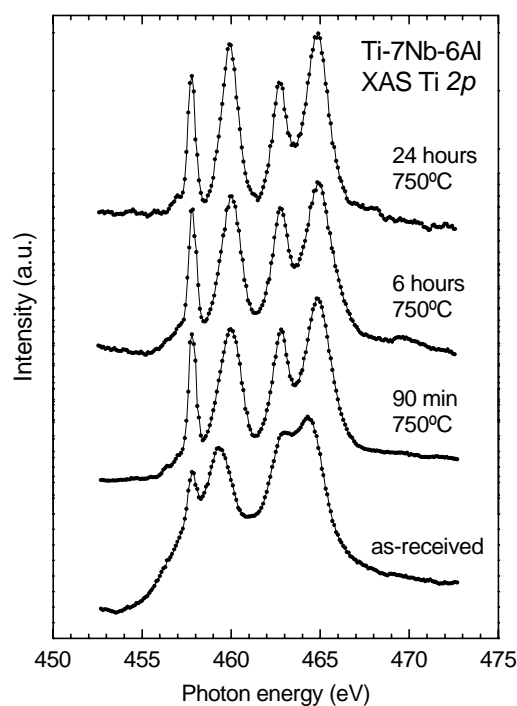

Fig. 1: Ti *2p* XAS spectra of Ti-13Nb-13Zr.　　Fig. 2: Ti *2p* XAS spectra of Ti-7Nb-6Al.

In order to study the oxidation behaviour of Ti-13Nb-13Zr, Ti-15Zr-4Nb and Ti-7Nb-6Al (wt %), some samples were isothermally heated at 750ºC in air for three different exposure times, 90 min, 6 hours and 24 hours. XAS measurements were carried out at the VLS-PGM soft x-ray monochromator at BESSY. XAS spectra were obtained by recording the total yield of electrons from the samples surfaces, i.e., in TEY mode. The base pressure in the UHV-chamber during the measurements was better than 2 x 10^{-10} mbar.

The Ti *2p* XAS spectra of the Ti-13Nb-13Zr and Ti-7Nb-6Al alloys are represented in Figs. 1 and 2, respectively. For Ti-13Nb-13Zr, the spectral shapes of all heat-treated samples are very similar to that of TiO_2, as can be deduced by comparison with previous works [3]. The Ti-15Zr-4Nb alloy exhibits a similar behaviour against oxidation in air to that of the Ti-13Nb-13Zr alloy. For Ti-7Nb-6Al, all heat-treated alloy spectra are very similar, but their shape is different to that of TiNbZr alloys. A comparison of these spectra with those of previous works, leads to the conclusion that they correspond to Al_2TiO_5 [4]. Both as-received spectra are, however, very similar and correspond to the native oxide.
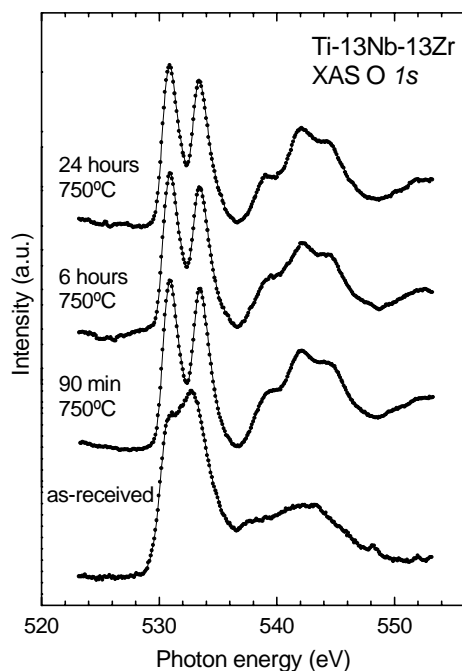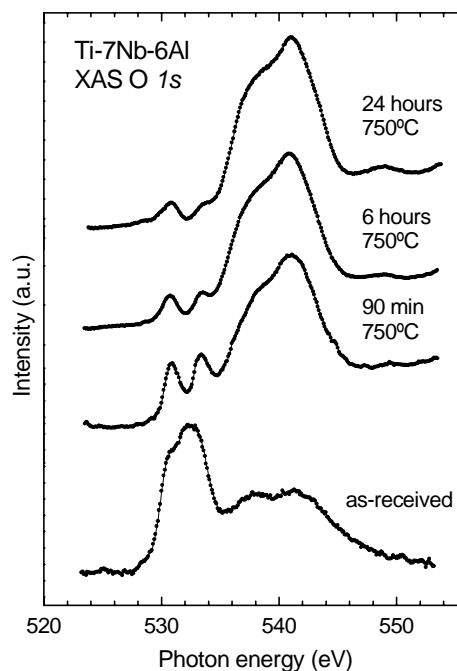

Fig. 3: O *1s* XAS spectra of Ti-13Nb-13Zr.

Fig. 4: O *1s* XAS spectra of Ti-7Nb-6Al.

Figs. 3 and 4 show the O *1s* XAS spectra of Ti-13-Nb-13Zr and Ti-7Nb-6Al, respectively. All Ti-13Nb-13Zr oxidized samples exhibit the typical O *1s* spectrum of rutile TiO_2, in agreement with the Ti *2p* spectra showed previously. In contrast, for the oxidized Ti-7Nb-6Al samples a broad feature at ≈ 540 eV is observed. By comparing the spectral shape of the oxidized samples with that of previous works, it can be concluded that this broad structure corresponds to Al_2O_3. The intensity of this feature increases by increasing the treatment time. These results suggest that the early state of oxidation promotes the formation of an Al_2TiO_5 layer on the material, as deduced from the Ti *2p* XAS spectra. As the exposure time increases, an Al_2O_3 layer grows on the previous oxide becoming thicker for longer oxidation times. Thus, the presence of Al in Ti-7Nb-6Al leads to a different oxidation tendency. The oxidation process of TiNbZr alloys promotes the TiO_2 formation contrary to Ti7Nb6Al alloys where Al_2TiO_5 and Al_2O_3 were formed.

[1] M. F. López, A. Gutiérrez, J. A. Jiménez, *Surf. Sci.* 2001; **482**: 300.
[2] M. F. López, A. Gutiérrez, J. A. Jiménez, *Electrochim. Acta (in print)* 2002.
[3] F. M. F. de Groot, J. C. Fuggle, B. T. Thole, G.A. Sawatzky, *Phys. Rev. B* 1990; **41**: 928.
[4] L. Soriano, M. Abbate, A. Fernández, A. R. González-Elipe, J. M. Sanz, *Surf. Interface Anal.* 1997; **25**: 804.

X-ray fluorescence analysis at the BAM*line*

A. Berger, K.-H. Ecker, W. Görner, S. Merchel, M. Procop, M. Radtke, H. Riesemeier
Bundesanstalt für Materialforschung und –prüfung (BAM), 12200 Berlin, Germany

As referred in the last annual report, the BAM*line* at the 7T Wavelength shifter (WLS) has been in operation since October 2000. Meanwhile a variety of successful X-ray fluorescence (XRF) experiments have been performed.

Set-up

At the moment a standard SY-XRF set-up is used. The sample is positioned under 45° and the detector under 90° with respect to the incoming beam to suppress scattered radiation effectively. The sample is mounted on an XYZ stage with µm resolution and on a rotation table with 0.001° resolution. The sample position can be monitored by a video system. Routinely a Si(Li) detector with an ultra thin window is used. An HPGe detector is also available for detection of the characteristic K-shell radiation of heavy elements. Both detectors are able to achieve a resolution of better than 140 eV at 5.9 keV and can be operated with a digital signal processor or analogue electronics. A double crystal monochromator (DCM) delivers monochromatic radiation for excitation. More detailed specifications of the beamline and the optical components can be found elsewhere [1].

Applications

Beside the analysis of Dürer's silver point drawings, which are presented in an own contribution to this annual report [2], we followed one of BAM's main duties, namely the characterization of reference materials. In this context first attempts were made to determine the sulphur content in oil and carbon black samples. Furthermore, it was demonstrated, that 15 ppm Ni can be determined in a Cu matrix using different excitation energies above and below the Ni K–edge and data processing of difference spectra. The option to vary the excitation conditions is one of the main advantages using a synchrotron as a radiation source. The results for measurements on thin layer reference materials are shown in more detail below.

As a contribution to the development of thin film reference materials in the nanometre range, the thickness of nominal 10 to 30 nm Ni- and Pt-layers has been measured by means of XRF. The initial measurement uncertainty could be significantly reduced after installation of an ionisation chamber to monitor the X-ray beam intensity. Converting the resulting area density (gram per cm^2) to layer thickness (nm), assuming bulk density, a reasonable agreement could be achieved with the GIXR (Grazing Incidence X-ray Reflectometry) data obtained by PTB at BESSY.

The small spot size (diameter of about 0.1 mm) and the high beam intensity enable to scan the beam over the entire layer on the 60×20 mm^2 substrate within reasonable time. Hence, we gained information about the homogeneity of the layer thickness that cannot be obtained by any other method in this direct way and in a comparably short measurement time.
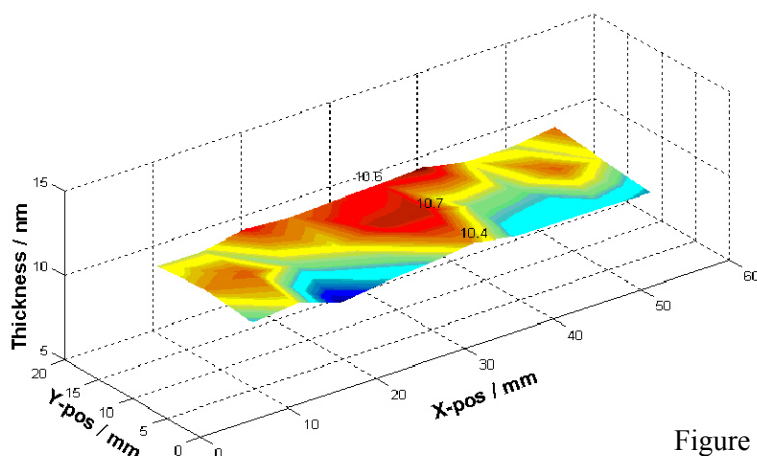
As an example Fig. 1 shows the thickness variation of a nominal 10 nm Ni-layer on quartz.

The investigations are a contribution of BAM to the BMBF-project "Kalibrierte Schichtdicken-Maßverkörperungen für Nanometerschichten", project number 13N7704.

Figure 1: Thickness variation of a nominal 10 nm Ni-layer on quartz.

XRF was also used to determine the homogeneity of another thin layer reference material [3]. It consists of a thin layer of Sb atoms (5×10^{16} cm^{-2}) implanted in a 3-inch silicon waver and subsequently cut into chips of 1cm×1cm. Since this material is intended to be used with beam techniques analysing only a fraction of the chip surface at a time, it is of prime importance for the certification of this reference material to know the lateral inhomogeneity of the areal density of Sb on a single chip and between chips. Homogeneity measurements, first carried out using Rutherford Backscattering Spectrometry (RBS) [4] with an ion beam of 1 mm diameter, could be improved considerably by XRF measurements. SY-XRF is an ideal method for fast high precision relative measurements. An intense monochromatic photon beam of size 0.3 mm x 0.3 mm with energy of 7 keV was used to excite the fluorescence radiation. The intensity of the Sb-L lines from the implanted atoms is measured relative to the Si-K lines from the substrate acting as an internal standard. Figure 2 shows a comparison of XRF and RBS measurements of the between chip homogeneity. The standard deviation, which is set to be the contribution to the uncertainty due to inhomogeneity, is reduced by a factor of 2 by XRF measurements. In turn the present XRF measurements lead to a reduction of the uncertainty of the certified value by a factor of 1.6. In addition, showing a very good micro-homogeneity of the material, the certified value is now valid for a considerably smaller fraction of the chip surface.
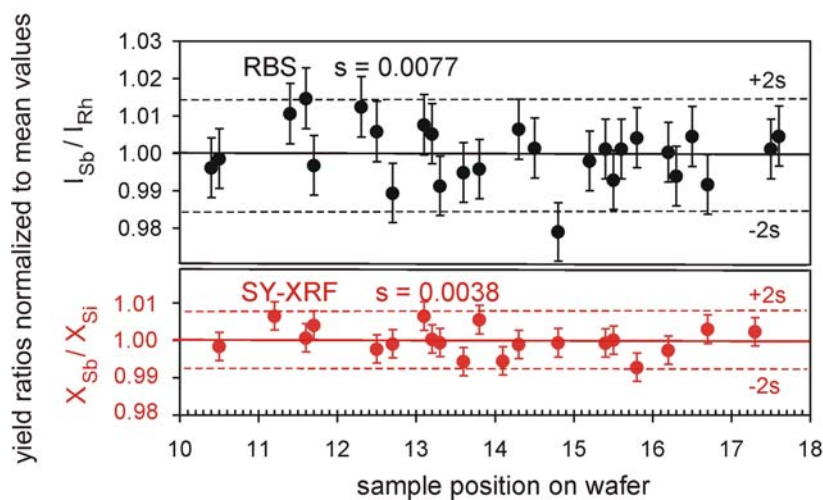

Figure 2: Results of homogeneity measurements for implanted antimony, expressed as ratios of net peak areas normalized to the respective mean value.

Outlook

Encouraged by these successfully performed XRF measurements, several upgrades are planned for the next future. The use of the recently installed double multi-layer monochromator will allow to perform experiments with a significantly higher flux. Besides components to use other techniques like µ-XRF or TXRF will be installed and the new power supply scheme for the superconducting wavelength shifter will enhance the stability of the WLS source.

Furthermore, the installation of a vacuum chamber will extend the range of accessible elements to lower Z materials. The characterization of the different components, especially of the detectors, will be continued to allow a more precise quantification on the base of fundamental parameter programs or Monte-Carlo simulations. An X-Flash detector, which is able to process count rates as high as 500,000 cps, will also be integrated into the set-up.

References

[1] W. Görner, M. P. Hentschel, B. R. Müller, H. Riesemeier, M. Krumrey, G. Ulm, W. Diete, U. Klein, R. Frahm, *Nucl. Instr. and Meth. A* **467-468** (2001) 703-706.

[2] I. Reiche, A. Berger, W. Görner, S. Merchel, M. Radtke, J. Riederer, H. Riesemeier, *BESSY Annual report* (2001).

[3] K. H. Ecker, U. Wätjen, A. Berger, L. Persson, W. Pritzkow, M. Radtke, H. Riesemeier, *Nucl. Instr. and Meth. B* (2002) in press.

[4] K. H. Ecker, A. Berger, R. Grötzschel, L. Persson, U. Wätjen, *Nucl. Instr. and Meth. B* **175** (2001) 797-801.

Configuration mixing in Pr and Nd transition-metal compounds

S.L. Molodtsov[1], Yu. Kucherenko[2], M. Finken[1], M. Heber[1], G. Behr[3], and C. Laubschat[1]

[1]Institut für Oberflächenphysik und Mikrostrukturphysik, TU Dresden, D-01062 Dresden, Germany

[2]Institute of Metal Physics, National Academy of Sciences of Ukraine, UA-03142 Kiev, Ukraine

[3]Institut für Festkörper- und Werkstofforschung Dresden, Postfach 270016, D-01171 Dresden, Germany

In Ce systems hybridization of 4f states is frequently studied by means of photoemission (PE) where it leads to characteristic splittings of the 4f-derived PE signal [1]: Instead of a single $4f^0$ electron-removal state at about 2 eV binding energy (BE) expected from photoionization of an unhybridized $4f^1$-ground state one observes the appearance of a second 4f-derived feature close to the Fermi energy, E_F, that reproduces essentially the $4f^1$ ground-state and is commonly referred as "Kondo-peak". This phenomenon may quantitatively be described in the framework of the single-impurity Anderson model (SIAM) [1] where the appearance of additional 4f-derived features in the PE spectra is explained in terms of configuration mixing. From the observed relative intensities and energy positions of the individual spectral features model parameters may be derived that allow for a consistent description of both PE results and ground-state properties of the system. Energy splittings of the 4f emissions have also been reported for Pr and Nd compounds and an interpretation in analogy to Ce systems was proposed [2]. A quantitative analysis of these phenomena that allows conclusions on the ground-state configurations, however, was never attempted.

In the present contribution we show that resonant PE spectra of Pr compounds may quantitatively be understood in the framework of the same SIAM applied usually for the description of Ce systems. Main parameters in this approach are the energy of the bare $4f^1$ state, ε_f, and the hybridization, Δ, describing the interaction of the 4f state with the valence-band via hopping. Introduction of the on-site Coulomb-repulsion energy, U_{ff} allows consideration of further configurations with higher 4f occupations; hereby, $2\varepsilon_f + U_{ff}$ and $3\varepsilon_f + 3 U_{ff}$ describe the energies of the $4f^2$ and $4f^3$ states, respectively. Shifting the energy zero to the position of the $4f^1$ state and replacing ε_f by the energy necessary to transform a $4f^1$ into a $4f^2$ configuration, $(\varepsilon_f + U_{ff})_f$, one gets formally a projection of Pr back to the Ce problem. An analogous treatment is also possible for Nd systems. In the following we apply a simple approach to SIAM that allows consideration of a realistic density of states (DOS) [3].

Resonant PE experiments on Pr compounds with Rh, Pd, and Ag were performed at the $3d \rightarrow 4f$ absorption threshold exploiting synchrotron radiation from the U49/2-PGM1 undulator beamline of BESSY II. Polycrystalline samples were prepared by arc-melting and cleaned in-situ by scraping with a diamond file. On- and off-resonance spectra are shown in fig. 1 together with a numerical simulation in the light of SIAM. In order to extract the 4f contributions the on-resonance spectra ($h\nu$ = 930 eV) were corrected by subtraction of the respective off-resonance data ($h\nu$ = 923 eV). In contrast to Pr metal where the 4f emissions consist of a sharp peak at 3.3 eV BE the 4f spectrum of Pr_5Rh_4 reveals a strong splitting with maxima at about 1.5 eV and 4.0 eV and a minimum arround 3 eV BE that coincides in energy with the maximum of the Rh 4d derived DOS (maximum in the off-resonance spectrum). In PrPd the respective splitting degenerates to an assymmetric line-broadening that disappears almost completely in case of the Ag compound. At the same time, the DOS maxima shift to

higher BE reflecting the filling of the 4d bands as a function of atomic number. The experimental result is well reproduced in the light of SIAM: For the Rh compound the energy degeneracy of ε_f with the narrow 4d band is lifted by hybridization leading to an almost symmetrical splitting of the 4f emission into two components separated from each other by about 2Δ. This is in analogy to the splitting of atomic orbitals into bonding and antibonding states. Consequently, both 4f components reveal almost the same 4f occupancy close to n=1 in contrast to related splittings in Ce systems where the individual spectral components correspond to different $4f^n$ configurations. The Pr_5Rh_4 spectrum was fitted modelling the DOS by a Gaussian at 2.5 eV BE and using ε_f and Δ as fit parameters (U_{ff}= 7.5 eV). As a result we obtain ε_f = -2.6 eV and Δ = 1.3 eV corresponding to a ground-state 4f occupancy of 2.05. For PrPd and PrAg the same ε_f and Δ parameters were used shifting only the DOS to the positions observed in the off-resonance spectra. Even this crude approach describes the experimental results rather well. An almost perfect fit may be obtained optimazing the fit parameters and considering surface effects. Similar results were obtained for Nd compounds.

References:
1) O. Gunnarsson and K. Schönhammer, Phys. Rev. Lett. **50**, 604 (1983)
2) R. D. Parks et al., Phys. Rev. Lett. **52**, 2176 (1984); G. Kalkowski et al., Solid-State Commun. **55**, 977 (1985); S. Suga et al., Phys. Rev. B **52**, 1584 (1995)
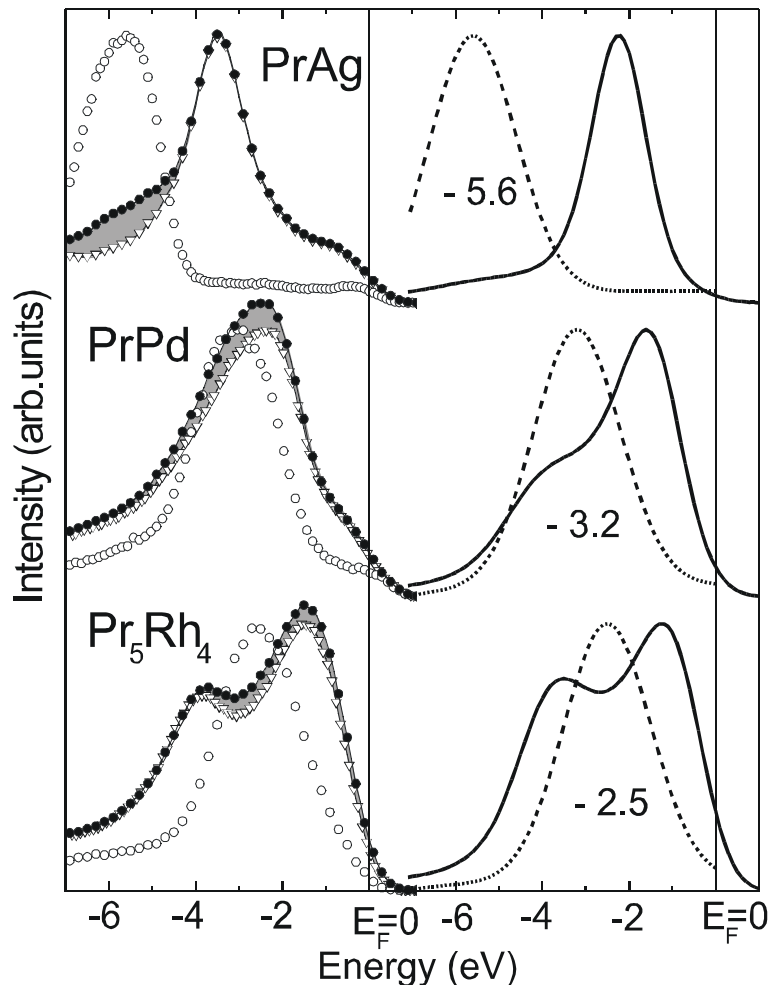3) R. Hayn et al., Phys. Rev. B **64**, 115106 (2001)

Fig. 1: 3d→4f resonant PE spectra (on-resonance: black circles, off-resonance: open circles: non-resonant contribution to on-resonance spectra: shaded area, corrected data: triangles) together with results of a numerical simulation in the light of SIAM (solid line: SIAM, dotted: DOS; numbers denote the position of the DOS maximum; ε_f = -2.6 eV).

Photoelectron diffraction determination of the local adsorption geometry of CO on Cu(210)

R. Terborg, P. Baumgärtel, J.T.Hoeft, M.Polcik, A.M. Bradshaw
Fritz-Haber-Institut der Max-Planck-Gesellschaft, Berlin, Germany

R.L.Toomes, D.P.Woodruff
Physics Department, University of Warwick, UK

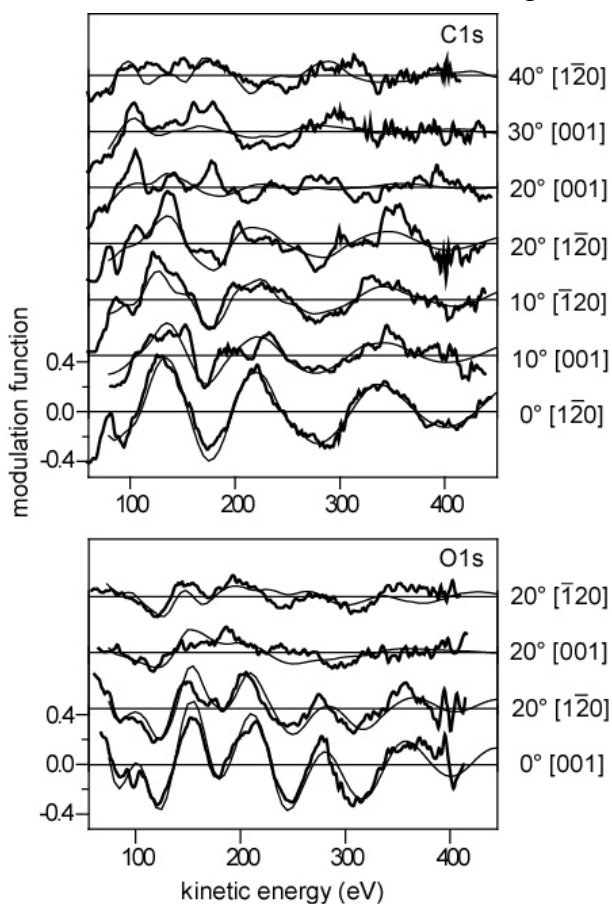While there have been extensive studies of the structure of low index surfaces of crystalline solids, there are far fewer studies of high-index or vicinal surfaces. Such surfaces are, however, of both intrinsic and practical interest because they include not only low-index terraces, but also steps (ledges) and (in some cases) kinks; these surface "defect" sites have been implicated in many surface reactions which are structure sensitive. Here we present the results of a study of a particularly simple model system, CO on Cu(210).

The experiments were conducted at the BESSY synchrotron facility on the HE-TGM 1 monochromator. The saturation coverage of CO was prepared and measured at 110K.

The experimental C 1s and O 1s scanned-energy photoelectron diffraction (PhD) modulation curves together with the results of calculations for the best-fit structure are shown in Fig. 1. The structural model is presented in Fig. 2 and the optimised values of the parameters defined in Fig. 2 are listed in Table 1. Our study has shown that the adsorption occurs at atop sites with C-Cu and C-O bondlengths consistent with previous studies on low-index Cu surfaces. Within the plane perpendicular to the [001] step edges the C-O axis is tilted to an angle intermediate between the surface normal to the

Fig. 1 Comparison of the experimental (thick) and simulated (thin) PhD spectra

average surface and that perpendicular to the (110) terraces. In addition, however, there is a component of the tilt parallel to these steps.
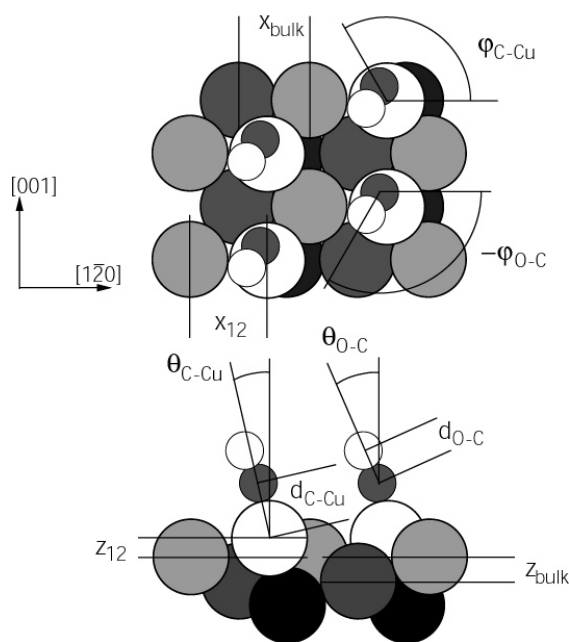

Fig.2 Structural model of the Cu(210)-CO system

Parameter	Optimum value
Z_{12}	0.68±0.19 Å (bulk =0.81 Å)
X_{12}	2.54±0.75 Å (bulk =2.42 Å)
d_{C-Cu}	1.87±0.02 Å
θ_{C-Cu}	6±5°
ϕ_{C-Cu}	150±57°
d_{O-C}	1.16±0.03 Å
θ_{O-C}	18±6°
ϕ_{O-C}	-112±37°

Table 1 Optimised values of structural parameters.

Cu(100)c(2x2)-N: a new type of adsorbate-induced surface reconstruction

J.T.Hoeft, M.Kittel, M.Polcik,

Fritz-Haber-Institut der Max-Planck-Gesellschaft, Berlin, Germany

R.L.Toomes, J.-H.Kang, D.P.Woodruff

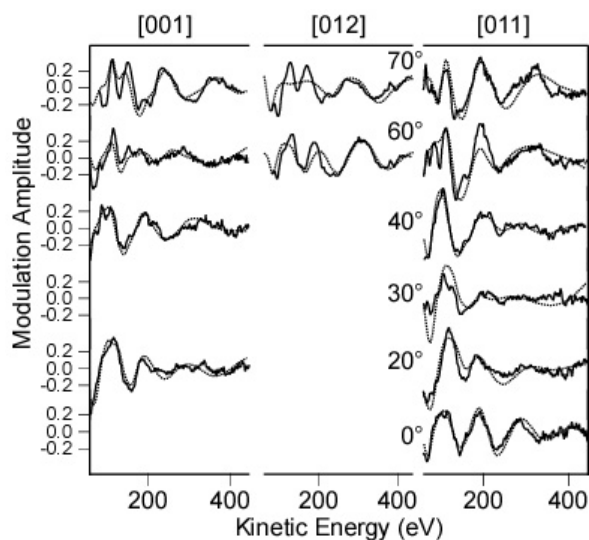*Physics Department, University of Warwick, UK*

Fig. 1 The experimental and simulated PhD modulation curves.

It is now well established that some clean metal surfaces and many adsorbate-covered metal surfaces reconstruct [1] i.e. the substrate atoms in the outermost layer(s) adopt a structure significantly different from those in the underlying bulk. In many cases these reconstructions are believed to relate to the relief of surface stress. Here we present a scanned-energy photoelectron diffraction (PhD) study of the c(2x2)Cu-N system in order to understand the novel self-organization of the c(2x2) islands previously reported in this system [2].

The PhD experiments have been performed at the BESSY storage ring facility using the HE TGM 1 monochromator. Nitrogen was sputtered on the clean Cu(100) surface at 300K. The c(2x2) structure was observed by low energy electron diffraction (LEED).

$d_{N1U} =$ (-0.07 ± 0.10)Å
$d_{N1L} =$ (0.27 ± 0.06)Å

$d_{N2} =$ (1.99 ± 0.06)Å

$d_{N3} =$ $(3.8 ^{+inf}/_{-1.7})$Å

vibration amplitudes
$<u_{nn,1}>^2$ $=$ $0.004 (\pm 0.003)$Å^2
$<u_{nn,2}>^2$ $=$ $0.010 (+0.010/-0.004)$Å^2
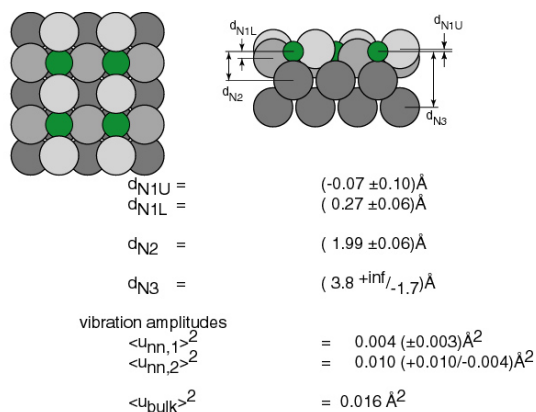
$<u_{bulk}>^2$ $=$ 0.016 Å^2

Fig 2. The structural model of the c(2x2)Cu(100)-N

The best agreement between the experimental and simulated PhD modulation curves, see Fig 1, has been achieved for the structural model shown in Fig. 2. The large amplitude of the rumpling (0.34Å) and the symmetry lowering are the primary signatures of the reconstruction. Although this type of reconstruction of a metal surface has not previously been observed, it seems clear that this could also be understood in terms of the relief of adsorbate-induced compressive surface stress. Indeed on a macroscopic scale bending or rumpling is the most common form of such
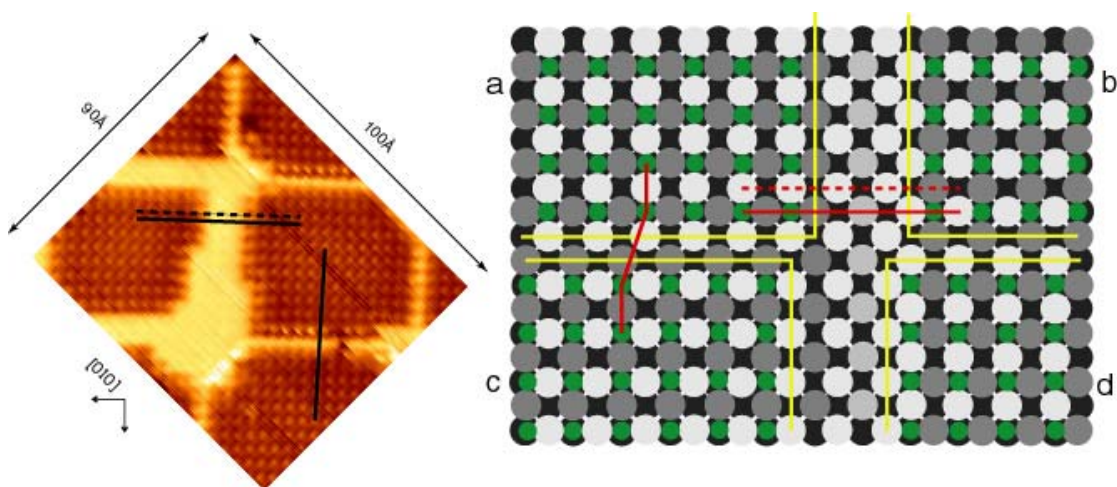
Fig.3 left: STM image of the c(2x2)Cu(100)-N surface[3]; right: Schematic diagram of the different types of structural domains and antiphase domain boundaries to be expected on the rumpled Cu(100)c(2x2)-N structure. The N atoms are shown as green circles; the upper Cu atoms in the outermost layer are white, the lower Cu atoms are grey. Domains a and c have opposite parity of Cu top layer rumpling to domains b and d leading to the wide vertical anti-phase boundary. Domains a and b involve different N atom site occupation from domains c and d leading to the narrow horizontal boundary wall.

relief. The rumpling also allows us to understand the unusual nature of the interaction of adjacent c(2x2) islands, see Fig. 3.

References

1 D.A. King and D.P. Woodruff (eds) 1994) The Chemical Physics of Solid Surfaces Vol 7 (Amsterdam: Elsevier)

2 F.M. Leibsle, C.F.J. Flipse and A.W. Robinson, Phys. Rev. B 47 15865

3. S.Driver, J.T. Hoeft, M. Polcik, M. Kittel, R.Terborg, R.L. Toomes, J.-H. Kang, D.P. Woodruff, J. Phys. Condens Mat, 13 L601 (2001)

Local structure of CO coadsorbed with O on Ni(111): A temperature-dependent study

J.-H. Kang, R.L.Toomes, J. Robinson, D.P.Woodruff

Physics Department, University of Warwick, UK

R. Terborg, P. Baumgärtel, J.T.Hoeft, M.Polcik, A.M. Bradshaw

Fritz-Haber-Institut der Max-Planck-Gesellschaft, Berlin, Germany

Especially for the case of CO adsorption, vibrational spectroscopy has been used routinely to infer the local adsorption geometry on surfaces [1]. In particular, the 0.5 monolayer coverage phase of CO on Ni(111), which forms an ordered c(4x2) phase, had long been interpreted in terms of bridge site adsorption, whereas the true structure was found to comprise equal occupation of the two inequivalent hollow sites 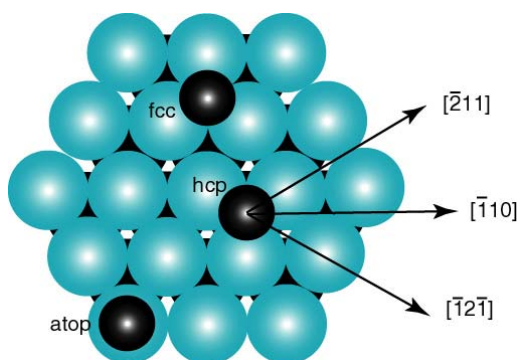[2], see Fig. 1. In the case of CO/O coadsorption the photoelectron diffraction (PhD) study [3] also found hollow sites whereas a vibrational spectroscopic study shows a C-O stretching frequency in the range of normally associated with atop adsorption [4]. In view of these results we have undertaken a new PhD study of the Ni(111)(2x2)-O/CO system at different temperatures.

Fig. 1 Plan view of a Ni(111) surface showing the atop, hcp hollow, and fcc hollow sites.

The experiments were conducted at the BESSY synchrotron facility on the HE-TGM 1 monochromator. The initial Ni(111)(2x2)-O surface was prepared by exposing the surface at 300-350K to 3×10^{-6}mbars of oxygen followed briefly annealing to approximately 400K to yield sharp (2x2) LEED pattern. CO was then dosed by exposing the surface to approximately 1×10^{-6}mbars at 150K, followed by annealing to 265-270K. All C 1s PhD spectra were collected at 140K. The results of the structural analysis are summarized in Table 1.

Preparation or annealing temperature (K)	Proportion of atop sites (%)	C-Ni layer spacing (atop) (Å)	C-Ni layer spacing (hcp hollow) (Å)
265	95(+5/-25)	1.77±0.02	1.26
170	70±20	1.79±0.03	1.28±0.12
120	35(+20/-25)	1.81±0.08	1.29±0.04

Table 1 Summary of the best-fit structural parameters for CO in the Ni(111)(2x2)-O/CO phase for different preparation and annealing temperatures.

Our analysis is in agreement with the XPS study [5], in which CO adopts atop sites in the presence of coadsorbed O when the surface is formed at around room temperature, whereas if the surface is prepared at sufficiently low temperatures a large fraction of the CO molecules occupy the hollow sites as they do in the absence of preadsorbed O. However, more careful consideration of the result of the vibrational study [4] indicates that a further key factor is the exact precoverage of oxygen. In particular this early study shows that while the coverage of exactly 0.25ML appeared to indicate only atop adsorption, even at 90K, lower predoses led to spectra indicative of co-occupation of more highly coordinated sites. We therefore conclude that hcp site occupation in the low temperature data is related to adsorption on regions which are depleted of oxygen. We then conclude from our new study that CO adsorption on an ideal (2x2)-O surface almost certainly is entirely in atop sites.

References

1 N. Sheppard, N.T. Nguyen, Adv. IR Raman Spectrosc,5, (1978), 67

2 L. Becker, S. Aminpirooz, B. Hillert, M. Pedio, J. Haase, D.L. Adams, Phys. Rev. B47 (1993) 9710

3 V. Fernandez, K.-M. Schindler, O. Schaff, P. Hofmann, A. Theobald, A.M. Bradshaw, V. Fritzsche, R. Davis, D.P. Woodruff, Surf. Sci 351 (1996) 1

4 Z. Xu, L. Surnev, K.J. Uram, J.T. Yates Jr., Surf. Sci. 292 (1993) 235

5 G. Held, J. Schuler, W. Sklarek, H.-P.Steinrück, Surf. Sci. 398 (1998) 154

Molecular Adsorption Bond-lengths at Metal Oxide Surfaces: Failure of Current Theoretical Methods

J.T.Hoeft, M.Kittel, M.Polcik, S.Bao

Fritz-Haber-Institut der Max-Planck-Gesellschaft, Berlin, Germany

R.L.Toomes, J.-H.Kang, D.P.Woodruff

Physics Department, University of Warwick, UK

M.Pascal and C.L.A.Lamont

Centre for Applied Catalysis, University of Huddersfield, UK

Very substantial advances in computational density functional theory during the last few years have shown that adsorbate bonding on metal surfaces can be described very precisely, achieving agreement with experimental results in local structural parameters within a few hundredths of an Ångstrom unit. There is now increasing interest in oxide surfaces, which are widely recognised as being of great importance in applications such as heterogeneous catalysis, but the state of knowledge concerning these surfaces is far more limited. We have performed quantitative structure determinations of the model systems of CO and NH_3 adsorbed on NiO(100).

The thin NiO(100) film was grown *in* situ on Ni(100) using the approach of Kuhlenbeck *et al* [1]. The scanned-energy photoelectron diffraction (PhD) experiments were conducted using the BESSY synchrotron radiation source in Berlin on a HE TGM 1 monochromator. A representative data set of PhD spectra recorded in 10 different emission directions for the NiO(100)/CO system is shown in
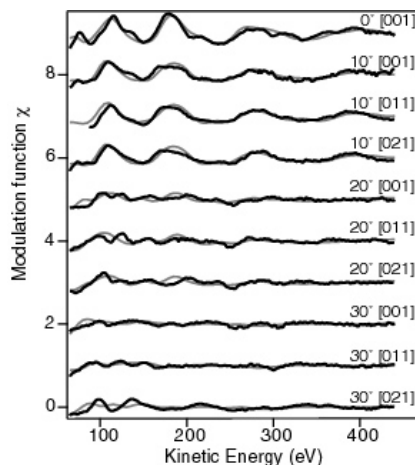

Fig.1 Comparison of experimental (faint lines) C 1s PhD modulation spectra from CO adsorbed on NiO(100) recorded at four different polar emission angles in three different azimuths with the results of multiple scattering simulations (full lines) for the best-fit structure.

Fig. 1. The structural parameters defined in Fig. 2 are listed in Table 1. While the local adsorption site and orientation for CO (and for NO[2]) are in good qualitative agreement with the results of the previous theoretical studies, the quantitative values of the local Ni-molecule bond-lengths are in very poor agreement. The theoretical Ni-N
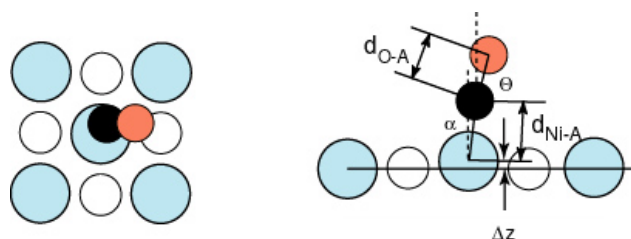

Fig. 2 Schematic side view of the best-fit adsorption geometry of CO on NiO(100), including a definition of the structural parameters given in Table 1. The shaded and open circles correspond to Ni and O atom

Adsorbate	CO	NH₃
d_{Ni-C}, d_{Ni-N}	2.07±0.02 Å	2.06±0.02 Å
d_{O-C}	1.15(+0.10/-0.08) Å	
θ_{Ni-C}, θ_{Ni-N}	7(+5/-3)°	7±6°
θ_{O-C}	12±12°	
Δz_{Ni}	0.03(+0.06/-0.08) Å	0.11±0.02 Å

Table 1

Optimum values of the structural parameters found in this experimental study of NiO(100)/CO and NiO(100)/NH₃

bond-length for NO adsorption is 0.22 Å longer than the experimental value, while the Ni-C distances for CO adsorption found in the two theoretical treatments are 0.42 Å and 0.79 Å longer than the experimental value. The adsorption bondlengths measured on NiO(100) are sufficiently short to indicate true bond formation, and not simply electrostatic interaction as has been concluded for CO adsorption on NiO(100) on the basis of current theoretical treatments.

References

1 H.Kuhlenbeck, G.Odörfer, R.Jaeger, G.Illing, M.Menges, Th.Mull, H.-J.Freund, M.Pöhlchen, V.Staemmler, S.Witzel, C.Scharfschwerdt, K.Wennemann, T.Liedtke and M.Naumann, Phys.Rev.B 43, 1969 (1991)

2 R.Lindsay, A.Theobald, T.Gießel, O.Schaff, A.M.Bradshaw, N.A.Booth and D.P.Woodruff, Surf.Sci. 405, L566 (1998)

3 F.Illas, G.Pacchioni, A.Pelmenschikov, L.G.M.Pettersson, R.Dovesci, C.Pisani, K.M.Neyman and N.Rösch, Chem.Phys.Lett. 306, 202 (1999)

4 R.Wu and Q.Zhang, Chem.Phys.Lett, 306, 205 (1999)

Si K-edge NEXAFS spectroscopy of amorphous silicon monoxide (SiO)

A. Hohl[1], T. Wieder[1], V. Joco[1], H. Fuess[1], M. Fieber-Erdmann[2], and F. Schäfers[2]

[1]*TU Darmstadt, FB Material- und Geowissenschaften, FG Strukturforschung, D-64287 Darmstadt*
[2]*BESSY GmbH, D-12489 Berlin, Germany*

The atomic structure of the black, coal-like modification of amorphous silicon monoxide (SiO) is a controversial issue and still could not be clarified. Some authors see SiO disproportionated into Si and SiO_2 on a microscopic scale [1]. Other authors suppose SiO as a phase of its own [2]. We performed NEXAFS (near-edge X-ray absorption fine structure) measurements as a part of our structural characterization by combination of several experimental methods [3]. NEXAFS spectroscopy gives information about the bonding conditions (i. e. the distribution of different tetrahedral Si and O coordination of absorbing silicon atoms), as the Si atoms take sp^3 hybridization. We studied SiO films of about 1 μm thickness, which had been produced at ca. 300 °C with a deposition rate of about 1 nm/s on germanium substrate in an induction vacuum sintering system. In comparison, bulk samples of commercially available Patinal® from Merck KGaA (Darmstadt, Germany) were investigated. They had been deposited at ca. 600 °C with a deposition rate of about 200 nm/s.

The present experiments were performed at room temperature at the KMC-1 beamline. The InSb(111) monochromator was used. The samples were measured in reflection mode. We recorded spectra at the Si K-edge (1839 eV). The estimated energy resolution was $E/\Delta E \approx 3500$. We simultaneously tried three detection modes while scanning the photon energy. We tried total electron yield (TEY) detection by directly detecting the sample current through a wire, which was in conductive contact to the sample surface. The TEY signals did not show sufficient signal-noise-ratio due to the low conductivity of the SiO samples. Furthermore, we used partial electron yield (PEY) detection using a channeltron, which was fixed in the chamber opposite to the sample surfaces. The use of a backward voltage of about 50 - 150 V reduced the sensivity for electrons from the outer surface. In addition, we used fluorescence yield (FY) detection using a photo diode, which exhibits a good signal-to-background ratio. We had fixed angles between incident beam and samples (45°), between samples and fluorescence detector (45°), and between samples and channeltron detector (90°). The raw data was corrected for the energy dependence of the incident beam intensity I_0 by division through spectra of monitored I_0, which were obtained using a gold net, that was fixed on the primary side before the sample chamber.

Here the results from six samples are presented. Sample A was a native SiO film. Sample B and sample C were SiO films, which had been annealed in (humide) air for 10 minutes at 400 °C and for 15 minutes at 600 °C respectively. Sample D and sample E were SiO films, which had been annealed in (dry) nitrogen atmosphere for 5 minutes at 850 °C and for 15 minutes at 700 °C respectively. Sample F was a native bulk SiO sample. Fig. 1 shows a comparison of the different NEXAFS spectra from FY detection mode. The results were confirmed by similarity to those, which were obtained from PEY detection mode (not shown). They exhibit spectral features which can be attributed to pure silicon (edge at 1838 - 1839 eV) and to pure silicon dioxide (peak at about 1845 - 1846 eV), which can be found in the literature [4]. The origin of the features is the amount of $Si(Si_4)$ and $Si(O_4)$ tetrahedral building units in the measured sample volume. From Fig. 1, the trend for disproportionation into Si and SiO_2 can be seen, which is probably related to the annealing temperature of the SiO films. Furthermore,
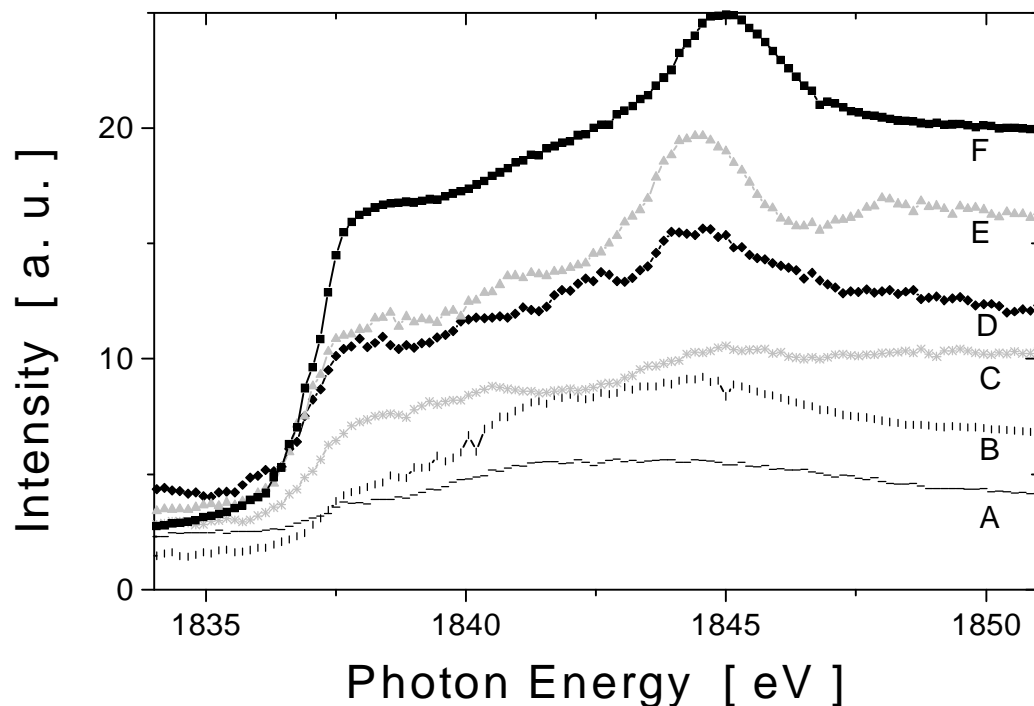
Fig. 1. Si K NEXAFS spectra for different samples A - F as described in the text, obtained from fluorescence yield detection. Different scaling factors have been applied to clarify the features of the spectra.

structural differences between native film and bulk samples are verified, probably related to the different deposition rate.

More results will soon be available from http://homepages.tu-darmstadt.de/~wieder/sio.html.

Acknowledgements

References

[1] R. J. Temkin, An Analysis of the Radial Distribution Function of SiO_x, Journal of Non-Crystalline Solids 17 (1975) 215-230.
[2] J. A. Yasaitis and R. Kaplow, Structure of Amorphous Silicon Monooxide, Journal of Applied Physics 53 (1972) 995.
[3] C. Deneke, Strukturuntersuchung an nicht-kristallinem Siliziummmonoxid, diploma thesis, Technische Universität, Darmstadt (2000)
[4] C. Laffon, A. M. Flank, and P. Lagarde, XANES studies of some silicon compounds, in: S. S. Hasnain (Ed.), X-ray absorption fine structure, Ellis Horwood, Chichester, 1991, p. 604-606.

EXAFS spectroscopy of amorphous iron-scandium alloys $Fe_{100-x}Sc_x$

A. Hohl[1], T. Wieder[1], V. Joco[1], H. Fuess[1], S. Gottschalk[2], A. Volland[2], M. Ghafari[2], and M. Fieber-Erdmann[3]

[1]*TU Darmstadt, FB Material- und Geowissenschaften, FG Strukturforschung, D-64287 Darmstadt, Germany*
[2]*TU Darmstadt, FB Material- und Geowissenschaften, FG Dünne Schichten, D-64287 Darmstadt, Germany*
[3]*BESSY GmbH, D-12489 Berlin, Germany*

Amorphous iron-scandium alloys $Fe_{100-x}Sc_x$ have found interest due to their magnetic properties (e. g. antiferromagnetic coupling at high scandium amount) [1,2]. The magnetic order strongly depends on the local atomic structure of these alloys. We performed EXAFS (extended X-ray absorption fine structure) measurements as a part of structural characterization by several experimental methods [3]. Samples of about 100 nm $Fe_{100-x}Sc_x$ deposited on crystalline silicon substrates had been produced by simultaneous electron beam evaporation of iron and scandium under UHV conditions. We studied samples with Sc composition in the range $8 \leq x \leq 86$.

The present experiments were performed at room temperature at the KMC-2 beamline. The samples were measured in reflection mode. We recorded spectra at the Fe K-edge (7112 eV) and at the Sc K-edge (4493 eV). The estimated energy resolution was $E/\Delta E \approx 7000$. We simultaneously used three detection modes while scanning the photon energy. We used total electron yield (TEY) detection by directly detecting the sample current through a wire, which was in conductive contact to the sample surface. Furthermore, we used partial electron yield (PEY) detection using a channeltron with a backward voltage of about 50 - 150 V to reduce the relative sensivity for slow electrons from the outer surface. In addition, we used fluorescence yield (FY) detection using a photo diode, which exhibits a high signal-to-background ratio. The comparison of PEY with TEY and FY shows the influence of surface oxide, resulting from handling the samples in air. We had fixed angles between incident beam and samples (45°), between samples and fluorescence detector (45°), and between samples and channeltron detector (90°). The raw data were corrected for the energy dependence of the incident beam intensity I_0 by division through spectra of monitored I_0, which were obtained from an ionization chamber on the primary side of the sample chamber. The ionization chamber was filled with N_2 gas.

The EXAFS spectra were fitted using the program XAFS [4]. The models for the fitting were constructed using the program FEFF7 [5]. The total absorption cross section μ_{tot} with contributions of both elements at the Fe K-edge and at the Sc K-edge has a magnitude of about 10^3 cm^{-1}. As the thicknesses of our samples were smaller than $1/\mu_{tot}$, it was not necessary to correct $\chi(k)$ for self-absorption effects [6,7]. Some EXAFS oscillations and corresponding Fourier transforms are shown in Fig. 1. The comparison of radial distribution functions from TEY and FY shows possible differences between the first neighbouring shell peaks due to surface oxidation. For fitting the EXAFS spectra the best appropriate data from the three experimental methods should be used. Hence, the fluorescence yield spectra were used to obtain fitting parameter values, whereas the TEY and PEY data provided an estimation of the corresponding errors. The first fitting results for the first neighbouring shells are shown for $Fe_{64}Sc_{36}$ (x = 36). At the Fe K-edge, the Fe-Fe coordination number was $N_1 \approx 3.66 \pm 0.3$, the Fe-Fe nearest-neighbour distance was $R_1 \approx 2.46$ Å ± 0.05 Å, and the Debye-Waller factor was $A_1 \approx 0.061$ Å$^2 \pm 0.002$ Å^2. For Fe-Sc we obtained $N_2 \approx 2.37 \pm 0.05$, $R_2 \approx 2.55$ Å ± 0.05Å, and $A_2 \approx 0.094$ Å$^2 \pm 0.022$ Å^2. At the Sc K-edge, the Sc-Fe coordination
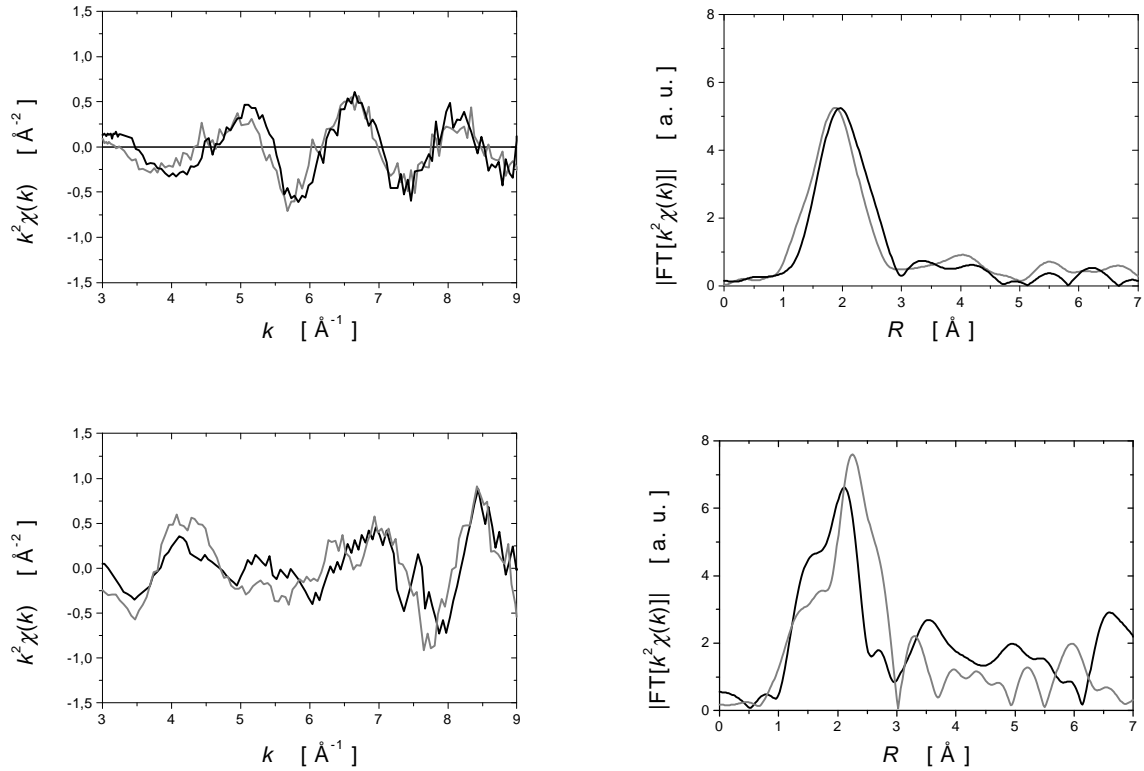
Fig. 1. EXAFS oscillations $k^2\chi(k)$ (left) and the corresponding Fourier transforms $|FT[k^2\chi(k)]|$ (right) for $Fe_{64}Sc_{36}$ at the Fe K-edge (top) and at the Sc K-edge (bottom) from FY (black line) and TEY (gray line).

number was $N_3 \approx 2.90 \pm 0.3$, the Sc-Fe nearest-neighbour distance was $R_3 \approx 2.44 \text{ Å} \pm 0.05 \text{ Å}$, and the Debye-Waller factor was $A_3 \approx 0.052 \text{ Å}^2 \pm 0.002 \text{ Å}^2$. For Sc-Sc we obtained $N_4 \approx 2.42 \pm 0.58$, $R_4 \approx 2.75 \text{ Å} \pm 0.08 \text{ Å}$, and $A_4 \approx 0.053 \text{ Å}^2 \pm 0.008 \text{ Å}^2$.

More results will soon be available from http://homepages.tu-darmstadt.de/~wieder/fesc.html.

References

[1] M. Ghafari, R. K. Day, J. B. Dunlop, and A. C. McGrath, Spin coupling in amorphous $Fe_{90}Sc_{10}$ alloy, Journal of Magnetism and Magnetic Materials 104-107 (1992) 1668-1670.

[2] S. K. Xia, E. Baggio-Saitovitch, V. A. Rodriguez, E. Passamani, A. Y. Takeuchi, M. Ghafari, R. R. Avillez, and F.C. Rizzo Assunçao, The effect of mechanical milling on the structure and magnetic properties of Fe_2Sc Laves phase, Journal of Alloys and Compounds 242 (1996) 85-89.

[3] H. Fueß, M. Ghafari, A. Hohl, B. Stahl, T. Wieder, and M. Winterer, Nahordnung in $Fe_{100-x}Sc_x$ aus EXAFS-Spektren, Zeitschrift für Kristallographie Supplement 17 (1999) 104

[4] M. Winterer, XAFS - A Data Analysis Program for Materials Science, Journal de Physique IV France 7 (1997) Issue C2, 243-244.

[5] S. I. Zabinsky, J. J. Rehr, A. Ankudinov, R. C. Albers, and M. J. Eller, Multiple-scattering calculations of x-ray absorption spectra, Physical Review B 52 (1995) 2995-3009.

[6] L. Tröger, D. Arvanitis, K. Baberschke, H. Michaelis, U. Grimm, and E. Zschech, Full correction of the self-absorption in soft-fluorescence extended x-ray-absorption fine structure, Physical Review B 46 (1992) 3283-3289.

[7] M. Katsikini, E. C. Paloura, M. Fieber-Erdmann, J. Kalomiros, T. D. Moustakas, H. Amano, and I. Akasaki, N K-edge x-ray-absorption study of heteroepitaxial GaN films, Physical Review B 56 (1997) 13380-13386.

Chemical Analysis of Electrochemically Modified Semiconductor Surfaces by Synchrotron Induced Photoelectron Spectroscopy

Th. Mayer, M. Beerbom, J. Ell, D. Ensling, R. Hunger, A. Thißen, W. Jaegermann
Department of Materials Science, Darmstadt University of Technology,

Wet chemical processes are widely applied in semiconductor device production because unique properties of surfaces and interfaces may be reached and costs are low as compared to vacuum processing. A detailed characterization of the chemical composition of surfaces after electrochemical treatment with modern UHV surface science techniques is hindered by the pressure gap and contaminations when electrodes are emersed from the electrolyte and transferred into the UHV analysis chamber. Therefore, we have directly attached an electrochemical cell to a UHV system, allowing for wet chemical processing under clean inert gas atmosphere and transfer into UHV without exposure to ambient air. A drop of the solution is deposited on top of the sample surface and, in the case of electrochemical preparation, the counter and reference electrodes are immersed into the drop. After preparation the liquid is blown off by a jet of N_2 gas and the sample is transferred to a buffer chamber which is rapidly pumped down.
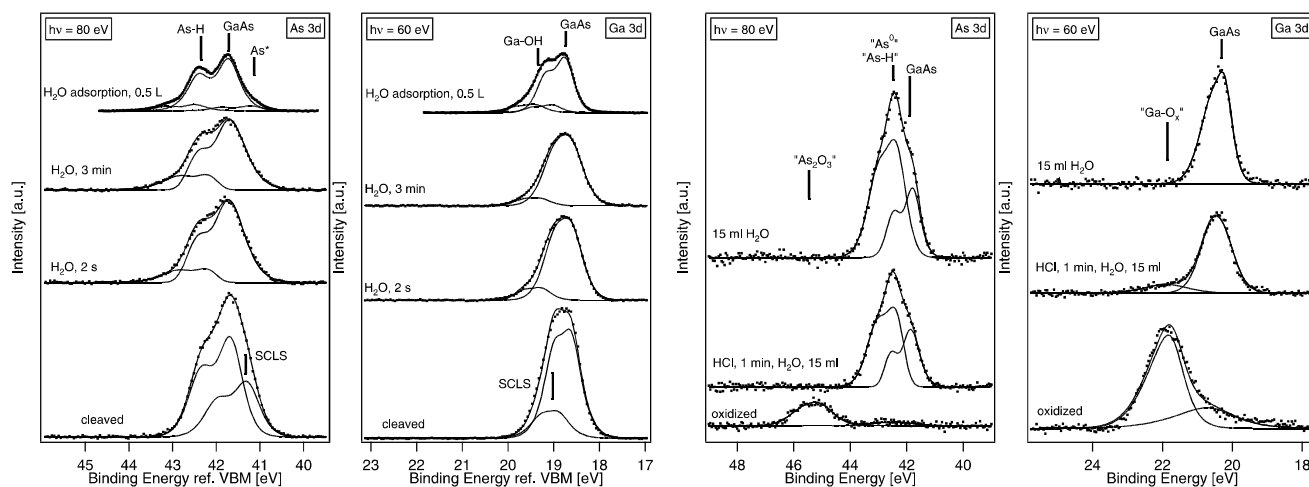

Fig.1. GaAs (110) cleaved, emersed from water after 2s and after additional 3min compared to H_2O adsorption at 100K. As 3d and Ga 3d core level lines are displayed.

Fig.2. Etching of an oxidized GaAs (110) surface with aqueous HCl (3%). After rinsing with water an elementary As layer with a thickness of about 2 atomic layers is left on the surface.

Synchrotron spectra obtained with this system on wet processed samples are of comparable quality as spectra taken after all vacuum processing as demonstrated for GaAs/H_2O interaction displayed in fig.1. Here As and Ga core emissions of the UHV cleaved GaAs (110) surface, this surface emersed from deionized H_2O after 2s and after additional 3min are compared to spectra taken on a different sample after adsorption of

0.5L H_2O at 100K [1]. The surface sensitivity reached is indicated by the intensity ratio of the single layer surface emission (SCLS) to the bulk emission of the freshly cleaved sample. Despite the great discrepancy in preparation conditions, both processes give similar results namely dissociative adsorption of H_2O creating a layer of As-H and Ga-OH surface molecules.
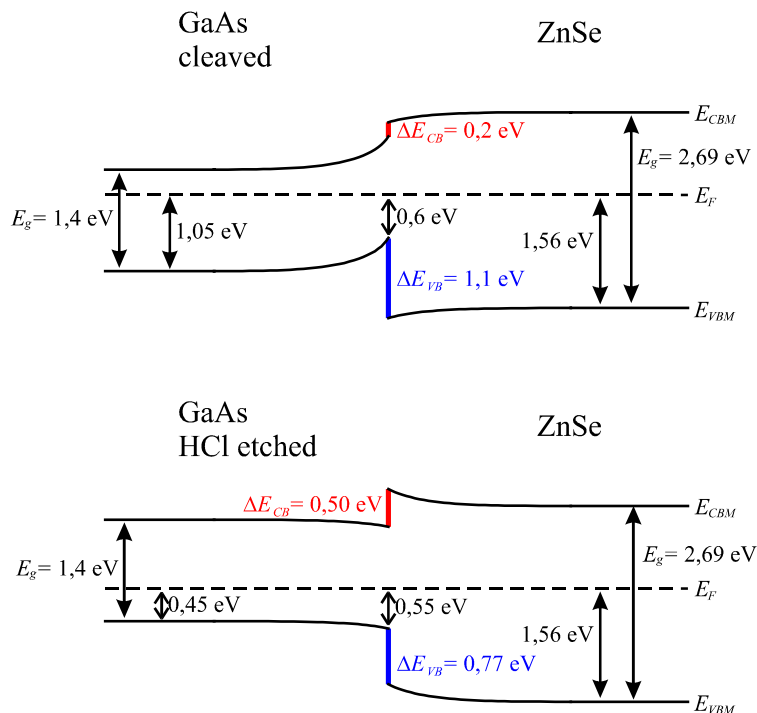

Fig.3. GaAs / ZnSe band alignment for cleaved GaAs (110) and the HCl-etched substrate. The valence band offset is decreases by 300 meV after the electrochemical processing step.

Wet chemical surface modifications may find applications e.g. in engineering band alignments of heterojunctions. Interfaces of II-VI and III-V materials have to be optimized for optoelectronic integration. As an example we compare the band alignment of lattice matched ZnSe on GaAs (110) as obtained by XPS for CVD layers of ZnSe on cleaved and on etched GaAs samples. From the spectra displayed in Fig. 2 the chemical composition of a HCl etched sample is determined to be elementary As and some leftover Ga-oxide, which is rinsed of by deionized water. After the electrochemical processing the sample is covered with about 2 atomic layers of elementary As. As compared to the cleaved sample the valence band offset is reduced by 300 meV due to the As interlayer. The course of the bands for a cleaved n-doped and an etched p doped sample is depicted in Fig.3.

Examples of technically relevant processes analyzed with this system so far are: Te back contact formation of CdTe solar cells by preferential etching of Cd, Schottky contact formation by pulse plating of Pt on GaAs wavers and electrochemical oxidation and reduction of different GaAs surfaces. The work on interface modification of III-V/II-VI heterostructures will be continued in the near future.

[1]   M. Beerbom, O. Henrion, A. Klein, Th. Mayer, W. Jaegermann;
       Electrochimica Acta 45, (2000), 4663

Ferrimagnetic spin order in O/Gd surface monoxide

O. Krupin, F. Heigl, J.E. Prieto, G. Kaindl, and K. Starke

Oxygen adsorption on Gd(0001) leads to the formation of an epitaxial O(1x1)/Gd-surface monoxide. Similar to the Gd metal surface, the surface-monoxide 5d-valence bands reveal a temperature dependent exchange splitting, which changes Stoner-like below the Gd-bulk Curie temperature [1]. While this temperature dependence of the valence bands indicates the existance of long-range order of the localized 4f-spins in the topmost oxide layer, neither the 4f-spin structure within this layer nor the coupling strengths are known.

We have studied the O(1x1)/Gd(0001) monoxide surface employing magnetic dichroism in core-level photoemission (MDPE) [2] at the Gd-4f level. To this end we used circularly polarized (at UE56/2-PGM2) as well as linearly polarized radiation (at U49/1-SGM). Standard 10 nm thick Gd(0001) films were prepared on W(110) by metal-vapor deposition in UHV [2]. For fabrication of the surface monoxide we followed the recipe given in [1], controlled in situ by PE and LEED. Samples were magnetized in the film plane along the b direction of the Gd hcp lattice, using a 0.2-Tesla electromagnet inside the chamber.
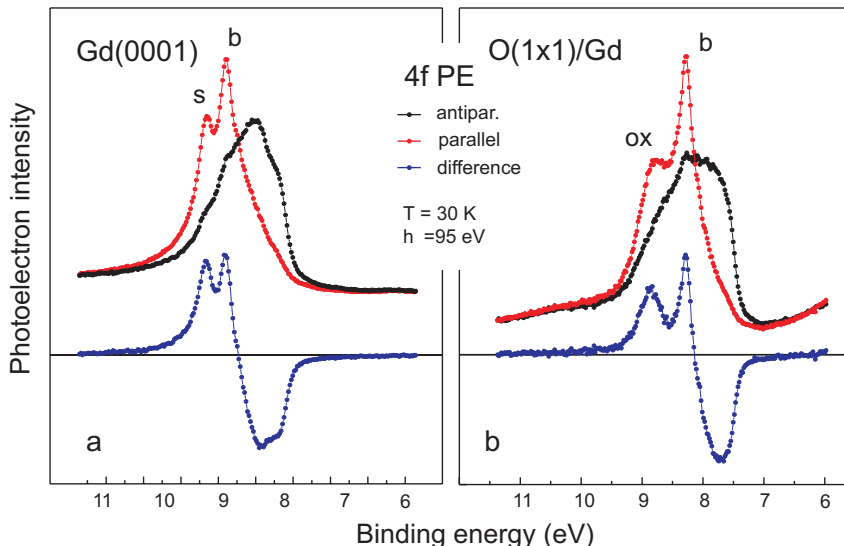

Figure 1: 4f-PE spectra from in-plane magnetized Gd samples excited with circularly polarized light for nearly parallel (red) and antiparallel orientation (black) of sample magnetization and photon spin. (**a**) Gd(0001) metal surface with surface (*s*) and bulk (*b*) line. (**b**) O(1x1)/Gd(0001) (*ox*: surface monoxide line). The intensity of the difference spectrum underneath (blue) is roughly proportional to the sample magnetization.

The clearly shifted Gd-4f photoemission (PE) line at the metal surface (0.3 eV with respect to the bulk line, see Fig. 1a) becomes separated by 0.5 eV from the bulk line (Fig. 1b) upon formation of the surface monoxide. This chemical shift allows one to monitor the oxidation process and to spectroscopically seperate surface and bulk layers in both cases. Upon reversal of the sample magnetization from nearly parallel to antiparallel with respect to the photon spin (light propagation axis) the relative intensities of the Gd-4f ^7F line components clearly change. Without further analysis the difference spectra ('dichroic' spectra, Fig. 1, bottom) reveal a non-vanishing net magnetization within the topmost atomic layer not only the metal surface (a) but also of the oxide surface (b).

For a quantitative spectral analysis we applied a *simultaneous* least-squares fit procedure of the dichroic spectra; the result is shown in Fig. 2. Each of the Gd-4f ^7F photoemission lines for the surface and sub-surface ('bulk') layers comprises seven spin-orbit components that cannot be resolved, owing to their lifetime width; yet their relative component intensities are well known [2,3]. Unlike magnetic dichroism in absorption, MDPE spectra in angle-resolved PE contain higher order components (which are not proportional to the sample magnetization) [3]; they have been included in the fit analysis.
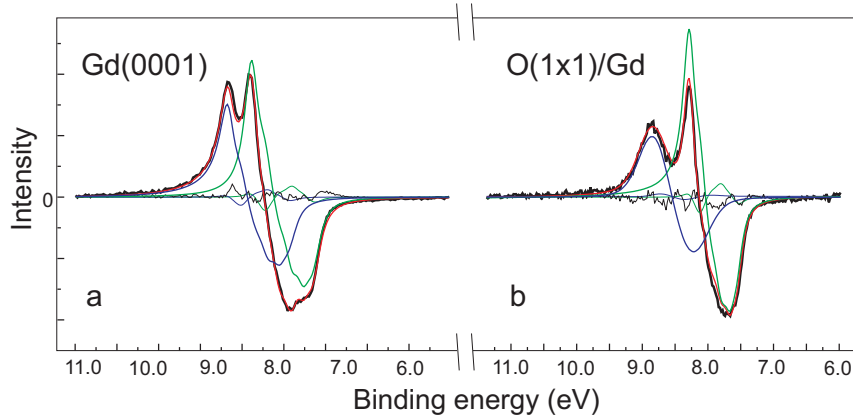
Figure 2: Least-squares fit analysis of the difference 4f-PE spectra (from Fig. 1): (**a**) metal surface and (**b**) O(1x1)/Gd(0001) monoxide. Experimental data (black curves); fit (red curves); residuum (noisy black curve). First order components, proportional to the magnetization: bulk (green), surface (blue). Thin curves of the same colors represent small higher order contributions to the PE line intensity.

A detailed comparison of metal and oxide surface [4] reveals that the in-plane magnetization component of the monoxide surface layer is reduced by a factor of two. – This experimental finding is presently compared with Monte-Carlo model calculations of the layer-dependent spin structure, in order to quantify the effective exchange-coupling constants acting within and between the Gd-monoxide layer and the ferromagnetic Gd-metal sub-surface layers.

[1] C. Schüssler-Langeheine *et.al.* Phys.Rev. B **60**, 3449 (1999)
[2] K. Starke, *Magnetic Dichroism in Core-Level Photoemission* (Springer, Berlin, Heidelberg, 2000)
[3] B.T. Thole and G. van der Laan, Phys.Rev. B **49**, 9613 (1994)
[4] O. Krupin, F. Heigl, J.E. Prieto, G. Kaindl, and K. Starke (to be published)

Photoemission study of Aluminium Steel cold welded joints

D.R. Batchelor [1], P. Hoffman [2] and D. Schmeißer [2]

[1] BESSY GmbH, Albert-Einstein-Str. 15, D-12489 Berlin, Germany
[2] LS Angewandte Physik- Sensorik, BTU Cottbus, 03044 Cottbus, Germany

Introduction

Aluminium and Stainless Steel bi-metal material is extremely versatile and is used in a wide range of products; from cooking utensils to high technology applications such as automobile manufacture and Synchrotron radiation instrumentation. As a consequence of this wide range of applications the study of the formation of Aluminium Steel junctions and the bonding mechanism is of considerable industrial importance [1-3].

In a previous publication [4] evidence for a chemical bond, alloying at the interface was found. As the monochromator focus and welded region are similar in size ≈200μm (the actual interface from SEM is an order of magnitude smaller) a simple photoemission experiment of translating the sample perpendicular (vertically, weld horizontal) to the weld and measuring spectra was performed.

Experiment and Results

Three samples were investigated. After Argon ion sputtering spectra were taken from ±2mm either side of the interface and at the interface. The interface position was judged by moving the sample until half the bulk Aluminium or Iron signal was observed. Two photon energies were used 186eV and 570eV to exploit surface sensitivity. To reduce the oxide contamination the sample was sputtered between taking data at the different photon energies.

Figure 1. shows the results for Aluminium 2p photoemission. The red and blue curves are spectra from the Iron and Aluminium sides of the weld respectively. The interface region is depicted as green. The high photon energy spectra from the interface region shows a better resolved 2p

doublet which is shifted by 100mev. This together with the attenuation length of the electrons at this energy, ≈1.4nm, clearly indicates that the Aluminium is chemically different at the interface and the difference extends over the volume of the beam (SEM shows that the interface is ≈20μm wide).
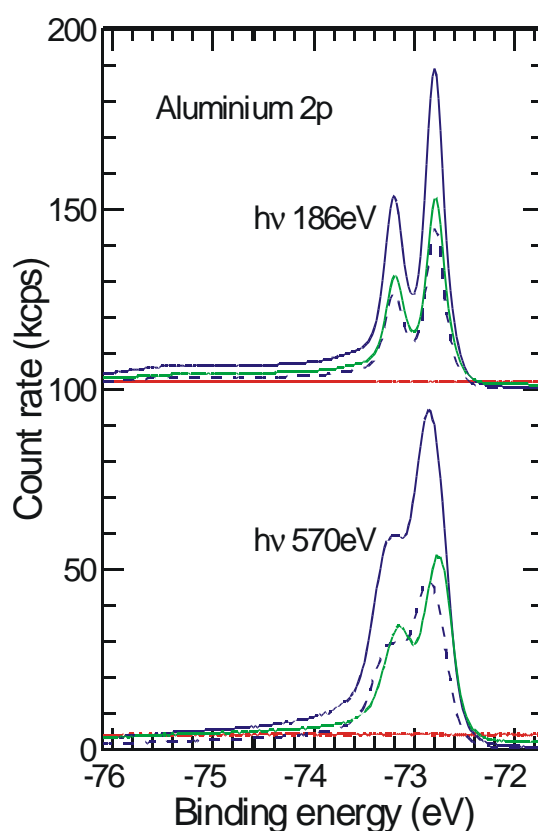
Figure 1. Aluminium 2p Photoemission spectra for the two photon energies 186eV and 570eV. The red and blue curves are from the iron and aluminium sides respectively. The green curve is from the interface region. The dashed lines are spectra from the aluminium side scaled by 50%. The 186eV photon energy spectra have been displaced by a factor 100kcps.

The shift of the spectra is approximately that seen for surface core level shifted Aluminium. The low photon energy spectra

show the doublet clearly resolved but with a much smaller shift ≈40meV between the aluminium side and interface. This discrepancy is perhaps explained by surface sensitivity and or differences at the surface. The small oxide peak visible in the spectrum is estimated as ≈0.8ML (λ≈0.6nm). The difference in the resolution of the 2p doublet at the two photon energies is not entirely due to monochromator resolution but material related; the resolution for the high photon energy and slit was ≈3000.
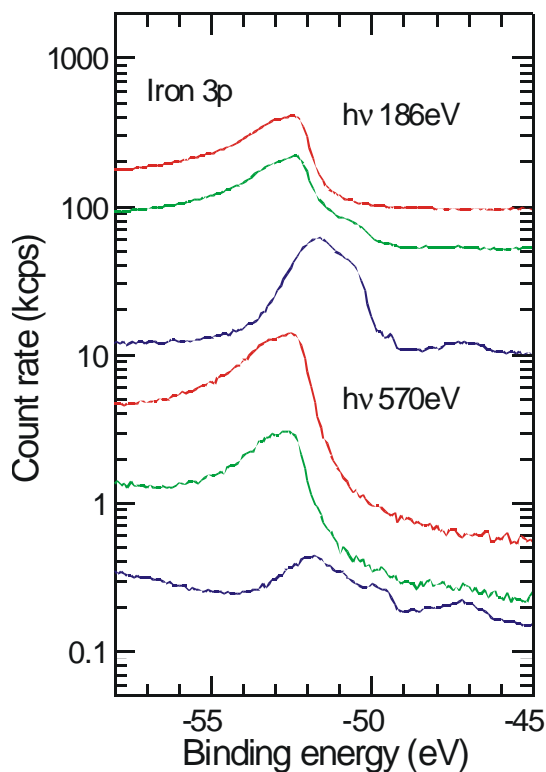
Figure 2. Iron 3p Photoemission spectra for the two photon energies 186eV and 570eV. The red and blue curves are from the iron and aluminium sides respectively. The green curve is from the interface region. The 186eV spectra have been scaled by a factor of 50.

The results for the Iron 3p spectra are shown in the logarithmic plot Figure 2. Here the Iron 3p contribution is clearly visible in spectra taken from the Aluminium side but it is more complicated than the broad asymmetric peak taken from the Iron side. The main peak is shifted by 0.8eV and has shoulders at 1.0 and 2.0 eV. There is also an additional peak at a binding en-

ergy of 47eV which is perhaps manganese which should be present in the steel <0.1% however it is not visible on the Iron side and the binding energy is too low. The above spectra may be due to a sputtering effect but this is thought to be unlikely.

Summary

The results show that changes in the photoemission are visible from a cold welded junction over a region of 100μm. Calculations as to the origin of the shifts and in particular the form of the Iron 3p peak are being pursued.

References

1. Miller M.A. and Oyler G.W., Welding Journal,30(1951)486
2. Keller D.V.: Wear, 6(1963)353
3. Tylecote R.F., The solid phase welding of metals, Edward Arnold ltd. London 1968
4. I. Hulea, P. Hoffmann, M. Brinza, D.R. Batchelor and D. Schmeisser, Proc. of ASST 2000 pg 251-257

Surface Amorphization of InP

N. Darowski[a], I. Zizak[a], E. Wendler[b], G. Schumacher[a], S. Klaumünzer[a]

[a] *Hahn-Meitner-Institut Berlin, Glienicker Straße 100, D-14109 Berlin, Germany*
[b] *Friedrich-Schiller-Universität, Institut für Festkörperphysik, Max-Wien-Platz 1, D-07743 Jena*

Irradiation of InP induces amorphization when the electronic energy loss exceeds the critical value of about 13 keV/(nm) [1]. A detailed analysis of the damage production at room temperature showed that individual tracks of 340 MeV Xe ions in virgin InP are not completely amorphous. Rather, each volume element needed to be impinged by three or four ions (corresponding to fluences $\Phi t = 10^{14}$ Xe/cm^2) in order to induce complete amorphization in the bulk. However, Rutherford backscattering spectrometry (RBS) and transmission electron microscopy (TEM) analysis revealed the existence of a 35 nm thick almost defect-free surface layer. This finding was ascribed to the migration and relaxation of defects at the free surface [1].

While RBS can hardly distinguish between heavily damaged and amorphous structures, TEM analysis provides detailed structural information, but only of a very small volume. Grazing incidence x-ray diffraction (GID) and x-ray reflectometry are complementary methods to TEM and RBS in providing detailed structural information on a larger sample volume. Additionally, the thickness and interface roughness of surface layers can be determined. This report presents first results from GID and x-ray reflectometry on irradiated InP. The investigations were carried out at room temperature at the 6-axes diffractometer at KMC-2 at BESSY II using a photon energy of 8.048 keV. The specimen was cut from a commercially available InP-wafer and was irradiated at the cyclotron of the ISL/HMI at room temperature with 390 MeV Xe ions up to $\Phi t = 1.4 \times 10^{14}$ Xe/cm^2.

Fig. 1 shows the (220) reflection curves of both the irradiated and unirradiated specimen measured by means of GID. The angle of the incident beam with respect to the sample surface was 0.2° for the unirradiated specimen and 0.4° for the irradiated specimen. From these values information depths of 2 nm and 20 nm, respectively, were estimated. Both curves reveal relatively sharp (220) Bragg peaks. Hence, a layer of some few nm below the surface of the irradiated specimen remained crystalline. Further, the similar

Fig. 1.: (220) reflection curves of both the irradiated and non-irradiated specimen

widths of the Bragg peaks of irradiated and unirradiated specimen suggest a low damage level in the near surface zone of the irradiated specimen in agreement with previous RBS measurements.
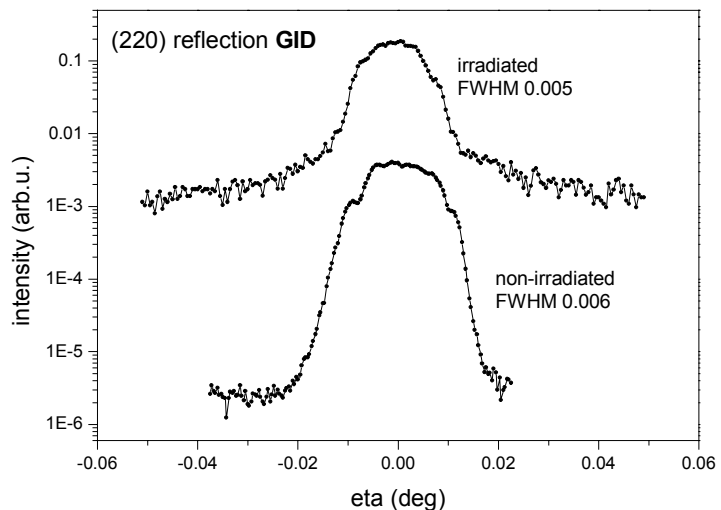
Fig. 2 shows (002) Bragg peaks of the unirradiated and of the irradiated specimen measured by conventional diffraction (XRD). From the Bragg angle of the (002) reflection an information depth of about 1.9 μm can be estimated. The Bragg peak of the unirradiated specimen is fairly sharp. The irradiated specimen reveals a Bragg peak of much lower intensity because most photon scattering takes place in the amorphous zone. The presence of the Bragg peak itself is due to the nearly undamaged surface layer. The width of the peak indicates coherently scattering structures of the order 30 nm. This length matches with the thickness of the crystalline surface layer as determined by RBS [1].
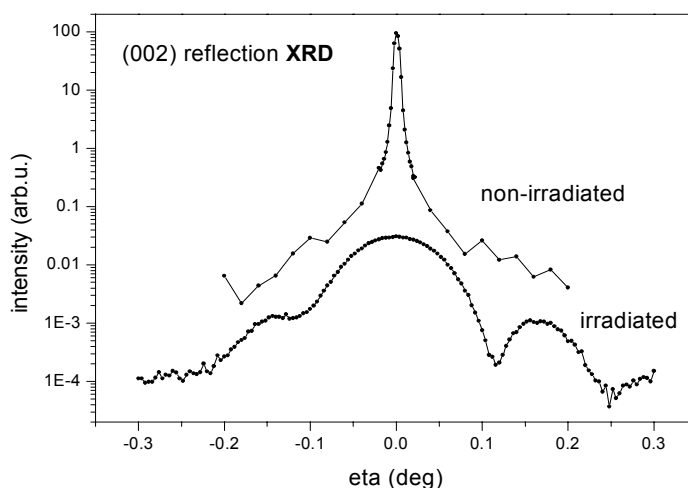
Fig. 2: (002) Bragg peaks of the non-irradiated and of the irradiated specimen measured by XRD.

The curve shown in Fig. 3 has been measured by means of reflectometry. The critical angle for total external reflection α_c was determined to be 0.29° in agreement with the theoretical value. The strong decrease of intensity above α_c as a function of the scattering vector Q_z points to a high roughness of the surface. This result seems to be in disagreement with the findings of Singh and coworkers [2,3]. Further investigations are necessary to clarify this point.
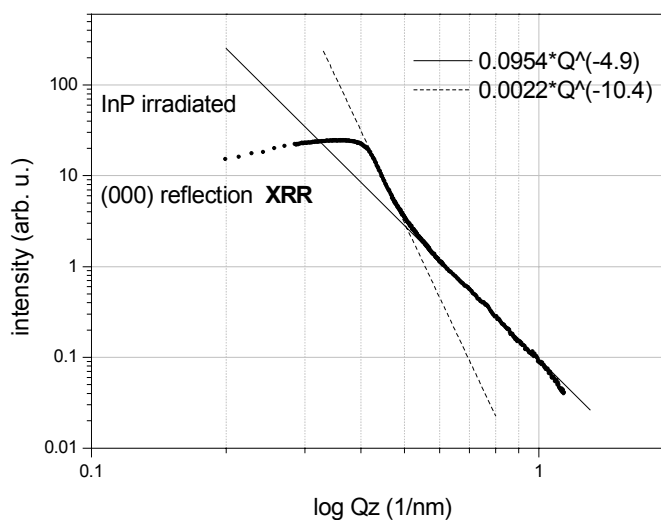

Fig. 3: Intensity of the reflected beam measured by means of reflectometry

References

1. W. Wesch, O. Herre, P.I. Gaiduk, E. Wendler, S. Klaumünzer and P. Meier, Nucl. Instr. & Meth.B146 (1998) 341.
2. J.P. Singh, R. Singh, N.C. Mishra, D. Kanjilal and V. Ganesan, Journal of Applied Physics 90 (2001) 5968.
3. J.P. Singh, R. Singh, N.C. Mishra, V. Ganesan and D. Kanjilal, Nucl. Instr. & Meth.B179 (2001) 37.

Protein crystallography at BESSY II:
Determination of two new protein structures

Timm Maier, Wolfram Saenger, Jacinta Lodge and Norbert Sträter

Institut für Chemie, Abteilung Kristallographie, Freie Universität Berlin, Takustr. 6, 14195 Berlin, Germany

Synchrotron radiation plays an important role in the determination of protein structures by single crystal X–ray crystallography: Firstly, a better resolution and more accurate structures are obtained because of the higher brilliance of the X–ray beam compared to a rotating anode home source. Secondly, the wavelength tunability greatly facilitates structure determination by increasing the anomalous scattering of metal ions, selenium or sulfur atoms.

We have determined two novel protein structures using data collected at the BAMline at BESSY II. In both experiments, the crystallographic phase problem was solved by heavy atom derivatives utilizing the anomalous contribution of metal ions (multiple isomorphous replacement with anomalous scattering – MIRAS). The heavy atoms could be located using Patterson maps and after phase refinement the electron density maps were of good quality so that complete protein models could be built.

A novel thermophilic glucosidase

Many of the industrially important enzymes are used in food processing, in particular in the degradation or processing of starch. For biotechnological applictions, enzymes from thermophilic organisms have the advantage of an increased stability and the possibility to use higher temperatures.

We have analysed the structure of a thermophilic glucosidase, that degrades maltose to glucose. The enzyme retains more than 50 % of its activity after 48 hours at 50°C. Structures of homologous enzymes of this family are currently not known.
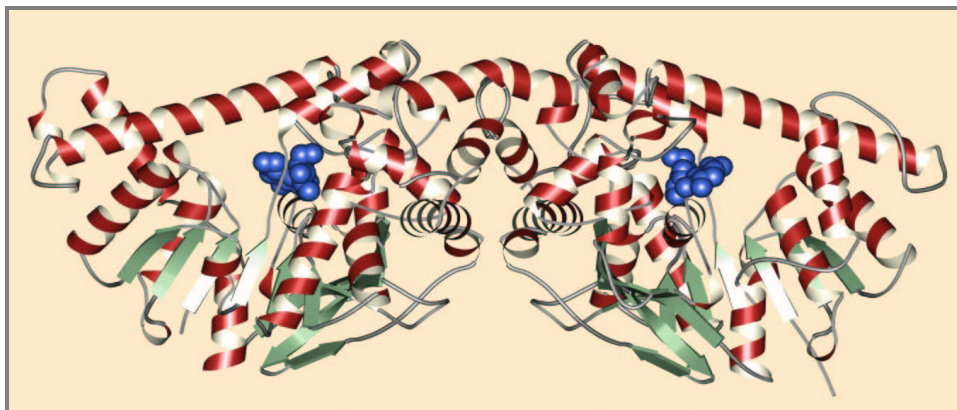
Figure 1

Fold of the dimeric glucosidase. The maltose substrate is shown in blue.

Substrate binding

Cocrystallization of the protein with substrates or substrate analogue inhibitors is a powerful approach to characterize the catalytic mechanism. We have cocrystallized the glucosidase with maltose, a natural substrate of the enzyme. The substrate is not turned over, because the enzyme needs to be reduced for activation. Figure 2 shows the electron density map of the active site with a bound maltose molecule.
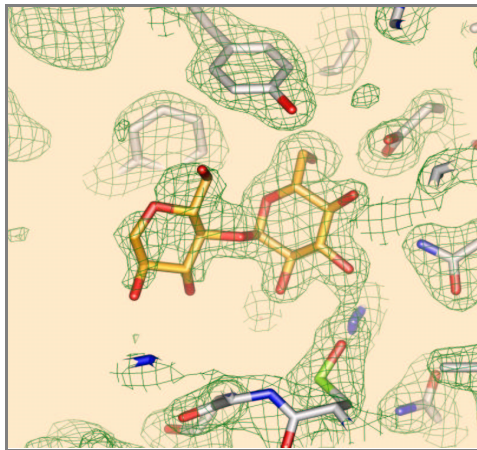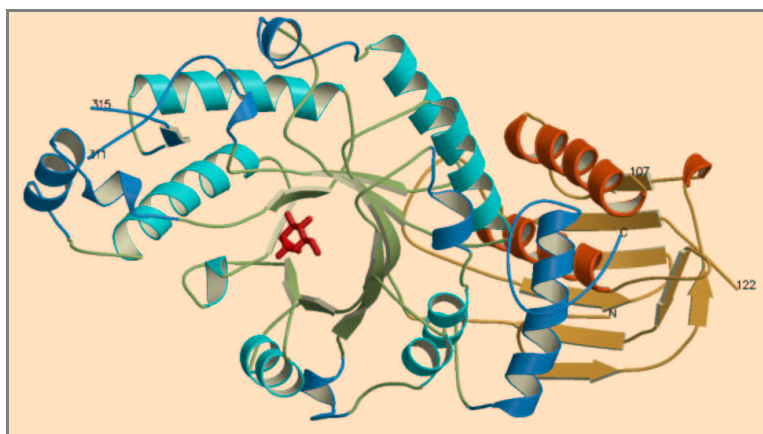

Figure 2

Electron density map ("chicken wire" representation in green) of a maltose molecule (yellow carbon atoms) bound to the catalytic site of the glucosidase.

A human lysosomal hydrolase

Lysosomes are the degradative compartment of animal cells. These acidic organelles contain a battery of specific and non–specific hydrolases to decompose all kinds of cell constituents and material uptaken by the cell, e.g proteins, lipids, nucleic acids. Genetic defects in lysosomal enzymes often results in severe diseases caused by the accumulation of non–degraded substances. The structure of a lysosomal hydrolase presented here will aid in the understanding of a fatal inborn error of metabolism and might help to develop strategies to prevent the outbreak of the disease in affected children.
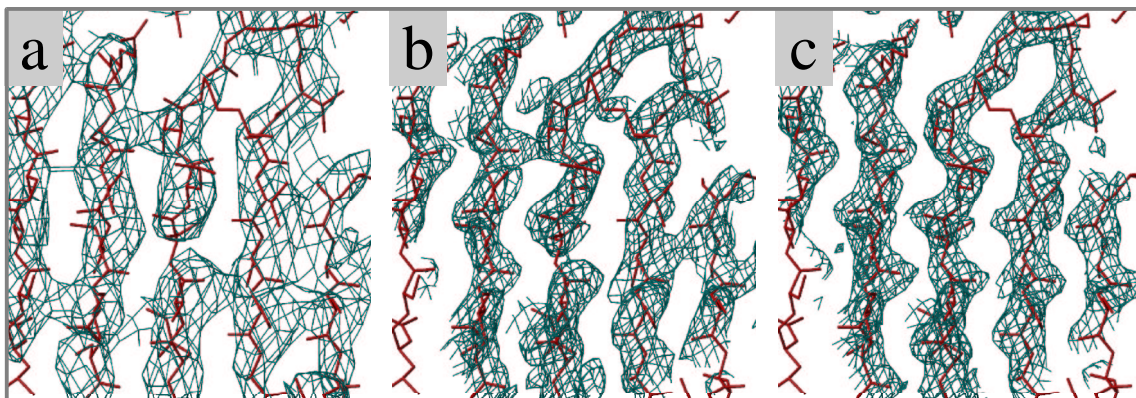

Figure 3

Cartoon representation of one monomer of the lysosomal hydrolase. A bound inhibitor molecule is shown in red.

Phase determination

Both crystal structures were determined by the MIRAS method, utilizing the isomorphous differences as well as the anomalous scattering of heavy metal ions. For each of the two proteins we collected data sets on 5 derivatives containing Pt, Hg, Pb, Ta, Br or Xe. All data have been collected at a wavelength of 0.9 Å. The heavy atom positions were located from Patterson maps. For the glucosidase 4 derivatives and for the lysosomal hydrolase 2 derivatives were used for phasing. The phases were improved and extended to the resolution of the native data set by solvent flattening and non–crystallographic symmetry averaging.

Binding of the heavy atom derivatives (approx. 5 mM in the drop) was not checked before the synchrotron experiment in this case. Considering the fact that data collection becomes increasingly faster at synchrotron sources and semi–automatic location of heavy atom binding sites is facilitated by modern crystallographic software, the conventional MIR or MIRAS approach might turn out to be an alternative powerful approach compared to phasing procedures using the anomalous contribution of proteins labeled with selenomethionine, if one considers the time to prepare and crystallize Se–Met protein. The anomalous signal from sulfur, however, could have been helpful to facilitate the positioning of the amino acid sequence into the electron density map.

Figure 4
Electron density maps of the lysosomal hydrolase , (a) experimental map at 4Å , (b) map after phase extension and density modification at 2.3Å, (c) 2fo–fc map at 2.3Å resolution

Vacuum Pressure Estimates for the SESAME RF Section

D. Richter

1. Introduction

The pressure distribution of the SESAME rf cavity section was calculated to obtain a better understanding of the influence of gas sources and the pumping speed of vacuum pumps. Transforming the vacuum system into an electrical network, the conductance of vacuum components and the pumping speed are equivalent to the inverse of a resistor. The gas flow corresponds to constant current sources. While the voltages at every node give directly the pressure distribution. Thus the cavity section with its components was modelled to the following network (fig. 1).
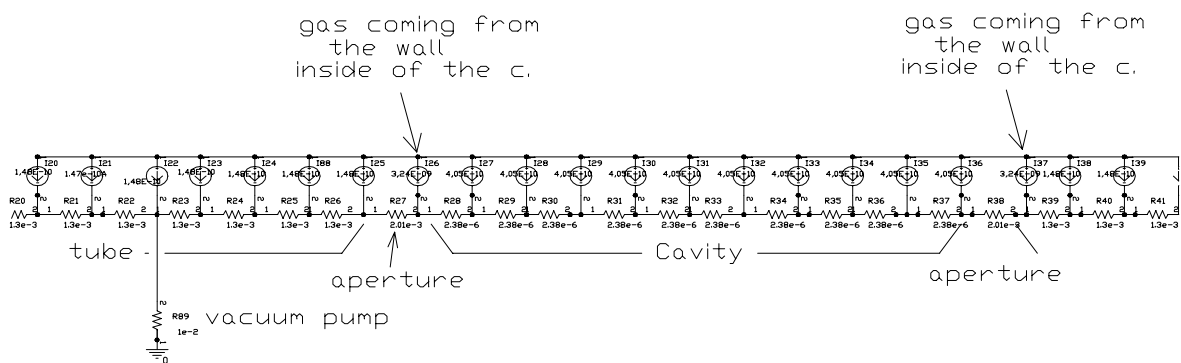
Fig. 1: Section part of electrical network describing ¼ of rf section

2. The pressure distribution

Assuming a constant degassing rate of $1 \cdot 10^{-12}$ mbar for all chamber walls,

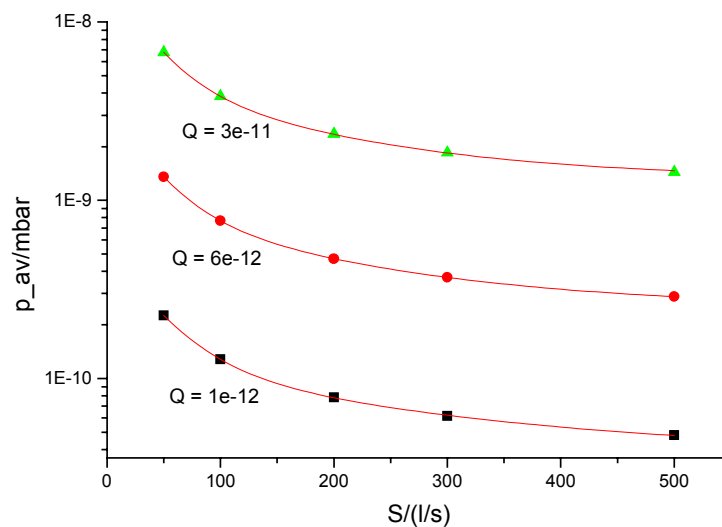Fig. 2: Average pressure p_av vs. effective pumping speed S for different degassing rates Q in (mbar·l)/(s·cm²)

the resulting average pressure as function of the pumping speed is plotted in fig. 2. A degassing rate of $1 \cdot 10^{-12}$ mbar l/(s cm²) is reasonable for cavities, therefore a basis pressure in the range of some 10^{-10} mbar can be expected.

Calculation in presence of a beam and realistic rf conditions were made also. The degassing rate of the tubes was assumed to be $5 \cdot 10^{-12}$ mbar l/(s cm²) [1] while for the chamber walls inside the cavities was assumed a value of $3 \cdot 10^{-11}$ mbar l/(s cm²) [2]. The nominal pumping speed was taken as 500 l/s. Figure 3 shows the pressure distribution and the average pressure which turned out to $2 \cdot 10^{-9}$ mbar. As it is unrealistic to assume a lower degassing rate of the connection tubes, it will be necessary to reduce to $1 \cdot 10^{-11}$ mbar l/(s cm²) the degassing rates inside the cavities to meet the required average pressure of $1 \cdot 10^{-9}$ mbar at the SESAME rf section.
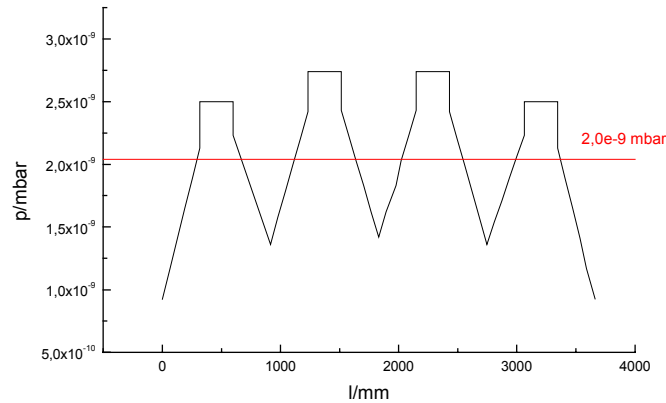

Fig. 3: Pressure distribution under realistic conditions

References

[1]: D. Richter, Technical report Nr. 219/00, BESSY
[2]: E. Weihreter, private conversation, BESSY

The First Synthetic X-Ray Hologram: Results.

A.A. Firsov[a,b], A.A. Svintsov[b], S.I. Zaitsev[b], A. Erko[a], V.V. Aristov[b]

[a] BESSY, Berliner Elektronenspeicherring-Gesellschaft für Synchrotronstrahlung mbH, Albert-Einstein-Str. 15, D-12489, Berlin, Germany.

[b] Institute of Microelectronics Technology RAS, Chernogolovka, Moscow distr., 142432, Russia.

In 1948 the Nobel Prize Laureate Denis Gabor proposed his famous "method of wave-front reconstruction" which opened the era of holography [1]. In the 1960's with the development of optical lasers, E. N. Leith and J. Upatnieks demonstrated the first wave-front reconstruction by a hologram with a reference beam [2]. Since this first successful hologram demonstration the method of holographic reconstruction has found applications in many different fields of art, science and technology. The possibility of crating holograms in the x-ray range has been also discussed in a number of works [3]. However, such holograms have neither been fabricated nor tested until now except the case of simple holograms, focusing zone plates. Due to the absence of sensitive and high-resolution materials for x-ray holography, it seems to be more effective to use x-rays only in the reconstruction stage to produce images with micron resolution. A so-called "synthetic hologram" [4] can be generated by computer and transferred into material using modern methods of microelectronics technology [5]. The topic has become even more important with the construction of x-ray lasers in Germany and the USA. The word
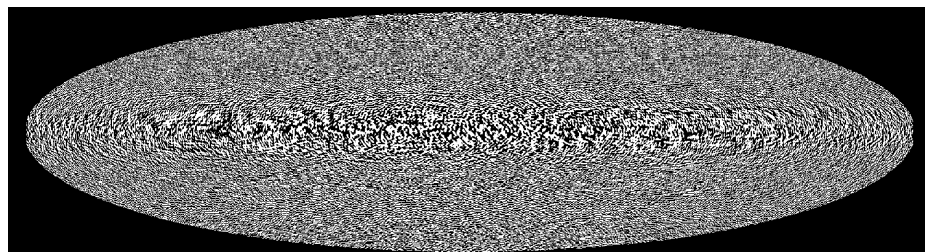

Figure 1. The test-object.   Figure 2. Fabricated synthetic hologram structure.

"X - RAY" composed of δ-function pixels has been chosen as the object (Figure. 1). For the hologram fabrication we employ the principle employed in the generation of Bragg-Fresnel optical elements: a combination of Bragg diffraction on a single crystal and Fresnel focusing on a surface profile [6]. The synthetic hologram has been designed as a phase shift mask placed on a polished surface of a Si (111) crystal. An initial hologram structure on the resist was fabricated by electron-beam lithography in the JSM-840 microscope controlled by the "Proxy for Windows" program package. After the development of the resist, a Ni layer was deposited, followed by the

lift-off procedure. The thickness of the Ni layer was 340 nm, calculated to produce a π phase-shift at the energy of 8 keV and Bragg incidence angle of 14.2°. Thus, the hologram is a phase-shifting layer of a Ni film on a silicon substrate simultaneously serving both as a Bragg mirror and as monochromator for the incident radiation (Figure 2). The design parameters of the hologram are the following: photon energy 8 keV (λ = 0.155 nm), aperture 270 microns, minimum period of interference fringes 0.6 μm, hologram-image distance 500 mm. The synthetic hologram is fabricated assuming an ideal

Figure 3. The image reconstructed from the synthetic hologram.

coherent source. The only limitation on spatial resolution is the minimum structure period of the e-beam writing process. The resolution of a synthetic hologram reconstruction is similar to the resolution of an x-ray Fresnel zone plate in partially coherent illumination. Each point of the source reconstructs the whole hologram image with a resolution defined by the size of the emitting source area. The reconstructed image was recorded on a high-resolution x-ray film and enlarged using an optical microscope. The result of the reconstruction is shown in Figure 3. At the distance of 500 mm from the hologram we have obtained an image "X-RAY". The image resolution was estimated to be on the order of 2.4 μm using micro-densitometery of the image edges. The estimated theoretical resolution is still better than the measured value. The loss of resolution could be explained by error in alignment, by film resolution or by inaccuracy of technological steps in reproducing of the smallest details of the hologram.

References.

1. D. Gabor, *Nature*, 161, (1948), 777.

2. E.N.Leith, J.Upatnieks.. *J.Opt.Soc.Am.,* 54, 11, (1964), 1295.

3. A.I.Erko V.V.Aristov, B.Vidal, *Diffraction X-Ray Optics*, IOP Publishing Bristol 1996)

4. A.W. Lohmann, D.P. Paris, *Appl. Opt.*, 6, (1967), 1739.

5. C. Jacobsen M. Howells, *Journal Vacuum Science and Technology* B10, (1992), 3177.

6. A. Erko, Yu. Agafonov, L.A. Panchenko, A. Yuakshin, P. Chevallier, P. Dhez, F. Legrand, *Optics Communications*, 106, (1994), 146

Spatially resolved synchrotron-X-ray fluorescence analysis

Max Wilke, *Institut für Geowissenschaften, Universität Potsdam, 14415 Potsdam, Germany*
Robert Lauter, Jörg Grenzer, Ulrich Pietsch, *Institut für Physik, Universität Potsdam, 14415 Potsdam, Germany*

In Earth Sciences trace elements concentrations are used for understanding geological processes, such as genesis and development of the earth's crust including the magmatic processes involved.

Due to the high photon flux at synchrotron facilities, synchrotron-XRF measurements provide the possibility of determining the trace-element concentrations by using the intensity of the X-ray fluorescence emission lines (K- and L-lines). Since the incoming beam can be collimated down to a small spot size measurements of concentrations with spatial resolution are possible. Thus, enabling the determination of distributions of elements among different phases within a sample or the determination of concentration profiles within one phase.

Test measurements at beam line D-13-2 using a energy-dispersive detector (Si(Li)) were performed to test which elements are detectable at trace element level using the energy spectrum of BESSY II. In first experiments, the incoming beam was collimated using the available cross slits. In a second set of measurements a pin hole was used for collimation. Samples used for the test runs were a rhyolitic glass standard (ATHO-G, Jochum et al. 2000), a monazite (Ce-phosphate) and a synthetic andesite glass that was doped with a suite of trace elements (Koepke & Behrens 2001).

Shown in Fig. 1a are spectra of the glass standard acquired with a beam size of 50 x 50 μm^2 and various sampling time. This graph indicates, that K-lines of elements with atomic numbers from 19 – 41 can be detected. The reference concentration levels are: K: 2.22 wt%, Ca: 1.19 wt%, Ti: 0.147 wt%, Mn: 798 ppm, Fe: 2.5 wt%, Cu: 21 ppm, Zn: 139 ppm, Rb: 63 ppm, Sr: 96 ppm, Y: 94, Nb: 62, Zr: 524 ppm.

If no overlap with K-lines of major elements occurs L-lines of elements with atomic numbers greater than 47 can also be detected. Measurements on monazite would be a suitable example. Monazite mainly fractionates light rare-earth elements as well as U and Th. Values of U, Th and Pb may be used for age determination. The spectrum is shown in Fig. 1b. Element oxide concentrations for monazite are in the range of 2 (Sm) to 30 (Ce) wt% for the rare-earth elements, 4 – 6 wt% for Th, 0.5 – 2 wt% U and 0.3 –0.5 wt% Pb.

For higher spatial resolution pinholes were tested for collimation of the incoming beam. The graph in Fig. 2 shows a comparison for measurements on a synthetic glass using either cross slits or a pinhole of 50 μm in diameter. The glass was doped with trace elements at a concentration level of 300 ppm (all elements shown except Ca; Ca: 7.6 wt%). A severe drop in the measured count rate is observed when using the pinhole. If this observed drop is really related to the decreased beam size cannot be ruled out. A potential possibility for a too low

flux is the proper alignment of the pinhole, which could not be optimized during the experiment.
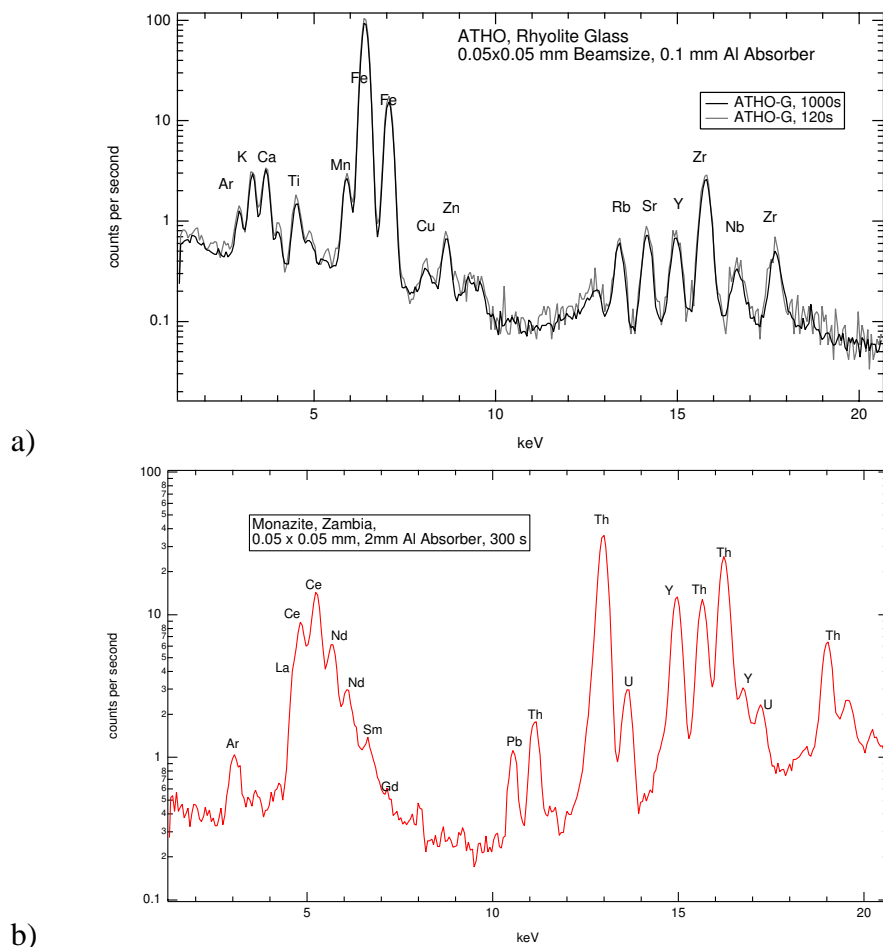

a)

b)

Fig. 1: XRF spectra acquired with a beam collimated by cross slits.
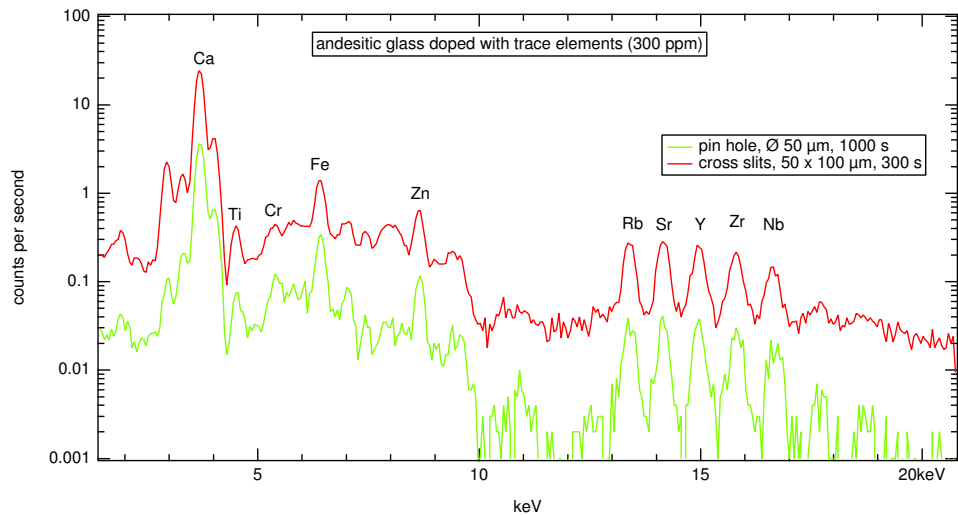

Fig. 2: Comparison of XRF-spectra acquired using cross slits or pinhole.

References:

Jochum KP et al. (2000) Geostandards Newsletter, 24, 87-133

Koepke J & Behrens H (2001) Geochimica et Cosmochimica Acta, 65, 1481-1498

Focus IS-PEEM investigations at U49/II: experimental determination of a magnification function, the contrast mechanism and the spectral resolution

B. Jäckel[1], A. Thißen[1], R. Hunger[1], A. Klein[1], W. Jaegermann[1], P. Hoffmann[2], D. Schmeißer[2]

[1]*TU Darmstadt, FB Materialwissenschaft, FG Oberflächenforschung, D-64287 Darmstadt*
[2]*BTU Cottbus, Lehrstuhl Angewandte Physik-Sensorik, D–03013 Cottbus*

Microspectroscopy as carried out with a photoemission electron microscope (PEEM) bears the chance to relate laterally resolved spectroscopic information (element distribution, electronic structure, surface potentials) directly to microscopic images of the sample surface. Therefore PEEM is a powerful tool for the investigation of lateral inhomogeneous samples like polycrystalline thin film materials, as used, for example, for thin film solar cells. The use of synchrotron radiation as a light source in a PEEM experiment is crucial, not only for its tunability, but also for the high brilliance making small area detection of photoelectrons with reasonable count rates possible. Although the PEEM used in this study is a commercial design (Focus IS-PEEM), experimental performance data are still not completely reported. Therefore the aim of this work has been to determine the magnification in dependence of the PEEM parameters (=electrostatic voltages at the extractor, focus, column and the projective lenses). Also the relationship between contrast and the spectral distribution of the photoelectrons must be clarified for the interpretation of data obtained at real sample surfaces.

For the magnification calibration a defined test sample of Au squares (5x5µm^2) on a Si(111) surface has been formed by electron beam lithography and subsequent PVD. For the determination of the magnification function no further surface cleaning has been done to avoid damage of the structures. In Fig.1 the dependence of the image size ($\varnothing$-PEEM-screen) on the voltages at the projective lenses P1 and P2 is presented. The PEEM images have been taken using the polychromatic radiation of a deuterium lamp. The image size has been fitted as a function of all five PEEM parameters. The given 3-dim function $\varnothing$-PEEM-screen=f(P1, P2) is the projection of the general magnification function into the P1/P2-plane. This function is a good approximation of the experimental data and also fits well to theoretical ray-tracing calculations done by Focus.
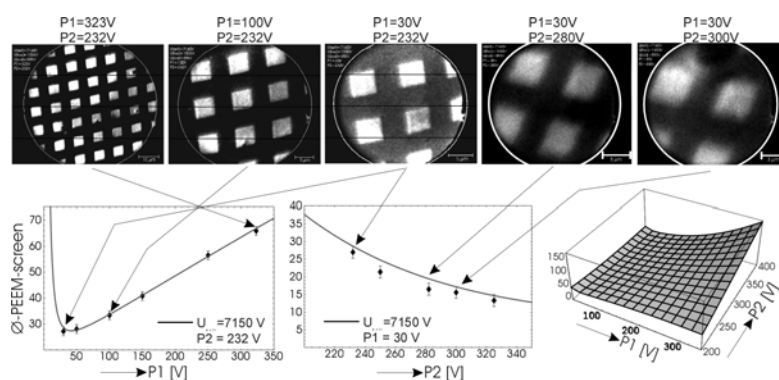

Fig.1.: Determination of a magnification function using a micro-structured Au/Si(111) sample.

For the investigation of the contrast mechanism in the PEEM experiment, the surface of the Au/Si(111) test sample has been cleaned by slight Ar$^+$-ion-bombardment. No obvious damages in the surface structure appeared due the cleaning. The PEEM images for different photon energies (Hg-Lamp: 4.9eV, synchrotron: 84, 100, 120, 150, 190, 250 and 490eV) are given in Fig.2. The contrast clearly depends on the photon energy. For 4.9eV Au is dark and Si is bright. For energies higher than about 15 eV (21.22eV (=HeI, not shown here), 84eV and 100eV) the contrast is reversed. For 120-190eV Au is dark and Si is bright again. And for photon energies above 200eV Au stays bright and Si dark. This contrast changes for different energies can be explained in terms of the total atomic photoionization cross section, as given for example in the atomic calculations of Yeh and Lindau (Fig.2). From that result it is clear, that the contrast observed in the PEEM experi

ment reflects the total photoelectron yield, as long as the sample is reasonable flat, and the electronic contrast is not obscured by the topographic contrast. For such samples the contrast of surfaces of known element distribution can be predicted and thus an chemical identification of surface structures in the PEEM images (µ-XAS) is possible.

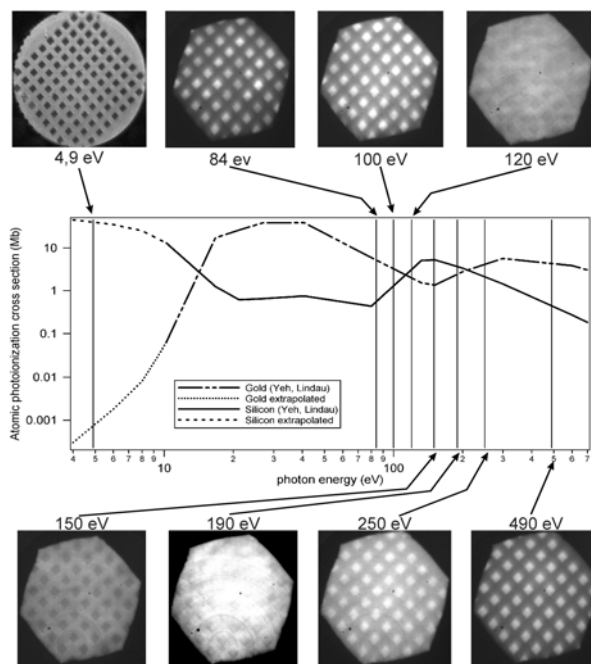Fig.2.: PEEM-contrast and photoionization cross section (after Yeh and Lindau) versus photon energy.

To determine the spectral resolution of the PEEM analyzer and to probe chromatic aberrations, as well, as the influence of different surface potentials on the spectra, an in-situ mask-deposited Au-dot ($\varnothing$=0.5mm, d=50Å) on a vacuum-cleaved MoTe(0001)-surface has been studied with PEEM. The PEEM-images (hv=4,9eV) (left part) and the spectra (hv=150eV, pass energy=10eV), as obtained in the hexagonal regions ($\varnothing$=60µm), respectively (right part), are shown in Fig. 3. The sharp boarderline between the MoTe substrate and the Au-dot is visible at the lower right boundary between the dark and the bright region (dashed line), so that spectrum 3 includes nearly equal parts of the MoTe substrate and the Au-covered region. The overal spectral resolution is about 0.9eV for Au4f and Te4d. No Au-signal has been found in the region of the uncovered MoTe substrate. Therefore no evident chromatic aberration could be detected for kinetic energies up to 100eV and even not up to 250eV (spectra not shown). A band bending has not been observed for that system.
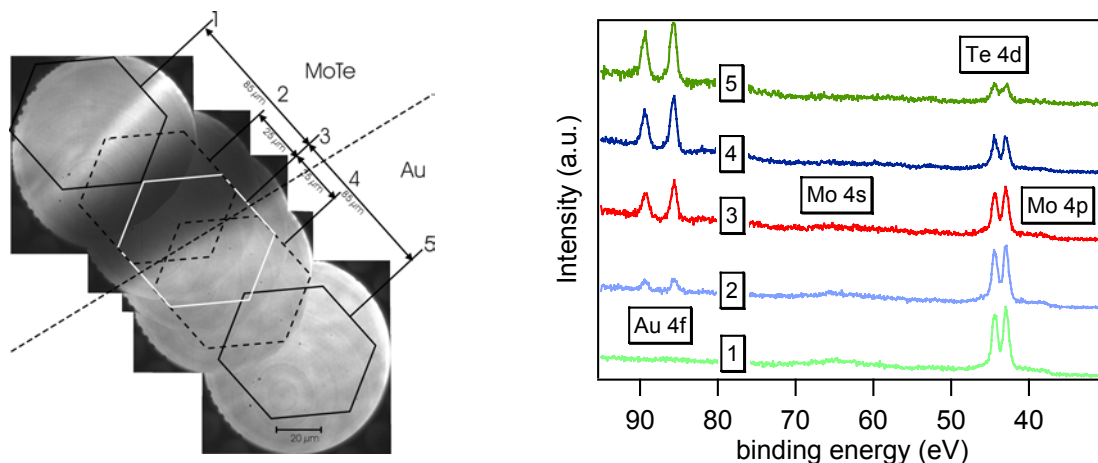

Fig.3.: PEEM-imaging (hv=4.9eV) and spectroscopy (hv=150eV) from an Au-dot ($\varnothing$=0.5mm, d=50Å) on MoTe(0001).

NEW INFRARED BEAMLINE AT BESSY

U. Schade, T. Noll, and W. B. Peatman
BESSY GmbH, Albert-Einstein-Straße 15, 12489 Berlin,Germany

A. Röseler, and E. H. Korte,
ISAS Berlin, Albert-Einstein-Str. 9, 12489 Berlin, Germany

F. Bartl, and K. P. Hofmann
Institut für Medizinische Physik und Biophysik, Ziegelstraße 5-9, 10098 Berlin, Germany

Abstract

In recent years it has become apparent that synchrotron radiation is a unique source of IR radiation that is being increasingly exploited at synchrotron radiation facilities around the world. The highly brilliant VUV and soft X-ray source BESSY II was augmented this year by a large acceptance infrared beamline. This new facility will be utilized for spectroscopic investigations of biological systems, for microscopy of same and for investigations on the structural and functional interactions of proteins. In addition, vibrational, structural and electronic properties of surfaces and thin layers will be studied using infrared ellipsometry. It will provide useful IR intensities over the energy range from about 5000 down to 50 cm^{-1} and lower. The beamline is equipped with several experimental stations consisting of two Fourier transform infrared spectrometers, an infrared microscope and an infrared ellipsometer. In a later stage of the project an ultra high vacuum chamber will be installed for surface science experiments. After commissioning the first beamline section in the spring of the year 2001 first quantitative measurements on the performance have been made in the near and mid infrared wavelength region.

Optical Design

The optical design of the infrared beamline at BESSY has been presented in detail[1] and is schematically shown in Figure 1. The geometrical constraints of the storage ring define the maximum horizontal and vertical acceptance of the beamline: ± 30 mrad horizontally and ± 20 mrad vertically. The first mirror M1, which is planar, is placed at a distance of 900 mm from the source, the first
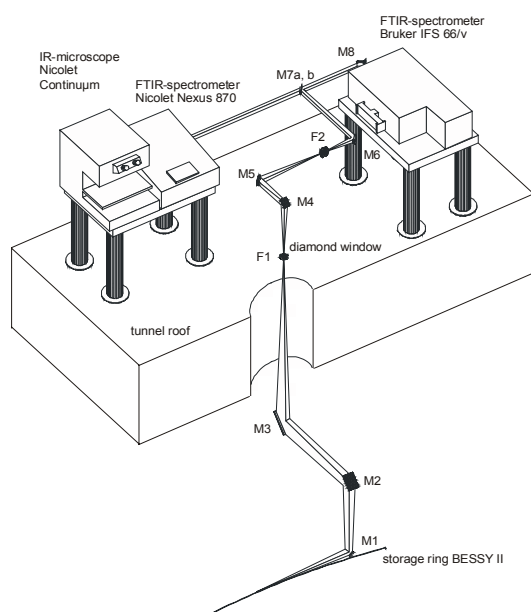

FIG. 1: Optical layout of the beamline.

position possible outside the poles of the dipole magnet. We have chosen to split the first (plane) mirror into two halves, leaving a gap of 6 mm for the high energy portion of the beam to pass through to a water cooled absorber at the rear of the dipole chamber. The second and third mirrors, M2 and M3, of the optical system are both cylindrical and focus the IR radiation vertically and horizontally to an intermediate focus, F1, just behind a wedge window of polycrystalline CVD diamond with a free circular aperture of 20 mm diameter providing broad band IR transmission. The window separates the ultra-high vacuum system of the front end from the fore-vacuum environment of the next part of the optical path. The mirrors M4 and M5, both cylindrical, transfer and refocus the radiation at the second focus F2. They are so arranged that the very asymmetric intermediate focus is made more symmetric before being collimated by the toroidal mirror M6. The following mirror pair M7a, b is mounted on a translation stage and consists of two plane mirrors which direct the collimated beam either through a KBr window to the

optical bench of the Nicolet microscope or to the toroidal mirror M8. The latter mirror refocuses the radiation to match the entrance requirements of the Bruker spectrometer. Near the second focus, F2, two gate valves are equipped with a KBr and a crystalline quartz window in the gate, respectively. This makes possible necessary alignment procedures for the experiments in the near and mid infrared wavelength region under atmospheric pressure without having a pressure difference of one atmosphere on the diamond window

Commissioning

The commissioning of the modified dipole chamber, the front end, and the beamline (up to the second focus) was finished in the first half of 2001 after installation during the first and second shutdown periods of 2001. First experimental tests of the beamline were performed on the radiation behind the intermediate focus by means of a mapping ellipsometer. The ellipsometer set-up is described elsewhere.[2] It allows one to scan the radiation distribution over an area of up to 50×50 mm^2 and to derive the distribution of the Stokes parameters and the ellipsometric parameters. In this specific application the accessible area of investigation in the plane of the diverging radiation was about 23×23 mm^2, limited by the divergence of the beamline optics and the angular acceptance of the mapping ellipsometer. The horizontal length of the actual footprint of the radiation at this position is about 100 mm. Two narrow bandpass filters were utilized for the measurements with a center wavelength of 1.95 and 4.60 μm, a full width at half maximum of 0.07 and 0.05 μm and peak transmittance of 75 and 60 %, respectively. In order to obtain absolute flux densities (photons/s·mm^2) the detector was calibrated for the two bandpass filters with a black body source at 1076 and 1176 K. All measurements have been normalized to a ring current of 1 A and a bandwidth of 0.1 %.

Figure 2 shows the distribution of the measured flux density of the diverging beam in the plane 1200 mm behind the intermediate focus for 1.95 μm and 4.60 μm wavelength at a ring energy of 1.7 GeV. The influence of the split first mirror for both wavelengths in the horizontal direction is apparent. The flux distribution arising from the two parts of the first mirror above and below the storage ring plane is asymmetric, probably caused by a small misalignment of the vertical position of the mirror gap. However, from the flux distribution no misalignment of the two parts of the split mirror against each other is discernable.

Measurements with a polarizer set to four different azimuth angles, both with and without a retarder (a phase shifting prism as an optical element of the ellipsometer) in the optical path, provides us with the necessary data for a complete characterization of the polarisation state at every spatially resolved element. The immediate results are the four elements of the Stokes vector as a convenient representation of the total flux and the relative amounts of linear and circular polarization. From the Stokes vector the so-called ellipsometric parameters, tan Ψ, the absolute ratio of the amplitudes between horizontally and vertically linear polarized radiation, and Δ, the phase shift between the two components can be derived.
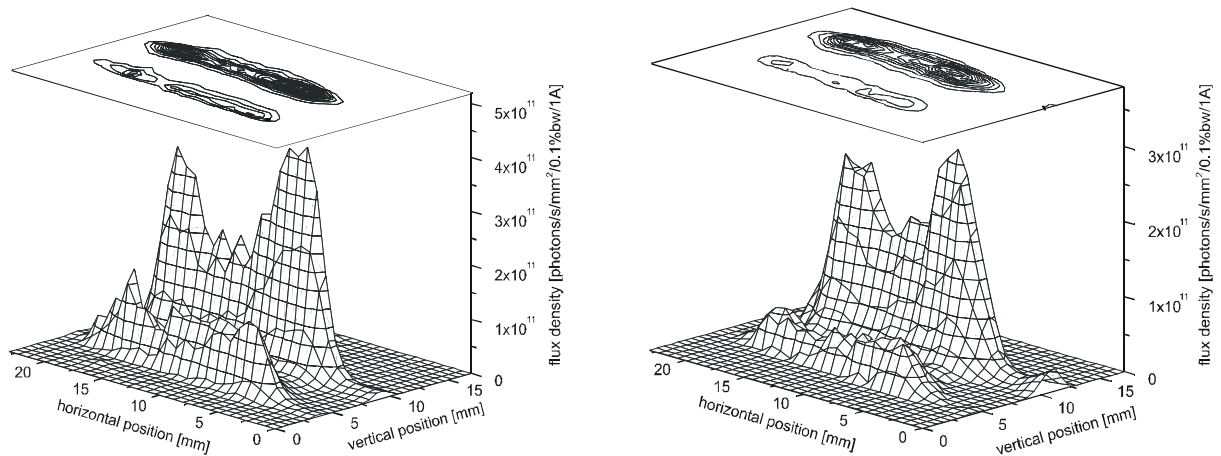
FIG. 2: Measured flux distribution of the diverging beam in the plane 1200 mm behind the intermediate focus for 1.95 μm (left) and 4.60 μm (right) wavelength at 1.7 GeV normalized to a beam current of 1 A and a band width of 0.1 %.
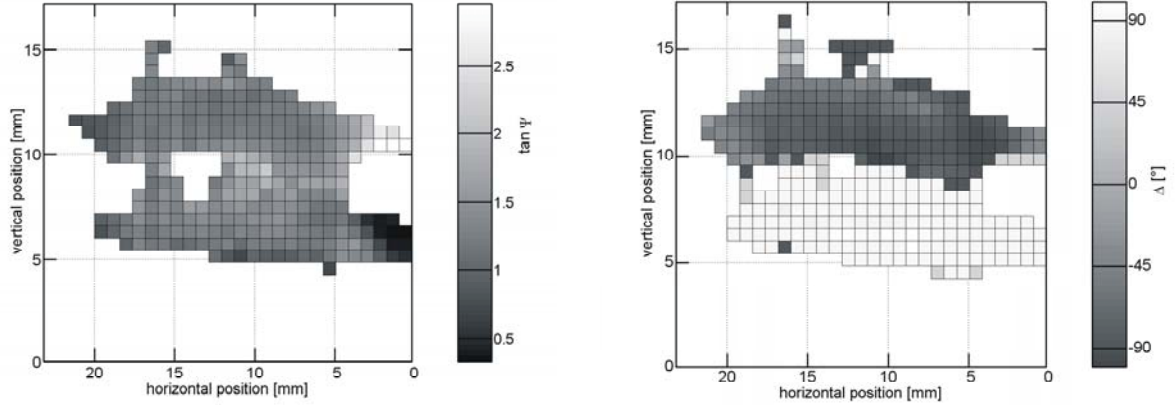
FIG. 3: Distribution of the experimentally derived tan Ψ (left) and of the experimentally derived Δ (right) of the diverging infrared beam in the plane 1200 mm behind the intermediate focus for 1.95 μm at 1.7 GeV.

Figure 3 shows the distribution of the ellipsometric parameters of the diverging infrared beam in the plane 1200 mm behind the intermediate focus for 1.95 μm at 1.7 GeV. Tan Ψ is almost homogeneously dispersed over the area investigated. The value of about 1 indicates that the amplitudes of the two linearly polarized components of the corresponding spatially resolved element are almost equal to each other. The phase difference, Δ, measured between the horizontally and vertically polarized radiation is - 90° above and + 90° below the storage ring plane, respectively, and agrees with theory for radiation from a homogeneous dipole field. In this context it should be mentioned that similar experiments at BESSY on infrared edge radiation have been performed showing completely different phase shift distributions above and below the ring plane.[2] Since tan Ψ ≈ 1 over the area accessible to our experiment, each spatially resolved element represents radiation which is either left-handed circularly polarized and radiated above the storage ring plane or right-handed circularly polarized and radiated below the storage ring plane.

Summary

The optics of the IR beamline at BESSY deliver a high IR flux. First experimental investigations on the total flux and on the polarization characteristics of the transmitted radiation in the near and mid-infrared wavelength region have confirmed the design expectations.

Acknowledgements

References

[1]   Peatman W. B., and Schade U. *Rev. Sci. Instr.* **72** (2001) 1620.

[2]   Schade U., Röseler A., Korte E.H., Scheer M., and Peatman W.B. *Nucl. Instrum. Methods A* 455, 476-486 (2000).

Non-destructive investigation of Dürer's silver point drawings by Sy-XRF

I. Reiche[1], A. Berger[2], W. Görner[2], S. Merchel[2], M. Radtke[2], J. Riederer[1], H. Riesemeier[2]

[1]Staatliche Museen zu Berlin, Rathgenforschungslabor, Schloßstr. 1a, 14059 Berlin, Germany
[2] Bundesanstalt für Materialforschung und –prüfung (BAM), 12200 Berlin, Germany

Introduction

Albrecht Dürer travelled together with his wife Agnes from July 1520 to August 1521 to the Netherlands. During this journey he drew his impressions into a travel book. In the late 19th century this travel book was separated and the sheets are now conserved in different international art collections. This book contained about fifteen sheets each 13 to 16 cm^2 in size. The sketches on the sheets are silver point drawings, a technique very appreciated in the 15th century. Even if many studies on the composition of art objects have now been performed, only little is known about this graphical technique.

The metal point lines are composed of thin layers of different metal alloys and deposited on a rag paper usually covered with a layer of bone white, a calcium phosphate obtained from burnt bone. As these metal deposits are extremely thin and, as the identification of the silver point line on the precious drawings must be non-destructive, only a few analytical methods enable the exact characterisation of the metal points.

The aim of this project is thus to characterise the silver point drawings of Dürer's travel book by synchrotron induced X-ray fluorescence (Sy-XRF) and to compare the results to those of six others already measured in Paris by 3 MeV Proton Induced X-ray Emission (PIXE) [1].

Experimental

We used Sy-XRF at the BAM*line* [2] to determine major and minor element contents in the silver point lines of the drawings. First test measurements with Sy-XRF clearly showed the non-destructiveness of the technique and evidenced that this technique provides the sensitivity required for the quantitative determination of the chemical composition of the silver point.

At the BAM*line* set-up a super conducting wavelength shifter (WLS) with a maximum field of 7 Tesla is used as an X-ray source. For the presented measurements, a Si(111) Double-Crystal-Monochromator (DCM) was used to produce an X-ray beam with an energy of 28 keV. The drawings were mounted in air in a sample frame on a motorized xyz-stage with an angle of 45° to the X-ray beam. Fluorescence signals were collected by a Si(Li)-detector covered with an Al filter (<30 µm) at 90° with respect to the incident beam. During measurements, drawings could be supervised by a video system. Data evaluation was performed by means of AXIL. Relative concentrations of the silver points were determined after background subtraction using a thin layer approximation.

Results and discussion

Up to now three sheets containing several silver point drawings of Dürer's travel book from the Kupferstichkabinett Berlin were investigated at the BAM*line*: "Thronender Bischof; Brustbild eines Mannes mit Pelzmütze" (March 1521), "Liegender Hund; Hundekopf und Löwenkopf" (April 1521) and "Brustbild eines Mannes aus Antwerpen; Der Krahnenberg bei Andernach" (June 1521) (Fig. 1a).

It was possible to quantify Ca, Mn, Fe, Cu, Zn, Sr, Ag, Hg, and Pb in the drawings. In the majority of the analysed lines, silver was affirmed to be the major element. Three other minor elements, Cu, Hg and in one case Zn could be attributed to the silver alloy as concentrations are significantly higher in the silver lines than in the backing. Determined Ag concentrations varied between 80.0 – 92.0 wt.%. Lines also contain about 10.0 ± 3.5 wt.% of Cu, and variable concentrations of Hg (Fig. 1b). Zn concentrations are generally in the range of those in the backing. Only in one drawing "Brustbild eines Mannes mit Pelzmütze" a Zn

concentration of about 6.0 wt.% was found in the silver line. This drawing could be realised with another silver point. In addition, some lead point lines were also detected in this drawing.
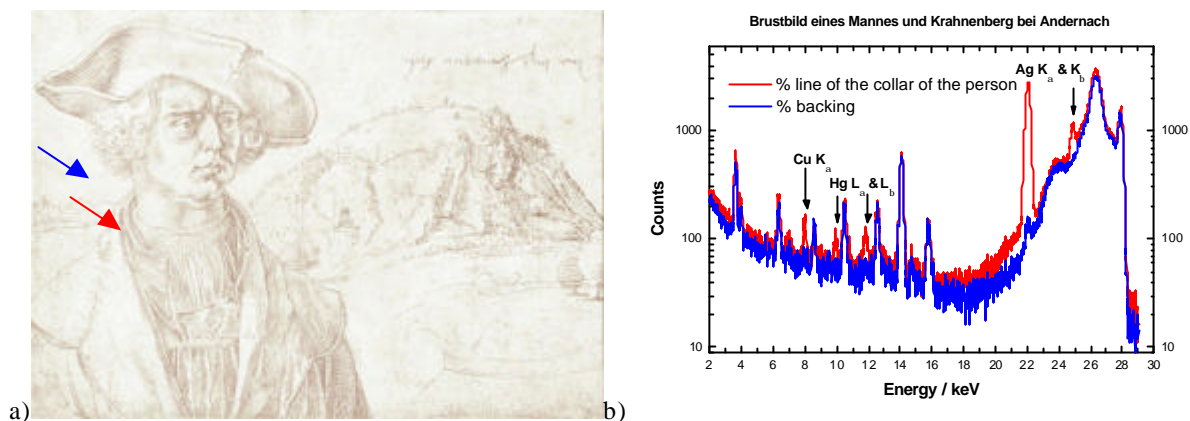
Figure 1. a) Albrecht Dürer drawing "Brustbild eines Mannes aus Antwerpen; Der Krahnenberg bei Andernach" (June 1521) from the Kupferstichkabinett Staatliche Museen zu Berlin (Inv.Nr. KdZ 33r) and b) Sy-XRF-spectra (28 keV excitation energy) of a silver point line and of the preparation layer.

The preliminary results are consistent with those obtained by Duval and Guicharnaud on six other sheets of the travel book [1]. They determined lines composed of Ag alloys with about 6 to 10 wt.% Cu, less than 1 % Zn and variable Hg concentrations depending on the thickness of the silver line. To our knowledge, no metal point containing Hg, even in minor concentration, were used for drawings during the Renaissance. Its presence is very likely caused by contamination of the drawings due to their exposure to the atmosphere. A large amount of Hg is released every year into the earth atmosphere. Silver has a strong affinity to Hg and forms a very stable amalgam. The uptake of Hg by the small Ag layers presenting a high surface area seems to be a general alteration phenomenon of these drawings as it was observed on different drawings analysed in Paris and at the BAM*line* in Berlin. This observation has important consequences for the conservation of these drawings and gives also the possibility to distinguish original drawings from recent ones.

Conclusion

We reported first successful non-destructive analyses of silver point drawings by Sy-XRF and showed the potential of this method to give more precise insights in the graphical technique and its alteration phenomena. These results indicate that drawings of Dürer's travel book from 1520 to 1521 were made with a similar silver point composed of a silver alloy containing copper, mercury and traces of zinc. This composition seems to be typical for Dürer's drawings. The presence of mercury could be attributed to contamination by the atmosphere.

References

[1] H. Guicharnaud, A. Duval, Sept dessins d'Albrecht Dürer au Laboratoire des Musées de France, *L'Estampille/L'Objet d'Art*, **362** (2001) 76-82.

[2] W. Görner, M.P. Hentschel, B.R. Müller, H. Riesemeier, M. Krumrey, G. Ulm, W. Diete, U. Klein, R. Frahm, BAM*line*: The first hard X-ray beamline at BESSY II, *Nucl. Instr. and Meth. A* **467-468** (2001) 703-706.

Normal and 45°-incidence mirrors for water window

Alexei Nefedov and Hartmut Zabel

Institut für Experimentalphysik/Festkörperphysik, Ruhr-Universität Bochum,
Universitätstr. 150, 44780 Bochum, Germany

F. Schäfers

BESSY, Albert-Einstein-Strasse 15, 12489 Berlin, Germany

Imaging with soft x-rays is a very important part of present day thin film technology. In recent years, remarkable progress has been made in the development of high reflectance multilayer mirrors for the vacuum UV range up to 280 eV. For the water window (280 eV - 530 eV) highly reflecting multilayer mirrors are rare. For normal incidence an optimized multilayer mirror has to have a period Λ which is half the wavelength λ of the incident x-ray beam. Therefore, one goal of x-ray optics is to produce a multilayer mirror with the smallest period possible. In addition, since at higher energies more and thinner layers are needed in order to approach the theoretical limit for reflectance, the interdiffusion and interface roughness become a serious problem due to the increasing ratio of interface roughness σ to period Λ. The interest in multilayers containing $3d$-transition elements (Ti, V) is called forth by the high reflection in this energy range at their L absorption edges. At the upper end of the water window, which is interesting for biological applications, the situation is even worse because of a lack of sufficiently transparent spacer materials. We proposed to use Al_2O_3 as the spacer layer due to its low absorption coefficient in the soft x-ray region and a smooth growth behavior. In this report new experimental data on the reflectance V/Al_2O_3 and Ti/Al_2O_3 multilayers obtained by synchrotron radiation in the soft x-ray energy range are presented.

Multilayers with periods Λ from 1.2 to 6.045 nm and numbers of double layers varying from 30 to 75 were deposited by conventional RF sputtering on $(11-20)Al_2O_3$ at room temperature in an atmosphere of $5 \cdot 10^{-3}$ mbar Ar. All measurements have been performed with the BESSY reflectometer chamber at beamline PM1. We have carried out $\theta - 2\theta$ scans in the vicinity Bragg reflections at different photon energies as well as energy scans at fixed angles of incidence. The reflectances of the multilayers were investigated from normal to grazing incidence. In Fig. 1 the reflectances at normal incidence for V/Al_2O_3 (a) and Ti/Al_2O_3 (b) multilayers are presented. The period of these multilayers was adjusted in order to have a multilayer "Bragg" peak near 90° (the 1st or higher orders). It is clearly seen that the intensity of the 3rd order peak of Ti/Al_2O_3 multilayer with Λ=4.13 nm is by an order of magnitude higher than for the 1st order peak for one with Λ=1.39 nm (Fig.1 (b)). Moreover, the intensity of the 1st order "Bragg" peak for the thinnest V/Al_2O_3 multilayer with Λ=1.2 nm is practically the same as the 5th order "Bragg" peak of V/Al_2O_3 multilayer with Λ=6.045 nm. These results confirm the previous conclusions about the crucial influence of the interfacial roughness on reflectance values, especially for multilayers with the smallest periods Λ. We also mention, that for the incident photon energy E=92 eV the V/Al_2O_3 multilayer with $\Lambda = 6.045$ nm has a normal incidence reflectance R=1.5% (the 1st order "Bragg" peak).

Next we characterized out multilayers near the Brewster angle ($\theta = 45^o$). In Fig. 2 we show $\theta - 2\theta$ scans for V/Al_2O_3 multilayer with $\Lambda = 1.745$ nm (Fig.2 (a)) and Ti/Al_2O_3 multilayer with $\Lambda = 2.07$ nm (Fig.2 (b)) at fixed energies of 510 eV and 451 eV, i.e. just below the corresponding L absorption edges, where the reflectance is resonantly enhanced. Well pronounced Kiessig fringes are clearly seen near the Bragg peaks indicating a high homogeneity of the individual
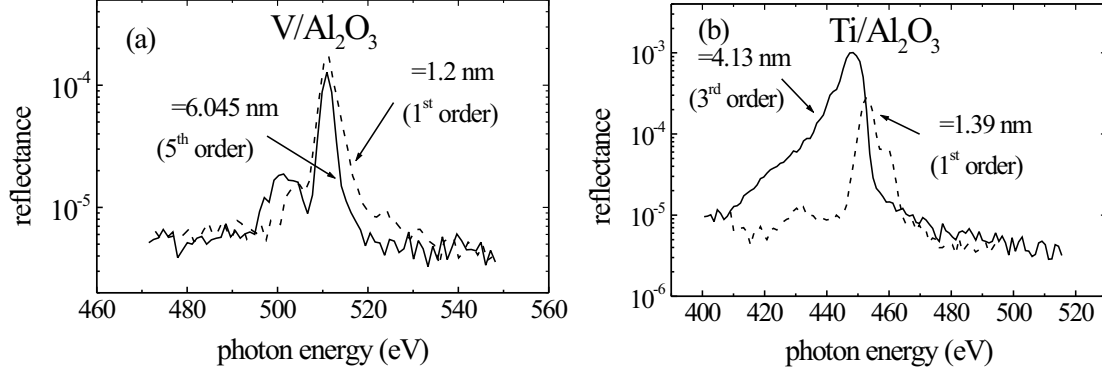
Fig.1 Intensity reflected from V/Al$_2$O$_3$ (a) and Ti/Al$_2$O$_3$ (b) multilayers as a function of photon energy at incidence angle of $\theta = 86^o$ (for Ti/Al$_2$O$_3$ with Λ=1.39 nm $\theta = 75.8^o$).

layers. We note that the position of multilayer "Bragg" peaks is indeed close to the Brewster angle for both multilayers ($\theta = 43.3^o$ for V/Al$_2$O$_3$ and $\theta = 41^o$ for Ti/Al$_2$O$_3$).
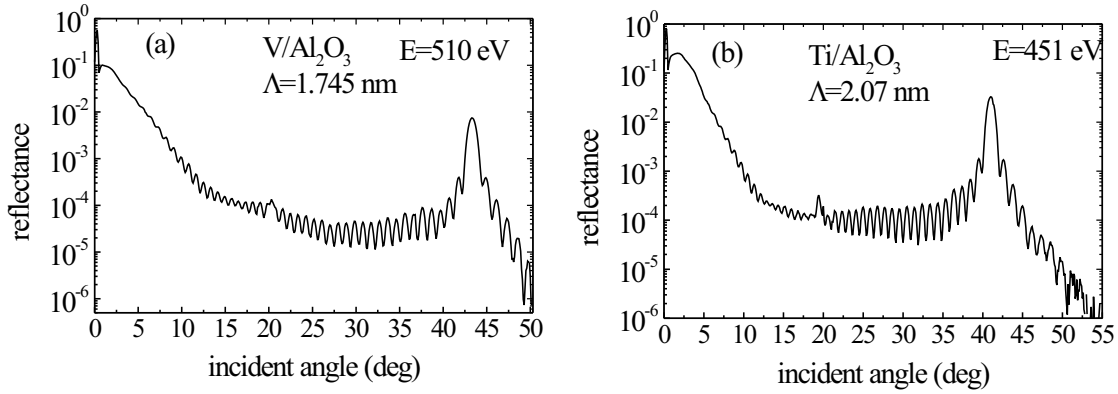

Fig.2 Reflectivity measurements on V/Al$_2$O$_3$ multilayer with $\Lambda = 1.745$ nm (a) and Ti/Al$_2$O$_3$ multilayer with $\Lambda = 2.07$ nm (b) at a fixed energies of 510 eV and 451 eV.

The energy resolution of the multilayers was extracted from the FWHM of the reflection curves of both energy scans and $\theta - 2\theta$ scans according to E/ΔE=tgθ/$\Delta\theta$. Generally, the resolving power is proportional to the number of periods which determines also its theoretical limit. The best resolving power (E/ΔE=70) is obtained for the sample with $\Lambda = 2.15$ nm and number of double layers N=75. Above the absorption edge the resolving power is reduced due to the increased absorption (i.e. reduced penetration length) resulting in a reduced number of contributing interfaces.

The peak reflectances of the V/Al$_2$O$_3$ multilayer with $\Lambda = 2.54$ nm and the Ti/Al$_2$O$_3$ multilayer with $\Lambda = 2.07$ nm are plotted in Fig. 3 as a function of incident photon energy. Each data point was extracted from energy or/and $\theta - 2\theta$ scans like those shown in Fig.1 and Fig.2. The inset in Fig.3 (b) shows peak reflectances for the samples with $\Lambda = 1.39$ nm and $\Lambda = 4.13$ nm (3rd order) close to the $L_{3,2}$ absorption edges of Ti. Here we also observe an intensity difference (by an order of magnitude) in the peak reflectances, which we earlier obtained for the normal incidence data. As expected, all spectra show a strong enhancement of reflectance at the

L edges of V and Ti and a sharp cut-off beyond this edge. Moreover, two peaks corresponding to the L_3 and L_2 edges are clearly resolved for all multilayers. The additional sharp cut-off of reflectance takes place near E=530 eV corresponding to the absorption edge of oxygen. At higher photon energies the reflectance increases again due to the decreasing angle of incidence.
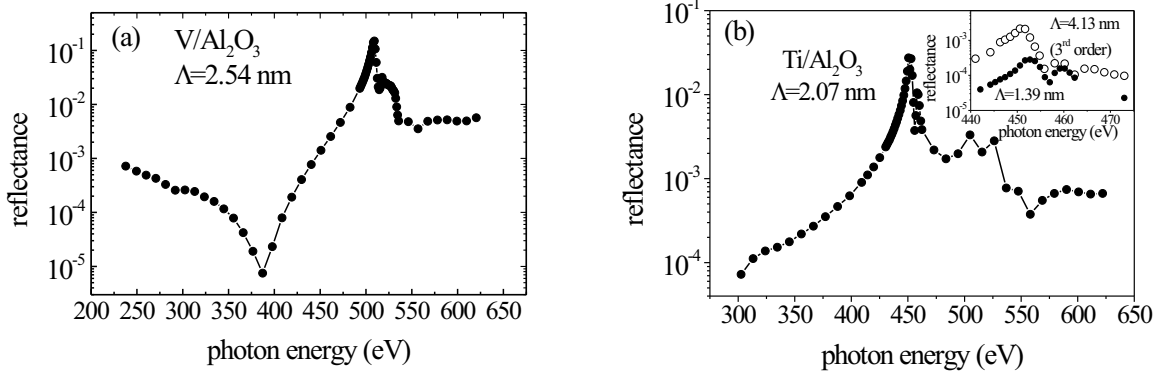

Fig. 3 The peak reflectances of V/Al$_2$O$_3$ and Ti/Al$_2$O$_3$ multilayers are plotted as a function of incident photon energy. Inset shows peak reflectances for multilayers with $\Lambda = 1.39$ nm and $\Lambda = 4.13$ nm close to $L_{3,2}$ absorption edges of Ti.

In a conclusion, we found that Me/Al$_2$O$_3$ (Me=V, Ti) multilayers are very good potential candidates for an application as x-ray mirrors within the "water window" energy range, because resonance phenomena close to the absorption edges provide a high material contrast between $3d$ metals and Al$_2$O$_3$. Moreover, due to the low absorption coefficient in the soft x-ray region and its smooth growth behavior Al$_2$O$_3$ appears to be an excellent spacer material in this energy range. We believe, that such multilayers have a chance to become good normal incidence mirrors, because their normal incidence reflectance of 0.1% and their reflectance near the Brewster angle of 3.3 % obtained at an energy close to the L_3 edge of Ti are brightly competitive. For such multilayer structures we found that it is better to use the 3rd order reflection of thicker multilayer instead of the 1st order "Bragg" peak for the thinner one, because of smoother growth conditions for the thicker multilayer. The similar results have also been obtained for V/Al$_2$O$_3$ multilayers.

The helical Undulator UE46 - Design and Construction

U.Englisch[1], H.Maletta[1], J.Bahrdt[2], W.Frentrup[2], A.Gaupp[2],
M.Scheer[2], W.Gudat[2], W.Eberhardt[2]

[1] Hahn-Meitner-Institut, Glienicker Str. 100, 14109 Berlin, Germany
[2] BESSY mbH, Albert-Einstein-Str. 15, 12489 Berlin, Germany

Introduction

Application of the x-ray and neutron measurements enables detailed investigation of the magnetic structure of thin films and nanostrucutres. We have built a new elliptical undulator UE46, which will be installed in a low beta section. It provides soft X-rays with variable polarization and with highest brilliance at highet possible energies (200 to 2000 eV) for magnetic circular dichroism (X-MCD) measurements at the $L_{2,3}$-edges in transition metals and the $M_{4,5}$-edges in Rare Earths. We report on the design and construction of the undulator.
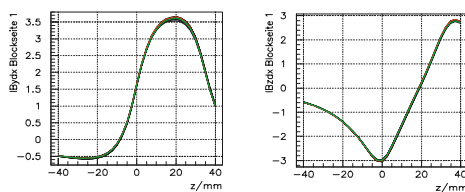
Design

The insertion device has a magnetic design of APPLE-II type [1] consisting of NdFeB-magnets. Symmetric or antisymmetric movement of the magnet rows create variable polarization: circular, linear or linear polarization under various angles. Variation of gap and shift controls the energy and the state and degree of polarization of the light. The tuning ranges of the first, third, fifth and seventh harmonic for the symmetric mode are reported in [2]. The design of the magnet structure guarantees an overlap of the first and third harmonic for horizontal linear and elliptical polarization. The row phase for 100% circular polarization, characterized by $S_3/S_1=\pm 1$, varies slightly with the gap. The helicity can be switched mechanically from right to left circular in about 3s. For the antisymmetric operation mode, which provides linear polarized light under various angle relativ the horizontal plane, the ranges of the various harmonics are shorter and do not overlap.

Construction

The construction of the UE46 is characterized by three steps. The magnet block quality was controlled by measuring the field integrals with the Stretched-Wire-System and th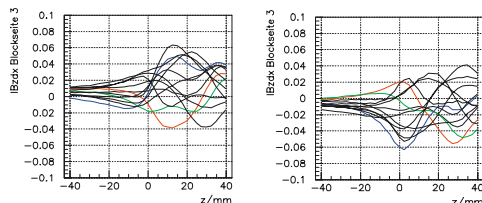e dipole errors with the Helmholtz-Coil. Measurements with the Stretched-Wire-System provides information about the field inhomogeneties in the single block. The magnets were moved relative to a 0.5m long single wire at a distance of 7.5mm. Via the measured induced voltage the contribution to the horizontal and vertical field integrals of each magnet at lowest gap (15mm) within a region of ±40mm was determined. The rms-reproducibility of the set-up is 0.0003 Tmm for the horizontal magnetized blocks (A) and 0.003 Tmm for the vertical magnetized (B), at least a factor of 10 lower than the amplitudes of the inhomogeneties [3]. Characteristic spectra for one side of the single magnet blocks of A- and B-
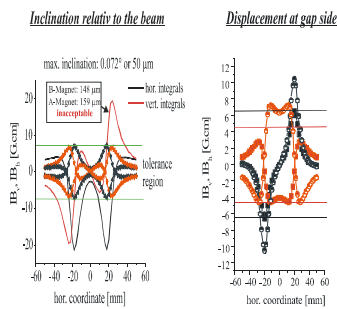

Fig. 1: Magnetic signals of single blocks

type are dislayed in Fig. 1. The blocks are magnetized half by half in two opposite directions with respect to the pressing direction, called S or N to cancel systematic fabrication errors [3]. Therefore four different types of magnets had to be distinguished, labelled AN, AS, BN, BS. For the A-magnets 4 block sides had to be measured and for the B-magnets two block sides.

The dipole magnetization errors of the A- and B-magnets were investigated using an automated Helmholtz-Coil setup. In case of the A-magnets we observed statistical distributions of the main component with rms-values below 0.25% in contrast to the minor-components, which had broader distributions with rms-values varying from 0.7% up to 1%. The B-magnets had shown a completely different behaviour. Because the magnets have been fabricated in two batches two main componets were observed which differed about 2%. In case of the magnet type BS one minor component revealed the same behaviour. The rms-values of the other minor components varied from 0.23% up to 0.74%.

The Helmholtz-Coil data were used together with the measurements of the Streched-Wire-System in a sorting procedure employing the simulated annealing algorithm. The single magnet blocks were sorted with respect to the spectral performance and minimum interaction with the storage ring. Minimizing of the first integrals and the phase error in horizontal and vertical direction were the criteria.

In the next steps the magnets were glued to pairs and then glued onto the keepers. To fulfil the strict displacement tolerances of ±25µm at the gap and slit side and the inclination of the single magnet blocks relativ to the beam (≤ 0.072°) the used mechanical devices had to be adjusted carefully. The quality of the assembly was controlled mechanically using a 3D coordinate measurement system and magnetically using the Stretched-Wire-System. Displacement and inclination errors larger than the quoted tolerances increased the magnetic errors, as shown in Fig. 2 on the left side. The statistics on the right side of Fig. 2 shows that the requirements for most magnet assemblies were fulfilled. So we could expect an optimized field integral for the whole magnetic structure due to the sorting procedure.

Finally the keeper units had to be mounted onto the girder using lamellated spacers to adjust the
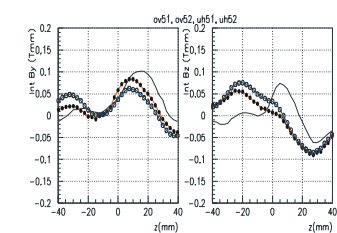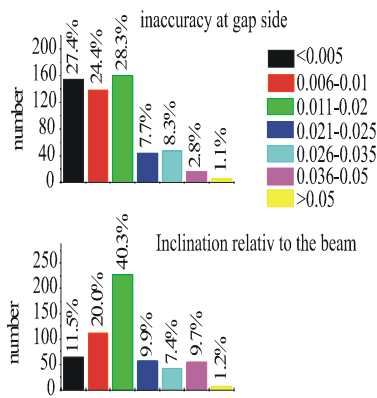

Fig. 2: left: Calculated (a) and measured (b) magnetic signals by inaccuracies in the glue glue process. The measured magnetic signal show a difference to the sorted one due to large discrepancies of the height mismatch at the gap side and the parallelism.

right: Statistics of the glue process of the UE46

keeper. The thickness of the spacers was calculated by a new program [4] including the deflection of the girder. The program yielded also the correct sequence of the keeper in each row by comparing the sorting lists before and after the field-integral measurements of the magnet assemblies with the Stretched-Wire-System.

Control and optimization of performance

After completing the assembly of the insertion device the magnetic properties were optimized at the granite bench. The granite bench is equipped with a Hallprobe for local field measurements and a moving wire for int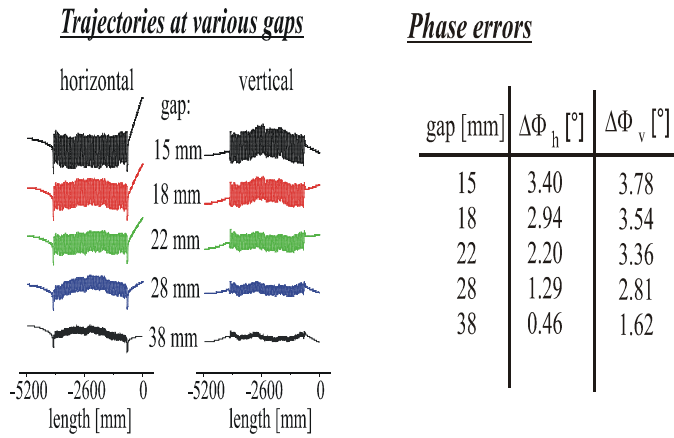egral measurements. The performance of an insertion device can be described in terms of the phase smear of the optical wave. The phase difference between the electron and the optical wave depends on the electron motion in the horizontal and vertical plane, whereas the electron trajectory is influenced by the vertical and the horizontal magnetic field. RADIA [5] calculations showed that a translation of 0.1mm of one block in horizontal and vertical direction adds 0.03 Tmm to the field integrals. Therefore movements of the keeper minimized the kicks in the trajectories and optimized the phase error (Fig. 3).

Trajectories at various gaps   *Phase errors*

gap [mm]	$\Delta\Phi_h$ [°]	$\Delta\Phi_v$ [°]
15	3.40	3.78
18	2.94	3.54
22	2.20	3.36
28	1.29	2.81
38	0.46	1.62

Fig. 3: Trajectories and phase errors after block movement

To reduce the shift dependence of the field integrals we used Fe-shims which are glued onto the magnets. The position and the size of the various shims were calculated using the shim response functions calculated with RADIA via a matrix diagonalization procedure. The shimming technique minimized the shift dependence of the field integrals within ±10mm for the horizontal and vertical component up to 10^{-3} Tmm [6].

Four magic fingers were used to compensate the multipoles. They were mounted at the ends of the girders and are symmetric relativ t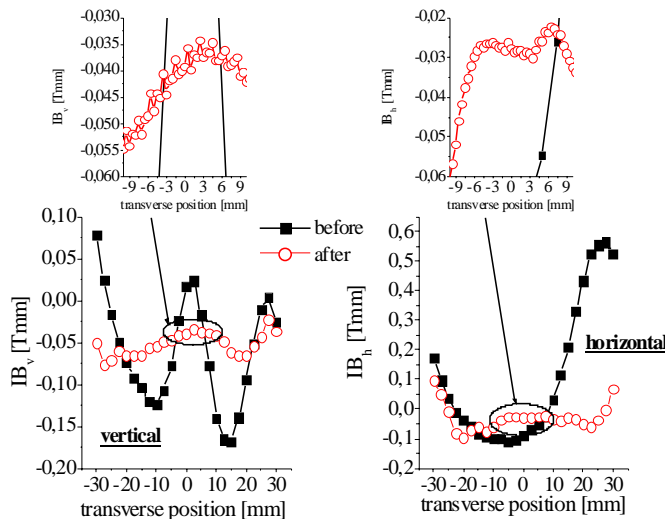o the middle of the magnetic structure. One magic finger has 25 vertical slots which were filled with shim magnets of various sizes. The algorithm to get the optimized magnet configuration was the same as used for the Fe-shims. After several iterations the field integrals within ±10mm were reduced down to $3.5*10^{-2}$ Tmm (vertically) and $2.5*10^{-2}$ Tmm (horizontally), respectively (Fig. 4).

Fig. 4: Measured field integrals before and after the shimming with the magic finger

Due to the comprehensive optimization in design and construction of the undulator the performance of the UE46 is at least a factor of 2 to 3 better than other elliptical insertion devices at BESSY.

References

[1] S.Sasaki, *Nucl. Instr. and Meth.* **A 347** (1994) 83

[2] U.Englisch, H.Rossner, H.Maletta, J.Bahrdt, S.Sasaki, F.Senf, K.J.S.Sawhney, W.Gudat
     Nuclear Instr. and Meth. **A 467-468** (2001) 541

[3] J.Bahrdt, W.Frentrup, A.Gaupp, M.Scheer, W.Gudat, I.Ingold, S.Sasaki
     Nuclear Instr. and Meth. **A 467-468** (2001) 21

[4] Software developed by U.Englisch: program ″montage″, unpublished

[5] RADIA, ESRF software developed by P.Elleaume, O.Chubar, J.Chavanne
     IEEE-Proc. of PAC'97, **Vol. 3** (1998) 3509

[6] J.Bahrdt et al., in preparation

Nanometer Optical Components for Synchrotron Radiation Beamlines

Heiner Lammert
Berliner Elektronenspeicherring-Gesellschaft für Synchrotronstrahlung - BESSY -
Albert Einstein Straße 15, D 12489 Berlin
e-mail: Lammert@Bessy.de

Abstract
A cooperative research project with 11 partners in Germany from industries and science was founded with the goal to provide optical components for use in synchrotron radiation research with an exactness that exceeds the present technological limit of 0.1 arcsec rms for the slope error. The necessity of more exact components, their generating processes and measuring methods and the goal of the cooperative project NOK are discussed.

Introduction
In connection with the construction of the storage ring for Synchrotron Radiation BESSY II in Berlin-Adlershof a new generation of monochromators has been developed, achieving a resolving power of E/ΔE > 100000, diffraction limited. This limit was been reached because some new engineering principles in beamline design have been implemented [1]: the metrology of the optical elements to be employed with up to 0.05 arcsec accuracy; the determination of the turning angle of the grating and mirror movement to 0.001 arcsec resolution; precision engineering of the mechanical parts and cooling of optical elements limiting deformations. A result of these developments is among other things the recognition, that the limit of the storage ring effectiveness mainly is specified of the quality of the optical components [2]. And the all-important quality criterion of the optical surface is, beside the microroughness the slope error. However with the slope error of optical components of 0.1 arcsec rms today, optical technology is at its limit. At BESSY we have identified this 0.1 arcsec limit with more than 100 LTP-measurements of SR components mainly for BEESY II. In most cases the 0.1 arcsec limit was not reached and only in a very small number of cases was this limit undershot.

The present technological limit
The technological limit of 0.1 arcsec is conditional upon the different methods of the shaping process by manufacturing and upon the measurement accuracy. A definite undershooting of this limit means that the geometrical shape accuracy of the surface must be in the range of 1 nm to subnanometer. For the use in SR such nanometer optical components are necessary. In view of this necessity - by the way a problem of the SR facilities all over the world - we at BESSY asked the question how this insufficiency may be overcome: how is to do better than the technological limit of 0.1 arcsec rms, how are to get nanometer optical components (NOK) for high quality use in the SR-research.

The solution for reducing the 0.1 arcsec limit is to be found in improved finish processes in manufacturing and in improved measuring facilities.

Methods of modern optical technology
The developments in the fields of the optical technology to the present has led to four surface material removal and smoothing methods:

1. The classical method is the polishing procedure with contact between a large surface part of the tool and the optical component. This method has been exercised for hundreds of years with little changes in the principle surface formation process. It allows a very high geometry accuracy, but is as a matter of principle only practical for plane or spherical shapes. The ultimate accuracy depends on the measuring accuracy employed. In the 1980s at BESSY plane mirrors made by classical polishing methods were used, which last year we measured with help of our high accuracy Long

Trace Profiler (LTP-) methods to an accuracy of better than 0.08 arcsec rms. This example shows, that 20 years the manufacturers already could make mirrors of higher accuracy with classical polishing methods, but that this accuracy could not be measured.

2. The second finishing method consists of computer aided polishing method (CAP) with small tools, in range of 1 cm^2. The local different polish height is computer controlled over the local polishing time and other polishing parameters in dependent upon the previously gained measuring result. Together with interferometric measuring methods this polishing method is in practice about 15 to 20 years. Mainly the measuring method determined the whole accuracy of the CAP method.

3. Ion beam material removal enables a very small height (0.1 nm) to be removed, after time of ion bombardment on a local, limited surface of about some 100 mm^2 . The process is computer controlled over the residence time of the ion beam or over the ion beam energy. Also necessary is a measuring result of the surface geometry before the ion bombardment. The finish accuracy is determined by the measuring accuracy, the dimension of the treated surface and the surface quality before the ion beam removal process.

4. The magnetorheological polishing method employs a with magnetic fluid polishing suspension which at the local tangent district between the moving tool and the workpiece is of solid consistence because of a magnetic field in this working area. This method mainly is utilized for shape conserving polishing of ground axially symmetrical nonspherical components.

All four of these technological methods are qualified to address the problem of the above mentioned so-called Nanometer Optical Components (NOK) for SR. But, of course, they all need highly qualified measuring methods.

Measuring methods
The common measuring facilities present in the optic shops of the producers are computer aided interferometers. The main problem with interferometric measuring methods is the necessity of having a reference surface. All over the world there are no surface standards for spherical, for plane and least of all, for nonspherical surface shapes. Thus it is imaginable, that the measuring results of the different producers may be different. For instance an inter-laboratory comparison of 11 different interferometers in 11 different Great Britain companies and laboratories inclusive the UK National Physical Laboratory [3] shows different measuring results: 11 plane surface measuring results has an average value for the "form error" of 120 nm p-v in a deviation range of 55 nm. Thus there is about by 50 % measuring deviation of the whole shape deviation and a standard deviation for the measuring results of 13 nm rms. Here one can see, that the precision measuring of nanometer optical components must be significantly improved in on the same way as the technology for their finish shape generation.

Not as widely-spread as interferometers are Long Trace Profilers (LTP) invited by P. Takacs and S. Qian [4]. These were developed some ten years ago and are mainly found in SR laboratories. The method is based on a scanning procedure for large radius nanometer optical components in dimensions up to more than 1000 mm length. At BESSY we were able to increase the accuracy of measuring results with different measuring strategies, mainly special calibration and auto-calibration methods and especially temperature controlling with temporal temperature gradients in range of less than 1 mK/min [5;6]. For some years we are able to determine our LTP measuring uncertainty by comparing our LTP-measuring reports with the measuring results obtained by other measuring methods of the producer. As result of these comparisons the veracity of the BESSY LTP-results has been verified. For instance, the BESSY-LTP measuring result of a spherical 130 mm grating substrate of (0.064 +/- 0.01) arcsec rms (Fig. 1) agree to less than 0.5 nm with the measuring results of a producer's coordinate measuring machine [7] (see table 1). The nearly identical results of both fully different measuring methods in respect of the curve radius of the same sample is in range of 0.001 % and the sagitta difference of 1 nm by a curve radius of 10044 mm.
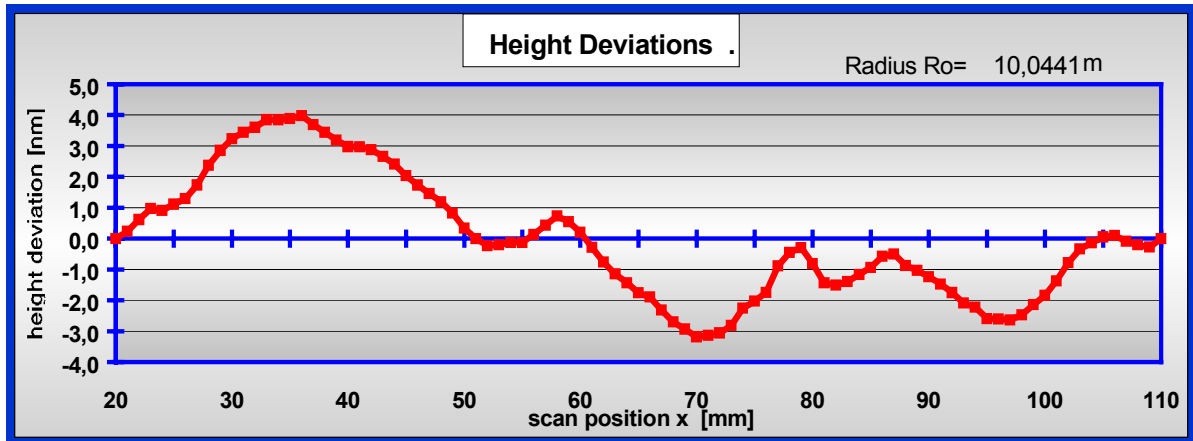
Fig.1: BESSY-LTP measuring result of a spherical grating substrate (values in Tab.1)

Sample: spherical grating substrate 140 mm Zerodur	measuring results of two different methods		comparison of the methods
	Long Trace Profiler LTP	coordinate measuring machine	difference
slope and shape deviations:			
angle [nrad rms]	310 +/- 65	437	127 nrad
angle [arcsec rms]	0.064 +/- 0.01	0.09	0.026 arcsec
height [nm rms]	2.0 +/- 0.5	ca 2	**< 0.5 nm**
height [nm p-v]	7.2 +/- 4	ca 10	**0.001 % *)**
average curve:			
radius [mm]	10044 +/- 1	10044	0.001 % *)
sagitta [mm]	0.100806 +/- 0.000002	0.100807	1 nm

Table 1: High accuracy and agreement in the measuring results on a spherical grating substrate of two different methods.   [*) in relationship to the sagitta of 0.1 mm]

Although there are some optical components with slope errors lower than 0.1 arcsec rms and measuring methods with uncertainties lower than 1 nm, such instances are only exceptions and demonstrate, that a major effort will be necessary to undershoot the common present technological 0.1 arcsec rms limit.

The cooperative project Nanometer-Optikkomponenten (NOK)
To approach the goal of SR nanometer optical components in Germany a union of 7 optical companies und 4 public scientific institutes was founded in a research cooperation project named "Nanometer-Optikkomponenten" (NOK). The start of the cooperative project was in February 2001 under promotion of the German Federal Government (Bundesministerium für Bildung und Forschung) within the scope of the research direction "Nanotechnology" in the Competence Center "Ultraprecision Technology of Optical Surfaces" (CC UPOB e.V.). The goal of the NOK-project is the manufacturing und measuring of supersmooth surfaces for optical components with emphasis on components with specifications, which are beyond the present technological limits. The coordination function of this project is performed by BESSY. The cooperation is organized in two working groups: a) technological development (WGT) and b) measurement development (WGM). In the working group for technological development special optical companies and institutes are banded together: representing the four aforementioned finishing methods for surface material removal and surface smoothing. The working group for measuring development precision consists of relevant institutes

and companies. The relationship of technical expense in these two groups is about 50:50, together 3 Million Euro.

Nanometer Optical Components (NOK)	optic dimen-sion	goal tolerances for **manufacturing**				goal **measuring** uncertainty		
		slope deviation		surface shape deviation		slope deviation		shape deviation
surface form	mm length	Nrad rms	arcsec rms	nm rms	nm p-v	nrad rms	arcsec rms	nm rms
1 plane	300 / 150	150 / 100	0.03 / 0.02	3 / 1.5	10 / 7	50 / 30	0.01 / 0.007	1 / 0.5
2 sphere	300 / 150	250 / 100	0.05 / 0.03	3 / 1.5	10 / 7	80 / 50	0.017 / 0.01	1 / 0.5
3 nonsphere cylinder, torus, ellipse	300 / 150	300 / 200	0.06 / 0.05	6 / 3	20 / 15	80 / 50	0.017 / 0.01	2 / 1

Tab. 2 Goals of the surface precision for Nanometer Optical Components (NOK)

The specified goal of the cooperative project is presented with some values (Tab.2). In the technologically working group the project partners apply the four different finishing methods to produce components, for instance, at a 100 mm long plane substrate with 0.02 arcsec rms for the slope error, and shape deviations of less than 1 nm rms. The microroughness of the nanometer optical components, of course, must be in the range needed, in SR research, less than 0.5 nm rms. The measurement working group develops measuring methods and facilities with the goal of about 30 % measuring uncertainty of that top values, e.g. < 0.01 arcsec rms for the slope measuring uncertainty, respective high measuring uncertainty in the range of 0.3 nm rms. On the way of the realization for these high requirements a new ultraprecision coordinate measuring facility for nanometer optical components is in construction at BESSY. In other institutes and companies other new measuring methods will be developed. Plane calibration mirrors will be produced and proofed at the different measuring labors of the relevant project partners and the measuring results will be subjected to comparisons and discussions about the measuring uncertainties in ranges of less than 1 nm rms.

Some nanometer optical components produced and measured in this way will ultimately serve as demonstrators and utilized as mirrors or gratings in a SR beamline at BESSY.

References
[1] Lammert, H, F. Senf, F. Eggenstein, U. Flechsig, R. Follath, S. Hartlaub, T. Noll,
    G. Reichardt, J.S. Schmidt, M. Weiss, T. Zeschke, W.B. Peatman, and W. Gudat;
    Nucl. Instr. and Meth. A 467-468 (2001) 488 - 491
[2] Lammert, H, Senf, F.; NOK-Ausarbeitung. BESSY, NOK-internal, Aug.8, 2000
[3] Biers, J.D.; J.Opt.A: Pure Appl. Opt. (UK) 1 (1999) 1-14,
[4] Takacs, P.Z., Qian, S.-N.; US Pat. 4,884,697; Intern'l Class: G01B 009/02, filed: June 21, 1988
[5] Lammert, H.; Senf, F.; Berger M.; Proc. of SPIE, Vol 3152 (July 1997), 168-179
[6] Lammert, H., Int. Workshop Metrology for X-ray and Neutron-Optics,
                                APS Argonne US, March 2000
[7] Lammert, H., Statusbericht NOK-Forschungsverbundprojekt, CC UPOB e.V.-internal
                                Braunschweig, Okt.26, 2001

Nanometer Optik Komponenten

Variable Orientation of Linear Polarisation from UE56-1

A.Gaupp, D.Abramsohn, J.Bahrdt, W.Frentrup, H.-Ch.Mertins, M.Scheer, F.Senf, Th.Zeschke, BESSYmbH

The polarisation of synchrotron radiation is widely used. In particular the study of magnetic phenomena has greatly benefitted from the large circular dichroism available at the 2p and 3p edges of transition metals. Anti-ferromagnetic effects are of special interest as they have found extensive technical applications in e.g. exchange-bias read-heads and spin valves.

Since anti-ferromagnets have no net magnetisation the magnetic circular dichroism can not be exploited. The approriate effect is the linear dichroism, i.e. the dependence of the response of the sample (like photoemission intensity, reflection, transmission etc.) on the orientation of the linear polarisation with repect to some axis inherent to the sample is to be detected.

To detect the linear dichroism requires either a rotation of the probe or a rotation of the plane of polarisation. There are situations when a rotation of the sample is not feasable, e.g. when a bulky cryostat is involved. Also a rotation of the sample usually exposes a different spot on the sample surface (cf. [1]). Usually an arbitrary orientation with respect to the laboratory is needed, and a continuous tuning of the plane of polarisation between horizontal and vertical orientation is desirable.

In this note we report on the coherent superposition of the radiation from the two units of undulator UE56-1 using the plane grating monochromator beamline to yield linearly polarised radiation with an adjustable orientation.

The APPLE II design [2] is made to generate circularly polarised radiation from a planar undulator. It consists of two rows of magnets above and two rows below the ring plane. One row from each pair can longitudinally be shifted controlling the polarisation [3]. Simultaneously moving both rows into the same direction changes the polarisation from horizontal linear into circular and into vertical linear. The substantial magnetic force between the upper and lower magnetic structure (in the order of 10 kN/m) changes its sign from maximum attraction

to maximum repulsion. Changing the shift parameters in an antisymmetric mode linear polarisation at an adjustable orientation is generated. This causes *longitudinal* magnetic forces on the upper and lower pair of rows of comparable strength.

These forces must have been taken care of by construction. The BESSY double undulators of type UE56 allow only for symmetric motion of the rows, and linear polarisation can only be generated in the horizontal and in the vertical plane (besides, of course, circular polarisation). Intermediate orientations of the plane of linear polarisation are not possible.
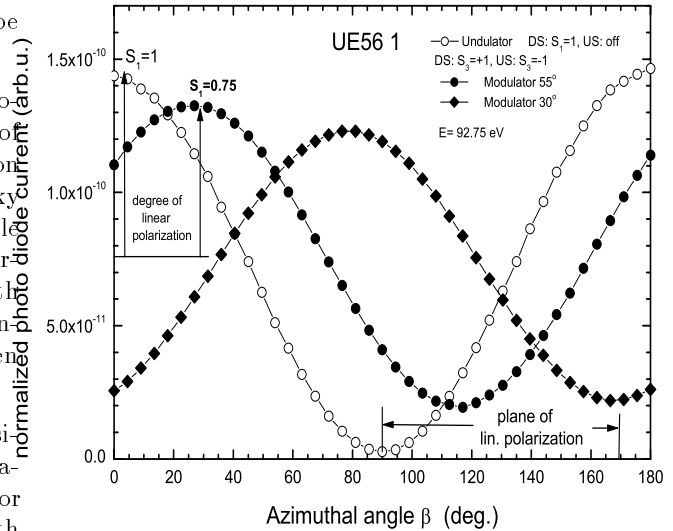

Figure 1: Azimuthal scan of the analyser taken with only one undulator unit with shift=0 (open symbols), and with both undulator units with opposite shifts set for $S_3 = \pm 1$ for two different settings of the modulator. Data are normalised to have a common mean value. The phase slippage in the modulator rotates the plane of polarisation as indicated in one case by the distance between two minima. Finite emittance reduces the maximum linear polarisation which is the modulation depth of the curves.

We use the modulator of UE56-1 to superimpose two circularly polarised beams of the same wavelength and of opposite helicity to generate linearly polarised light at a controllable orientation. The modulator is a magnetic chicane in between the two undulator units causing a phase shift between the two light waves generated in the two undulators without any net deflection to the electron beam. It is adjusted by mechanically rotating cylindrical permanent magnets.
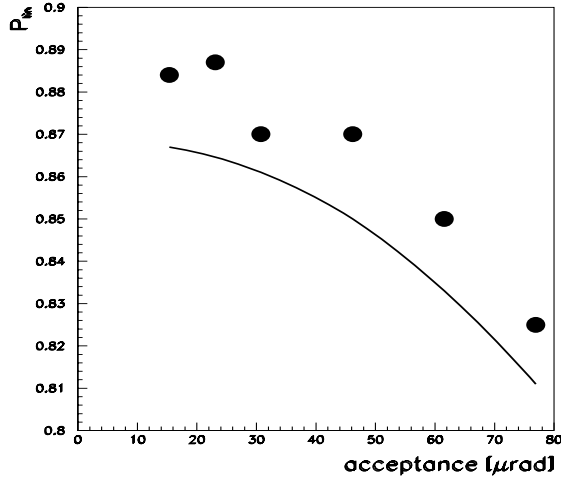

Figure 2: Measured degree of linear polarisation versus beam line acceptance (symbols) in comparision to WAVE calculations (line).

The measurement were done using the BESSY polarimeter [4] at the UE56-1/PGM-1 beamline at a photon energy in first harmonic of undulator radiation near 93 eV. The natural photon beam divergence of $\sqrt{\lambda/L} = 80\,\mu rad$ is much larger than the electron beam divergence which is less than $10\,\mu rad$. An analytic estimate of the degree of polarisation [5] gives values from 0.4 up to 0.98 depending on the acceptance of the beamline. Experience indicates the existence of other so far unknown polarisation reducing mechanisms [6]. - The spectral resolution was $\frac{E}{\Delta E} = 2500$.

As optical elements in the polarimeter we use Mo/Si multilayers. A transmission multilayer with 50 periods of 10 nm each was used as a phase shifter, and a reflecting multilayer at an incident angle around 45° with 100 periods of 9.4 nm each was used as an analyser. In part of the measurements only the analyser was used (see fig. 1). - Data are normalised to the current measured at the refocussing mirror of the beamline.
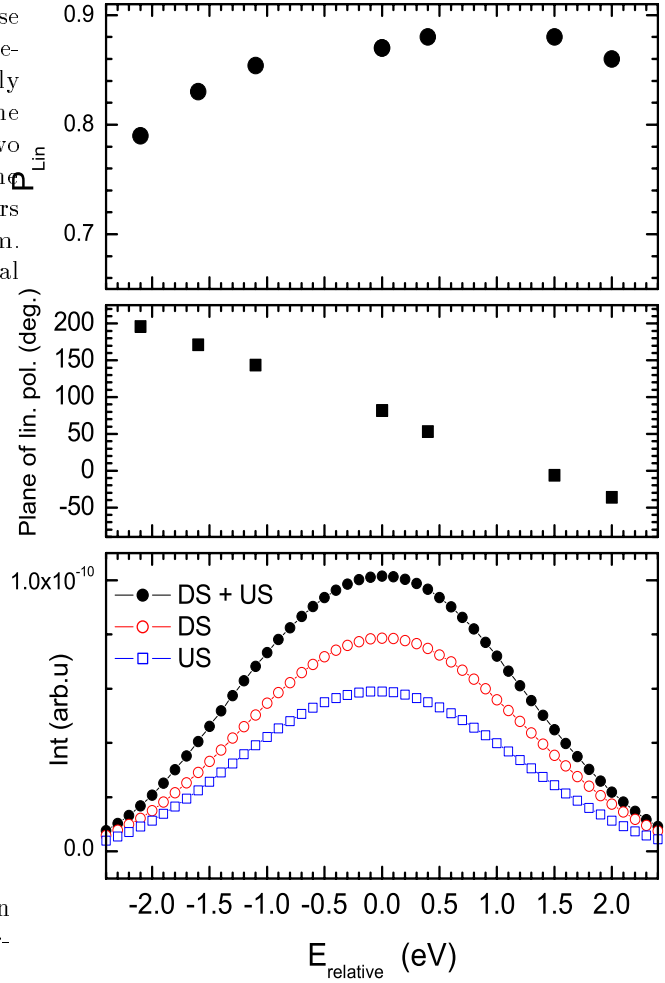

Figure 3: Degree of linear polarisation (top panel), orientation of the plane of polarisation (center panel), and intensity of the undulator units separately (bottom panel, open symbols) and of both undulator units (full symbols, not to scale) near the first undulator harmonic.

The data with phase shifter are analysed as described in [4]. This yields among others the analysing power of the reflector. The measurements using the analyser only thus result in the degree of linear polarisation and in the orienation of the plane of the polarisation (see fig. 1).

Using both undulators in helical mode with different settings of the modulator we observe a degree of polarisation $P \approx 0.85$. The remaining intensity is mostly unpolarised. The distribution between S_1 and S_2 depends on the setting of the modulator. S_i are the normalised Stokes parameters [4].

In fig. 2 the dependence of the degree of polarisa-

tion versus acceptance is shown. The uncertainty of the experiment is estimated to be a few percent. The solid line is the simulation done with the code WAVE [7]. The trend of the data is well reproduced. The systematic difference is considered to be non significant. The analytic estimate [5] (not shown) does not fit the data at all.

The variation of the linear polarisation within the first undulator harmonic was analysed as shown in fig. 3 An unequal intensity of the two modules (bottom panel) was accepted to maintain the two harmonics at the same photon energy. (Note: In the experiment the pass band of the monochromator was fixed and the undulator harmonic was tuned). As shown in the central and upper panel the orientation of the polarisation ellipse and the degree of linear polarisation vary significantly with photon energy.

Fig.4 shows the orientation of the linear polarisation as function of the phase shift introduced by the modulator. The phase shift is obtained from magnetic measurements of the modulator magnets by calculating the electron path lengthening due to the deflection in the modulator. The linear de-
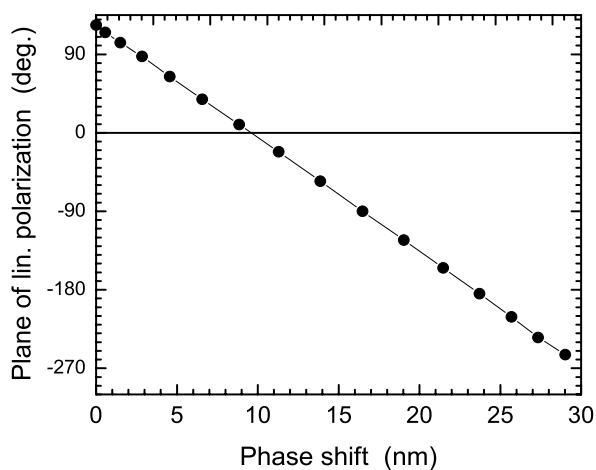
Figure 4: Orientation of the linear polarisation against horizontal plane *vs.* phase shift (in nm) in the modulator. Data have been taken by rotating the modulator magnets in steps of 5°.

pendence indicates a good consistency. The degree of polarisation is found to be independent of the modulator.

In summary it has been shown that the two circularly polarised beams of opposite heliticity from the UE56-1 double undulator can be superimposed to yield linearly polarised radiation with an arbitrary, easily variable orientation of the polarisation ellipse. The degree of polarisation exceeds 0.85. The performance at higher photon energies needs to be determined.

References

[1] H.Ch.Mertins, F.Schäfers, A.Gaupp, Deutsches Patent DE 199 63 537 A 1 (1999) and Euro Phys.Lett.55 (2001) 125.

[2] S.Sasaki, K.Miyata, T.Takada, Jpn.J.Appl.Phys. 31 (1992) L1794.
S. Sasaki, K. Kakuno, T. Takada, T. Shimada, K. Yanagida, . Miyahara, Nucl. Instr. Meth. A331 (1993) 763-767.

[3] M.Weiss, R.Follath, K.J.Sawhney, F.Senf, J.Bahrdt, W.Frentrup, A.Gaupp, S.Sasaki, M.Scheer, H.-Ch.Mertins, D.Abramsohn, F.Schäfers, W.Kuch, W.Mahler, Nucl.Instr.Meth. A467-468 (2001) 449.

[4] F.Schäfers, H.Ch.Mertins, A.Gaupp, W.Gudat, M. Mertin, I.Packe, F.Schmolla, S.DiFonzo, G.Soullie, W.Jark, R.Walker, X. LeCann, R.Nyholm, M.Eriksson, Appl.Optics 38 (1999) 4074.

[5] K.J.Kim, Nucl.Instr.Meth. 222 (1984) 11.
K.J.Kim estimates the polarisation including inhomogeneous broadening by divergence σ_θ at a wavelength λ for an undulator of length L as
$P = \frac{1}{\sqrt[4]{1 + (\frac{2\pi}{\lambda} \frac{L}{2} \sigma_\theta^2)^2}}$

[6] W.B.Peatman, J.Bahrdt, A.Gaupp, F.Schäfers, F.Senf, BESSY Annual Report 1992, 499. the two units of undulator UE56-1 to yield linearly polarised radiation with an adjustable orientation.

[7] M.Scheer, BESSY, unpublished.
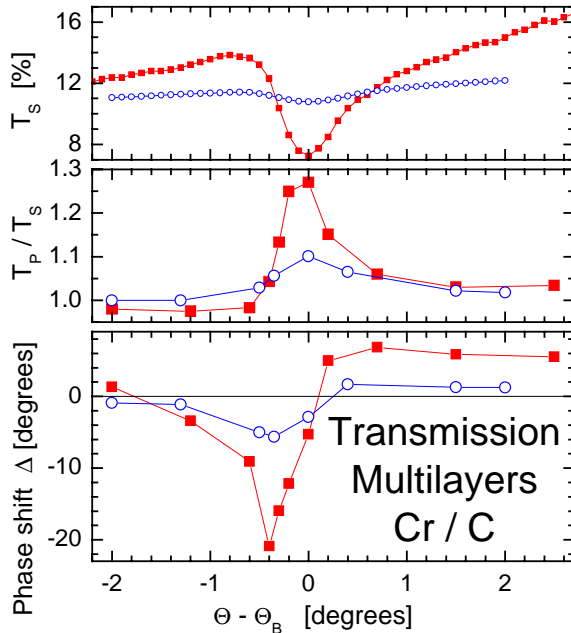
DEVELOPMENT OF COMPONENTS FOR POLARIZATION ANALYSIS

H. Grimmer [1],   O. Zaharko [1],   M. Horisberger [1],   H-Ch. Mertins [2],   D. Abramsohn [2],   F. Schäfers [2], Ch. Klemenz [3]

[1]*Laboratory for Neutron Scattering, ETHZ & PSI, CH-5232 Villigen PSI, Switzerland*
[2]*BESSY GmbH, Albert-Einstein-Strasse 15, D-12489 Berlin, Germany*
[3]*AMPAC, University of Central Florida, Orlando, Fl 32816-2455, USA*

The polarization state of a soft X-ray beam can be determined using a transmission multilayer as phase shifter and a reflection multilayer at a grazing angle $\Theta = 45°$ (Brewster angle) as analyser for photon energies E < 600 eV; for higher energies either magneto-optic effects or single crystals may be used [1]. A transmission multilayer with much larger phase shift than available previously and a corresponding reflection multilayer, both consisting of 100 Cr/C bilayers, have been developed at PSI and tested at BESSY. The analyser has a period d = 3.13 nm and a reflectance for s-polarized radiation R_S >19% for energies close to the Carbon K edge (274-281 eV). Its reflectance ratio for s- and p- polarized radiation is R_S/R_P > 400 in this range with a peak value 1400 at 278 eV, where the Bragg angle $\Theta_B = 45°$ [2]. Calculations gave a period d = 3.96 nm for a Cr/C phase shifter with maximum figure of merit $\sin \Delta \cdot \sqrt{T}$, where Δ denotes the phase shift and T the transmission. The following figure shows that the phase shift is about 3 times larger than obtained previously [3].

These multilayers can be used for unambiguous polarisation determination at the Carbon K edge. New reflecting optics for linear polarization analysis above 700 eV has also been investigated. $YBa_2Cu_3O_x$ epitactical layers with c-axis perpendicular to the surface, i.e. a period of 1.174 nm, were grown at EPFL by liquid phase epitaxy on (110) $NdGaO_3$ substrates. Measurements at the BESSY undulator beamline UE56/1-PGM gave $R_S = 10\%$, $R_S/R_P = 200$ at the Barium M_5 edge (780 eV) and $R_S = 3.6\%$, $R_S/R_P = 3400$ at 750 eV, where Θ_B is equal to the Brewster angle.
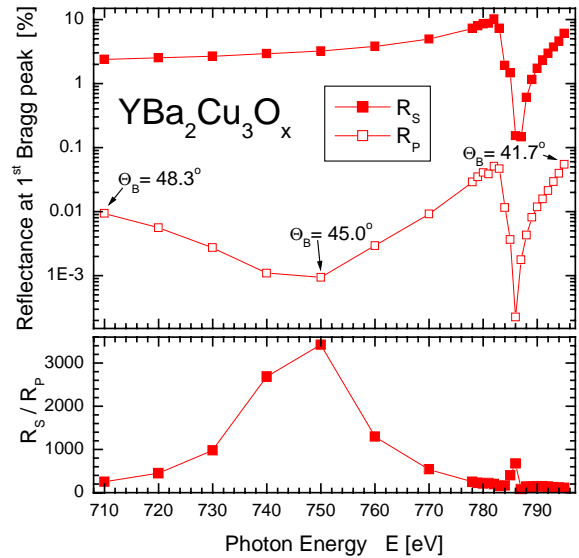
Fig. 2: Bragg peak reflectances R_S and R_P in % and their ratio R_S / R_P. Θ_B is the grazing angle at which the Bragg peak appears.

A reflectance maximum at the Cu L_3 edge of 932 eV was also observed. Further investigations have to show the applicability of this sample for polarization analysis in this energy range.

Fig. 1: Transmission T_S, ratio T_P/T_S, and phase shift Δ as functions of the deviation between grazing angle and Bragg angle. Results at 277 eV for our sample (filled squares) and at 275 eV from ref. [3] (open circles).

[1]   F. Schäfers et al., Appl. Optics, **38** 4074 (1999)

[2]   H. Grimmer et al., Surface Rev. and Letters, (in press)

[3]   S. Di Fonzo et al., Rev. Sci. Instrum. **66** 1513 (1995)

X-ray fluorescence spectroscopy at U41-PGM by means of ROSA - present status and first results

1) R. Szargan, K.-H. Hallmeier, R. Hesse, A. Kopczynski, S. A. Krasnikov, L. Zhang; 2) T. Chassé; 3) O. Fuchs, C. Heske, E. Umbach; 4) S. Molodtsov, F. Schiller, C. Laubschat; 5) C. Jung, W. Braun

1) Wilhelm-Ostwald-Institut für Physikalische und Theoretische Chemie der Universität Leipzig; 2) Institut für Oberflächenmodifizierung e.V. Leipzig; 3) Lehrstuhl für Experimentelle Physik II der Universität Würzburg; 4) Institut für Oberflächen- und Mikrostrukturphysik der Universität Dresden; 5) BESSY G.m.b.H. Berlin

Introduction

The **ro**tatable **s**pectroscopy **a**pparatus ROSA was built in order to open research opportunities for exploiting new features of the soft X-ray emission spectroscopy (SXES). Basing on the high brightness and the polarization selectivity of the monochromatized BESSY II radiation excitation the present ROSA experiments are focused on the following SXES probing capabilities [1]:

- site selective local and partial density-of-states probing at chemically non-equivalent sites of the same atomic species applying tuned energy selective excitation;
- enhancing of the inelastic X-ray scattering by tuning the excitation energy to specific absorption states. This resonant one-step scattering (RIXS) process may give an ultimate resolution below the core-state-lifetime limitation;
- probing of the various symmetry states of the valence band of two-dimensional as well as ordered and non- ordered multilayer systems by detection of electron and fluorescence emission at different angles with respect to the polarization plane of the synchrotron radiation.

Probing of the molecular alignment and bonding in highly oriented layers by detecting the X-ray absorption (via electron yield measurement) at different angles between the sample surface and the polarization plane of the synchrotron radiation supplements the SXES research.

This paper reports on the first ROSA beam time application in October/November 2001.

ROSA design and instrumentation

ROSA is a two-chamber system for UHV preparation and analysis of solid samples and thin layers by means of LEED, photoemission and X-ray fluorescence spectroscopy (Fig. 1). The preparation chamber was designed for standard surface treatment, monolayer and multilayer deposition from gaseous atmospheres and epitaxial growing procedures. The spectroscopic investigations can be carried out rotating the whole analysis chamber equipped with the electron energy analyser and the X-ray fluorescence monochromator perpendicularly arround the beam axis. By this rotation the angle resolved information on polarization and symmetry dependence of the X-ray absorption and emission can be obtained simultaneously with the energy dependence of the resonantly excited electron and fluorescence emission at the absorption thresholds.

Presently ROSA is equipped with:

- X-ray monochromator XES 300 for the range 50 eV ... 1000 eV [2,3];
- Electron energy analyser EA 10;
- Er LEED 150;

- Manipulation system for sample cooling/heating (180K/1200K) and two-axis rotation/tilting [4].
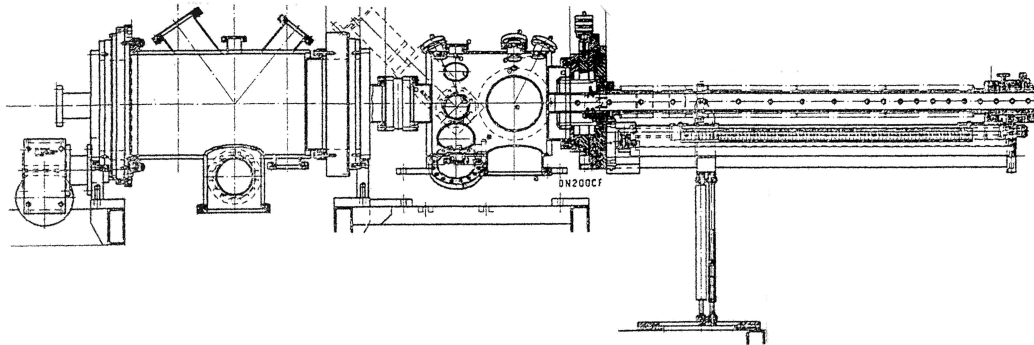

Fig. 1. Schematic side view of ROSA: Manipulator (right), preparation chamber (center) and rotatable analysis chamber with beam entrance (left) [4].

The first commercially available X-ray monochromator XES 300 (Fig. 2) equipped with three spherical blazed gratings using Rowland circle geometry optimized for photon energies 400 eV, 280 eV and 100 eV, respectively, was commissioned after substantial software development [5] in October 2001.
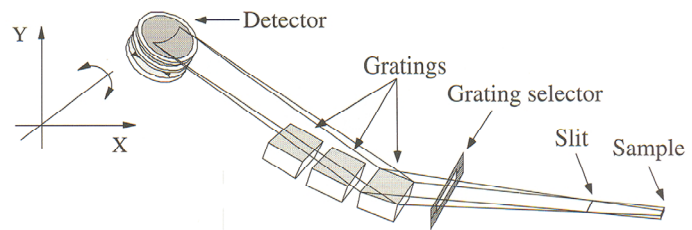
Fig. 2. Schematic setup of the X-ray mono-chromator XES 300 [2,3].

Results

The first X-ray fluorescence spectra measured at the U41-PGM beamline cover the energy range between 100 eV and 850 eV from the Si $L_{2,3}$ to Ni $L_{2,3}$ emission bands. In Fig. 3 the S L emission spectra of oxidized CdS crystals are shown consisting of a strong peak and some features below 160 eV which can be assigned to "3s"→2p transitions from the lower (S3s), central (Cd4d) and upper valence band (UVB). The progressing oxidation of the material during the UV exposition creates S-O species contributing transitions from S3d dominated electronic states above 160 eV.
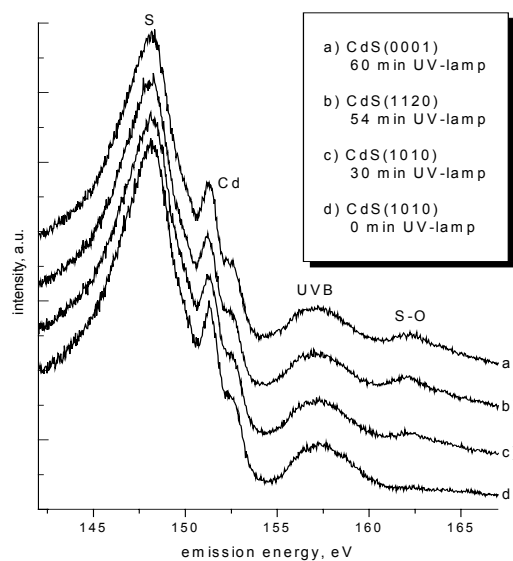
X-ray fluorescence spectra of the Si L emission from the buried Si layers inside a stack composed of 50 Mo/Si double layers (single thickness 6.7 nm) have been recorded in dependence on the energy of the exciting photons and displayed in Fig. 4. The Si L spectra are governed by contributions from amorphous Si and some Mo-silicides, which have formed at the internal Mo-Si interfaces. The individual

Fig. 3. Non-resonant $SL_{2,3}$ emission spectra from oxidized CdS crystals.

spectra reveal only minor differences compared to the reference spectrum taken at 175 eV, which is shown in the top part of the figure. These differences may be traced back to a peak shifting systematically with the exciting radiation as demonstrated in the difference spectra in the bottom part of the figure.
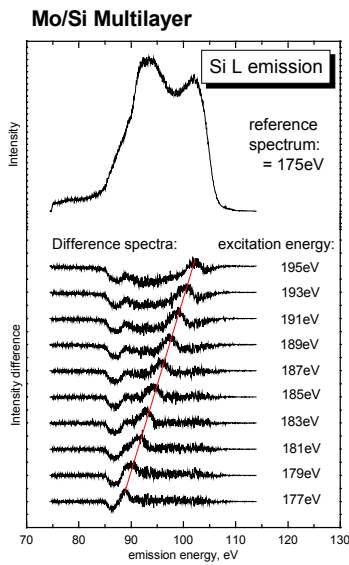

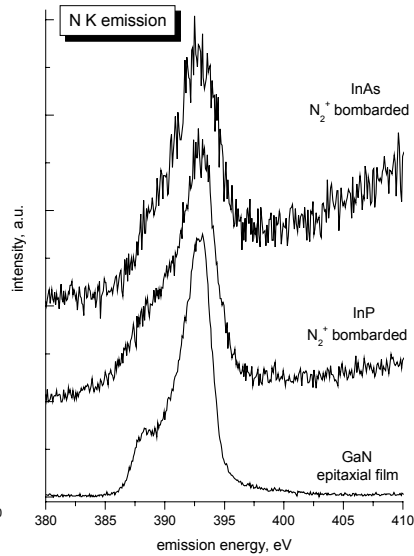Fig. 4. X-ray fluorescence spectra of the Si L emission in Mo/Si multilayer.
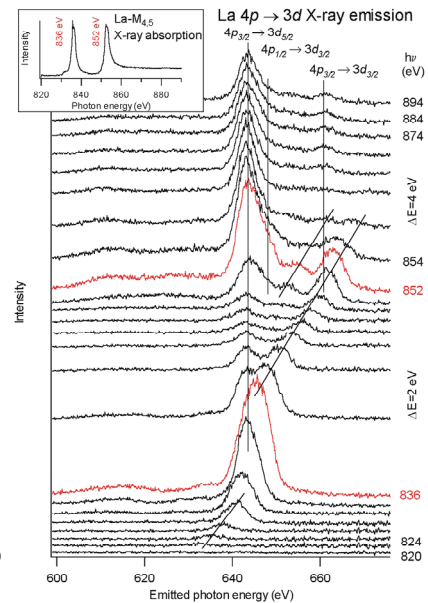
Fig. 5. N K emission of nitrogen ion bombarded surface.

Fig. 6. 1st order La 4p → 3d X-ray emission.

The X-ray fluorescence spectra of the N K emission recorded from semiconductor surfaces following nitrogen ion beam-assisted nitridation have been recorded in comparison to N K emission spectra of an epitaxial film (300 nm) of hexagonal GaN, shown in Fig. 5. In-N species could be detected in both samples also known from photoemission investigations of nitrided InAs surfaces.

Figure 6 displays 1st order XES spectra of La metal taken in the region of the 4p radiative decay of the 3d core holes excited at the $M_{4,5}$ absorption thresholds (see inset). The spectra reveal two different groups of features. Emission peaks, which do not change their positions upon variation of excitation energy, can be assigned to the direct 4p→3d decays. Features rigidly shifted toward higher emission energies with increasing excitation energy can be interpreted as due to Bremsstrahlung of resonantly excited 4p photoelectrons or due to an energy-loss caused by a 4p→4f electron transitions in the radiative decay of the 3d hole. Both groups of features reveal resonant enhancements at the M_4 and M_5 thresholds. Between these two edges the intensities are suppressed presumably due to a Fano-antiresonance-like behavior.

References:
[1] J. Nordgren, E. Z. Kurmaev, J. Elec. Spec. Rel. Phen. Special Issue, 110-111 (2000).
[2] Gammadata/Scienta AB, Uppsala.
[3] J. Nordgren, J. Guo, J. Elec. Spec. Rel. Phen. 110-111 (2000) 1.
[4] PINK GmbH, Vakuumtechnik, Wertheim.
[5] O. Fuchs, Diplomarbeit, Universität Würzburg, 2001.

Characterization of the new transmission X-ray microscope at BESSY II

P. Guttmann, B. Niemann, S. Rehbein, D. Rudolph, G. Schmahl

Institut für Röntgenphysik, Georg-August-Universität Göttingen,
Geiststraße 11, 37073 Göttingen, Germany

The new Göttingen transmission X-ray microscope (TXM) is the first instrument working at an undulator beamline in the soft X-ray region. The undulator U41 at the electron storage ring BESSY II was especially optimized for this application. The optical layout and the new condenser-monochromator concept are shown in Fig.1 [1,2].
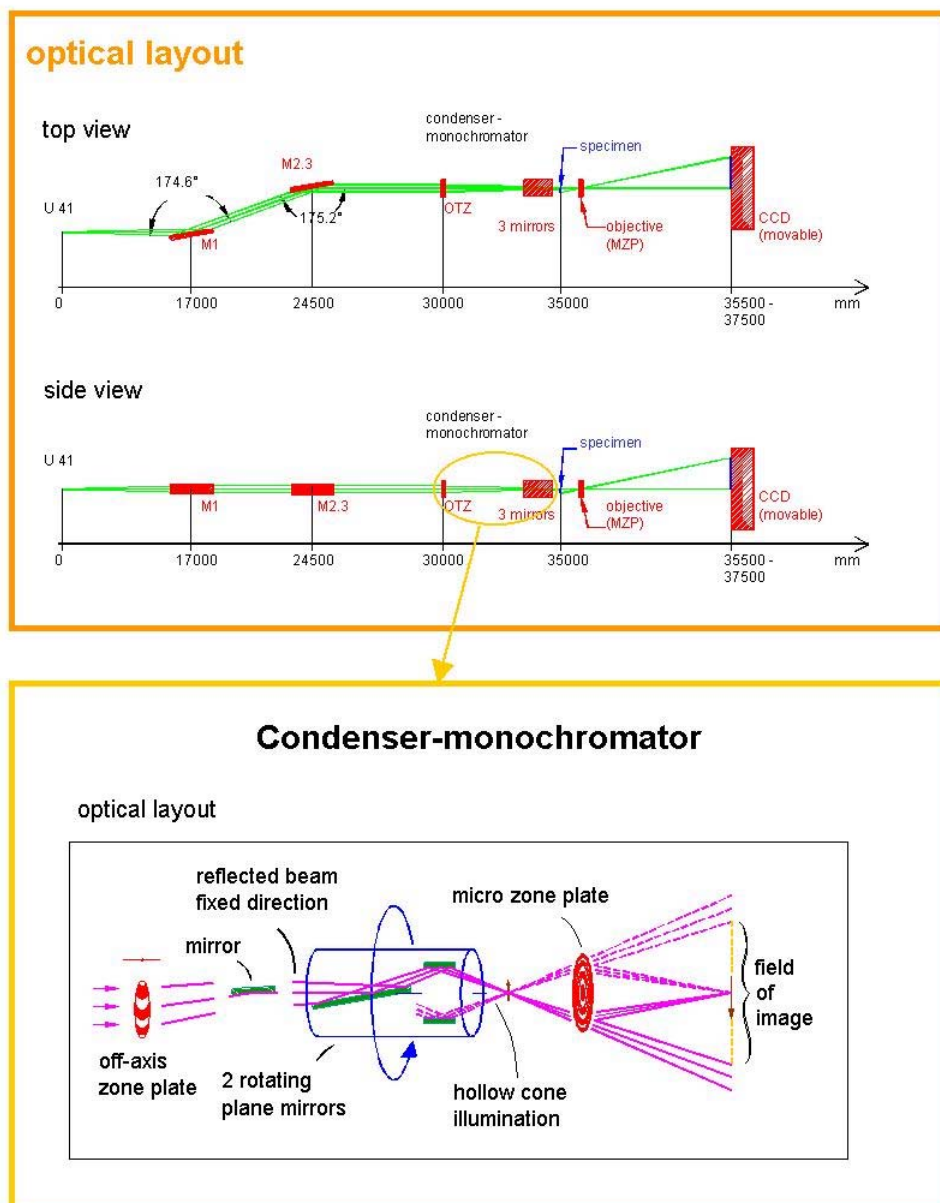

Fig. 1. The optical layout of the transmission X-ray microscope at BESSY II.

For adjustment purposes several beam monitors are incorporated. A vertical movable hole with 1 mm diameter is placed in 1.1 m distance downstream from the first mirror M1 to adjust it. Two luminescent screen pairs with adjustable perpendicular slits in a distance of 1.8 m resp. 8.4 m downstream from mirror M2.3 are used to adjust this mirror and the off-axis transmission zone plate (OTZ). A vertical movable GaAsP-photodiode 8.5 m downstream to M2.3 give the possibility for quantitative measurements e.g. of the efficiency of the OTZ. Two luminescent screens in the middle above the mirror M3 display the position of the incoming beam. In a distance of about 15 cm behind the micro zone plate MZP a luminescent screen with a central hole monitors the zero order radiation of the MZP.

A rotating mirror system RK35 which has the same aperture as a micro zone plate (objective) with 35 nm outermost zone width was used to demonstrate the possibilities of the instrument. The mirrors of this system have to be fixed on a support plate with exactly 90° between the support plate and the mirror surfaces otherwise the beam will oscillate in horizontal direction during the rotation of the mirrors. The rotation axis of the system has to be adjusted in the direction of the beam. This is done by using a laser beam defining the optical axis of the microscope which is identical to the incoming beam direction. The fine adjustment can be done with the X-rays. The focal spot of the condenser monochromator can be adjusted by moving the RK35 in beam direction separately to the outlet window of the system. For this, a luminescent screen can be fixed on the micro zone plate holder at the object position. A normal CCD camera with an optical system is used to magnify the resulting light spot. Figure 2 shows the dependence of the horizontal oscillation from the distance to the luminescent screen.
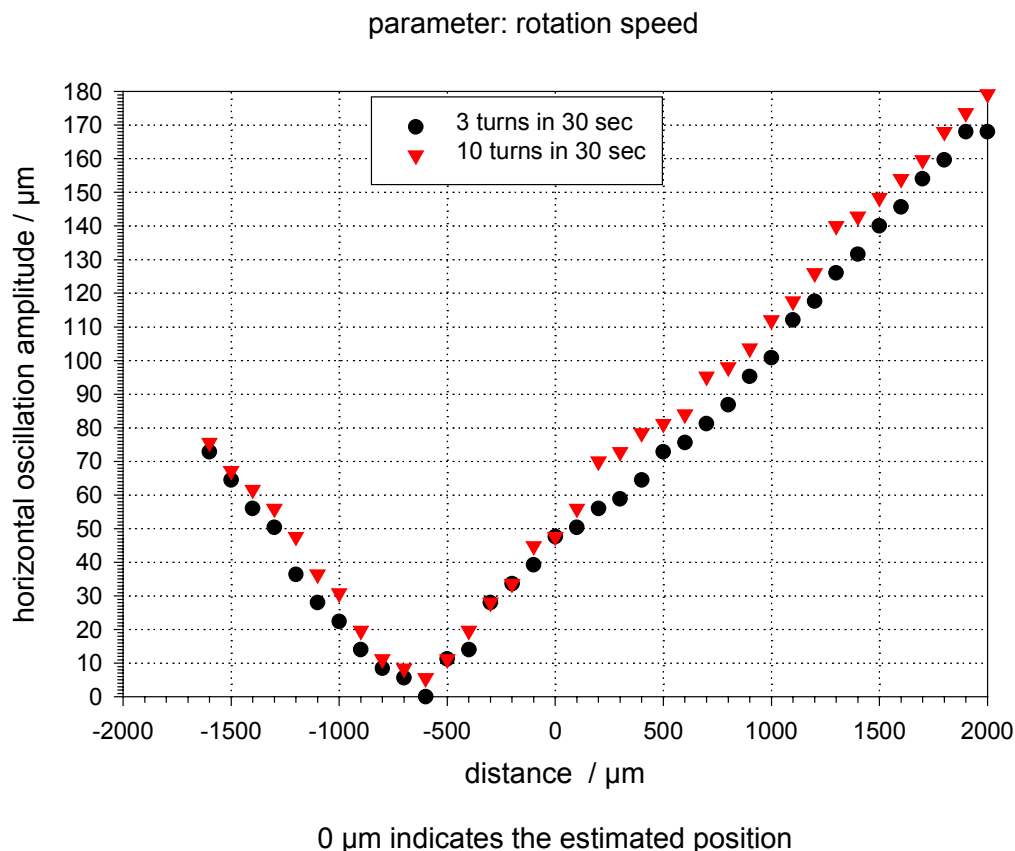

Fig. 2. The dependence of the horizontal oscillation of the light spot produced by the rotating mirror system RK35 from the distance of it to the object plane.

The off-axis transmission zone plate OTZ has a focal length of 4.2857 m for 2.4 nm wavelength and is built by electron-beam lithography. Only a segment of 4 mm diameter is needed with radii of the zones between 15.55 mm and 19.55 mm, resp. zone widths between 327 nm and 260 nm. OTZs with Ni or Au for the zone structures are not stable in the undulator beam unless the thickness of the zones are very low which results in a low efficiency. The reason for this is, that the higher order radiation of the undulator is absorbed effectively in the "opaque" zones and will heat the OTZ. These problems can be avoided by using Si for the zone structures because Si is more transparent for higher order radiation present when using the TXM in the water window. In this case the zone plate structure is transferred directly into the Si-support foil. The best efficiency reached recently for this type of zone plates is 12% at 2.4 nm wavelength. There will be the possibility to increase this by optimizing the production steps.
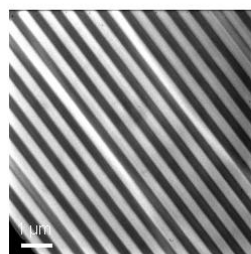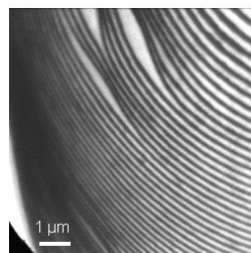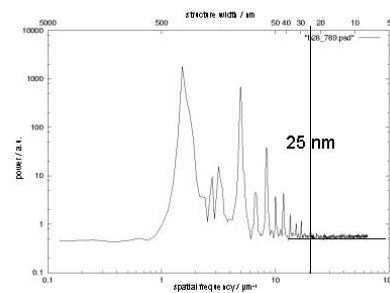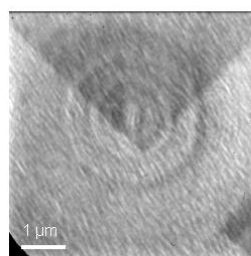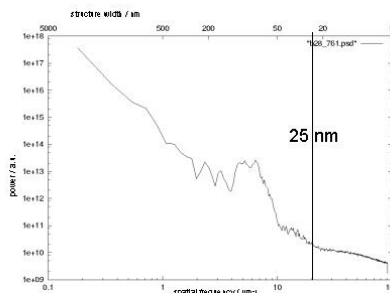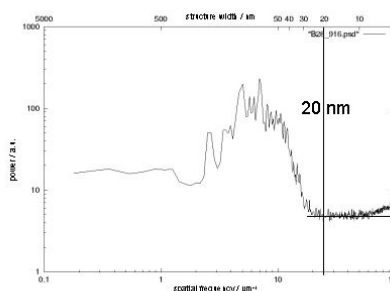

Fig. 3. Images of test patterns and the power spectra calculated from them to determine the cutoff frequency of the microscope.

In the past we could not reach the expected flux in the object plane because we have used OTZs with about 3% efficiency and we have problems due to the C-contamination of the RK35 mirrors. By using a RK70 the influence of the contamination can be reduced due to the smaller incident angles. For the RK35 a flux reduction in the order of one magnitude was measured which is explainable with the increased micro-roughness of the C- contamination layer of about 5 nm rms instead of 1 nm rms for the original micro roughness of the Ni coating. Very recently we could demonstrate that with the RK70 exposure times in the order of 1 sec for wet specimens are possible at an X-ray magnification of 3156 x using a micro zone plate with $dr_n = 30$ nm.

Images of test pattern (Fig.3) were made to demonstrate the resolution reached with the new transmission X-ray microscope at BESSY II using a RK35 mirror system. A power spectrum of the image is used to determine the cutoff frequency of the microscope [3].

At the scanning transmission X-ray microscope beamline a chamber was installed to perform radiation induced cross-linking of polymers which are necessary to produce high resolution zone plates [4]. In this case the used undulator beam was only reflected by the first mirror M1 in the beamline. No further optical components are in the beam.

Acknowledgements

References

1. P. Guttmann, B. Niemann, J. Thieme, D. Hambach, G. Schneider, U. Wiesemann, D. Rudolph, G. Schmahl: „Instrumentation advances with the new X-ray microscopes at BESSY II", in: Nucl. Instrum. Meth. A (2001), 849-852

2. B. Niemann, P. Guttmann, D. Hambach, G. Schneider, D. Weiß, G. Schmahl: „The new condenser-monochromator with dynamical aperture synthesis for the TXM at an undulator beamline at BESSY II", ibid., 857-860

3. S. Vogt, G. Schneider, A. Steuernagel, J. Lucchesi, E. Schulze, D. Rudolph, G. Schmahl: „X-ray microscopic studies of the *Drosophila* dosage compensation complex", J. Struct. Biol. **132** (2000), 122-132

4. D. Weiss, M. Peuker, and G. Schneider: „Radiation-enhanced network formation in co-polymer galvanoforms for diffractive nickel optics with high aspect ratios", Appl. Phys. Lett., **72** (15), (1998), 1805-1807

U41-PGM: some thoughts on improving the photon flux

Ch. Jung and M. Mast

BESSY mbH, Albert Einstein Straße 15,
D 12489 Berlin, Germany

A driving force for the development of the U41-PGM beamline was the future use of x-ray emission spectroscopy in the VUV-range for the analysis of buried interfaces and thin adsorbate films. Despite the opportunities of this technique it suffers from the fact that the efficiency of x-ray emission in the VUV-range is rather poor compared to that of electron emission. Thus, highly brilliant sources are required being able to deliver a high photon flux.

During the first $1^1/_2$ years of operation the U41-PGM has demonstrated that it offers a photon flux of more than 10^{12} photons per second over its working range [1]. For a reasonable energy resolution, this flux is obtained with an exit slit width of 40 μm, resulting in a spot size of 15μm by 55 μm full width at half maximum in the vertical and horizontal direction, respectively.

In fall 2001, a dedicated XES-instrument was put into operation at the U41-PGM. Although the working conditions were not ideal during the first beam time, the results obtained were promising. Part of the characterisation of the beamline was the determination of the available photon flux as a function of the exit slit width. The U41-PGM is equipped with a slit plate carrying seven fixed slits, ranging from 20 μm up to 3 mm (!). For a fixed photon energy of the source (fixed undulator gap) we recorded the undulator harmonic for each of the exit slits using a GaAsP-diode. For the peak current, the absolute photon flux (normalized to 100 mA beam current) was determined.

For a photon energy of 200 eV the result is presented in figure 1. The left hand side shows the resulting photon flux as function of the exit slit width. Up to a slit width of 500 μm, the flux increases linearly with increasing slit width. For a slit size of 2 mm and 3 mm, the gain in
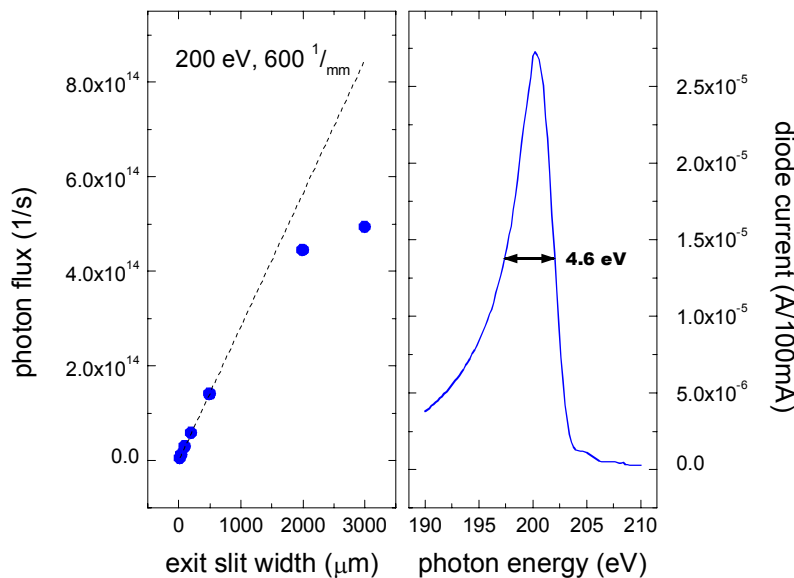

Fig. 1: Left: photon flux at 200 eV for different exit slit widths (the dashed line indicates the expected dependence extrapolated from slit width data below 500 μm). Right: first undulator harmonic at 200 eV (full width at half maximum is indicated).

flux does no longer follow the linear behaviour. This result is not surprising, since the reason for this is quite simple: above 500 μm, the energy resolution is on the order of the full width at half maximum of the undulator harmonic (4.6 eV at an energy of 200 eV, see figure 1). Nevertheless, the flux reaches about 4 x 10^{14} photons per second, about two orders of magnitude higher than for 40 μm slit width.

Unfortunately, this impressive gain in photon flux is accompanied by a significant increase in the size of the focal spot. In addition, the area illuminated on the refocusing toroidal mirror also increases, with the result of significant coma contribution. All in all, the focal spot size for 3 mm exit slit width is about 0.8 mm x 0.2 mm (vertical x horizontal, see figure 2).

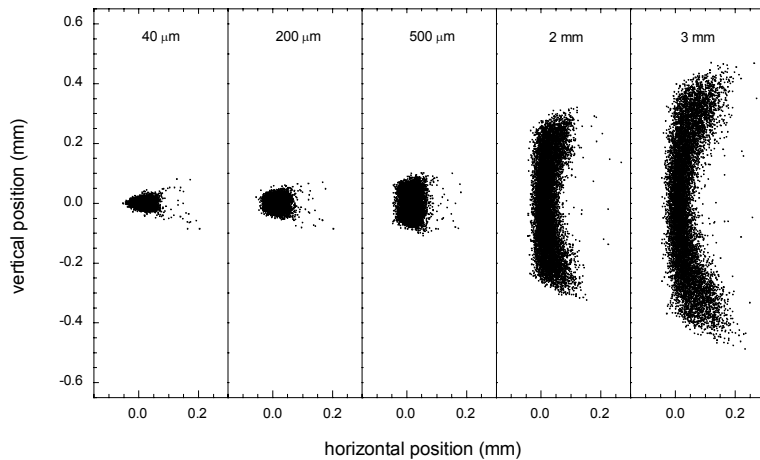It is obvious, that this spot size is not acceptable for x-ray emission experiments. The spectrometers usually are operated with an entrance slit with a width of about 100 μm or less. Opening the mono-chromators exit slit thus does not really improve the experi-mental result. In contrast to this it is desireable to shape the focus in such a way that an entrance slit is no longer required for the spectrometer. The question thus arises: is it possible for the given optical design of the beamline to concentrate the desired photon flux of about 10^{14} photons per second on a spot size of a few square microns?

Fig. 2: Focal spot size for different exit slit widths.

The U41-PGM beamline is currently equipped with a single blazed grating with a line density of 600 $^1/_{mm}$ and a blaze angle of 0.8°. From a detailed mapping of the photon flux as a function of both photon energy and c_{ff}-value, the path for optimal photon flux has been determined [1]. In most experiments the monochromator is operated with optimised photon flux (beside the x-ray emission experiments also EXAFS studies on thin adsorbate films require high photon flux), if required, the c_{ff}-value can be set to obtain a moderate energy resolution.

One way to increase the flux density at the focal spot is modify the line density at the grating. To determine the proper values for line density and groove profile we decided to optimise two gratings: one covering the energy range up to 300 eV (including the carbon K-edge), and a second one for energies up to 600 eV (N 1s, O 1s). Both gratings should still allow to fulfill the on-blaze condition to obtain optimal flux with varying energy. This specification influences the line density, since even for the upper energy limit of each grating the c_{ff}-value needs to be variable between 0.5 and 1.

According to the latter limitation, the turning range (c_{ff}-value as a function of photon energy) of each grating was determined as a function of line density. It turned out, that for the low energy grating a line density of 120 $^1/_{mm}$ is appropriate. Using the well known software code REFLEC [2] we calculated the grating efficiency for different energies as a function of blaze angle and c_{ff}-
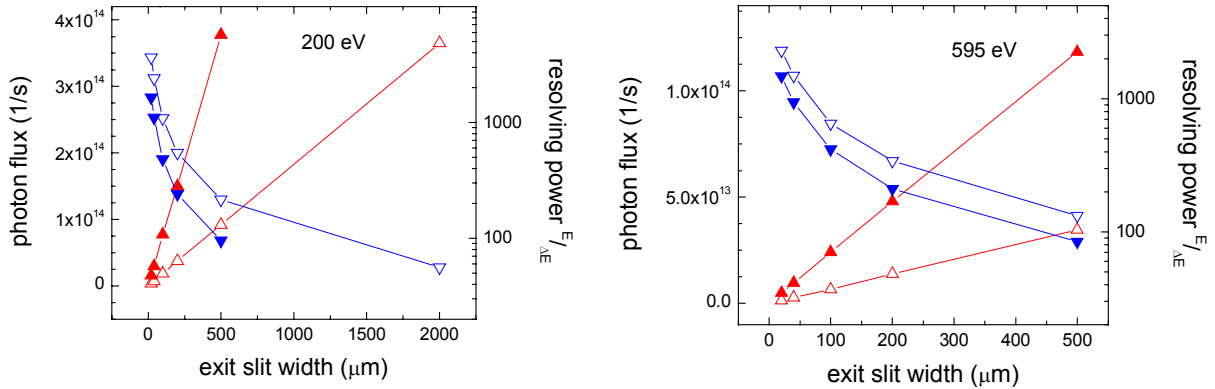
Fig. 3: Photon flux and resolving power as function of exit slit width for two photon energies. Left: 120 $^1/_{mm}$ grating, 0,45 ° blaze; right: 240 $^1/_{mm}$ grating, 0,45 ° blaze (filled symbols). Open symbols: 600 $^1/_{mm}$ grating; up triangle: photon flux; down triangle: resolving power.

value. Best photon flux over the whole energy range is obtained for a blaze angle of 0.45 °. Finally, the calculations were performed for the second grating, resulting in a line density of 240 $^1/_{mm}$ at the same blaze angle.

With these parameters, the performance of the beamline was calculated for different photon energies (with the optimal c_{ff}-value for each energy). The photon flux data and the resolving power for 200 eV (120 $^1/_{mm}$ grating) and 595 eV (240 $^1/_{mm}$ grating) are presented in figure 3 (data for 1st undulator harmonic). From this figure it is obvious that the reduced line density leeds to an increased photon flux at a given exit slit width. In fact, for 200 eV and the 120 $^1/_{mm}$ grating a 500 µm exit slit gives about the same photon flux as the 600 $^1/_{mm}$ grating at 2 mm exit slit width. About the same result is achieved for the 240 $^1/_{mm}$ grating.

As expected, the modification of the line density allows to reduce the focal spot size significantly. Unfortunately it is not possible to feed the desired photon flux through an exit slit of 40 µm width. In addition, the gain in flux is accompanied by a loss in resolving power. A further limitation comes from the fact that a blaze angle of 0.45° is required for the optimised gratings. This angle is on the border of what can be manufactured today.

A second way of improving the flux density available on the sample surface is to design a proper refocusing stage tailored to give a smaller spot often required by the experimental set-up. In this case, the refocusing stage, being part of the experiment, replaces the toroidal mirror used under normal operating conditions of the beamline.

The U41-PGM is well prepared for both options: its grating holder can be equipped with up to three gratings (currently, only one slot is used), and its refocusing stage can be moved out of the synchrotron beam *in situ*.

References:

[1] Ch. Jung et al., Nucl. Instr. Meth. **A 467-468** (2001) 485 – 487;
    see also www.bessy.de/users_info/

[2]   F. Schäfers, M. Krumrey, Technischer Bericht, BESSY TB 201, 1-17 (1996)

RF Cleaning of the U125/1-PGM Beamline

R. Follath and F. Eggenstein
BESSY, Albert-Einstein-Straße 15, 12489 Berlin

Most of the beamlines at BESSY II show a more or less distinctive carbon contamination of the optical elements [1–5]. It is assumed, that gaseous carbon compounds are cracked under the influence of VUV irradiation on the illuminated areas of the mirrors and gratings. In some beamlines even the footprints of the VUV-beam on the optical surfaces are identifiable by brown colorations. The reduction in transmitted flux at the carbon K-edge (284 eV) and above extends to one or two orders of magnitude.

In a recent paper [6] one of us described an in situ cleaning method using a RF induced plasma discharge process in an argon-oxygen mixture to remove the contamination from the optical surfaces. This cleaning procedure was applied to several beamline compounds in the past. In August 2001 all optical elements of the beamline U125/1-PGM [7] were cleaned by this process within one shutdown. It was the first time that all elements of a beamline at BESSY were cleaned without intermediate illumination with synchrotron light.

To judge the impact of the method, the photon flux behind the beamline was determined with an GaAsP-Photodiode before (July 2000, see figure 1) and immediately after the shutdown (Sept. 2001, see figure 2). Figure 3 shows the photon flux in January 2002 after twelve weeks of user operation. In all measurements the photocurrent of the electrically isolated last mirror (M_5) was recorded simultaneously. This is of special importance, because it is usually used as an I_0-signal for the users experiment.

In the flux curves recorded before the cleaning process the carbon contaminations give rise to a strong absorption dip at 284 eV. Approximately 80% of the light is absorbed at this energy before it leaves the beamline. The absorption at the oxygen K-edge at 532 eV extends to 35%. The reason for the small 20% dip at 685 eV is yet unknown. Concerning the absorption dips, the M_5 mirror current shows the same behaviour as the photon flux determined with the GaAsP-photodiode.

Figure 2 shows the photon flux and the M_5 photocurrent after the cleaning process. The dip at the carbon edge is strongly reduced and only 15% of the photon flux is absorbed. Contrary the oxygen dip has increased to 50%. This is certainly due to the oxygen used in the plasma discharge. Obviously the oxygen itself or oxidized compounds stick on or in the optical surfaces even after bakeout. Noticeable is also an overall reduction of photon flux by approximately 10%. It is not clear if this is due to the cleaning process itself or caused by other reasons.

In the measurement after the shutdown, the fifth undulator harmonic is much higher than before. This is no effect of the cleaning process but most probable due to a software failure in the undulator - monochromator - coupling in the measurements before the cleaning process. Unfortunately — as shown in figure 3 — the carbon dip recurred after only twelve weeks of regular user operation and causes an absorption of 65%. Besides that, the photon flux as recorded with the GaAsP-diode remains nearly unchanged.
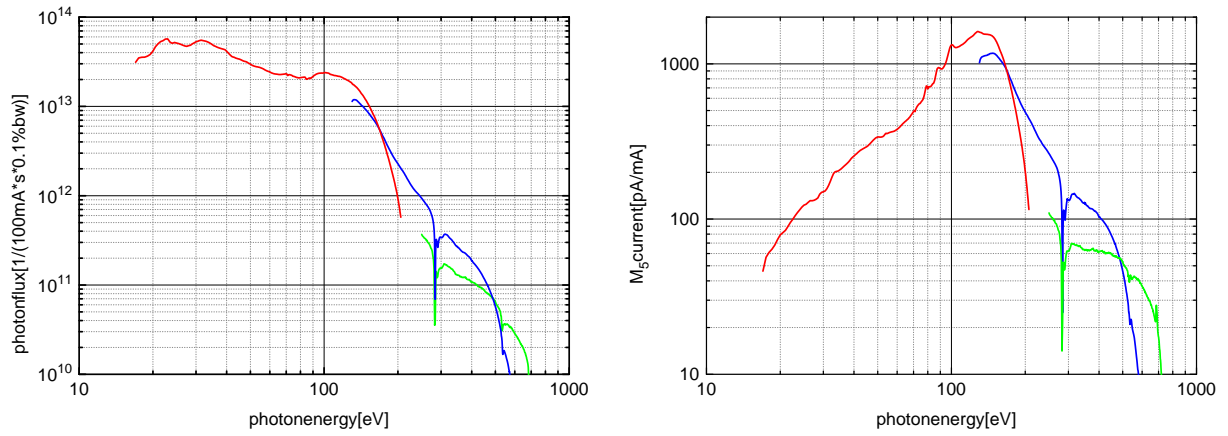
Fig. 1: Measurements before cleaning (July 2000). The flux curves are recorded using the first, third and fifth undulator harmonic. The 300 l/mm grating was operated with c=2.25.
Left: Photon flux measured with a GaAsP photodiode at the end of the beamline.
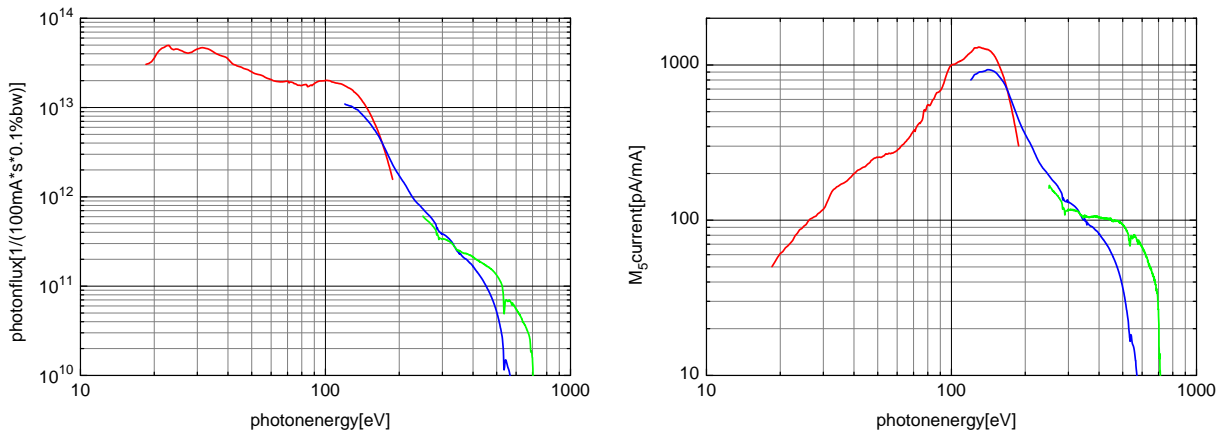Right: Photocurrent of last mirror in the beamline.

Fig. 2: Same as above, measured immediately after cleaning process in September 2001.
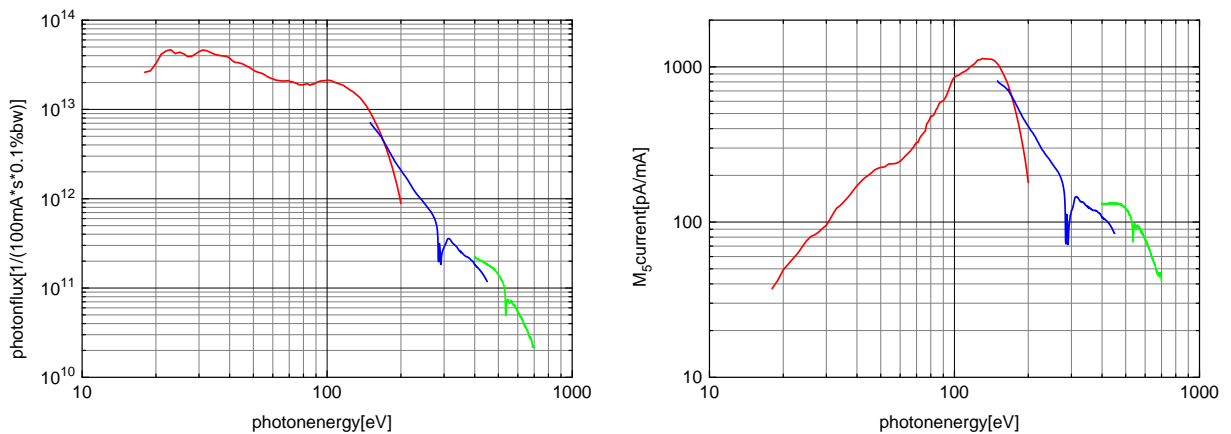

Fig. 3: Same as above, measured after twelve weeks of user operation in January 2002.

In contrast to that, the photocurrent of M_5 showed a systematic change with photon energy after the twelve weeks. The signal was reduced below 170 eV and enlarged above. At 500 eV it was already 30% higher than immediately after the cleaning process. This may indicate that some carbon accumulated on the last mirror.

The effect of a carbon contamination onto the photocurrent is visibly very pronounced on the gold mesh in the ionization chamber. Figure 4 shows the photocurrent of the gold mesh which is used as I_0 detector in the ionization chamber. This section is located before the refocusing mirrors M_4 and M_5. It contains no optical element and was thus never subject to a cleaning process. The signal was recorded simultaneously with the data shown in figure 2. It shows a strong increase when scanning over the carbon edge. This very distinctive step proves that the surface of the mesh is highly contaminated with carbon.
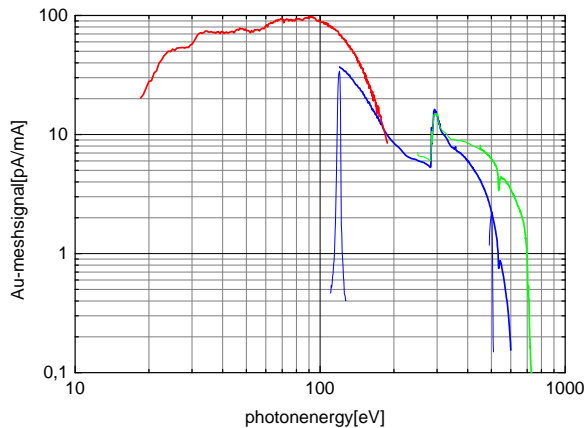

Fig. 4: Photocurrent of a gold mesh located in the ionization chamber measured in Sept. 2001. It was not subject to the RF cleaning process. Its carbon contamination causes a strong increase in photocurrent, when the photon energy is scanned over the K-edge of carbon.
The thin curves are recorded with fixed undulator gap and prove that the undulator - monochromator matching is very good.

The carbon emitts additional photoelectrons when the photon energy is higher than the corresponding binding energy.

The dip in the photocurrent signal at the oxygen edge indicates, that no oxygen contamination is located on the surface of the mesh and the absorption of this photons occurs at the optical surfaces before the gold mesh.

conclusion

The described RF-cleaning process removes carbon contaminations on optical surfaces very efficiently, leading only to a small increase of oxygen contamination. It does not prevent the surfaces effectively from being contaminated again. The rate of contamination will be monitored over the next year.

References

[1] F. Senf et al.: *annual report* **1999**, p. 512.

[2] D. Batchelor et al.: *annual report* **2000**, p. 303.

[3] R. Follath et al.: *annual report* **2000**, p. 322.

[4] C. Jung et al.: *annual report* **2000**, p. 339.

[5] R. Follath: *Nucl. Instrum. and Methods* **A 467-468**, 418 (2001).

[6] F. Eggenstein et al.: *Nucl. Instrum. and Methods* **A 467-468**, 325 (2001).

[7] R. Follath et al.: *annual report* **1998**, p. 465.

Enhancement of Imaging Performance in Photoemission Electron Microscopy by Means of Time-of-Flight Selection

A. Oelsner[1], A. Krasyuk[1], G.H. Fecher[1], S. Nepijko[1], C.M. Schneider[2], G. Schönhense[1]

[1]*Johannes Gutenberg - Universität, Institut für Physik, 55099 Mainz, Germany*
[2]*Institut für Festkörper- und Werkstofforschung, 01099 Dresden, Germany*

The excitation with synchrotron radiation of variable energy allows to obtain element specific information in photoemission electron microscopy (PEEM) by choosing a suitable photoabsorption edge of the selected element [1]. In the imaging process, the secondary electron yield is exploited which is a measure of the photoabsorption signal. Further, magnetic domain distributions on ferromagnetic surfaces can be visualized by calculating the difference or asymmetry between two images of this photoabsorption yield for circularly polarized light with opposite helicity (XMCD) [2]. A main limitation of the spatial resolution in this procedure is given by the chromatic aberration of the electron optics. This aberration contribution is much stronger for X-ray absorption experiments than for the threshold regime due to the broad energy distribution of secondary electrons. Conventional designs of electron optics overcome the problem by inserting very small apertures in the focal plane of the objective lens system. One disadvantage of this solution is its restriction to a fixed kinetic energy of electrons contributing to the signal at the detector. The lower intensity turns out to be the main practical disadvantage due to handling problems in adjustments of lenses, of the aperture position, and in the optimization process of the measurements, particularly in observing magnetic domains. A straight forward but very demanding solution is the use of imaging dispersive energy filters as was demonstrated in E. Bauers group [3].

This work demonstrates the use of a simple imaging energy filter based on electron time-of-flight (ToF) selection. The spatial resolution could be improved drastically although the instrument was optimized using a contrast aperture of 50 µm. A special delayline detector replaces the conventional combination of phosphor screen and CCD-camera at this ToF-PEEM [4]. The detector readout system sorts every incoming electron signal into a 3 dimensional organized histogram memory device by x-y-position and time. Time measurements are made with respect to a phase locked photon marker signal of the synchrotron single bunch mode. At present, this device has a time resolution limit of about 150ps, which is still beyond the photon puls length of about 50ps. The time dispersion in the electron trajectories can be controlled by setting different voltages to the last section of the microscope, that is the drift tube. This voltage differs largely from the PEEM column voltage in order to neglect the time dispersion in the rest of the instrument. For the presented dataset, the drift voltage was set to +50V leading to an electron drift energy $E_d = 50\,eV + E_{kin}$ where E_{kin} describes the start energy of the photoelectron when leaving the sample surface.

Fig. 1 shows the ToF-spectrum for photoemission from a structured FeCo film on Cu. It is spatially integrated over an field of view of approximately 25 µm x 25 µm. A photon energy of $h\nu = 780\,eV$ (Co-L_3-edge) has been chosen in order to obtain the maximum image contrast. The complete ToF distribution is shown at the inserted plot using a logarithmic intensity scale. Its maximum appears at a kinetic energy of about 1eV and the region of high electron energies exibits still some structure although their intensity is two orders of magnitude smaller. The large plot represents the low-energy part of the distribution which is mainly contributing to the image with a FWHM of 4ns for the chosen settings. This time difference corresponds to an energy width $\Delta E = 4.3$ eV and is determined by the instrument transmission function for the given size of the contrast aperture of 50 µm.

Large improvements of the image quality have been observed when cutting narrow time slices from the ToF distribution and forming images only with these electrons. An example is
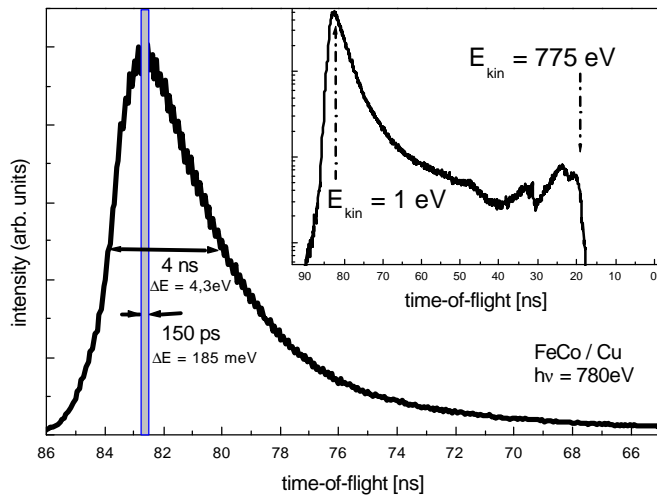
Fig.1: *Time-of-flight distribution of photoelectrons integrated over the complete PEEM-image at drift energy E$_d$ = 50eV + E$_{kin}$. The aperture of 50 µm yields PEEM-images with a FWHM of 4.3eV in energy corresponding to 4ns ToF-width.*
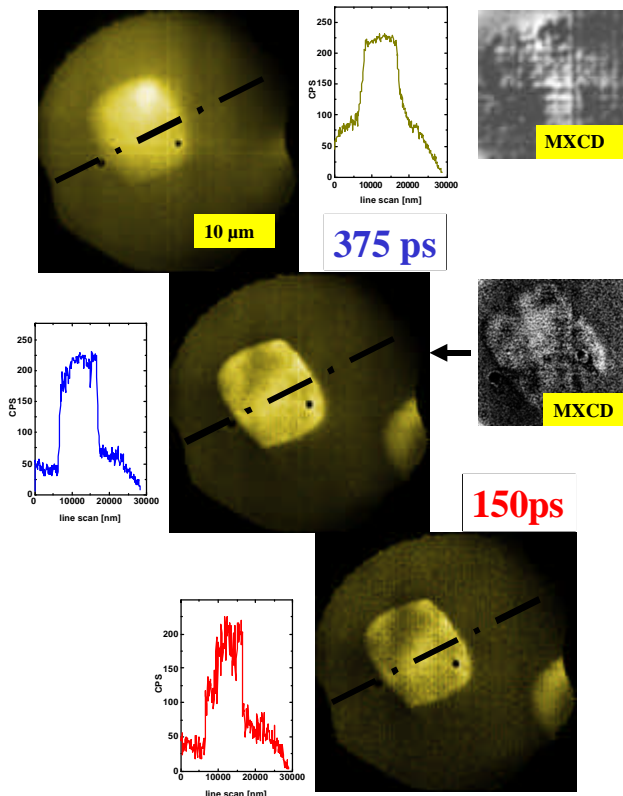
Fig.2: *Enhancement of image performance by ToF selection, comparison of the images and the line scans (dash dot line) crossing the image of an FeCo island, without ToF selection (top), a time slice of 375ps width (middle), and one at the resolution limit of 150ps (bottom). A ToF-selected energy window (bar in Fig.1) of 185meV improves the present resolution by more than a factor of 20.*

demonstrated in the image set of Fig. 2. The microscope has been adjusted as good as possible without the ToF option for displaying a FeCo island with a medium scale magnification. The topmost image resolution is rather poor, the slopes of the line scan at the island rims are about 1.8 µm in width. While the unfiltered energy distribution contributes to the topmost image, only electrons with certain time-of-flight conditions have been used to produce the other two plots. In the centre image, a time slice of 375 ps width was chosen corresponding to an energy width of about 400 meV. The improvement is already obvious, the edges in the line scan become sharp and some details like the neighboring island at the right side of the image as well as some structure on top of the island appear. These structures on top of the object become more detailed in the bottom image, where the time resolution is set to the present limit of 150ps. It corresponds to the shaded area in Fig.1 and to an energy width of ΔE = 185 meV. The widths of the edges in the line scan are determined finally to 80 nm, an improvement factor better than 20. This improvement also shows up in the magnetic domain pattern shown on the right hand side viewed via MXCD. In concluion, ToF selection provides a simple maens to reduce the chromatic aberration in a PEEM. The technique does not require demanding electron optical elements and retains a linear microscope column. Funded by BMBF: (05KS1UM1/5 and 05KS1BDA/9)

[1] B. P. Tonner and G. R. Harp, Rev. Sci.. Instrum. **59** (1988) 853
[2] J. Stöhr et al., Science **259** (1993) 658
[3] E. Bauer et al. in H. Ade, J. Electron Spectrosc. Relat. Phenom. **84** (1997) 201
[4] A. Oelsner et al., Rev. Sci. Instrum. **72** (2001) 3968

Nano-XAS and Nano-XPS with X-PEEM

Ch. Ziethen, F. Wegelin, P. Bernhard, G. Schönhense
Johannes Gutenberg Universität, Institut für Physik, D-55099 Mainz
R. Ohr, H. Hilgers
IBM Speichersysteme Deutschland GmbH, Werk Mainz
M. Escher, M. Merkel
FOCUS GmbH, D-65510 Hünstetten-Görsroth

Research projects, especially in the field of applied physics, follow both scientific and technical goals. In the present report, we would like to show that spectromicroscopy using standard electron optical devices is even capable to do chemical spectroscopy and imaging well below the 'micrometer limit'. The term micro -XAS, -XPS, -Auger for laterally resolved spectroscopic techniques describes the resolution capability of the respective techniques. For our technique of 'photoemission spectromicroscopy' see [Zie98]. Here, we report the present milestone results of two research projects, showing ways to do nano-XAS (X-ray absorption spectroscopy) and nano-XPS (X-ray photoelectron spectroscopy, using a rather simple electron energy filter). The techniques establish spectroscopy and imaging with high signal-to-noise ratio and a lateral resolution clearly below the micrometer scale. The spectromicroscope used was a FOCUS Photoemission Electron Microscope.
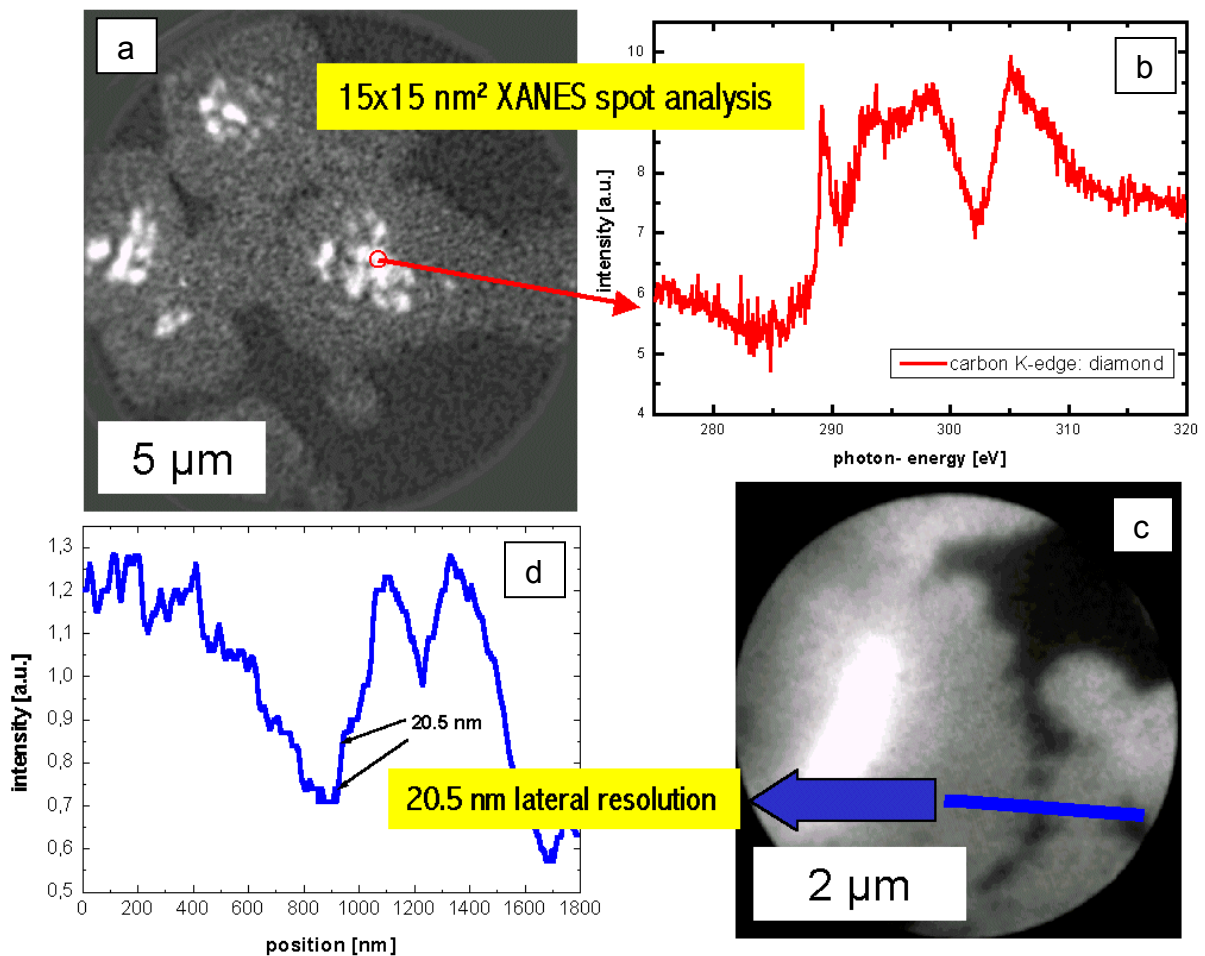

Figure 1: Diamond nucleation on Iridium. a) Secondary electron image (orbital map) at hν=289.5 eV b) XANES of the carbon K-edge c) highly resolved image of domain boundaries (at hν=289.5 eV) d) line scan, revealing a lateral resolution of 20.5 nm. Sample courtesy M. Schreck, Augsburg)

Nano-XAS spectromicroscopy

Previously we analyzed ultra-thin (< 5nm) amorphous carbon (a-C) and carbon nitride (CN_x) hard-disk coatings aiming at local chemical information [Zie00]. In 2001, we focused the analysis on two questions: the chemical structure of the CN_x films, especially the bonding sites of carbon and nitrogen, and the corrosion of the underlying magnetic storage layer. In both cases, we determined the information from the XANES- features of the carbon, nitrogen and oxygen K-edges [Zie02]. Beside this, the final technical goal of the project, i.e. imaging of carbon- based hard coatings with lateral resolution of around 20 nm, has been reached.

Figure 1 gives a typical result, obtained at the beamline U49/1-SGM at the carbon K-edge. We examined the nucleation of single crystalline diamond films. The samples have been provided by the group of Stritzker and Schreck (University of Augsburg). These films were grown on biased $SrTiO_3$ single crystals and an iridium buffer layer [Sch01]. Fig. 1a shows the orbital map at the photon energy hν=289.5 eV. The iridium buffer (dark) is covered by diamond islands, some of them showing submicron 3D diamond crystallites at the center. Fig.1b is the nano-XAS spectrum obtained from a 15x15 nm² area centered at one of these crystallites. It shows a typical near edge structure (XANES) of diamond. We get these spectra by recording images (formed by secondary electrons) for every photon energy, and analyzing the intensity of regions of interest. Examining grain boundaries with higher magnification (Fig 1c), we determined the lateral resolution (15 to 85% intensity jump) to be 21±5 nm (Fig. 1d).

Fig. 2 shows an evaporated silver structure on a tantalum surface, with the same magnification used as in Fig. 1c. Image was obtained at photon energy of hν=600 eV. Line scan analysis determines again a lateral resolution of 21 nm. These results show the resolution limit of the FOCUS X-PEEM at an undulator beamline, imaging the low energy secondary electrons without energy filter. It should be noted that the bright spots in the left part of Figs. 1c and 2a are due to the primary photoelectrons from the sample, which are not focused due to their higher kinetic energy.
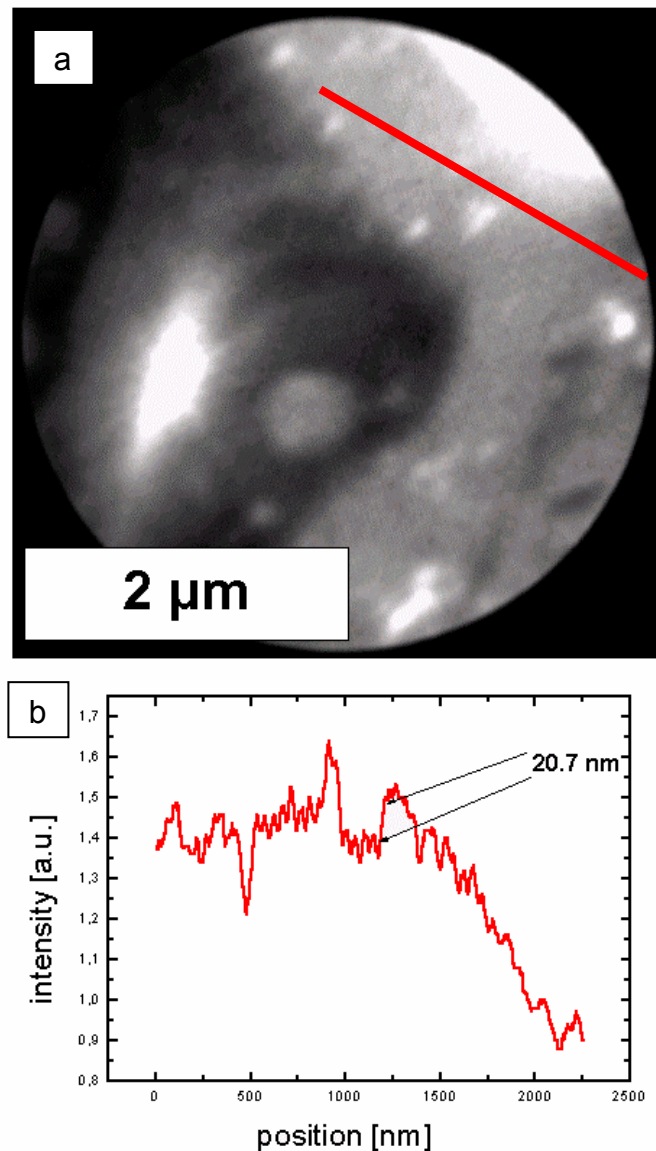

a

2 µm

b

20.7 nm

Figure 2: Microstructured silver on tantalum. a) Secondary-electron image (XAS-PEEM) taken at hν=600eV. b) Line scan for resolution determination

Nano-XPS spectromicroscopy

Changing the settings of the electron optics and keeping the photon energy fixed leads to nano-XPS. The in-column retarding field imaging energy filter (IEF) was used to select the XPS- signal, here Ta 4f. Applying a variable negative voltage to the grid at fixed sample potential (or keeping the grid fixed and varying the sample bias), it acts as a high- pass energy filter with an energy resolution of about $\Delta E=0.5$ eV [Mer01]. XPS- spectra of the sample are recorded as integral spectra of electrons with higher energy than the cut off of the grid. Every photoelectron or Auger peak is identified as a step. Numerical differentiation then leads to differential XPS spectra. Images of a XPS- peak are obtained as the difference of images taken at both sides of the step. Figure 3 shows such an image of the Ta $4f_{7/2}$ peak, taken at photon energy $h\nu=700$ eV. The lateral resolution of this XPS-image was determined to be 140nm. At the given conditions (U49/1 SGM), typical nano- XPS- spectra can be obtained from 250x250nm² sample regions. The lateral resolution using this simple electron optical design is about one order of magnitude higher than commercially available imaging ESCA/ XPS probes (PHI, Kratos, VG). Higher resolution requires e.g. an imaging hemispherical energy filter [Sch98] or even aberration corrected instruments, i.e. a much more demanding experimental setup [Wic98].
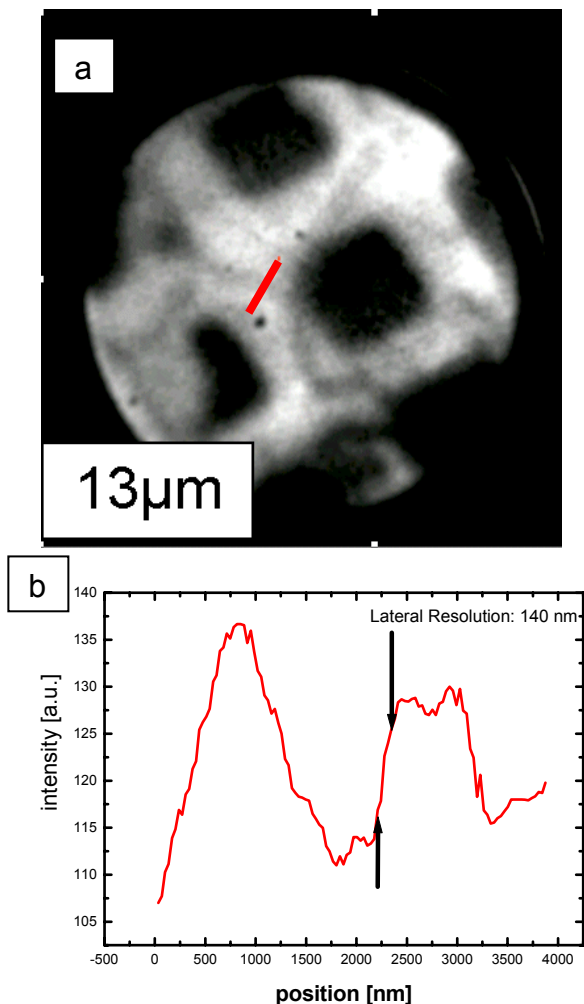
[Mer01] M. Merkel, M. Escher, J. Settemeyer, D. Funnemann, A. Oelsner, Ch. Ziethen, O. Schmidt, M. Klais, G. Schönhense, Surf. Sci. 480 (2001)
[Sch98] Th. Schmidt, S. Heun, J. Slezak, J. Diaz, K. C. Prince, G. Lilienkamp, E. Bauer, Surf. Rev. and Lett. 5 (1998) 1287
[Sch01] M. Schreck, F.Hörmann, H. Roll, J.K.N. Lindner, B. Stritzker, Apl. Phys. Lett. 78 (2001) 192
[Zie98] Ch. Ziethen O. Schmidt, G.H. Fecher, C.M. Schneider, G. Schönhense R. Frömter, M. Seider, K. Grzelakowski, M. Merkel, D. Funnemann, W. Swiech, H. Gundlach, J. Kirschner, J. Electron. Spectr. Relat. Phenom. J. Electron Spectr. Relat. Phenom. 88-91 (1998) 983
[Wic98] R. Wichtendahl, R. Fink, H. Kuhlenbeck, D. Preikszas, H. Rose, R. Spehr, P. Hartel, W. Engel, R. Schlögl, H.-J. Freund, A. M. Bradshaw, G. Lilienkamp, Th. Schmidt, E. Bauer, G. Benner, E. Umbach, Surface Review and Letters 5 (1998) 1249
[Zie00] Ch. Ziethen, O. Schmidt, G.K.L. Marx, G. Schönhense, R. Frömter, J. Gilles, J. Kirschner, C.M. Schneider, O. Gröning, J. Electron Spectr. Relat. Phenom. 107 (2000) 261; Ch. Ziethen, F. Wegelin, R. Ohr, G. Schönhense, M. Neuhäuser, H. Hilgers, BESSY annual report 2000 (2001) 286
[Zie02] Ch. Ziethen, F. Wegelin, G. Schönhense, R. Ohr, M. Neuhäuser, H. Hilgers, Diamond and Related Materials (2002), in print;

Figure 3: a) XPS- PEEM image taken at the Ta $4f_{7/2}$ peak and $h\nu=700$ eV (sample as Fig 2) b) Line scan analysis revealing a resolution of 140nm.
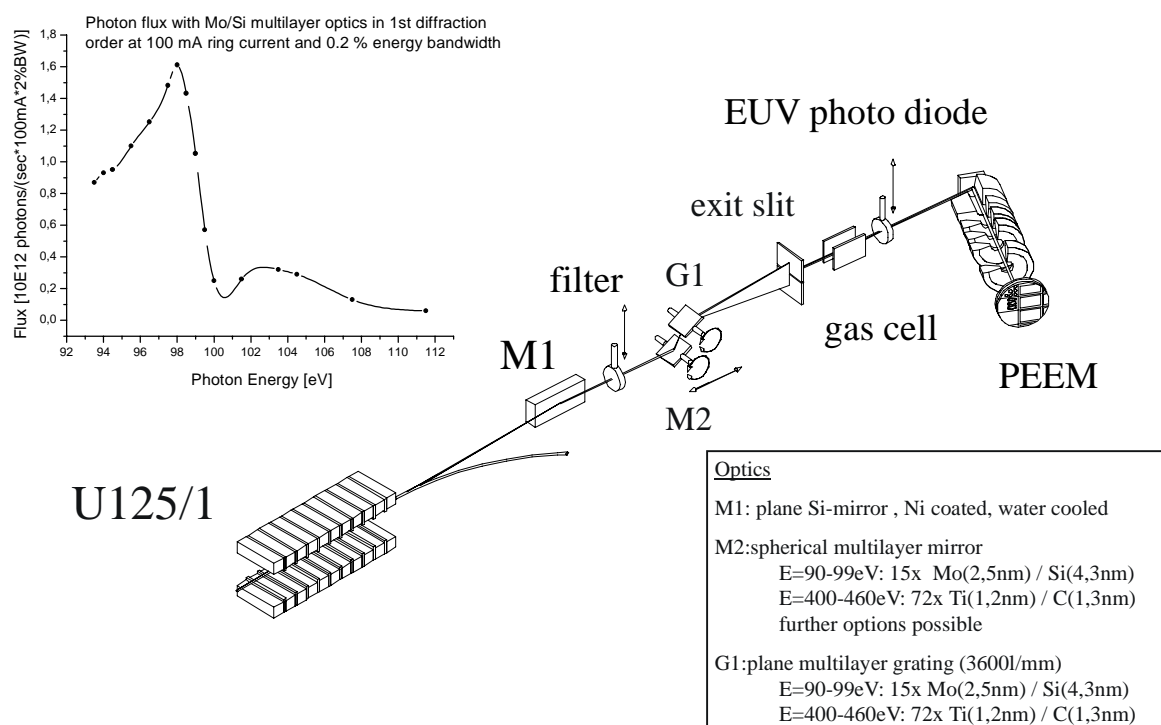
X-PEEM Spectromicroscopy at the Multilayer Monochromator Beamline U125/1-ML at BESSY II

M. Pohl, M. Sundermann, A. Brechling, U. Kleineberg, U. Heinzmann
mpohl@physik.uni-bielefeld.de; kleineberg@physik.uni-bielefeld.de
University of Bielefeld, Faculty of Physics, Universitaetsstr. 25, D-33615 Bielefeld, Germany

Photoemission microscopy utilizing electron core level excitation by extreme ultraviolet or soft X-ray radiation (X-PEEM) is well known to be a powerful spectromicroscopy tool for the characterization of mesoscopic properties of surfaces and thin films. Besides the potential for high spatial resolution the chemical sensitivity achievable near X-ray absorption edges of sample materials is a highly valuable X-PEEM feature. A Synchrotron Radiation beamline providing tunable radiation of high flux and high spectral purity at moderate energy resolution in the soft X-ray range is best suited for this application.

In order to meet these requirements we have set up a beamline dedicated to photoemission microscopy within a 90-460 eV photon energy range at the linear undulator U125/1 (Fig. 1).

Figure 1 : Setup scheme and photon flux measurement (with Mo/Si multilayer optics) of the multilayer monochromator beamline U125/1-ML for X-PEEM spectromicroscopy

Linearly (horizontally) polarized undulator radiation emitted from the linear undulator U125/1 is horizontally deflected by an actively cooled plane Ni-coated silicon mirror at a grazing incidence angle of 3 degree. The reflectivity properties of the premirror coating set a high-energy cutoff at a photon energy of about 500 eV. A further spectral filtering of the polychromatic radiation is possible by using transmission foil filters located in front of the multilayer monochromator.

The deflected radiation is spectrally dispersed by means of a multilayer monochromator operating at non-grazing incidence angles and focused onto a variable exit slit.

The optical elements within the monochromator are three *in-vacuo* interchangable sets of spherical multilayer mirrors (concave radius 2000 mm) and 3600 l/mm plane laminar multilayer gratings, each pair coated with different reflection multilayers for covering three

different spectral ranges from 90-105 eV (Mo/Si multilayer coating) up to 400-460 eV (C/Ti multilayer coating). Wavelength tuning according to the multilayer Bragg equation $n\lambda = 2*d*\cos(\alpha)$ is achieved by changing the angle of incidence α on the multilayer mirror and multilayer grating simultaneously with an angular tuning range of about 15 degrees to 65 degrees (with respect to the surface normal).

The spectral resolution and photon flux of the radiation behind the monochromator can be measured by means of an inline ionization gas cell and a retractable and calibrated GaAsP EUV photodiode (Hamamatsu G1127-02), respectively. A very high photon flux reaching $1.7*10^{12}$ photons/sec at 100 mA ring current and approximately 0.2 % spectral bandwidth has been reached using the 1st undulator harmonic and with Mo/Si multilayer optics operating at 1st grating order at 99 eV (see inset of Fig. 1).

The radiation enters an electrostatic photoemission microscope (Focus IS-PEEM) in reflection geometry illuminating the sample surface at an angle of about 25 degrees (with respect to the sample surface). A special operation in transmission geometry using transparent photocathodes is optionally possible. The beamline is especially useful to characterize silicon-based layer systems and nanostructures by recording spectromicroscopic images at two photon energies just below and above the Si-L absorption edge (99 eV).

We have investigated the effect of ultrathin (2-3 nm) organic monolayers preadsorbed as Self-Assembled Monolayers (SAM) onto hydroxilated silicon wafer surfaces on the interdiffusion and silicide reaction of evaporated copper layers with the underlying substrate initiated by *insitu* annealing at temperatures up to 350° C.
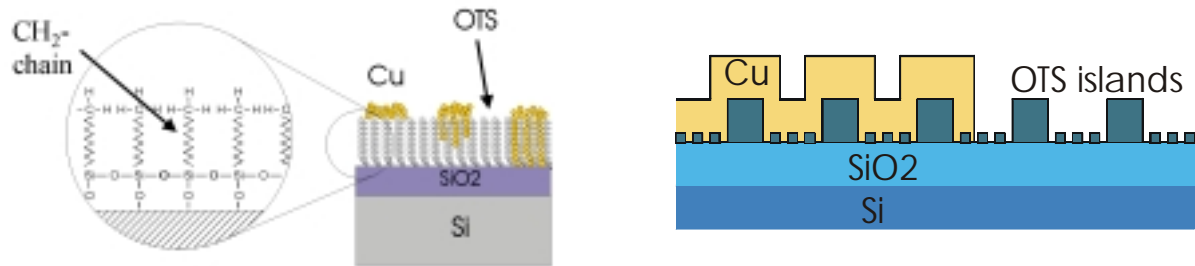

Figure 2 : Copper growth on OTS and sample crossection of Cu/OTS-islands/SiO$_2$/Si samples

Three different types of samples have been prepared for X-PEEM analysis by evaporating thin (5-10 nm) copper layers *in-vacuo* onto bare Si(100) wafer substrates (with 1.5 nm native siliconoxide coverage), onto hydroxilated Si-wafer substrates with a closed organic monolayer coverage of Octadecyltrichlorosilane (OTS) and Si-substrates covered with OTS islands (see Fig. 2 for schematic scetch).
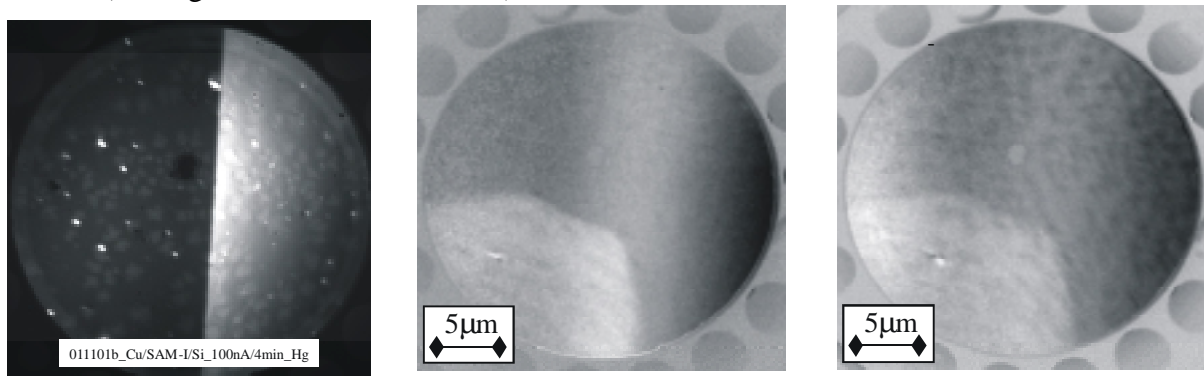

Figure 3 : PEEM images (20 μm field diameter) of Cu(10 nm)/OTS-islands(2.5 nm)/SiO$_2$(1.5 nm)/Si(100); left : work function contrast (hν = 4.9 eV); middle : differential image (hν =106 eV – 99 eV) before annealing; right : same sample area after annealing (300°C, 300 sec)

Figure 3 displays a series of PEEM images recorded on a sample of a thin (10 nm) copper film evaporated at UHV conditions onto an OTS-island covered hydroxilated silicon substrate. A part of the sample has been shadowed during the copper evaporation in order to create copper coated and uncoated surface areas. These two different surface areas (copper : bright, non-copper : dark) result in a large UV-PEEM image contrast (Fig. 3, left image) due to the work function difference of Cu (~4.7 eV) and Si (5.1 eV). Additionally, the larger islands of the organic monolayer film (500-700 nm in size, work function ~4.5 eV) buried underneath the copper layer as well as those adsorbed onto the hydroxilated silicon surface are also clearly visible while smaller islands (< 40 nm) detected by Atomic Force Microscopy are not resolved in the UV-PEEM image. XPEEM spectromicroscopy of the same sample performed by recording differential images below and above the Si-L edge at 106 eV and 99 eV photon energy reveals information about the lateral silicon(-oxide) distribution on the sample surface which appears as bright areas while non-silicon areas appear dark. While a clear differential image contrast between the copper-coated and uncoated areas is displayed before sample annealing (Fig. 3, center) the contrast is decreased after sample annealing at 300°C for 300 seconds (Fig. 3, right). It should be noted that the visibility of the copper-buried OTS-islands (dark spots) hardly visible before the annealing procedure is now significantly enhanced. The result can be explained in terms of the copper-silicon interdiffusion followed by silicide reaction occuring at elevated substrate temperatures. While strong copper-silicon interdiffusion can occur at surface areas not covered with OTS-islands, the interdiffusion is probably decreased in the presence of the OTS-film acting as ultrathin barrier layer. Additionally, the chemical reaction between the siliconoxide surface and the copper film leading to copper-oxide films is inhibited.
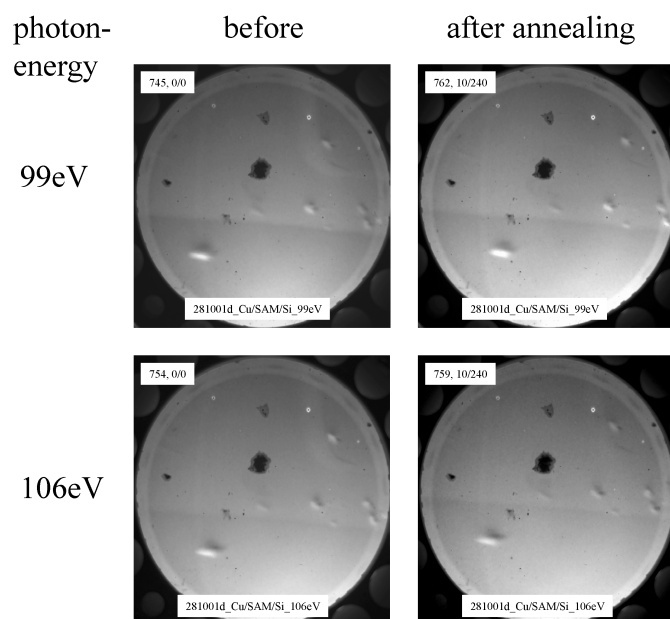
This explanation is verified by similar annealing experiments performed on Cu/OTS/Si samples with *closed* OTS interlayer (Fig. 4). XPEEM images recorded at photon energies of 99 eV (< Si-L edge, top images) and 106 eV (> Si-L edge, bottom images) show almost no changes in contrast between the copper-covered (upper half) and uncovered areas (lower half) before and after annealing thus pointing to an inhibited interdiffusion in the presence of the OTS monolayer film.

photon-energy	before	after annealing
99eV	745, 0/0 ... 281001d_Cu/SAM/Si_99eV	762, 10/240 ... 281001d_Cu/SAM/Si_99eV
106eV	754, 0/0 ... 281001d_Cu/SAM/Si_106eV	759, 10/240 ... 281001d_Cu/SAM/Si_106eV

Figure 4 : XPEEM images of Cu/OTS/SiO$_2$/Si

Acknowledgments :

References :
M. Pohl, A. Brechling, M. Sundermann, S.A. Nepijko, U. Kleineberg, U. Heinzmann;
Copper overlayers on Self-Assembled Monolayers studied by soft X-ray photoelectron microscopy; Abstracts Dreiländertagung für Elektronenmikroskopie, Innsbruck, 9.-14. September 2001, p. 161

Commissioning of the Russian-German beamline

S.I. Fedoseenko,[#] D.V. Vyalikh,[§] I.E. Iossifov,[#] S.L. Molodtsov,[#,&] R. Follath,[£]
S.A. Gorovikov,[§,#*] J.-S. Schmidt,[£] V.K. Adamchuk,[#] W. Gudat,[£] and G. Kaindl [§]

[§] *Institut für Experimentalphysik, Freie Universität Berlin, 14195 Berlin, Germany*
[#] *Institute of Physics, St.Petersburg State University, 198904 St.Petersburg, Russia*
[&] *Institut für Oberflächen- und Mikrostrukturphysik, TU Dresden, 01062 Dresden, Germany*
[£] *BESSY GmbH, 12489 Berlin-Adlershof, Germany*

In October 2001, the installation of the Russian-German beamline at the bending magnet D16-1A was successfully completed by the co-operation partners: Freie Universität Berlin, St.-Petersburg State University, BESSY GmbH, and Technische Universität Dresden, and first light could be transmitted through its optical system. This high resolution beamline is the first soft x-ray beamline at BESSY II, which was specially designed for operation at a bending magnet. Therefore, the performance of this beamline is of crucial importance for the further exploitation of dipole-source instrumentation at BESSY II.

The optical layout of the beamline is shown in Fig. 1: The toroidal mirror M1, upstream of the plane grating monochromator (PGM), accepts 3.4-mrad horizontal slice of synchrotron light from the bending-magnet source. This mirror focuses the source horizontally onto the exit slit and collimates the beam vertically in the dispersion plane. The collimated light from
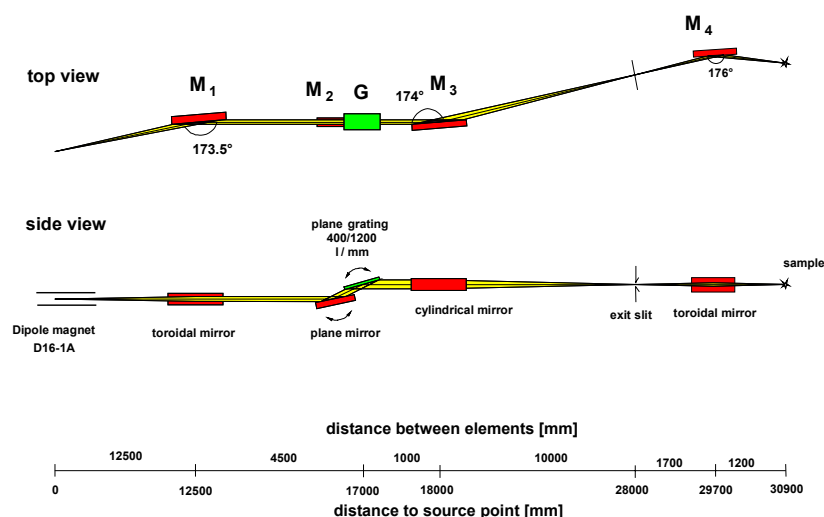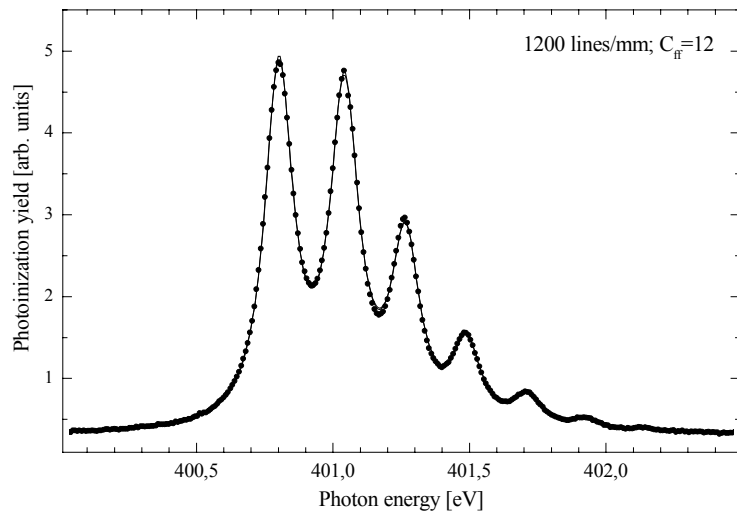

Fig. 1 Optical layout of the Russian-German beamline

M1 is diffracted by the vertically deflecting gra-ting (400 lines/mm and 1200 lines/mm) in the Petersen-type PGM geo-metry (plane mirror M2-plane grating) [1]. The cylindrical mirror M3 focuses the diffracted light vertically onto the exit slit. The image at the exit slit is refocused by the toroidal mirror M4 onto the sample position in the experimental station. An essential difference of the present layout with respect to the Peterson design [1] (taken as a basis for our calculations) is the operation of the monochromator with collimated light due to saggitally focusing mirror M1 [2]. This allows to achieve high energy resolution, effective suppression of higher order light and high transmitted photon flux without any movements of the exit slit or optical elements; only a change of the fix-focus constant $C_{ff} = \cos\beta/\cos\alpha$ is required (α and β are the angle of incidence and the angle of diffraction relative to the grating normal, respectively). Further details of the layout can be found in Ref. [3]. Ray-tracing calculations revealed a state-of-the-art performance of the beamline in the photon energy range 30 eV to

1500 eV, with a resolving power up to 25.000 and a photon flux up to 3 x 10^{10} photons/s/100 mA for a slit width of 20 μm at fix-focus ratios C_{ff} = 5 and 2.25, respectively.

For the experimental characterization of the spectral resolution of the Russian-German beamline, a home-built photo-ionization chamber was used. It is an integral part of the beamline and is located between the exit slit and the chamber of refocusing mirror M4. During operation the gas cell is separated from the exit slit by a removable 120-nm thick polyamide window and allows to perform measurements with gas pressures up to 1 mbar: The gas is photo-excited by the beam and the resulting ions and electrons are collected by two plane electrodes. Photoionization spectra of nitrogen and helium were taken to optimize the resolution of the beamline at various photon energies. The experiments were carried out at pressures in the range from 1×10^{-3} to 1×10^{-1} mbar and applied voltages of up to 100 V. All spectra were recorded with the 1200 lines/mm grating and the largest possible C_{ff} value (C_{ff} = 12), providing the highest resolving power.

Fig. 2 Photoionization spectrum of nitrogen (1s - π* resonance

Figure 2 shows the photoionization spectrum of nitrogen molecules in the region of the 1s - π^* resonance. The solid curve represents the best fit with Voigt functions of constant linewidth, where the Gaussian (experimental resolution) and Lorentzian (natural linewidth) width contribute by (117±1) meV and (34±1) meV, respectively. The resolving power of the beamline obtained from this fit is higher than 12.000. It is well known, that in case of N_2 the resolving power can be estimated from the parameter r, which is the ratio between the intensities of the first dip and the third peak in the 1s - π^* photoionization spectrum [4]. Already for the first 1s - π^* spectrum recorded at the Russian-German beamline, r = 0.74 was obtained, which clearly demonstrates perfect alignment of the optical components of the beamline with only standard geodesic devices. After subsequent adjustment of the deflection angle of the first mirror and the position of the exit slit, the r value could be improved to 0.69.

A determination of the energy resolution at high photon energies is complicated by the
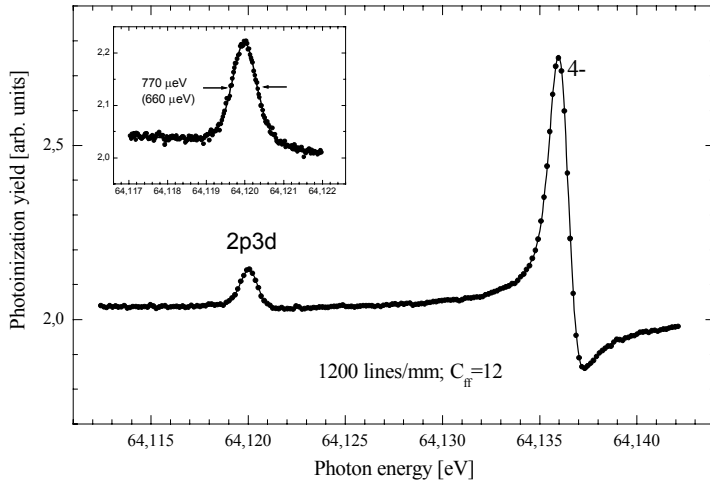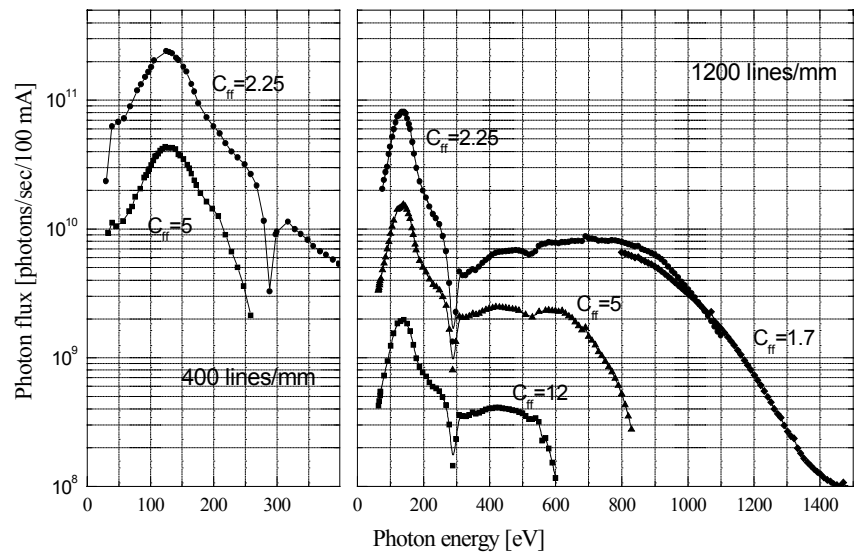

Fig. 3 Photoionization spectrum of He (2d3d resonance)

rather large natural linewidth of the available atomic resonances. For low photon energies, much sharper resonances can be used to this purpose. The 2p3d and 4⁻ autoionization profiles of the N=2 series of doubly-excited He were selected to examine the energy resolution at photon energies close to 64 eV (Fig. 3). The inset in Fig. 3 shows the vicinity of the 2p3d profile. The theoretical linewidth of this resonance is about 3 μeV. However, Doppler broadening at room temperature already gives rise to a spectral width of 400 μeV. The linewidth obtained in the present experiment is about 770 μeV. Taking into account the Doppler broadening, this value corresponds to a monochromator bandwidth of 657 μeV, which yields a resolving power of approximately 98.000. To our knowledge, this is the best resolution ever achieved on a bending-magnet beamline in the grazing incidence regime.

The photon flux at the sample position in the experimental station was estimated from the total photoelectron yield of a gold mesh, which is installed behind refocusing mirror M4, as a function of the settings of the mono-chromator. The flux measurement was carried out for both gratings: 1200 lines/mm and 400 lines/mm at an exit-slit width of 200 μm and a set of C_{ff} values specified in Fig. 4. The data were taken for a stored electron energy of 1.7 GeV and are normalized to 100 mA current. The quantum yield of gold and the transparency of the gold mesh were taken into account. As seen in Fig. 4, the beamline provides up to 2×10^{11} photons/s/100mA at this exit slit, in agreement with the results of our calculations [3]. The flux curves show a smooth

Fig. 4 Photon flux

dependence on photon energy with a dip at 280 eV caused by a carbon contamination of the mirror surfaces. At large C_{ff} values, the acceptance of mirror M2 and of the grating is reduced causing a low transmission. At high photon energies, the flux curves exhibit sharp decays, since the length of M2 does not allow to set the required small deflection angles for the grating operating with the specified C_{ff} values. An increasing part of the incident beam hits the front side of the mirror substrate and is no longer reflected by the mirror surface.

The Russian-German beamline will go into regular user operation by February 2002.

References and footnotes:
*present address: MAX-Lab, Hamtstalle 9, 22100 Lund, Sweden
[1] H. Petersen, Opt. Commun. 40, (1982), 402.
[2] R. Follath and F. Senf, Nucl. Instr. and Meth. A 390 (1997) 388.
[3] S.A. Gorovikov *et al*., Nucl. Instr. and Meth. A 441, 506-512 (1998) 506; S.A. Gorovikov *et al*., Nucl. Instr. and Meth. A 467-468 (2001) 565; S.I. Fedoseenko *et al*., Nucl. Instr. and Meth. A 470 (2001) 84.
[4] D. Cvetko *et al*., Proc. SPIE, 3150 (1997) 86; C. Quaresima *et al*., Nucl. Instr. and Meth. A 364 (1995) 374; C.T. Chen and F. Sette, Rev. Sci. Instr. 60 (1989) 1616.

Instrumentation for IR-Ellipsometry at the IRIS beamline

M. Gensch[1], K. Hinrichs[1], E.H. Korte[1], U. Schade[2], N. Esser[3], and A. Röseler[1]

[1] Institut für Spektrochemie und Angewandte Spektroskopie, Institutsteil Berlin,
Albert-Einstein-Str. 9, D-12489 Berlin

[2] Berliner Elektronenspeicherring Gesellschaft für Synchrotronstrahlung mbH,
Albert-Einstein-Str. 15, D-12489 Berlin

[3] Institut für Festkörperphysik der TU Berlin, Hardenbergstr Str. 36 , D-10623 Berlin

There is a growing interdisciplinary interest in reliable optical constants in the infrared (IR) spectral range of surfaces, thin organic and inorganic films as well as small crystal samples [1,2,3]. However, the rather poor brilliance of conventional IR sources (e.g. globar) limits investigations with state-of-the-art IR-ellipsometers to rather large samples (some 10 mm^2) and the opening angle of the irradiating cone in the experiment is large (2°-4°).

For these reasons an IR-ellipsometer is currently designed to take full advantage of the superior properties of synchrotron radiation (high brilliance, polarization). The small opening angles that can be achieved with the new set-up will generally improve the accuracy of the experimental data. The expected gain in irradiance will enable quantitative analysis of smaller samples or smaller sample areas.
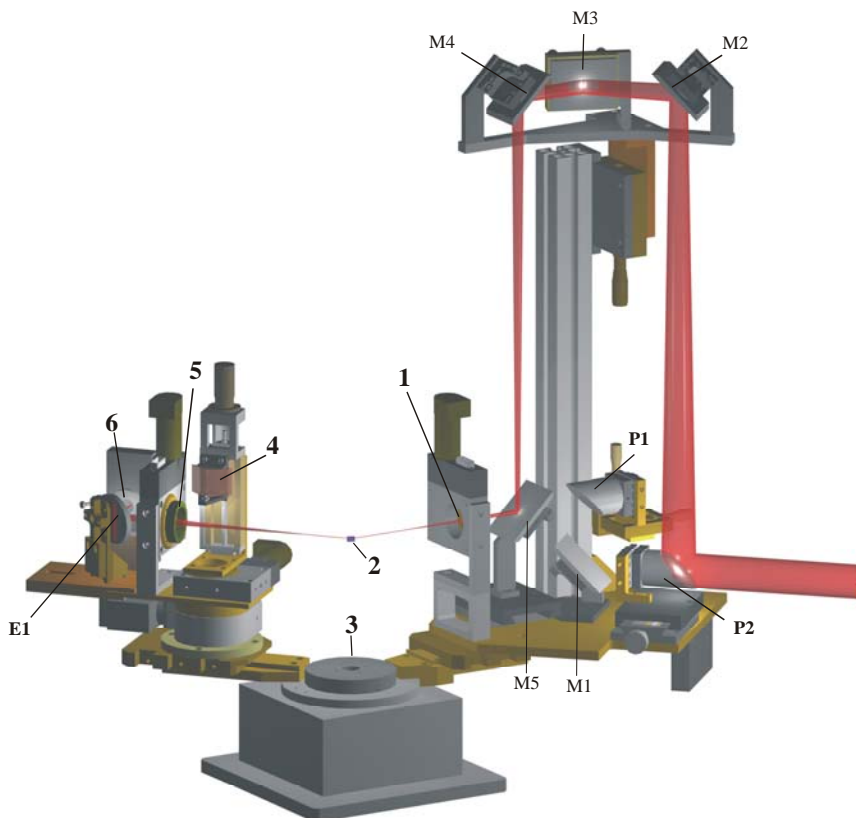
IR-ellipsometer:

P1,P2 parabolic off-axis mirrors, M1-M5 plane mirrors, E1 elliptic off-axis mirror, 1 polarizer, 2 sample, 3 goniometer, 4 retarder, 5 analyzer, 6 detector. The focal length is chosen by moving P2 in or out of the beam

Optical design

A detailed description of the parameters and facilities of the IRIS beamline is given elsewhere [4]. The ellipsometer will be attached to a port of a BRUKER IFS66 spectrometer. The collimated beam has a diameter of 17 mm and can alternatively be focussed onto the sample with two different mirror systems. One system (I) is optimized to gain maximum irradiance with still acceptable opening angles. It consists of a plane mirror (M1) and a parabolic mirror (P1, f=290 mm). The polarization of the radiation is rotated by an angle of 45° to make use of the polarization of the synchrotron radiation. The irradiance is increased by a factor of 20 compared to a conventional set up. The second system (II) is optimized to achieve a small opening angle and focus the light onto a 5x5 mm^2 sample area (standard sample size in surface science experiments). The radiation is focussed with a parabolic mirror (P2, f=1375 mm) and guided into the ellipsometer by a system of 4 plane mirrors (M2, M3, M4, M5). The opening angle here is an order of magnitude smaller than in a conventional set-up.

Source	opening angle*	irradiance (normalized)*	typical area*
IRIS (I)[#]	±1.8°	20	<1mm^2
IRIS (II)[#]	±0.35°	1	<25mm^2
Globar[+]	±3.5°	1	<100mm^2

* for 1000 cm^{-1}, [#] for a beamcurrent of 0.4 A, [+] for 1200 K

An UHV chamber has been designed to be implemented into the ellipsometer for surface science experiments. A cryostat will also be available for temperature dependent investigations.

The ellipsometer is planned to be in operation by April 2002. The first projects will be investigations of adsorbates on III-V semiconductor surfaces and the determination of optical constants of terrestrial rock-forming minerals.

References

[1] A. A. Sirenko et al, Soft mode hardening in SrTiO3 thin films, Nature 404, 373 (2000)

[2] M. Schubert et al, Infrared optical Properties of mixed-phase thin films studied by spectroscopic ellipsometry using boron nitride as an example, Phys Rev B 56, 13306 (1997)

[3] K. Hinrichs et al, Comparative study of an anisotropic layer by infrared spectroscopic techniques, Appl. Spectr. (in press)

[4] Peatman W.B. and Schade U., Rev. Sci. Instr. 72, 1620-1624 (2001)

Reconstruction of Magnetic Domain Arrangements from Resonant Coherent Scattering Patterns

S. Eisebitt[1,2,*], M. Lörgen[1,2,*], W. Eberhardt[2,*], J. Lüning[1], J. Stöhr[1], A. Rahmim[3], T. Tiedje[3]

[1] SSRL, Stanford Linear Accelerator Center, Menlo Park CA 94025, USA
[2] IFF, Forschungszentrum Jülich, 52425 Jülich, Germany
[3] AMPEL, University of British Columbia, Vancouver B.C., V6T 1Z4 Canada
[*] present address: BESSY GmbH, Albert-Einstein-Str. 15, 12489 Berlin, Germany

In coherent x-ray scattering, a sample volume smaller than the coherence volume of the incident x-ray beam is illuminated. As a consequence, the scattering pattern contains a fine structure called „speckle", which is due to the fact that radiation scattered at different points in the sample can interfere. The envelope of the scattered intensity, corresponding to incoherent small angle x-ray scattering, contains information about the statistical properties of the sample only. Beyond this averaged information, the speckle fine structure contains information about the individual spatial arrangement in the sample.

The problem in extracting this information from a measurement of the scattered intensity is that the phase information is lost in the intensity measurement. It has been shown mathematically, that the phase information can be retrieved when the scattering pattern is measured with a point density corresponding to at least twice the Nyquist sampling frequency [1]. This procedure is known as "oversampling". In this case, the phase can be reconstructed in an iterative process starting with a random phase guess. The measured scattering pattern and some trivial information about the sample (such as that it is confined in a certain area on the sample holder) is then used as a constraint in the iterations [2,3,4]. Recent experiments exploiting charge scattering from gold dots have demonstrated the viability of this approach in reconstructing the real space structure of submicron structures using soft x-ray scattering [5].

In this work, we are trying to lay the foundations in order to extend this concept to the investigation of magnetic domain patterns. Such patterns can be probed by resonant magnetic scattering. Circular and linear x-ray dichroism give rise to magnetization dependent contributions to the scattering cross-section and can be used as a contrast mechanism for small angle scattering. A scheme of the experiment is presented in Fig. 1. A circular pinhole (A) with 5.0 μm diameter [6] is mounted in front of the sample, restricting the sample illumination to the transverse coherence length of our x-ray beam. Sufficient longitudinal coherence is achieved by monochromatization of the x-ray beam. The sample (B) consists of a Co/Pt thin film multilayer medium with perpendicular anisotropy, which forms worm domains magnetized parallel or antiparallel to the sample normal [7]. The magnetic medium was grown on a SiN_x membrane and illuminated in a normal incidence transmission geometry. The scattering pattern (C) is recorded on a position sensitive detector with the energy of the incident photons tuned to the Co L_3 edge. In addition, the polarization of the incident beam was varied between right and left circular and linear. The experiments were carried out at the SGM beamline of the BESSY II UE56/1 undulator.
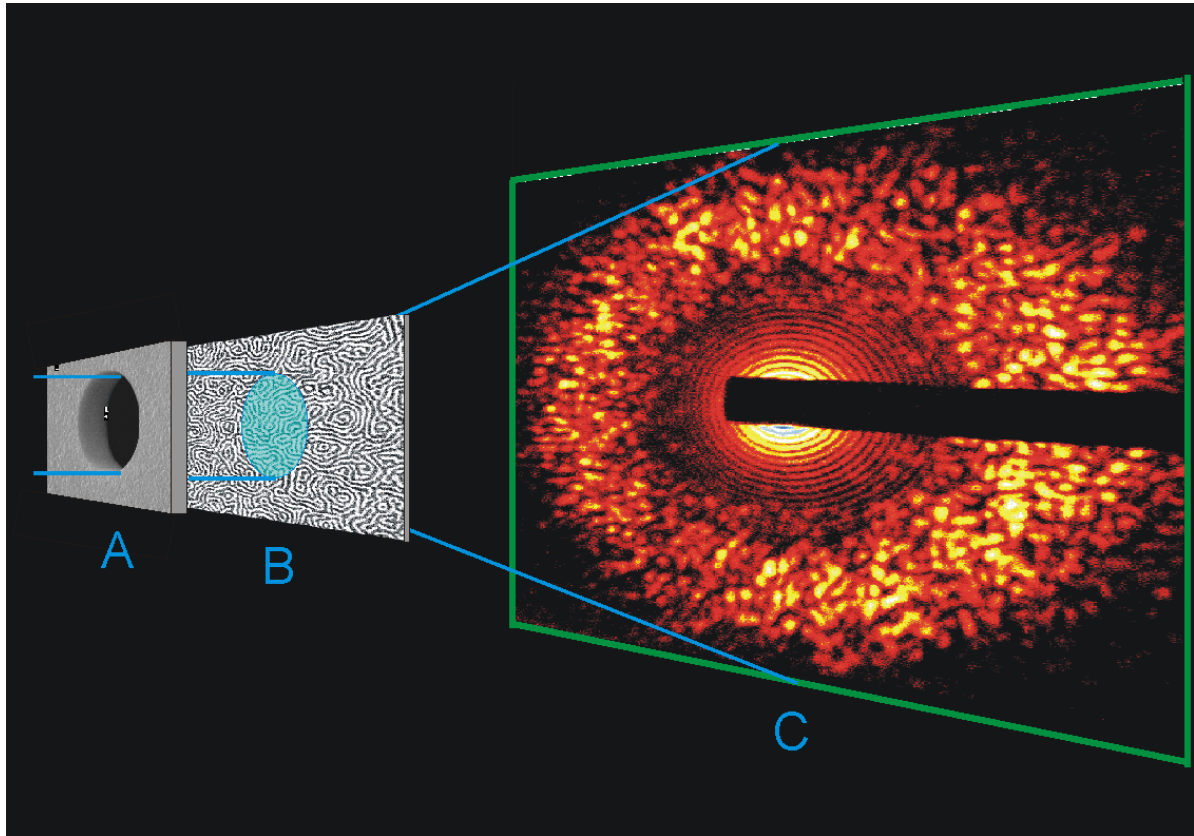
Fig.1 Schematic of a coherent scattering experiment. The illuminated area on the sample is defined by a pinhole (A), which in the experiment described here has a diameter of 5.0 μm, located 380 μm in front of the sample surface. The Co/Pt multilayer sample (B) is grown on a SiN_x membrane and mounted in a transmission geometry. The scattered intensity is observed on a 2D position sensitive detector (C). The central beam was blocked by a rod in front of the detector. Intensity is shown on a false color log scale. The images of the Pinhole (A: SEM [6]), worm domains (B: XM1[8]) and scattering pattern (C) have been distorted to create a 3D effect.

Using circularly polarized radiation at the Co L_3 resonance, we observe scattering patterns as the one shown in Fig. 1. In the vicinity of zero momentum transfer q, the scattering is dominated by the charge scattering from the pinhole, generating a Fraunhofer pattern. Magnetic small angle scattering from the domain pattern is observed at higher momentum transfer, corresponding to a in plane domain correlation length centered at about 216 nm, in agreement with results from STM and x-ray microscopy [7,8]. Speckle fine structure is clearly visible. Apart from this fine structure, the in-plane momentum transfer in the multilayer sample is isotropic. The small angle scattering ring is reduced by several orders of magnitude in intensity when the incident photon energy is lowered 10 eV below the Co L_3 resonance, illustrating the magnetic origin of this scattering feature. When the magnetic contrast is inverted by switching from right circular to left circular polarized illumination, the speckle pattern does *not* change. This is an illustration of Babinet's theorem, which states that the scattering pattern from a given object is the same as the scattering pattern from the inverted object. Charge scattering from the pinhole and magnetic scattering from the domains are fairly well separated in the reciprocal space (q-space) due to the different real space lengthscales. Charge scattering arising from the sample roughness is located in a q-range exceeding the detection range. As a result, charge-magnetic interference terms can be neglected in first approximation over a large q-range and the prerequisites for Babinet's theorem are fulfilled for the magnetic scattering ring. One at first hand surprising

consequence is that again the same speckle fine structure is observed, when illuminating the sample with *linearly* polarized radiation. This is due to the fact that the right circular and left circular channels can not interfere. Consequently, this type of experiments can be performed at beamlines that deliver linearly polarized radiation only – given the prerequisites for Babinet's theorem are fulfilled.

We have adapted reconstruction algorithms to the case of resonant magnetic scattering, taking the magnetooptic details of the scattering process into account. A preliminary reconstruction of part of the worm domain structure in a Co/Pt multilayer sample from the measured data in Fig.1 is shown in Fig. 2. We are now in the process of rigorously checking the reconstruction procedure by independently measuring the magnetic real space structure of the sample area illuminated in the scattering experiment.
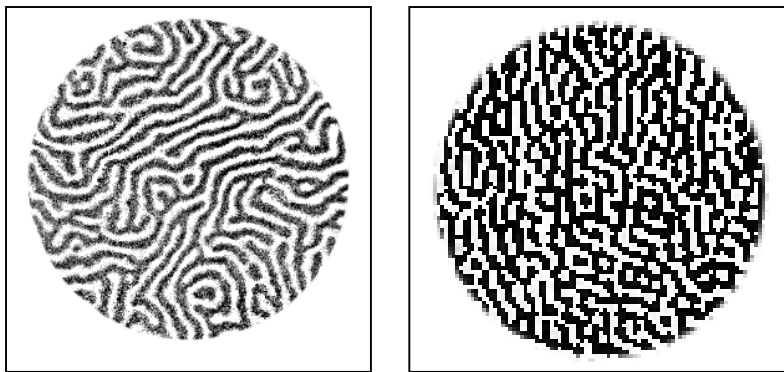
Fig.2. Real space image of the magnetic domain distribution in a Co/Pt multilayer sample as measured by x-ray microscopy (left) and obtained in a preliminary reconstruction from the coherent resonant scattering data presented in Fig.1 (right). The field of view is 4 µm. Different areas of the sample are shown.

References and Acknowledgements

[1]   R. Barakat, G. Newsam, J. Math. Phys. **25**, 3190 (1984)
[2]   R.W. Gerchberg, W.O. Saxton, Optik **35**, 237 (1972)
[3]   J.R. Fienup, Opt. Lett. **3**, 27 (1978)
[4]   J.R. Fienup,Appl. Opt. **21**, 2758 (1982)
[5]   J. Miao, P. Chararlambous, J. Kirz, D. Sayre, Nature **400**, 342 (1999)
[6]   We thank C. Rettner at IBM Almaden for the fabrication and characterization of the pinholes.
[7]   We thank E. Fullerton and O. Hellwig at IBM Almaden for the fabrication and characterization of the worm domain samples.
[8]   Magnetic X-ray microscopy of a worm domain sample was performed in collaboration with G. Denbeaux at the XM-1 x-ray microscope at the ALS, Berkeley. We would like to thank G. Denbeaux and A.L. Pearson for their help.

SMART – A SPECTROMICROSCOPE WITH ENERGY-FILTER

SMART collaboration (coordinator: E. Umbach, authors: R. Fink, Th. Schmidt)

(Univ. Würzburg - Fritz-Haber-Institut der Max-Planck Gesellschaft Berlin - TU Darmstadt - TU Clausthal – LEO Oberkochen – BESSY)

Worldwide, spectromicroscopy activities are steadily increasing. XPEEM (x-ray photoelectron emission microscopy) has become a routine technique. Especially the recent results based on the combination of XPEEM with magnetic linear or circular dichroism has recently demonstrated the importance of this method. At present one of the major disadvantages of XPEEM is the limited lateral resolution due to spherical and chromatic aberrations and due to the limited transmission of conventional PEEM optics. Two major spectromicroscopy projects are presently under way which shall overcome these limitations: the SMART project, an aberration corrected, energy-filtered XPEEM/LEEM at BESSY-II [1], and the PEEM-3 project at the Advanced Light Source [2]. Common to both instruments is a correction scheme proposed by Rose and Preikszas, which consists of an electrostatic tetrode mirror in combination with a highly symmetric magnetic beam splitter [3].

The SMART project has made significant progress in 2001. All single modules were successfully tested independently and are operational. However, due to the complexity of the final setup, a stepwise installation has been favored. At present, the SMART spectromicroscope is operated as an XPEEM with band pass energy filter at the BESSY U49/1-PGM beamline. It presently consists of an electromagnetic immersion lens, an electrostatic transfer optics, the aberration corrected energy filter (so-called OMEGA filter) and 2D projection optics. In particular, the implementation of the OMEGA filter offers interesting possibilities.

Here, we will particularly focus on the use of this filter, which already demonstrates the variability of methods of the final version: energy-filtered microscopy, spectroscopy and angular distributions. *Microscopy* is performed with (a) a fixed acceptance angle obtained by an aperture, (b) usually in normal emission, (c) at a chosen kinetic electron energy E_0 (start energy of the electrons at the sample), and (d) at fixed energy window ΔE set by the energy slit. *Spectroscopy* has been performed mainly by imaging the dispersion plane of the analyzer directly at fixed angular acceptance and with a chosen "surface area of interest". For the *angular distributions* the image of the emitted electrons is directly projected onto the detector at a chosen start energy E_0 with a selected energy window ΔE and with a chosen "surface area of interest". From a so-called stack analysis (the angular distribution is recorded for many different kinetic energies) one gets direct access to valence band structures or analyze photoelectron diffraction patterns.

a. Energy-filtered microscopy

As a test system we used three-dimensional graphite islands on a Ag(111) single crystal which were obtained by photolytic decomposition of NTCDA crystallites. Fig. 1 shows on the left the surface image at a moderate magnification of 2200 with secondary electrons at $E_0 = 0.9$ eV. The image on the right-hand side was taken with the Ag 3d photoemitted electrons at $E_0 = 71.2$ eV. The energy window of the filter was set to $\Delta E = 0.5$ eV; the photon energy was $h\nu = 450$ eV with an energy resolution of $\Delta E_{ph} = 0.1$ eV.
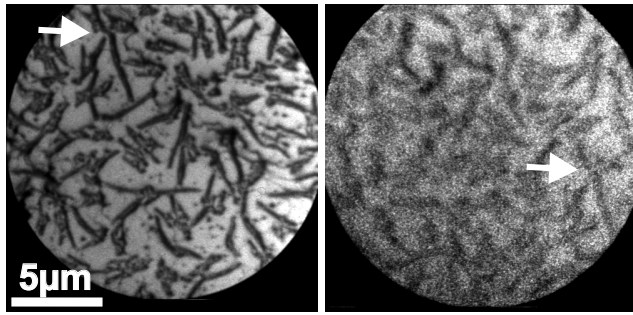
Fig. 1: Energy-filtered microscopy. Image of graphite islands on Ag(111) taken with secondary electrons at E_0 =0.9 eV (left) and with the Ag $3d_{3/2}$ photoemitted electrons at E_0 = 71.2 eV (right). The arrows mark the same surface spot.

The secondary electron image reveals a strong contrast due to the different gain of secondary electrons from the Ag substrate and the graphite islands. In this case we tuned the electron energy to the photoemission peak of Ag $3d_{3/2}$ (Fig.1 right). Under this condition the image intensity can be analyzed qualitatively: the bright areas are due to the Ag substrate, the dark areas to the graphite islands. Though the surface is shifted in the observed field of view, identical surface spots can be identified, as indicated by the arrows. Unfortunately, the quality of the Ag 3d photoemitted electron image is still rather poor due to a misalignment of the objective lens and a lack of intensity which could not be optimized because of the termination of the experiment.

Experiments to improve and demonstrate the lateral resolution of the present setup have not yet been performed since presently the here used objective lens is being reconstructed. However, in previous laboratory experiments a lateral resolution of 50 nm was achieved which - under the conditions at that time (no correction, defective objective) - was considered to be a rather good starting point.

b. Spectroscopy

For a comprehensive analysis of chemical states and compounds the spectroscopic mode is the best choice. Fig. 2 shows the Ag 3d doublet and the C 1s peak, both taken with 450 eV photon energy using a photon energy resolution of ΔE_{ph} = 0.1 eV. The top row shows the dispersion plane imaged on the detector with horizontal energy axis. In order to enhance the dynamical range of the detector system by up to two orders of magnitude, the energy focus is stretched perpendicular to the energy axis by a specific quadrupole in the OMEGA-filter. This procedure results in quite smooth spectra which are taken with a simple 8 bit camera.
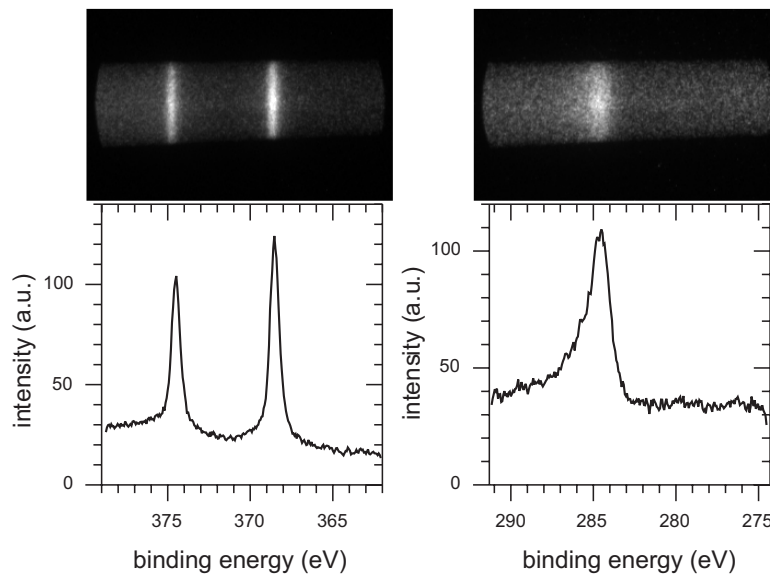

Fig. 2: Spectroscopy mode: imaging of the dispersion plane of the analyzer. Left: Ag 3d doublet, right: C 1s; top row: raw data on the detector screen, bottom row spectra generated simply by numerical integration of the raw data. The photon energy was $h\nu$ = 450 eV. The detected energy range in this specific measurement was 17 eV, but can be increased up to 30 eV, mainly by changing the settings of the projector optics.

For these spectra an object area with a diameter of 3 μm was selected by the field aperture. The magnification of the transfer optics of the SMART in principle allows sizes of selected areas down to less than 10 nm. The measured full width at half maximum of the Ag 3d peaks is 0.65 eV. A deconvolution gives an overall spectral resolution of less than 0.5 eV (at 15 KeV kinetic energy), which for first test measurements is a good value for this kind of microscope.

c. Angular distribution / Photoelectron diffraction (PED)

A special setting of the electron optics exchanges the image of the object plane with that of the back focal plane in which the angular distribution is available. Fig. 3 shows the angular distribution of secondary electrons for different kinetic energies in the range between 11 eV and 19 eV taken with an energy window $\Delta E = 0.5$ eV set by the OMEGA filter. The size of the object area selected by the aperture is 1 μm in diameter in all cases. Due to the strong acceleration of the electrons from the initial energy to the base energy of 15 keV, the instrument is able to utilize the *full angular half sphere*, i.e. the electrons at the edge start parallel to the surface. The origin of the pronounced threefold pattern of the secondary emission is a combination of the electron energy dispersion $E(\mathbf{k})$ (i.e. the band structure) and of diffraction processes of the emitted electrons (i.e. photoelectron diffraction). A quantitative analysis is complicated and hence has not been tried for the present preliminary data
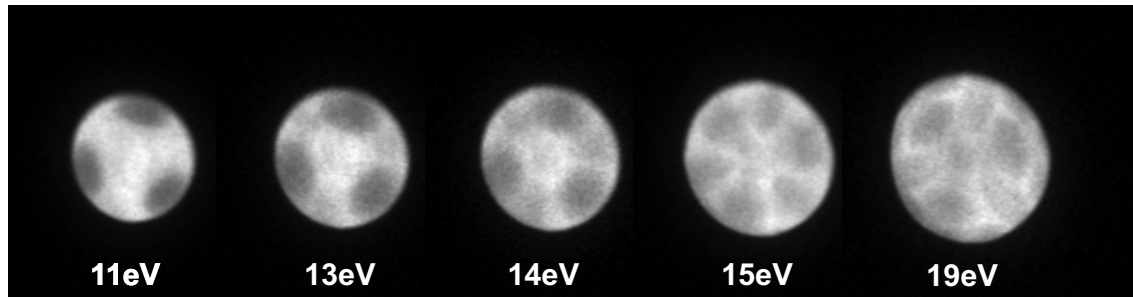

Fig. 3: Imaging of the angular distribution of the secondary electrons at a photon energy hν = 450 eV. The kinetic energy of the electrons is varied from 11 eV to 19 eV.

The present version of the SMART microscope already shows up all the three methods for comprehensive characterization of surfaces: microscopy, spectroscopy and diffraction. When the complete instrument is installed we will try to reach a lateral resolution hopefully close to the theoretical resolution limit of 0.5 nm at an energy resolution of ≤100 meV together with an increase in transmission by a factor of about 50. As a result new possibilities in surface science and investigations of nanoscaled samples will be opened.

References:

[1] R. Fink et al., J. Electr. Spectrosc. Rel. Phen. **84** (1997) 231.

[2] D. Preikszas and H. Rose, J. Electr. Micr. **1** (1997) 1; D. Preikszas, Dissertation D 17, Technische Hochschule, Darmstadt, Germany (1995)

[3] J. Feng, A. Scholl, private communication.

Measurements of bendable mirrors with a Long Trace Profiler

Frank Siewert, Heiner Lammert, Jan Schmidt, Brian N. Jensen*, Ulf Johansson*
BESSY GmbH, Albert-Einstein-Str. 15, D-12489 Berlin, Germany
*MAX-lab, Box 118, S-22100 Lund, Sweden

Introduction:

The use of bendable mirrors to generate x-ray micro-foci has become an interesting option in the designing of beamlines [1]. Here we describe a test of the optics for a new refocusing system for the I311-beamline at MAXLAB[2]. Beamline I311 is an undulator based VUV, soft X-ray beamline as described in [2] for high resolution XPS and XAS including the option for scanning photoelectron and photoabsorption microscopy with sub-micron lateral resolution. It covers the spectral range between 30 and 1300 eV. In the new design two Kirk-Patrick Baez pairs of bendable elliptical mirrors, exchangeable in situ, will allow for 1; a final focus at the experimental position (mirrors M4a and M5) or 2; an intermediate focus 1m before the experimental position (mirrors M4b and M6). The specified elliptical surface is produced by the controlled bending of a near shape polished elliptical cylinder ("plane-elliptical") mirror. A micrometer screw setting enables the mirror to be adjusted to defined sagitta and radii. The substrate material is GlidCop© Al-15 electroless nickel coated, the optical coating is gold (thickness: 40 nm). The mirror systems were manufactured by SESO.

Specifications: The mirrors M4a/M4b (useful length 150 mm) are specified for a slope of < 5 µrad rms and the M5/M6 couple (useful length 300 mm / 50 mm) for < 20 µrad rms (specification of the radius see at Table 1).

Measurement:

The mirrors were measured by using a Long Trace Profiler (LTP) [3]. In a non contact scan the slope error can be detected with an accuracy in the range of better than 40 nrad [4] and [5]. The mirrors were measured along a single line located in the central long axis. The mirror couple M5/M6 were measured at one radius setting while the second mirror couple M4a/M4b were measured at different radius settings. Due to the scan length the lateral resolution was settled in the range of 0,5 mm for mirror M6, 1,5 mm for mirror M4a/M4b and 3,0 mm for mirror M5. So that the complete optical length was characterised the scan length was a few millimeter longer than required.

Analysis:

Result of the LTP-measurement are raw intensity data converted to original slope data. The next step is to take a reference beam correction. The slope data at this point usually needs to have the mean subtracted as a zero order polynomial from current data (see figure 2a). Subsequently a subtraction of a 1st order polynomial from the slope data gives the residual slope error of the scanned surface compared to a circle and the base curvature as shown in figure 3a. Finally the reference corrected original slope values have to be best fitted to the parameter of an ellipse - see figure 4a.

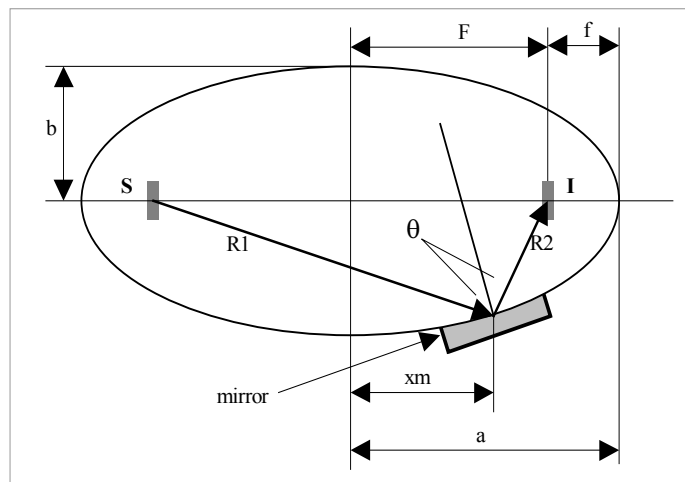|	
F	-distance minor axis - focus
xm	-distance minor axis to center of mirror
R1	-distance source – center of mirror
R2	-distance center of mirror - image
S	-source point
I	-image point
a	-major semiaxis
b	-minor semiaxis
f	-focal distance
θ	-grazing angle

Figure 1: Ellipse layout and parameter

The beamline design requires a source point **S** a mirror to focus the rays from source to image and an image point **I**. Assumed that the mirror surface is a segment of a ellipse the source point is one of the foci and the image point is at the other focus. The parameters specifying the ellipse are shown in Figure 1. The common way of specifying an elliptical mirror means to give the parameters for major semiaxis **a** and minor semiaxis **b.** To provide a complete picture it is useful to view the surface height profile as seen in figures 2b – 5b. By means of integration the surface height profile is derived from the slope function.

Results:

Table 1 shows the results for the four mirrors in comparison with the specification and inspection report of the manufacturer. We can notice a good consistency with the specification for the mirror radii. In the case of the slope results for three tested mirrors M4b, M5 and M6 a deviation from the specified values of the original ellipse parameters has been assigned. The slope error of mirror M4a complies with the specification. As shown in Table 1 a variation of the ellipse parameter **b** (a few millimeters or less) can be used to adjust a slope optimum better than specified for each mirror (see also figure 5a/b). All other ellipse parameters continue in position as calculated (see also at figure 1). In a setting range of 5 positions the bending mirror M4b has been tested. To demonstrate the performance of the mirror bender (see figure 7) each tested position was measured for the turn in and turn out case. As expected a hysteresis curve for the radius-displacement-relation was recorded (see figure 7). The sagitta-displacement-relation as well was recorded (see figure 6). The Figure 7 also shows a good reproducibility of return of shape to that at the starting position at 5,81 mm. The results for both measurements comply with the required specification of radius and sagitta. Of course for any positioning of the mirror this hysteresis can be avoided by driving the mirror in the same direction to the desired position. The results of the two measurements at the position of 7,4 mm demonstrate an admissible stability of shape. The time between the two measurements accounted to 16 hours. But over a longer period a stability check is recommended.
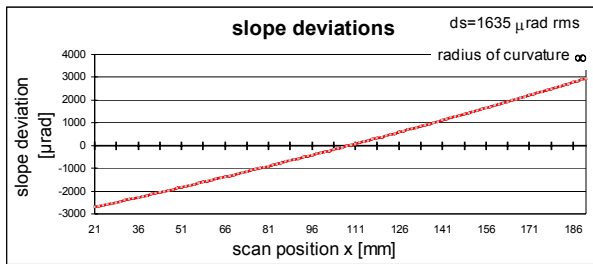

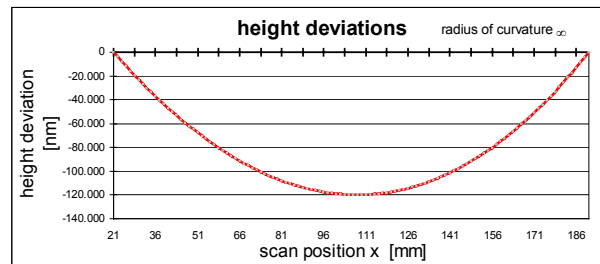
Figure 1a : Mirror M4b original slope profile

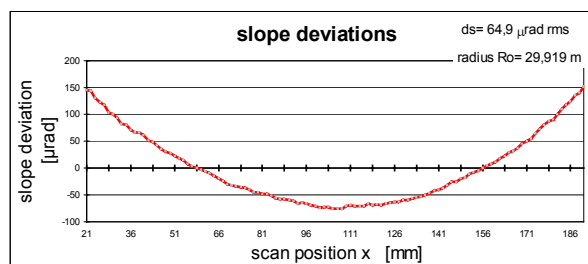Figure 1b: Mirror M4b surface height profiler derived from slope data

Figure 2a: Mirror M4b residual slope profile compared to sphere and base curvature
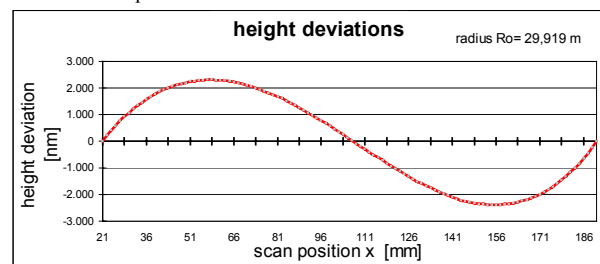

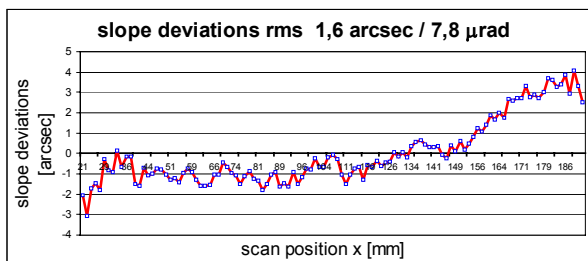Figure 2b: Mirror M4b surface height profile derived from from residual slope data

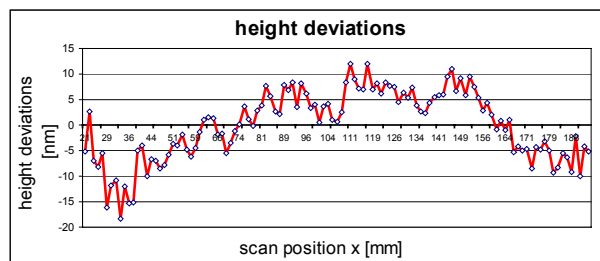Figure 3a: Ellipse parameter converted slope profile for mirror M4b

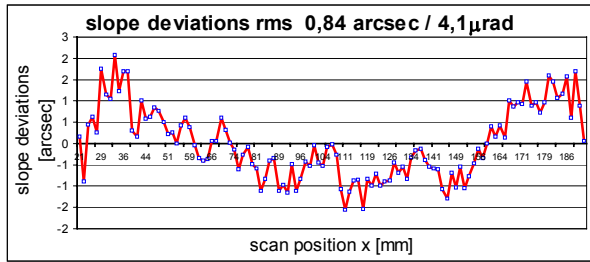Figur 3b: Surface height profile derived from ellipse converted slope data

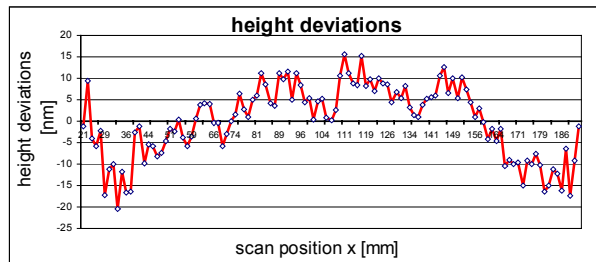Figure 4a: Mirror M4b surface gheight profile derived from ellipse slope data with slope optimized parameter b

Figure 4b: Mirror M4b ellipse converted slope profile with slope optimized variation of parameter b

Mirror	Specification		inspection report		BESSY – LTP-results			
	range of curvature		radius		radius at best fit			
	r [m]	slope error [µrad rms]	r [m]	slope error [µrad rms]	r [m]	slope error [µrad rms]	slope error [µrad rms] **with variation of parameter b**	
M4a	56,0 – 64,5	< 5	63,57	3,1	64,73	5,0	4,5	(0,23mm)
M4b	30,4 – 32,0	< 5	31,04	4,3	29,92	7,8	4,1	(-0,202mm)
M5	48,0 – 58,0	< 20	51,51	5,4	48,0	99,4	4,3	(3,712mm)
M6	7,8 – 8,72	< 20	8,26	14,7	8,52	138	9,7	(-1,762mm)

Table 1: Measurement results of radius and slope error in comparison with specification
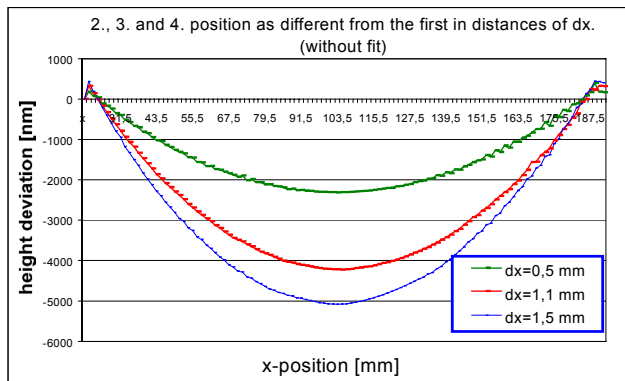

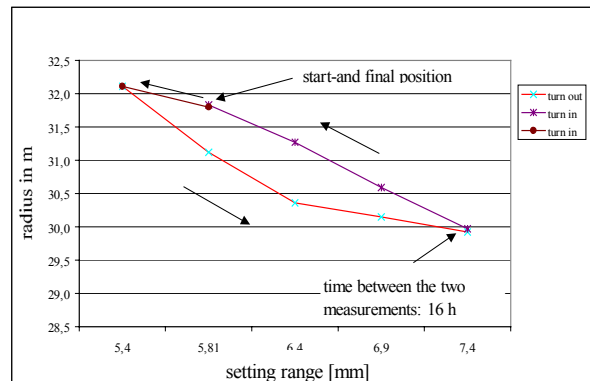Figure 6: Mirror M4b, sagitta difference at various setting positions

Figure 7: Mirror M4b, radius – displacement relation

Conclusions:

By use of a LTP a detailed quality check of bending mirrors enables good results of slope and shape deviation and variation as well. The interaction between micrometer setting and mirror shape were tested and shows an admissible reproducibility of shape. Considering the range of slope and radii in question and allowing a slight variation of the ellipse parameter **b** we notice a good consistency with the inspection report of the manufacturer and in general the results are in the range of specification.

References:

[1]   H.A. Padmore, M.R. Howels, S. Irick, T. Renner, R. Sandler and Y.-M. Koo; "Some New Schemes for Producing High-Accuracy Elliptical X-ray Mirrors by Elastic Bending", 1996, SPIE Conference, Denver

[2]   R. Nyholm, J.N. Andersen, U. Johansson, B.N. Jensen, I. Lindau; "Beamline I311 at MAX-lab; a VUV/soft X-ray undulator beamline for high resolution electron spectroscopy", 2001, Nucl. Instr. and Meth. in Phys. Res A *467-468*, P.520-524

[3]   Takacs, P.Z., Qian, S.-N.; US Pat. 4,884,697; Intern`l Class: G01B 009/02, filed: June 21, 1988

[4]   H. Lammert, F. Senf, M. Berger, „Improvement of Synchrotron Radiation Mirrors below the 0.1 arcsec rms Slope Error Limit with the Help of a Long Trace Profiler" 1997, SPIES`s International Symposium, San Diego

[5]   H. Lammert, "Subnanometer Accuracy Measurements with the LTP at BESSY" March 2000; Int. Workshop on Metrology for X-ray and Neuron Optics, APS Argone Nat. Lab.

Broad Band, Far Infrared Coherent Synchrotron Radiation at BESSY II

M. Abo-Bakr, K. Holldack, H.-W. Hübers*, D.Ponwitz, G. Wüstefeld
BESSY GmbH, Albert-Einstein-Str. 15, 12489 Berlin, Germany
*DLR GmbH, Rutherfordstrasse 2, 12489 Berlin, Germany

Synchrotron radiation is emitted in form of coherent waves (CSR), if the wavelength of the radiation is comparable or longer than the typical electron bunch length. In this case the electromagnetic waves superimpose with equal phase leading to constructive interference. This process yields highly enhanced intensities compared to the incoherent intensity. The enhancement factor at wavelength λ is proportional to the number of involved electrons, typically of around 10^9 , and a bunch shape factor f(λ), given by the square of the Fourier transform of the longitudinal bunch shape /1/. This emission process was demonstrated already in LINAC based machines /2/. At BESSY II it was now shown for the first time, that steady state coherent emission of the radiation is also possible in electron storage rings. Because the bunches are typically of mm length, these results are of interest for designing and building intense, broad band far infrared synchrotron radiation sources. Recent results of CSR experiments at BESSY II are presented /3/.

At BESSY II the rms electron bunch length of the regular user optics is about 5 mm.

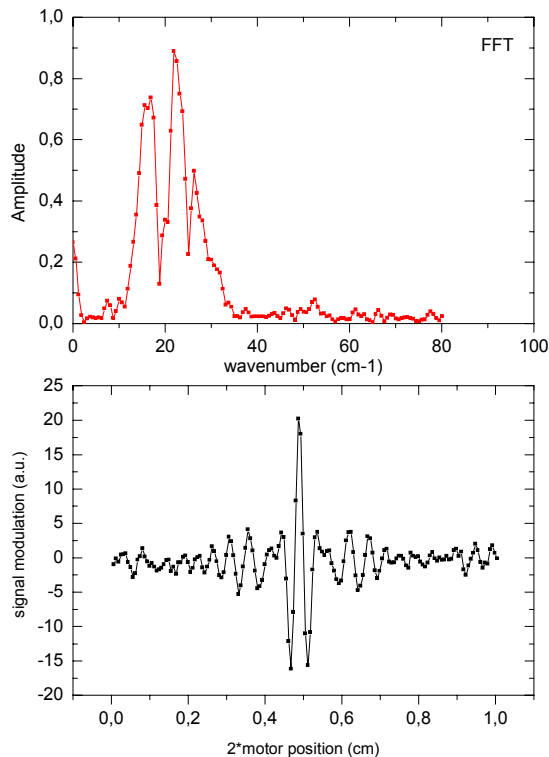Fig. 1: Interferogram and Fourier spectrum measured at 1.5 mm bunch length.
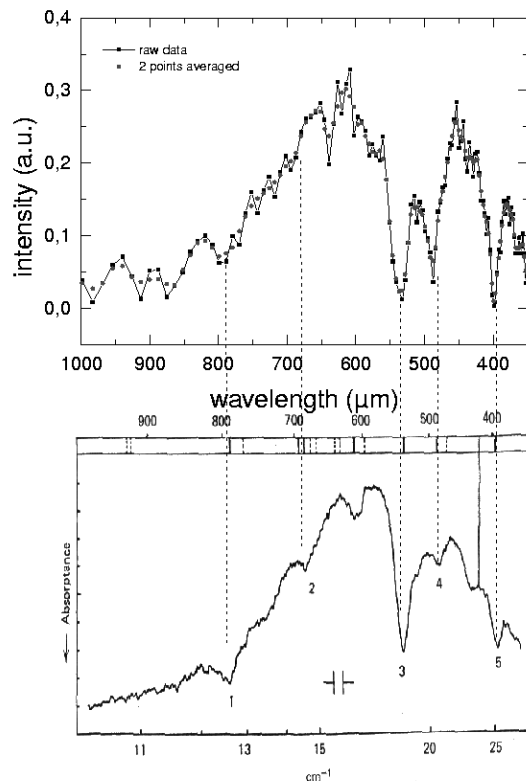
Fig.2: Comparison of the FTIR spectrum with a water spectrum /4/.

Incoherent or coherent radiation of comparable wavelength can not be observed, it is suppressed by screening effects of the vacuum chamber which has a cut off of around 4 mm wavelength. However, far infrared (FIR) coherent synchrotron radiation can be generated and

observed at the BESSY II storage ring by operating the ring in a dedicated 'low alpha mode' /5/. The low alpha optics is a special setting of the ring magnets to shorten the bunch length. This dedicated optics can be characterized at fixed rf accelerating voltage by the synchrotron oscillation tune f_s. In the limit of zero beam current, where current dependent bunch lengthening effects are absent, the rms bunch length is proportional to the synchrotron tune. Compared to the user optics with a synchrotron tune of $f_s = 7.5$ kHz, the BESSY low alpha optics can be tuned down to $f_s = 0.35$ kHz. There are no systematic measurements of the bunch length yet, but at fs=2.2 kHz a bunch length reduction by a factor of 3 was recently verified by streak camera measurements /6/.

The synchrotron radiation is detected with a liquid helium cooled InSb-detector, most sensitive in the 0.5 mm - 2 mm wave length range respective 5 cm^{-1} to 20 cm^{-1} wave numbers. The detector is sufficiently fast to resolve the 1.25 MHz revolution frequency of the beam in the storage ring. It is placed about 15 m away from the source point in the dipole and the FIR is directed through 3 m air being reflected by a set of metal coated plane mirrors into a Michelson-Fourier Spectrometer and a LnHe-cooled InSb-bolometer. The detector signal is conducted into a spectrum analyzer and the strength of 1.25 MHz signal line is recorded as a function of the interferometer path length difference.
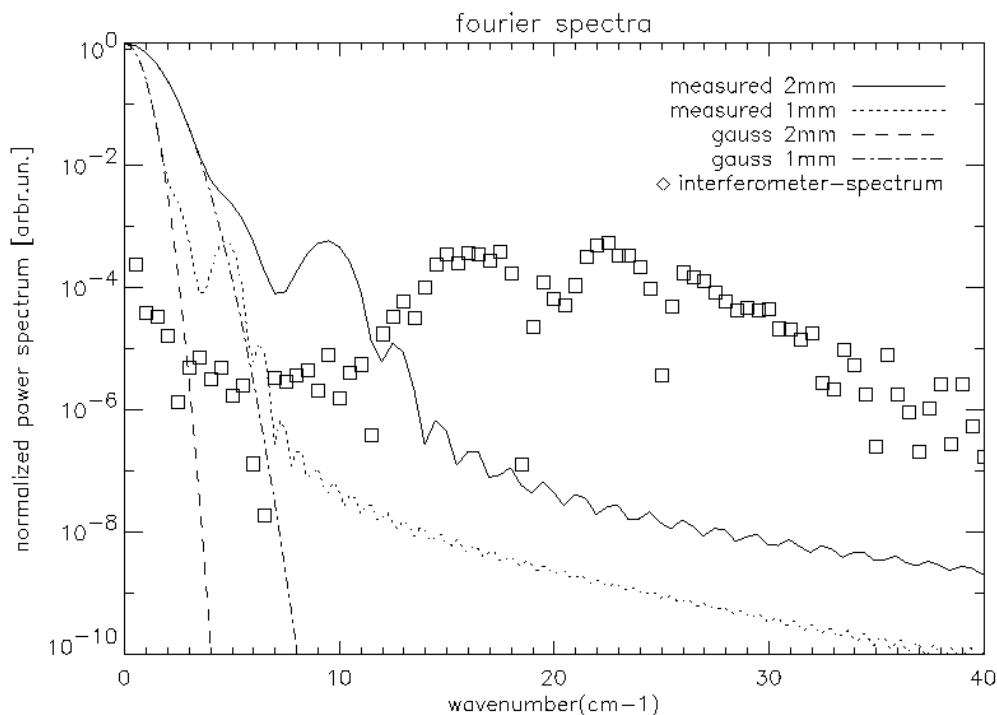
Fig 3: Comparison of the expected CSR spectra for different bunch shapes and lengths to a measured spectrum at f_s=1.5 kHz which is dominated by humid air transmission.

The coherent character of the radiation was already demonstrated, by showing that the FIR signal strength is not growing linearly but with the square of the beam current /7/. The absolute value of the enhancement compared to the incoherent case could not be derived, because the incoherent signal was always below the back ground level. The maximal recorded coherent signal strength was about 3000 stronger than the background, the incoherent signal was below the background level and not visible. By time and frequency resolved measurements it was further shown that the radiation is of steady state character and not bursting /3/.

Recent measurements could now demonstrate the broad band character of the radiation by performing measurements with a Michelson interferometer. For a storage ring current of 12 mA distributed in 100 adjacent bunches and a tuning parameter of fs = 1.5 kHz an example of the interferometer measurement and its Fourier transform is shown in figure 1. An expanded portion of the Fourier transform in a different scale is seen in figure 2, compared with a published result of a water vapor absorption spectrum. Our measured signal, without any correction with respect to the beam bunch shape or the spectrometer transmission shows a similar absorption characteristic by residual water in the air. More important is the conclusion from the measurements, that the FIR is emitted as a broad band radiation, at least ranging from wave numbers 10 cm^{-1} to 40 cm^{-1}.

As demonstrated in figure 3, the detection window as limited by the detector and the transmission of the setup is illuminated by the coherent emission of non-Gaussian bunches. Gaussian bunches show a steep decaying power spectrum with increasing wave numbers which probably would not be sufficient to explain the detected signal intensity beyond 10cm^{-1} wave numbers. By scaling the length of a measured (non-Gaussian) bunch to shorter values, the power spectrum becomes wider and more intensity covers the detection window leading to an enhancement of the FIR signal similar as observed /7/. In this comparison a bunch shape measured with a streak camera /5/ was used and scaled to 1 mm and 2 mm rms length.
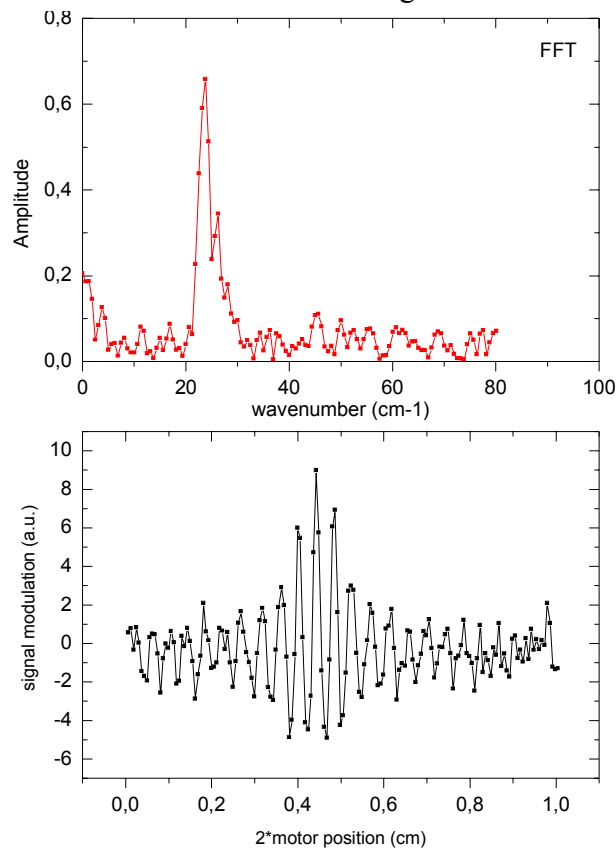
Figure 4 shows a spectrum were a high pass filter /8/ is placed in front of the detector entrance. A steep cut off for frequencies lower than 20 cm^{-1} is visible. The corresponding interferogram in the lower graph shows only the high frequency components as compared to figure 1.

From the measured spectrum and also from the interferogram itself basically the bunch length can be reconstructed, but this demands for water-absorption free measurements, especially in the wavelength range comparable to the bunch length and for a precise determination of the detector transmission function.

Fig.4: Interferogram and Fourier spectrum of CSR after passing a high pass filter /8/.

References

/1/ see for example, H. Wiedemann, Particle Accelerator Physics I, chapter 9.2 'Coherent Radiation'

/2/ Observation of Coherent Synchrotron Radiation, T. Nakazato, M. Oyamada, N. Niimura et al., Phys. Rev. Letters, (63) number 12, p. 1245, 1989

/3/ Steady State Far Infrared Coherent Synchrotron Radiation detected at BESSY II, M. Abo-Bakr, J. Feikes, K. Holldack, G. Wüstefeld, BESSY mbH Berlin and H.-W. Hübers, DLR Berlin, submitted to Phys. Rev. Letters November 2001

/4/ H. Yoshinaga et al. J. Opt. Soc. Am. (48), 315 (1958)

/5/ see for example, H. Wiedemann, Particle Accelerator Physics I, chapter 8.2.3 'Bunch Length'

/6/ P. Kuske, BESSY, private communication

/7/ Coherent mm-Radiation Experiments at the BESSY II Storage Ring, M. Abo-Bakr, J. Feikes, K. Holldack, D. Ponwitz, G. Wüstefeld, BESSY mbH, H.-W. Hübers, DLR, Proceedings of the 7th European Particle Accelerator Conference, Vienna, 2000

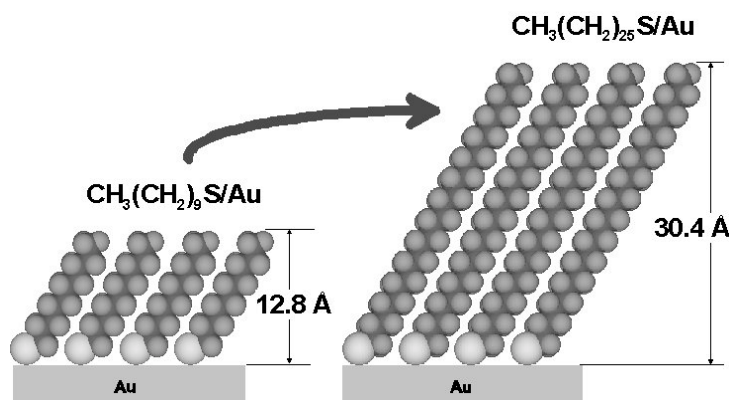/8/ by courtesy on leave from Ake Andersson, MAX-Lab, Lund (Sweden)

An extension of the mean free path approach to X-ray absorption spectroscopy

M. Zharnikov, S. Frey, K. Heister, and M. Grunze

Angewandte Physikalische Chemie, Universität Heidelberg, Im Neuenheimer Feld 253, 69120 Heidelberg, Germany

A proper interpretation and quantitative analysis of the Auger electron and X-ray photoelectron spectra requires knowledge of the electron inelastic mean free path (IMFP), which is an extensively studied parameter over a broad range of materials and kinetic energies. This parameter describes the attenuation and effective escape depth of the primary Auger- or photoelectrons due to inelastic scattering events. Any such event that results in an energy loss larger than the given energy resolution of the spectrometer reduces the number of acquired electrons.

The situation is, however, completely different in the case of the X-ray absorption spectroscopy (XAS). In the partial electron yield (PEY) acquisition mode, which is commonly used in XAS experiments, both elastically and inelastically scattered electrons contribute to the signal with the latter contribution dominating. In this situation, the majority of inelastic scattering events will not result in an overall signal attenuation as in the case of Auger electron and X-ray photoelectron spectroscopy (AES and XPS, respectively) since some of the inelastically scattered electrons still have a kinetic energy in the acquisition range of the spectrometer (PEY detector). The respective values of the effective mean free path (MFP or λ) should, therefore, be somewhat larger than the IMFPs for electrons of definite kinetic energy.

Fig. 1. A schematic drawing of the Cn SAMs used in this study. The length of the aliphatic chains was changed from 10 to 26 CH_2/CH_3 entities to vary the film thickness (the theoretical values are shown in the figure for C10 and C26) in a controlled way.

To obtain reliable quantitative information on the MFP for the PEY acquisition mode we performed XPS and near edge X-ray absorption fine structure (NEXAFS) spectroscopy measurements for a series of alkanethiol (AT or Cn: $CH_3(CH_2)_{n-1}SH$, n = 10 - 26) SAMs on gold substrates, which are well-defined and densely packed two-dimensional arrangements of the chain-like AT molecules anchored through a thiolate group to the substrate (Fig. 1).[1] The length of the alkyl chains and, subsequently, the film thickness was systematically varied which allowed us to estimate the MFP in both the XPS and NEXAFS experiment. The NEXAFS measurements were performed at the C 1s absorption edge, which is especially important for analysis of thin organic films and polymers. Our aims were to prove whether a standard MFP formalism is applicable in the case of the PEY acquisition mode and to get a quantitative information on the PEY MFP and its dependence on the detector settings.

The conventional IMFP for the Au 4f photoelectrons and the effective PEY MFP for the electrons originated from gold (λ_{Au}) were derived from standard expression[2,3]

$$ln\ [\ I(Au)_{Cn/Au}\ /\ I(Au)_{Au}\ ] = -\ nd\ /\ (\lambda_{Au}\ sin\theta\ ) + constant, \qquad (1)$$
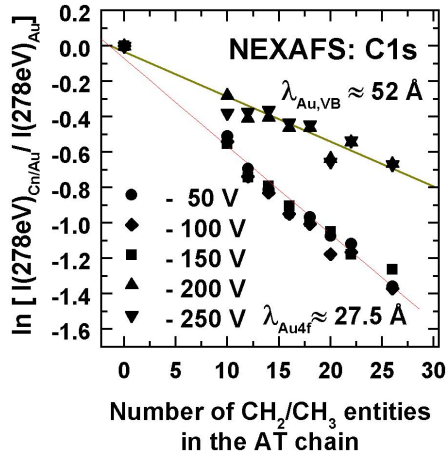
Fig. 2. Plots of *ln [I(278eV)$_{Cn/Au}$ / I(278eV)$_{Au}$]* versus *n* for retarding voltages of -50 V (circles), -100 V (diamonds), -150 V (squares), -200 V (up triangles), and -250 V (down triangles). The straight solid lines are the fits according to Eq. 1. The values of *I(278eV)$_{Cn/Au}$* and *I(278eV)$_{Au}$* were derived from the raw NEXAFS spectra. *I(278eV)* represents an average intensity in a pre-edge region. The derived values of the effective PEY MFP for the photoelectrons originated from the Au substrate are shown near the respective fits.
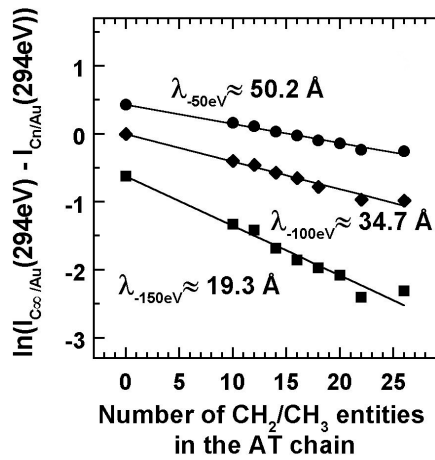
Fig. 3. The plots of *ln[I(C$_{KLL}$)$_{C\infty/Au}$ - I(C$_{KLL}$)$_{Cn/Au}$]* versus *n* for retarding voltages of -50 V (circles), -100 V (diamonds), -150 V (squares). The the straight solid lines are the fits according to Eq. 2. The C$_{KLL}$ PEY signal was derived from the raw NEXAFS spectra, in which the contribution of the Au substrate was subtracted. As a measure of this signal, the intensity at 294.0 eV was taken, close to the absorption edge at 287.8 eV. The derived values of the effective PEY MFP for the C$_{KLL}$ electrons are shown at the respective fits.

where $I(Au)_{Cn/Au}$ and $I(Au)_{Au}$ are either the intensities of the Au 4f signal or the pre-edge PEY intensities from the raw NEXAFS spectra for the IMFP and PEY MFP, respectively, and θ is the take-off angle of the electrons. The Au4f IMFP (32.5 Å) at a given kinetic energy of the Au 4f photoelectrons (~1169 eV) agrees well with literature values of 34 Å[3] and 31 Å[4]. The derived PEY MFPs are shown in Fig. 2. These values are noticeably larger than the respective IMPF values for the elastically scattered Au 4f electrons with a kinetic energy of ~190 eV (~8-10 Å) or the valence electrons of Au with the a kinetic energy of ~270 eV (11-12 Å).

Besides the effective PEY MFP for the electrons originated from the Au substrate, the PEY MFP for the C KLL Auger electrons λ_C in hydrocarbon Cn films was also estimated from an expression[2]

$$ln [I(C)_{C\infty/Au} - I(C)_{Cn/Au}] =$$
$$ln [I(C)_{C\infty/Au}] - nd / (\lambda_C \sin\theta), \quad (2)$$

where $I(C)_{Cn/Au}$ and $I(C)_{C\infty/Au}$ are the C$_{KLL}$ PEY signals from a conventional Cn/Au film and an infinitely thick Cn film (n → ∞), respectively. The derived values of λ_C are shown in Fig. 3. These values are 19.3 Å, 34.7 Å, and 50.2 Å for retarding voltages of -150 V, -100 V, and -50 V, respectively. In the same manner as the effective PEY MFP for the electrons originated from gold, they are noticeably larger than the respective IMFP for the C$_{KLL}$ electrons (11 Å). Moreover, the obtained values exhibit the expected increase of the PEY MFP with decreasing retarding voltage of the PEY detector, which is related to the increasing contribution of the inelastically scattered electrons to the signal.

References:

(1) M. Zharnikov, S. Frey, K. Heister, and M. Grunze, J. Electron Spectrosc. Relat. Phenom., in press.
(2) C. D. Bain, G. M. Whitesides, J. Phys. Chem. 93 (1989) 1670.
(3) P. E. Laibinis, C. D. Bain, G. M. Whitesides, J. Phys. Chem. 95 (1991) 7017.
(4) P. Harder, M. Grunze, R. Dahint, G. M. Whitesides, P. E. Laibinis, J. Phys. Chemistry B 102 (1998) 426.

X-Ray Magnetic Circular Dichroism investigation of the magnetization of ultrathin Fe on a V(110) single crystal complementary to Polarized Neutron Reflectometry

D. Schmitz, J. Hauschild, Y.T. Liu, H. Fritzsche, H. Maletta

Hahn-Meitner-Institut Berlin, Abt. SF2 Magnetismus, Glienicker Str. 100, D-14109 Berlin

We investigated ultrathin Fe films on a V(110) single crystal, a system which was hardly studied before. By Polarized Neutron Reflectometry (PNR) and Magneto-Optical Kerr Effect (MOKE) measurements [Naw99, Naw00] a reduced total magnetization has been found which would correspond to a magnetically dead Fe layer with a thickness of 2 ML. The main open question is, to which extent the apparent reduction of magnetization is caused by magnetically dead layers of Fe or by antiparallel coupling between the Fe moment and the induced V moment. It cannot be answered by PNR because under the conditions which were used this technique is sensitive to the total magnetization averaged over Fe and V. Therefore we studied this system at the $L_{2,3}$ absorption edges of Fe and V with XMCD, which is ideally suited to answer the open question. In particular, the advantages of XMCD were utilized to be surface sensitive in electron yield detection and element-specific. Therefore we were able to detect the induced V polarization and to determine the coupling between the magnetic moments of Fe and V, respectively. Our investigation with a V single crystal as substrate is a complement to XMCD experiments by other groups who studied superlattices [Scw98, Sch01a] and trilayers [Sch01b].

According to theoretical predictions [Veg93, Izq01] V at the interface to Fe is ferromagnetically ordered with antiparallel coupling to Fe, and the Fe at the interface is ferromagnetically ordered with reduced magnetic moment. Furthermore it has been calculated that interdiffusion at the interface amplifies both, the absolute value of the induced V moment and the reduction of the Fe moment. Assuming 6 ML of an $Fe_{0.5}V_{0.5}$ alloy at the interface as a model for the interdiffusion can explain the reduced total magnetization as determined with PNR.

Before the beamtime the V(110) single crystal was cleaned over weeks in order to minimize S, C and O contaminations. Cleaning the bulk of the V crystal would require several hundred hours of sputtering at different temperatures [Ada81, Beu00]. Considering this large effort we decided to clean only the surface region of the crystal. In order to achieve this sputtering and annealing cycles were performed using Ar ions with 500 eV kinetic energy and a maximum annealing temperature of 800°C. After this cleaning procedure the Auger intensity ratios of residual surface contaminations were below the detection limit for S_{152eV}/V_{473eV}, about 2.5% for C_{272eV}/V_{473eV} and about 2.5% for O_{493eV}/V_{473eV}.

The *in-situ* XMCD measurements were performed at beamline PM-1 at BESSY II. Elliptically polarized radiation with 0.94 degree circular polarization of fixed helicity was used. In order to measure the XMCD the magnetization direction of the sample was reversed. The base pressure of the chamber was $3 \ 10^{-10}$ mbar and the films were deposited with a rate of about 0.3 ML/min. V was deposited at a substrate temperature of 320 K in order to get a flat surface [Naw98] and Fe was deposited at room temperature.

As a first step XMCD of Fe was measured as a function of Fe thickness at room temperature. As an example the spectra of 5 ML Fe/V(110) are shown in Fig.1a where the asymmetry, defined as dichroism intensity devided by the sum, at the Fe L_3 maximum is -0.22. In Fig.1b the Fe L_3 asymmetry is shown as a function of Fe thickness. It turns out that the onset of the Fe magnetization at room temperature appears at 2 ML in accordance with the PNR results. Above 2 ML the Fe magnetization quickly increases and saturates at 4 ML.
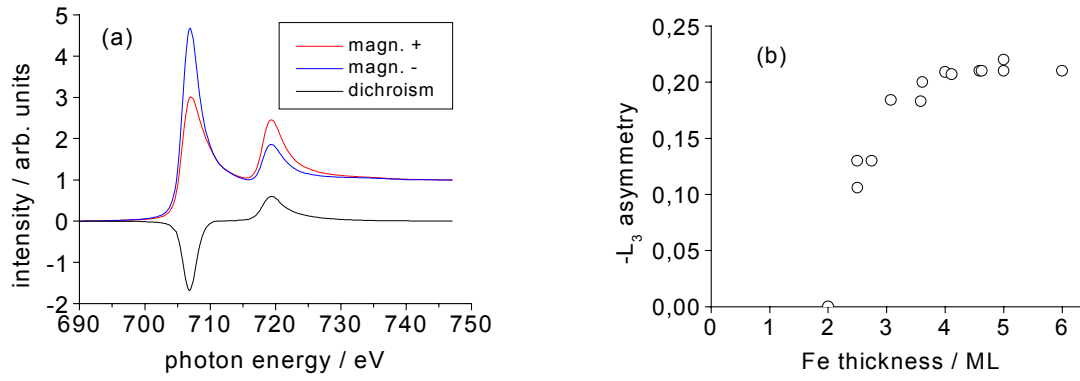
Fig.1a: Fe $L_{2,3}$ absorption spectra for two magnetization directions (red, blue line) and dichroism signal (black line) of 5 ML Fe/V(110); *b:* Fe L_3 asymmetry of Fe/V(110) as a function of Fe thickness at room temperature.

The sum rule analysis reveals that the Fe XMCD asymmetry above 4 ML corresponds to an average total magnetic Fe moment of 2.2 ± 0.1 μ_B per atom. This value is similar to the Fe bulk moment. Combining the Fe moment determined by XMCD with the average total magnetic moment determined by PNR, 1.3 ± 0.05 μ_B per Fe atom for 5 ML Fe [Naw99], enables us now to estimate the average V moment. Assuming that the V magnetization is located only within the first two monolayers at the interface to Fe implies an average value for the V moment of 2.3 ± 0.3 μ_B per atom oriented antiparallel to the Fe moment. Compared with the values of the experimental V moment in Fe_4/V_2 superlattices of 1.06 μ_B per atom [Sch01a] and the calculated V moment in an $Fe_{0.5}V_{0.5}$ alloy of at most 1.23 μ_B per atom [Izq01], our value of 2.3 μ_B per atom in 2 ML V seems to be too large. Future experiments are going to be performed to explain this contradictory result.

In Fig.2 XMCD spectra of V are presented which demonstrate that a net V magnetization with antiparallel alignment to the Fe moment is present. Please note that the dichroism signals in Fig.2 have been multiplied by 30 for illustration. The measured XMCD asymmetry of V at the rising edge of the L_3 white line is between 0.4% (Fig.2a) and 1% (Fig.2b) depending on the sample preparation. It is so small in both cases because the V magnetization is only located in the first few monolayers at the interface to Fe, whereas deeper V layers are not ferromagnetic but still contribute to the electron yield signal due to the escape depth of the secondary photoelectrons. In this sense the dichroism signal of the few ferromagnetic V layers close to the interface is diluted by the non-ferromagnetic V layers underneath. Nevertheless, reproducible measurements of the small V dichroism signal were possible due to the high stability of the storage ring BESSY II.
In Fig.2a and Fig.2b XMCD spectra of V are shown for 5 ML Fe/V(110) and 5 ML Fe/1 nm V/V(110), respectively. In the first case Fe was deposited directly onto the V single crystal, whereas in the second case a V buffer with a thickness of 1 nm was deposited before the Fe deposition. Obviously the XMCD asymmetry of V increases by more than a factor of 2 due to the V buffer layer. According to earlier LEED investigations [Naw98] the V buffer layer changes the island sizes along the in-plane [001] and [1-10] directions from 5.5 nm to 8.7 nm and from 6.3 nm to 4.8 nm, respectively. Thus the V buffer layer increases the area of the islands by 20% for rectangular islands and results in a decrease of the fraction of V atoms which are located at a kink. Since the V magnetic moment at the interface to Fe is enhanced at a kink [Izq01] this should decrease the V magnetization, in contrast to the experimental finding. Thus there must be another mechanism which explains the observed increase of the V

magnetization by the V buffer layer. One starting point for future investigations is that the V buffer layer strongly suppresses the C concentration at the surface as observed in the Auger spectra.
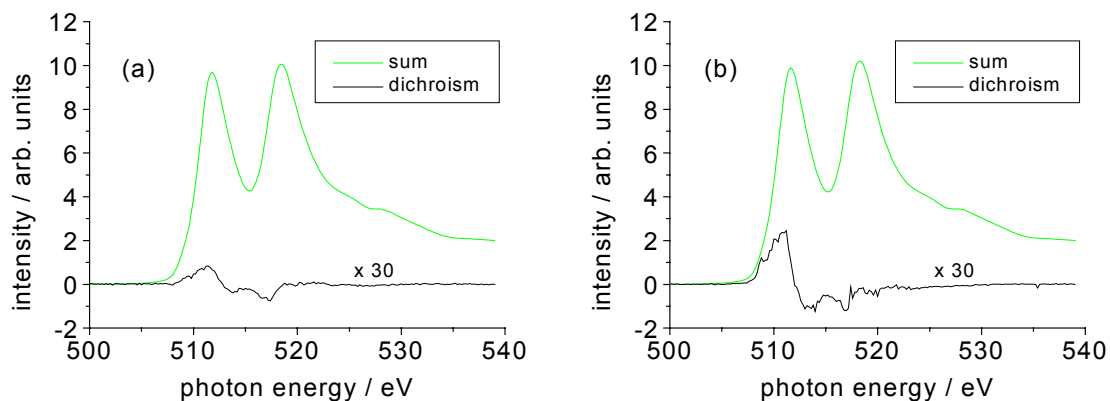
Fig.2a: V L$_{2,3}$ absorption and dichroism spectra of (a) 5 ML Fe/V(110) and (b) 5 ML Fe/1 nm V/V(110). The asymmetry is increased by a factor of 2 by the V buffer layer.

No increase in the XMCD asymmetry of V is observed when capping the Fe with 2 ML V. This finding is in accordance with the PNR results [Naw99]. An increase in the XMCD asymmetry of V by a factor of 2 or so would be observed if the V cap layer was ferromagnetic. Further investigations are needed to explain the observed behavior of the V magnetization.

[Naw99] T. Nawrath, H. Fritzsche, F. Klose, J. Nowikow, H. Maletta, Phys. Rev. B 60, 9525 (1999)
[Naw00] T. Nawrath, H. Fritzsche, H. Maletta, Journ. Magn. Mag. Mat. 212, 337-346 (2000)
[Scw98] M.M. Schwickert, R. Coehoorn, M.A. Tomaz, E. Mayo, D. Lederman, W.L. O'Brien, Tao Lin, G.R. Harp, Phys. Rev. B 57, 13681 (1998)
[Sch01a] A. Scherz, H. Wende, P. Poulopoulos, J. Lindner, K. Baberschke, P. Blomquist, R. Wäppling, F. Wilhelm, N.B. Brooks, Phys. Rev. B 64, 180407 (2001)
[Sch01b] A. Scherz, P. Poulopoulos, H. Wende, G. Ceballos, K. Baberschke, F. Wilhelm, J. Magn. Magn. Mater. proc. (2001)
[Veg93] A. Vega, L.C. Balbás, H. Nait-Laziz, C. Demangeat, H. Dreyssé, Phys. Rev. B 48, 985 (1993)
[Izq01] J. Izquierdo, R. Robles, A. Vega, M. Talanana, C. Demangeat, Phys. Rev. B 64, 060404 (2001)
[Ada81] D.L. Adams, H.B. Nielsen, Surface Science 107 (1981) 305
[Beu00] M. Beutl, J. Lesnik, E. Lundgren, C. Konvicka, P. Varga, K.D. Rendulic, Surface Science 447 (2000) 245
[Naw98] T. Nawrath, H. Fritzsche, H. Maletta, Surface Science 414 (1998) 209

Resonant magnetic scattering with polarized X-rays from Co/Cu multilayers

M. Hecker[1], C.M. Schneider[1], H.-C. Mertins[2], D. Tietjen[1], D. Abramsohn[2], F. Schäfers[2]

[1]*Institut f. Festkörper- u. Werkstofforschung Dresden, Helmholtzstraße 20, 01069 Dresden, Germany*
[2]*Berliner Elektronenspeicherring-Gesellschaft für Synchrotronstrahlung m.b.H. (BESSY), Albert-Einstein-Straße 15, 12489 Berlin, Germany*

Nanoscale Co/Cu multilayers have received strong interest because of their unique magneto-transport properties (giant magnetoresistance, GMR). Less is known, however, about the correlation between their structural and magnetic properties, e.g., the influence of the interface roughness on the GMR which has been controversely discussed in the past. Using polarized soft X-rays opens the possibility to simultaneously investigate structural and magnetic features of the layer stacks.

We investigated Co/Cu multilayers with a nominal structure corresponding to the second antiferromagnetic (afm) coupling maximum ($40\times$[Co(1nm)/Cu(2nm)]/Co(1nm)). These were prepared by dc magnetron sputtering onto thermally oxidized (100)-Si and showed a typical GMR value of 27%. The scattering experiments were performed at the BESSY II UE56-PGM undulator beamline utilizing the polarimeter set-up described in [1]. Both T-MOKE and L-MOKE geometry were applied for the measurements.

Reflectometry curves measured with linearly polarized radiation at the Co L_3 edge (Fig. 1a, top curves) and with Cu-K_α radiation (bottom curve) show characteristic differences. For instance, the Kiessig fringes appearing in the bottom curve are nearly completely suppressed at the Co-L_3 edge due to the lower penetration depth. Also the plateau region observable in the first part of the curve measured with hard X-rays is missing in the top curves. This is due to the real part of the refractive index of Co exceeding 1 at wavelengths close to the L_3-edge (cf. [2]) thus precluding total reflection. Apart from the structural Bragg peaks caused by the chemical modulation in the multilayer (with 3 nm periodicity length), an additional peak of magnetic origin ("1st order magn. peak", Fig. 1a) is observed at the Co-L_3 edge. The appearance of this magnetic peak agrees with the measurements by Hase et al. [3], confirming the antiparallel magnetic coupling of adjacent Co layers in our multilayer structure (according to 6 nm periodicity length).

In contrast to previous reports [3], however, we also find a pronounced 3rd order magnetic peak. The larger angle of incidence results in a lower charge scattering background in this angular region. Therefore, the influence of an external magnetic field B is more accentuated than on the 1st order peak (Fig. 1b). As can be clearly seen in Figs. 1a,b, the most striking effect of B is the nearly symmetric intensity reduction of the magnetic peaks for opposite signs of B. This reduction is found to be almost independent of the orientation of B with respect to the scattering plane and is caused by a partial break-up of the afm coupling with increasing magnetic field. The maximum B field available in the polarimeter chamber was not sufficient to obtain magnetic saturation. Therefore the residual magnetic alignment of the adjacent layers still gives rise to small magnetic peaks.

Using Parratt's formalism [4] for the calculation of reflectometry curves on the basis of a structural model (an established approach in the hard X-ray region) and taking into account the magnetically induced variation of the refractive index n of the Co layers at the L_3-edge, the observed reflectometry curve can be reproduced (cf. Fig. 2). Within this model, a reduction of the afm coupling by ~70% must be assumed to fit the decrease of the magnetic peak heights at $B = 40$ mT.

In addition to intensity modulations which are even in *B*, also a difference in the reflectometry curves being *odd* in *B*, i.e., an asymmetry is visible in Fig. 1. In contrast to the general decrease of the magnetic peaks, this asymmetry effect was only observed for properly chosen orientations of the scattering geometry and B according to $f_{magn} \sim (e_i \times e_f) \bullet M$ [3], i.e. for T-MOKE and L-MOKE geometry, whereas for other orientations of *B* no significant asymmetry occurs. Details of the magnetic switching are inferred from additional hysteresis loop measurements. Depending on the angle of incidence, either the degree of antiparallel coupling or the magnetization of the multilayer as a function of the applied field can be derived from the loop measurements (Fig. 3).
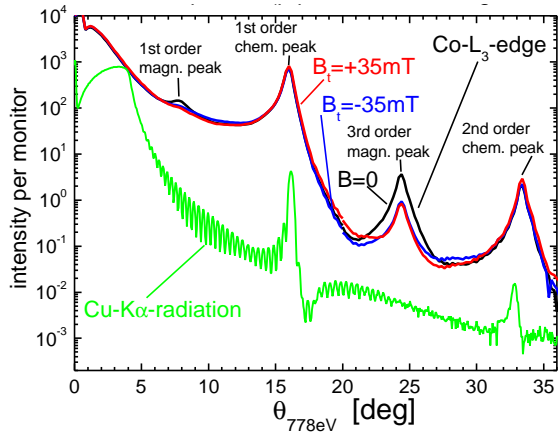

Fig. 1a: Reflectometry curves measured with Cu-Ka radiation (q recalculated for 778eV; green line), and at the Co-L3 edge with linearly p-polarized radiation (black line). The latter measurement was also performed with applied magnetic field (blue, red line).
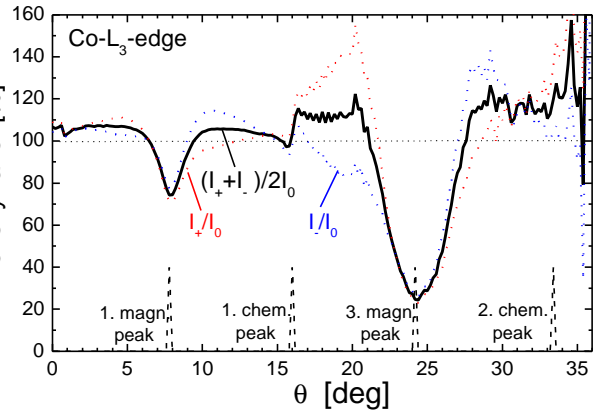

Fig. 1b: Ratio of the specular reflected intensity measured at the Co-L3 edge with applied magnetic field normalized to that without magnetic field (red, blue for + and - 35mT, black: average).
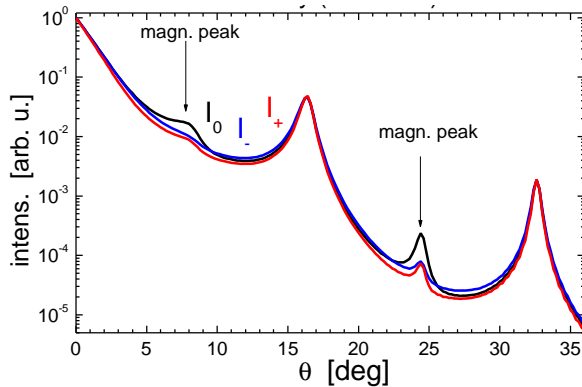
Fig. 2: Reflectometry curves calculated using a structural model of the multilayer and B-dependent optical constants for E=778eV (black: B = 0, red: B= +40mT, blue: B= -40mT).
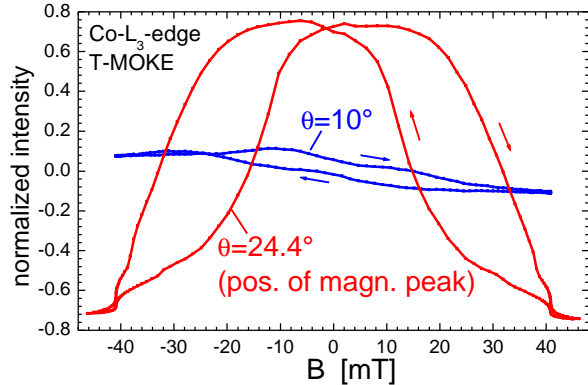
Fig. 3: Hysteresis loops measured at different positions of the reflectometry curve. The measured intensity I is normalized according to $2I/(I_{min}+I_{max})-1$.

References
[1] F. Schäfers, H.-Ch. Mertins, A. Gaupp, W. Gudat et al. , Appl. Opt. 37 (1999) 4074.
[2] H.-Ch. Mertins et al., to be published.
[3] T.P.A. Hase, I. Pape, D.E. Read, B.K. Tanner et al., Phys. Rev. B 61, 15331, 2000.
[4] L.G. Parratt, Phys. Rev. 95 (1954) 359.

Element-selective investigation of magnetic switching in transition metal layers

M. Hecker[1], C.M. Schneider[1], H.-C. Mertins[2], D. Elefant[1], D. Abramsohn[2], F. Schäfers[2]

[1]*Institut f. Festkörper- u. Werkstofforschung Dresden, Helmholtzstraße 20, 01069 Dresden, Germany*
[2]*Berliner Elektronenspeicherring-Gesellschaft für Synchrotronstrahlung m.b.H. (BESSY), Albert-Einstein-Straße 15, 12489 Berlin, Germany*

One of the unique advantages of resonant X-ray magnetic scattering is its element-selectivity. This feature has been employed to investigate magnetic switching in giant magnetoresistance (GMR) multilayers and spin-valve structures. The understanding of hysteresis phenomena in such structures is mandatory for a further improving materials systems for applications (cf. e.g. [1]). Our measurements were performed at the BESSY II UE56-PGM undulator beamline using the polarimeter setup [2] in T- and L-MOKE scattering geometries.

Fig. 1a shows reflectometry measurements of a [CoFe/Cu/NiFe/Cu]$_{20}$ layer stack with individual layer thicknesses close to the 2nd antiferromagnetic (afm) coupling maximum. The relatively low GMR of ~5% for this sample indicated that the coupling of adjacent magnetic layers in this sample is only weak. This is also reflected by the absence of additional magnetic peaks in Fig. 1a; i.e. all observed peaks arise due to the chemical modulation in the multilayer structure and are well reproduced also at measurements far away from the absorption edges. However, a significant asymmetry in the reflectometry curves appears in between the Bragg peaks for the near-edge measurements, thus enabling the determination of element-selective hysteresis loops (Fig 1b). The curves clearly show the simultaneous (ferromagnetic) switching of all constituent elements. The magnitude of the effect is strongest in Fe and weakest in Ni.
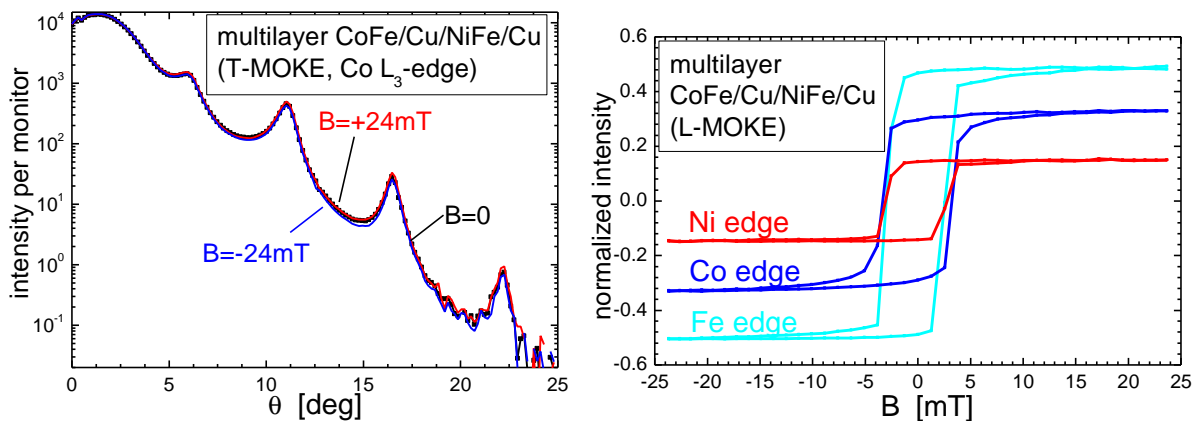
Fig. 1: Reflectometry measurements of a multilayer with 20 bilayers of alternating CoFe/Cu and NiFe/Cu (left) and hysteresis loops measured at different L_3 edges (intensity I normalized according to $2I/(I_{min}+I_{max})-1$, right).

Another more complex behaviour is observed in the spin-valve structure depicted in Fig. 2a. The upper CoFe layer is magnetically pinned to an IrMn antiferromagnet, whereas the lower NiFe layer acts as a free layer, its magnetization following the direction of an external field. Scanning the intensity of the specularly reflected radiation at fixed incidence angle versus the energy of the radiation, the resonant enhancement of the scattering at the absorption edges allows one to select precisely those wavelengths where both the magnetic scattering and the element-selectivity of the measurements are maximum (Fig. 2b).

In contrast to multilayer systems with a repeating bilayer structure, singular magnetic Bragg peaks cannot be expected in reflectometry measurements from spin-valve systems. Nevertheless, also this layer stack reveals asymmetry effects in the reflectometry curves which are typical for magnetic switching, as a detailed inspection of the signals for opposite signs of B reveals (Fig. 3a). Accordingly, hysteresis loops have been measured at the various absorption edges for comparable values of the scattering vector q. These loops differ not only in amplitude, but also distinctly in shape (Fig. 3b). In particular, the Ni (or synonymously, the free layer) switches already at small external fields according to loop 1, whereas the complex loop obtained from the Co and Fe signals reveals the switching of the ultrathin lower CoFe layer at small fields, and subsequently the switching of the CoFe pinned layer at larger fields.
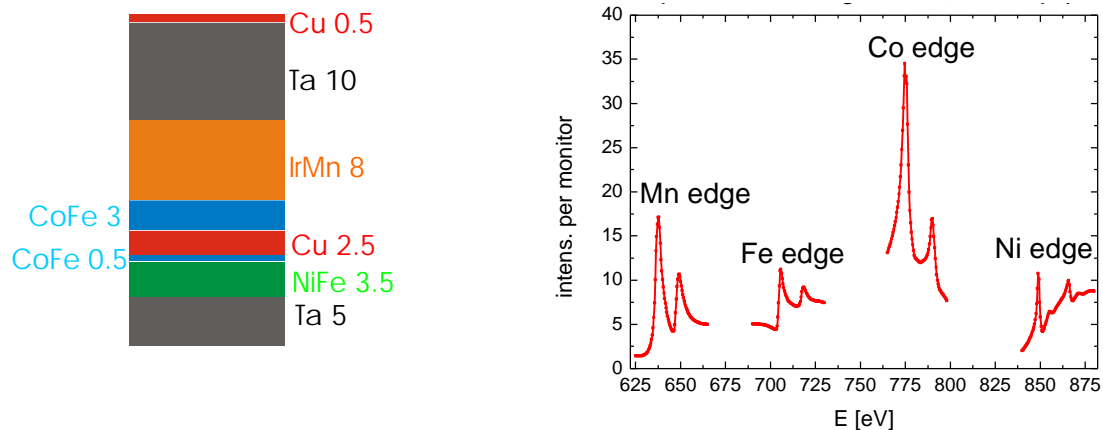
Fig. 2: Layer structure of the spin-valve system (layer thickness in nm, left) and enhanced charge scattering in the specularly reflected intensity utilized for precise assignment of photon energies for element-selective measurements.
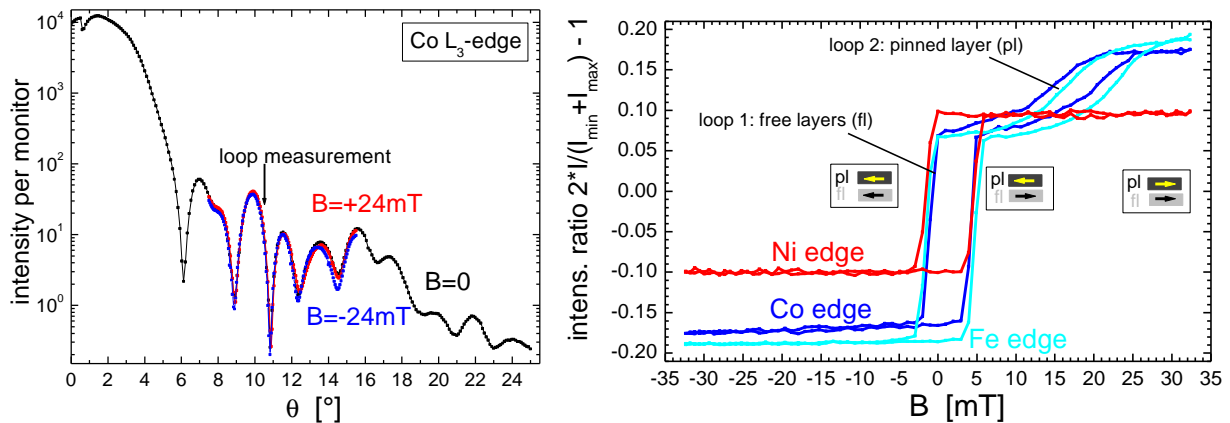
Fig. 3: Reflectometry measurement and hysteresis loops measured at the IrMn-based spin-valve system (L-MOKE geometry; intensity normalized as in Fig.1).

References
[1] A. M. Goodman, K.O'Grady et al., Journ. Magn. Magn. Mat. 198-199 (1999) 12.
[2] F. Schäfers, H.-Ch. Mertins, A. Gaupp, W. Gudat et al. , Appl. Opt. 37 (1999) 4074.

Inner shell excitation-induced dynamics in chemisorbates

P. Feulner[1], A. Föhlisch[2], R. Romberg[1], R. Schneider[1], G. Tyuliev[3], W. Weimar[1],
W. Wurth[2], D. Menzel[1]

[1] Physik-Department E20, Technische Universität München, Garching, Germany
[2] II. Institut für Experimentalphysik, Universität Hamburg, Germany
[3] Bulgarian Academy of Science, Sofia, Bulgaria

Excitation of core levels by narrow bandwidth synchrotron radiation allows us to investigate many aspects of the electronic and chemical dynamics of adsorbed particles. For example, the time scales of adsorbate/substrate electron transfer, which extend well below the femtosecond range, can be analyzed with the Resonant Auger Raman Effect by utilizing the lifetime of the core hole as an internal clock [1]. Inner shell excitations which are well localized in most cases, are also well suited for tailoring molecules by atom selective bond breaking [2]. The coupling of the electronic and nuclear dynamics underlying these photochemical processes is strongly modified on the surface, and the atom selectivity as well as the branching into charged and neutral reaction products are changed [3,4]. The coupling of core holes in heterogeneous systems termed MARPE (multi atom resonant photoemission) finally is an interesting and controversially discussed topic that recently has attracted considerable interest, mainly due to the experimental difficulties to reliably discriminate true (small) MARPE effects from experimental artifacts [5].

In our contribution we focus on selected aspects of surface effects on core excitation induced dynamics. We first present data on photodesorption (PSD) of fragment ions from chemisorbed N_2, which we then use to look for excitation transfer processes from the Ni substrate to chemisorbed N_2 at the Ni 2p edge. The last part of our contribution is devoted to a comparison of core-to-LUMO induced fragmentation of chemisorbed CO from different substrates.
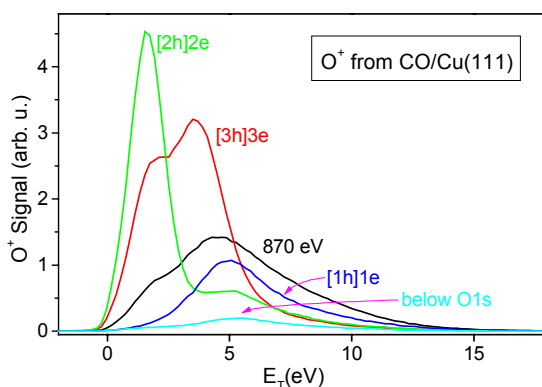
Fig. 1: Kinetic energy distributions of O^+ ions desorbed from CO/Cu(111) by one- and multi-electron O1s excitations (normal emission, after [4]).
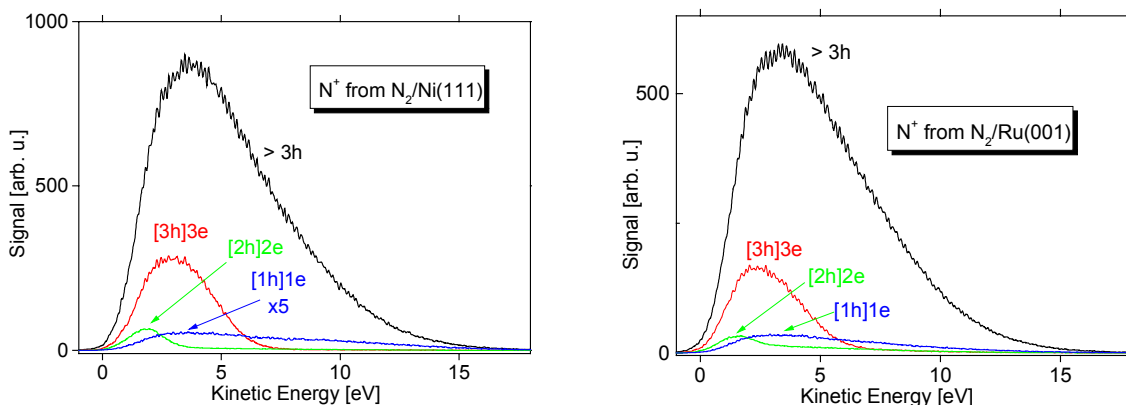
Fig. 2: Kinetic energy distributions of N^+ ions desorbed from $\sqrt{3}\times\sqrt{3}$ layers of N_2/Ni(111) (left) and N_2/Ru(001) (right) for primary one- and multi-electron excitations in the N1s range.

Due to fast electron transfer, the yield of ions from core induced dissociation and desorption of chemisorbates is strongly suppressed compared to the isolated molecules. It is strong only for repulsive multi-electron states

leading to highly charged final states upon core decay. Because of this selectivity, PSD of fragment ions is a versatile tool for the investigation of highly excited states. Triply excited N1s resonances which now are experimentally accessible in the gas phase were first detected in our PSD experiments [6]. In previous experiments we have shown that the kinetic energy distributions (KEDs) of fragment ions depend on the number of primary holes. For CO/Cu(111), e.g., different maxima appear for primary 1h, 2h, 3h and >3h excitations (see Fig.1; data for CO/Ru(001) yield similar energy values, but different amplitudes [4]). For n≥2 the kinetic energies increase monotonically with n reflecting the increasing repulsive nature of the primary states. The large value for n=1 is due to a minority channel in core decay (see [4] for details). These translational energy data are important inputs for the modeling of the bond breaking process by MD calculations. By applying TOF techniques during the single bunch beamtime of BESSY (UE56-1-PGM) we were recently able to measure also the KEDs of N^+ ion desorbed by N1s excitation from N_2/Ru(001) and N_2/Ni(111). The data are very similar for the two substrates, indicating a common molecular origin (Fig.2). The individual shapes of the distributions also closely resemble those obtained for CO (compare Fig.1). The relative amplitudes of the peaks belonging to lower excitation energies however are much smaller for N_2 than for CO. Although the chemisorption energies are comparable for CO/Cu(111) and N_2/Ni(111)/Ru(001), we find much more efficient quenching of ionic products by rapid charge transfer for N_2 compared with CO. Without the high sensitivity of our TOF apparatus [7] and the narrow, intense bunches of BESSY these measurements would not have been possible.

Further evaluation of the data of Fig.2 on the basis of MD simulations, and calculations of potential energy curves are under way. Here, we will use them as fingerprints for the investigation of possible MARPE events. From Fig.2 it is clear that primary excitations of 1, 2, 3, or more holes corresponding to excitations of a N1s electron with 0,1,2 additional shake-up/(-off) events lead to very different KEDs. In previous experiments at HASYLAB and ELETTRA we found strong variations of the N1s photoemission signal and of the N^+ PSD yield at the Ni 2p edges, which could be due either to interatomic transfer of core excitations (MARPE), to a modulation of the electric field of the light at the surface by x-ray optics, or to beam damage [5]. It certainly would have been the best approach to vary the angle of photon incidence for all of these experiments. Unfortunately, this was not possible in our apparatus because of geometrical reasons. While PES could be measured at 7° and 45° of photon incidence, all PSD experiments were restricted to grazing incidence conditions. We instead use here the shape of the KEDs to discriminate between MARPE and field enhancement/depletion by x-ray optics in PSD. MARPE is an interatomic Auger process whose coupling to the higher continua seen in N^+-PSD should exhibit a different branching than the direct dipolar excitation process, and the shape of the N^+-KEDs is expected to change at the Ni 2p resonance if significant contributions by MARPE beyond x-ray optics exist.
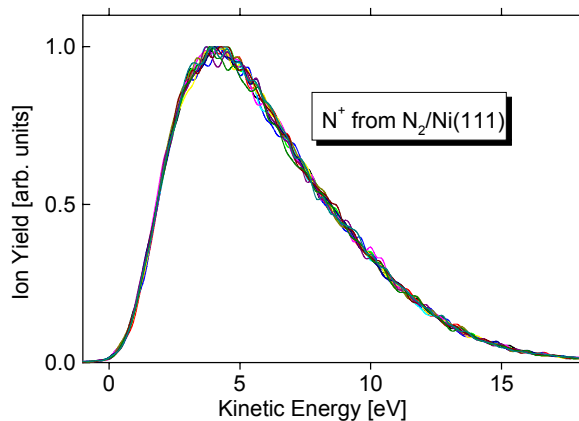

Fig. 3: Comparison of 13 normalized N^+ KEDs recorded for photon energies across the Ni $3p_{3/2}$ edge. No changes of the spectral shapes are visible.

In Fig.3 we show 13 normalized N^+-KEDs from N_2/Ni(111) recorded for different photon energies across the Ni$2p_{3/2}$ resonance. Although their amplitudes vary by about 30% (not shown), their shapes remain unchanged, indicating influence by x-ray optics, but minimum contributions of MARPE. Later N1s-PES experiments at the U41-PGM, and the investigation of PSD of neutral N atoms and N_2 molecules under multi bunch conditions have corroborated these findings. A very high cross section for *electron* stimulated desorption of neutrals increases the rate of beam damage at the Ni2p edge, where the yields of decay and secondary electrons rise dramatically (by more than one order of magnitude). N1s photoemission spectra not affected by beam damage could only be obtained by very rapid scanning of the light spot over the surface area during data acquisition in order to minimize the photon dose. In summary, we could not detect any angle independent MARPE effect within the limits of our experimental errors for this system.

Photon stimulated desorption by core-to-LUMO excitations is our last example. In previous studies of π-resonant bond breaking of N_2/Ru(001), N_2/Ni(111), and CO/Ru(001) we have shown that molecular *and* surface

properties govern excitation site selectivity. For N_2 we found strong fragmentation for excitation of the inner N atom close to the surface [3,4,8]. Here we compare results from CO/Cu(111) with previously obtained data for CO/Ru(001) [3] which clearly show the influence of the surface. According to the equivalent core approximation, C1s excited CO, and N_2 with an N1s excitation of the outer N atom, should become chemically similar, namely equivalent to NO. This Z+1 equivalency is indeed nicely seen in the decay spectra of the two adsorbates [3]. According to this Z+1 equivalency, fragmentation of CO should be weak for C1s, and strong for O1s excitation. Inspecting Fig.4 we find this only to be true for the weakly coupled CO/Cu. For CO/Ru, the branching is reversed due to the stronger surface bond. Although the overall dissociation yield is lower, it is differentially increased for excitation at the C end compared with the Cu case. We note that in the ion signal C1s induced fragmentation remains completely invisible [9]. If we had monitored only ions, we simply would have overlooked the most important fragmentation channel for this adsorbate.
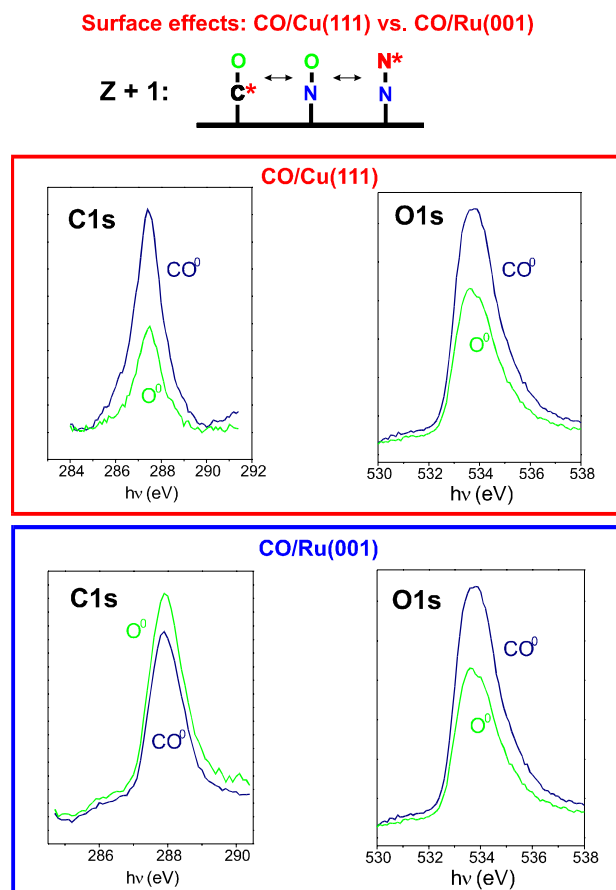
Fig.4: Modification of the relative fragment yields from CO on Ru and Cu for C1s and O1s excitation by surface effects. By Z+1 equivalency, C1s excitation of CO corresponds to N1s excitation of the N_2 molecule at the outer N atom (see text).

References:
1. W. Wurth and D. Menzel, Chem. Phys. **251** (2000) 141.
2. W. Eberhardt et al., Phys. Rev. Lett. **50** (1983) 1038¸Kenichiro Tanaka et al., J. Electron Spectrosc. Rel. Phen. **119** (2001) 255.
3. D. Menzel and P. Feulner, J. Phys: Cond. Matter **13** (2001) 11249; D. Menzel, Physik.Blätter 56 (2000) 81.
4. P. Feulner et al., Surf. Rev. Lett. (in press).
5. See, e.g., A.W. Kay et al., Phys. Rev. **B 63** (2001) 5119, and references therein.
6. Shigemasa et al., VUV-13, Mo 076 and in preparation; P. Feulner et al., Surf. Sci. **451** (2000) 41.
7. R. Weimar et al., Surf. Sci. **451** (2000) 124.
8. R. Romberg et al., Phys. Rev. Lett. **84** (2000) 374.
9. R. Treichler et al., Chem. Phys. **153** (1991) 259.

The BESSY II Storage Ring

A typical day at BESSY:

Operation energy: 1.7 GeV
Filling: 250 mA at injection
Eight hours after injection: 110 mA left
Beam lifetime: 7 to 12 h

In 2001 the BESSY light source has been operating during six user runs of four to five weeks each. The total beamtime delivered to users added up to more than 3900 h. Installations were carried out during ten weeks of shutdowns in April, July and August. Major additions to the storage ring were the replacement of the superconducting wavelength shifter for micro-engineering and the replacement of ID vacuum chambers by narrow 11 mm high vessels.

In machine-dedicated shifts special emphasis was laid upon further improvements on beam stability and improvements to beam lifetime. Routinely, the ring is currently filled to 250 mA.

MACHINE IMPROVEMENTS

Orbit Stability at the Highest Level

Orbit stability at a level well below 10% of the electron beam-size becomes more and more important for many experiments. Thus, at the end of 2000 a powerful 20 (24) bit resolution orbit correction system had been implemented. The new system uses the same magnets and power supplies as before; but to allow sensitive correction of a fraction of about 10^{-6} radian all DACs were replaced by 24-bit units. Beam orbit is measured at 112 locations in horizontal and vertical direction

and is corrected every 6 s using a Singular Value Decomposition (SVD) algorithm. Thermally induced drifts as well as remaining orbit displacements from undulator gap drives are thus adjusted. The beam stays constant in space at a level of less than 5 μm at any location during a day with a constancy of the rms orbit of $\pm$ 25 nm, fig.1.
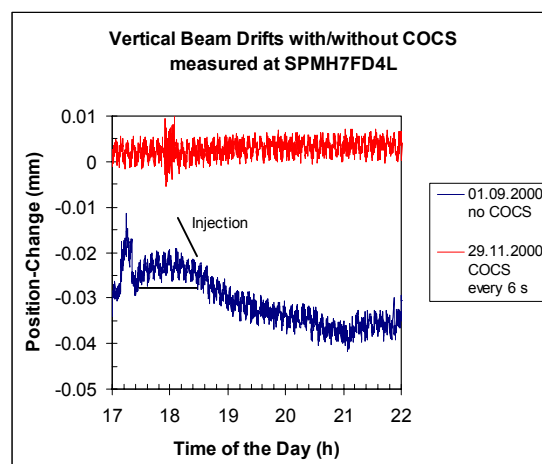
Fig.1: Vertical photon beam stability during filling. Upper graph with closed orbit correction system (COCS) active, lower graph without stabilization.

At the beginning of each new user run the centers of all beam position monitors are recalibrated using beam-based alignment methods. A long-term reproducibility of the beam orbit of better than 100 μm and/or 50 μrad is ensured over the year.

Tune Stabilization Feed Forward

The focusing effects of undulators during gap drives cause changes to the working point (tune) of the machine. Whereas the effect of a single undulator is negligibly small, ten such devices active in parallel sum up to

yield an intolerably large tune shift. Thus, all IDs had to be characterized and a gap-dependent correction to the quadrupole power supplies has been generated. Each ID is connected to typically 32 pairs of quadrupoles to stabilize the tune globally. Moreover, in order to compensate for the distortion in the optical function of the ring, local nearby quadrupoles are powered separately to minimize the beating of the amplitude functions.

By this means the variations of the working point are reduced by a factor of more than 20 bringing back stable conditions.

Optimizing Beam Lifetime

Improving beam lifetime, which is already a factor of three higher than the design value, still is a subject of machine studies. Measurements on the harmonic sextupole magnet circuits resulted in new field settings which yield a substantial increase in beam lifetime. Comparing the lifetime for the "old" and the "new" setting versus beam current a 25% improvement when all undulators are at open gap position, fig. 2. is seen
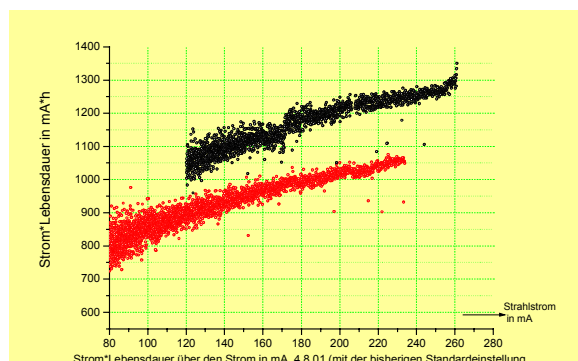
Fig. 2: Beam lifetime vs. beam current for the "old" harmonic sextupole setting (lower red dots) and the improved setting (upper black dots).

Lifetime Effects by APPLE II

Since installation of the elliptically polarizing APPLE II type undulators, a lifetime reduction of the electron beam was observed while operating at low gap settings. The reason for the effect is a variety of higher order multipole fields that drive resonances. In particular a dominant skew octupole field error causes electrons to get lost on the $3Q_y+Q_x=38$ resonance near the actual working point. To minimize the effect the tune was readjusted, and together with operation of a tune feed forward the lifetime degradation now mostly is less than 25%. Fig. 3 shows electron loss rates for open and closed APPLE II gaps respectively; the tune area of present machine operation is indicated.
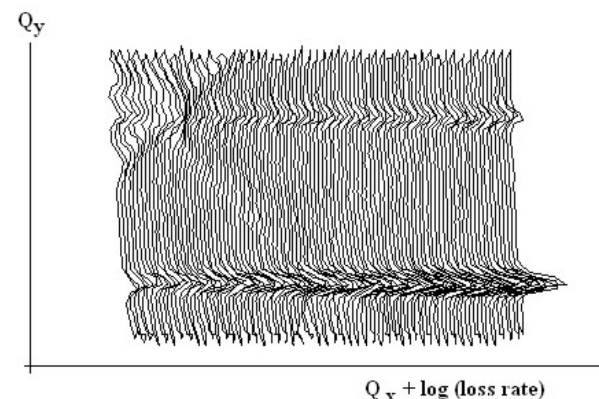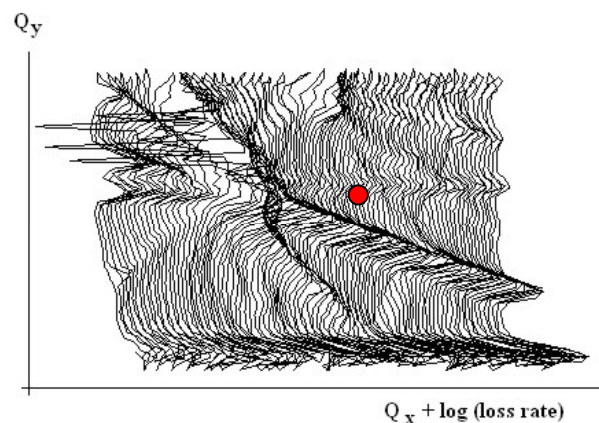
Fig. 3: Electron loss rates for different working points Q_x, Q_y. Lower graph: undulator gap opened. Upper graph: undulator gap closed. The dominant resonance excited is $3Q_y+Q_x=38$.

At open gaps, electron loss rates are dominated by sextupole and octupole driven resonances $3Q_y = 20$ and $4Q_y = 27$. At minimum gap the undulator drives a variety of additional resonances. The dominant most harmful one is the skew octupole resonance $3Q_y+Q_x=38$ causing enhanced electron losses.

Efforts to compensate the undulator field errors were not successful since the field strength of two dedicated electromagnets, installed on both sides of the ID turned out to be too weak.

OPERATION IN 2001

Filling modes

Standard filling mode throughout the year was multi-bunch mode where 320 out of the 400 rf-buckets available are filled and a 80 ns long "empty" clearing gap is generated by a knock-out kicker. The ring was filled typically to intensities of 250 mA: 8h after injection the current had decreased to 110 mA and a new injection was started.

For the first time single-bunch mode was scheduled for a two-week period. One rf bucket was filled to 15 mA circulating current (see fig. 4). The injection rates were about 2 mA/min. As beam lifetime for this current is only about 2 h due to the large charge density in the bunch, an rf-quadrupole field was used for slightly increasing the vertical beam-size; thus the Touschek effect was reduced and lifetime increased to 4 h typically.

During the single-bunch period also a hybrid mode was offered to users. In this mode 310 buckets of the ring are filled to 200 mA - similar to multibunch mode - while in the clearing gap one bucket is filled to 10 mA.
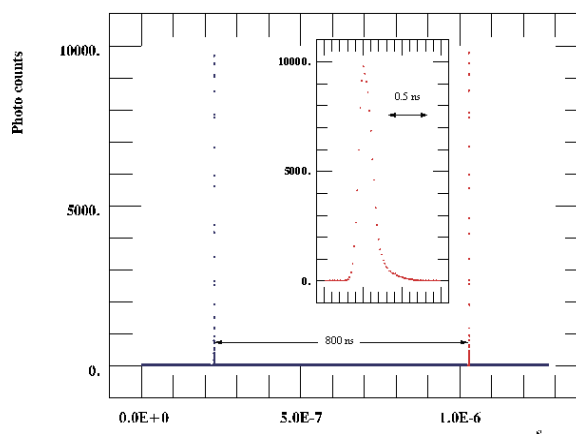
Fig. 4 Filling pattern in Single-Bunch mode.

The technique used was to switch the electron gun parameters from multi-bunch to single-bunch by reloading appropriate settings from file, fig. 5. Total injection time to fill the machine in hybrid mode was 30 min typically.
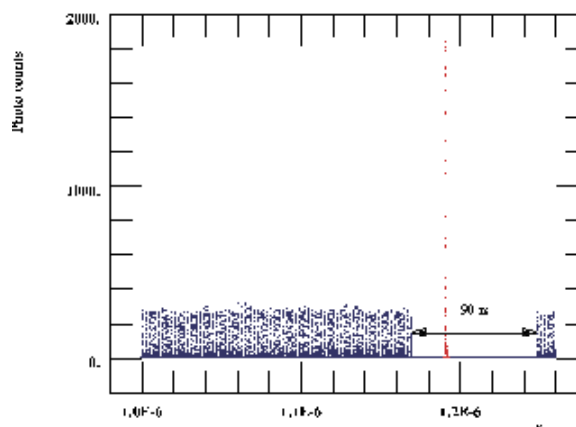
Fig. 5: Filling pattern of the ring in the hybrid mode: 320 bunches are filled to 0.6 mA/bunch with the 10 mA single-bunch in the empty clearing gap.

Operation Statistics

Throughout the year 2001 the source delivered photon beam to the experiments for 3900 h in total. This is about 10% more than the 3600 h scheduled resulting from the trouble-free night operation where the machine is run without human intervention.

The general operation schedule was made up of six periods of user

operation adding up to a total of 28 weeks on a basis of seven days per week, 24 h a day. Figure 6 outlines the total beam time per year since the start of BESSY II.
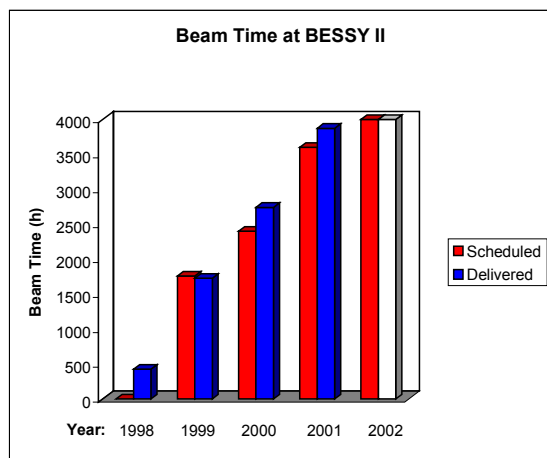
Fig. 6: Annual operation times during the years 1998 to 2001 comparing scheduled and delivered user hours

The storage ring was operated during additional 13 weeks for dedicated machine development as well as for undulator and beamline commissioning.

During three installation phases of altogether ten weeks all necessary installations were done in the machine tunnel, such as the integration of a 6T Siemens WLS (fig. 7), the replacement of a cavity, the replacement of a dipole chamber for an IR beamline, the substitution of ID-chambers by 11 mm high vessels at U49-1 and U180, and the installation of connecting chambers to four front-ends.

Failures and Preventive Maintenance

The overall availability of the BESSY light-source was 94%. About half of the down-time was associated with technical malfunctions, the other half originated from injection.

The major hardware problem was one rf-resonator which developed a vacuum leak in a damping antenna. To replace the device the rf-section had to be vented. All rf-cavities needed one week of re-conditioning. By shifting the single bunch period from User Run #4 to #5 the down-time could be limited to four days. Additional valves in the rf section are under preparation to allow faster reconditioning in case a similar accident should appear again in the future.

Fig.7: Photo of the 6 T WLS, formerly operated at BESSY I, that replaced the 4 T device

Current Activities and Future Plans

The 3rd harmonic cavities successfully used for bunch-lengthening are being replaced by new high-power versions. Thus, it is planned to operate at considerably higher voltages to further increase beam lifetime. A super conducting cavity, presently under fabrication, is expected to be installed in early 2003 to exploit this technique to the limit.

A second 7T wavelength shifter for protein structure analysis and a 7T multipole wiggler for material research are in a well advanced production state at BINP (Novosibirsk). Installation of the devices is scheduled in 2002.

As space for future insertion devices is of most importance the last non-occupied straight section will be cleared from the many diagnostic elements in the course of the next 18 months.

Status of BESSY II

- in operation
- under construction
- planned
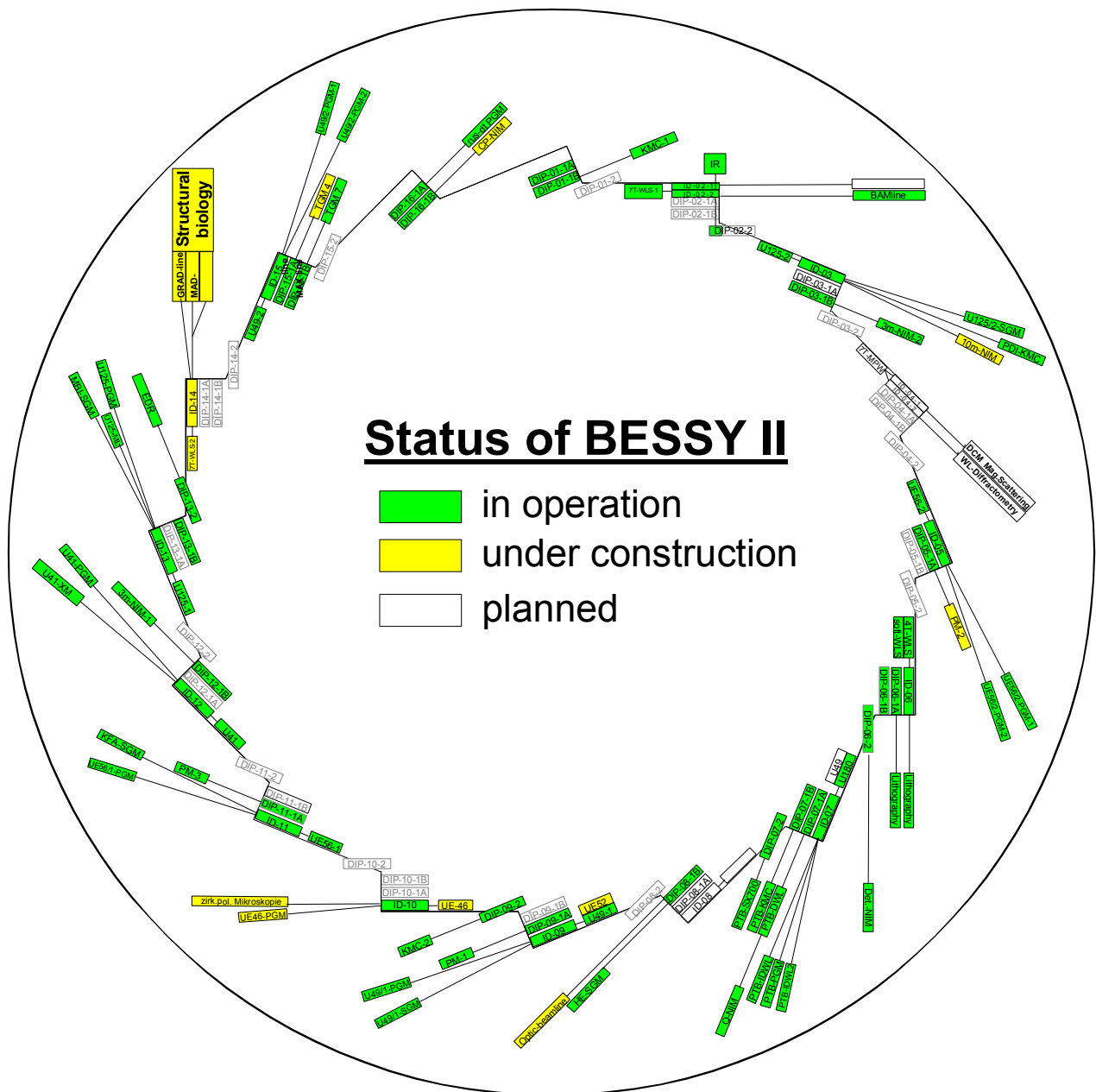
Since the start of the new facility BESSY II three years ago, 36 beamlines have been put into operation, an average of one beamline per month. At the end of 2001 21 insertion device monochromators / beamlines at 8 undulators, 2 wavelength shifters and 15 bending magnet beamlines were in operation. Due to the limited number of straight sections the main phase of installation of new ID-monochromators is coming to an end. On the other hand, the installation of bending magnet beamlines, new ones and those transferred from BESSY I, is still in progress. In 2001 two new and three transferred bending magnet beamlines went into operation.

Meanwhile a major task of the experimental systems group has become the instruction of an increasingly large user community in exploiting the capabilities of our beamlines. A further main focus is the continuous improvement and exploitation of the special characteristics of the beamlines.

INSTALLATION OF BEAMLINES

The Installation and commissioning of undulator based PGM's has become a

highly standardized procedure. The experiences gained in the last three years with this monochromator type enabled us to put the U49/2-PGM-1 with only four weeks of commissioning successfully into user operation. The beamline shows a very high resolving power combined with a small spot size and excellent flux values up to more than 2 keV.
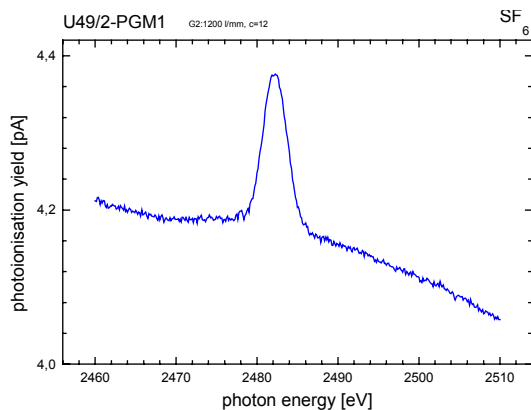
Fig.1:. *Even at energies as high as 2.5 keV the U49/2-PGM shows reasonable results. The pronounced structure in the photoionisation yield of SF_6 at the sulphur K-edge is clearly visible*

With the first grating delivered after more than 2 years of delay the U125/2-SGM finally went into operation in 2001. Due to two gratings which are still outstanding the energy range is still limited. Nevertheless first experiments could be performed on this monochromator which is operated by the Berlin universities HU, TU and FU. Following the commissioning of the U125/2-KMC the experiments of Paul-Drude-Institute started and delivered first promising results.

A further hard X-ray beamline, the BAM/PTB-KMC at 7T-WLS/I went into user operation in 2001. This beamline, devoted to materials research and detector calibration, also serves as first source for protein crystallography at BESSY II.

With the excellent results obtained at the newly installed Russian-German-PGM, the virtues of the BESSY collimated PGM design, which lead to unprecedented high performance beamlines at our undulator sources have been confirmed this time on a bending magnet, DIP16.1A. A resolving power of 100.000 has been demonstrated at 65 eV and flux and focus size have reached their design values.
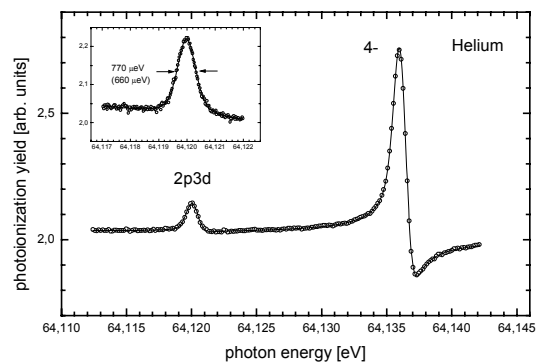
Fig.2:. *After Doppler correction the He 2s3d resonance shows a line width of 660 μeV revealing a resolving power of 100.000 achieved at the German-Russian PGM on Dipole DIP16.1A.*

The IR-system installed at dipole-frontend DIP2.2 went successfully into operation. The focussing system delivers 60 mrad (h) and 40 mrad (v) infrared radiation from 5000 cm^{-1} to 50 cm^{-1} to a Fourier Transform Spectrometer and an IR-Microscope.
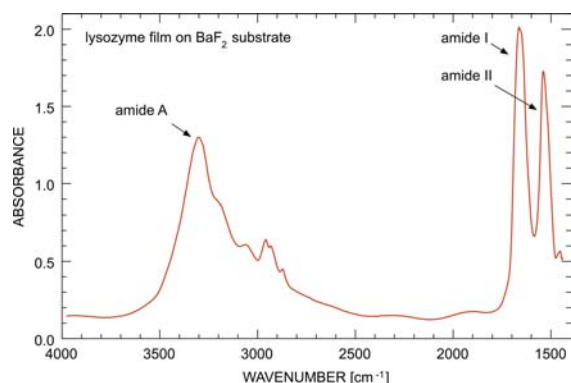
Fig.3:. *Fourier Transform Infrared (FT IR) spectrum of the protein lysozyme measured at the commissioned infrared beamline*

After adaptation to the new source and careful set-up even monochromators like the almost 20 year old 3m-NIM-2 show now an outstanding resolving power of 60.000 at 11 eV. Focus size of 400 µm x 100 µm and flux values in the 10^{10} range meet or even exceed the design values.
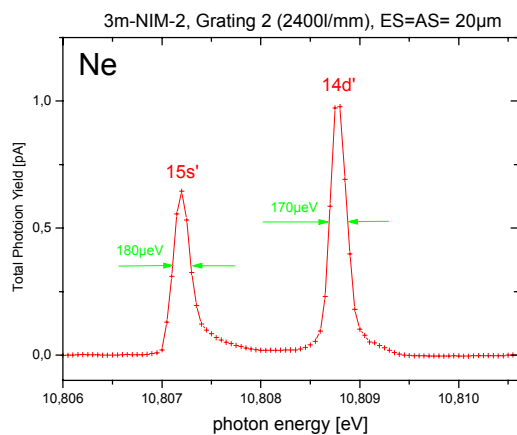
Fig.4:. *A resolving power of 60.000 at 11 eV was achieved with the almost 20 year old 3m-NIM-2.*

In order to upgrade the performance of the KMC-1 we decided to replace the original crystal chamber and drives by a new one which will provide the necessary precision resulting from the smaller source size and the longer optical path compared to the former set-up at BESSY I.

IMPROVEMENT OF BEAMLINES

In order to maintain and improve the unprecedented high performance of the BESSY-beamlines, a permanent process of characterisation and optimisation during regular commissioning shifts has become a major task of the experimental systems group. Only the close cooperation of specialists for undulators, beam position diagnostics, optics and computer control could guarantee for the successful continuous improvement of the beamlines. Now users have full control over gap and shift of all undulators. It is now easily possible to scan on top of the undulator harmonic with a well defined degree of polarisation.

The in-beamline ionisation chambers have proven to be an indispensable tool. By an elaborate procedure it is now possible to introduce an absolute energy scale for our PGM's with an uncertainty of less than 0.1%.

For optimisation of focal position and spot size a focus test chamber, based on a high resolution fluorescent screen combined with a microscope-CCD-system, has been developed. The test chamber can be adjusted in all three directions under vacuum. Thus, the results of alignment actions can be seen online and quantitative values of the focus size are automatically determined.

UE56-Dual-Beam-Mode
The adjustments of the dual-beam-mode of the UE56-PGM was one of the most demanding tasks we had to perform on our beamline systems. The absolute energy position of both beams in addition to their ideal geometrical overlap and intensity homogeneity had to be optimised. Ionisation chamber, focus test system and in-beamline dichroism detectors had to be used for this purpose.

A severe problem was the inhomogeneity of the focus in the horizontal direction (fig. 5 left). Even with the best mirrors available a significant intensity modulation remained, which was different for both beams due to the fact that they pass over different portions of the optical components. The solution of this problem was a modification of the last mirror chamber, allowing for well defined micro-oscillations of the refocusing mirror. They produce an almost uniform intensity distribution

without enlarging the spot size by more than 10% (Fig. 5 right).
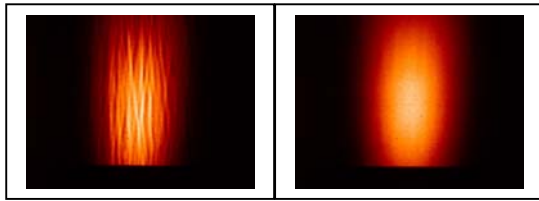
Fig.5: *Intensity distribution in the focus of the UE56/1-PGM without (left) and with (right) micro-oscillation of the refocusing mirror.*

For an appropriate usage of this dual beam mode, e.g. for MCD measurements the data acquisition- and beamline control software was adopted to give the users full access to the chopper for switching of the helicity. First MCD spectra recorded with this technique show an improved quality (Fig. 6) compared to spectra recorded successively.
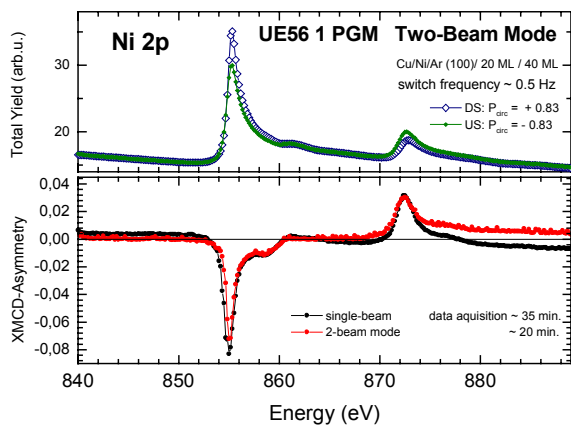
Fig.6: *Comparison of MCD-spectra recorded in dual-beam-mode and successively.*

RF Carbon Decontamination
Due to the contamination of the optical components with carbon a strongly diminished intensity at the carbon K-edge can result. This is a severe blemish of all beamlines working in this energy range.

Since several years BESSY has good experience with removing carbon contamination by in-situ application of an Ar/O_2 low-energy RF-discharge in the mirror chambers. All chambers of the BESSY-beamlines are equipped such that the cleaning procedure can be applied quickly. Fig.7 shows the result of a cleaning procedure at the U125/1-PGM. Before cleaning, the flux at the carbon K-edge dropped more than an order of magnitude. After cleaning almost no intensity loss could be detected.
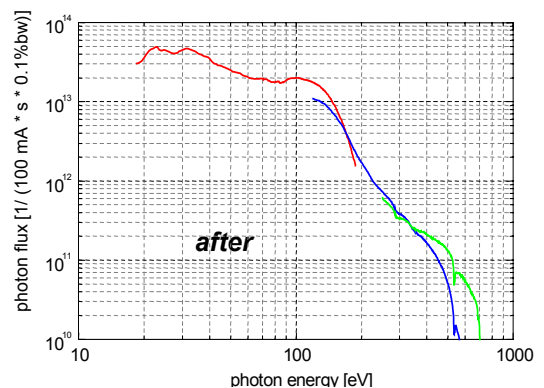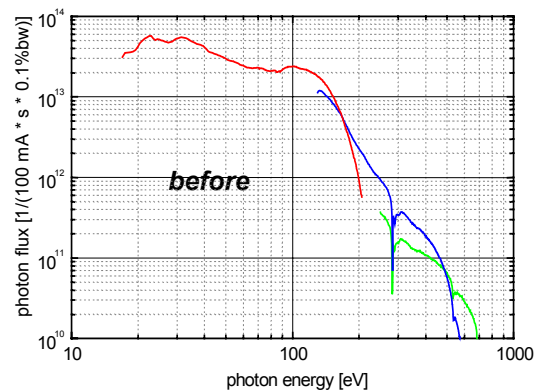
Fig.7:. *Photon flux of the U125/1-PGM before and after carbon decontamination.*

Status of BESSY II

- in operation (green)
- under construction (yellow)
- planned (white)

G.R., 06.02.2002

ID Beamlines at BESSY II (January 2002)

21 ID-BLs in operation

BESSY II
1.7 GeV, 200 mA

For general information on beamlines see BESSY website under www.bessy.de
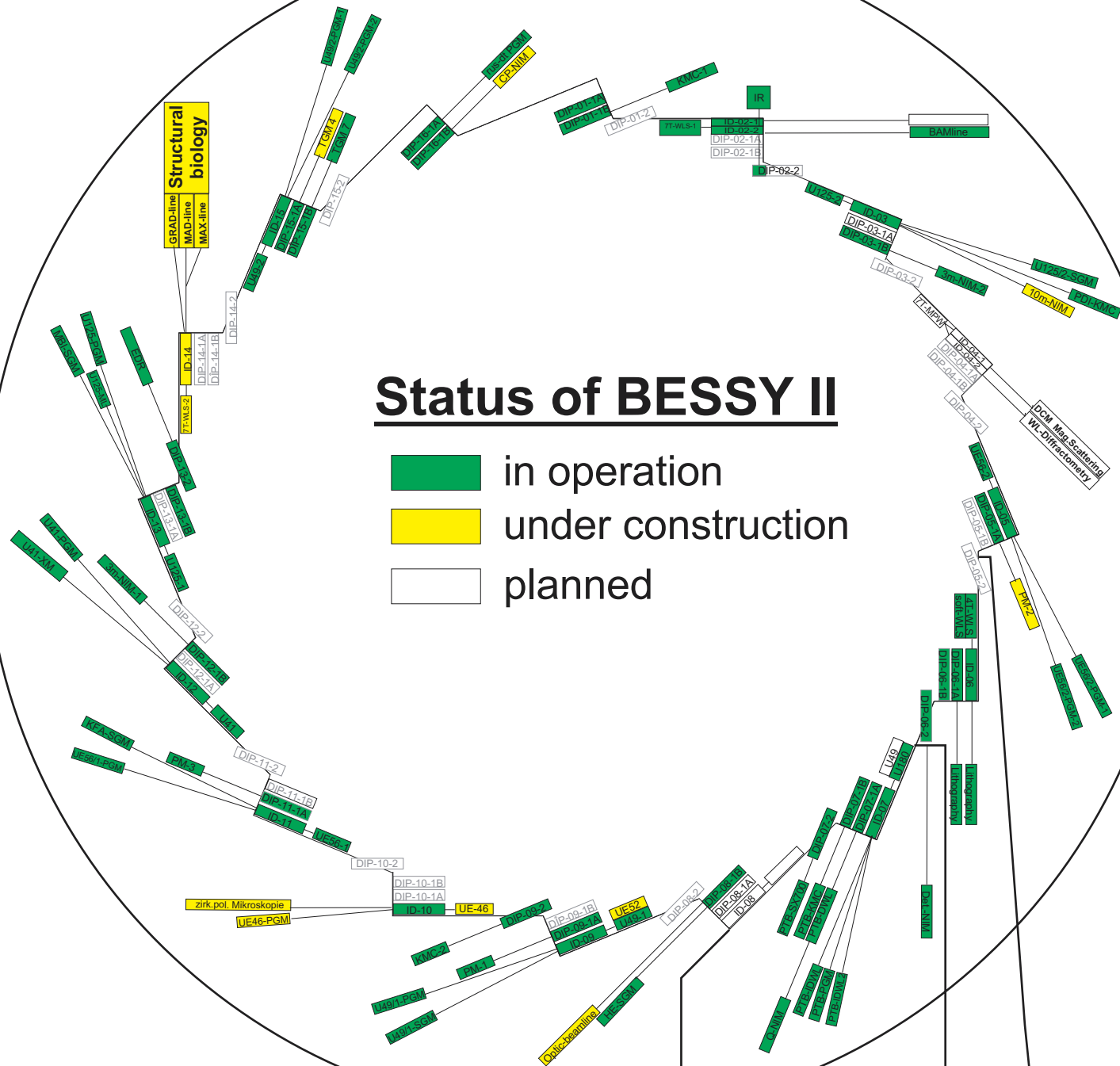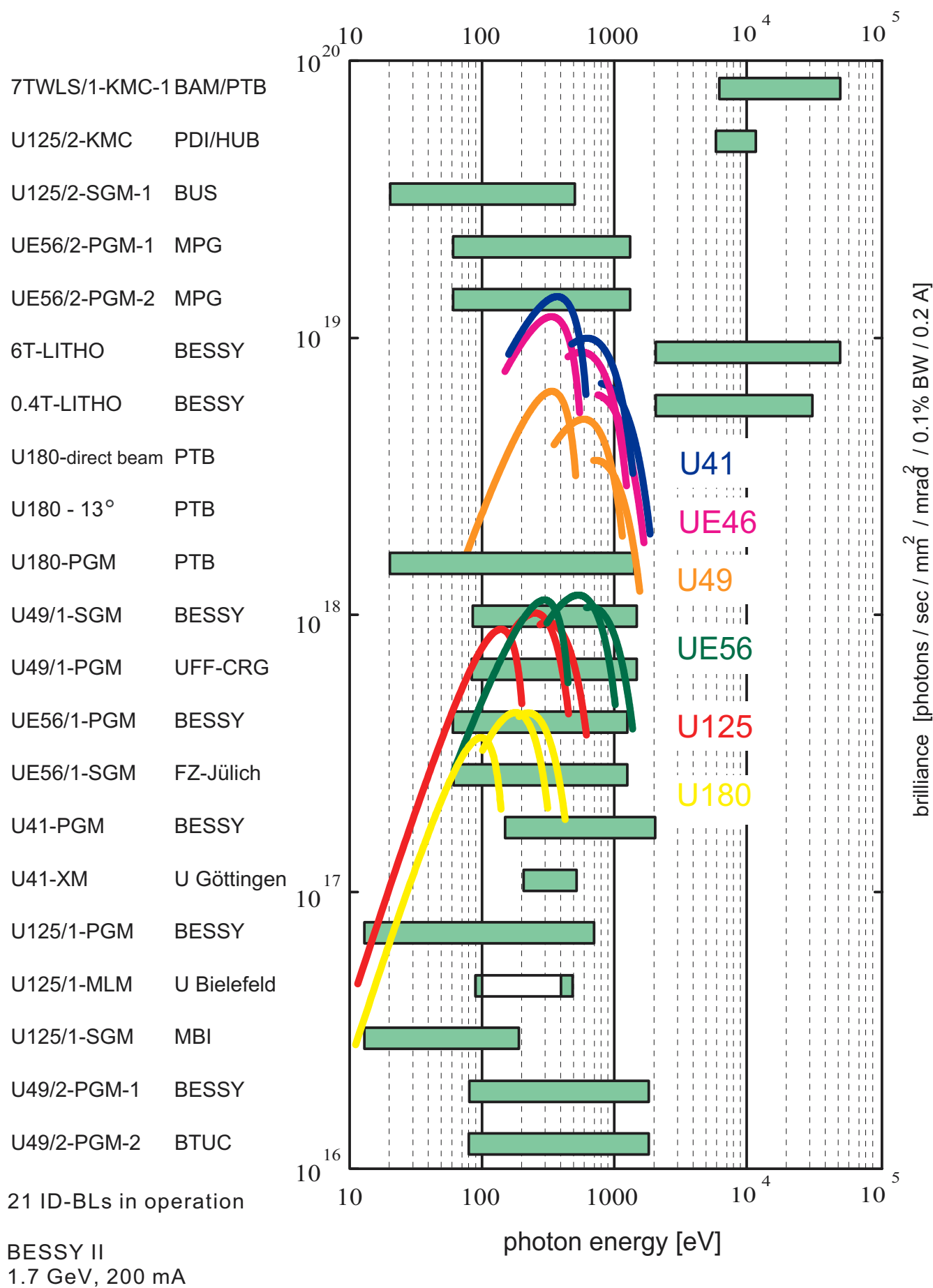
Beamlines on Insertion Devices

Insertion Device	Monochromator	Energy Range (eV)	Contact Persons	
7 T WLS/1	KMC-1	6 k – 50 k	H. Riesemeier (BAM) A. Erko	B. Müller (BAM)
U 125-2	KMC	6 000 – 12 000	Wolfgang Braun (PDI) A. Erko	B. Jenichen (PDI)
U 125-2*	NIM	< 10 – 35	A. Ehresmann (U Kl) G. Reichardt	I. Packe P. Rotter
U 125-2	SGM	20 – 500	R. Püttner (FUB) G. Reichardt	
UE 56-2	PGM 1	60 – 1 300	W. Mahler (MPG) H.-C. Mertins	B. Zada (MPG)
UE 56-2	PGM 2	60 – 1 300	W. Mahler (MPG) H.-C. Mertins	B. Zada (MPG)
6 T WLS	LITHO	> 2000	B. Löchel H.-U. Scheunemann	H. Köhrich M. Bednarzik
0.4 T	LITHO	> 2 000	B.Löchel H.-U. Scheunemann	H. Köhrich LM. Bednarzik
U 180 / (U 49*)	-	direct beam	R. Klein (PTB)	
U 180 / (U 49*)	13°		R. Klein (PTB)	A. Gottwald (PTB)
U 180 / (U 49*)	PGM	20 – 1 900	B. Beckhoff (PTB)	
U 49-1 / (UE 52*)	SGM	85 – 1 600	F. Senf	T. Zeschke
U 49-1 / (UE 52*)	PGM	85 – 1 600	T. Schmidt (U Wü) C. Jung	
UE46*	PGM	120 – 1 700	H. Rossner (HMI) F. Senf	D. Schmitz (HMI)
UE 56-1	PGM	60 – 1 300	H.-C. Mertins	T. Zeschke Julia Schmidt

UE 56-1	SGM	60 – 1 300	S. Cramm (FZJ)	
U 41	PGM	170 – 1800	C. Jung	M. Mast
U 41	XM	~ 200 – ~600	P. Guttmann (U Gö)	
U 125-1	PGM	20 – 700	NN (BESSY)	F. Eggenstein
U 125-1	Multilayer	80 – 700	M. Pohl (U Bi)	
U 125-1	SGM	15 – 180	B. Winter/T. Gießel/W. Widdra (MBI)	
7T WLS/2*	KMC-1	4.5 k – 17.5 k	U. Müller (PSF)	K. Höppner (PSF)
7T WLS/2*	KMC-2	4.5 k - 17.5 k	U. Müller (PSF)	K. Höppner (PSF)
7T WLS/2*	KMC-3	13.7	U. Müller (PSF)	K. Höppner (PSF)
U 49-2	PGM-1	85 – 1 600	R. Follath	J.-S. Schmidt
U 49-2	PGM-2	85 – 1 600	P. Hoffmann (BTUC) D. Batchelor	

* under construction

BAM	Bundesanstalt für Materialforschung und -prüfung
BTUC	Brandburgische Technische Universität Cottbus
FUB	Freie Universität Berlin
FZJ	Forschungszentrum Jülich
HMI	Hahn-Meitner-Institut
HUB	Humboldt-Universität zu Berlin
MPG	Max-Planck-Gesellschaft
PSF	Proteinstrukturfabrik
PTB	Physikalisch-Technische Bundesanstalt
TUB	Technische Universität Berlin
U Bi	Universität Bielefeld
U Gö	Universität Göttingen
U Kl	Universität Kaiserslautern
U Wü	Universität Würzburg

DIPOLE Beamlines at BESSY II (January 2002)

For general information on beamlines see BESSY website under www.bessy.de
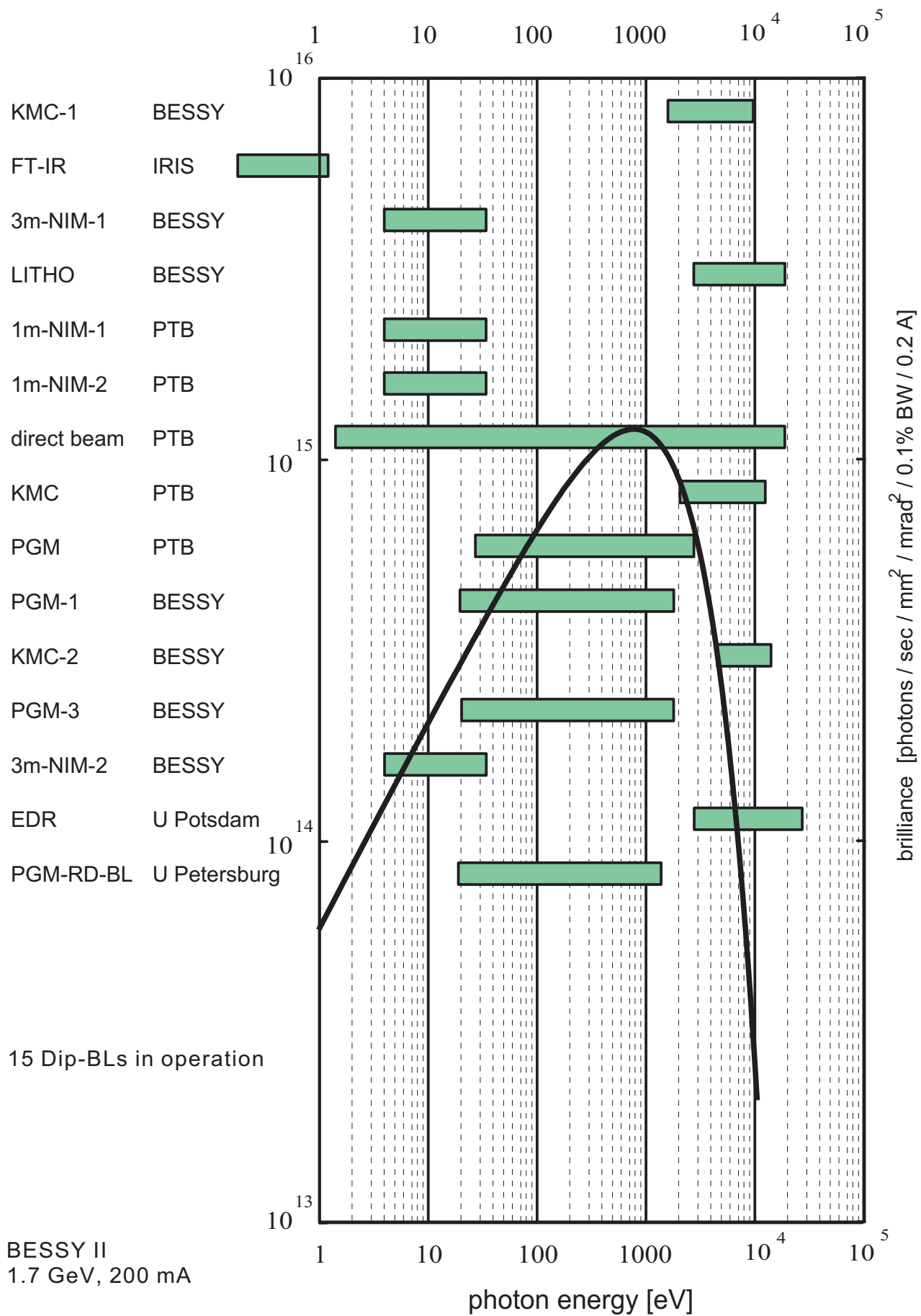
Beamlines on Dipole Magnets

Monochromator	Energy Range (eV)	Contact Persons	
KMC-1	1700 – 10 000	F. Schäfers F. Neißendorfer	M. Mertin
FT-IR	IR	F. Bartl (HUB) U. Schade	
3m-NIM-1	4 – 35	T. Schroeter G. Reichardt	I. Packe
LITHO	direct beam	B. Löchel H.-U. Scheunemann	H. Köhrich M. Bednarzik
1m-NIM-1	3 – 35	M. Richter (PTB)	
1m-NIM-2	3 – 35	M. Richter (PTB)	
	direct beam	R. Thornagel (PTB)	
KMC	1750 – 10 000	M. Krumrey (PTB)	
PGM	30 – 1 800	F. Scholze (PTB)	
HE-SGM*	200 – 700	A. Lippitz (BAM) O. Schwarzkopf	
PGM-1	20 – 1 900	T. Kachel	F. Eggenstein
KMC-2	4.5 k – 15 k	A. Erko	I. Packe
PGM-3	20 – 1 900	T. Kachel	F. Eggenstein
3m-NIM-2	4 – 35	T. Schroeter G. Reichardt	I. Packe
EDR	2 k – 12 k	J. Grenzer (U Po) A. Erko	
TGM-7*	8 – 120	C. Pettenkofer (HMI)	S. Tiefenbacher (HMI)
TGM-4*	8 – 120	K. Godehusen	M. Mast
PGM-RD-BL	30 – 1 500	D. Vyalikh (FUB) A. Shikin	S. Molodtsov (TUD)
CP-NIM*	4 – 35	F. Neißendorfer F. Schäfers	M. Mertin

*under construction

BAM	Bundesanstalt für Materialforschung und -prüfung
FUB	Freie Universität Berlin
HMI	Hahn-Meitner-Institut
HUB	Humboldt-Universität zu Berlin
PTB	Physikalisch-Technische Bundesanstalt
TUD	Technische Universität Dresden
U Po	Universität Potsdam

Experimental stations

The aim of BESSY is to make the unique opportunities offered by synchrotron radiation accessible to a large user community. Thus, those scientists who plan to perform experiments at BESSY but do not have dedicated experimental equipment find below a list of experimental stations available for common use. The list merges setups which are already available with those designed to exploit the enhanced performance of BESSY II.

In addition to the stations already available several new experimental stations are under construction for future use at BESSY. These experiments will be put into operation during 2003. For further information on the experimental stations please contact W. Braun (braun @ bessy.de) or Ch. Jung (jung @ bessy.de)

Experimental systems available at BESSY	UPS / XPS	Microscopy	Electron yield	Fluorescence	X-ray emission	Contact
HIRES – high resolution electron spectrometer	●	●				rader @ bessy.de
PHOENEXS – photoemission and near edge x-ray spectroscopy	●		●	●		bressler @ bessy.de
Multi-user-multi-purpose measuring station	●		●	●		tepper @ bessy.de
Fluorescence spectrometer			●	●		ruediger.mitdank @ physik.hu-berlin.de
Two-photon-photoemission experiment	●					bwinter @ mbi-berlin.de
XPEEM photoemission microscopy		●				pohl @ physik.uni-bielefeld.de
HIRE-PES – highest energy resolution photoemission	●					christoph.jannowitz @ physik.hu-berlin.de
Soft x-ray emission spectrometer					●	eisebitt @ bessy.de
ROSA – rotatable spectrometer apparatus	●				●	szargan @ rz.uni-leipzig.de
SMART – spectro-microscope with highest spatial resolution	●	●				thomas.schmidt @ physik.uni-wuerzburg.de
XM – x-ray microscopy		●				guttmann @ bessy.de

IRIS – infrared spectroscopy experiment		schade @ bessy.de
Infrared ellipsometry		hinrichs @ isas-berlin.de
VUV / XUV ellipsometry		norbes @ gift.physik.tu-berlin.de
Scattering experiments in the VUV / XUV range		eugen.weschke @ physik.fu-berlin.de
X-ray diffraction during molecular beam epitaxy		ploog @ pdi-berlin.de
Reflectometry		schaefers @ bessy.de
Polarimetry		mertins @ bessy.de

Experiments under construction	UPS / XPS	Microscopy	Electron yield	Fluorescence	X-ray emission	Absorption	Scattering
Investigations on stored nano particles	●			●			●
X-ray emission on organic substances and biomaterials			●		●		
So-Li-AS – the solid-liquid-analysis system	●						
Photoemission microscope for time resolved spectroscopy in the ps-regime	●	●					
High resolution spinpolarization photoelectron spectroscopy	●						
UVIS – circular dichroism spectroscopy for biological investigations						●	

Annual operation times during the years 1998 to 2001 comparing scheduled and delivered user hours.
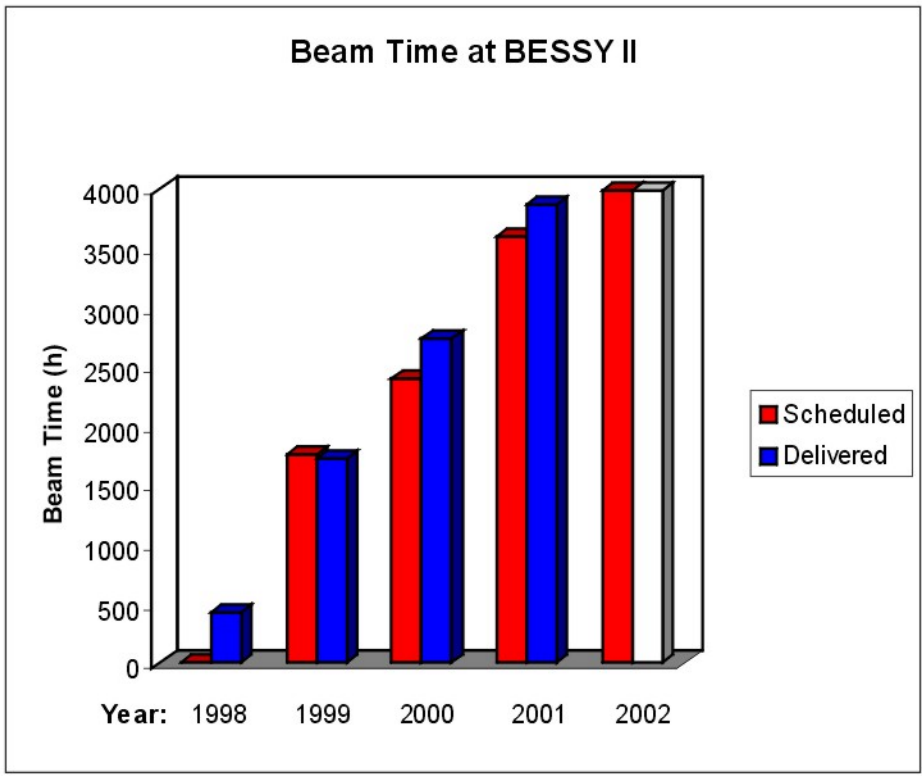
Allocation of beam time at BESSY II (2001)

Insertion Device Beamlines

Total: 3259,35 shifts
at 16 ID-Beamlines

Beamtime [shifts]

- MPG (510,95)
- WGL (350,65)
- Grossforschung (104,4)
- German Universities (1365,1)
- EU-HPP-Programme (142,4)
- non-German Universities (10,5)
- BESSY in house research (85,1)
- Bundesanstalten (230)
- Commissioning (460,25)

Institution

Bending Magnet Beamlines

Total: 1888 shifts
at 6 Dipole Beamlines

Beamtime [shifts]

- MPG (177,6)
- WGL (69)
- Grossforschung (134)
- German Universities (904,5)
- EU-HPP-Programme (173,7)
- non-German Universities (34,3)
- BESSY in house research (200,3)
- Commissioning (88,1)
- Test experiments (106,5)

Institution

Number of User Runs:	160
Projects in the EU-HPP-Programme:	20
Average Beamtime per User Run:	32,2 shifts

MPG = Max-Planck-Gesellschaft, WGL= Wissenschaftsgemeinschaft Gottfried Wilhelm Leibniz, Grossforschung= Members of Helmholz Gemeinschaft, Bundesanstalten= BAM, PTB

BESSY

```
                    ┌─────────────────┐
                    │   Supervisory   │
                    │      Board      │
                    └────────┬────────┘
                             │
┌──────────────┐    ┌────────┴────────┐    ┌──────────────┐
│  Scientific  │    │    Board of     │    │  Beam Time   │
│Advisory Board├────┤   Directors     ├────┤  Committee   │
└──────────────┘    └────────┬────────┘    └──────────────┘
                             │
    ┌──────────┬─────────────┼─────────────┬──────────┐
┌───┴────┐ ┌───┴────┐   ┌────┴─────┐   ┌────┴────────┐
│Experi- │ │Accele- │   │ Central  │   │Administration│
│mental  │ │rators  │   │ Services │   │             │
│Division│ │        │   │          │   │             │
└────────┘ └────────┘   └──────────┘   └─────────────┘
```

Supervisory Board

Scientific Advisory Board — Board of Directors — Beam Time Committee

Experimental Division

Accelerators

Central Services

Administration
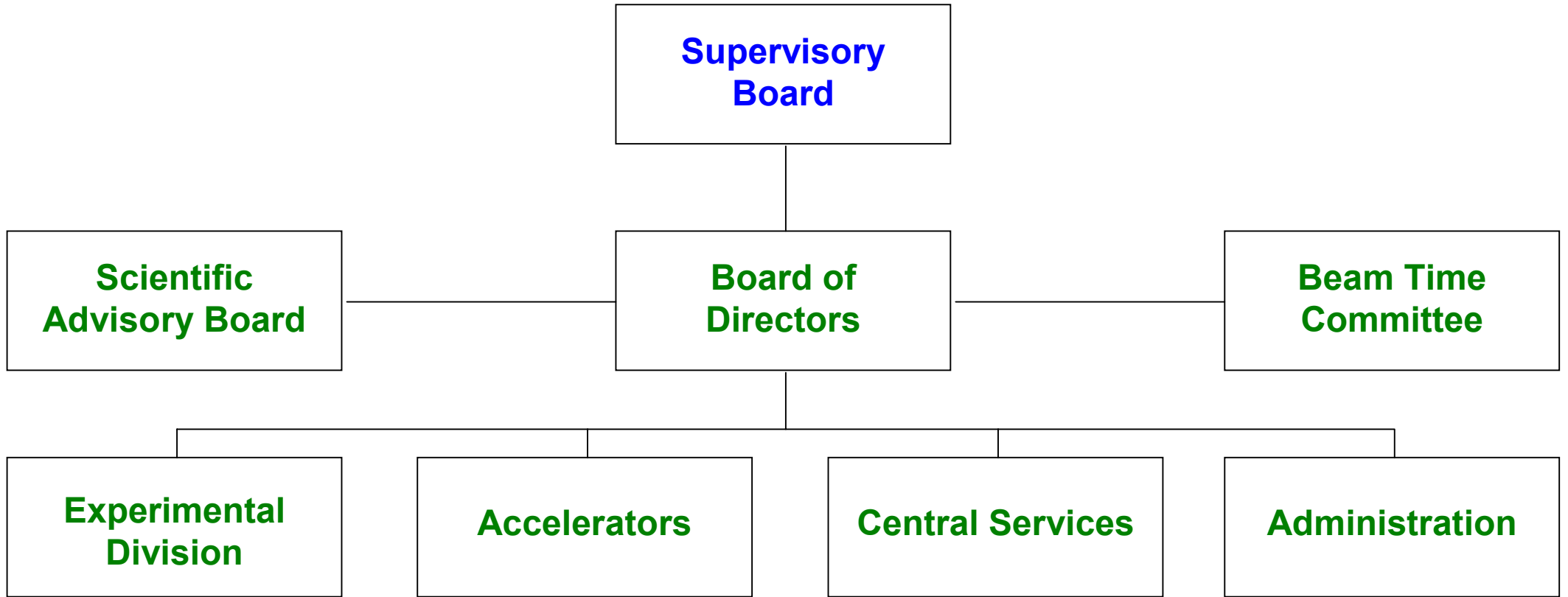
Advisory Boards

(January 2002)

Supervisory Board

Prof. Dr. J. Treusch (Chairman)	Forschungszentrum Jülich
Prof. Dr. A. Goldmann (Vice-Chairman)	Gesamthochschule Kassel
ORR C. Brandt	BMBF
Prof. Dr. E. O. Göbel	PTB Braunschweig
M. Meinecke	Max-Planck-Gesellschaft München
Prof. Dr. R. Maschuw	Forschungszentrum Karlsruhe
Dr. D.-M. Polter	FhG München
Prof. Dr. W. Saenger	Freie Universität Berlin
Prof. Dr. J. Schneider	DESY Hamburg
MinRat Dr. J. Schöttler	BMWi
Prof. Dr. M. Steiner	HMI Berlin
Ltd. Senatsrat J. Stoehr	Senatsverwaltung für Wissenschaft, Forschung und Kultur Berlin

Financal Committee

Dr. H. Krech (Chairman)	DESY Hamburg
Dr. W. Buck	PTB Berlin
OAR H. Diermann	BMBF
R. Kellermann	Forschungszentrum Jülich
A. Röhr	Max-Planck-Gesellschaft, München
Dr. R. Schuchardt	Senatsverwaltung für Wissenschaft, Forschung und Kultur Berlin

Scientific Advisory Committee

Prof. Dr. M. Grunze (Chairman)	Universität Heidelberg
Prof. Dr. V. Saile (Vice-Chairman)	Forschungszentrum Karlsruhe
Prof. Dr. D. S. Chemla	ALS, Berkeley, USA
Prof. Dr. M. Eriksson	MAXLab Lund, Schweden
Prof. Dr. H.-J. Freund	Fritz-Haber-Institut, Berlin
Prof. Dr. K.C. Holmes	Max-Planck-Institut für medizinische Forschung, Heidelberg
Prof. Dr. Y. Petroff	Lawrence Berkeley Lab, Berkeley, USA
Prof. Dr. W. Sandner	Max-Born-Institut, Berlin
Prof. Dr. G. Schütz	Max-Planck-Institut für Metallforschung, Stuttgart
Prof. Dr. J. Stöhr	Stanford Synchrotron Radiation Laboratory (SSRL), USA
Dr. A. F. Wrulich	Paul-Scherrer-Institut Villigen, Schweiz

permanent guests:

ORR C. Brandt	BMBF
Prof. Dr. R. Gerhardt-Multhaupt	Universität Potsdam
Prof. Dr. H. Hahn	TU Darmstadt
Dr. T. Möller	HASYLAB/DESY Hamburg
Dr. R. Schuchardt	Senatsverwaltung für Wissenschaft, Forschung und Kultur, Berlin

Beam Time Committee

Prof. Dr. J. Fink (Chairman)	IFW Dresden
Prof. Dr. H.-P. Steinrück (Vice-Chairman)	Universität Würzburg
Prof. Dr. D. Arvanitis	Universität Uppsala
Prof. Dr. H. Bertagnolli	Universität Stuttgart
Prof. Dr. M. Grunze	Universität Heidelberg
Prof. Dr. E. Rühl	Universität Osnabrück
Prof. Dr. K.-H. Schartner	Universität Gießen
Prof. Dr. R. Schlögl	Fritz-Haber-Institut Berlin
Prof. Dr. G. Schütz	Max-Planck-Institut für Metallforschung, Stuttgart

Berliner Elektronenspeicherring-Gesellschaft für Synchrotronstrahlung mbH - BESSY

Albert-Einstein-Strasse 15 phone +49 (0)30 / 6392 2999
12489 Berlin fax   +49 (0)30 / 6392-2990
Germany http://www.bessy.de
  info@bessy.de

Scientific Director: Prof. Dr. Wolfgang Eberhardt
  Eberhardt@bessy.de

  Secretariat (Ines Maupetit)
  phone +49 (0)30 / 6392 4633
  fax   +49 (0)30 / 6392 2989
  Maupetit@bessy.de

Technical Director Prof. Dr. Eberhard Jaeschke
  Jaeschke@bessy.de

  Secretariat (Nikoline Hansen)
  phone +49 (0)30 / 6392 4651
  fax   +49 (0)30 / 6392 4632
  Hansen@bessy.de

Administration Thomas Frederking
  Frederking@bessy.de

  Secretariat (Katrin Rosenblatt)
  phone +49 (0)30 / 6392 2901
  fax   +49 (0)30 / 6392 2990
  Rosenblatt@bessy.de

Beamtime Coordination

  Dr. Walter Braun
  phone +49 (0)30 / 6392 2927
  Braun@bessy.de

  Dr. Gerd Reichardt
  phone +49 (0)30 / 6392 4983
  Reichardt@bessy.de

  Secretariat (Stine Mallwitz)
  phone +49 (0)30 / 6392 2904
  fax   +49 (0)30 / 6392 4673
  Mallwitz@bessy.de

User Office

Maha Krämer
phone +49 (0)30 / 6392 4734
fax   +49 (0)30 / 6392 4746
MahaKraemer@bessy.de

Daniela Baum
phone +49 (0)30 / 6392 4734
fax   +49 (0)30 / 6392 4746
Baum@bessy.de

Public Relations

Regina Bost
phone +49 (0)30 / 6392 2907
fax   +49 (0)30 / 6392 2925
pr@bessy.de

Dr. Heike Henneken
phone +49(0)30-6392-2922
fax   +49(0)30-6392-4972
Heike.Henneken@bessy.de

Dr. Markus Sauerborn
phone +49(0)30-6392-2921
fax   +49(0)30-6392-4972
Markus.Sauerborn@bessy.de

News & Events

Prof. Dr. Wolfgang Gudat's term of office as scientific director of BESSY expired at the end of 2000. His successor is Prof. Dr. Wolfgang Eberhardt *(left picture below),* formerly of the FZ Jülich. On the occasion of the official inauguration in July, Prof. Gudat *(picture below on the right)* handed over the official business of the BESSY light source symbolized by an oil lamp.

Construction works along the Albert Einstein Strasse were comleted in 2001. Prof. Dr. Hans Olaf Henkel *(right)*, president of the Wissenschaftsgemeinschaft Gottfried Wilhelm Leibniz, spoke at the ceremonial completion of the BESSY building extension in October. Scientific talks were held by Prof. Dr. B. Keimer (Max-Planck Institute Stuttgart) and Prof. Dr. J. Stöhr, (Stanford Synchrotron Radiation Laboratory, USA).

The new lecture hall is being used to promote scientific exchange: There are jour fix for the "User Treff" (USER/BESSY meetings regarding operations) and for "Science on the Fly", informal seminars of research in progress.

The inauguration of the Russian-German Laboratory, a joint venture of the University of St. Petersburg, the Freie Universität Berlin and BESSY was accompanied by the "Third Russian-German Workshop" on Synchrotron Radiation Research in November 2001.

USERS' MEETING 2001

The BESSY Users' Meeting 2001 was held on December 6th and 7th, 2001 according to tradition. The scientific director, Prof. Dr. Wolfgang Eberhardt, in office since May 2001, opened the meeting by reviewing some of the highlights of the 3rd year of user operation. Life science increases its importance for BESSY as demonstrated by the first protein structure resolved at BESSY. The BESSY in house research will be extended to further areas particularly related to the new BESSY project, the SASE FEL. Among these are clusters and cluster cased caterials, magnetic thin film systems and nanostructures and the development of coherent scattering methods for the investigation of novel materials and processes. The new project, the SASE FEL, operating in the energy range up to 1000 eV with pulses as short as 20 fs is one of the special activities at BESSY. Less spectacular are the ongoing activities in the microstructure lab and in the radiometry lab operated by PTB. The PTB is also making plans for a low energy storage ring for radiometry to be built next to the BESSY II ring and also basic research at long wavelengths to come in operation around the year 2007.

In further contributions the Visions of Science relating to the future FEL was presented. It started with an introduction to the project by W. Eberhardt who stated that time is just right to build such a facility. The increase in performance justifies thinking about it as a new project and not as an extension of the existing source. The peak power increases by a factor 10^9, the pulse length decreases by a factor of 10^3 as compared to the BESSY II source, and the photon energy increases by a factor 10^3 as compared to existing laser sources. The complete transverse coherence of the radiation is one of the new features that allow to extract useful information from diffraction to be obtained without an extended regular lattice (cf. Visions of Sciences).

Michael Wolf from the Free University Berlin discussed fs chemistry as another field of applications of the FEL. He pointed out that the time evolution of the electronic and the geometric structure occurs on a scale between 20 fs and 200 fs. As an example he discussed the surface catalytic reaction $CO/Ru(0001) \rightarrow CO_2$. Using pulse correlation techniques in the visible the reaction channel - hot electron mediated vibrational excitation - was identified. An FEL will allow the evolution of electronic structure with element selectivity to be studied using techniques as time resolved UPS and X-ray emission. Time resolved EXAFS investigations can be used to obtain geometric information from the same sample.

J. Ullrich from Heidelberg discussed the potential of the FEL in atomic physics. He identified the areas of multiphoton processes when the number of photons and the number of electrons are both simultaneously well defined, of molecular ion interaction, and of precision spectroscopy on ions. In all cases experiments with the FEL will allow to come closer and even reach the situation of a complete experiment (in a quantum mechanical sense). Examples are the two and three photon absorption of He like systems, the chemistry of interstellar clouds, and the fine structure and Lamb shift for high Z H-like ions with nuclear charges up to Z=90. Hyperfine structure studies on highly charged ions probe nuclear physics.

G. Schütz concentrated on the magnetism of nanostructures. Such investigations are triggered by the requirement of high switching rates in magnetic data storage systems. A typical technique would be time resolved resonant XMCD in composite systems. Relaxation times of spin systems are one of the topics to be addressed by the BESSY FEL.

Michael Grunze from Heidelberg pointed out that presently the most important question in life science is functional genomics. This requires high spacial resolution of the order of 1 nm and better, and chemical resolution as achieved e.g. by NEXAFS techniques *in vivo* i.e. in a state close to the living cell. As an example he showed the amino acids cystein and methionine. Both molecules contain a sulfur atom but in chemically different environments. The chemical contrast of XES helps to disentangle the systems. Solar cells using electrolytes are a further field of relevance where the FEL may contribute.

J. Feldhaus reported on the recent results from the TTF in Hamburg . With a gain length of about 0.7 m saturation is regularly achieved where there are some 10^{17} photons/cm^2 in the focus (more than 4 orders of magnitude more than one can hope to get from ordinary synchrotron radiation). First experiments include the investigation of a 40 nm layer of carbon on a Si surface which is a system representing a future typical mirror. Also Xe clusters where investigated. It was found, that upon irradiation highly charged Xe ions are observed which are not generated when atomic Xe is irradiated.

On the second day of the users' meeting different results obtained at BESSY in the past year were presented (see also special reports). The poster session was held in the BESSY storage ring hall. The posters are to remain in the hall until next year's meeting so that the results of the experiments can be discussed by visitors and by other user groups the whole year round.

As in the last years the best poster was honoured with a voucher for scientific literature. This year the poster prize was awarded to Lutz Kipp, University of Kiel (right picture).

Parallel to the Users' meeting a **vendor exhibition** was held in the Einstein- and Newton-Kabinett of the WISTA-building.

The following companies participated in the exhibition:

Accel Instruments GmbH, Bergisch Gladbach	Leybold Vakuum GmbH, Berlin
Astro- und Feinwerktechnik Adlershof GmbH, Berlin	Optikkomponenten & Kristalle, Berlin
BESTEC GmbH, Berlin	Omikron Vakuumphysik GmbH, Taunusstein
Caburn-MDC GmbH, Berlin	Oxford Danfysik, Oxford
FMB Feinwerk- und Meßtechnik GmbH, Berlin	Pfeiffer Vakuum GmbH, Asslar
Gammadata Scienta AB, Uppsala	piezosystem jena GmbH, Jena
GMS Frank Optic Products, Berlin	PINK Vakuumtechnik GmbH, Wertheim
Goodfellow GmbH, Bad Nauheim	SAGEM (Roeosc Products), Nanterre
Hamamatsu Photonics Deutschland GmbH, Herrsching	SIS Struck Innovative Systeme GmbH, Hamburg
Hositrad/Holland, Hoevelaken	SPECS GmbH, Berlin
Huber Diffraktionstechnik GmbH, Rimsting	Thermo Eberline ESM, Eiche
IfG-Institut für Gerätebau GmbH, Berlin	Thermo Vacuum Generators, Hennstedt
ILMVAC GmbH, Ilmenau	VACOM GmbH, Jena
Jenoptik Mikrotechnik GmbH, Jena	Varian GmbH, Darmstadt
Just Vakuumtechnik GmbH, Landstuhl	VAT Deutschland GmbH, Grasbrunn
Jobin Yvon GmbH, Grasbrunn	

Ernst Eckhard Koch Prize

The Ernst Eckhard Koch prize is annually awarded for an outstanding PhD thesis using synchrotron radiation at BESSY or HASYLAB. Like the years before, the prize was awarded at the Users' Meeting by the Society of Friends and Sponsors of BESSY. This year Dr. Karin Heister from the University Heidelberg received the prize for her thesis on selfassembled monolayers of large molecules on Au and Ag surfaces. The molecules investigated contain a sulfur head group, aliphatic and/or aromatic spacers and an endgroup which is chosen to be inert. She showed that the reconstructed gold surface is modified by the adsorption of the molecules the Ag surface does not show any modification as demonstrated by line shifts as small as 0.05 eV! She showed further that this result is independent of the details of the spacer part of the molecule. The radiation damage mechanism was shown to be mediated by secondary electrons. Lateral structuring by selective irradiation with synchrotron radiation was also demonstrated.

Karin Heister from the University of Heidelberg received the Ernst Eckhard Koch Prize 2001. The Prize was handed over by Prof. Dr. P. Zimmermann.

Innovation Award on Synchrotron Radiation

At this year's Users' Meeting the Society of Friends and Sponsors of BESSY awarded for the first time the Innovation Award on Synchrotron Radiation. It is granted for an excellent achievement which has contributed significantly to the further development of techniques, methods or uses of synchrotron radiation. The award which includes a monetary prize of € 2550 was given to Rolf Follath and Friedmar Senf, both from BESSY, for the development and manufacturing of high resolution plane grating monochromators. These monochromators yield the highest energy resolution in the XUV spectral region ever achieved, as well as a high photon flux and a very small focus.

Bestowal of the Innovation Award on Synchrotron Radiation:
from left to right: Dr. K. F. Beckstette, president of the jury, Technology Center Carl Zeiss, Oberkochen, the winners Dr. Rolf Follath and Dr. Friedman Senf and the president of the Society of Friends and Sponsors of BESSY, Prof. Dr. P. Zimmermann.

VISITORS

In 2001 BESSY enjoyed great popularity as ever: 76 groups - thereof 18 groups from primary and secondary schools and 16 groups from universities - visited BESSY to get a view inside the facility and the scientific work that is done there. Overall nearly 1500 participants attended guided tours at BESSY. The importance of BESSY for the WISTA and greater area of Berlin concerning science and technological development was also expressed by the visits of high ranking persons like the Klaus Wowereit, (Governing Mayor of Berlin), Adrienne Goehler (Berlin Senator of science, research and culture), Werner Müller (Federal Minister of Economy).

On September the 15th nearly 4000 interested visitors joined the Open House which was arranged by BESSY in the framework of the "**Lange Nacht der Wissenschaft**" (Long Night of Science).

Almost 4000 visitors took the opportunity to talk to BESSY researchers and to get detailed information about the facility and the research that is done there.

Demonstrations and exhibits were a special attraction for the visitors.

Visitors in 2001

JANUARY

Hr. Holstein (FZK) und Kollegen, 4 Teilnehmer

BAM, Mitglieder des Präsidiums und Abteilungsleiter, 16 Teilnehmer

Teilnehmer eines deutsch-chilenischen Workshops, Prof. Jaenichen (IGAFA), 8 Teilnehmer

Studierende der TU, FB Chemie, Prof. Lubitz, Hr. Messinger, 12 Teilnehmer

Journalisten aus Österreich, 10 Teilnehmer

Studierende der TUB, AG Prof. Zimmermann, 20 Teilnehmer

FRBRUARY

Mitarbeiter Daimler Chrysler AG, 22 Teilnehmer

MARCH

Projektleiter der Proteinstrukturfabrik, 40 Teilnehmer

High School Norwegen, 10 Teilnehmer

Herr Ohff und ehem. Lehrerkollegium, 15 Teilnehmer

Mitarbeiter der Fa. JOTEV, Adlershof, 6 Teilnehmer

Studierende der TUB, FB Physik, Institut fürMetallforschung, 15 Teilnehmer

APRIL

Junior Experts japanischer Firmen aus den Sektoren Informationstechnik, Energie,
    Chemie;

Prof. Meinnicken, GF des Deutsch Japanischen Konzils

Fa. VAT München, Hr. Doll und Kollegen, 4 Teilnehmer

Gesamtpersonalrat der PTB Braunschweig u. Berlin, 15 Teilnehmer

Studierende der Westsächsischen Hochschule Zwickau, 40 Teilnehmer

Teilnehmer einer Tagung der DLR, 30 Personen

Studierende der Universität Leipzig, FB Physik, Prof. Freude,15 Teilnehmer

Sts Dr. Meister-Scheufelen+ Mitarbeiter der Senatsverwaltung

VDE, Studierende der Nachrichtentechnik, 20 Teilnehmer

Informatiker der Daimler Chrysler AG, 15 Teilnehmer

Informatiker der Humboldt Universität, 3 Teilnehmer

Mitarbeiter des Max-Planck-Instituts für Metallforschung, Stuttgart, 55 Teilnehmer

Studierende der HU, Grundstudium Physik, 15 Teilnehmer,

MAY

Pohang Accelerator Laboratory, Korea Dr. Sang H. Nam , 3 Teilnehmer

Dr.Grover Dr.Sahni , BARC Indore

Mitarbeiter des Max-Planck-Instituts für Kernphysik, Heidelberg, 27 Teilnehmer

JUNE

MinR Dr. Jürgen Arnold, BMBF Ref. 123 (Russland, Ukraine u.a. GUS Staaten)

Prof. Hans-Olaf Henkel, WGL

Studierende der Universität Kaiserslautern, AG Schmoranzer, 50 Teilnehmer

Mitglieder des Verbands der Medizintechniker Berlin/Brandenburg, 30 Teilnehmer

Mitarbeiter der Generalverwaltung der MPG ca. 40 Personen

Mitarbeiter der Proteinstrukturfabrik, 6 Teilnehmer

Studierende der FH Brandenburg, FB Physikalische Technik, 25 Teilnehmer

Studierende der TU Berlin, FB Chemie, 20 Teilnehmer

Delegation des chinesischen Institute Atomic Energy, Peking, 5 Teilnehmer

JULY

Katsuyoshi Takano, Gunma University Japan

Vertreter des Interdisziplinären Verbundes Serviceeinrichtungen (IVS) der WGL

Bundeswirtschaftsminister Dr. Müller

Fr. Haddatney, ZDF- Redaktion "aspekte", Filmaufnahmen zur Kunstausstellung

Dr. Schmidt, TUB (AG Prof. Lehr) mit 15 Studierende

Senatorin für Wissenschaft, Forschung und Kultur, Fr. A. Goehler

Mr. Masashi Ishii, SPring-8

Ms Dr. Akane Aguii, SPring-8

Mitarbeiter der Botschaft Malaysias, 4 Teilnehmer

AUGUST

Hr. Render, Deutsche Bank Berlin

Prof. Mitituka Terasawa, Japan, Himeji Institute of Technology

Australian Synchrotron Project, 3 Teilnehmer

Regierender Bürgermeister Wowereit

ACCEL Delegation, Prof. Edmonds, Dr. R. Fischetti, D.Dougherty, J. Durge

SEPTEMBER

Architekturstudenten aus Barcelona, 20 Teilnehmer

Delegation aus China, Besuch des Anwenderzentrums, 15 Teilnehmer

Mitarbeiter des HMI, 25 Teilnehmer

Teilnehmer des MBE Workshop des Paul Drude Instituts, ca 10 Personen

Teilnehmer der 4.Weltkonferenz ü. Oxidationskatalysatoren, 8 Teilnehmer

OCTOBER

Prüfer des Deutschen Patentamts München, 3 Teilnehmer

Mitglieder des Fördervereins der Technologiestiftung Berlin, 30 Teilnehmer

Studierende der TUB, Prof. Lehr, 20 Teilnehmer

Prof. Andersen, Niels-Bohr-Institute Kopenhagen , Prof. Grande, Brasilien und 7 HMI-Mitarbeiter

NOVEMBER

Mitarbeiter der oetv, 10 Teilnehmer

Studierende der TFH Wildau, FB Physikalische Technik, 25 Teilnehmer

Mitarbeiter der BAM und Studierende der TFH Berlin, FB Chemie & Pharmazie, 14 Teilnehmer

2 Mitarbeiter Agilent Technologies

DECEMBER

50 Besucher des IRIS-Workshops

Mitarbeiter des Instituts für Medizinische Physik & Biophysik, 20 Teilnehmer

Besucher der PTB, 15 Teilnehmer

Hr. Schulz, MBI mit Studenten, 15 Teilnehmer

Studierende der TU Berlin (Umwelttechnik), 35 Teilnehmer

Visiting Schools

FEBRUARY

Nelly-Sachs-Schule-Oberschule, 15 Teilnehmer

MARCH

Werner-von-Siemens-OS, LK Physik, 17 Teilnehmer

Zehlendorfer Gymnasium, GK+LK Physik, 18 Teilnehmer

Erich-Hoepner-OS, Hr. Schleissing, 34 Teilnehmer

Alexander-von-Humboldt-OS, LK Physik, 16 Teilnehmer

APRIL

Alexander-von-Humboldt-OS, LK Physik, 25 Teilnehmer

JUNE

Paulsen-Gymnasium, Steglitz, 20 SchülerInnen der 8.-10. Klasse

Schulklasse aus Würzburg, 28 Teilnehmer

John F. Kennedy Schule, Zehlendorf, 15 Teilnehmer

JULY

Max -Planck-OS, Mitte, LK Physik, 15 Teilnehmer

Barnim-Oberschule, Hohenschönhausen, 8 Teilnehmer

Herder-Oberschule, Charlottenburg, 16 Teilnehmer

SEPTEMBER

Ernst-Friedrich-OS, Treptow, 13 Teilnehmer

Oberstufenzentrum KFZ, B-Charlottenburg, Kurs Chemie/Physik, 21 Teilnehmer

Robert-Blum-Schule, 8 Teilnehmer

WISTA Tage der Forschung 93 Teilnehmer

NOVEMBER

Gymnasium Hildesheim, LK Physik, 8 Teilnehmer

Robert-Blum-Oberschule, LK Physik, 18 Teilnehmer

Workshop on the Scientific Case of a
BESSY VUV-Soft-X-Ray FEL
January 12 - 17, 2001

Friday, January 12th

Arrival and Check-In Hotel Sachsenstern, Holzhau

Welcome and Introduction

R. Bakker   The BESSY FEL

J. Feldhaus Concepts for Seeding and Monochromators

Saturday, January 13th

I. Lindau   Experimental Possibilities at LCLS

Cluster

K.H. Meiwes-Broer Multi-ionization of metal clusters by strong VUV-FEL pulses

G. Gantefoer Innershell photoabsorption of free mass-selected clusters

M. Neeb Photoionisationsexperimente on mass selected clusters and cluster-adsorbates

Th. Möller Electronic Structure and Dynamics of Clusters

Magnetism

K. Starke Spin dynamics in itinerant and localized magnetic systems

H. Dürr Femtosecond Magnetization Dynamics of Nanoscale Devices

W. Sandner Experimental Possibilities with fs-Lasers

Sunday, January 14th

Chemistry, Environmental Sciences

O. Schaff Spectro-microscopy with extreme lateral resolution: the SMART

E. Rühl Excited-State Dynamics of atmospheric Molecules, Radicals, and Aggegates

Atoms and Molecules

B. Sonntag Triple Photoionization of Li atoms, Photoexcitation and decay dynamics of hollow atoms, Multiphoton inner-shell excitation/ionization of atoms

U. Becker Configuration and conformation changes during molecular discoiation

J. Ullrich Resonant Single and Multi-Photon Excitation and Ionisation of Highly Charged Ions by FEL Radiation; Multiphoton Multiple-Ionization of Atoms and Molecules using Reaction-Microscopes

A. Wolf Fast Beam Photodissociation Spectroscopy of Molecules

High Resolution Spectroscopy

S. Hüfner High Resolution Photoemission

L. Kipp Angle Resolved Photoelectron Nanospectroscopy using VUV-FEL Radiation

M. Golden Angle-scanned photoemission of HTSC with high k and E resolution: present status and perspective

Soft X-Ray Resonant Scattering

S. Eisebitt Electronic Structure of Nanomaterials

J.E. Rubensson Resonant Soft X-ray Inelastic Scattering on Atoms and Molecules

H. Dürr Resonant Scattering from oxide materials

Monday, January 15th

Coherence und Biology

S. Eisebitt Speckle and Coherent Resonant Scattering

G. Schmahl Biological investigations using FELs

Pump-Probe Spectroscopy

M. Aeschlimann Pump-Probe Experiment in the VUV region

M. Wolf Dynamics of femtosecond laser-induced surface reactions studied with time-resolved pump-probe experiments

C. Pettenkofer Pump-Probe Spectroscopy of Semiconductor Heterostructures

W. Wurth Pump-Probe Spectroscopy involvin core electrons

W. Eberhardt Setup of working groups

Discussion in working groups and draft of the report

Tuesday, January 16th

Discussion in working groups and draft of the report

Reports from working groups

Final discussion and conclusion

End of Workshop

Wednesday, January 17th

Check Out and Departure

Indo-German Workshop on
Nano-Materials & Technologies
18th and 19th June, 2001

Monday, June 18th, 2001

Welcome / Introduction
Prof. Dr. W. Eberhardt (BESSY)

Mr. A. Chakraborty (Indian Embassy)

Prof. Dr. C. Streffer (Uni Essen)

Quantum confinement effect and interfacial properties in nanocomposites
Prof. D. Chakravorty (IACS Kalkutta)

Stability and properties of nano-embedded particle of metals and alloys
Prof. K. Chattopadhyay (IISc Bangalore)

Deposition massenselektierter Cluster auf Oberflächen
Dr. R. Klingeler (FZ Jülich)

Nanomaterials: Structural characterization
Dr. V.S. Raghunathan (IGCAR Kalpakkam)

Nanomachining
Mr. G. Gouthaman (BARC Mumbai)

Synthesis, properties and self-assembly of semiconductor nanoparticles
Prof. Dr. H. Weller (Universität Hamburg)

Novel properties of nanostructure semiconductors and Sb & Se clusters
Dr. S.N. Sahu (IOP Bhubhaneswar)

Electronic structure and optical properties of carbon nanostructures
Dr. M.S. Golden (IFW Dresden))

Semiconductor and biomolecular
Dr. R.P. Bajpai (CSIO Chandigarh)

Development of nanostructured materials by mechanical methods:
The Indian scenario
Prof. S.K. Pabi (IIT Kharapur)

Nanocrystalline materials with interface-controlled properties
Dr. J. Weissmüller / Dr. R. Viswanath (FZ Karlsruhe)

Radiolytic preparation and physico-chemical characteristics of nano-sized metal particles
Dr. S.K. Kulshreshtha (BARC Mumbai)

Hydrogel and smart hydrogel nanoparticles – applications to drug delivery and targeting
Prof. A.V. Maitra (University of Delhi)

Tuesday, June 19th, 2001

Structural and opto-electronic properties of sputter-deposited nanocrystalline thin films
Prof. P. Ayyub (TIFR Mumbai)

Spektroskopie magnetischer Nanostrukturen
Prof. Dr. W. Gudat (Dr. O. Rader) (BESSY GmbH)

Nanostrukturen auf Oberflächen
Prof. Dr. K. Kern (MPI für Festkörperforschung Stuttgart)

Structure of nano-crystalline alloys and intermetallics produced by rapid solidification
Dr. S. Banerjee (BARC Mumbai)

Stress, strain and magnetostriction in epitaxial films
Dr. D. Sander (MPI für Mikrostrukturphysik Halle)

Effects of processing conditions on grain size and physico-chemical properties of thin films
Dr. V.C. Sahni (BARC Mumbai)

Nanostructured materials for future storage applications – a synthetic approach
Dr. Christoph Frommen (FZ Karlsruhe)

Tour of the facility
 (Dr. W. Braun)

ESF Exploratory Workshop on Time Resolved Investigations of Structural Changes in Soft and Solid matter with Neutrons and X-rays

5.-7. September 2001, Sommerfeld/Berlin, Germany

Wednesday, September 5th, 2001

Introduction

G. Vogl (HMI)	Welcome address
P. Day (ESF-PESC)	Presentation of the ESF standing committee for physical and engineering sciences (PESC)
C. Wilson (ISIS)	Pulsed neutron diffraction: New opportunities in time-resolved crystallography
A. Kvick (ESRF)	Time-resolved studies in material sciences using synchrotron radiation

Instruments and novel applications

W. Bras (NWO)	Time-resolved x-ray scattering techniques
S. Techert (MPI Göttingen)	Topochemistry probed by time-resolved photo-diffraction
I. Grillo (ILL)	Application of SANS real time experiments with a stopped flow apparatus: a study of anionic vesicle growth
P. Van Esch (ILL)	Fast, real time SANS detectors

Spectroscopy & Scattering

D. Clarke (Daresbury)	Synchrotron radiation as a superior light source for CD; facilities at Daresbury Laboratory
M. Haumann (FU Berlin)	X-ray absorption studies on the tetra-manganese complex of photosystem II
R. Frahm (Uni Wuppertal)	Piezo-EXAFS in the millisecond range
R. Abela (SLS)	Structural dynamics with current and future x-ray sources
G. Grübel (ESRF)	Probing slow dynamics with coherent x-rays
G. Vogl (HMI)	Diffusion in solids: Studied by nuclear resonant x-ray and neutron scattering
R. Röhlsberger (Uni Rostock)	Picosecond time resolution via nuclear resonant scattering from rotating media
I. Sikharulidze (FOM)	Dynamic x-ray scattering from smectic membranes

Thursday, September 6th, 2001

Soft matter and biology I

S. Egelhaaf (Uni Edinburgh)	What can time-resolved SANS tell us about surfactant phase transitions?
H.-D. Bartunik (Hasylab)	Studying structural transitions in proteins by X-ray crystallography
K. Moffat (Uni Chicago)	Time-resolved macromolecular crystallography: Molecular movies?
J. Holzinger (ILL)	Chasing experiments on the binding of co-chaperonins
U. Pietsch (Uni Potsdam)	Time-resolved x-ray scattering at thin organic films
J. Bordas (Uni Barcelona)	Time-resolved x-ray diffraction: muscle structure and function

Hard matter I

D. O'Hare (Uni Oxford)	Studying solid state reactions using time-resolved x-ray and neutron diffraction
G. Eckold (Uni Göttingen)	Stroboscopic studies on the kinetics of phase transitions
G. Bruno (HMI)	Neutron and synchrotron radiation study of the γ^+ nucleation and growth kinetics in the Nickelbase superalloy SC16
K.-H. Liß (GKSF)	Time-resolved study on laser-shocked silicon crystals with high resolution x-ray diffraction

New horizons

R. Bakker (BESSY)	Free-Electron Lasers as the next generation light source for the VUV and x-ray spectral range
W. Eberhardt (BESSY)	Visions of sciences at the BESSY-FEL
F. Mezei (HMI)	The time variable in neutron scattering experiments and the ESS

Friday, September 7th, 2001

Hard matter II

B. David (ISIS)	Parametric high resolution neutron powder diffraction
T. Hansen (ILL)	One-shot and stroboscopic neutron powder diffraction at ILL
K. Ellmer (HMI)	In situ energy dispersive x-ray diffraction system for time-resolved thin film growth studies
Ch. Pietzker (HMI)	Real-time XRD studies on the sequential formations of $CuInS_2$

Soft matter and biology II

H. Amenitsch (ELETTRA)	Time-resolved SAXS in mesoscopic systems: Its applications from bulk to surfaces
T. Kiefhaber (Uni Basel)	Monitoring protein folding on the millisecond time-scale with time-resolved small-angle x-ray scattering
P. Fratzl (Uni Leoben)	Structure and mechanical properties of collagen studied by time-resolved x-ray diffraction

2. Seminar zur Nutzung des Wellenlängenschieber-Messplatzes bei BESSY II
8. - 9. November 2001

Mit Unterstützung des Adolf-Martens-Fonds e.V.
und der BESSY GmbH

Die BAM betreibt seit Anfang des Jahres 2001 eine Beamline (BAMline) am 7T-Wellenlängenschieber bei BESSY II am Wissenschaftsstandort Berlin-Adlershof. Das Seminar soll die Teilnehmer über die Aktivitäten der BAM und ihrer Partner bei BESSY II informieren und zu weiteren Nutzungsmöglichkeiten der BAMline in Chemie- und Materialtechnik durch eingeladene Vorträge anregen.

Die Physikalisch-Technische Bundesanstalt (PTB) unterstützt den Aufbau des Messplatzes und nutzt ihn für metrologische Untersuchungen. Die BAM entwickelt den Messplatz für folgende eigene Projekte:

Röntgenfluoreszenzanalyse
>   als Referenzverfahren zur Optimierung von Analysenverfahren in Reinststoff- und Umweltanalytik

Mikrocomputertomographie
>   zur bildlichen Darstellung kleinster Fehler und Risse sowie Dichtefluktuationen bei der Werkstoff- und Bauteilentwicklung

Röntgentopographie
>   für die Untersuchungen von Hochleistungsverbundwerkstoffen und Bauteilen aus faserverstärkten Keramikwerkstoffen

EXAFS
>   für die Untersuchungen von nicht-kristallinen Werkstoffen z.B. Katalysatoren für Industrie und Kraftfahrzeuge (in Zusammenarbeit mit dem ACA Berlin)

Darüber hinaus hat bereits eine rege Nutzung durch externe Institutionen begonnen.

Begrüßung und Eröffnung
M. Hennecke, Vizepräsident der BAM
J. Schöttler, BMWi
B. Wende, Leiter des Instituts Berlin der PTB

Röntgenstrahlen - ein neues Spektralsegment bei BESSY II
W. Eberhardt, BESSY

Röntgenfluoreszenzanalyse - Status und Trends
P. Wobrauschek, Universität Wien

Röntgenfluoreszenzanalyse (Chair: P. Wobrauschek & B. Kanngießer)

Ortsabhängige Bestimmung von Schadelementen in Lungengewebe von Bergarbeitern der SDAG Wismut
A. Knöchel, F. Lechtenberg, M. Paulsen, S. Staub, Universität Hamburg

Neue Anwendungsfelder der Mikrofokus-Beamline L am HASYLAB
G. Falkenberg, HASYLAB Hamburg

Bestimmung von Fundamentalparametern für die Röntgenfluoreszenzanalyse bei BESSY
B. Kanngießer, TU Berlin

Erste tiefensensitive micro-RFA-Experimente an der BAMline
W. Malzer, TU Berlin

RFA von Metallstiftzeichnungen aus dem Kupferstichkabinett Berlin
I. Reiche[1], J. Riederer[1], H. Bevers[2], [1]Rathgen-Forschungslabor und Kupferstichkabinett, SMBPK, Berlin

Pilotstudien zur Identifizierung metall-haltiger Proteine mit Hilfe der SY-RFA
G. Weseloh, D. Behne, M. Kühbacher, A. Kyriakopoulos, Hahn-Meitner-Institut, Berlin
Quantitative RFA im Radiometrielabor der PTB am Elektronenspeicherring BESSY II
B. Beckhoff, PTB

Schichtdickenbestimmung für Nanometer-Kalibriernormale mittels XRF
M. Procop, BAM

Pflichtprogramm der BAM an der BAMline
S. Merchel, M. Radtke, BAM

Metrologie

Radiometrische Anwendungen hochenergetischer Synchrotronstrahlung
M. Krumrey, G. Ulm, R. Klein, PTB

Offizielle Eröffnung der BAMline mitkleinem Imbiss und Umtrunk mit freundlicher Unterstützung von ACCEL Instr. GmbH, Bergisch-Gladbach

Instrumente (Chair: H.-U. Klein)

X-Ray Optic Developments at BESSY
A. Erko, BESSY

Schlüsselfertige Beamlines und Beamline-komponenten aus industrieller Fertigung
W. Diete, ACCEL Instr. GmbH

Anwendungen unterschiedlicher Glaskapillar-optiken an Beamlines
V. Arkadiev, A. Bjeomikhov, N. Langhoff, Institut für Gerätebau GmbH

BAMline - Status und Zukunft
H. Riesemeier, BAM

EXAFS (Chair: G. Ulm)

Poly-capillary based micro-XANES by means of bending magnet radiation
K.H.A. Janssens, Universität Antwerpen

XANES und EXAFS an Materialien unter dynamischen Bedingungen
S.L.M. Schroeder, FU Berlin

Zeitaufgelöste Röntgenabsorptionsspektroskopie schneller Prozesse
M. Richwin, R. Frahm, Universität Wuppertal

Strukturanalytik (Chair: A. Zschunke)

Die Proteinstrukturfabrik – Einkristall-Diffraktionsexperimente bei BESSY
U. Müller, U. Heinemann, FU Berlin & Max-Delbrück-Centrum, Berlin

Röntgen-Refraktions-Topographie an der BAMline
B.R. Müller, M.P. Hentschel, BAM

Bestimmung der Dichteverteilung in keramischen Bauteilen mit Computer-Tomographie an der BAMline
J. Goebbels, BAM

Schlusswort
W. Görner, BAM

Organisation
• Wolf Görner (wolf.goerner@bam.de), Silke Merchel, Heinrich Riesmeier
  Tel.: 030-8104 1140, Fax: 030-8104 1147
• Victoria von Malotky (victoria.von_malotky@bam.de), Tel.: 030-8104 3021
• Walter Braun (braun@bessy.de), BESSY, Tel.: 030-6392 2927
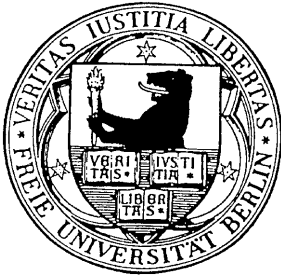
Third Russian-German Workshop on

Synchrotron Radiation Research

Nov. 18-20, 2001, Berlin, Germany

Workshop Chairmen

Günter Kaindl   Freie Universität Berlin
Wolfgang Gudat   BESSY GmbH, Berlin

Sponsors

BESSY GmbH Berlin

Bundesministerium für Bildung und Forschung

Deutsche Forschungsgemeinschaft

Freie Universität Berlin

Förderverein BESSY

Stifterverband für die Deutsche Wissenschaft

Russian Foundation for Basic Research

Ministry of Science and Technology of Russian Federation

Sunday, November 18, 2001

Registration for the Workshop at the 'Clubhaus' of the Freie Universität Berlin, Goethestraße 49, 14163 Berlin-Zehlendorf. The 'Clubhaus' can be easily reached by 'U-Bahn' No. 1, which should be taken to the final destination 'Krumme Lanke'. From there, it is just a 5-minutes walk to the 'Clubhaus'.

Welcome Reception for all participants of the Workshop, with German-Russian buffet dinner, at the 'Clubhaus' of the Freie Universität Berlin. The Reception will end at 22:30. Adlershof can be easily reached after the Reception by 'U-Bahn' and 'S-Bahn'.

Monday, November 19

Registration for the Workshop at BESSY II, Albert-Einstein-Straße 15, 12489 Berlin-Adlershof.

Opening Session

W. Eberhardt (BESSY GMBH Berlin): *Welcome address*

G. Kaindl (Freie Universität Berlin): *Opening address*

Session A: *Facilities and Instrumentation*

     Chair: W. Gudat (BESSY GmbH Berlin)

W. Braun (BESSY GmbH Berlin):
BESSY II: Facilities and beamlines

S.L. Molodtsov (Technische Universität Dresden):
Russian-German Laboratory at BESSY II

V.G. Stankevich (Kurchatov Institute, Moscow):
Kurchatov synchrotron radiation source: status and research programs

1G.N. Kulipanov (Budker Institute, RAS, Novosibirsk):
Progress in synchrotron radiation research at Novosibirsk

M.V. Kovalchuk (Shubnikov Institute of Crystallography, RAS, Moscow):
Photoelectron yield induced by x-ray standing waves
W. Eberhardt (BESSY GmbH Berlin):
Visions of science at the future BESSY SASE free-electron laser

Session B: *Chemistry, Catalysis, Materials Science*

         Chair: E. Umbach (Universität Würzburg)

Yu.A. Ossipyan (Institute of Solid State Physics, RAS, Chernogolovka):
Fullerenes: from discovery to applications as a new object for studies with synchrotron radiation

J. Fink (Institut für Festkörper u. Werkstofforschung, Dresden):
Valence and core-electron spectroscopy applied to doped fullerenes and nanotubes

V.M. Mikoushkin (A.F. Ioffe Physico-Technical Institute, RAS, St. Petersburg):
Modification of fullerite C_{60} by irradiation

W. Wurth (Universität Hamburg):
X-ray absorption spectroscopy of size-selected supported transition metal clusters

Yu.A. Babanov (Institute of Metal Physics, RAS, Yekaterinburg):
EXAFS studies of solid-state solutions

A.S. Vinogradov (St. Petersburg State University, St. Petersburg):
Chemical bonding effects in iron compounds studied by x-ray absorption

Session C: *Atoms, Molecules, Interfaces, and Thin Films*

         Chair: N. Mårtensson (MAX-Lab Lund)

V.L. Sukhorukov (Rostov State University of Transport Communications):
Dynamics of decay of excited atomic and molecular states studied by photon-induced fluorescence spectroscopy

P. Zimmermann (Technische Universität Berlin)
2p multiplet splitting in 3d-transition-metal atoms

C. Laubschat (Technische Universität Dresden):
Cooper minima in photoemission and resonant photoemission from solids

A.M. Shikin (St. Petersburg State University and BESSY GmbH Berlin):
Quantum-size effects in ultra-thin epitaxial Au and Ag films on W(110)

C. Heske (Universität Würzburg):
X-ray emission study of buried interfaces in Cu(In,Ga)(S,Se)$_2$ thin-film solar cells

Session D: Poster Session

Chair: Yu.S. Gordeev (A.F. Ioffe Physico-Technical Institute, RAS, St. Petersburg)

Tuesday, November 20

Session E: *Electronic Structure and Magnetism*

Chair: V.K. Adamchuk (St. Petersburg State University)

S. Hüfner (Universität des Saarlandes, Saarbrücken):
High-resolution photoemission applied to superconductors and highly correlated material

A.M. Ionov (Institute of Solid State Physics, RAS, Chernogolovka):
Resonant photoemission study of Chevrel phase materials

K. Starke (Freie Universität Berlin):
Magneto-optics with soft x-rays of rare-earth materials

H.C. Mertins (BESSY GmbH Berlin):
Observation of the x-ray magneto-optical Voigt effect at the 2p edge of Co

W. Kuch (MPI für Mikrostrukturphysik, Halle)
Layer-resolved magnetic imaging in exchange-coupled Co/Cu/Ni-trilayers

Session F: X-Ray Scattering and Spectroscopy

> Chair: S.N. Mazurenko (Institute of Physical Problems, Moscow/Zelenograd)

D. Hupfeld (Forschungszentrum Jülich):
Investigation of element-specific magnetic correlations with synchrotron radiation

H. Dürr (BESSY GmbH):
Soft x-ray resonant magnetic scattering of magnetic ordering phenomena

E. Weschke (Freie Universität Berlin):
Magnetic structure of ultrathin Ho metal films studied by soft x-ray resonant scattering

S.I. Zheludeva (Shubnikov Institute of Crystallography, RAS, Moscow):
X-ray scattering in characterization of organic and inorganic nanostructures

E.Z. Kurmaev (Institute of Metal Physics, RAS, Yekaterinburg):
Band mapping in MgB_2 and graphite using resonant x-ray inelastic scattering

A.E. Voloshin (Shubnikov Institute of Crystallography, RAS, Moscow):
Quantitative measurements of crystal inhomogeneities by x-ray topography

V.V. Kvardakov (Kurchatov Institute, RAS, Moscow):
Non-linear magneto-acoustic vibrations in weak ferromagnets studied by means of x-ray diffraction and topography

Inauguration of the Russian-German Laboratory at BESSY II (separate Program)

Reception with buffet dinner for all participants in the Lobby of the BESSY building

GAMMADATA

Scienta Users' Meeting

Dear Scienta user,

Gammadata Scienta has the honour to invite you to the first users' meeting, which is going to take place in connection to the BESSY users meeting in Berlin. The meeting is open to all group members affiliated with the owner group. Registration is mandatory.

Location: BESSY building/lecture hall,
                 Albert-Einstein-Strasse 15, Berlin

Time: Dec. 5, 2001 at 18:00

Program:

Buffet dinner

Introduction, Scienta news presentation

User presentation: **Dr. Sergey Borisenko**, IFW-Dresden is presenting research work done both with a Scienta SES-200 and a SES-100 analyzer.

Software demonstration. **Mr. Henrik Ohman**, Gammadata Scienta explores the possibilities of the new Scienta spectrometer software.

Open discussion

GAMMADATA

XES Workshop

Location: BESSY building/lecture hall,
Albert-Einstein-Strasse 15, Berlin

Time.   Dec. 5, 2001 at 14:30

Program:

Soft X-ray emission spectroscopy of buried interfaces
and first results at BESSY
Dr. Clemens Heske, Universität Würzburg

Soft X-ray emission spectroscopy of nanostructures
Mr. Mirko Freiwald

Coffee break

Visions and future direction for soft X-ray emission spectroscopy
Prof. Joseph Nordgren, Uppsala University

Discussions
        * What are the demands on an optimized soft x-ray
        emission setup?
        * What are the possibilities today at BESSY for soft
        x-ray emission spectroscopy?

infrared initiative
synchrotron radiation

IRIS

IRIS Workshop
am 5. Dezember 2001
in Berlin-Adlershof

Programm:

Begrüßung

K.P. Hofmann (Charité, Berlin), W. Eberhardt (BESSY, Berlin),
L. Incoccia-Hermes (Projektträger DESY-HS, Hamburg)

Vorträge
Chairman: E.H. Korte (ISAS, Berlin)

- **D. Naumann (RKI, Berlin)** "FT-IR Mikrospektrometrie an Zellen und Geweben"

- **Ch. Bernhard (MPI, Stuttgart)** "Fern-Infrarot Ellipsometrie an einem Synchrotron - Ergebnisse an Kuprat Hoch-Tc Supraleitern und anderen Oxidverbindungen"

- **K. Gerwert (Ruhruniversität, Bochum)** "Proteine bei der Arbeit: Untersuchungen mit zeitaufgelöster FT-IR"

Besichtigung und Eröffnung des IRIS-Messplatzes bei BESSY
L. Incoccia-Hermes (Projektträger DESY-HS), W.B. Peatman (BESSY),

Arbeitstreffen der IRIS-Interessenten
Chairmen: W.B. Peatman (BESSY), U. Schade (BESSY)

- **W.B. Peatman (BESSY)** "Begrüßung, Einleitung"

- **U. Schade (BESSY)** "Erste Ergebnisse am IRIS-Messplatz"

- **K. Holldack (BESSY)** "Erstmalige Beobachtung kohärenter Fern-IR Strahlung am Speicherring"

- **K. Hinrichs (ISAS, Berlin)** "Instrumentierung für IR-Ellipsometrie am IRIS-Messplatz"

- **N. Esser (TU Berlin)** "In situ IR-Spektroskopie an metallorganischen Molekülen auf III-V Oberflächen"

- **F. Siebert (Universität Freiburg)** "Erste Erfahrung über TR-IR Untersuchungen mit Synchrotronstrahlung am NSLS Brookhaven"

- **F. Bartl (Charité, Berlin)** "FTIR-Spektroskopie an photosensorischen Proteinen"

- **Ch. Zscherp (Universität Frankfurt)** "Untersuchung von Proteinen mit photolabilen Effektormolekülen."

- **Ch. Jung (MDC, Berlin)** "Hochdruck IR-Spektroskopie an Häm-Proteinen"

Veranstalter: Charité, ISAS, BESSY   Organisation: KoSt

Kontakt:

Ulrich Schade
BESSY GmbH
Albert-Einstein-Straße 15
D-12489 Berlin
fon +49 30 6392-3550, fax -3544
Email: schade@bessy.de

Markus Sauerborn, KoSt
c/o BESSY GmbH
Albert-Einstein-Straße 15
D-12489 Berlin
fon +49 30 6392-4921, fax -4972
Email: sauerborn@bessy.de

Der Verein der Freunde und Förderer der Berliner Elektronenspeicherring-Gesellschaft mbH BESSY e.V.

Albert-Einstein-Straße 15, D-12489 Berlin

lädt zum BESSY-Forum ein

Am Montag, dem 17. Dezember 2001 um 15:00 Uhr

spricht

Herr Prof. Dr. Jürgen Mlynek
Präsident der Humboldt-Universität

über

"Kalte Atome - ein heißes Thema "

*Die Veranstaltung findet im Hörsaal der
BESSY GmbH,
Albert-Einstein-Str. 15, 12489 Berlin
statt.*

*Über Ihre Teilnahme würden wir uns freuen.
Zum anschließendem Empfang mit Buffet
laden wir Sie herzlich ein.*

Prof. Dr. P. Zimmermann
Vorsitzender des Vorstandes

How to become a BESSY user

The Berliner Elektronenspeicherring-Gesellschaft für Synchrotronstrahlung mbH (BESSY) operates the 1.7 GeV electron storage ring BESSY II in Berlin-Adlershof to produce highly brilliant synchrotron radiation from the infrared to the hard X-ray region (photon energy range below 50 keV) of the electromagnetic spectrum for basic research, for metrology and for instrumental development purposes. In general, BESSY provides monochromatized synchrotron radiation while the user is responsible for his/her own measuring chamber/preparation chamber. Data acquisition systems and central computer facilities are provided by BESSY. Presently there are 36 beamlines in operation at BESSY II: 21 are located at undulators and 15 at bending magnets. Typically a user group is granted a beam time period which lasts from 2 - 4 weeks.

Besides complying with general safety rules of a large laboratory potential users must ensure that the measuring equipment also fulfills certain requirements which depend, at least in part, on the beam line used. Most importantly the measuring station has to be operated under such conditions that an impairment of the beam line and storage ring vacuum is prevented. In general this means the station itself runs under ultra high vacuum conditions. Furthermore, one may use either so-called common facilities, which are operated under the responsibility of a user group, or measuring equipment which belongs to BESSY (see attached list "Experimental stations at BESSY"). The use of equipment must be coordinated with the scientists responsible for the equipment. In addition to this safety rules it is necessary that your Institution has a valid Radiation Protection Delimitation Contract with BESSY. Access to BESSY cannot be granted without such a contract.

BESSY charges fees for beam time to cover the operational costs. The German Federal Ministry of Education and Research (BMBF) and the corresponding state ministries cover fees and provide funds for user groups from German universities and research institutes of the "Leibniz-Gemeinschaft". These funds are administered by the "Projektträger" (DESY HS, Dr. L. Incoccia-Hermes, Notkestr. 85, D-22603 Hamburg, phone: +49-40/8998-3702, FAX: +49-40/8994-4301). Further information may be obtained there. Beam time fees for projects funded by the Deutsche Forschungsgemeinschaft (DFG) will also be covered by the BMBF. Through the "Human Potential Programme" (HPP) of the Commission of the EU, groups from countries of the European Union and Associated States may receive funds to carry out projects at BESSY.

In addition, BESSY can make arrangements to cover project costs for short test and preliminary experiments at BESSY. These should be sent prior to the semi-annual application deadlines. Applications forms and further information are available on this CD and on the BESSY web site www.bessy.de.

When planning an experiment it is recommended that one contacts the scientific director as early as possible. In addition to providing synchrotron radiation, the BESSY services include assessment of the feasibility of the intended project, scientific-technical consulting and help in contacting competent partners within the BESSY user community.

Beam time is allocated twice a year for a the subsequent semesters. The beam time schedule can be found on www.bessy.de. Applicants are invited to submit their beam time requests by mid-February or mid-July, respectively. Allocations take into account the recommendations of BMBF or DFG referees and the BESSY Beam Time Committee of independent external scientists.

For further information please contact the beam time coordinator

                Dr. W. Braun   (Tel.: +49-30/6392-2927,
                                      e-mail: walter.braun@bessy.de)
or   Dr. G. Reichardt (Tel.: +49-30/6392-4983,
                                      e-mail: gerd.reichardt@bessy.de)

General information for BESSY users as well as the performance of the monochromtors and of the experimental facilities are summarized in the BESSY user handbook which is available on the web site www.bessy.de.

Berlin, February 2002

**Berliner Elektronenspeicherringgesellschaft
für Synchrotronstrahlung m.b.H.**

⬡ **BESSY**

....
Proposal number (to be completed by BESSY)

Albert-Einstein Straße 15
D-12489 Berlin
Germany

Tel.:   ++49-30-6392 - 2999
FAX: ++49-30-6392 - 2989
e-mail: buero@bessy.de

Application for beam time at BESSY

Proposer / Project leader	
Name, Title:……………………………………	Phone:…………………………………
Institute:……………………………………	FAX:……………………………………
Address:……………………………………	e-mail:…………………………………
……………………………………	…………………………………

Project Title:
……………………………………………………………
……………………………………………………………
……………………………………………………………
……………………………………………………………

Status of project	
❒ **New project**	❒ **Continuation of an ongoing project**

❒ **Collaboration with**
    partner group:………………………………
             ………………………………
	❒ **Shared experimental set up**
	  with :…………………………………………
	         …………………………………………

Funding of project
❒ **BMBF**   ❒ **DFG**   ❒ **EU/HPP**
Contract No. : …………………………………

Beam time at other SR facilities for this project
❒ no
❒ yes, at……………………………………………………………………………

Enclosures	included
1)Description of the project	❒
2)Report of the latest measurements at BESSY	❒
List of BESSY related publications of the last 2 years, refereed publications only!	❒

1,2) see remarks next page

Technical requirements:

Monochromator:

Prioriry	Beam line requested	Mode*)	number of weeks required	preferred period(s)	unacceptable periods
❐ 1st choice ❐ alternative		❐ MB ❐ SB		……. KW to ……KW(incl.)	
❐ 1st choice ❐ alternative		❐ MB ❐ SB		……. KW to ……KW(incl.)	
❐ 1st choice ❐ alternative		❐ MB ❐ SB		……. KW to ……KW(incl.)	
❐ 1st choice ❐ alternative		❐ MB ❐ SB		……. KW to ……KW(incl.)	

*) MB: Multi Bunch, SB: Single Bunch, Double Bunch or Hybrid Mode

Experimental chamber:

❐ own system

❐ system of partner group

❐ BESSY-experimental chamber , specify experimental requirements:……………………………………………
………
………
………
………
………
………

Date:... Signature:...

[1] **Description of the project**

The description of the project is an essential criterion for the allocation of beam time. The project will be evaluated by the BESSY Beam Time Committee and it will be put into one of four priority categories. Because of the large number of projects **only two pages of text** can be accepted at most.

To provide the Beam Time Allocation Committee with a suitable database for evaluating the projects, please make sure that your description of the project includes brief but incisive paragraphs on the following topics:
- aims of the experiment and the relevant scientific background
- experimental method, technical requirements (energy range, resolution, flux, polarisation, etc.)
- results expected
- why must synchrotron radiation be exploited for the experiment? Alternative methods
- list of relevant references

[2] **Report of latest measurements at BESSY**

In case you had beamtime at BESSY in the last 12 months, please include a one page report on the results obtained.

G.R., XII/2001

Anmeldeformular für Nutzer von BESSY-Adlershof
Registration form for users of BESSY-Adlershof

Bereich/field:

- ☐ Grundlagenforschung / basic research
- ☐ Metrologie / metrology
- ☐ Lithographie / lithography
- ☐ Sonstige / other

Angaben zur Person/personal data:

Name/last name _____ Vorname/first name _____

Titel/title _____ Geburtsname, frühere(r) Nachname(n)/birth name, former family name(s)

Berufsbezeichnung/profession _____ Geburtsdatum/date of birth (DD-MM-YYYY) ☐☐☐☐☐☐☐☐

Projektleiter/head of group _____ Beschäftigt bei/employed with _____

Institution (bitte volle Anschrift)/complete name and address of institution

_____

_____

_____

_____

_____

Telefon/phone _____ **Fax** _____

homepage (of institution) **e-mail**

Hiermit bestätige ich, dass die o.a. Angaben korrekt sind; ich bin damit einverstanden, dass meine Daten in die BESSY-Adressdatenbank aufgenommen werden. / Herewith I confirm the correctness of above data and agree that they are recorded in the BESSY database.

Datum/date _____ Unterschrift/signature _____

Hiermit bestätige ich den Erhalt eines BESSY-Ausweises. Die dazu gehörige Erklärung habe ich zur Kenntnis genommen. / I herewith confirm the receipt of a BESSY ID card and have read accompanying explanations.

Datum/date _____ Unterschrift/signature _____

BESSY

Registration for Radiation Protection

Institution:	....
Name:	....
Address:	....
Phone:	....
e-mail:	....

Following members of staff will carry out experiments at BESSY during the periods stated and therefore have to be registrated for radiation protection .

Last Name	First Name	Presence at BESSY II (if possible please specify for the next 6 months)	
		from yy/mm/dd	up to yy/mm/dd

Date: .... Signature Group Leader: ....

(Name printed): ....

Safety Registration

Project

Project director:
(name / phone / fax / e-mail)

....
....

Responsible scientist:
(name / phone / e-mail)

....
....

Project-titel:

....

Project number:

....

Time & Location

from:.....................................

unitl: ....

Beam line:

Preparation

❏ space inside the experimental hall
is required before the beam time

....
....

Required BESSY equipment

❏ Safety locker for gases

❏ exhausted

....

❏ not exhausted

....

❏ Admittance to Chemistry Lab. ....
(probably after April 2002)

❏ Laser-shielding (tent)

....

❏ oil free pumping stage

....

❏ liquid nitrogen tank

....

❏ others (please note)

....
....

Safety Registration - continued-

Substances to be used

❑ Substances/Quantities

....
....

....

❑ Gases

....

Dangerous Substances

❑ Gases

....

quantity / consumption rate

....

❑ Other chemicals

....

quantity / consumption rate

....

! **Data sheets and operating instructions for these substances must be enclosed.** **!**
Operating instructions must be available at the experimental station during beam time.

Dangerous Equipment

❑ High voltage

....

❑ High current

....

❑ Laser (safety classification)

....

! **Operating instructions must be available at the experimental station during beam time.** **!**

Other sources of danger (use additional pages if necessary)

....

....

The required DIN-safety regulation data sheets and operation instructions are enclosed. I / We pledge to observe the legal accident prevention regulations and the safety regulations valid at BESSY as well as to comply with suchwise instructions on the BESSY staff.

Liability will be undertaken only in the scope of the legal provisions. Irrespective of the legal provisions liability for personal injury or damage to property is restricted to intent or gross negligence. Liability for consequential damage or consequential harm caused by a defect is excuded

Date: ....

....
Signatur Project director

....
Project number (repeated)

....
Signature Responsible Scientist

Acknowledgment of receipt BESSY:

Date: ....

....
Signature

Projects in Basic Research
(January 2002)

Projektleiter	Institution	Projekttitel	Förderung	Förder-kennzeichen
Aksela	University of Oulu	Hochauflösende Rumpfniveauspektroskopie an Molekülen	EU	
Baberschke/Wende	Freie Universität Berlin	Dichroismus und Magnetismus von 3d und 4f Monolagen	BMBF	05 SC8 KEA3 05 KS1 KEB4
Baberschke/Wende	Freie Universität Berlin	Oberflächen EXAFS und NEXAFS an adsorbierten Atomen und Molekülen	BMBF	05 SF8KEA2 05 KS1KEB4
Bakker	BESSY	Planung und Entwicklung eines Freie Elektronen Lasers bei BESSY	Zukunfts-fonds Land Berlin	
Bansmann/Meiwes-Broer	Universität Rostock	Magnetismus von Nanopartikeln auf Oberflächen	BMBF	05 SC8HRA6
Bansmann/Meiwes-Broer	Universität Rostock	Magnetismus von Inselschichten und Clustern auf Oberflächen	BMBF	ME 813/14-3
Becker	Fritz-Haber-Institut Berlin	Coherence properties in atomic and molecular photoionization		
Becker/Kleinpoppen	Fritz-Haber-Institut Berlin University of Stirling	Photoelectron and ion spectroscopy of polarized atoms	EU	
Bertagnolli	Universität Stuttgart	EXAFS Untersuchungen an organometallischen Nickel (II) Komplexen		
Boscherini	University of Bologna	Structural origin of the electronic and optical properties of InGaAsN quantum wells	EU	
Bradshaw/Polcik	Fritz-Haber-Institut Berlin	Photoelektronenbeugung an adsorbierten Atomen, Molekülen und dünnen Schichten	MPG	05 SF8EBA4
Braun/Jenichen/ Kaganer/ Schulz/Ploog	Paul-Drude-Institut Berlin	Oberflächenstrukturanalyse mittels Dreistrahlinterferenz; Stepbunching auf Vizinalflächen: Kinetik und Thermodynamik Nitride, Antimonide, Phosphide und ferromagnetische Metalle auf GaAs		

Projektleiter	Institution	Projekttitel	Förderung	Förder-kennzeichen
Brehmer/Reiche/Schulz	Universität Potsdam	Textur und in-plane Anisotropie in ultradünnen organischen Schichten		
Brezesinski/Möhwald	MPI f. Kolloid und Grenzflächenforschung Golm	In-plane Beugung von Lipidschichten an der Luft-Wasser Grenzfläche		
Bridge	Trinity College Dublin	Coverage dependence of site occupancy of simple adsorbates on stepped surfaces: CO, NO and N_2O on Pt (331)	EU	
Chassé	Universität Leipzig	Bindung, Struktur und elektronische Struktur von Sulfidoberflächen und -grenzflächen	DFG	Ch 132/9-1
Chassé	Universität Leipzig	Beugung und Spektroskopie an ionengestützt abgeschiedenen Gruppe III-V Epitaxieschichten	BMBF	AG IXZHCX
Chassé	Universität Leipzig	Chemisch modifizierte Oberflächen und Grenzflächen von III-V Halbleitern	BMBF	05 SE8OLA
Claessen	Universität Augsburg	Photoemissionsspektroskopie an Übergangsmetalloxiden	DFG	SFB 484/TPA7
Cramm/Eberhardt	FZ Jülich BESSY	MoS_2 nanotubes: electronic structure studied by soft X-ray emission absorption spectroscopy		
Dähne-Prietsch	Technische Universität Berlin	Photoemission spectroscopy at epitaxial metal-semiconductor multilayer structures		
Dau	Freie Universität Berlin	Vorversuche am KMC-2 zu XAS-Messungen an biologischen Proben (BioXAS)		
de Groot	Utrecht University	Characterisation of ZSM-5: Fe zeolite catalysis under reaction conditions of the NO_x process	EU	
Dürr/Eberhardt	FZ Jülich BESSY	Soft X-ray resonant magnetic scattering from exchange biased ferromagnetic/antiferromagnetic films		

Projektleiter	Institution	Projekttitel	Förderung	Förder-kennzeichen
Ehresmann/ Schmoranzer	Universität Kaiserlautern	Zustandselektive Wirkungsquerschnitte für Doppelphotoionisationsprozesse im Stickstoffmolekül mit und ohne anschließender Dissoziation; Charakterisierung eines unbekannten molekularen Zustands in CO um 27 eV		
Ehresmann/ Schmoranzer	Universität Kaiserlautern	Selektiver Elektroneneinfang während der Dissoziation von NO und CO nahe der jeweiligen $N1s^{-1}$, $C1s^{-1}$ und $O1s^{-1}$ Ionisationsschwellen	DFG	Schm 379/11
Eisebitt/Eberhardt	FZ Jülich BESSY	Speckle und kohärente magnetische Streuung		
Erko/Firsov	BESSY IPMT Chernogolovka	White beam holography		
Esser/Richter/Braun	Technische Universität Berlin BESSY	$In_{1-x}Ga_xP$: Oberflächenstruktur und epitaktisches Wachstum von Kobalt	DFG	ES 127-4/3 SFB 290TPB6
Evans	University of Wales Aberystwyth	NEXAFS studies of organic semiconductor growth	EU	
Faubel	Max-Planck-Institut f. Strömungsforschung Göttingen	Photoelektronenspektroskopie an solvatisierten Ionen in flüssigem Wasser	DFG	251/FA-1
Fauth/Schütz	Universität Würzburg/MPI f. Metallforschung Stuttgart	Elektronische Struktur und Magnetismus in Übergangsmetallclustern		
Fauth/Schütz	Universität Würzburg/ MPI f. Metallforschung Stuttgart	Charakterisierung von Übergangsmetallclustern mittels resonanter Photoemission		
Fieber-Erdmann	BESSY	Fluoreszenz-EXAFS an GeSi- und FeNOC-Proben		
Figueiredo	New Univ. Lisbon	Electronic state of oxygen vs. cationic environment in oxide minerals and structurally afine materials	EU	

Projektleiter	Institution	Projekttitel	Förderung	Förder-kennzeichen
Freund/Kuhlenbeck	Fritz-Haber-Institut der MPG Berlin	Elektronische Struktur molekularer Schichten auf reinen und modifizierten Oxid-, Karbid- und Nitridsubstraten	BMBF	05 SF8EBB-7
Gabel	Universität Bremen	NEXAFS-Spektren von Bor in biologischem Material		
Galan	Universidad Autonoma de Madrid	X-ray absorption and photoemission spectroscopy of materials for antimultifactor applications	EU	
Gießel/Hertel	Max-Born-Institut Berlin	Temperaturabhängige Photoelektronenbeugung an dünnen Metallfilmen		
Glass-Maujean	Université P. et M. Curie Paris	Decay dynamics of doubly excited states in molecular hydrogen investigated by time resolved fluorescence analysis	EU	
Goebbels/Riesemeier	BAM Berlin	Charakterisierung von Strukturkeramiken und Bauteilen aus der Mikro-Strukturtechnik mittels Mikrocomputertomographie	DFG	GO 530/1-3
Goering/Maletta	Universität Würzburg/ HMI Berlin	XMCD-Untersuchungen und Reflektometrie an Co/Pt Schichtsystemen		
Goering/Schütz	Universität Würzburg/ MPI f. Metallforschung Stuttgart	Magnetische Sauerstoffpolarisation in Eisen-Granaten und Zirkulardichroismus an Systemen mit großem magnetischen Tunnelwiderstand		
Görner/Radtke/Procop	BAM Berlin	Zertifizierung von Referenzmaterialien, Oberflächen- und Ultraspurenanalyse mit (µ-)RFA	BMBF	13N7704
Golden/Fink	IFW Dresden	Electronic structure and physical properties of novel fullerene-based materials	EU	ERB FMRXCT 9701551

Projektleiter	Institution	Projekttitel	Förderung	Förder-kennzeichen
Golden/Fink	IFW Dresden	Elektronenstruktur quasi-1D Übergangsmetallverbindungen; Elektronische und mikromagnetische Struktur in neuen magnetoelektronischen Materialien	BMBF	05 KS1BD1/0
Golden/Fink	IFW Dresden	Elektronenstruktur von korrelierten Materialien	BMBF	05 SB8BDA-6
Golden/Fink	IFW Dresden	Korrelierte Elektronenzustände in quasi-eindimensionalen Kupratketten	DFG	FI 439/7-1
Golden/Fink	IFW Dresden	Elektronische Struktur von Grenz- und Multischichten aus organischen Molekülen und Metallen	BMBF	05 SF8BD1-1
Gonzalez-Elipe	Instituto de Ciencia de Materiales de Sevilla	X-ray absorption spectroscopy characterization of doped TiO_2 thin films prepared by ion beam induced CVD	EU	
Grimmer	Paul-Scherrer-Institut Villigen	Optische Komponenten für die Polarimetrie weicher Röntgenstrahlung		
Grimmer	Paul-Scherrer-Institut Villigen	Exchange coupling in Fe/NiO/Co trilayers		
Grunze/Zharnikov	Universität Heidelberg	Photoelektronenspektroskopie und Röntgenabsorption an chemischen Strukturen in selbstaggregierenden organischen Schichten	BMBF	05 SF8VHA1
Güntherodt	RWTH Aachen	Hochauflösende spinpolarisierte Photoemission von Ferromagnet-Oxid-Grenzflächen und oxidischen halbmetallischen Ferromagneten	BMBF	05 KS1PAA/7
Gudat/Mertins	Universität Potsdam/ BESSY	Magnetooptische Polarisationsspektroskopie mit Synchrotronstrahlung an magnetischen Schichtsystem	BMBF	05 KS1IPB8
Gudat/Rader	Universität Potsdam/ BESSY	Magnetism of rare-earth quantum-well systems		

Projektleiter	Institution	Projekttitel	Förderung	Förder-kennzeichen
Gudat/Rader	Universität Potsdam/ BESSY	Quantum size effects in rare-earth and noble-metal stripes and wires on stepped W and Ni surfaces		
Gudat/Rader	Universität Potsdam/ BESSY	Elektronische Struktur von Spin-Gapmaterialien an Grenzflächen	BMBF	05 KS1IPA/0
Hasinger	Astrophysikalisches Institut Potsdam	Reflektivitätsbestimmungen an astronomischen Spiegelsystemen		
Heinzmann/ Drescher	Universität Bielefeld	Spinpolarisationstransfer an Auger-Elektronen aus freien Atomen	BMBF DFG	05 SP8PB10 HE 1049/72
Heinzmann/ Kleineberg	Universität Bielefeld	In-vitro Transmissions-Photoelektronenemissions-Mikroskopie im Wasserfenster am Messplatz U125/1-ML bei BESSY II	BMBF	05 KS1PBA/8
Heinzmann/ Kleineberg	Universität Bielefeld	XPS-Mikroskopie mit abbildenden Emissionsmikroskop und fokussierender Multilayeroptik im direkten Undulatorstrahl U125 von BESSY II	BMBF	05 SL8PB1-1
Hergenhahn	Fritz-Haber-Institut der MPG Berlin	Hochaufgelöste Photoelektronen-spektroskopie innerer Schalen an gasförmigen Molekülen	DFG	HE 3060/3-3
Hergenhahn	Fritz-Haber-Institut der MPG Berlin	Hochaufgelöste Photoelektron-Auger-Elektron Koinzidenzspektren von gasförmigen Molekülen	DFG	HE 3060/3-3 und BE 860/18-1
Heyn/Otto	Freie Universität Berlin	Strukturänderungen in funktionell wichtigen Zwischenzuständen der Retinalproteine Bacteriorhodopsin und Rhodopsin	BMBF	03 HE4 FUB-3
Hillebrecht	MPI für Mikrostrukturphysik Halle	Two electron photoemission from solids and adsorbates		
Horn	Fritz-Haber-Institut der MPG Berlin	Quantum Size-Effekt und elektronische Struktur von dünnen metallischen Schichten	BMBF	05 622OLA3

Projektleiter	Institution	Projekttitel	Förderung	Förder-kennzeichen
Horn	Fritz-Haber-Institut der MPG Berlin	Magnetismus und Quantum Size-Effekte in metallischen Schichten auf Halbleiteroberflächen		
Horn	Universität Augsburg	Untersuchung zeitlicher und räumlicher Korrelationen mittels Neutronen- und Röntgenstreuung	BMBF DFG	05 SB8WAA8 SFB 484-00
Horn	Universität Augsburg	Spektroskopie hochkorrelierter Materialien in der Nähe eines Metall-Isolator Übergangs	BMBF DFG	05 SB8WAA8 SFB 484-00
Hüfner	Universität des Saarlandes	Elektronische Struktur stark korrelierter Materialien, insbesondere nahe der Fermi-Energie	BMBF	05 SB8TSA2
Jaegermann	Technische Universität Darmstadt	Grenzflächen polykristalliner leitender Oxide	BMBF	01 SF0034
Jaegermann	Technische Universität Darmstadt	Elektronische Struktur von van der Waals-Epitaxiequanten-Schichten	DFG	JA 859/7-1
Jaegermann/Klein	Technische Universität Darmstadt	Potentialinhomogenitäten an Halbleiteroberflächen und -grenzflächen	BMBF	BEO 141/29857
Jaegermann/Mayer	Technische Universität Darmstadt	Charakterisierung von Festkörper-Elektrolyt-Grenzflächen	DFG	JA 859/3-1
Kaindl/Martins/Püttner	Freie Universität Berlin	Hochauflösende Photoelektronen-spektroskopie von Lathanidmetallfilmen	BMBF DFG	05 KS1KED/0 DO 561/1-3
Kaindl/Martins/Püttner	Freie Universität Berlin	Hochauflösende Rumpfniveau-spektroskopie an Atomen und Molekülen	BMBF DFG	05 KS1KED/0 DO 561/1-3
Kanngießer/ Zimmermann	Technische Universität Berlin	Bestimmung von Fluoreszenz- und Augerausbeuten im weichen Röntgenenergiebereich mit Hilfe der Photoelektron-Photoion Koinzidenztechnik		
Kirschner/Kuch	Max-Planck-Institut für Mikrostrukturphysik Halle	Elementspezifische Abbildung magnetischer Mikrostrukturen an Oberflächen und in dünnen epitaktischen Schichtsystemen	BMBF	05 SL8EFI

Projektleiter	Institution	Projekttitel	Förderung	Förder-kennzeichen
Kjeldgaard	Uppsala University	Endohedral doping of fullerenes: an electron spectroscopy study	EU	
Klaumünzer/ Darowski	Hahn-Meitner-Institut Berlin	Untersuchung des Kristallisationsverhaltens amorpher Legierungen an der Oberfläche und in dünnen Schichten		
Klaumünzer/ Darowski	Hahn-Meitner-Institut Berlin	Röntgendiffraktion an metallischen Nichtgleichgewichtsphasen		
Knop-Gericke/ Anderson	Fritz-Haber-Institut der MPG Berlin	Charcterisation of ZSM-5: Ga Zeolites catalysts under reaction conditions		
Knop-Gericke/ Conrad	Fritz-Haber-Institut der MPG Berlin	Charakterisierung der Sauerstoffzustände im Volumen der sauerstoffreichen Ru(0001) Oberfläche		
Lammert	BESSY	Verbundprojekt zu Arbeiten zur hochgenauen Vermessung von Nanometer-Optikomponenten	BMBF	13 N7929
Lamont	University of Huddersfield	Quantitative structural determination of di-oxygen and carbonate species on Ag(110)	EU	
Langer/Hertel	Max-Born-Institut Berlin	Photoion-photoelectron coincidence spectroscopy on fullerenes		
Laubschat	Technische Universität Dresden	Epitaktische Dünnschichten seltener Erden	BMBF DFG	05 SF80D1-4 SFB 463 TPB4
Leitenberger	Institut für Kristallzüchtung Berlin	Characterization of homepitaxial 4H-SiC layers by X-ray white beam diffraction topography		
Lewerenz	Hahn-Meitner-Institut Berlin	Photoelektronenspektroskopie an elektrolytischen Doppelschichten auf Halbleiterelektroden		
Ley	Universität Erlangen-Nürnberg	Photoemissionsuntersuchungen am SiC	BMBF	05 SE8WEA0

Projektleiter	Institution	Projekttitel	Förderung	Förder-kennzeichen
Ley	Universität Erlangen-Nürnberg	Elektronische und strukturelle Eigenschaften der Ober- und Grenzflächen von Halbleitern mit großer Bandlücke: SiC, Diamant, GaN	BMBF	05 SE8WEA0
Maletta/Schmitz	Hahn-Meitner-Institut Berlin	Element-specific, in-situ investigation of the magnetization at the interface of Fe on V(110)		
Manzke	Humboldt Universtität zu Berlin	Photoelektronenspektroskopie an II-VI- und Schichthalbleitern mit höchster Auflösung	BMBF	05 622KHA5
Manzke	Humboldt Universtität zu Berlin	Photoelektronenspektroskopie höchster Auflösung an Hochtemperatur-Supraleitern und niederdim. Systemen: Röntgen-Absorptionspektroskopie an Hochtemperatur-Supraleitern	BMBF	05 SB8KH10
Menzel/Feulner	Technische Universität München	Interatomarer Anregungstransfer und atomselektiver Bindungsbruch	DFG	SFB 338C10
Meyer	LURE	Symmetry and dynamics of inner-shell excited molecules	EU	
Möhwald/Riegler	MPI f. Kolloid- und Grenzflächenforschung Golm	Reflexion und Diffraktionsmessungen an Alkanfilmen		
Müller/ Hentschel/Riesemeier	BAM Berlin	Synchrotron-Topographie heterogener Werkstoffe mittels Kleinwinkelstreuung		
Mukherjee/ Bhatthacharya/ Sanyal	Saha Institute of Nuclear Physics, Calcutta/ BESSY	Temperature dependence of thicknesses and surface tension of polymer films		
Niehus	Humboldt Universität zu Berlin	Untersuchung der Oxidationszustände von epitaktisch gewachsenen Vanadiumoxidfilmen auf Cu_3Au		
Paloura	Aristotle University of Thessaloniki	X-ray absorption measurements on ion implanted GaN	EU	

Projektleiter	Institution	Projekttitel	Förderung	Förder-kennzeichen
Pettenkofer	Hahn-Meitner-Institut Berlin	Untersuchung der elektronischen Struktur der initiellen Wachstumsphase von heteroepitaktischen $CuInS_2$ Filmen		
Piancastelli	University "Tor Vergata" Rom	Surface-induced circular dichroism in adsorbates	EU	
Pietsch	Universität Potsdam	Energiedispersive Röntgenstreuung an organischen dünnen Filmen auf festen und flüssigen Trägern		
Pfohl	Universität Ulm	Dünne Flüssigkristallfilme auf glatten und lithographischen Oberflächen		
Powis	University of Nottingham	Circular dichroism in the photoionisation of free chiral molecules	EU	
Reiche/Riederer/ Riesemeier	BAM Berlin/ Rathgen-Forschungslabor, SMPK Berlin	Ortsaufgelöste Ultraspurenanalyse an mittelalterlichen Metallstiftzeichnungen mit RFA	DAAD	PROCOPE D/0122896
Rühl	Universität Osnabrück	Größenabhängige Veränderungen der Struktur und Dynamik von organischen van der Waals Clustern im Bereich der Rumpfniveauanregung	DFG	RU 420/4-1 436RUS113/ 339/0(R)
Rühl	Universität Osnabrück	Rumpfniveauanregung von freien Clustern: Hochaufgelöste NEXAFS-Spektroskopie	DFG	436RUS113/ 339/0(R)
Schäfers/Mertins	BESSY	Broad-band polarisation detectors	EU	ERB FMGECT 980105
Schartner/ Schmoranzer	Justus-Liebig-Universität Gießen/ Universität Kaiserslautern	Spektrale Analyse strahlender Zerfälle doppelt angeregter He-Atome		
Schartner/ Schmoranzer	Justus-Liebig-Universität Gießen/ Universität Kaiserslautern	Alignmentwechsel auf Resonanzen der Ar^+-$4p\,^2P_{3/2}$ und $^2P_{3/2}$-Satelliten	DFG	Scha /235/16 Schmo 379/12

Projektleiter	Institution	Projekttitel	Förderung	Förder-kennzeichen
Schartner/ Schmoranzer	Justus-Liebig-Universität Gießen/ Universität Kaiserslautern	Parity-unfavoured Beiträge bei der photoneninduzierten Ne$^+$3p ^{2}D$_{3/2}$-^{2}D$_{3/2}$ und F$_{7/2}$ Satellitenproduktion	DFG	Scha 235/16 Schmo 379/12
Schlögl/ Knop-Gericke	Fritz-Haber-Institut der MPG Berlin	Katalytische Oxidation: Röntgenabsorption im weichen Röntgenbereich unter Reaktionsbedingungen		
Schlögl/ Knop-Gericke	Fritz-Haber-Institut der MPG Berlin	Charakterisierung der katalytisch relevanten Oberflächenzustände von Vanadium-Pyrophosphat-Oxid Katalysatoren für die n-Butanoxidation		
Schmahl	Georg-August-Universität Göttingen	Weiterentwicklung des röntgen-mikroskopischen Messplatzes am Undulator U41 am BESSY II und röntgenmikroskopische Experimente	BMBF	05 KS1MG1/9
Schmahl	Georg-August-Universität Göttingen	Aufbau eines Röntgenmikroskops und eines Rasterröntgenmikroskops am Undulator U41 am BESSY II	BMBF	05 SL8MG11
Schmeißer	Brandenburgische Technische Universität Cottbus	Al-Fe Legierungsbildung durch Reibschweißen		
Schmeißer	Brandenburgische Technische Universität Cottbus	ZnS-CuInS$_2$ Legierungen		
Schmeißer	Brandenburgische Technische Universität Cottbus	Multiatomare resonante Photoemission zum Studium der Wechselwirkung von Gold und Silber mit Polypyrrol		
Schmidt-Böcking/ Hillebrecht	Johann Wolfgang Goethe Universität Frankfurt(M)/ MPI für Mikrostrukturphysik Halle	Experimente im Single-Bunch-Modus mit Flugzeitspektrometer und Multi-Hit-Detektor		
Schmoranzer/ Schartner	Universität Kaiserslautern/ Justus-Liebig-Universität Gießen	Beeinflussung des Aligments von Kr II Satelliten durch Bevölkerung über autoionisierende Zweielektronenresonanzen	DFG	Schm 379/12 Scha 235/16

Projektleiter	Institution	Projekttitel	Förderung	Förder-kennzeichen
Schneider	IFW Dresden	Elektronische und mikromagnetische Struktur in neuen magnetoelektronischen Materialien	BMBF	05 KS1BD1 0
Schoenes	Technische Universität Braunschweig	Winkelaufgelöste Photoemissionsspektroskopie an epitaktischen MnBi-Filmen		
Schönhense	Johannes-Gutenberg-Universität Mainz	Abbildung magnetischer Domänen in eisenhaltigen natürlichen Mineralien in Kombination mit spektromikroskopischen Untersuchungen und µSpot-CDAD-Holographie	BMBF	05 SC8UMA0
Schönhense	Johannes-Gutenberg-Universität Mainz	Picosekunden PEEM. Photoemissionsmikroskop für die zeitaufgelöste Beobachtung dynamischer Prozesse	BMBF	05 KS1UM1/5
Schönhense	Johannes-Gutenberg-Universität Mainz	Innovative Reaktoren und in-situ Analytik für Nano-Schutz-schichten. Chemisch selektive Schichtabbildung mit höchster Ortsauflösung	BMBF	13N 7759
Schönhense	Johannes-Gutenberg-Universität Mainz	Nano-ESCA-Entwicklung eines abbildenden Photoelektronen-spektrometers zur hochauflösenden Material- und Defektanalyse. Elektronenoptische Rechnungen und Evaluierung der bildgebenden Detektionsverfahren	BMBF	13N 7863
Schrader	Universität Potsdam	UPS and NEXAFS investigations on conjugated organic materials for photonics		
Schrader	Universität Potsdam	Röntgenographische Untersuchungen an organischen Schichtstrukturen für Anwendungen in der Photonik		
Schwentner	Freie Universität Berlin	Verstärkungsprozesse und elektronische Anregungen beim photochemischen Ätzen von dünnen Metallen und Halbleitern	DFG	Schw 230/12-2
Soinski	Technische Universität Czestochowa	Gußeisen mit Kugel- und Vermiculargraphit	EU	

Projektleiter	Institution	Projekttitel	Förderung	Förder-kennzeichen
Soriano	Universidad Autonoma de Madrid	Study of the electronic structure of small particles and ultra-thin films of metal oxides, nitrides and carbides	EU	
Starke/Kaindl	Freie Universität Berlin	Röntgenmagnetooptik und Magnetismus von nanostrukturierten Lanthanidmaterialien		
Starke/Kaindl	Freie Universität Berlin	Magnetischer Zirkulardichroismus in der Photoemission (MCD-PE): Anwendung auf nanostrukturierte Lanthanidmaterialien	BMBF	05 SC8KEB-6
Steinrück	Universität Erlangen-Nürnberg	Charakterisierung und Veränderung molekularer Schichten auf dünnen Metallschichten	DFG	STE 620/2-2
Steinrück	Universität Erlangen-Nürnberg	Elektronische Struktur von Eisen- und Iridiumsiliziden	DFG	SFB 292
Steinrück	Universität Erlangen-Nürnberg	Charakterisierung und Veränderung molekularer Schichten auf modifizierten Metalloberflächen	BMBF	05 SF8 WEA7
Steinrück/ Denecke	Universität Erlangen-Nürnberg	In situ XPS Untersuchung von chemischen Reaktionen an Oberflächen	BMBF	05 SF8 WEA7
Steinrück/ Denecke	Universität Erlangen-Nürnberg	Höchstaufgelöste Photoelektronenspektroskopie mit Synchrotronstrahlung zur in-situ Untersuchung von Oberflächenreaktionen	DFG	STE 620/4-1
Sträter/Saenger	Freie Universität Berlin	Protein crystallography at BESSY II: Determination of two novel protein structures	DFG	
Szargan	Universität Leipzig	Elektronenkonfiguration, Koordination und Reaktivität von Fe-Ionen an Grenzflächen von modifizierten Sulfidhalbleitern		
Szargan	Universität Leipzig	Röntgenemissionsspektroskopie mit Synchrotronstrahlung an dünnen Schichten von Übergangsmetalloxiden	BMBF	05 KS1 OL1/3

Projektleiter	Institution	Projekttitel	Förderung	Förder-kennzeichen
Szargan	Universität Leipzig	Photoemissionsspektroskopie mit Synchrotronstrahlung an dünnen Schichten von Übergangsmetalloxiden		
Tonnerre	Centre National de Recherches Scientifiques Grenoble	Soft X-ray resonant magnetic scattering from nanoscale magnetic particles	EU	
Umbach/Fink	Universität Würzburg	Elektronische und vibronische Feinstruktur in grenzflächenmodifizierten organischen Dünnschichten	BMBF	05 SF8 WWA7
Umbach/Fink	Universität Würzburg	Höchstauflösende Röntgenabsorption und Photoelektronenspektroskopie an organischen Molekülen und organischen Dünnschichten	BMBF	05 SF8 WWA7
Umbach/Heske	Universität Würzburg	Röntgenemissionsspektroskopie an modifizierten Festkörperoberflächen, Halbleitergrenzflächen und korrelierten Materialien	BMBF	05 SR8 OL12
Umbach/Heske	Universität Würzburg	Charakterisierung innerer Grenzflächen von Dünnschicht-Solarzellen und organischen Heterostrukturen	DFG	SFB 410
Umbach (Koordinator)	Universität Würzburg	Höchstauflösende Elektronen-Spektromikroskopie mit durchstimmbarer XUV-Strahlung	BMBF	05 SL8 WW1-8 05 KS1 WW2/0
Vinogradov	St. Petersburg State University	Electronic structure of 3d metal cyanide complexes by X-ray absorption and resonant photoemission		
Vollmer	University of Cambridge	Electron yield X-ray absorption spectroscopy using gas microstrip detectors	EU	
Weschke/Kaindl	Freie Universität Berlin	Grenzflächenbedingte Materialmodifikation von Lanthanidmetallen	BMBF	05 SF8KEC-8 05 KS1KEE/8
Westphal	Westfälische Wilhelms-Universität Münster	Photoelektronenbeugungs-Untersuchungen an der SiO_2/Si (III) Grenzschicht	BMBF	05 SE8PMB-9

Projektleiter	Institution	Projekttitel	Förderung	Förder-kennzeichen
Widdra/Hertel	Max-Born-Institut Berlin	Pump-Probe Untersuchungen zur Dynamik von Halbleiteradsorbat- und Oberflächenzuständen		
Wieder	TU Darmstadt	EXAFS an amorphem $Fe_{100-x}Sc_x$ zur Strukturbestimmung und zur Ableitung des magnetischen Phasendiagramms		
Wieder	TU Darmstadt	EXAFS an amorphem Siliziummonoxid zur Strukturbestimmung		
Wilke/Oberhänsli	Universität Potsdam	Bestimmung der Selten-Erd-Konzentration in Mineralien mit Hilfe der SY-RFA		
Winter/Hertel	Max-Born-Institut Berlin	Electron spectroscopy from a liquid water jet and solutions		
Winter/Hertel	Max-Born-Institut Berlin	Experiment with time correlated laser and synchrotron pulses: 2-colour-2photon-photoemission from adsorbate systems		
Wöll	Ruhr-Universität Bochum	Charakterisierung organischer Dünnschichten mittels Absorptionspektroskopie im weichen Röntgenbereich	BMBF	05 SF8PCA1
Woodruff	University of Warwick	Scanned-energy mode photoelectron diffraction at BESSY II	EU	
Wurth	Universität Hamburg	Magnetische Eigenschaften kleiner, größenselektierter, deponierter Übergangsmetallcluster	BMBF DFG	05 KS1GUB/5 Me 266/22-2
Zabel	Ruhr-Universität Bochum	Structural and thermal properties of metal/ceramics multilayers		
Zahn/Braun	Technische Universität Chemnitz/ BESSY	Photoemissionsmessungen an ultradünnen organischen Schichten	BMBF	05 KS1OCA/1
Zahn/ Braun/Kachel	Technische Universität Chemnitz/ BESSY	Wechselwirkung von Metallen mit organischen Halbleitern: Ag und In auf PTCDA		

Projektleiter	Institution	Projekttitel	Förderung	Förder-kennzeichen
Zimmermann	Technische Universität Berlin	Hochauflösende Elektronenspektroskopie an freien Atomen der 3d-Übergangselemente	DFG	Zi 183/16-1

LIST OF PUBLICATIONS 2001

S.S. Andreev, H.-Ch. Mertins Y.Y. Platanov, N.N. Salashchenko, F. Schäfers, E.A. Shamov, L.A. Shmaonek
Multilayer Dispersion Optics for X-Ray Radiation
Nucl. Instr. Meth. A, **448**, 133 - 141, (2001)

V. Arkadiev, A. Bjeoumikhov, N. Langhoff, J. Rabe, P. Roth, R. Wedell, B. Ham, F. Diekmann, K. Richter, M. Krumrey, U. Linke, G. Ulm, R. Lawaczeck, W.-R. Press, K. Schön und H.-J. Weinmann
Aufbau und Charakterisierung eines Röntgen-Monochromatormoduls für Mammographiegeräte
Medizinische Physik 2001, Hrsg. K. Welker und K. Zink, 123, (2001)

D. Arvanitis, N. Haack, G. Ceballos, H. Wende, K. Baberschke, A.L. Ankudinov and J.J. Rehr
Shape resonances of oriented molecules
J. Electr. Spectr. Relat. Phenom. , **113**, 57, (2000)

L. Assoufid, O. Hignette, M. Howells, S. Irick, H. Lammert, P. Takacs
Future metrology needs for synchrotron radiation grazing-incidence optics
Nuclear Intruments & Methods in Physics research A , **467-468** , 267-270, (2001)

P. Srivastava, K. Baberschke
New opportunities in soft-X-ray absorption to characterize the adsorbate bonding.
Topics in Catalysis , **10**, 199, (2000)

K. Baberschke
Anisotropy in Magnetism
Lecture Notes in Physics, Springer, **580**, 27, (2001)

K. Baberschke, M. Donath, W. Nolting
Band - Ferromagnetism: Ground-State and Finite-Temperature Phenomena
Lecture Notes in Physics, Springer, **580**, (2001)

D.R. Batchelor, R. Follath, D. Schmeisser
Commissioning results of the BTUC-PGM beamline
Nucl. Instrum. and Methods , **467**, 470-473 , (2001)

A. Bayer
Zirkulardichroische Untersuchungen und Momentenanalyse an epitaktisch gewachsenen CrO2-Filmen , Diplomarbeit
(2001)

B. Beckhoff, R. Fliegauf, G. Ulm, G. Pepponi, C. Streli, P. Wobrauschek, L. Fabry and S. Pahlke
Improvement of a total reflection X-ray fluorescence analysis of low Z elements on silicon wafer surfaces at the PTB monochromator beamline for undulator radiation at BESSY II
Spectrochimica Acta B , **56**, 2073, (2001)

M. Beijersbergen, M. Bavdaz, A. Peacock, E. Tomaselli, R. Fairbend, J.-P. Boutot, S.O. Flyckt, A. Brunton, G. Price, G. Fraser, C. Herrmann, M. Krumrey, E. Ziegler and A. Freund
High-resolution micro-pore X-ray optics peoduced with micro-channel plate technology
Proc. SPIE , **4145**, 188, (2001)

G. Ceballos, H. Wende, K. Baberschke and D. Arvanitis
Molecular Geometry Modifications upon Adsorption for N2O: N and O K-edge NEXAFS.
Surf Sci. , **482-485**, 15, (2001)

G. Ceballos, N. Haack, H. Wende, R. Püttner, D. Arvanitis and K. Baberschke
High-resolution X-ray absorption spectra of the p* resonance of N2, directly physisorbed on metallic Cu (100)
Nuclear Instruments and Methods in Physics Research A, **467-8**, 1560 , (2001)

J.D. Coates, R. Chakraborty, S.M. Connor, C. Schmidt, J. Thieme
The Geochemical Effects of Microbial Humic Substances Reduction
Acta hydrochim. Hydrobiol. , **28**, 420-427, (2000)

A. Dallmeyer, K. Maiti, O. Rader, L. Pasquali, C. Carbone, W. Eberhardt
Magnetism and interlayer coupling in fcc-Fe/Co films
Phys. Rev. B , **63**, 104413-1--5 , (2001)

M. Dickow
Polarisationsmessungen an lasergepumpten 3d-Atomen für Dichroismusexperiment mit Synchrotronstrahlung ,
Diplomarbeit
TU-Berlin, (2001)

N. Dimakis, G. Bunker, M. Katsikini, E.C. Paloura
Verification of a distortion in the microstructure of GaN detected by EXAFS using ab initio DFT
J. Synchrotron Rad, **8**, 258, (2001)

S. Dreiner, M. Schürmann, C. Westphal , H. Zacharias
Local atomic environment of Si suboxides at the SiO2/Si(111) interface determined by angle-scanned photoelectron diffraction
Phys. Rev. Lett. , **86**, 4068-4071, (2001)

M. Dähne, S. Vandre, C. Preinesberger, S.K. Becker, W. Busse, and T. Kalka
Rare-earth silicide films on silicon surfaces
Advances in Solid State Physics, **41**, 227, (2001)

A. Ehresmann, H. Liebel, M. von Kröger, H. Schmoranzer
Dissociation of NO b3II0,1,2 npl 2L (v = 0) Rydberg states into O((4S)3s 3S1) + N(4S) fragments
J. Phys. B: At. Mol. Opt. Phys. , **34**, 2893, (2001)

A. Ehresmann, H. Liebel, M. von Kröger, H. Schmoranzer
Final state selectively observed autoionisation and predissociation processes in NO for Eexc = 16.9 eV - 19.6 eV
J. Phys. B: At. Mol. Opt. Phys. , **34**, 3119, (2001)

T. Eimüller, P. Fischer, M. Köhler, M. Scholz, P. Guttmann, G. Denbeaux, S. Glück, G. Bayreuther, G. Schmahl, D. Attwood, G. Schütz
Transmission X-ray microscopy using X-ray magnetic circular dichroism
Appl. Phys. A, **73**, 697-701, (2001)

T. Eimüller, P. Fischer, G. Schütz, P. Guttmann, G. Schmahl, M. Scholz, M. Köhler, G. Bayreuther
Magnetization reversal of a multilayered FeGd dot array imaged by MTXM
J. Appl. Phys., **89**, 7162-7164, (2001)

A. Erko, N. Langhoff, A.A.Bjeoumikhov, V.I.Beloglasov
High-Order Harmonic Suppression by a Glass Capillary Array
Nuclear Instruments and Methods in Physics Research , **467-468**, 832-835, (2001)

A. Erko, I. Packe, W. Gudat, N. Abrosimov, A. Firsov
The Crystal Monochromator Based on graded SiGe Crystals
Nuclear Instruments and Methods in Physics Research , **467-468** , 358-361, (2001)

S.I. Fedoseenko, I.E. Iossifov, S.A. Gorovikov, J.S. Schmidt, R. Follath, S.L. Molodtsov, V.K. Adamchuk, G. Kaindl
Development and present status of the Russian-German soft X-ray beamline at BESSY II
Nucl. Instrum. and Methods , **470**, 84-88 , (2001)

A. Firsov, A. Svintsov, A. Erko, W. Gudat, S. Kuznetsov, M. Grigoriev, A. Asryan, M. Ferstl, S. Shapoval, V. Aristov
Crystal-based diffrction Focusing Elements for Third-Generation Synchrotron Radiation Sources
Nuclear Instruments and Methods in Physics Research, **467 - 468** , 366-369, (2001)

R. Follath
The versatility of collimated plane grating monochromators
Nucl. Instrum. and Methods , **467**, 418 - 425, (2001)

H.-J. Freund, H. Kuhlenbeck, J. Libuda, G. Rupprechter, M. Bäumer, H. Hamann
Bridging the Pressure and Materials Gaps Between Catalysis and Surface Science: Clean and Modified Oxide Surfaces
Topics in Catalysis, **15**, 201, (2001)

H.-J. Freund, H. Kuhlenbeck, T. Risse
Molecules on Well Structured Oxide Surfaces
The Chemical Physics of Solid Surfaces/Elsevier, **vol 9, chapter 8**, (2001)

H.-J. Freund, N. Ernst, M. Bäumer, G. Rupprechter, J. Libuda, H. Kuhlenbeck, T. Risse, W. Drachsel, K.A.-Shamery, H. Hamann
Model Systems for Heterogeneous Catalysis: Quo Vadis Surface Science
in "Surface Chemistry and Catalysis" /Kluwer-Plenum, (2001)

R. Fritsche, E. Wisotzki, A.B.M.O. Islam, A. Thissen, A. Klein, W. Jaegermann, D. Tonti, R. Rudolph, C. Pettenkofer
Electronic passivation of Si(111) by Ga-Se half-sheet termination
Applied Physics Letters, in press, (2002)

R. Früke
Holografisch erzeugte Laminargitter mit variabler Liniendichte für das Göttinger Rasterröntgenmikroskop ,
Diplomarbeit
Institut für Röntgenphysik, Georg-August-Universität Göttingen, (2001)

G.G. Fuentes
Recubrimientos de nitruros y carbonitruros de titanio crecidos mediante depssitos asistidos con haces de iones de baja energma. , Dissertation
Universidad Autsnoma Madrid, (2001)

J. Geissler, E. Goering, M. Justen, F. Weigand, G. Schütz, J. Langer, D. Schmitz, H. Maletta, R. Mettheis
Pt magnetization profile in a Pt/Co bilayer studied by resonant magnetic X-ray reflectometry
Phys. Rev. B, **65**, 020405(R), (2001)

M. Glass-Maujean, S. Lauer, H. Liebel, H. Schmoranzer
Direct evidence of collisional disalignment decay time: case of H(3) + H2
J. Phys. B: At. Mol. Opt. Phys. , **34**, 5121, (2001)

Th. Gleim, C. Heske, E. Umbach, C. Schumacher, W. Faschinger, Ch. Ammon, M. Probst, H.P. Steinrück
Reduction of the ZnSe/GaAs(100) valence band offset by a Te interlayers
Appl. Phys. Lett., **78(13)**, 1867, (2001)

E. Goering, J. Will, J. Geissler, M. Justen, F. Weigand, G. Schütz
X-ray magnetic circular dichroism - an universal tool for magnetic investigations
J. Alloys and Compounds, **328**, 14-19, (2001)

E. Goering, A. Fuss, W. Weber, J. Will, G. Schütz
Element specific X-ray Magnetic Circular Dichroism magnetization curves using Total Electron Yield
Journal of Applied Physics, **88**, 5920, (2000)

E. Goering, S. Gold, A. Bayer,G. Schuetz
Non symmetric influences in the Total Electron Yield X-ray Magnetic Circular Dichroism signal in applied magnetic fields
Journal of Synchrotron Radiation, **8**, 434, (2001)

E. Goering, S. Gold, G. Schütz
HoFe - Garnet soft XMCD measurements below and above the compensation temperature
Journal of Synchrotron Radiation , **8**, 422, (2001)

S.A. Gorovikov, R. Follath, S.L. Molodtsov, G. Kaindl
Optimization of the optical design of the Russian-German soft-X-ray beamline at BESSY II
Nucl. Instrum. and Methods , **467**, 565-568 , (2001)

H. Grimmer, O. Zaharko, H.-Ch. Mertins, F. Schäfers
Polarizing mirrors for soft X-ray radiation
Nucl. Instr. and Meth. A, **467-468**, 354-357, (2001)

H. Grimmer, M. Horisberger, U. Staub, H.-Ch. Mertins, F. Schäfers
Multilayer optics for soft X-rays
Czech and Slovak Crystallographic Association, Praha, **Article in book: "Advances in Structure Analysis", Editors: R. Kuzel, J. Hasek**, 311-318, (2001)

H. Grimmer, O. Zaharko, M. Horisberger, H.-Ch. Mertins, F. Schäfers
Optical Components for Polarization Analysis at the Vanadium L3 edge and the Carbon K edge
Surface Review and Letters (Proceedings VUV-XIII 2001) , (2001)

P. Grübling
Untersuchung der Strahlungscharakteristik eines resonant mikrowellengeheizten Plasmas im Vakuum-UV ,
Dissertation
Dissertation an der Fakultät II Mathematik und Naturwissenschaften der Techn. Universität Berlin, (2001)

C. Gude, W. Rettig
Radiative and nonradiative excited state relaxation channels in squaric acid derivates bearing differently-sized donor subsituents
J. Phys. Chem. A, **104**, 8050, (2000)

P. Guttmann, B. Niemann, J. Thieme, D. Hambach, G. Schneider, U. Wiesemann, D. Rudolph, G. Schmahl
Instrumentation advances with the new X-ray microscopes at BESSY II
Nucl. Instrum. Meth. A, **467/8**, 849-852, (2001)

W. Görner, M.P. Hentschel, B.R. Müller, H. Riesemeier, M. Krumrey, G. Ulm, W. Diete, U. Klein, R. Frahm
BAMline: the first hard X-ray beamline at BESSY II
Nucl. Instr. And Meth., **467-468**, 703, (2001)

A.G. Gürek, G. Appel, R.P. Mikalo, D. Schmeißer
Synthesis of dihydroxy silicon phthalocyanine tetrasulfonic acid and poly-5-oxo silicon phthalocyanine tetrasulfonic acid
Journal of Porphyrins and Phthalocyanines, **5**, 751-757, (2001)

N. Haack, G. Ceballos, H. Wende, K. Baberschke, D. Arvanitis, A.L. Ankudinow and J.J. Rehr
Shape resonances of oriented molecules: ab initio theory and experiments on hydrocarbon molecules.
Phys. Rev. Lett., **84**, 614 , (2000)

D. Hambach, M. Peuker, G. Schneider
Nanostructured diffractive optical devices for soft X-ray microscopes
Nucl. Instrum. Meth. A, **467/8**, 877-880, (2001)

D. Hambach
Nanostrukturen mit hohem Aspektverhältnis als lichtstarke diffraktive Röntgenoptiken für hohe Beugungsordnungen ,
Dissertation
Institut Für Röntgenphysik, Georg-August-Universität Göttingen, (2001)

K. Hasche, K. Herrmann, M. Krumrey, G. Ulm, S. Schädlich, W. Frank, M. Procop
Calibrated reference standards for films in the nanometer range
Proc. of 2nd euspen International Conference (Turin, Italy, May 27th - 31st), 396, (2001)

J.-D. Hecht, F. Frost, A.B. Preobrajenski, D. Hirsch, H. Neumann, A. Schindler, T. Chassi
Observation of interstitial nitrogen in the low-energy ion beam nitridation of AIII-BV semicon-ductor surfaces by means of X-ray
J. Applied Physics, **90** , 6066-69, (2001)

J.-D. Hecht, F. Frost, T. Chassi, D. Hirsch, H. Neumann, A. Schindler, F. Bigl,
In situ characterization of the nitridation of AIII-BV semiconductor surfaces by means of
Appl. Surface Science, **179** , 196-202, (2001)

M. Hecker, U. Muschiol, C.M. Schneider, H.-Ch. Mertins, D. Abramsohn, F. Schäfers
Effect of annealing on structural and magnetic properties of Co/Cu multilayers investigated by resonant X-ray scattering
Journal of Magnetism and Magnetic Materials (proceedings MMM Aachen June 2001), (2001)

H. Henneken, F. Scholze, M. Krumrey and G. Ulm
Quantum efficiencies of gold and copper photocathodes in the VUV and X-ray range
Metrologia, **37**, 485, (2000)

U. Hergenhahn, O. Kugeler, A. Rüdel, E.E. Rennie, A.M. Bradshaw
Symmetry-selective observation of the N 1s shape resonance in N2
J. Phys. Chem. A , **105**, 5704-5708, (2001)

J. Hollandt, U. Becker, W. Paustian, M. Richter and G. Ulm
New developments in the radiance calibration of deuterium lamps in the UV and VUV spectral range at the PTB
Metrologia, **37**, 563, (2000)

K. Holldack, D. Ponwitz, W.B. Peatmann
Beam stability of undulator and dipole radiation on BESSY II obtained by synchrotron radiation monitors
Nuc. Instrum. Meth. A, **467-468**, 213-220, (2001)

H. Hunter-Dunn, D. Arvanitis, K. Baberschke, A. Hahlin, O. Karis, R. Carr and N. Mertensson
A comparative study of x-ray absorption spectroscopy at various synchrotron facilities and the effect of transverse source coher
J. Electr. Spectr. Relat. Phenom. , **113**, 67 , (2000)

M. Jäger
Untersuchungen zur Darstellung von Kernproteinen mit Laserscan- und Röntgenmikroskop , Diplomarbeit
Institut für Röntgenphysik, Georg-August-Universität Göttingen, (2001)

C. Jung, F. Eggenstein, S. Hartlaub, R. Follath, J.S. Schmidt, F. Senf, M.R. Weiss, T. Zeschke, W. Gudat
First results of the soft X-ray microfocus beamline U41-PGM
Nucl. Instrum. and Methods , **467**, 485-487 , (2001)

B. Kanngießer, S. Brünken, K. Godehusen, Ch. Gerth, W. Malzer, M. Richter and P. Zimmermann
A Photoelctron-Photoion Coincidence Method for the Investigation of Decay Probabilities after Inner-Shell Photoionization
Nucl. Instr. And Meth., **467-468**, 1477, (2001)

S. Kapelle, W. Rettig, R. Lapouyade
Aniline Dimers and Trimers as Model Compunds for Polyaniline
Chem. Phys. Lett., **348**, 416, (2001)

M. Katsikini, E.C. Paloura, T.D. Moustakas
Study of group-III binary and ternary nitrides using near edge X-ray absorption measurements
Journal of Crystall Growth, **230 (3-4)**, 405, (2001)

M. Katsikini, J. Bollmann, W.T. Masselink, E.C. Paloura
On the effect of ion implantation in the microstructure of GaN: A XAFS study
Journal of Synchrotron Radiation, **6**, 552, (1999)

M. Katsikini, H. Rossner, M. Fieber-Erdmann, E. Holub-Krappe, T. D. Moustakas, E. C. Paloura
Gallium K-edge EXAFS measurements on cubic and hexagonal GaN
Journal of Synchrotron Radiation , **6**, 561, (1999)

M. Katsikini, T. D. Moustakas, E. C. Paloura
Nitrogen K-edge EXAFS measurements on Mg and Si doped GaN
Journal of Synchrotron Radiation , **6**, 555, (1999)

M. Katsikini, M. Fieber-Erdmann, E. Holub-Krappe, D. Korakakis, T.D. Moustakas, E.C. Paloura
Nitrogen K-edge NEXAFS measurements on Group-III binary and ternary nitrides
Journal of Synchrotron Radiation , **6**, 558, (1999)

M. Katsikini, E.C. Paloura, J. Bollmann, E. Holub-Krappe, W.T. Masselink
Nitrogen K-edge X-ray absorption measurements on N and O implanted GaN
Journal of Electron Spectroscopy and Related Phenomena, **101-103**, 689, (1999)

M. Katsikini, E.C. Paloura, M. Fieber-Erdmann, E. Holub-Krappe, D. Korakakis, T.D. Moustakas
Nitrogen K-edge NEXAFS measurements on group-III binary and ternary nitrides
Journal of Electron Spectroscopy and Related Phenomena , **101-103**, 695, (1999)

M. Katsikini, E.C. Paloura
NEXAFS and EXAFS studies of GaN and its alloys
Proceedings of the Electrochemical Society, **98-18**, 64, (1999)

P. Kavouras, M. Katsikini, N. Vouroutzis, C.B. Lioutas, E.C. Paloura, J. Antonopoulos, Th. Karakostas, P. Bressler
Ion implantation effects on the microhardness and microstructure of GaN
Journal of Crystal Growth, **230 (3-4)**, 454, (2001)

V. Kharlanov, W. Rettig
Multiple emission of n-(1-naphthyl)-Pyridinium
J. Photoechem. Photobiol. A:Chemistry, **141**, 127, (2001)

V.A. Kilin, D.A. Lazarev, Dm.A. Lazarev, V.M. Zelichenko, M.Ya. Amusia, K.-H. Schartner, A. Ehresmann, H. Schmoranzer
Test of a q-fractional V(N-q) Hartree-Fock potential for the calculation of double photoionization cross sections of neon
J. Phys.B:At. Mol. Opt. Phys., **34**, 3993, (2001)

A. Kleibert
Magneto-optische Untersuchungen an ultradünnen Kobaltschichten auf W(110) mit sichtbarem Licht und im weichen Röntgenbereich , Diplomarbeit
Universität Rostock, (2001)

R. Klein, A. Gottwald, F. Scholze, R. Thornagel, J. Tümmler, G. Ulm, M. Wedowski, F. Stietz, B. Mertens, N. Koster, J.V. Elp
Lifetime testing of EUV optics using intense synchrotron radiation at the PTB radiometry laboratory
Proc. SPIE , **4506**, 105, (2001)

N. Koch, D. Pop, R.L. Weber, N. Böwering, B. Winter, M. Wick, G. Leising, I.V. Hertel, W. Braun
Radiation induced degradation and surface charging of organic thin films in ultraviolet photoemission spectroscopy
Thin Solid Films, **81**, 391, (2001)

M. Krumrey, C. Herrmann, P. Müller and G. Ulm
Synchrotron-radiation-based cryogenic radiometry in the X-ray range
Metrologia, **37**, 361, (2000)

M. Krumrey, G. Ulm
High-accuracy detector calibration at the PTB four-crystal monochromator beamline
Nucl. Instr. And Meth. , **467-468**, 1175, (2001)

W. Kuch, C.M. Schneider
Magnetic dichroism in valence band photoemission
Rep. Prog. Phys., 64, 147-204, (2001)

S.K. Kulkarni, U. Winkler, N. Deshmukh, P.H. Borse, R. Fink, and E. Umbach
Investigations of Chemically Capped CdS and ZnS Nanoparticles
Appl. Surf. Sci, **169/170**, 438, (2001)

J. Kunes, P.M. Oppeneer, H.-Ch. Mertins, F. Schäfers, A. Gaupp, W. Gudat, P. Novak
X-Ray Faraday Effect at the L2,3 Edges of Fe, Co and Ni: Theory and Experiment
Phys. Rev. B, **64**, 174417-1, (2001)

J. Kunes, P.M. Oppeneer, H.-Ch. Mertins, F. Schäfers, A. Gaupp, W. Gudat, P. Novak
X-Ray Faraday Effect of ferromagnetic films: contribution of the core exchange splitting
Journal of Magnetism and Magnetic Materials (proceedings MMM Aachen June 2001) , (2001)

H. Lammert, F. Senf, F. Eggenstein, U. Flechsig, R. Follath, S. Hartlaub, T. Noll, G. Reichardt, J.S. Schmidt, M. Weiss, T. Zeschke, W.B. Peatman, and W. Gudat
Engineering aspects for the conception of the BESSY II beamlines
Nuclear Intruments & Methods in Physics research A , **467-458** , 488-491, (2001)

H. Liebel, R. Müller-Albrecht, S. Lauer, F. Vollweiler, A. Ehresmann, H. Schmoranzer
Fine-structure selectivity of neutral dissociation with excitation observed in O2
J. Phys. B: At. Mol. Opt. Phys. , **34**, 2581, (2001)

H. Liebel
Spektroskopische Untersuchungen der Neutraldissoziation des Sauerstoffs nach Anregung mit monochromatischer Synchrotronstrahlung , Dissertation
Dissertation, Universitat Kaiserslautern, (2001)

J. Lindner, P. Poulopoulos, F. Wilhelm, M. Farle and K. Baberschke
Atomic exchange processes at the interface and their role on the magnetic moments of ultrathin Ni/Cu(001) films
Phys. Rev. B , **62**, 10431 , (2000)

K. Maiti, A. Dallmeyer, M.C. Malagoli, C. Carbone, W. Eberhardt, O. Rader, L. Pasquali, A. Banerjee, S. Turchini, S. Zennaro, N. Zema
Oscillatory interlayer coupling mediated by fcc-Fe/Co(100) films
Appl. Surf. Sci., **182**, 302-307, (2001)

M. Martins
Photoionization of open-shell atoms: the chlorine 2p excitation
J. Phys. B, **34**, 1324, (2001)

M. Maus, W. Rettig
Comparison of the Bandshape and Lifetime Data Analysis of Temperature-Dependent Fluorescence Measurements
Phys. Chem. Chem. Phys., **3**, 5430, (2001)

H. Meiling, B. Mertens, F. Stietz, M. Wedowski, R. Klein, R. Kurt, E. Louis, A. Yakshin
Prevention of MoSi multilayer reflection loss in EUVL tools
Proc. SPIE , **4506**, 93, (2001)

E. Meltchakov, W. Jark, H.-Ch. Mertins, F. Schäfers
Magnetic Circular Dichroism of Gd/Transition Metal Multilayer Structures around the Gd M5,4 Edges
Nucl. Instrum. Meth. A, **467-8**, 1411 - 1414, (2001)

E. Meltchakov, W. Jark, H.-Ch. Mertins, M. Scheer, F. Schäfers
Two-band magneto-optical elements for soft x-ray polarisation analysis at the Fe (Co) 2p and Gd 3d edges
Surface Review and Letters (Proceedings VUV-XIII 2001), (2001)

E. Meltchakov, H.-Ch. Mertins, M. Scheer, S. DiFonzo, W. Jark, F. Schäfers
Soft x-ray resonant magnetic reflectivity of Gd/TM multilayers
Journal of Magnetism and Magnetic Materials (proceedings MMM Aachen June 2001) , (2001)

H.-Ch. Mertins, F. Schäfers, A. Gaupp
Soft-X-Ray Magneto-Optical Faraday Effect on Fe and Co Films
Europhys. Lett., **55**, 125 - 131, (2001)

H.-Ch. Mertins, P.M. Oppeneer, J. Kunes, D. Abramsohn, F. Schäfers, A. Gaupp
Observation of the X-Ray Magneto-Optical Voigt Effect
Phys. Rev. Lett., **87**, 047401-1, (2001)

H.-Ch. Mertins, O. Zaharko, F. Schäfers, A. Gaupp, D. Abramsohn, M. Weiss, H.-Grimmer
Resonant Magnetic Scattering of Linearly Polarised Soft X-rays from Fe-Layers and Fe/C-Multilayers
Nucl. Instrum. Meth.A, **467-8**, 1415-1418, (2001)

H.-Ch. Mertins, F. Schäfers, A. Gaupp, W. Gudat, J. Kunes, P.M. Oppeneer
Soft X-Ray Magnetic Dichroism and Farady-Rotation Measured with Linearly Polarised Light
Nucl. Instrum. Meth.A, **467-8**, 1407-1410, (2001)

H.-Ch. Mertins, F. Schäfers, A. Gaupp, W. Gudat
Faraday-Effekt mit weicher Röntgenstrahlung
Physikalische Blatter, **57**, 53 - 55, (2001)

H.-Ch. Mertins, O. Zaharko, A. Gaupp, F. Schäfers, D. Abramsohn, H. Grimmer
Soft x-ray magneto-optical constants at the Fe 2p edge determined by Bragg scattering and Faraday effect
Journal of Magnetism and Magnetic Materials (proceedings MMM Aachen June 2001) , (2001)

A. Nefedov, H. Zabel, F. Schäfers
Sputtered V/Al2O3 multilayer x-ray mirrors for the water window
Nucl. Instr. and Meth. A, **345**, 345-348, (2001)

A.I. Nesvizhskii, A.L. Ankudinov, J.J. Rehr and K. Baberschke
Interpretation of X-ray magnetic circular dichroism and X-ray near-edge structure in Ni
Phys. Rev. B, **62**, 15295 , (2000)

A. Ney, P. Poulopoulos, F. Wilhelm, A. Scherz, M. Farle and K. Baberschke
Absolute determination of the magnetic moments of Co monolayers: A combination of UHV magnetometries
J. Magn. Magn. Mat., **226**, 1570 , (2001)

B. Niemann, P. Guttmann, D. Hambach, G. Schneider, D. Weiß, G. Schmahl
A rotating condenser and off-axis zone plate monochromator for the TXM at the undulator U41 at BESSY II
Nucl. Instrum. Meth. A, **467/8**, 857-860, (2001)

T. Noll, Th. Zeschke, G. Reichardt, H. Lammert, W. Gudat
Six-strut arrangements for cartheisan movements of mirors
Nuclear Intruments & Methods in Physics research A , **467-468** , 775-777, (2001)

B. Obst, T. Richter, M. Martins, P. Zimmermann
Photoionisation of atomic Scandium in the region of the 2p resonances
J. Phys. B, **34**, L657, (2001)

J. Okabayashi, A. Kimura, O. Rader, T. Mizokawa, A. Fujimori, T. Hayashi, M. Tanaka
Electronic structure of Ga1-xMnxAs studied by angle-resolved photoemission spectroscopy
Physica E, **10**, 192-195, (2001)

J. Okabayashi, A. Kimura, O. Rader, T. Mizokawa, A. Fujimori, T. Hayashi, M. Tanaka
Angle-resolved photoemission study of Ga1-xMnxAs
Phys. Rev. B, **64**, 125304-1--5 , (2001)

E.C. Paloura, M. Katsikini, A. Markwitz, R.W. Michelmann
An X-ray absorption study of SixNyOz films
Proceedings of the Electrochemical Society, **98-22**, 327, (1999)

C. Pampuch, O. Rader, R. Kläsges, C. Carbone
Evolution of the electronic structure in ultrathin Co, Ni, and Cu films
Phys. Rev. B, **63**, 153409-1--4 , (2001)

S. Park, T.U. Kampen, W. Braun, D.R.T. Zahn
Photoemission study of Mg/PTCDA/Se-GaAs Schottky contacts
Appl. Surf. Sci., **175/176**, 249, (2001)

S. Park, T.U. Kampen, D.R.T. Zahn, W. Braun
Energy level alignment driven by electron affinity difference at 3, 4, 9, 10 perylentetracboxylic dianhydride/n-GaAs (100) interfaces
App. Phys. Lett. , **79**, 4124, (2001)

W.B. Peatman, U. Schade
A brilliant infrared light source at BESSY
Review of Scientific Instruments, **72**, 1620-1624, (2001)

P. Petrashen, A. Erko
Graded SiGe Crystals as X-Ray Collimators
Nuclear Instruments and Methods in Physics Research , **467-468** , 358-361, (2001)

M. Peuker
High-efficiency nickel phase zone plates with 20 nm minimum outermost zone width
APL, **78**, 2208-2210, (2001)

P. Poulopoulos, K. Baberschke
Phase Transitions in Coupled Two-Dimensional Ferromagnetic Layers
Lecture Notes in Physics, Springer , **580**, 283 , (2001)

G. Prümper, O. Geßner, B. Zimmermann, J. Viefhaus, R. Hentges, H. Kleinpoppen, U. Becker
Absorption of Circularly Polarized VUV Radiation in Polarized Iron Vapor
J. Phys. B. atomic molecular and optical physics , **34** , 2707 , (2001)

G. Prümper, B. Zimmermann, N.A. Cherepkov, U. Becker, H. Kleinpoppen
Complete Photoionisation Experiments unsing polarised atoms
Complete Scattering Experiments; Plenum Press, New York, 141-154 , (2001)

G. Prümper, B. Zimmermann, B. Langer, J. Viefhaus, R. Hentges, N.A. Cherepkov, B. Schmidtke, M. Drescher, U. Heinzmann
Sudden interchannel coupling in the Tl 6p ionization above the 5d threshold
Phys. Rev. Lett. , **85**, 5074-5077 , (2000)

R. Püttner, B. Grimaud, D. Delande, M. Domke, M. Martins, A.S. Schlachter, G. Kaindl
Statistical Properties of Inter-Series Mixing in Helium: From Integrability to Chaos
Phys. Rev. Lett., **86**, 3747, (2001)

O. Rader, T. Mizokawa, A. Fujimori, A. Kimura
Structure and electron correlation of Mn on Ni(110)
Phys. Rev. B, **64**, 165414-1--5, (2001)

O. Rader, A.M. Shikin
Quantization of electronic states in a rare-earth film: Gd/W(110)
Phys. Rev. B, **64**, 201406(R)-1--4 , (2001)

G. Reichardt, J. Bahrdt, J.-S. Schmidt, W. Gudat, A. Ehresmann, R. Müller-Albrecht, H. Molter, H. Schmoranzer, M. Martins, N. Schwentner, S. Sasaki
A 10m-normal incidence monochromator at the quasi-periodic undulator U125-2 at BESSY II
Nucl. Instr. Meth. in Physics Research, **467-468**, 462, (2001)

D. Richter
Simulation of the BESSY II Vacuum System
Nuclear Instruments and Methods in Physics Research A , **470**, 18, (2001)

M. Richter, U. Johannsen, P. Kuschnerus, U. Kroth, H. Rabus, G. Ulm and L. Werner
The PTB high-accuracy spectral responsivity scale in the ultraviolet
Metrologia, **37**, 515, (2000)

M. Richter, J. Hollandt, U. Kroth, W. Paustian, H. Rabus, R. Thornagel, G. Ulm
The two normal-incidence monochromator beam lines of PTB at BESSY II
Nucl. Instrum. and Meth. A , **467-468**, 605, (2001)

M. Richter, F. Becker, K. Grützmacher, U. Kroth, H. Rabus, K. Vogler, E. Bergmann, and U. Stamm
Metrology of Laser Radiation in the DUV for Lithography
Laser Beam and Optics Characterization, Hrsg. H. Weber, H. Laabs, 301, (2000)

A. Rüdel
Elektronenspektroskopische Untersuchungen zur Photoionisationsdynamik freier Moleküle nach Anregung mit Synchrotronstrahlung , Dissertation
Wissenschaft&Technik Verlag, (2001)

F. Schäfers, M. Mertin, D. Abramsohn, H.-Ch. Mertins, N.N. Salashchenko
Cr/Sc Nanolayers for the Water Window: Improved Performances
Nucl. Instrum. Meth. A, **467-468**, 349-352, (2001)

K.-H. Schartner, B. Zimmermann, S. Kammer, S. Mickat, H. Schmoranzer, A. Ehresmann, H. Liebel, R. Follath, G. Reichardt
Radiative cascades from doubly excited He-states
Phys. Rev. A, **64**, 040501(R), (2001)

A. Scherz, F. Wilhelm, U. Bovensiepen, P. Poulopoulos, H. Wende and K. Baberschke
Separate Curie temperatures in magnetic trilayers and the effect of spin fluctuations
J. Magn. Magn. Mat., **236**, 1, (2001)

A. Scherz, F. Wilhelm, P. Poulopoulos, H. Wende and K. Baberschke
Element-specific Magnetization Curves and Crossover in Co/Cu/Ni/Cu(001) Trilayers Studied by XMCD
J. Synchrotron Rad., **8**, 472 , (2001)

E. Schierle
Der Einfluß des magnetische finite-size-Effektes auf elektronische Struktur und Gitterparameter schwerer Lanthanidmetalle: Gadolinium und Holmium , Dissertation
(2001)

N. Schmidt
Die Untersuchung des Kaskadenzerfalls von Magnesium nach Innerschalenionisation mit Hilfe der Synchrotronstrahlung , Diplomarbeit
TU-Berlin, (2001)

B. Schmidtke, T. Khalil, M. Drescher, N. Müller, N.M. Kabachnik, U. Heinzmann
The Kr M4,5N1N2,3 1P1 Auger decay: measurement of the transferred spin polarization and analysis of Auger amplitudes
J. Phys. B: At. Mol. Opt. Phys., 34, 1-18, (2001)

H. Schmoranzer, S. Lauer, H. Liebel, A. Ehresmann, Ph.V. Demekhin, B.M. Lagutin, I.D. Petrov, V.L. Sukhorukov
Manifestation of Strongly Delocalized Atomic States in the Photoionization Cross Sections of Ar, Kr, and Xe
J. Electron Spectrosc. Relat. Phenomena , **114-116**, 135, (2001)

H. Schmoranzer, H. Liebel, F. Vollweiler, R. Müller-Albrecht, A. Ehresmann, K.-H. Schartner, B. Zimmermannn
Photon-induced fluorescence spectroscopy (PIFS)
Nuc. Instrum. and Meth. in Phys. Res. A, **467-8**, 1526 - 1528, (2001)

F. Scholze, R. Thornagel, G. Ulm
Calibration of energy-dispersive X-ray detectors at BESSY I and BESSY II
Metrologia, **38**, 391, (2001)

F. Scholze, B. Beckhoff, G. Brandt, R. Fliegauf, A. Gottwald, R. Klein, B. Meyer, U. Schwarz, R. Thornagel,
J. Tümmler, K. Vogel, J. Weser, and G. Ulm
High-Accuracy EUV Metrology of PTB Using Synchrotron Radiation
Proc. of SPIE , **4344**, 402, (2001)

F. Scholze, M. Procop
Measurement of detection efficiency and response functions for an Si(Li) x-ray spectrometer in the range 0.1 - 5 keV
X-Ray Spectrom. , **30**, 69, (2001)

T. Schröder, A. Hammoudeh, M. Pykavy, M. Adelt, M. Bäumer, H.-J. Freund
Single Crystalline Silicon Dioxide Films on Mo(112)
Solid State Electronics, **45**, 1471, (2001)

C. Schüßler-Langeheine, E. Weschke, A. Yu. Grigoriev, H. Ott, A. Möller, R. Meier, Chandan Mazumdar, G. Kaindl
Magnetic effects in the band structure of ferromagnetic and antiferromagnetic lanthanide metal films
J. Electron Spectrosc. Relat. Phenom. , **114-116**, 795, (2001)

C. Schüßler-Langeheine, E. Weschke, A.Yu. Grigoriev, H. Ott, R. Meier, D.V. Vyalikh, Chandan Mazumdar,
C. Sutter, D. Abernathy, G. Grübel, G. Kaindl
Resonant magnetic x-ray scattering from ultrathin Ho-metal films down to a few atomic layers
J. Electron Spectroscop. Relat. Phenom. , **114-116**, 953, (2001)

F. Senf, F. Eggenstein, U. Flechsig, R. Follath, S. Hartlaub, H. Lammert, T. Noll, J.S. Schmidt, O. Schwarzkopf,
G. Riechardt, M. Weiss, T. Zeschke, and W. Gudat
Set-up and Performance of the first undulator beamline U49-1-SGM at BESSY II
Nuclear Intruments & Methods in Physics research A , **467-468** , 474-478, (2001)

F. Senf, F. Eggenstein, U. Flechsig, R. Follath, S. Hartlaub, H. Lammert, T. Noll, J.S. Schmidt, G. Reichardt,
O. Schwarzkopf, M. Weiss, T. Zeschke, W. Gudat
Performance of the first undulator beamline U49-1-SGM at BESSY II
Nucl. Instrum. and Methods , **467**, 474-478 , (2001)

V. Senz
Größeneffekte magnetischer Strukturen: Eisen-Inseln und -Cluster , Dissertation
Universität Rostock, (2001)

N. Sieber, Th. Seyller, R. Graupner, L. Ley, R. Mikalo, P. Hoffmann, D.R. Batchelor, D. Schmeißer
PES and LEED Study of Hydrogen and Oxygen terminated 6H-SiC(0001) and (000-1) Surfaces
Appl. Surf. Sci. , **184**, 280, (2001)

N. Sieber, T. Seyller, B.F. Mantel, J. Ristein, L. Ley
Preparation and characterization of hydrogen terminated 6H-SiC
Mater. Sci. Forum , **353-356** , 223, (2001)

N. Sieber, B.F. Mantel, T. Seyller, J. Ristein, L. Ley, T. Heller, D.R. Batchelor, D. Schmeisser
Electronic and chemical passivation of hexagonal 6H-SiC surfaces by hydrogen termination
Applied Physics Letters , **78**, 1216, (2001)

N. Sieber, Th. Seyller, L. Ley, M. Polcik, D. James, J.D. Riley, R.G.C. Leckey
A high resolution photoemission study of hydrogen terminated 6H-SiC surfaces
Mater. Sci. Forum, in print, (2001)

N. Sieber, Th. Seyller, R. Graupner, L. Ley, R. Mikalo, P. Hoffmann, D. Batchelor, D. Schmeißer
Wetchemical preparation of silicate adlayer terminated SiC(0001) surfaces studied by PES and LEED
Mater. Sci. Forum, in print, (2001)

G. Snell, M. Martins, E. Kukk, W.-T. Cheng, N. Berrah
High Resolution Electron Spectroscopy of a Strongly Correlated System: Atomic Barium
Phys. Rev. A, **63**, 062715, (2001)

C. Streli, P. Wobrauschek, B. Beckhoff, G. Ulm, L. Fabry and S. Pahlke
First results of TXRF measurements of low-Z elements in Si wafer surfaces at the PTB plane grating monochromator beamline for undulator radiation at BESSY II
X-Ray Spectrom., **30**, 24, (2001)

B. Tepper
Elektronenspektroskopische Untersuchungen an Vanadiumoxidoberflächen , Dissertation
(2001)

R. Thornagel, R. Klein, G. Ulm
The electron storage ring BESSY II as a primary source standard from the visible to the x-ray range
Metrologia, **38**, 385, (2001)

K. Tiedtke, Ch. Gerth, M. Martins, P. Zimmermann
Term-dependent lifetime broadening in the 3p photoelectron spectra of atomic Fe and Co
Phys. Rev. A, **64**, 022705, (2001)

S. Vandre, C. Preinesberger, W. Busse, and M. Dähne
Conservation of flat-band conditions for DySi2 monolayers on n-type Si(111)
Applied Physics Letters , **78**, 2012, (2001)

S. Vogt, M. Jäger, G. Schneider, E. Schulze, H. Saumweber, D. Rudolph, G. Schmahl
Visualizing specific nuclear proteins in eukaryotic cells using soft X-ray microscopy
Nucl. Instrum. Meth. A, **467/8**, 1312-1314, (2001)

S. Vogt
Investigations of Immunolabelled Structures in the Cell Nucleus by X-Ray and Light Microscopy , Dissertation
Institut für Röntgenphysik, Universität Göttingen, (2001)

M.R. Weiss, R. Follath, K.J.S. Sahawney, F. Senf, J. Bahrdt, W. Frentrup, A. Gaupp, S. Sasaki, M. Scheer, H.-Ch. Mertins, D. Abramsohn, F. Schäfers, W. Kuch, W. Mahler
The Elliptically Polarised Undulator Beamlines at BESSY II
Nucl. Instrum. Meth. A, **467-8**, 449-452, (2001)

M.R. Weiss, R. Follath, K.J.S. Sawhney, T. Zeschke
Absolute energy calibration for plane grating monochromators
Nucl. Instrum. and Methods , **467**, 482-484 , (2001)

D. Weiß, G. Schneider, S. Vogt, P. Guttmann, B. Niemann, D. Rudolph, G. Schmahl
Tomographic imaging of biological specimens with the cryo transmission X-ray microscope\",
Nucl. Instrum. Meth. A, **467/8**, 1308-1311, (2001)

H. Wende, F. Wilhelm, P. Poulopoulos, K. Baberschke, J.W. Freeland, Y.U. Idzerda, A. Rogalev, D.L. Schlagel, T.A. Lograsso and D. Arvanitis
On the Temperature Dependence of Multiple- and Single-Scattering Contributions in Magnetic EXAFS
in "Theory and computation for synchrotron radiation spectroscopy" AIP Proceedings , **514**, 140, (2000)

Ph. Wernet, B. Sonntag, M. Martins, P. Glatzel, B. Obst, P. Zimmermann
Multiplet splitting and valence shell recoupling in the core-level 2p photoelectron spectrum of atomic Mn and of Mn comp
Phys. Rev. A, **63**, R050702, (2001)

Ph. Wernet, J. Schulz, B. Sonntag, K. Godehusen, P. Zimmermann, A.N. Grum-Grzhimailo, N.M. Kabachnik, and M. Martins
2p photoelectron spectra and linear alignment dichroism of atomic Cr
Phys. Rev. A, **64**, 042707, (2001)

E. Weschke, G. Kaindl
Magnetic exchange splitting in lanthanide metals
J. Phys.: Condens. Matter , **13**, 11133, (2001)

C. Westphal, S. Dreiner, M. Schürmann, F. Senf, H. Zacharias
The role of the Si-suboxide structure at the interface: an angle-scanned photoelectron diffraction study
THIN SOLID FILMS , **400**, 101-105 , (2001)

U. Wiesemann, J. Thieme, R. Früke, P. Guttmann, B. Niemann, D. Rudolph, G. Schmahl
Construction of a scnanning transmission X-ray microscope at the undulator U41 at BESSY II
Nucl. Instrum. Meth. A, **467/8**, 861-863, (2001)

F. Wilhelm, U. Bovensiepen, A. Scherz, P. Poulopoulos, A. Ney, H. Wende, G. Ceballos and K. Baberschke
Manipulation of the Curie temperature and the magnetic moments of ultrathin Ni and Co films by Cu-capping
J. Magn. Magn. Mat. , **222**, 163 , (2000)

F. Wilhelm
Magnetic Properties of Ultrathin Films, Coupled Trilayers and 3d/5d Multilayers Studied by X-ray Magnetic Circular Dichroism , Dissertation
Dissertation.de-Verlag im Internet GmbH, Berlin (2000), ISBN 3-89825-177-2, (2000)

K. Wilhelm, U. Schühle, W. Curdt, I.E. Dammasch, J. Hollandt, P. Lemaire and M.C.E. Huber
Solar spectroradiometry with the telescope and spectrograph SUMER on the Solar and Heliosperic Observatory SOHO
Metrologia, **37**, 393, (2000)

O. Zaharko, A. Cervellino, H.-Ch. Mertins, H. Grimmer, F. Schäfers, D. Arvanitis
Soft X-Ray Magnetic Circular Dichroism in Fe and Fe0.5Co0.48V0.02 Films: quantitative Analysis of Transmission
Eur. Phys. J. B, **23**, 441 - 448, (2001)

O. Zaharko, H. Grimmer, H.-Ch. Mertins, F. Schäfers
Resonant X-ray Magnetic Scattering from an Fe-Film and Fe/C-Multilayers
Nucl. Instrum. Meth. A, **467-8**, 1419 - 1422, (2001)

O. Zaharko, H.-Ch. Mertins, H. Grimmer, F. Schäfers
Soft X-ray resonant magnetic scattering from Fe/C multilayers
Nucl. Instr. and Meth. A, **467-468**, 1419-1422, (2001)

Keyword Index

(click on page number to open selected page)

Authors Index
(click on page number to open selected page)